

Contents lists available at ScienceDirect

Environmental Technology & Innovation

journal homepage: www.elsevier.com/locate/eti



Investigating and correlating the photocatalytic activity of synthesised strontium titanate nanopowder with calcination temperature

Zhengisbek Kuspanov^{a,b}, Aigerim Serik^{a,b,*}, Alisher Tattibay^{b,c}, Aibol Baratov^{a,b}, Ulzhan Abdikarimova^{a,b}, Madina Bissenova^{a,b}, Mukhtar Yeleyov^{a,b,d}, Sayabek Sakhiyev^b, Chingis Daulbayev^{a,b}

ARTICLE INFO

 $\label{eq:Keywords:Photocatalysis} Factor of the Strio of the Strio$

ABSTRACT

In this study, SrTiO3 nanoparticles were synthesised in high yield using a simple and low-cost method, followed by calcination. The effect of the calcination temperature in the range from 700 to 1100 °C on the morphology, phase structure, crystallite size, and photocatalytic activity of SrTiO₃ nanoparticles was investigated. Analysis of the morphology and structure of the synthesised samples revealed an increase in the average particle size from 70.4 to 361.72 nm as well as crystallite growth with increasing calcination temperature (from 800 to 1100 $^{\circ}$ C), likely due to the fusion of smaller crystallites into larger ones. A possible pathway for the growth mechanism of strontium titanate grains was also proposed. The SrTiO3 sample calcined at 800 °C exhibited the highest methylene blue (MB) photodegradation efficiency, achieving 100 % degradation within 30 min of irradiation. The pseudo-first-order reaction rate constant k for this sample was determined to be 0.156 min⁻¹, which is almost 1.8 and 14.19 times higher compared to those of commercial P25 and SrTiO3, respectively. The analysis indicated that the high photoactivity of this sample was due to its high crystallinity, relatively small particle size, and optimal light absorption, which enhanced the separation and transport of the photogenerated charges and increased the number of active sites, thereby positively affecting the photocatalytic properties. Additionally, the effects of the initial dye concentration and amount of photocatalyst loaded on the photodegradation efficiency were investigated.

1. Introduction

Since Domen's pioneering work in 1980, which highlighted the promising use of strontium titanate (SrTiO₃) as a photocatalyst, it has been extensively studied for its potential to decompose water into hydrogen (Kudo et al., 2023). Recently, the application of SrTiO₃ in a photocatalytic panel reaction system with a total area of 100 m^2 was reported (Nishiyama et al., 2021). Notably, Al-doped SrTiO₃

https://doi.org/10.1016/j.eti.2024.103852

^a Satbayev University, Almaty, Kazakhstan

^b Institute of Nuclear Physics, Almaty, Kazakhstan

^c Al-Farabi Kazakh National University, Almaty, Kazakhstan

d Bes Saiman Group, Almaty, Kazakhstan

^{*} Corresponding author at: Satbayev University, Almaty, Kazakhstan. E-mail address: aigerim.serik3508@gmail.com (A. Serik).

exhibited a quantum efficiency exceeding 90 % in the near-UV region when selectively loaded with hydrogen- and oxygen-evolution cocatalysts (Takata et al., 2020). Despite the significant potential of SrTiO₃, its commercial application in photocatalysis has been hindered by the high recombination rate of photogenerated electron-hole pairs on its surface or within its lattice (Kuspanov et al., 2023b). Nonetheless, enhancing the photocatalytic activity of SrTiO₃ remains a critical challenge in heterogeneous photocatalysis. In recent years, various methods have been employed to address this issue, including defect engineering, morphology optimisation, co-catalyst deposition, and the creation of composite semiconductors (Daulbayev et al., 2021; Oin et al., 2021; Sultanov et al., 2020; Vijay and Vaidya, 2021; Wang et al., 2021). However, these studies mainly utilised commercial SrTiO₃ powder, highlighting the need for a detailed investigation of synthetic methods and their parameters, as these critically affect the chemical and physical properties of SrTiO₃. Typically, SrTiO₃ nanoparticles are synthesised using hydrothermal/solvothermal (Kobayashi et al., 2018; Ramos-Sanchez et al., 2020), solid-state (Youssef et al., 2018), sol-gel (Deshmukh et al., 2021), and other methods (Aravinthkumar et al., 2022). Each method has its own advantages and limitations. Chemical synthesis methods generate more homogeneous and finely dispersed powders at low temperatures but require long reaction times, high equipment standards, and typically yield small quantities of product (Ma et al., 2019). The solid-state method is characterised by simplicity, low cost, and mass production capability; however, it requires high synthesis temperatures, which can lead to the presence of undesirable impurities and coarse grain textures (Youssef et al., 2018). Furthermore, it has been reported that the crystallite sizes vary with the calcination temperature, which directly correlates with the photocatalytic activity of the synthesised photocatalyts (Ma et al., 2019). Therefore, the development of a simple method for synthesising high-purity and homogeneous SrTiO₃ nanoparticles that enables mass production at low temperatures is an urgent priority.

In this study, $SrTiO_3$ nanoparticles were synthesised in high yield using a simple and cost-effective method followed by calcination. The effect of the calcination temperature on the morphology of the nanoparticles and their photocatalytic activity towards the degradation of methylene blue dye was investigated. The synthesised samples were characterised using X-ray diffraction (XRD), scanning electron microscopy (SEM), transmission electron microscopy (TEM), and high-resolution X-ray photoelectron spectroscopy (XPS) to determine their morphologies and crystal structures.

2. Materials and methods

2.1. Materials

All reagents and chemicals, including titanium dioxide (TiO₂, < 25 nm, 99.7 %, Sigma–Aldrich, USA), strontium nitrate (Sr(NO₃)₂, \geq 98 %, Sigma–Aldrich, USA), oxalic acid ((COOH)₂·2 H₂O, > 98 %, Laborpharma, Kazakhstan), strontium titanate (SrTiO₃, Sigma–Aldrich, USA, \geq 99 %), strontium titanate (SrTiO₃, Amazon, USA, 99.95 %, 100 nm), methylene blue (C₁₆H₁₈ClN₃S·xH₂O, dye content \geq 82 %, Sigma–Aldrich, CIIIA), and nitric acid (HNO₃, < 90 %, Sigma–Aldrich, USA), were of analytical grade and used without any additional purification. Double-distilled deionised water was used for the synthesis of the photocatalysts and photocatalytic degradation experiments.

2.2. Synthesis of SrTiO3

SrTiO $_3$ nanoparticles were synthesised using a simple and economical chemical precipitation method (Kudaibergen et al., 2023; Serik et al., 2024). For this purpose, a 0.12 M aq. solution of Sr(NO $_3$) $_2$ and TiO $_2$ with a 1:1 Sr/Ti molar ratio was mixed in distilled water and subjected to ultrasonic treatment for 30 min. As a reducing agent, a 0.4 M solution of (COOH) $_2$ ·2 H $_2$ O was added dropwise to the previous suspension under vigorous stirring. The pH of the suspension was adjusted to 6–7 by adding 30 % ammonium solution. The resulting white precipitate was washed five times by centrifugation and dried for 16 h at 60 °C. The product was then calcined at 700, 800, 900, 1000, and 1100 °C for 60 min in a muffle furnace under an air atmosphere. The obtained samples were designated as STO-700, STO-800, STO-900, STO-1000, and STO-1100. Commercial SrTiO $_3$ purchased from Sigma-Aldrich (STO-com, Sigma) and Amazon (STO-com, Amazon) were used for comparison. After calcination, the synthesised samples were incubated for 30 min in a 1 M HNO $_3$ solution to remove remaining impurities, such as SrCO $_3$, then washed with distilled water several times and dried for 16 h at 60 °C.

2.3. Photocatalytic reaction

The photocatalytic activities of the synthesised $SrTiO_3$ samples were evaluated based on the photodegradation of MB in an aqueous solution within a specialised photochemical reactor (Shanghai Leewen Scientific Instrument Co., Ltd., China) at room temperature. A 10-watt high-pressure mercury lamp ($\lambda_{max}=254$ nm) served as a UV light source, and a cut-off filter ($\lambda \geq 400$ nm) was utilised to obtain visible light. The experimental setup involved preparing a suspension by adding 20 mg of the photocatalyst to 50 mL of an MB solution at a concentration of 10 mg/L (ppm) positioned 10 cm away from the irradiation source. To ensure the establishment of an adsorption-desorption equilibrium on the catalyst surface, the solution was stirred for 30 min in the dark before irradiation. The experiments were conducted at a neutral pH of 7 for the MB solution. During irradiation, the suspension was continuously stirred for 60 min using a magnetic stirrer. At 15-min intervals, 0.7 mL of the reaction mixture was sampled, and the photocatalyst was separated using a syringe filter with a pore size of 2.5 μ m. Selected aliquots were analysed using a UV-Vis spectrophotometer (I5 Hanon Advanced Technology Group Co., Ltd.). Each measurement was performed in duplicate, and the mean values with standard deviations were considered. The photocatalytic degradation efficiency was calculated using the following Eq. (1):

Degradation efficiency(%) =
$$\frac{C_0 - C_t}{C_0} \times 100\%$$
, (1)

where % is the photocatalytic degradation percentage, C_0 is the initial absorbance of the MB solution, and C_t is the final absorbance after illumination.

2.4. Characterisation

To characterise the morphology and elemental composition of the obtained samples, a scanning electron microscope (SEM) (Zeiss Crossbeam 540, Germany) with an accelerating voltage of 5–20 kV, equipped with an energy-dispersive X-ray spectrometer (EDX) (INCA X-Sight, Oxford Instruments), was used. A high-resolution TEM (JEM-2100 LaB6 HRTEM, JEOL, Japan) operated at 80 kV was used to define the morphology of the samples. To investigate the structure of the synthesised samples, XRD patterns were obtained using a Drone-8 setup with detection unit rotation angles ranging from 5 to 70° in 0.01° steps, with an allowable deviation of $\pm 0.015^{\circ}$. The XPS spectra for analysing the valence states and elemental structure of SrTiO₃ were obtained using a VG Microtech Multilab 3000 instrument with Mg and Al as the X-ray sources. The binding energies were calibrated using the C1s peak (284.8 eV) as a reference. A Perkin Elmer Lambda 35 spectrophotometer in the 200–800 nm range was used to obtain ultraviolet reflectance spectra (UV-Vis DRS).

3. Results and discussion

3.1. Characterisation of the obtained samples

The morphological features of photocatalytic materials play a crucial role in photochemical processes, and controlling their grain size is an effective method for enhancing the photocatalytic properties. The morphology and elemental composition of the synthesised SrTiO₃ were investigated using SEM, TEM, and EDX to determine their evolution with temperatures ranging from 800 to 1100 °C. As shown in Fig. 1a-d, the SEM micrographs reveal large agglomerations of cube-like particles. The particle size of each sample was analyzed using ImageJ software, and the particle size distribution histograms are shown in Fig. 2(a)-(d). A log-normal fit was applied to each histogram, from which the mean particle size and the distribution width δ were determined. Compared to the SrTiO₃ particles calcined at 800 °C, those calcined at 1100 °C exhibited more sintering and increased size. The particle sizes of the STO-1100 sample ranged from 100 to 600 nm, with an average size of 361.72 nm. In contrast, the particles of the STO-800 sample were distributed between 25 and 150 nm, with an average size of 70.4 nm. High-resolution TEM images confirm that the average nanoparticle size of the STO-800 sample is 41 nm. Elemental analysis of the STO-800 sample using EDX (Fig. 3b) confirmed the presence of Sr (43.7 %), Ti (27.2 %), and O (29.1 %). Generally, an increase in particle size with increasing calcination temperatures may be attributed to crystallite growth and particle fusion. As the energy available to the atoms in the material increases at higher calcination temperatures, atomic diffusion and recrystallisation are promoted, leading to crystallite growth and an increase in particle size (Ma et al., 2019).

The XRD patterns of the obtained samples were studied in detail to analyse their crystal structures and crystallite sizes. Fig. 3(a) shows the XRD patterns of $SrTiO_3$ synthesised at different temperatures. These XRD patterns are consistent with the ICDD database #860178 for $SrTiO_3$, confirming the successful synthesis of the material. The peaks marked with (\blacksquare) correspond to $SrCO_3$ according to the JCPDS database #71–239. Despite the successful formation of the $SrTiO_3$ phase, some $SrCO_3$ impurities remained, indicating incomplete carbonate decomposition at these sintering temperatures. Other studies also indicated that the formation of the $SrCO_3$ impurity is inevitable during the preparation of $SrTiO_3$ using various methods described in the literature (Aktaş and Ay, 2022; Ma et al., 2019; Rocha-Rangel et al., 2020; Roy and Bera, 2005). $SrCO_3$ remains as an intermediate product during the synthesis of $SrTiO_3$

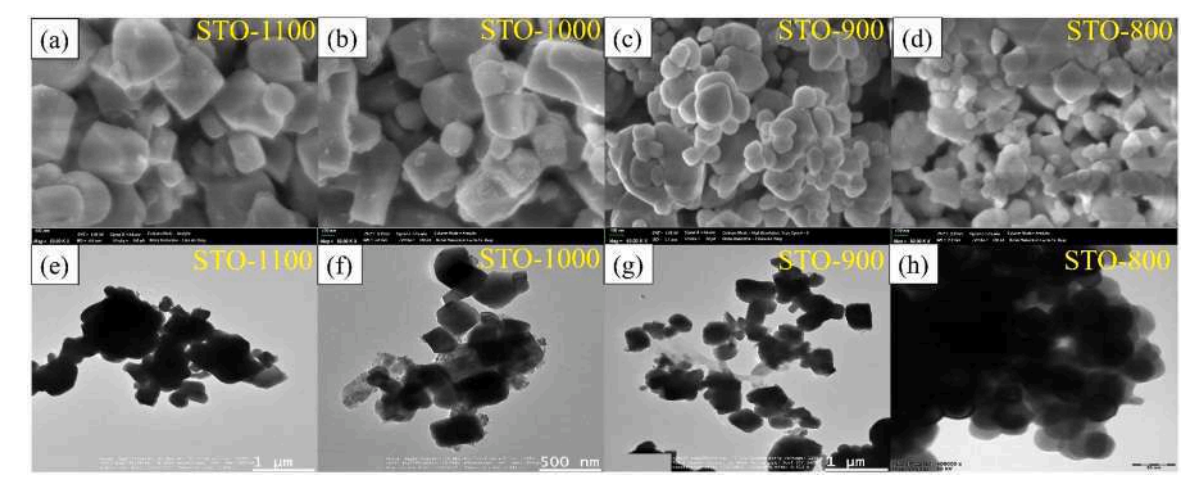


Fig. 1. (a-d) SEM and (e-h) TEM images of the obtained samples.

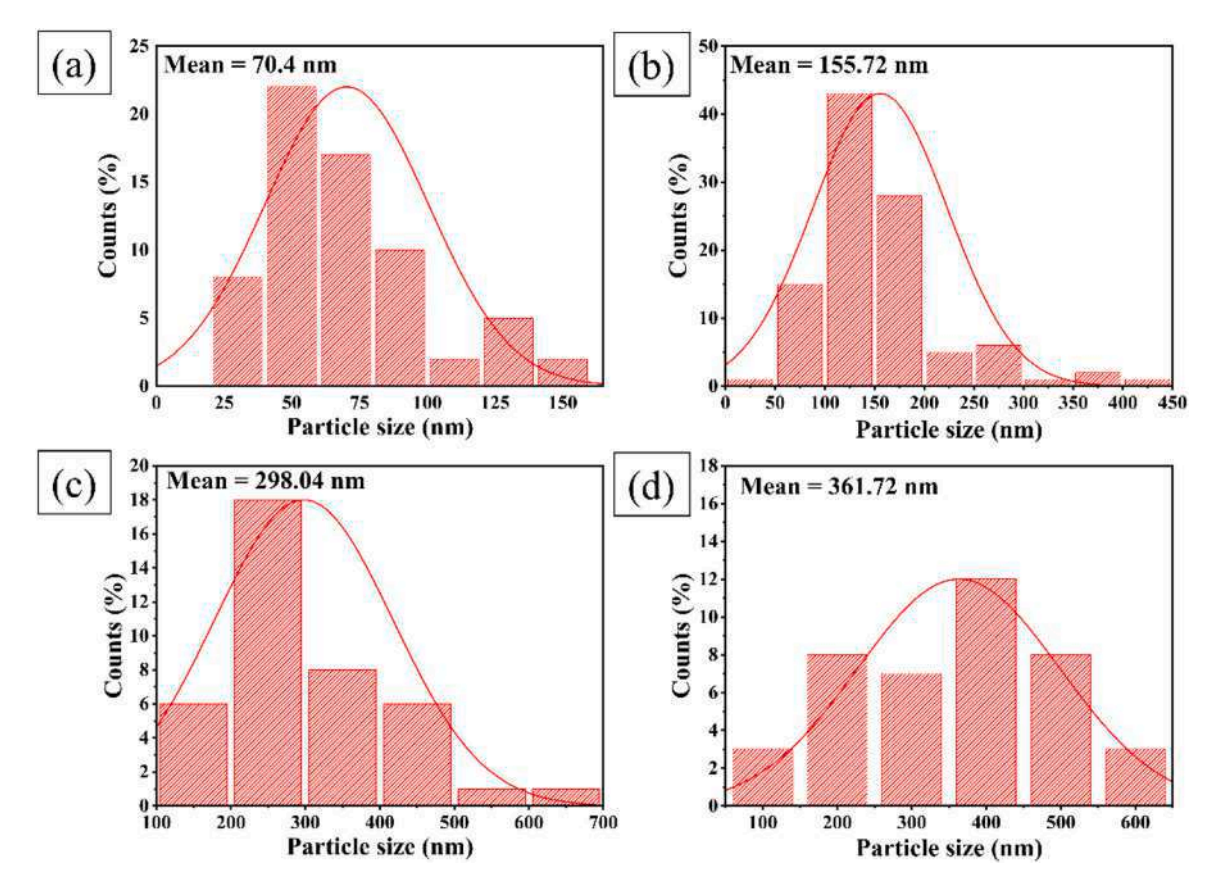


Fig. 2. Histogram illustrating the particle size distribution corresponding to SEM images of STO after calcination at (a) 800 $^{\circ}$ C, (b) 900 $^{\circ}$ C, (c) 1000 $^{\circ}$ C, and (d) 1100 $^{\circ}$ C.

and acts as a contaminant after its formation (Kiran et al., 2022).

The intensity of the $SrTiO_3$ peaks increased at temperatures of 1000 and 1100 °C, indicating an increase in the crystallinity of the material and grain growth. The obtained X-ray diffraction patterns were in good agreement with the $SrTiO_3$ data presented elsewhere (Jiang et al., 2020; Kiran et al., 2022).

To calculate the crystallite sizes, the reflections with the highest intensities along the (110), (111), and (200) directions were chosen. The average sizes of SrTiO₃ crystallites were determined using the Debye-Scherrer formula (2):

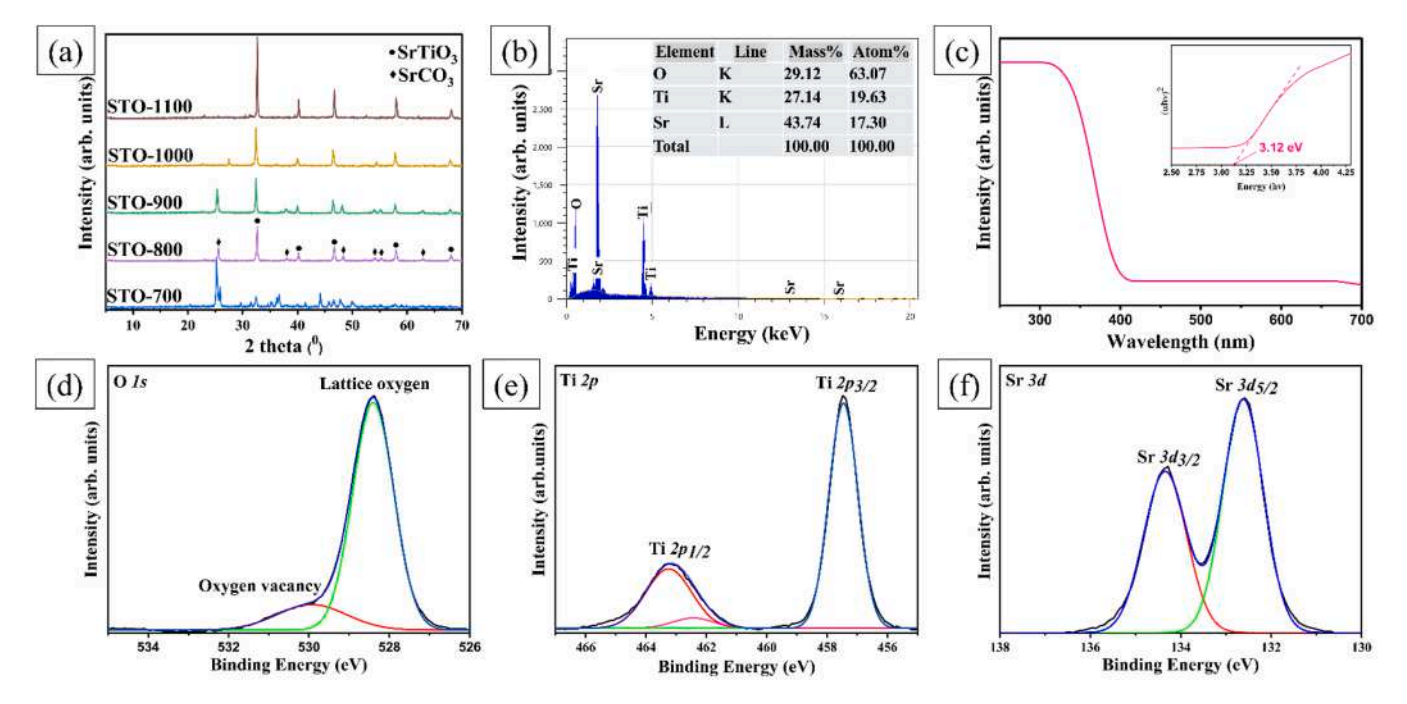
$$d = \frac{k\lambda}{\beta \cos \theta},\tag{2}$$

where K is the crystallite shape factor, λ is the X-ray wavelength (1.5406 nm for Cu K α), β is the width of the diffraction peak, and θ is the Bragg angle.

Calculations showed that the crystallite size increased from 26.89 to 32.25 nm with increasing sintering temperatures. In smaller particles, both surface electrons and holes, as well as those migrating from the interior, have a shorter diffusion distance to the active sites on the catalyst surface. This facilitates quicker participation in photocatalytic reactions, reducing the likelihood of recombination and enhancing relatively overall photocatalytic efficiency. Surface electrons and holes play a critical role by directly engaging in oxidation and reduction processes, contributing significantly to the reaction dynamics and overall performance of the photocatalyst (Agustina et al., 2023; Bakbolat et al., 2020).

The table illustrates the relationship among the calcination temperature, crystallite size, and FWHM of the synthesised $SrTiO_3$. As the calcination temperature increases, FWHM values decrease, indicating crystallite growth and a reduction in crystal defects. For instance, the FWHM for the (110) plane decreases from 0.32567 for STO-800-0.26543 for STO-1000, with a slight increase to 0.28383 for STO-1100. A similar trend is observed for the (111) and (200) planes. Grain size increases from 26.89 nm for STO-800-32.25 nm for STO-1100, suggesting particle sintering and crystal growth due to enhanced atomic mobility at higher temperatures. The most significant increase in grain size occurs between STO-1000 and STO-1100, corresponding to a sharp reduction in STO-11000 plane, possibly due to particle agglomeration and larger grain formation.

Based on the morphological and structural analyses as well as a comprehensive review of the literature, we proposed a mechanism for the growth of strontium titanate grains (Roy and Bera, 2005), which can be outlined as follows.



ū

Fig. 3. (a) XRD patterns of the obtained samples, (b) EDX, (c) UV-Vis DRS and (d-f) high-resolution XPS spectra for the STO-800 sample.

- 1. Uniform Chemical Deposition: The synthesis of $SrTiO_3$ begins by dissolving strontium nitrate ($Sr(NO_3)_2$) in a solution, followed by the addition of titanium dioxide (TiO_2) to achieve a 1:1 molar ratio of strontium to titanium. Oxalic acid is then added dropwise while stirring vigorously, and the pH is adjusted to 6–7 using an ammonia solution. As the reaction proceeds, strontium oxalate forms and deposits uniformly on the surface of the TiO_2 particles through heterogeneous nucleation, where TiO_2 acts as a substrate for grain formation. This controlled deposition is crucial for the subsequent growth and crystallization of $SrTiO_3$ nanoparticles, leading to uniform particle formation.
- 2. Calcination and Interaction: During the calcination process, strontium oxalate (SrC₂O₄·6H₂O) on the surface interacts with the inner layer of TiO₂, leading to the formation of SrTiO₃. This process comprises three sequential reaction steps.
- Dehydration of Strontium Oxalate:

Strontium oxalate dihydrate is dehydrated to form strontium oxalate:

$$SrC_2O_4 \cdot xH_2O + TiO_2 \rightarrow SrC_2O_4 + TiO_2 + xH_2O.$$
 (3)

This reaction occurs at temperatures ranging from 150 to 350 °C.

• Decomposition of Strontium Oxalate:

Strontium oxalate decomposes to form SrCO₃ at temperatures between 400 and 600 °C:

$$SrC_2O_4 + TiO_2 \rightarrow SrCO_3 + CO + TiO_2$$
. (4)

Carbon monoxide then reacts with oxygen to form carbon dioxide (CO2):

$$CO + O_2 \rightarrow CO_2$$
. (5)

Formation of SrTiO₃:

At temperatures of 800-1100 °C, strontium carbonate decomposes and reacts with titanium dioxide to form SrTiO3:

$$SrCO_3 + TiO_2 \rightarrow SrTiO_3 + CO_2$$
 (6)

This scheme outlines in detail the steps involved in the formation and growth of strontium titanate grains during calcination.

Thus, at the calcination temperature of 800 °C, smaller strontium titanate nanoparticles began to form. Increasing the temperature further enhanced the agglomeration of these nanoparticles, leading to the gradual growth of larger SrTiO particles owing to the forces acting at the grain boundaries. This growth process was characterised by Ostwald ripening, wherein smaller grains dissolve and reprecipitate into larger grains, thereby contributing to their growth (Bera and Sarkar, 2003; Roy and Bera, 2005). As the particle size increased, the surface energy of the system decreased, resulting in particle dispersion (Youssef et al., 2018).

XPS was employed to investigate the valence states and chemical composition of SrTiO₃ calcined at 800 °C. The XPS spectra, as shown in Fig. 3(d-f), confirm the presence of the elements Sr, Ti, and O in the SrTiO₃ composition. Fig. 3(d) displays the high-resolution XPS spectrum of O 1 s. The Gaussian-fitted peaks at binding energies of 528.4 and 530.0 eV corresponded to the lattice oxygen and surface-adsorbed oxygen, respectively. This finding was consistent with those of previous studies (Li et al., 2023; Niu et al., 2022; Ruan

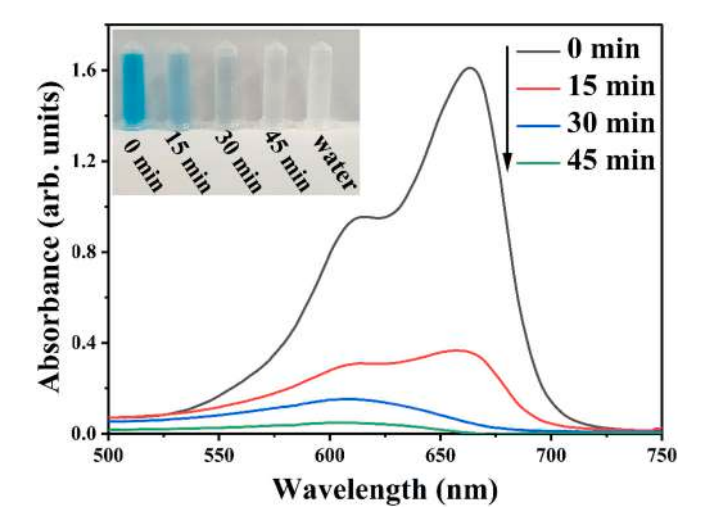


Fig. 4. UV-Vis analysis of the photodegradation processes of MB facilitated by the STO-800 sample under UV light irradiation, with the inset showing the colour change over time.

et al., 2023). The high-resolution XPS spectrum of Ti 2p, as shown in Fig. 3(e), reveals binding energies of 457.4 and 463.2 eV, which could be attributed to the Ti $2p_3/2$ and Ti $2p_1/2$ spin-orbitals, respectively (Ruan et al., 2023). These values are indicative of Ti⁴⁺ valence states (Li et al., 2023). Additionally, the presence of a peak at 462.4 eV suggested a minor amount of Ti³⁺ ions, typically formed during high-temperature processing (Zhao et al., 2019). The XPS spectra of Sr 3d, as shown in Fig. 3(f), exhibit binding energies of 132.3 and 135.2 eV, corresponding to Sr $3d_5/2$ and Sr $3d_3/2$ bonds, respectively. These values were associated with Sr²⁺ valence states (Ruan et al., 2023). Overall, the XPS results confirmed the successful synthesis of SrTiO₃ through calcination at 800 °C.

A key factor influencing the photocatalytic efficiency of photocatalysts is their light absorption capability. Fig. 3(c) presents the UV-Vis DRS for the $SrTiO_3$ sample calcined at 800 °C. The absorption edge of the STO-800 sample can be observed at approximately 400 nm, which corresponds to a bandgap energy of 3.12 eV. This value is notably aligned with and higher to the band gap energies reported for both commercial and other synthesised $SrTiO_3$ materials (Ham et al., 2016; Xiao et al., 2020), respectively.

3.2. Photocatalytic performance

The photocatalytic performance of $SrTiO_3$ nanoparticles, calcined at various temperatures, was evaluated through the degradation of MB at a concentration of 10 ppm under UV and visible light irradiation at room temperature. For comparison, commercial samples of $SrTiO_3$ (from Sigma and Amazon) and TiO_2 (P25) were also tested. The results depicted in Fig. 4 are based on changes in the intensity of the MB absorption peak at 664 nm following irradiation. The reduction in the peak intensity and MB concentration, as shown in Fig. 4, signified the effective decomposition of MB.

Fig. 5(a and b) illustrate the percentages of MB degradation over time under UV and visible light irradiation, respectively. It is evident that the calcination temperature significantly influenced the photocatalytic activity of SrTiO₃ to promote MB dye degradation. Specifically, the adsorption efficiencies of SrTiO₃ calcined at 800, 900, 1000, and 1100 °C were approximately 21.9, 14.9, 9.2, and 7.7 %, respectively. These findings correlated well with the results from electron microscopy and XRD analyses, which revealed a decrease in particle size and crystallite dimensions with decreasing calcination temperatures from 1100 to 800 °C. The reduction in particle size enhances the specific surface area of photocatalysts, positively affecting their adsorption capabilities (Ismael, 2021; Paul et al., 2019). Additionally, the increased surface area resulted in a higher number of active centres available for photocatalytic reactions.

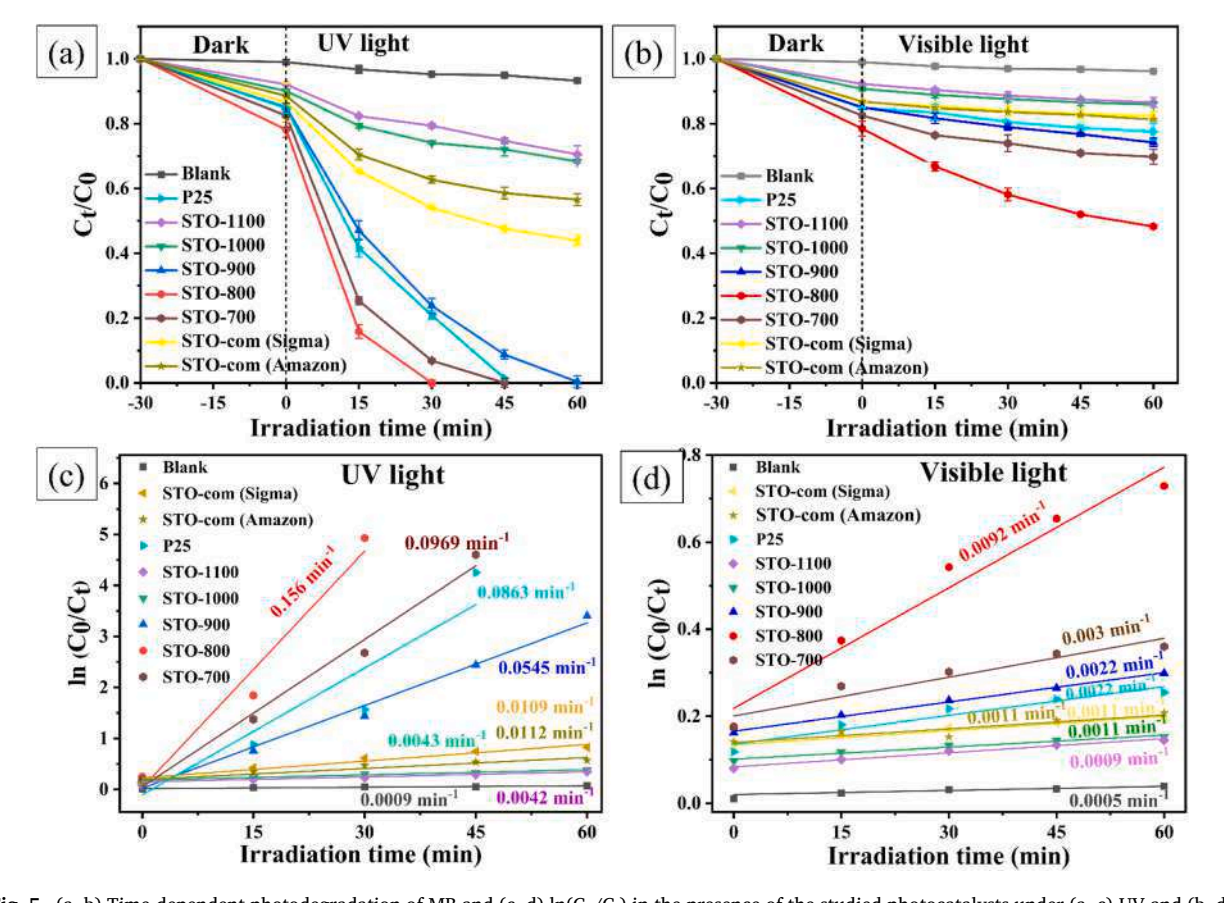


Fig. 5. (a, b) Time-dependent photodegradation of MB and (c, d) $ln(C_0/C_t)$ in the presence of the studied photocatalysts under (a, c) UV and (b, d) visible light irradiation.

The photocatalytic activity of SrTiO3 was observed to increase with the calcination temperature increasing from 700 to 800 °C but declined when the temperature was further raised to 900, 1000, and 1100 °C. The sample calcined at 800 °C exhibited the highest efficiency for methylene blue (MB) photodegradation, achieving 100 % degradation within 30 min of UV light exposure. In comparison, commercial P25 reached 100 % dye degradation in 45 min, while commercial SrTiO3 samples (Sigma and Amazon) demonstrated lower efficiencies of 56.1 and 43.5 % after 60 min. Under visible light irradiation, the photocatalytic efficiency decreased in the following order: STO-800 (51.7 %) > STO-700 (30.2 %) > STO-900 (25.8 %) > P25 (22.4 %) > STO-com (Sigma) (17.5 %) > STO-com (Amazon) (18.7 %) > STO-1000 (14.1 %) > STO-1100 (13.5 %). The results indicated that the STO-800 sample exhibited the highest photocatalytic activity in both UV and visible light spectra. This suggests that optimising the calcination temperature significantly enhanced the photocatalytic performance, whereas excessively high temperatures led to decreased activity. This reduction in activity was attributed to an increased particle size and the formation of large agglomerates, which hindered efficient light absorption and the generation of electron-hole pairs. Moreover, larger particle sizes exacerbate the recombination of photogenerated charges because the charges fail to efficiently migrate to the photocatalyst surface, thereby reducing the overall photocatalytic efficiency (Ismael, 2021).

To determine the rate kinetics of methylene blue (MB) photocatalytic degradation, the pseudo-first-order rate model was employed, as expressed by Eq. (7):

$$-\ln\left(\frac{c_t}{c_0}\right) = k_p t,\tag{7}$$

where C_0 and C_t (mg/L) are the initial concentrations and at time t, respectively, and k_p is the rate constant of the reaction.

Fig. 5(c,d) illustrates the relationships between $-\ln(C_t/C_0)$ and time t for the photodegradation of MB under UV (Fig. 5(c)) and visible (Fig. 5(d)) light irradiation, along with the calculated pseudo-first-order rate constants for the respective photocatalysts. The highest reaction rate constant k for MB photocatalytic degradation under UV light irradiation was observed for the STO-800 sample, with a value of 0.156 min⁻¹. This rate was approximately 1.6, 1.8, 2.86, 13.9, 14.19, 36.3, and 37.1 times greater than those of STO-700, P25, STO-900, STO-com (Amazon), STO-com (Sigma), STO-1100, and STO-1000, respectively. Under visible light irradiation, the STO-800 sample also demonstrated the highest reaction rate constant k of 0.0092 min⁻¹, significantly surpassing the performance of all other photocatalysts examined (Fig. 5(d)).

In this study, the impact of the photocatalyst mass loading and initial dye concentration on the photocatalytic degradation efficiency of MB using the STO-800 sample was evaluated under UV irradiation. Fig. 5(e) shows the MB (10 ppm) degradation efficiency after 30 min of irradiation at photocatalyst loading of 10, 20, and 30 mg. The results indicated that the MB degradation efficiency increased with the photocatalyst mass, achieving a maximum efficiency at 30 mg, where complete dye removal occurred within 20 min. This enhancement was attributed to the increased number of active sites on the photocatalyst surface, which facilitated the absorption of more photons, thereby improving the efficiency of the photocatalytic process (Singh et al., 2022).

Fig. 5(f) illustrates the effect of the initial dye concentration on the efficiency of the STO-800 sample (20 mg) for MB photo-degradation at initial concentrations of 5, 10, and 15 ppm under UV irradiation. The data show that the MB degradation efficiency improved as the dye concentration decreased. This could be attributed to the saturation of the photocatalyst surface with dye molecules at high concentrations. When the initial dye concentration reached 15 ppm, an excessive number of molecules formed a dense reaction medium, which hampered photon penetration. Additionally, an increased dye concentration may lead to a shortage of hydroxyl radicals necessary to decompose all dye molecules, further reducing process efficiency (Singh et al., 2022).

The $SrTiO_3$ sample calcined at 800 °C underwent a stability test over five cycles. As depicted in Fig. 6(c), the photocatalyst maintained nearly consistent photodegradation activity against a 10 ppm MB dye solution across all five cycles. A minor reduction in degradation efficiency from 100 % to 95.6 % was observed, which was likely attributable to the accumulation of adsorbed dye intermediates on the photocatalyst surface during repeated use. Cyclic stability tests confirmed that STO-800 exhibited high durability and remained effective for dye degradation across multiple cycles.

To define the efficiency of STO-800 as a photocatalyst for MB photodegradation, a comparison with the other photocatalysts is presented in Table 2. As indicated, the STO-800 sample demonstrated a significantly superior performance for MB degradation compared to other known photocatalysts. Notably, compared to Al-doped SrTiO₃ and Al-SrTiO₃ modified with cocatalysts, the pure STO-800 sample exhibited the highest photocatalytic activity under UV light, despite the lack of additional modifications. Furthermore, the STO-800 sample benefitted from a straightforward and cost-effective fabrication process while achieving excellent photocatalytic performance in the removal of organic dyes from aqueous solutions.

The fundamental mechanism underlying the photocatalytic degradation of organic dyes involves a sequence of surface redox reactions and other processes (Kuspanov et al., 2023b, 2023a). When SrTiO₃ is exposed to light with energy equal to or greater than its bandgap, electron-hole pairs are generated. Under ultraviolet irradiation, photoelectrons transition from the valence band to the conduction band of SrTiO₃, creating holes in the valence band (Rafiq et al., 2021). The excited electrons can then interact with oxygen molecules to produce superoxide radicals (O₂-). Photogenerated holes react with water molecules to generate hydroxyl radicals (OH•). These highly reactive radicals (OH• and O₂-) subsequently react with methylene blue dye molecules, leading to the formation of intermediate products that are eventually degraded into carbon dioxide and water. While our work provides valuable insights into the relationship between synthesis conditions and photocatalytic performance, we acknowledge that a comprehensive understanding of the degradation mechanism requires further investigation into the reactive species involved. Specifically, experiments using radical scavengers could help identify the predominant reactive radicals (e.g., OH* or O₂-) and elucidate the preferred reaction pathways. Such studies, as noted in relevant literature (da Silva et al., 2016; Grecu et al., 2024), typically involve trapping experiments that can

Fig. 6. (a) Effect of different mass loading and (b) initial dye concentration on MB photodegradation over the STO-800 sample under UV light irradiation; (c) cycle stability experiment of the STO-800

9

Table 1
Grain sizes of synthesised SrTiO₃ as a function of calcination temperature and full width at half maximum (FWHM).

Sample	FWHM			Grain size
	(110)	(111)	(200)	
STO-800	0.32567	0.28705	0.32346	26.89
STO-900	0.28211	0.30257	0.32089	27.75
STO-1000	0.26543	0.27318	0.31416	29.55
STO-1100	0.28383	0.18082	0.39383	32.25

Table 2
Comparison of the photocatalytic activity of the synthesised STO-800 photocatalyst with the results of recent studies conducted on other SrTiO₃ photocatalysts.

Nº	Photocatalyst	Light source	MB dye conc./ ppm	Irradiation Time (min)	Performance/	k_1/min^{-1}	Ref.
1	SrTiO ₃	UV light	10 (MB)	120	36	0.00565	(Aravinthkumar et al., 2022)
1	SrTiO ₃	UV light	10 (MB)	120	83.13	0.0170	(Vinod Kumar and Prakash Babu, 2024)
3	SrTiO ₃	UV light	10 (MB)	150	78.9	3.713×10^{-3}	(Kiran et al., 2022)
4	Al-doped SrTiO ₃	UV light	10 (MB)	300	54.91	0.16736	(Iriani et al., 2024)
5	PVA/SrTiO ₃ /Ag ₂ O	UV light	20 (MB)	150	88	0.0159	(Chen et al., 2022)
6	RhCr ₂ O ₃ /Al-SrTiO ₃ / CoOOH	UV light	10 (Congo Red)	90	81	0.0183	(Abd Elkodous et al., 2023)
7	N-ZnO/CD	UV-B light	10 (MB)	60	83.4	0.0299	(Ayu et al., 2023)
8	TiO ₂ /rGO	UV light	10 (MB)	60	91.48	0.0417	(Kusiak-Nejman et al., 2020)
9	SrTiO ₃	UV light	10 (MB)	30	100	0.156	This work
10	$SrTiO_3$	Visible light	10 (MB)	60	51	9.2×10^{-3}	This work

pinpoint the role of different reactive species during photodegradation. The possible reactions can be summarised as follows:

$$SrTiO_3 + h\nu \rightarrow e^- + h^+ \tag{8}$$

$$e^- + O_2 \rightarrow * O_2^- \tag{9}$$

$$h^+ + H_2O \rightarrow OH* \tag{10}$$

$$OH* + MB \rightarrow intermediate \ products \rightarrow CO_2 + H_2O$$
 (11)

$$O_2^- + MB \rightarrow intermediate \ products \rightarrow CO_2 + H_2O.$$
 (12)

These reactions illustrate the key steps in the photocatalytic process where SrTiO3 effectively utilises UV light to generate reactive species that drive the degradation of MB dye (Rafiq et al., 2021).

4. Conclusion

SrTiO₃ nanoparticles were successfully synthesised via a simple chemical precipitation method and calcined at various temperatures. The photocatalytic performance towards MB dye improved up to a calcination temperature of 800 °C, beyond which activity declined. The 800 °C sample achieved 100 % degradation of MB in 30 min under UV light and 51.7 % under visible light, outperforming commercial P25, which required 45 min for complete degradation. XRD, SEM, TEM, XPS, UV-Vis DRS analyses revealed that the enhanced photocatalytic activity of the 800°C sample is due to its high crystallinity and average particle size at 70.4 nm, which facilitate effective charge carrier separation and increased light absorption. Furthermore, factors such as catalyst and dye concentrations significantly impact the degradation process. These findings indicate that SrTiO₃ calcined at 800°C has strong potential for MB dye degradation and future photocatalytic applications, though its current efficacy is limited to the UV spectrum, necessitating further research to broaden its applicability.

CRediT authorship contribution statement

Chingis Daulbayev: Writing – review & editing, Project administration. Aigerim Serik: Methodology, Investigation, Conceptualization. Zhengisbek Kuspanov: Writing – original draft. Aibol Baratov: Methodology, Investigation, Conceptualization. Alisher Tattibay: Methodology, Conceptualization. Madina Bissenova: Methodology, Investigation, Conceptualization. Ulzhan Abdikarimova: Methodology, Investigation, Conceptualization. Sayabek Sakhiyev: Resources, Formal analysis. Mukhtar Yeleyov: Resources, Formal analysis.

Declaration of Competing Interest

The authors declare that they have no known competing financial interests or personal relationships that could have appeared to influence the work reported in this paper.

Data Availability

No data was used for the research described in the article.

Acknowledgments

This research was funded by the Science Committee of the Ministry of Science and Higher Education of the Republic of Kazakhstan (Grant No. AP14869381 and No BR24992935).

References

- Abd Elkodous, M., El-Khawaga, A.M., Abouelela, M.M., Abdel Maksoud, M.I.A., 2023. Cocatalyst loaded Al-SrTiO3 cubes for Congo red dye photo-degradation under wide range of light. Sci. Rep. 13, 6331. https://doi.org/10.1038/s41598-023-33249-1.
- Agustina, F.R., Suherman, B., Hasanah, L.U., Puspita, N.F.S., Sandi, D.K., Nurosyid, F., Handoko, E., Iriani, Y., 2023. Preparation of Nickel (Ni) doped SrTiO3 and effects of sintering temperatures on its properties as photocatalyst. J. Phys.: Conf. Ser. 2498, 012018. https://doi.org/10.1088/1742-6596/2498/1/012018.
- Aktaş, P.S., Ay, E., 2022. Influence of Synthesis Procedures on the Preparation of Strontium Titanate Nanoparticles and Photocatalytic application for Methylene blue degradation. https://doi.org/10.21203/rs.3.rs-2137722/v1.
- Aravinthkumar, K., Praveen, E., Jacquline Regina Mary, A., Raja Mohan, C., 2022. Investigation on SrTiO3 nanoparticles as a photocatalyst for enhanced photocatalytic activity and photovoltaic applications. Inorg. Chem. Commun. 140, 109451. https://doi.org/10.1016/j.inoche.2022.109451.
- Ayu, D.G., Gea, S., Andriayani, Telaumbanua, D.J., Piliang, A.F.R., Harahap, M., Yen, Z., Goei, R., Tok, A.I.Y., 2023. Photocatalytic Degradation of Methylene Blue Using N-Doped ZnO/Carbon Dot (N-ZnO/CD) Nanocomposites Derived from Organic Soybean. ACS Omega 8, 14965–14984. https://doi.org/10.1021/
- Bakbolat, B., Daulbayev, C., Sultanov, F., Beissenov, R., Umirzakov, A., Mereke, A., Bekbaev, A., Chuprakov, I., 2020. Recent Developments of TiO2-Based Photocatalysis in the Hydrogen Evolution and Photodegradation: A Review. Nanomaterials 10, 1790. https://doi.org/10.3390/nano10091790.
- Bera, J., Sarkar, D., 2003. Formation of BaTiO3 from Barium Oxalate and TiO2. J. Electroceram. 11, 131–137. https://doi.org/10.1023/B: JECR.0000026366.17280.0d.
- Chen, X., Qi, H., Zhang, C., Ma, L., Li, Z., Chen, P., Xing, Q., Sun, Q., Yan, Z., 2022. Synthesis and characterization of recyclable PVA/SrTiO3/Ag2O composite with photocatalytic degradation performance of methylene blue. Appl. Phys. A 128, 374. https://doi.org/10.1007/s00339-022-05510-3.
- Daulbayev, C., Sultanov, F., Korobeinyk, A.V., Yeleuov, M., Azat, S., Bakbolat, B., Umirzakov, A., Mansurov, Z., 2021. Bio-waste-derived few-layered graphene/SrTiO3/PAN as efficient photocatalytic system for water splitting. Appl. Surf. Sci. 549, 149176. https://doi.org/10.1016/j.apsusc.2021.149176.
- Deshmukh, V.V., Ravikumar, C.R., Kumar, M.R.A., Ghotekar, S., Kumar, A.N., Jahagirdar, A.A., Murthy, H.C.A., 2021. Structure, morphology and electrochemical properties of SrTiO3 perovskite: Photocatalytic and supercapacitor applications. Environ. Chem. Ecotoxicol. 3, 241–248. https://doi.org/10.1016/j.enceco.2021.07.001.
- Grecu, I., Enache, A.-C., Pascariu, P., Bele, A., Samoila, P., Cojocaru, C., Harabagiu, V., 2024. Modified spinel ferrite-based composite membranes with highly proficient photocatalytic activity. Surf. Interfaces 51, 104536. https://doi.org/10.1016/j.surfin.2024.104536.
- Ham, Y., Hisatomi, T., Goto, Y., Moriya, Y., Sakata, Y., Yamakata, A., Kubota, J., Domen, K., 2016. Flux-mediated doping of SrTiO 3 photocatalysts for efficient overall water splitting. J. Mater. Chem. A 4, 3027–3033. https://doi.org/10.1039/C5TA04843E.
- Iriani, Y., Sandi, D.K., Hikmah, D.N., Afriani, R., Nurosyid, F., Handoko, E., Faquelle, D., 2024. Comparison study of aluminum (Al)-doped strontium titanate (SrAlxTi1-xO3; x = 3% and 5%) photocatalyst for methylene blue degradation. Mater. Today.: Proc. https://doi.org/10.1016/j.matpr.2024.03.042.
- Ismael, M., 2021. Latest progress on the key operating parameters affecting the photocatalytic activity of TiO2-based photocatalysts for hydrogen fuel production: A comprehensive review. Fuel 303, 121207. https://doi.org/10.1016/j.fuel.2021.121207.
- Jiang, J., Kato, K., Fujimori, H., Yamakata, A., Sakata, Y., 2020. Investigation on the highly active SrTiO3 photocatalyst toward overall H2O splitting by doping Na ion. J. Catal. 390, 81–89. https://doi.org/10.1016/j.jcat.2020.07.025.
- Kiran, K.S., Shashanka, R., Lokesh, S.V., 2022. Enhanced Photocatalytic Activity of Hydrothermally Synthesized Perovskite Strontium Titanate Nanocubes. Top. Catal. https://doi.org/10.1007/s11244-021-01558-2.
- Kobayashi, M., Suzuki, Y., Goto, T., Cho, S.H., Sekino, T., Asakura, Y., Yin, S., 2018. Low-temperature hydrothermal synthesis and characterization of SrTiO3 photocatalysts for NOx degradation. J. Ceram. Soc. Jpn. 126, 135–138. https://doi.org/10.2109/jcersj2.17195.
- Kudaibergen, A., Kuspanov, Z., Issadykov, A., Beisenov, R., Yeleuov, M., Daulbayev, C., 2023. Synthesis, Structure, and Energetic Characteristics of Perovskite Photocatalyst SrTiO3: an Experimental and DFT Study | Eurasian Chemico-Technological Journal.
- Kudo, A., Sakata, Y., Kondo, J.N., Hara, M., Kubota, J., Ikeda, S., Takata, T., Abe, R., Takagaki, A., Hisatomi, T., 2023. A Career in Catalysis: Kazunari Domen. ACS Catal. 13, 6934–6955. https://doi.org/10.1021/acscatal.3c00951.
- Kusiak-Nejman, E., Wanag, A., Kapica- Kozar, J., Kowalczyk, Ł., Zgrzebnicki, M., Tryba, B., Przepiórski, J., Morawski, A.W., 2020. Methylene blue decomposition on TiO2/reduced graphene oxide hybrid photocatalysts obtained by a two-step hydrothermal and calcination synthesis. Catal. Today, SI: CarboCat. –VIII 357, 630–637. https://doi.org/10.1016/j.cattod.2019.04.078.
- Kuspanov, Z., Bakbolat, B., Baimenov, A., Issadykov, A., Yeleuov, M., Daulbayev, C., 2023a. Photocatalysts for a sustainable future: Innovations in large-scale environmental and energy applications. Sci. Total Environ. 885, 163914. https://doi.org/10.1016/j.scitotenv.2023.163914.
- Kuspanov, Z., Umirzakov, A., Serik, A., Baimenov, A., Yeleuov, M., Daulbayev, C., 2023b. Multifunctional strontium titanate perovskite-based composite photocatalysts for energy conversion and other applications. Int. J. Hydrog. Energy. https://doi.org/10.1016/j.ijhydene.2023.06.168.
- Li, R., Takata, T., Zhang, B., Feng, C., Wu, Q., Cui, C., Zhang, Z., Domen, K., Li, Y., 2023. Criteria for Efficient Photocatalytic Water Splitting Revealed by Studying Carrier Dynamics in a Model Al-doped SrTiO3 Photocatalyst. Angew. Chem. Int. Ed. 62, e202313537. https://doi.org/10.1002/anie.202313537.
- Ma, Y., Wu, Z., Wang, H., Wang, G., Zhang, Y., Hu, P., Li, Y., Gao, D., Pu, H., Wang, B., Qi, X., 2019. Synthesis of nanocrystalline strontium titanate by a sol–gel assisted solid phase method and its formation mechanism and photocatalytic activity. CrystEngComm 21, 3982–3992. https://doi.org/10.1039/C9CE00495E.
- Nishiyama, H., Yamada, T., Nakabayashi, M., Maehara, Y., Yamaguchi, M., Kuromiya, Y., Nagatsuma, Y., Tokudome, H., Akiyama, S., Watanabe, T., Narushima, R., Okunaka, S., Shibata, N., Takata, T., Hisatomi, T., Domen, K., 2021. Photocatalytic solar hydrogen production from water on a 100-m2 scale. Nature 598, 304–307. https://doi.org/10.1038/s41586-021-03907-3.
- Niu, J., Zhang, Y., Shi, J., Zhang, Z., Ma, Z., Yao, B., Yu, X., Wang, X., 2022. Microwave-based preparation of γ-Fe2O3/SrTiO3 photocatalyst for efficient degradation of organic pollutants in water. Mater. Chem. Phys. 288, 126357. https://doi.org/10.1016/j.matchemphys.2022.126357.
- Paul, D.R., Sharma, R., Nehra, S.P., Sharma, A., 2019. Effect of calcination temperature, pH and catalyst loading on photodegradation efficiency of urea derived graphitic carbon nitride towards methylene blue dye solution. RSC Adv. 9, 15381–15391. https://doi.org/10.1039/C9RA02201E.

- Qin, Y., Fang, F., Xie, Z., Lin, H., Zhang, K., Yu, X., Chang, K., 2021. La, Al-Codoped SrTiO3 as a Photocatalyst in Overall Water Splitting: Significant Surface Engineering Effects on Defect Engineering. ACS Catal. 11, 11429–11439. https://doi.org/10.1021/acscatal.1c02874.
- Rafiq, A., Ikram, M., Ali, S., Niaz, F., Khan, M., Khan, Q., Maqbool, M., 2021. Photocatalytic degradation of dyes using semiconductor photocatalysts to clean industrial water pollution. J. Ind. Eng. Chem. 97, 111–128. https://doi.org/10.1016/j.jiec.2021.02.017.
- Ramos-Sanchez, J.E., Camposeco, R., Lee, S.-W., Rodríguez-González, V., 2020. Sustainable synthesis of AgNPs/strontium-titanate-perovskite-like catalysts for the photocatalytic production of hydrogen. SI: 5th LACP3 Catal. Today 2017 (341), 112–119. https://doi.org/10.1016/j.cattod.2019.08.020.
- Rocha-Rangel, E., Pech-Rodríguez, W.J., Lopez Hernandez, J., Calles-Arriaga, C., Eddie Nahúm, A.-M., Castillo-Robles, J.A., 2020. Synthesis of SrTiO3 by the Calcination of SrCO3 and TiO2 Mixtures Intensively Ground by Means of High Energy Milling. Arch. Metall. Mater. 52 621–626. https://doi.org/10.24425/amm.2020.132801.
- $Roy,\ P.K.,\ Bera,\ J.,\ 2005.\ Formation\ of\ SrTiO3\ from\ Sr-oxalate\ and\ TiO2.\ Mater.\ Res.\ Bull.\ 40,\ 599-604.\ https://doi.org/10.1016/j.materresbull.2005.01.010.$
- Ruan, J., Zhong, T., Guo, Y., 2023. Enhanced water splitting over ethylenediaminetetraacetate treated SrTiO3 photocatalysts with high crystallinity, reduced size, and surface nanostructure. J. Colloid Interface Sci. 650, 1424–1433. https://doi.org/10.1016/j.jcis.2023.07.041.
- Serik, A., Kuspanov, Z., Bissenova, M., Idrissov, N., Yeleuov, M., Umirzakov, A., Daulbayev, C., 2024. Effective Photocatalytic Degradation of Sulfamethoxazole Using Pan/Srtio3 Nanofibers https://doi.org/10.2139/ssrn.4758700..
- da Silva, L.F., Lopes, O.F., de Mendonça, V.R., Carvalho, K.T.G., Longo, E., Ribeiro, C., Mastelaro, V.R., 2016. An Understanding of the Photocatalytic Properties and Pollutant Degradation Mechanism of SrTiO3 Nanoparticles. Photochem. Photobiol. 92, 371–378. https://doi.org/10.1111/php.12586.
- Singh, P., Mohan, B., Madaan, V., Ranga, R., Kumari, P., Kumar, S., Bhankar, V., Kumar, P., Kumar, K., 2022. Nanomaterials photocatalytic activities for waste water treatment: a review. Environ. Sci. Pollut. Res 29, 69294–69326. https://doi.org/10.1007/s11356-022-22550-7.
- Sultanov, F., Daulbayev, C., Azat, S., Kuterbekov, K., Bekmyrza, K., Bakbolat, B., Bigaj, M., Mansurov, Z., 2020. Influence of Metal Oxide Particles on Bandgap of 1D Photocatalysts Based on SrTiO3/PAN Fibers. Nanomaterials 10, 1734. https://doi.org/10.3390/nano10091734.
- Takata, T., Jiang, J., Sakata, Y., Nakabayashi, M., Shibata, N., Nandal, V., Seki, K., Hisatomi, T., Domen, K., 2020. Photocatalytic water splitting with a quantum efficiency of almost unity. Nature 581, 411–414. https://doi.org/10.1038/s41586-020-2278-9.
- Vijay, A., Vaidya, S., 2021. Tuning the Morphology and Exposed Facets of SrTiO3 Nanostructures for Photocatalytic Dye Degradation and Hydrogen Evolution. ACS Appl. Nano Mater. 4, 3406–3415. https://doi.org/10.1021/acsanm.0c03160.
- Vinod Kumar, S., Prakash Babu, D., 2024. Perovskite SrTiO3 for photo catalytic and optoelectronic applications. Mater. Today.: Proc. https://doi.org/10.1016/j.matpr.2024.02.040.
- Wang, S., Teramura, K., Hisatomi, T., Domen, K., Asakura, H., Hosokawa, S., Tanaka, T., 2021. Dual Ag/Co cocatalyst synergism for the highly effective photocatalytic conversion of CO 2 by H 2 O over Al-SrTiO 3. Chem. Sci. 12, 4940–4948. https://doi.org/10.1039/D1SC00206F.
- Xiao, F., Xu, J., Cao, L., Jiang, S., Zhang, Q., Wang, L., 2020. In situ hydrothermal fabrication of visible light-driven g-C3N4/SrTiO3 composite for photocatalytic degradation of TC. Environ. Sci. Pollut. Res 27, 5788–5796. https://doi.org/10.1007/s11356-019-07060-3.
- Youssef, A.M., Farag, H.K., El-Kheshen, A., Hammad, F.F., 2018. Synthesis of Nano-Structured Strontium Titanate by Sol-Gel and Solid State Routes. Silicon 10, 1225–1230. https://doi.org/10.1007/s12633-017-9596-z.
- Zhao, Z., Goncalves, R.V., Barman, S.K., Willard, E.J., Byle, E., Perry, R., Wu, Z., Huda, M.N., Moulé, A.J., Osterloh, F.E., 2019. Electronic structure basis for enhanced overall water splitting photocatalysis with aluminum doped SrTiO3 in natural sunlight. Energy Environ. Sci. 12, 1385–1395. https://doi.org/10.1039/C9EE00310J.

ELSEVIER

Contents lists available at ScienceDirect

Journal of the Taiwan Institute of Chemical Engineers

journal homepage: www.journals.elsevier.com/journal-of-the-taiwan-institute-of-chemical-engineers





Efficient photocatalytic degradation of methylene blue via synergistic dual co-catalyst on SrTiO₃@Al under visible light: Experimental and DFT study

Zhengisbek Kuspanov^{a,b}, Aigerim Serik^{a,b}, Nikita Matsko^c, Madina Bissenova^{a,b}, Aidos Issadykov^{b,c}, Mukhtar Yeleuov^{a,b,d}, Chingis Daulbayev^{b,e,f,*}

- a Satbayev University, Almaty, Kazakhstan
- ^b Institute of Nuclear Physics, Almaty, Kazakhstan
- ^c Joint Institute for Nuclear Research, Dubna, Russia
- ^d Bes Saiman Group, Almaty, Kazakhstan
- e Institute of Physics and Technology, Almaty 050032, Kazakhstan
- ^f Kazakh-British Technical University, Almaty, Kazakhstan

ARTICLE INFO

Keywords: Photocatalysis SrTiO₃ Composite DFT+U calculations Dual cocatalysts Photodegradation

ABSTRACT

Background: Photocatalytic oxidation is a green method for water purification. However, the operation of traditional photocatalysts depends on exposure to UV radiation, which only forms a small portion of the spectrum comprising sunlight. The expansion of photocatalyst absorption to the visible range of light could greatly improve the efficiency and economic viability of the process.

Methods: The photocatalyst was prepared by first synthesising SrTiO $_3$ nanoparticles by chemical precipitation followed by calcination. Then, SrTiO $_3$ was doped with aluminium using a flux method with Al $_2$ O $_3$ and SrCl $_2$ at 1150 $^{\circ}$ C. Finally, the dual co-catalysts, Rh/Cr $_2$ O $_3$ and CoOOH, were photodeposited onto SrTiO $_3$ @Al via sequential irradiation.

Significant findings: The Rh/Cr₂O₃/SrTiO₃@Al/CoOOH nanocomposite degraded 87% of methylene blue (MB) (10 mg/L) under visible light in 1 h, a 3.3-fold improvement over pure SrTiO3 and 2.1-fold over a similar commercial composite. This enhancement is due to efficient charge separation resulting from Al doping and improved carrier transport as a result of the anisotropic deposition of the co-catalysts. Optimisation showed that 20 mg of photocatalyst in 50 mL of MB solution (5 mg/L) degraded 100% thereof within 45 min. DFT calculations showed uneven electron distribution in SrTiO3's conduction band and structural changes with Al doping, further enhancing photocatalytic activity.

1. Introduction

The rapid development of textiles, pharmaceuticals, cosmetics, and other products has vastly increased the amount of industrial wastewater being discharged, and this has contributed to water resources becoming severely polluted. Dyes, even at low concentrations, can significantly degrade the water quality and negatively impact the environment. In addition, some dyes, such as methylene blue (MB), Congo red, and rhodamine B, are biodegradable and pose serious risks in terms of toxicity and carcinogenicity [1,2]. Moreover, the World Health Organisation has predicted that, by 2025, a severe shortage of water resources would exist in regions that are home to half of the world's population [3], thus highlighting the need to apply and improve

technological processes, including adsorption [4], filtration [5] and photocatalysis [6], to enhance the effectiveness of water treatment procedures. Owing to its high efficiency and lack of producing secondary pollutants, photocatalysis is currently considered the most environmentally friendly and sustainable method for wastewater treatment. In general, the photocatalytic degradation of organic pollutants on semiconductor photocatalysts usually involves three steps: (1) photon absorption; (2) generation, separation, and electron–hole pair transfer by photoexcitation; (3) reactions in the presence of photoexcited electrons and holes and the formation of highly reactive radicals to degrade the organic pollutants [7]. Hence, the prevention of the rapid recombination of electrons and holes inside the photocatalyst particles, which would otherwise lower the photocatalytic activity of the semiconductor

^{*} Corresponding author at: Institute of Nuclear Physics, Almaty, Kazakhstan. E-mail address: ch.daulbayev@inp.kz (C. Daulbayev).

catalysts, is important.

Among the various photocatalysts, the multifunctional perovskite strontium titanate ($SrTiO_3$) stands out due to its high oxidative activity and favourable physicochemical properties, including its non-toxicity, stability, resistance to photocorrosion, and high carrier mobility [8]. However, its wide band gap, low quantum efficiency, and limited pollutant removal capacity restrict its large-scale use for wastewater treatment [9]. To enhance its effectiveness across a broader range of UV–visible wavelengths, modifications are necessary. Efforts to improve the performance of $SrTiO_3$ include defect engineering [10], the development of structures with complex surface morphologies [11,12], the creation of composites [13], and the use of co-catalysts loaded onto these composites [14–16].

Recent research has shown that doping SrTiO₃ with metals can significantly enhance its photocatalytic activity [17-19]. The introduction of a dopant affects SrTiO₃ primarily by (1) altering the energy levels and creating new energy states within the photocatalyst, or (2) modifying the perovskite structure to boost the formation of photoinduced charge carriers. Additionally, because the size of the active surface area of SrTiO₃-based photocatalysts is affected by the particle size and shape, the photocatalytic performance in terms of surface reactions on the photocatalyst is impacted [20–23]. For example, substituting tetravalent Ti⁴⁺ with the lower-valence Al³⁺ in SrTiO₃ shifts the Fermi level [22], which limits the upward bending of the energy-state band and decreases the size of the region that is depleted of electrons. In turn, this facilitates the introduction of electrons, lowers the number of protons, and increases the charge separation efficiency. Takata et al. [24] emphasised the possibility of controlling the particle size by adjusting the alloying ratio after flux treatment at high temperatures—a strategy that promoted the formation of particles with optimal diameters that enhanced the photocatalytic activity.

Another approach to enhance the photocatalytic efficiency entails loading dual co-catalysts onto the surface of the SrTiO3-based photocatalyst. Oxidative and reductive co-catalysts play crucial roles by creating distinct oxidation and reduction centres on the photocatalyst surface [25]. These co-catalysts also ensure that the electrons and holes generated by the photocatalytic reaction are transported to different active centres on the photocatalyst surface [7,26]. According to Li et al., oxidation and reduction co-catalysts located on different facets of the BiVO₄ photocatalyst perform their usual functions during the reaction and align the internal electric field vectors of the photocatalyst particles [27]; this phenomenon favours the maximum separation and transfer of photogenerated electron-hole pairs. Other studies reported that SrTiO₃: Al, with the addition of RhCrO_x as a co-catalyst by the impregnation method, achieved a quantum yield of 56% at 365 nm for the photocatalytic decomposition of water [28]. In contrast, the simultaneous introduction of Rh/Cr₂O₃ and CoOOH as co-catalysts onto the Al-SrTiO₃ photocatalyst using the photodeposition method achieved a record 96% quantum yield in the range of 350-360 nm [24]. Based on these developments, a pilot plant that included panel reactors with a total area of 100 m² was established for mass-producing solar hydrogen [29]. Consequently, many studies involving the use of dual co-catalysts have been conducted to selectively decompose water photocatalytically [22, 30,31], reduce CO₂ [7,20,32] and decompose pharmaceutical pollutants [33-35]. However, to the best of our knowledge, few studies on the photocatalytic decomposition of organic pollutants in water using dual co-catalysts have been reported.

Thus, with this work, we aimed to synthesise and apply $SrTiO_3@Al$ -based photocatalysts loaded with Rh/Cr_2O_3 and CoOOH as dual co-catalysts for the highly efficient photocatalytic removal of organic pollutants from aqueous media. The photocatalytic activity of the newly fabricated photocatalysts was evaluated by assessing their ability to accomplish the photodegradation of MB, a precursor of organic dyes, under visible light (400 nm). The synthesised samples were characterised using X-ray diffraction (XRD), scanning electron microscopy (SEM), transmission electron microscopy (TEM), and high-resolution X-

ray photoelectron spectroscopy to clarify their morphology and crystal structure. In addition, the electronic structure and density of states of aluminium-doped $SrTiO_3$ were described using density functional theory (DFT). The results obtained in this study provide new insights into the photodegradation of organic pollutants in aqueous media using Rh/ $Cr_2O_3/SrTiO_3@Al/CoOOH$ photocatalysts.

2. Materials and methods

2.1. Materials

Titanium(IV) oxide, anatase (TiO $_2$, particle sizes<25 nm, 99.7%), strontium nitrate (Sr(NO $_3$) $_2$, \geq 98%), nitric acid (HNO $_3$, < 90%), strontium titanate (SrTiO $_3$, particle sizes<100 nm, 99%), aluminium oxide (Al $_2$ O $_3$, particle sizes<50 nm, 99.8%), rhodium(III) chloride hydride (RhCl $_3$ ·6H $_2$ O, Rh 38-40%), cobalt (II) nitrate hexahydrate (Co (NO $_3$) $_3$ ·6H $_2$ O, \geq 98%), and methylene blue (C $_1$ 6H $_1$ 8ClN $_3$ S·xH $_2$ O, dye content, \geq 82%) were purchased from Sigma–Aldrich (St. Louis, MO, USA). Oxalic acid ((COOH) $_2$ ·2H $_2$ O, \geq 98%), strontium chloride hexahydrate (SrCl $_2$ ·6H $_2$ O, 99.7%), potassium chromate (K $_2$ CrO $_4$, 99.5%), were purchased from Laborpharma (Almaty, Kazakhstan). All the chemicals were used without any additional treatment.

2.2. Synthesis of SrTiO₃

SrTiO $_3$ nanoparticles were synthesised by chemical precipitation followed by calcination, according to previously published methods [36–38]. Briefly, the TiO $_2$ powder was added to an aqueous solution of Sr(NO $_3$) $_2$ at a Ti:Sr molar ratio of 1:1 and incubated in an ultrasonic bath for 30 min. Then, an aqueous solution of (COOH) $_2$ ·2H $_2$ O (0.4 M) was gradually added under vigorous stirring, while the pH was maintained between 6 and 7 using an ammonia solution. The precipitate was then centrifuged, washed five times with distilled water, and dried for 16 h. The resulting powder was calcined in air at 900 °C for 1 h. The calcined powder was treated with a 1 M HNO $_3$ solution for 30 min to remove impurities of SrCO $_3$, washed five times with distilled water, and dried for 16 h.

2.3. Synthesis of SrTiO3@Al

The SrTiO₃ powder was doped with aluminium using a flux processing method based on research reported elsewhere [23,39]. For this purpose, we used the SrTiO₃ powder that had been prepared as described in Section 2.2, as well as Al₂O₃ and SrCl₂ (as fluxing reagents), in a molar ratio of 1:0.02:10. These components were thoroughly mixed in an agate mortar and placed in an aluminium oxide crucible. The powders were then heated to 1150 °C (heating rate: 7.5 °C/min) and kept at this temperature for 10 h in an oven under atmospheric conditions. The samples were then removed, ultrasonicated to completely remove the salt residue, washed thoroughly five times with distilled water, and then dried for 20 h. The same procedure was performed using commercial SrTiO₃ powder, with all steps repeated in the same order. As a result, two SrTiO3@Al samples were obtained: one from SrTiO3 obtained by chemical precipitation followed by calcination at 900 °C and the other from commercial SrTiO₃ powder. These samples were labelled STO(900)@Al and STO(com)@Al.

2.4. Photodeposition of Rh/Cr₂O₃ and CoOOH on SrTiO₃@Al

The dual co-catalysts Rh/Cr $_2$ O $_3$ and CoOOH were deposited on the STO@Al photocatalyst using an *in situ* photodeposition method, as described in the literature [24]. Initially, 0.1 g of the STO@Al powder was dispersed in 50 mL of distilled water and subjected to ultrasonication for 30 min. The resulting suspension was then placed in a photochemical reaction reactor and subjected to UV irradiation from a 10 W mercury lamp with vigorous stirring. In parallel, 50 μ L of freshly

prepared RhCl $_3$ ·6H $_2$ O solution with a precursor concentration of 2 mg/mL was added to the mixture and irradiated for 10 min under constant magnetic stirring. Then, 25 µL of K $_2$ CrO $_4$ solution (2 mg (Cr)/mL) was added, whereupon irradiation was continued for another 5 min. Next, 25 µL of freshly prepared Co(NO $_3$) $_3$ solution (2 mg(Co)/mL) was added to this suspension, followed by irradiation for 5 min. Notably, the photodeposition of the co-catalysts was conducted sequentially without changing the solvent. The obtained samples were washed several times and dried for 16 h at 60 °C. The amounts of the aqueous solutions of the co-catalysts that were added were calculated such that the mass concentrations of Rh, Cr, and Co were 0.1%, 0.05%, and 0.05%, respectively, eventually resulting in samples deposited by the photodeposition of dual co-catalysts based on the synthesised and commercial SrTiO $_3$. These co-catalysts were designated as Cocat/STO(900)@Al and Cocat/STO(com)@Al, respectively.

2.5. Photocatalytic reaction

The photocatalytic decomposition of MB in aqueous solution was conducted at room temperature (25°C) using a photochemical reactor (Shanghai Leewen Scientific Instrument Co., Ltd., China), where the radiation source was a high-pressure mercury lamp (10 W; λ_{max} =254 nm) using a line cut-off filter ($\lambda \ge 400$ nm). The distance between the quartz flask (50 mL) and the lamp was fixed at 10 cm. Next, 20 mg of photocatalyst was dispersed in 50 mL of an aqueous MB solution (10 mg L⁻¹) at the calculated pH value. Before photocatalytic irradiation, the mixtures were subjected to 30 min of magnetic stirring in the dark to achieve an adsorption-desorption equilibrium between MB and the photocatalyst. The duration of photocatalytic irradiation was 60 min for each sample, with aliquots (1 mL) collected every 15 min and filtered using a PVDF syringe filter. The obtained aliquots were then analysed by recording the UV-Vis spectra (I5 Hanon Advanced Technology Group Co., Ltd.) to quantify the extent to which the MB concentration had been lowered. All photocatalytic measurements were performed twice, with the mean values considered to account for deviations.

2.6. Characterisation

The synthesised samples were characterised using various techniques. XRD was performed on a Drone-8 with detection unit rotation angles ranging from $5-70^{\circ}$ in 0.01° steps, with an allowable deviation of $\pm 0.015^{\circ}$. The morphology and elemental composition of the samples were examined using SEM (Zeiss Crossbeam 540, Germany) at an accelerating voltage of 5-20 kV, equipped with an energy-dispersive Xray spectrometer (EDX) (INCA X-Sight, Oxford Instruments). Highresolution TEM (JEM-2100 LaB6 HRTEM, JEOL, Japan), operated at 80 kV, was used to study the morphology and distribution of co-catalysts on the surface of the photocatalysts. X-ray photoelectron spectroscopy (XPS) was conducted on a VG Microtech Multilab 3000 instrument with Mg and Al as the X-ray sources to analyse the valence states and elemental structure of the samples. The C1s peak at 284.8 eV was used as a reference for binding energy (BE) calibration. Ultraviolet reflectance spectra (UV-Vis DRS) were recorded on a Perkin Elmer Lambda 35 spectrophotometer in the range of 200-800 nm.

2.7. Theoretical analyses

The Quantum Espresso code [40] was used for the DFT calculations. Al-doped $SrTiO_3$ was modelled using a supercell containing $3\times3\times3$ elementary cubic cells with a 3.94 Å lattice parameter; an ideal crystal supercell contains 135 cells. The supercell structure was optimised using the Perdew–Burke–Ernzerhof-generalised gradient approximation (PBE-GGA) functional, 40 Ry plane wave cut-off energy, and a uniform $3\times3\times3$ k-points grid in the first Brillouin zone. The structures were relaxed until atomic forces became less than 10-4 Ry/Å. Because of the difficulties encountered by the standard DFT approach when processing

d- and f-electron materials (mainly related to the self-interaction errors for localised electron states), we employed the GGA+U method (Dudarev's formulation [41]) for electronic structure calculations of the SrTiO $_3$ and Al-doped SrTiO $_3$ structures. Owing to the hybridisation of the Ti 3d and O 2p electronic states [42–44], the on-site Coulomb correction U was applied to both Ti (5.9 eV) and O (4.2 eV) atoms, with the cut-off energy set to 60 Ry. The uniform k-grid contained 5 \times 5 \times 5 points in the first Brillouin zone.

3. Results and discussion

3.1. Characterisation of the prepared samples

Fig. 1 shows SEM and TEM images that were acquired to study the surface morphology of the samples. Pure STO calcined at 900°C successfully formed agglomerated nanocubes of regular shape with sizes ranging from 50 mm to 150 nm (Fig. 1a). The calcination temperature is known to be critical for determining the particle size [45]. In our work, even though smaller STO particles formed at calcination temperatures of 750-900°C, large amounts of impurities in the form of SrCO3 were observed to be present. In contrast, calcination at 1000–1100°C favours the decomposition of more carbonate; however, the STO particle size increases to reach micrometre-scale dimensions, possibly resulting in an increased probability of the recombination of photogenerated charges [46,47]. Thus, calcination at 900°C followed by treatment in an aqueous HNO3 solution to remove SrCO3 residues was selected as the optimal approach to synthesise STO nanocubes. Analysis of the elemental composition using energy-dispersive X-ray spectroscopy (EDX) (Supplementary Fig. S1) indicated the presence of Sr, Ti, and O in the structure without any impurities. Doping the STO with aluminium nanoparticles promoted the formation of truncated cubic particles with sizes ranging from 200 to 400 nm (Fig. 1e). Supplementary Fig. S2 presents the EDX analysis of the synthesised SrTiO3@Al particles and confirms the presence of aluminium in the SrTiO₃ structure. Elemental mapping further verifies the uniform distribution of Sr, Ti, O, and Al throughout the nanocomposite, as shown by the distinct colour-coded distribution maps for each of these elements. The formation of the truncated-cubic morphology for STO@Al by flux treatment followed by exposure to heat at 1150°C leads to an expansion of the {111} and a reduction of the {100} planes [20,48,49]. Considering that photocatalytic reactions occur on the catalyst surface, the presence of anisotropic crystal faces with different energies plays an important role in increasing the photocatalytic efficiency. The formation of anisotropic cubic STO improves the separation and transport efficiency of the photogenerated electrons and holes on the photocatalyst surface by inducing the subsequent formation of superoxide radicals (•O²⁻) and hydroxyl free radicals (•OH) in the reaction medium [50]. Subsequent photodeposition of the co-catalysts (Rh/Cr₂O₃ and CoOOH) revealed the separation of photogenerated electrons and holes along the spatial anisotropic crystallographic facets of the doped STO (Fig. 1c, d, g, and h). This seemed to suggest that the Rh/Cr₂O₃ nanoparticles were mainly distributed on the {100} faces, whereas the CoOOH co-catalyst was deposited on the truncated {111} and {110} faces. This assumption is based on the results of similar studies [7,20,24,31], in which the growth of co-catalysts on the STO surface was examined.

Fig. 2a shows the XRD patterns of all the synthesised samples. Analysis of the XRD pattern of the synthesised STO revealed an ordered diffraction pattern consistent with the perovskite structure [36]. The characteristic peaks of STO(900) appear at 2θ values corresponding to 32.40° , 40.50° , 46.50° , 58.50° and 68.50° , coincident with the lattice face positions of (110), (111), (200), (211), and (220) (JCPDS Card #35-0734) of the cubic STO phase. A comparison of the XRD patterns of the doped and undoped STO(900) revealed a marked increase in the peak intensity of the samples with STO@Al, indicating that the flux-doped Al doping process improved the crystallinity of STO(900). Furthermore, the presence of the Al dopant and co-catalysts did not

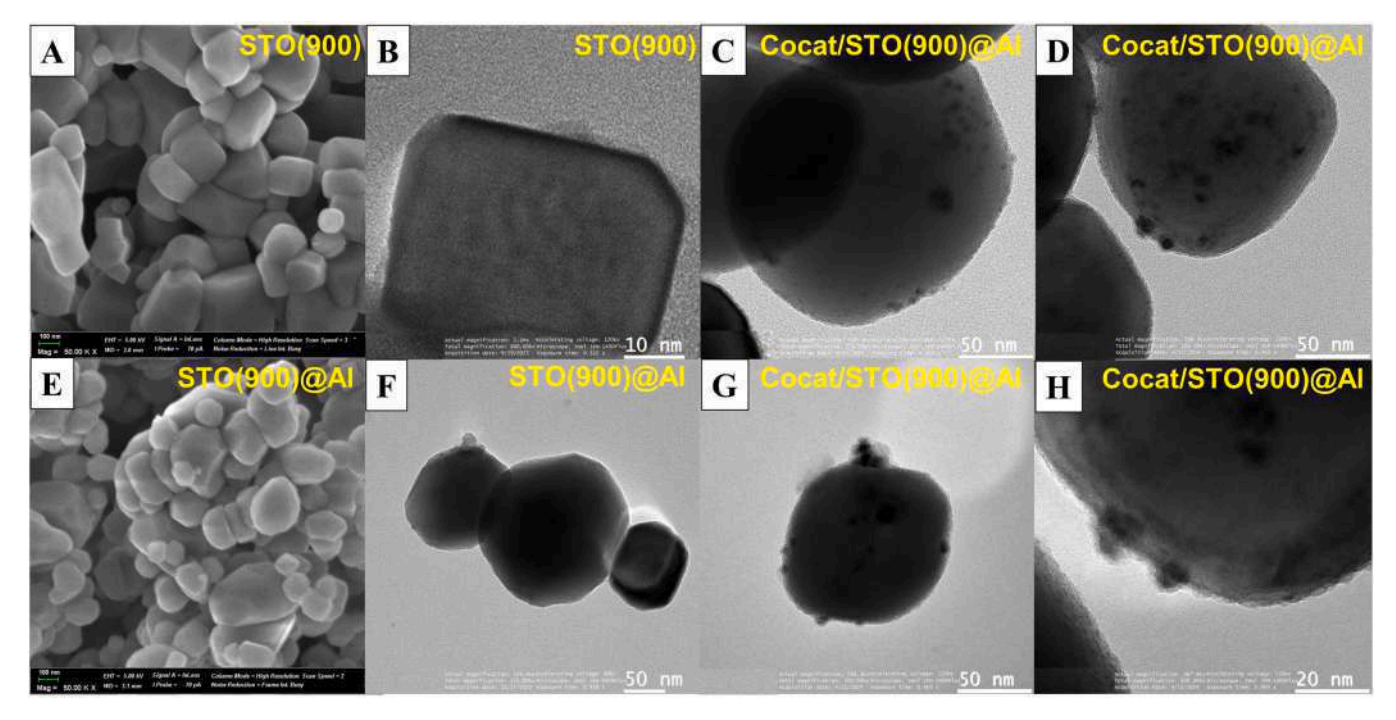


Fig. 1. SEM (a, e) and TEM (b-d, f-h) images of the prepared photocatalyst samples before and after doping with Al and before and after co-catalyst loading.

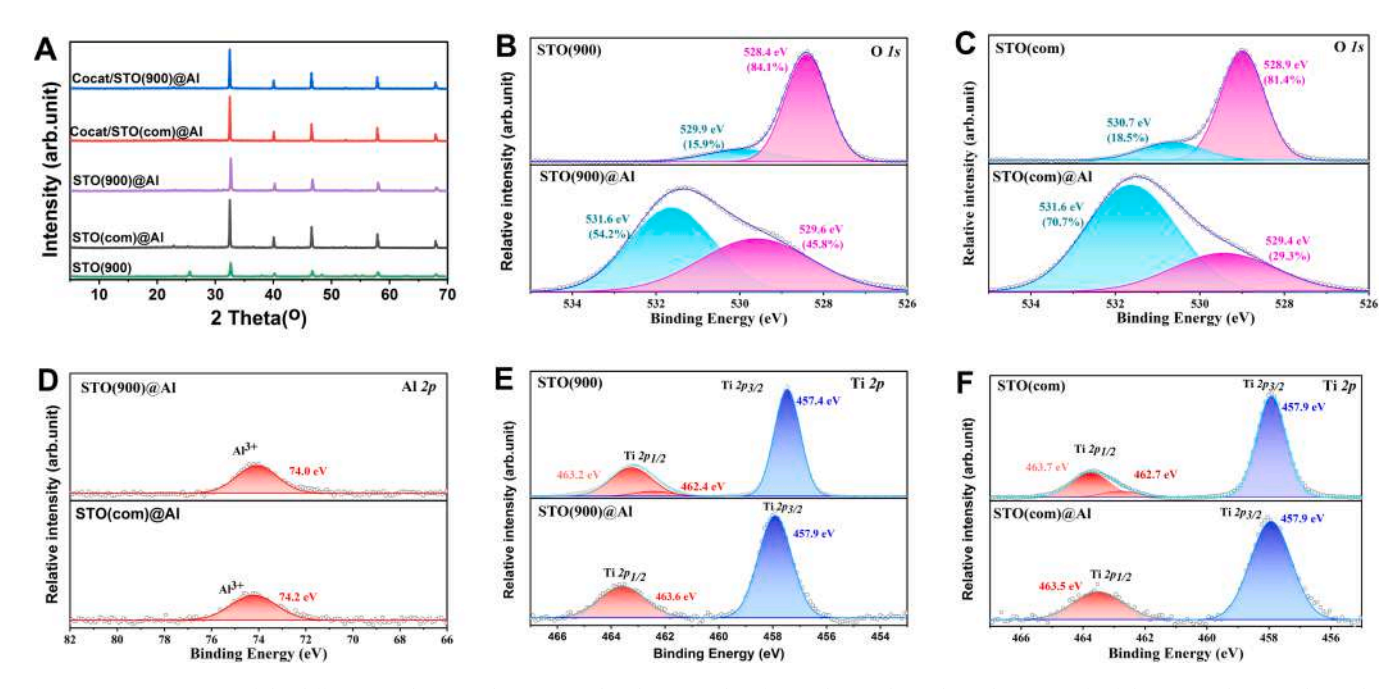


Fig. 2. (a) XRD patterns of the different catalyst samples. Deconvoluted XPS results of O 1s (b, c), Al 2p (d), and Ti 2p (e, f) of the STO and STO@Al samples.

affect the crystal structure of STO(900), and their characteristic peaks do not appear on the XRD patterns, probably because they are only present in small amounts and also due to their high dispersibility and low crystallinity [23,51].

XPS was used to investigate the chemical states and surface compositions of STO(900), STO(com), STO(900)@Al, and STO(com)@Al, with the results presented in Fig. 2(b–f). In particular, the Ti 2p spectrum of STO(900) in Fig. 2e consisted of two peaks—457.4 eV and 463.2 eV—corresponding to the Ti $2p_{3/2}$ and Ti $2p_{1/2}$ states, which indicate the presence of Ti⁴⁺ ions, whereas the peak at 462.4 eV indicates the presence of Ti³⁺ ions [11,51,52]. However, doping with Al completely suppresses the Ti³⁺ ions, and the Ti 2p spectrum of the STO(900):Al

sample is characterised by only two peaks at 457.9 and 463.6 eV, which represent ${\rm Ti}^{4+}$ ions. Similar patterns were observed for STO(com) and STO(com)@Al (Fig. 2f). The O 1s spectrum of the STO(900) sample (Fig. 2b) has peaks at two binding energies, with the peak at 528.4 eV attributed to ${\rm O}^{2-}$ ions in the crystal lattice and that at 530.0 eV to adsorbed oxygen (${\rm O}_{ads}$) [31,53]. The peak ratios changed for the STO (900)@Al-doped (increased from 15.9% to 54.2%) and STO(com) @Al-doped (increased from 18.5 to 70.7%) samples, consistent with prior results [51], indicating that increasing the ${\rm O}_{ads}$ content by doping with Al effectively prevents the recombination of photogenerated carriers, thereby positively affecting the photocatalytic properties. In general, the XPS results obtained for the synthesised samples were

consistent with those reported previously [11,21,31,51].

The optical properties of the prepared photocatalysts were examined by recording their UV-Vis diffuse reflectance spectra (DRS), and the energies corresponding to their energy-forbidden zones were obtained, as presented in Fig. 3. The energy-forbidden bands of the photocatalysts were estimated based on the analysis of the dependence of $(\alpha h \nu)^2$ on the photon energy [54]. The high absorbance of STO(com), STO(900), STO (com)@Al, STO(900)@Al, and Cocat/STO(com)@Al in the 380-400 nm range indicates the need for UV activation. The calculated energy range of the band gaps of these photocatalysts was 3.13-3.15 eV (Fig. 3b). The Cocat/STO(900)@Al sample exhibited significant sensitivity to visible light (430 nm) and is characterised by an energy band value of 3.07 eV. The improved light absorption ability of the Cocat/STO(900)@Al sample compared to that of STO(900)@Al indicates the potential influence of the co-catalysts on the light-harvesting efficiency in the visible spectrum, which, in turn, contributes to an increase in the number of photogenerated electrons available for participation in photocatalytic reactions. Additionally, other studies have indicated the significant contribution of co-catalysts to the overall light absorption capacity compared to pure photocatalysts [55,56]. In addition, the Mott-Schottky plot allows for the determination of the semiconductor type and its flat band potential [57,58]. In similar studies involving SrTiO₃-based photocatalysts and Al-doped SrTiO3 synthesised via the flux method, the positive slope of the $1/C^2$ vs. potential plot indicated the n-type nature of these materials [22,59,60]. It was noted that the flat band potential of SrTiO₃ shifts towards more negative values after doping with aluminium, which enhances the photocatalytic activity. Additionally, the deposition of co-catalysts such as RhCr₂O₃/CoOOH [60] and Pd [59] on the surface of STO@Al also results in a negative shift of the flat band potential.

The energy band diagrams of the studied samples, constructed on the basis of the UV-Vis DRS data and Mott-Schottky plots, show that the band gap becomes slightly narrower upon co-catalyst loading. This broadens the range of light absorption and is one of the reasons for the enhanced photocatalytic production of hydrogen. The experimental UV-Vis DRS data presented in this paper further confirm these findings.

3.2. Photocatalytic performance

3.2.1. Visible-light-driven photocatalytic degradation of MB

Photocatalytic degradation reactions were performed with the cationic dye MB in aqueous solution (pH 7) to evaluate the photocatalytic activity of the synthesised photocatalysts. In all cases, the samples were irradiated with visible light using a light filter (400 nm) for 60 min. The photocatalytic efficiency of the prepared samples as a function of irradiation time is presented in Fig. 4a. The percentage of MB dye that was removed (initial concentration of 10 mg/L, 50 mL) reached

21.8%, 37.2%, 16.7%, 19.3%, 41.7%, and 86.7% using the STO(com), STO(900), STO(com)@Al, STO(900)@Al, Cocat/STO(com)@Al, and Cocat/STO(900)@Al photocatalysts, respectively. The difference in the photodegradation efficiency between STO(900) and STO(900)@Al indicates the influence of the size of the crystallites and, consequently, the particle size during Al doping, as mentioned when discussing the morphology of the samples in Section 3.1. This increase in size increases the probability of the recombination of photogenerated charges, known to negatively affect the efficiency of photocatalytic reactions [46]. The Cocat/STO(900)@Al sample exhibited the highest photocatalytic activity in that its efficiency was 3.3, 4.5, and 2.1 times higher than that of STO(900), STO(900)@Al, and Cocat/STO(com)@Al, respectively. Efficient charge separation and charge transfer are significant advantages of dual co-catalysts that were separately photo-deposited in a co-catalyst/photocatalyst system. Furthermore, a prior study [51] revealed that Al doping successfully suppressed the Ti³⁺ recombination centres, which enabled the photogenerated electrons/holes to be spatially separated, transferred to different sites, and participate in subsequent photocatalytic pollutant decomposition reactions [51]. Thus, the Cocat/STO(900)@Al photocatalyst, which delivered the best photocatalytic degradation performance among all the samples, was used in subsequent experiments.

3.2.2. Effect of catalyst loading and MB concentration

Further experiments were conducted to investigate the effect of photocatalyst loading on MB decomposition of the synthesised Cocat/ STO(900)@Al sample (Fig. 4c). After photocatalytic irradiation for 60 min at photocatalyst doses of 10, 20, and 30 mg, the MB (10 mg/L) removal rates were 57.9, 73.9, and 86.7%, respectively. The process of photocatalysis is known to have an optimal level of photocatalyst loading at which the maximum number of active centres for redox reactions is reached and the maximum number of incident photons is absorbed [61]. The photodegradation efficiency increased as the loading amount increased from 10 mg to 20 mg; however, a further increase in the loading amount to 30 mg caused the photodegradation efficiency to decrease. This is likely the result of the excessive amount of catalyst, which led to strong turbidity in the solution that had the undesirable effect of light scattering. Thus, the optimum loading in the case of Cocat/STO(900)@Al for photocatalytic MB degradation was 20 mg per 50 mL of the solution, with a further increase in the catalyst mass being unnecessary.

MB solutions with concentrations of 5, 10, and 15 mg/L were used to evaluate the effect of the initial concentration of the dye on the efficiency of the Cocat/STO(900)@Al photocatalyst (20 mg per 50 mL solution) under visible light (400 nm). Fig. 4b shows that the photocatalytic degradation rate decreased as the substrate concentration increased, with complete removal achieved within 45 min at an

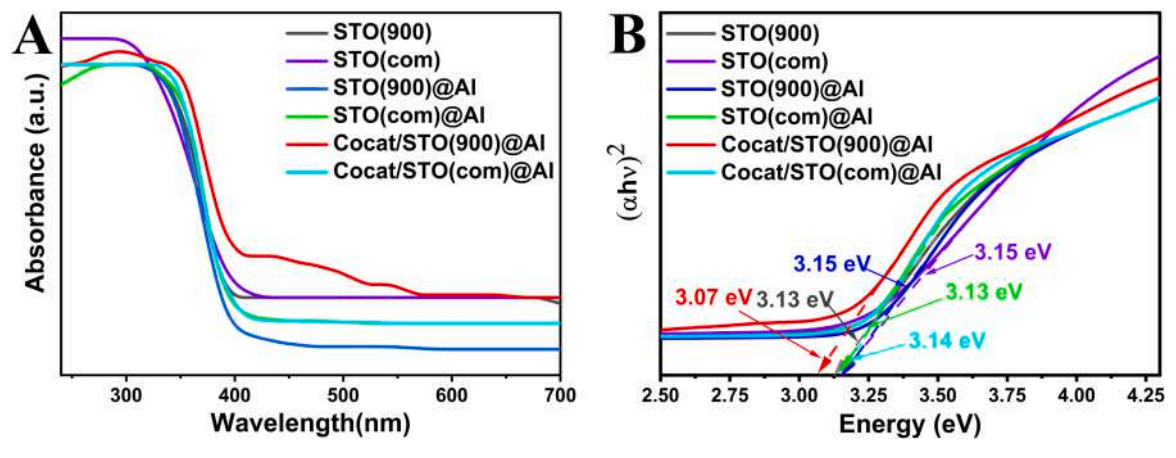


Fig. 3. UV-Vis diffuse reflectance spectra of the examined samples (a), and the corresponding calculated band gap values (b).

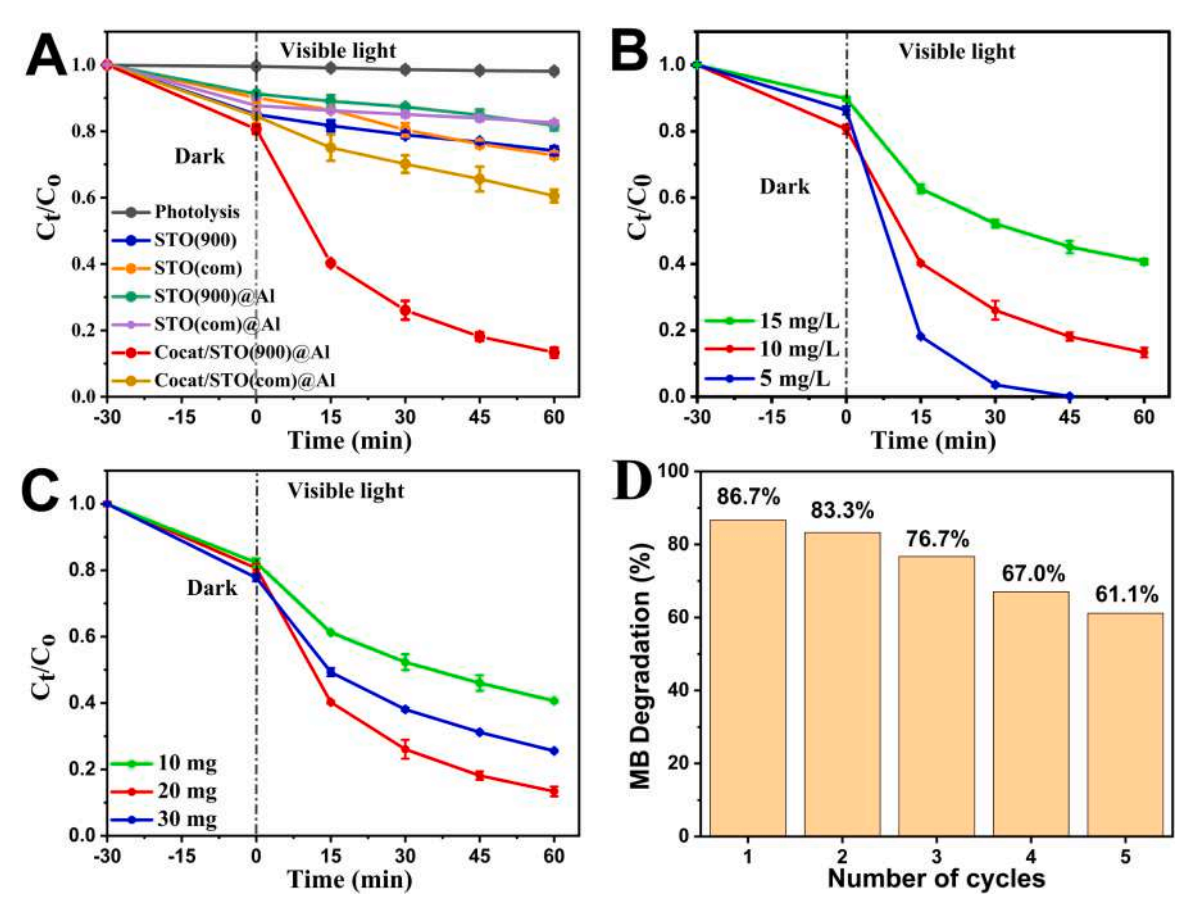


Fig. 4. Photodegradation curves of MB by different STO catalysts (a). Effect of the initial concentration of MB (b), photocatalyst dosage (c), and cyclic degradation rate of MB over Cocat/STO(900)@Al (d).

initial concentration of 5 mg/L. This decrease in efficiency can be attributed to the saturation of the photocatalyst surface by the dye molecules [62]. However, compared to 5 mg/L, a further increase in the dye concentration to 10 mg/L and 15 mg/L thickens the reaction medium, which makes it difficult for photons to penetrate the medium and activate the photocatalysts owing to the excessive number of ions. In addition, proportional amounts of oxidants and free radicals are required to form with increasing dye concentration to achieve a similar efficiency. However, the number of free radicals that formed in the reaction medium remained unchanged when the MB concentration was increased because the photocatalyst dosage remained unchanged (20 mg per 50 mL vessel), further explaining the decrease in photocatalyst efficiency with the increase in the MB concentration.

3.2.3. Reusability and photostability

Assessing the reusability of photocatalysts for environmental treatment is important for long-term waste management. After each experiment, the powdered photocatalysts were collected, centrifuged, washed with ethanol, and dried overnight for regeneration. The parameters used to evaluate the stability of Cocat/STO(900)@Al were similar to those described in previous experiments. Fig. 4d shows that, after five cycles, the photocatalytic decomposition rate decreases moderately (from 86.7% to 61.1%), and this was attributed to the deactivation process. This process is initiated by the accumulation of adsorbed reaction intermediates from the reaction medium on the surface of the photocatalyst, which can hinder the availability of the active centres of the photocatalyst, consequently decreasing its efficiency in subsequent cycles of use [63,64]. However, the involvement of gaseous reactants in the reaction would result in reaction products that may be less readily adsorbed onto the surface of the photocatalyst; hence, inhibitory layers are less likely to form on the surface, thus making it less susceptible to

such deactivation. For example, in the case of photocatalytic hydrogen generation or CO₂ reduction using similar photocatalysts, the products formed may be more readily desorbed from the photocatalyst surface, allowing it to regenerate and remain active for longer periods [39,48,65].

3.2.4. Study of photocatalytic decomposition kinetics

Studying the kinetics provides information about the mechanism of the photocatalytic removal of dyes. In this study, the pseudo-first-order and pseudo-second-order kinetic models for the photocatalytic degradation of MB were determined using Equations (1) [66] and (2) [67].

$$-ln\left(\frac{c_t}{c_0}\right) = k_1 t \tag{1}$$

$$\frac{1}{c_t} - \frac{1}{c_0} = k_2 t \tag{2}$$

where C_0 and C_t are the dye concentrations before and after photocatalytic reactions, respectively.

Fig. 5 (a–f) plots the linear dependence of (C_t/C_o) and separately $(1/C_t \cdot 1/C_0)$ on the reaction time. The values of the degradation rate constant (k) at different dye concentrations and catalyst mass loadings, together with their regression coefficients (R^2) , are presented in Table S1 in the supplementary materials. The R^2 values are well-correlated with the reaction kinetics of pseudo-first-order and pseudo-second-order reactions $(R^2 = 0.976$ and 0.968 for STO(900), $R^2 = 0.985$ and 0.981 for STO(900)@Al, and $R^2 = 0.975$ and 0.990 for Cocat/STO(900)@Al for pseudo-first- and pseudo-second-order, respectively). The calculations showed that the constants k_1 and k_2 for STO(900), STO(900)@Al, and Cocat/STO(900)@Al correspond to values of 0.0035, 0.0018, and

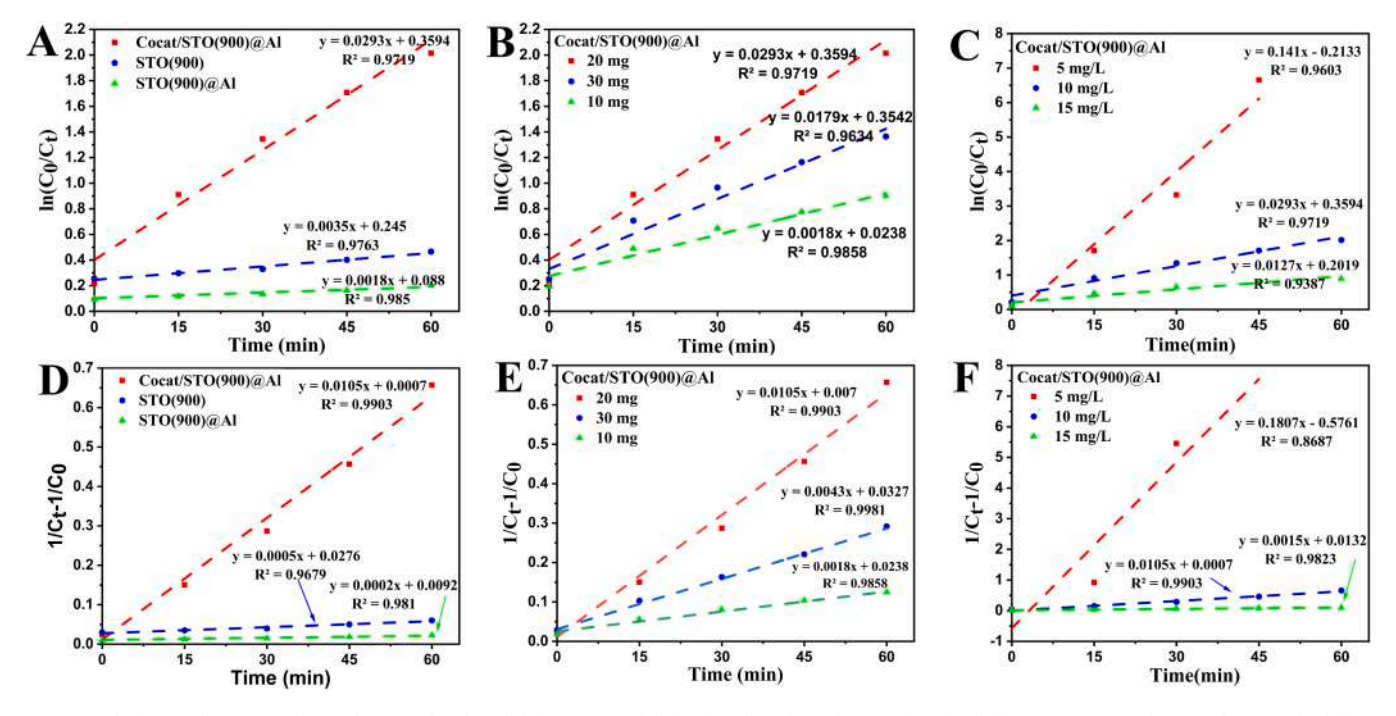


Fig. 5. Pseudo-first-order (a–c) and pseudo-second-order (d–f) kinetics models for the photodegradation of MB for different STO(900) photocatalysts (a, d), different initial concentrations (b, e), and photocatalyst dosages (c, f).

 $0.0293~\text{min}^{-1}$, and 0.0005, 0.0002, and $0.0105~\text{mol}^{-1}\text{L}^{-1}~\text{min}^{-1}$, respectively. The results further confirm that the Cocat/STO(900)@Al sample is the best photocatalyst for MB dye degradation, consistent with the above-described photodegradation results.

Table 1 summarises recent developments and research on the application of photocatalysts for degrading organic pollutants. The STO@Al photocatalyst photodeposited by dual split co-catalysts developed in this study exhibited higher efficiency and a higher degradation rate of MB compared with potential analogues based on SrTiO₃ [52, 68–71]. These results indicate the positive effect of separate photodeposition of the co-catalysts on the STO@Al photocatalyst surface and charge separation during visible-light irradiation, which promotes faster photoinduced charge transfer. Moreover, the co-catalysts can influence the photoabsorption ability in the visible range to enhance the overall photocatalytic activity compared to the photodegradation of MB.

Electrochemical impedance spectroscopy (EIS) measurements in a similar study showed that the sample with NiS and Rh/CrO $_{\rm x}$ /CoO $_{\rm y}$ cocatalysts loaded on Al-doped STO had the impedance semi-circle with the smallest radius, indicating more efficient photoelectron transfer [72]. This suggests that the deposition of co-catalysts such as NiS or RhCrCoO $_{\rm x}$ on STO lowers the interfacial charge transfer resistance and improves charge transport, thereby ultimately enhancing the photocatalytic activity of the material. A similar trend was observed in other studies of the photocatalytic hydrogen evolution reaction, in which EIS and photocurrent investigations were conducted on composite photocatalysts with dual co-catalysts deposited on Al-doped STO [59,73–75].

3.3. Photocatalytic mechanism

The putative mechanism of the photocatalytic decomposition of the

Table 1 Comparison of the synthesised Cocat/STO(900)@Al photocatalyst with recent research results.

Nº	Photocatalyst	Light source	Catalyst dose/ Volume of solution	MB dye conc./ ppm	Irradiation time (min)	Performance/ %	k1/ min ⁻¹	Refs.
1	SrTiO ₃ /rGO@Ag	Xenon lamp (150 W)	-	10	180	94	0.01457	[68]
2	Ag@SrTiO ₃ @CNT	Visible light; 150 W OSRAM lamp (< 420 nm)	0.8g/L	10	120	63	0.02416	[69]
3	Ag@SrTiO ₃ @CNT	Visible light; 150 W OSRAM lamp (< 420 nm)	0.8 g/L	5	105	100	-	[69]
4	GO-derived C-doped SrTiO ₃	Xenon lamp (ASB-XE-175-500 W)	0.25 g/	8	180	95	0.017	[52]
5	SrTiO ₃ /g-C ₃ N ₄	Visible light; six fluorescent lamps	10 mg/ 20 mL	10	420	40	0.00130	[70]
6	CdS–SnS	Visible light; (150 W) (>420 nm)	70 mg/ 70 mL	5	180	99	0.023	[76]
7	SrTiO ₃ /CZTS/Ag	Visible light; UV-filtered 150 W OSRAM lamp	1 g/L	10	90	90	0.0233	[71]
8	SrTiO ₃ /CZTS/Ag	Visible light; UV-filtered 150 W OSRAM lamp	1 g/L	5	90	100	0.0465	[71]
9	Rh/Cr ₂ O ₃ /SrTiO ₃ / CoOOH	Visible light; Mercury lamp (100W, >400 nm)	20 mg/ 50 mL	5	45	100	0.141	Our work
10	Rh/Cr ₂ O ₃ /SrTiO ₃ / CoOOH	Visible light; Mercury lamp (100W, ≥400 nm)	20 mg/ 50 mL	10	60	86.7	0.0293	Our work

MB dye and the physicochemical reaction characteristics of Rh/Cr₂O₃/ SrTiO3@Al/CoOOH were studied. As mentioned above, different cocatalysts were separately photodeposited on the anisotropic faces of the SrTiO₃@Al photocatalyst, where Rh³⁺ and Cr_(VI)O₄²⁻ were reduced and loaded on one face, whereas Co²⁺ was oxidised and loaded on the other face [24]. We assume that irradiation with visible light resulted in the photogenerated electrons being transferred from the conduction band of SrTiO₃@Al to the reductive Rh/Cr₂O₃ co-catalyst, where they react with the adsorbed O_2 and superoxide radicals $\bullet O_2^{2-}$ and $\bullet O_2^{-}$ [77]. Simultaneously, the photogenerated holes migrate from the valence band to the oxidative co-catalyst CoOOH, which promotes the oxidation of adsorbed MB or H₂O molecules to form •OH-. This proposed mechanism is consistent with that of previous studies involving SrTiO3-based photocatalysts with cocatalysts under similar experimental conditions [15,69,78,79]. Specifically, these studies suggest that photoirradiation produces both oxygen-centred radicals and hydroxyl radicals, with $\bullet O_2^$ playing a significant role in the degradation process [69,78]. These active species were identified in other research using scavengers such as isopropyl alcohol, benzoquinone, and ethylene-diaminetetraacetic acid to selectively capture $\bullet OH$, $\bullet O_2^-$, and h^+ , respectively. Therefore, although our study did not include additional experiments with scavengers, the proposed mechanism is supported by analogous work and experimental data from the literature. Further, active radicals in the form of $\bullet O^{2-}$, $\bullet O_2^{2-}$, and $\bullet OH$ initiate a series of oxidation reactions of MB molecules with final mineralisation to CO₂ and H₂O [57,78]. Consequently, the high photocatalytic activity for MB degradation was attributed to the synergistic effect of the separately photodeposited Rh/Cr₂O₃ and CoOOH co-catalysts (reductive and oxidative), which promoted the efficient separation and transfer of photogenerated electrons and holes.

3.4. DFT calculations

DFT modelling was used to analyse the electronic structures of STO and STO@Al and study their differences in the context of their energy band structures and densities of states. The supercells of pure STO, STO with oxygen vacancies, and STO doped with aluminium + oxygen vacancies (VO) are presented in Fig. 6. The results are consistent with those of previous studies [42,65,80]. The calculated value of the forbidden bandwidth using GGAs is 1.99 eV. This is narrower than the experimental value owing to the known underestimation of the GGA-DFT of the *in situ* Coulomb interaction for the d- and f-electrons. This problem is overcome by introducing the Hubbard parameter U (U = 5 and J = 4), which increases the value of the forbidden-zone width to 3.2 eV, which closely approximates the experimental value determined in this study. Fig. 7a shows the calculated zone structure of pure SrTiO₃ using the proposed computational model. The calculated value of the indirect forbidden gap of 3.19 eV is comparable to the experimental value of 3.15 eV. The anisotropy of the Ti 3d zones in the conduction band is clearly visible on the graph; as such, the almost dispersion-free characteristic of the zone in the GX direction can be observed. In the other directions, the quasiparticle energy increased rapidly. Thus, the excited electrons in the conduction zone are expected to preferentially occupy states in the GX direction and possess the lowest kinetic energy. This corresponds to the distribution of conduction electron impulses perpendicular to the cubic faces of the crystal, as observed in the experiment.

The total energies of the different supercell configurations with defects in the form of oxygen vacancies and the substitution of two Ti ions by Al ions were calculated. The configurations in which all three defects were unbound and uniformly distributed over the supercell exhibited the highest total energy. The location of one oxygen vacancy and one Al atom adjacent to each other lowered the system energy by 0.045 eV. The configuration in which an oxygen vacancy was located between two Al ions was the most stable (Fig. 6c). The formation energy of such a defect is 0.51 eV lower than that of the unbound configuration. The energy difference of 0.5 eV corresponds to the thermal energy kBT at temperatures of the order of 5000 K. Thus, at lower temperatures, oxygen vacancies and Al dopant ions tend to merge to form an Al-VO-Al structure. Fig. 7c, d shows the zone structure and density of electronic states, respectively, for a $3 \times 3 \times 3$ STO supercell with oxygen vacancies. The defect level formed by the electrons occupying the Ti atoms around the vacancy is clearly visible in the upper half of the forbidden gap, approximately 2.5 eV above the valence band boundary and 0.5 eV below the bottom of the conduction band. The presence of oxygen vacancies as defects in the crystallites explains the peculiarities of the photoabsorption measurements, exemplified by the peak at approximately 2.5 eV on the photoabsorption plot (Fig. 3a). In addition, the optical absorption measurements reveal a peak in the region of 0.4-0.8 eV [81,82]. This peak, which was observed for both pure STO and doped STO@Al, apparently corresponds to the excitation of electrons from the defect level to the conduction band, while the photoabsorption at 2.5 eV is associated with the excitation of valence band electrons to the defect level in the gap.

The addition of Al to STO as a dopant preferentially substitutes Ti ions, which would be expected based on the similar ionic radii of the Al³⁺ (54 pm) and Ti⁴⁺ (61 pm) ions in the SrTiO₃ lattice. The substitution of a trivalent Ti³⁺ ion by a trivalent Al³⁺ ion contributes to p-type conductivity [82-86], along with the formation of impurity Al levels near the valence band ceiling. We considered the effect of Al doping on the electronic structure of SrTi_{1-x}Al_xO₃ for x=0.04 and x=0.08, which correspond to one and two Al atoms in a $3 \times 3 \times 3$ supercell; x=0.04 corresponds to the doping level in the experiment (Supplementary Fig. S3). At such concentrations, the substitution had a limited effect on the electronic structure and left the size of the forbidden gap practically unchanged. In fact, the substitution mainly seems to have the effect of increasing the lifetime of excited electrons and holes owing to the substitution of Ti³⁺ recombination centres, and is consistent with the results of the XPS study (Fig. 2). Accordingly, the charge-separation efficiency on the faces of the nanocrystals increased.

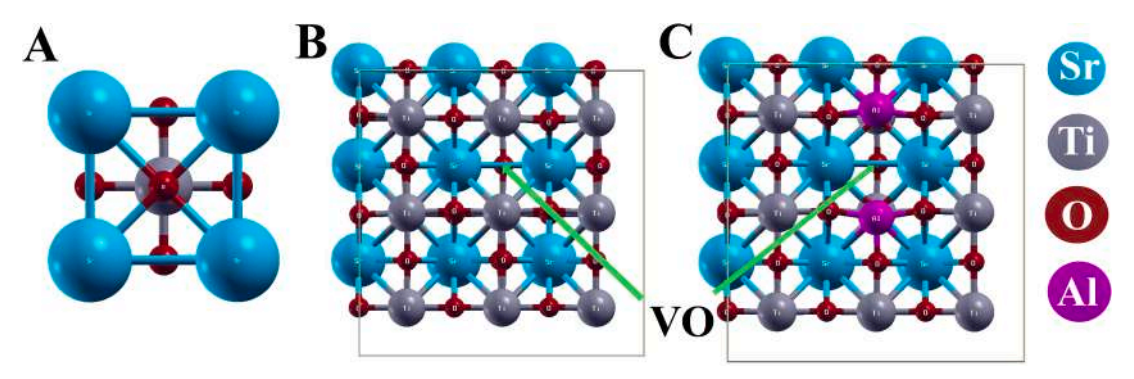


Fig. 6. Supercells of (a) undoped SrTiO₃, (b) SrTiO₃ with a single oxygen vacancy, and (c) Al-doped SrTiO₃ with a single oxygen vacancy (VO: oxygen vacancy).

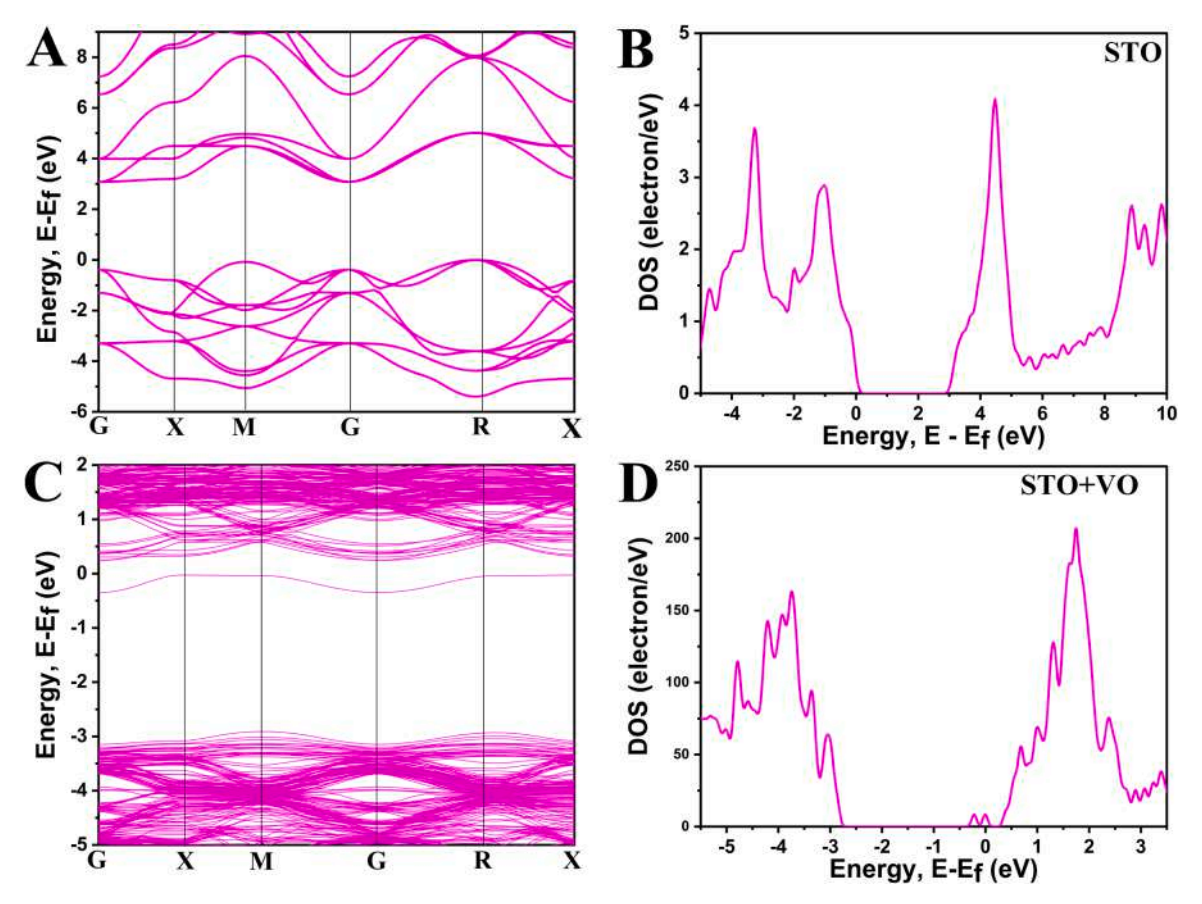


Fig. 7. DFT + U electronic band structure and density of states of bare STO (a, b) and STO + VO (c, d), respectively.

4. Conclusion

We reported the synthesis of a new composite, Rh/Cr₂O₃/ SrTiO₃@Al/CoOOH, with outstanding photocatalytic activity for the removal of MB under sunlight. Under the optimal synthesis conditions developed in this work, the composite proved highly efficient (over 87%) for the photocatalytic degradation of MB in visible light (400 nm). The advantageous properties of these composites are attributable to their controlled synthesis. The use of the molten flux method allowed the preparation of $SrTiO_3@Al$, wherein the Al^{3+} ions replaced the Ti^{3+} recombination centres, thus enabling more efficient photoinduced charge transfer. To further improve the charge separation and transfer and reduce the activation energy of the prepared photocatalyst, the cocatalysts Rh/Cr₂O₃ and CoOOH were deposited on the SrTiO₃@Al surface by photodeposition. The performance of the Rh/Cr₂O₃/SrTiO₃@Al/ CoOOH composite prepared in this way was 3.3 and 2.1 times higher than that of pure SrTiO3 and a similar composite based on commercial SrTiO₃, respectively. The efficiency of this process was attributed to several factors, including the effective separation of photoinduced charges, reduction of recombination, and, as a result, an increase in photocatalytic activity—achieved using anisotropically deposited dual co-catalysts capable of conducting both reductive and oxidative reactions during photocatalysis. DFT analysis revealed the inhomogeneity of the distribution of excited electrons in the conduction band and their preferred direction of motion in pure SrTiO3. The dynamics of the changes in the energy band and density of states of pure and aluminiumdoped SrTiO₃ were also analysed. The theoretical and experimental results confirmed the potential use of the developed photocatalytic composite for the efficient purification of water that contains organic pollutants.

CRediT authorship contribution statement

Zhengisbek Kuspanov: Writing – review & editing, Writing – original draft, Methodology, Investigation. Aigerim Serik: Methodology, Investigation. Nikita Matsko: Software, Methodology. Madina Bissenova: Methodology. Aidos Issadykov: Writing – review & editing, Supervision. Mukhtar Yeleuov: Writing – review & editing, Resources. Chingis Daulbayev: Writing – review & editing, Supervision, Resources, Project administration, Conceptualization.

Declaration of competing interest

The authors declare that they have no known competing financial interests or personal relationships that could have appeared to influence the work reported in this paper.

Acknowledgments

This research was funded by the Science Committee of the Ministry of Science and Higher Education of the Republic of Kazakhstan (Grant No AP14869381 and No BR18574073).

Supplementary materials

Supplementary material associated with this article can be found, in the online version, at doi:10.1016/j.jtice.2024.105806.

References

[1] Valadi FM, Ekramipooya A, Gholami MR. Selective separation of Congo Red from a mixture of anionic and cationic dyes using magnetic-MOF: experimental and DFT study. J Mol Liq 2020;318:114051. https://doi.org/10.1016/j. molliq.2020.114051.

- [2] Bagga V, Singh N, Khanuja M, Rani M, Kaur D. Enhanced photocatalytic degradation of Rhodamine B and Methylene blue by novel TiO2/SnSe-SnO2 hybrid nanocomposites under sunlight irradiation: correlation of photoluminescence property with photocatalytic activity. Mater Res Bull 2023;159:112109. https:// doi.org/10.1016/j.materresbull.2022.112109.
- [3] Niu J, Zhang Y, Shi J, Zhang Z, Ma Z, Yao B, et al. Microwave-based preparation of γ-Fe2O3/SrTiO3 photocatalyst for efficient degradation of organic pollutants in water. Mater Chem Phys 2022;288:126357. https://doi.org/10.1016/j. matchemphys.2022.126357.
- [4] Megbenu HK, Tauanov Z, Daulbayev C, Poulopoulos SG, Baimenov A. Effective removal of methylene blue dye by a novel 4-vinylpyridine-co-methacrylic acid cryogel: kinetic, isotherm, and breakthrough studies. J Chem Technol Biotechnol 2022;97:3375–84. https://doi.org/10.1002/jctb.7197.
- [5] Jin L, Sun X, Ren H, Huang H. Biological filtration for wastewater treatment in the 21st century: a data-driven analysis of hotspots, challenges and prospects. Sci Total Environ 2023;855:158951. https://doi.org/10.1016/j.scitotenv.2022.158951.
- [6] Megbenu HK, Daulbayev C, Nursharip A, Tauanov Z, Poulopoulos S, Busquets R, et al. Photocatalytic and adsorption performance of MXene@Ag/cryogel composites for sulfamethoxazole and mercury removal from water matrices. Environ Technol Innov 2023;32:103350. https://doi.org/10.1016/j.eti.2023.103350.
- [7] Wang S, Teramura K, Hisatomi T, Domen K, Asakura H, Hosokawa S, et al. Dual Ag/Co cocatalyst synergism for the highly effective photocatalytic conversion of CO 2 by H 2 O over Al-SrTiO 3. Chem Sci 2021;12:4940–8. https://doi.org/ 10.1039/D1SC00206F.
- [8] Kuspanov Z, Umirzakov A, Serik A, Baimenov A, Yeleuov M, Daulbayev C. Multifunctional strontium titanate perovskite-based composite photocatalysts for energy conversion and other applications. Int J Hydrog Energy 2023. https://doi. org/10.1016/j.ijhydene.2023.06.168.
- [9] Kuspanov Z, Bakbolat B, Baimenov A, Issadykov A, Yeleuov M, Daulbayev C. Photocatalysts for a sustainable future: innovations in large-scale environmental and energy applications. Sci Total Environ 2023;885:163914. https://doi.org/ 10.1016/j.scitotenv.2023.163914.
- [10] Su Z, Fang F, Li X, Han W, Liu X, Chang K. Synergistic surface oxygen defect and bulk Ti3+ defect engineering on SrTiO3 for enhancing photocatalytic overall water splitting. J Colloid Interface Sci 2022;626:662–73. https://doi.org/10.1016/j. jcis.2022.06.109.
- [11] Ruan J, Zhong T, Guo Y. Enhanced water splitting over ethylenediaminetetraacetate treated SrTiO3 photocatalysts with high crystallinity, reduced size, and surface nanostructure. J Colloid Interface Sci 2023;650:1424–33. https://doi.org/10.1016/j.jcis.2023.07.041.
- [12] Xiao J, Chen C, Chen S, Liu H, Peng T. Insight into the significantly enhanced photocatalytic CO2 reduction performance of Pt/MnOx dual cocatalysts on seaurchin-like anatase TiO2 microspheres. Chem Eng J 2021;425:131627. https://doi. org/10.1016/j.cei.2021.131627.
- [13] Daulbayev C, Sultanov F, Korobeinyk AV, Yeleuov M, Azat S, Bakbolat B, et al. Biowaste-derived few-layered graphene/SrTiO3/PAN as efficient photocatalytic system for water splitting. Appl Surf Sci 2021;549:149176. https://doi.org/10.1016/j.apsusc.2021.149176.
- [14] Bae HS, Patil RP, Hwang JH, Mahadik MA, Song MS, Chae WS, et al. Visible-light-responsive hydrogen-reduced CoOx loaded Rh/Sb:SrTiO3 nanocubic photocatalyst for degradation of organic pollutants and inactivation of bacteria. J Environ Chem Eng. 2023;11:109837. https://doi.org/10.1016/j.iecg.2023.109837
- Eng 2023;11:109837. https://doi.org/10.1016/j.jece.2023.109837.
 [15] Olagunju MO, Poole X, Blackwelder P, Thomas MP, Guiton BS, Shukla D, et al. Size-controlled SrTiO3 nanoparticles photodecorated with Pd cocatalysts for photocatalytic organic dye degradation. ACS Appl Nano Mater 2020;3:4904–12. https://doi.org/10.1021/acsanm.0c01086.
- [16] Yergaziyeva G, Kuspanov Z, Mambetova M, Khudaibergenov N, Makayeva N, Daulbayev C. Advancements in catalytic, photocatalytic, and electrocatalytic CO2 conversion processes: current trends and future outlook. J CO2 Util 2024;80: 102682. https://doi.org/10.1016/j.jcou.2024.102682.
- [17] Xu Y, Liang Y, He Q, Xu R, Chen D, Xu X, et al. Review of doping SrTiO3 for photocatalytic applications. Bull Mater Sci 2022;46:6. https://doi.org/10.1007/ s12034-022-02826-x.
- [18] Bantawal H, Shenoy US, Bhat DK. Vanadium-doped SrTiO3 Nanocubes: insight into role of vanadium in improving the photocatalytic activity. Appl Surf Sci 2020;513: 145858. https://doi.org/10.1016/j.apsusc.2020.145858.
- [19] Jiang J, Kato K, Fujimori H, Yamakata A, Sakata Y. Investigation on the highly active SrTiO3 photocatalyst toward overall H2O splitting by doping Na ion. J Catal 2020;390:81–9. https://doi.org/10.1016/j.jcat.2020.07.025.
- [20] Wang S, Teramura K, Hisatomi T, Domen K, Asakura H, Hosokawa S, et al. Effective driving of Ag-loaded and Al-doped SrTiO3 under irradiation at λ >300 nm for the photocatalytic conversion of CO2 by H2O. ACS Appl Energy Mater 2020;3:1468–75. https://doi.org/10.1021/acsaem.9b01927.
- [21] Zhao Z, Goncalves RV, Barman SK, Willard EJ, Byle E, Perry R, et al. Electronic structure basis for enhanced overall water splitting photocatalysis with aluminum doped SrTiO 3 in natural sunlight. Energy Environ Sci 2019;12:1385–95. https:// doi.org/10.1039/C9EE00310J.
- [22] Tian L, Guan X, Dong Y, Zong S, Dai A, Zhang Z, et al. Improved overall water splitting for hydrogen production on aluminium-doped SrTiO3 photocatalyst via tuned surface band bending. Environ Chem Lett 2023;21:1257–64. https://doi. org/10.1007/s10311-023-01580-8.
- [23] Wang S, Teramura K, Hisatomi T, Domen K, Asakura H, Hosokawa S, et al. Optimized synthesis of Ag-modified Al-doped SrTiO3 photocatalyst for the conversion of CO2 Using H2O as an electron donor. ChemistrySelect 2020;5: 8779–86. https://doi.org/10.1002/slct.202001693.

- [24] Takata T, Jiang J, Sakata Y, Nakabayashi M, Shibata N, Nandal V, et al. Photocatalytic water splitting with a quantum efficiency of almost unity. Nature 2020;581:411–4. https://doi.org/10.1038/s41586-020-2278-9.
- [25] Meng A, Zhang L, Cheng B, Yu J. Dual cocatalysts in TiO2 photocatalysis. Adv Mater 2019;31:1807660. https://doi.org/10.1002/adma.201807660.
- [26] Wang Z, Li C, Domen K. Recent developments in heterogeneous photocatalysts for solar-driven overall water splitting. Chem Soc Rev 2019;48:2109–25. https://doi. org/10.1039/C8CS00542G.
- [27] Zhu J, Pang S, Dittrich T, Gao Y, Nie W, Cui J, et al. Visualizing the nano cocatalyst aligned electric fields on single photocatalyst particles. Nano Lett 2017;17: 6735–41. https://doi.org/10.1021/acs.nanolett.7b02799.
- [28] Goto Y, Hisatomi T, Wang Q, Higashi T, Ishikiriyama K, Maeda T, et al. A particulate photocatalyst water-splitting panel for large-scale solar hydrogen generation. Joule 2018;2:509–20. https://doi.org/10.1016/j.joule.2017.12.009.
- [29] Nishiyama H, Yamada T, Nakabayashi M, Maehara Y, Yamaguchi M, Kuromiya Y, et al. Photocatalytic solar hydrogen production from water on a 100-m2 scale. Nature 2021;598:304–7. https://doi.org/10.1038/s41586-021-03907-3.
- [30] Di T, Deng Q, Wang G, Wang S, Wang L, Ma Y. Photodeposition of CoOx and MoS2 on CdS as dual cocatalysts for photocatalytic H2 production. J Mater Sci Technol 2022;124:209–16. https://doi.org/10.1016/j.jmst.2021.12.071.
- [31] Qin Y, Fang F, Xie Z, Lin H, Zhang K, Yu X, et al. La,Al-codoped SrTiO3 as a photocatalyst in overall water splitting: significant surface engineering effects on defect engineering. ACS Catal 2021;11:11429–39. https://doi.org/10.1021/ acceptal 1002874
- [32] Zhu S, Liao W, Zhang M, Liang S. Design of spatially separated Au and CoO dual cocatalysts on hollow TiO2 for enhanced photocatalytic activity towards the reduction of CO2 to CH4. Chem Eng J 2019;361:461–9. https://doi.org/10.1016/j. cei.2018.12.095.
- [33] Wang B, Li P, Du C, Wang Y, Gao D, Li S, et al. Synergetic effect of dual co-catalysts on the activity of BiVO 4 for photocatalytic carbamazepine degradation. RSC Adv 2019;9:41977–83. https://doi.org/10.1039/C9RA07152K.
- [34] Shi W, Shu K, Sun H, Ren H, Li M, Chen F, et al. Dual enhancement of capturing photogenerated electrons by loading CoP nanoparticles on N-deficient graphitic carbon nitride for efficient photocatalytic degradation of tetracycline under visible light. Sep Purif Technol 2020;246:116930. https://doi.org/10.1016/j. seppur.2020.116930.
- [35] Ren K, Lv M, Xie Q, Zhang C, Shi H. Dual BN quantum dot/Ag co-catalysts synergistically promote electron-hole separation on g-C3N4 nanosheets for efficient antibiotics oxidation and Cr(VI) reduction. Carbon 2022;186:355–66. https://doi.org/10.1016/j.carbon.2021.10.050.
- [36] Kudaibergen A, Kuspanov ZB, Issadykov A, Beisenov R, Mansurov Z, Yeleuov M, Daulbayev C. Synthesis, structure, and energetic characteristics of perovskite photocatalyst SrTiO3: an experimental and DFT study. Eurasian Chem-Technol J 2023.
- [37] Sultanov F, Daulbayev C, Bakbolat B, Daulbayev O, Bigaj M, Mansurov Z, et al. Aligned composite SrTiO3/PAN fibers as 1D photocatalyst obtained by electrospinning method. Chem Phys Lett 2019;737:136821. https://doi.org/ 10.1016/j.cnjett.2019.136821
- [38] Bissenova M, Umirzakov A, Mit K, Mereke A, Yerubayev Y, Serik A, et al. Synthesis and study of SrTiO3/TiO2 hybrid perovskite nanotubes by electrochemical anodization. Molecules 2024;29:1101. https://doi.org/10.3390/ molecules29051101.
- [39] Chiang TH, Lyu H, Hisatomi T, Goto Y, Takata T, Katayama M, et al. Efficient photocatalytic water splitting using Al-doped SrTiO3 coloaded with molybdenum oxide and rhodium-chromium oxide. ACS Catal 2018;8:2782–8. https://doi.org/ 10.1021/acscatal.7b04264.
- [40] Giannozzi P, Baroni S, Bonini N, Calandra M, Car R, Cavazzoni C, et al. QUANTUM ESPRESSO: a modular and open-source software project for quantum simulations of materials. J Phys Condens Matter 2009;21:395502. https://doi.org/10.1088/ 0953-8984/21/39/395502
- [41] Dudarev SL, Botton GA, Savrasov SY, Humphreys CJ, Sutton AP. Electron-energy-loss spectra and the structural stability of nickel oxide: an LSDA+U study. Phys Rev B 1998;57:1505–9. https://doi.org/10.1103/PhysRevB.57.1505.
- [42] Wang YR, Tao HL, Cui Y, Liu SM, He M, Song B, et al. Investigations on tuning the band gaps of Al doped SrTiO3. Chem Phys Lett 2020;757:137879. https://doi.org/ 10.1016/j.cplett.2020.137879.
- [43] Ph G, Gonze X, Ph L, Michenaud JP. Born effective charges of barium titanate: band-by-band decomposition and sensitivity to structural features. Phys Rev B 1995;51:6765–8. https://doi.org/10.1103/PhysRevB.51.6765.
- [44] Shah SH, Bristowe PD, Kolpak AM, Rappe AM. First principles study of three-component SrTiO3/BaTiO3/PbTiO3 ferroelectric superlattices. J Mater Sci 2008; 43:3750–60. https://doi.org/10.1007/s10853-007-2212-7.
- [45] Roy PK, Bera J. Formation of SrTiO3 from Sr-oxalate and TiO2. Mater Res Bull 2005;40:599–604. https://doi.org/10.1016/j.materresbull.2005.01.010.
 [46] Bakbolat B, Daulbayev C, Sultanov F, Beissenov R, Umirzakov A, Mereke A, et al.
- [46] Bakbolat B, Dauidayev C, Sultanov F, Beissenov R, Umirzakov A, Mereke A, et al. Recent developments of TiO2-based photocatalysis in the hydrogen evolution and photodegradation: a review. Nanomaterials 2020;10:1790. https://doi.org/ 10.3390/nano10091790.
- [47] Ma Y, Wu Z, Wang H, Wang G, Zhang Y, Hu P, et al. Synthesis of nanocrystalline strontium titanate by a sol-gel assisted solid phase method and its formation mechanism and photocatalytic activity. CrystEngComm 2019;21:3982–92. https:// doi.org/10.1039/C9CE00495E.
- [48] Shen Q, Kang W, Ma L, Sun Z, Jin B, Li H, et al. Tuning the anisotropic facet of SrTiO3 to promote spatial charge separation for enhancing photocatalytic CO2 reduction properties. Chem Eng J 2023;478:147338. https://doi.org/10.1016/j. cei.2023.147338.

- [49] Murthy DHK, Nandal V, Furube A, Seki K, Katoh R, Lyu H, et al. Origin of enhanced overall water splitting efficiency in aluminum-doped SrTiO3 photocatalyst. Adv Energy Mater 2023;13:2302064. https://doi.org/10.1002/aenm.202302064.
- [50] Din MI, Khalid R, Najeeb J, Hussain Z. Fundamentals and photocatalysis of methylene blue dye using various nanocatalytic assemblies- a critical review. J Clean Prod 2021;298:126567. https://doi.org/10.1016/j.jclepro.2021.126567.
- [51] Li R, Takata T, Zhang B, Feng C, Wu Q, Cui C, et al. Criteria for efficient photocatalytic water splitting revealed by studying carrier dynamics in a model Aldoped SrTiO3 photocatalyst. Angew Chem Int Ed 2023;62:e202313537. https:// doi.org/10.1002/anie.202313537.
- [52] Chang CW, Hu C. Graphene oxide-derived carbon-doped SrTiO3 for highly efficient photocatalytic degradation of organic pollutants under visible light irradiation. Chem Eng J 2020;383:123116. https://doi.org/10.1016/j.cej.2019.123116.
- [53] Tan H, Zhao Z, Zhu W, Coker EN, Li B, Zheng M, et al. Oxygen vacancy enhanced photocatalytic activity of pervoskite SrTiO3. ACS Appl Mater Interfaces 2014;6: 19184–90. https://doi.org/10.1021/am5051907.
- [54] Putri YE, Muharmi M, Wendari TP, Wellia DV. Growth of SrTiO3 thin film on a glass substrate by the sol-gel-assisted hydrothermal method. Surf Interfaces 2023; 40:103026. https://doi.org/10.1016/j.surfin.2023.103026.
- [55] Tan P, Zhu A, Liu Y, Ma Y, Liu W, Cui H, et al. Insights into the efficient charge separation and transfer efficiency of La,Cr-codoped SrTiO3 modified with CoP as a noble-metal-free co-catalyst for superior visible-light driven photocatalytic hydrogen generation. Inorg Chem Front 2018;5:679–86. https://doi.org/10.1039/ C70100769H
- [56] Nakamoto T, Iguchi S, Naniwa S, Tanaka T, Teramura K. Mg-doped SrTiO 3 photocatalyst with Ag–Co cocatalyst for enhanced selective conversion of CO 2 to CO using H 2 O as the electron donor. Catal Sci Technol 2023;13:4534–41. https://doi.org/10.1039/D3CY00576C.
- [57] Asgari S, Mohammadi Ziarani G, Badiei A, Vasseghian Y. A ternary composite nanofibrous photocatalyst: FcLR-gC3N4/polyisothianaphthene/polyacrylonitrile for degradation of organic dyes. J Taiwan Inst Chem Eng 2024;163:105672. https://doi.org/10.1016/j.jtice.2024.105672.
- [58] Asgari S, Ziarani GM, Badiei A, Varma RS, Iravani S, Mohajer F. Enhanced photocatalytic activity of modified black phosphorus-incorporated PANi/PAN nanofibers. RSC Adv 2023;13:17324–39. https://doi.org/10.1039/D3RA01744C
- [59] Jiang J, Zhou Y, Zhang J, Gao K, Pan J, Dong P. Accelerating the charge separation from the Schottky junction effect of Pd-loaded Al: SrTiO3 for highly efficient photocatalytic hydrogen evolution. Int J Hydrog Energy 2024;82:646–54. https:// doi.org/10.1016/j.ijhydene.2024.07.441.
- [60] Abd Elkodous M, El-Khawaga AM, Abouelela MM, Abdel Maksoud MIA. Cocatalyst loaded Al-SrTiO3 cubes for Congo red dye photo-degradation under wide range of light. Sci Rep 2023;13:6331. https://doi.org/10.1038/s41598-023-33249-1.
- [61] Falah S, Ghorbani M, Ahmadpour J. Photocatalytic degradation of anionic and cationic dyes over PPy/CuFe2O4 nanocomposite under visible-light and bactericidal action. J Taiwan Inst Chem Eng 2023;144:104767. https://doi.org/ 10.1016/j.itice.2023.104767.
- [62] Azimifar M, Ghorbani M, Peyravi M. Fabrication and evaluation of a photocatalytic membrane based on Sb2O3/CBO composite for improvement of dye removal efficiency. J Mol Struct 2022;1270:133957. https://doi.org/10.1016/j. molstruc.2022.133957.
- [63] Nguyen CH, Juang RS. Efficient removal of methylene blue dye by a hybrid adsorption-photocatalysis process using reduced graphene oxide/titanate nanotube composites for water reuse. J Ind Eng Chem 2019;76:296–309. https:// doi.org/10.1016/j.jiec.2019.03.054.
- [64] Mahanthappa M, Kottam N, Yellappa S. Enhanced photocatalytic degradation of methylene blue dye using CuSCdS nanocomposite under visible light irradiation.
 April Surf Sci 2010 477: 629 29 https://doi.org/10.1016/j.composite.2010.10170
- Appl Surf Sci 2019;475:828–38. https://doi.org/10.1016/j.apsusc.2018.12.178.
 [65] Fang F, Xu F, Su Z, Li X, Han W, Qin Y, et al. Understanding targeted modulation mechanism in SrTiO3 using K+ for solar water splitting. Appl Catal B Environ 2022;316:121613. https://doi.org/10.1016/j.apcatb.2022.121613.
- [66] Serik A., Kuspanov Z., Bissenova M., Idrissov N., Yeleuov M., Umirzakov A., et al. Effective photocatalytic degradation of sulfamethoxazole using Pan/Srtio3 nanofibers 2024. 10.2139/ssrn.4758700.
- [67] Verma N, Chundawat TS, Chandra H, Vaya D. An efficient time reductive photocatalytic degradation of carcinogenic dyes by TiO2-GO nanocomposite. Mater Res Bull 2023;158:112043. https://doi.org/10.1016/j. materresbull.2022.112043.

- [68] Guediri MK, Chebli D, Bouguettoucha A, Bourzami R, Amrane A. Interfacial coupling effects on adsorptive and photocatalytic performances for photoresponsive graphene-wrapped SrTiO3@Ag under UV-visible light: experimental and DFT approach. Environ Sci Pollut Res 2022;29:28098–114. https://doi.org/10.1007/s11356-021-17543-x.
- [69] Sharifian K, Mahdikhah V, Sheibani S. Ternary Ag@SrTiO3@CNT plasmonic nanocomposites for the efficient photodegradation of organic dyes under the visible light irradiation. Ceram Int 2021;47:22741–52. https://doi.org/10.1016/j. ceramint.2021.04.291.
- [70] Ferreira MA, da Silva G, Lopes OF, Mastelaro VR, Ribeiro C, Pires MJM, et al. Fabrication of SrTiO3/g-C3N4 heterostructures for visible light-induced photocatalysis. Mater Sci Semicond Process 2020;108:104887. https://doi.org/ 10.1016/j.mssp.2019.104887.
- [71] Alimohammadi E, Mahdikhah V, Alirezazadeh F, Sheibani S, Farzin YA. Plasmonic resonance and type-I heterojunction interface in SrTiO3/CZTS/Ag nanocomposite for enhanced photocatalytic degradation of organic pollutants. Mater Today Chem 2023;28:101378. https://doi.org/10.1016/j.mtchem.2023.101378.
- [72] Cheng H, Bai Z, Cong R, Zhou Z, Zhang Z. NiS modified SrTiO3:Al bifunctional photocatalyst for H2 generation and cathodic protection. Ceram Int 2024;50: 25518–27. https://doi.org/10.1016/j.ceramint.2024.04.286.
- [73] Zong S, Tian L, Guan X, Cheng C, Shi J, Guo L. Photocatalytic overall water splitting without noble-metal: decorating CoP on Al-doped SrTiO3. J Colloid Interface Sci 2022;606:491–9. https://doi.org/10.1016/j.jcis.2021.08.049.
- [74] Zhang J, Cao Y, Chen F, Cai M, Bai J, Xue J, et al. Modulating the electron interaction of Cu-Ni hybrid sites for boosting photocatalytic hydrogen evolution over Al-doped SrTiO3. Surf Interfaces 2024;46:104156. https://doi.org/10.1016/j. surfin.2024.104156.
- [75] Sahu AK, Pokhriyal M, Banerjee D, Rufford TE, Upadhyayula S. An indirect Z-scheme heterostructure of nano-gold layer immobilized Cu-Al-doped SrTiO3 and CoOx-WO3 for photocatalytic CO2 reduction. Chem Eng J 2024;487:150716. https://doi.org/10.1016/j.cej.2024.150716.
- [76] Alikarami S, Soltanizade A, Rashchi F. Synthesis of CdS–SnS photocatalyst by chemical co-precipitation for photocatalytic degradation of methylene blue and rhodamine B under irradiation by visible light. J Phys Chem Solids 2022;171: 110993. https://doi.org/10.1016/j.jpcs.2022.110993.
- [77] Wang B, Li P, Du C, Wang Y, Gao D, Li S, et al. Synergetic effect of dual co-catalysts on the activity of BiVO4 for photocatalytic carbamazepine degradation. RSC Adv 2019;9:41977–83. https://doi.org/10.1039/C9RA07152K.
- [78] Sohrabian M, Mahdikhah V, Alimohammadi E, Sheibani S. Improved photocatalytic performance of SrTiO3 through a Z-scheme polymeric-perovskite heterojunction with g-C3N4 and plasmonic resonance of Ag mediator. Appl Surf Sci 2023;618:156682. https://doi.org/10.1016/j.apsusc.2023.156682.
- [79] Garcia CR, Oliva J, Chávez D, Esquivel B, Gómez-Solís C, Martínez-Sánchez E, et al. Effect of Bismuth Dopant on the Photocatalytic Properties of SrTiO3 Under Solar Irradiation. Top Catal 2021;64:155–66. https://doi.org/10.1007/s11244-020-01301-z
- [80] Ahmed S, Hasan T, Faysal A, Nishat SS, Khan MNI, Kabir A, et al. A DFT+U approach to doped SrTiO3 for solar harvesting applications. Comput Mater Sci 2022;214:111743. https://doi.org/10.1016/j.commatsci.2022.111743.
- [81] Zhao Z, Goncalves RV, Barman SK, Willard EJ, Byle E, Perry R, et al. Electronic structure basis for enhanced overall water splitting photocatalysis with aluminum doped SrTiO3 in natural sunlight. Energy Environ Sci 2019;12:1385–95. https:// doi.org/10.1039/C9FF003101
- [82] Amor LB, Belgacem B, Filhol JS, Doublet ML, Yahia MB, Hassen RB. New p-type Alsubstituted SrSnO3 perovskites for TCO applications? Chem Commun 2020;56: 2566–9. https://doi.org/10.1039/C9CC09212A.
- [83] Blazey KW. Optical absorption edge of SrTiO₃ around the 105-K phase transition. Phys Rev Lett 1971;27:146–8.
- [84] Toyoda T, Yabe M. The temperature dependence of the refractive indices of fused silica and crystal quartz. J Phys D Appl Phys 1983;16:L97–100. https://doi.org/ 10.1088/0022-3727/16/5/002.
- [85] Higuchi T, Tsukamoto T, Yamaguchi S, Kobayashi K, Sata N, Ishigame M, et al. Observation of acceptor level of p-type SrTiO3 by high-resolution soft-X-ray absorption spectroscopy. Nucl Instrum Methods Phys Res Sect B Beam Interact Mater At 2003;199:255–9. https://doi.org/10.1016/S0168-583X(02)01580-X.
- [86] Guo H, Liu L, Fei Y, Xiang W, Lü H, Dai S, et al. Optical properties of p-type Indoped SrTiO3 thin films. J Appl Phys 2003;94:4558–62. https://doi.org/10.1063/ 1.1606510.

https://doi.org/10.18321/ectj1636

Efficient Photocatalytic Hydrogen Evolution via Cocatalyst Loaded Al-doped SrTiO₃

Zh. Kuspanov^{1,2}, A. Serik^{1,2}*, A. Baratov^{1,2}, U. Abdikarimova^{1,2}, N. Idrissov^{1,2}, M. Bissenova^{1,2,3}, Ch. Daulbayev^{1,2}

¹Satbayev University, 22 Satbayev str., 050013, Almaty, Kazakhstan ²Institute of Nuclear Physics, 1 Ibragimov str., 050032 Almaty, Kazakhstan ³Institute of Physics and Technology, 11 Ibragimov str., 050032, Almaty, Kazakhstan

Article info

Received: 6 May 2024

Received in revised form: 27 June 2024

Accepted: 15 August 2024

Keywords

Photocatalytic water splitting; SrTiO₃; Cocatalysts; H₂ evolution

Abstract

The growing reliance on fossil fuels is causing significant environmental issues, prompting the search for renewable energy sources. Hydrogen energy, which produces only water vapor, is a promising solution. This study focuses on developing an aluminum-doped $SrTiO_3$ photocatalyst with dual cocatalysts (Rh/Cr₂O₃ and CoOOH) for efficient photocatalytic water splitting. Using a simple chemical deposition method, high-purity and crystalline $SrTiO_3$ was synthesized and thoroughly characterized. The results show that the modified $SrTiO_3$ achieved significantly higher photocatalytic activity, with $Rh/Cr_2O_3/SrTiO_3@Al/CoOOH$ producing 11.04 mmol g^{-1} h^{-1} of H_2 and 4.69 mmol g^{-1} h^{-1} of O_2 . This work demonstrates the effectiveness of dual cocatalyst deposition and aluminum doping in enhancing photocatalytic performance by improving charge separation and reducing recombination.

1. Introduction

With population growth and technological advances, dependence on fossil energy sources is increasing, despite their limited reserves [1, 2]. The use of these fuels is accompanied by significant greenhouse gas emissions, leading to global environmental problems [3, 4]. Therefore, the scientific community is directing its efforts towards the development of renewable and clean energy sources [5, 6]. Hydrogen energy, of which water vapor is a by-product, is seen as one of the promising energy sources and requires innovative solutions to create cost-effective and environmentally friendly methods for mass production of hydrogen [7, 8, 9, 10]. One such method is the conversion of solar energy into green hydrogen through photocatalytic decomposition of water. In this context, the

development of efficient photocatalysts becomes a key challenge. Oxide semiconductors such as Sr-TiO₃ with a 3.2 eV forbidden bandgap have proven to be efficient photocatalysts for water splitting under UV irradiation without applying an external voltage [11]. However, high-temperature synthesis of SrTiO₃ often produces defects that reduce the photocatalysis efficiency [12]. In particular, oxygen vacancies promote the reduction of Ti⁴⁺ to Ti³⁺, which serve as recombination centers for the photogenerated electron-hole pairs [12]. Nevertheless, the ABO₃-type perovskite structure has considerable flexibility, which allows improving the photocatalytic activity by controlling and minimizing defects through cation substitution in the Aand B-sites [13]. Sources emphasize that efficient separation of photogenerated electron-hole pairs can significantly enhance photocatalytic activity [14]. Fine-tuning the physicochemical properties of the photocatalyst at the atomic level, e.g., through crystal facet engineering, contributes to charge

E-mail address: aigerim.serik3508@gmail.com

^{*}Corresponding author.

selective separation and increased activity. Different crystal faces can direct electrons and holes to separate regions for reduction and oxidation, as observed in photocatalysts such as BiVO₄, BiOBr, and SrTiO₃ [15]. In addition, one approach to increase the efficiency of photocatalytic reactions is the use of dual co-catalysts deposited on the photocatalyst surface. Oxidation and reduction co-catalysts play an important role by helping to form active centers and facilitating the transfer of electrons and holes to different zones on the photocatalyst surface. Studies have shown that this promotes better separation of photogenerated pairs of electrons and holes, which increases the quantum yield of the reaction [16]. While the quantum efficiency of existing photocatalysts for water splitting is usually less than 10% at UV light, T. Takata and his colleagues were able to achieve an external quantum efficiency of up to 96% at wavelengths from 350 to 360 nm [17] using a modified photocatalyst based on aluminum-doped strontium titanate. This allows the hydrogen and oxygen release reactions to be carried out separately on different crystal faces of semiconductor particles, achieving maximum quantum efficiency for water splitting and eliminating charge recombination losses. Nevertheless, studies on efficient photocatalytic total water splitting using dual co-catalysts are currently insufficient, which opens the door for further research in this area.

Previous studies in our research [18, 19, 20] extensively explored the synthesis of SrTiO₃ nanoparticles using a simple and cost-effective chemical precipitation method followed by calcination. This approach enables the production of SrTiO₃ nanoparticles with relatively high purity while maintaining good photocatalytic activity. However, modifying pure SrTiO₃ by aluminum doping to introduce defect engineering, followed by the photodeposition of dual co-catalysts, could further enhance the photocatalytic performance of this material, particularly for water splitting and hydrogen production.

The aim of this work is to develop and study a photocatalyst based on aluminum-doped SrTiO₃ with the addition of double separately photodeposited co-catalysts for efficient water splitting. A simple chemical precipitation method was employed to synthesize SrTiO₃ of high purity and crystallinity. The structure, morphology and photocatalytic activity of the obtained materials were studied in detail. The results demonstrate a new and simple approach to the controlled synthesis and modification of SrTiO₃, providing high efficiency of photocatalytic water splitting.

2. Materials and methods

2.1 Materials

The main reagents and chemicals were purchased from Kazakhstan and the USA. These include TiO_2 (particle size less than 25 nm, purity 99.7%, Sigma-Aldrich, USA), $Sr(NO_3)_2$ (purity \geq 98%, Sigma-Aldrich, USA), $(COOH)_2$ -2H $_2O$ (purity greater than 98%, Sigma-Aldrich, USA), $Sr(I_2-6H_2O)$ (particle size 50 nm, Sigma-Aldrich, USA), $Sr(I_2-6H_2O)$ (Laborpharma, Kazakhstan), $Sr(I_3-6H_2O)$ (Rh content 38–40%, Sigma-Aldrich, USA), $Sr(I_3-6H_2O)$ (purity \leq 98%, Sigma-Aldrich, USA), and $Sr(I_3-6H_2O)$ (purity \leq 98%, Laborpharma, Kazakhstan). All chemicals were of analytical grade and did not require additional purification. Double distilled water was used for synthesis and photocatalytic experiments.

2.2 Synthesis of SrTiO₃

SrTiO₃ powder was synthesized using a simple chemical precipitation method [18, 19, 20]. First, 0.12 M aqueous solution of Sr(NO₃)₂ was mixed with TiO₂ in distilled water at a Sr/Ti molar ratio of 1:1 and subjected to ultrasonic treatment for 30 minutes. A 0.4 M solution of (COOH)₂-2H₂O was used as a reducing agent, which was added to the suspension dropwise under active stirring using a magnetic stirrer. The pH value of the suspension was then adjusted to 6-7 using 10% aqueous ammonia solution. After precipitation, the mixture was purified from excess ammonia by removing the surface liquid layer. The resulting precipitate was washed 5 times using centrifugation and dried at 60 °C for 16 hours. Finally, the product was calcined at 1100 °C in a muffle furnace in air.

2.3 Synthesis of SrTiO₃@Al

The alloying of $SrTiO_3$ powder with aluminum is carried out by the fluxing method developed by the team of Domen [17]. To synthesize $SrTiO_3$ @ Al, powders of 1.835 g $SrTiO_3$, 20.39 mg Al_2O_3 , and 15.85 g $SrCl_2$ are mixed in an agate mortar for 15 min, or longer, until homogeneous. After thorough mixing, the mixture is calcined at 1150 °C for 10 h in a muffle furnace. The resulting powder is then ultrasonically treated to completely remove residual salt, after which it is washed 5 times with hot distilled water using centrifugation and dried for 20 h at 60 °C.

2.4 Photodeposition of Rh/Cr₂O₃/SrTiO₃@Al/CoOOH

Selective deposition of Rh/Cr₂O₃ and CoOOH double co-catalysts on the surface of SrTiO₃-based photocatalyst was carried out by photodeposition method. First, 0.1 g of SrTiO₃ or SrTiO₃@Al powder was mixed with 50 ml of distilled water and subjected to ultrasonic treatment for 30 minutes. The resulting suspension was placed in a photochemical reactor and irradiated with ultraviolet light from a 10 W mercury lamp under vigorous stirring. After magnetic stirring was started, 50 μl of RhCl₃-6H₂O solution (2 mg/ml concentration) was added to the mixture and irradiation was continued for 10 minutes. Then 25 μl of K₂CrO₄ solution (2 mg(Cr)/ml) was added and irradiation was continued for another 5 minutes. Finally, 25 μ l of Co(NO₃)₂ solution (2 mg(Co)/ml) was added and irradiated for 5 minutes. The resulting samples were washed several times and dried at 70 °C overnight.

2.5 Characterization

X-ray diffraction (XRD) on a Drone-8 instrument, scanning electron microscopy (SEM) with energy dispersive X-ray spectrometer (EDX), high-resolution transmission electron microscopy (HRTEM), and X-ray photoelectron spectroscopy (XPS) were used to characterize the synthesized samples. XRD measurements were performed over an angle range of 5-70° with a step size of 0.01° and an accuracy of ±0.015°. SEM and EDX were performed on a Zeiss Crossbeam 540 at an accelerating voltage of 5-20 kV. TEM was used to analyze the structure and distribution of co-catalysts on the photocatalyst surface using a JEM-2100 LaB6 at 80 kV. XPS was performed on a Microtech Multilab 3000 VG with Mg and Al sources, and the C1s level at 284.8 eV was used for calibration. Diffuse reflectance spectra (UV-Vis DRS) were recorded on a Perkin Elmer Lambda 35 spectrophotometer in the range of 200–800 nm.

2.6 Photocatalytic reaction

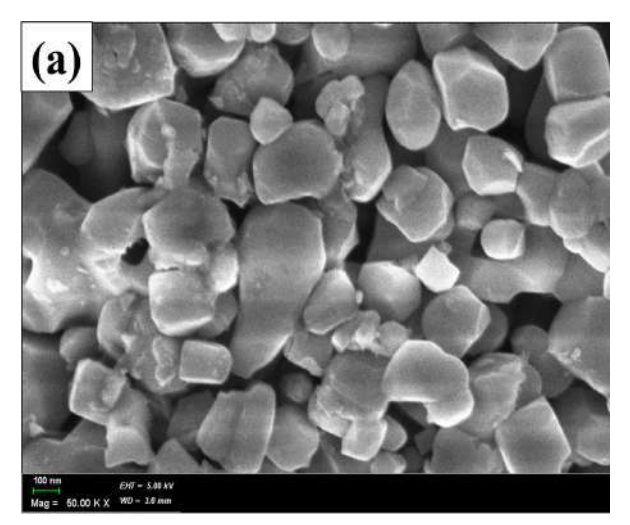
To determine the photocatalytic activity of the obtained samples, 25 mg of photocatalytic sample was suspended in 50 ml of distilled water and stirred for 30 min without the addition of sacrificial agents. The photocatalytic activity was evaluated by decomposition of water followed by release of hydrogen and oxygen. A Chromos-1000 chromatograph with 3 mm columns filled with NaX and PORAPAK Q was used to analyze the released gases. The photocatalytic water

decomposition process was carried out in a photochemical reactor (Shanghai Leewen Scientific Instrument Co., Ltd., China), where a 10 W high-pressure mercury lamp with wavelength λ_{max} = 254 nm was used as a radiation source. The distance between a 50 ml quartz flask and the lamp was fixed at 10 cm.

3. Results and discussion

3.1. Characterization of obtained samples

SEM and TEM techniques were used to investigate the surface morphology of the samples. In the case of SrTiO₃ calcined at 1100 °C, the formation of agglomerated nanocubes with sizes ranging from 150 to 250 nm was observed (Fig. 1a). The calcination temperature proved to be a critical factor in determining the particle size. For example, calcination in the range of 750-900 °C forms smaller SrTiO₃ particles, but this process is accompanied by the appearance of SrCO₃ impurities [21]. Calcination at 1100 °C promotes the decomposition of carbonates, which ensures high phase purity and improves crystallinity, thereby enhancing the transfer efficiency of photogenerated charge carriers. Based on this, 1100 °C was selected as the optimum temperature for the synthesis of SrTiO₃ nanocubes. EDX analysis showed the presence of Sr, Ti and O in the structure without any extraneous impurities (Fig. 2). The doping of SrTiO₃ with aluminum nanoparticles resulted in the formation of truncated cubic particles with sizes ranging from 200 to 400 nm (Figs. 1b and 3a). Flux treatment followed by aging at 1150 °C promoted the broadening of {111} facets and the reduction of {100} [22], which improved the separation and transport of photogenerated charge carriers. This increases the photocatalytic activity of SrTiO₃ due to more efficient water reduction with hydrogen formation and oxidation with oxygen release. Figures 3b and 3c show SrTiO₃@Al samples after separate photodeposition of co-catalysts (Rh/ Cr₂O₃ and CoOOH) on its surface. The images show that dark formations of 5-8 nm are concentrated on some faces, while less dispersed particles of 2-5 nm are localized on others. It is assumed that Rh/Cr₂O₃ nanoparticles are preferentially deposited on faces {100}, while CoOOH is distributed on faces {111} and {110}. These data are in agreement with previous studies that have examined in detail the growth of co-catalysts on the surface of SrTiO₃ [17, 22]. The unique distribution structure of the co-catalysts promotes efficient separation of photogenerated charges, which in turn facilitates the photocatalytic water splitting process.



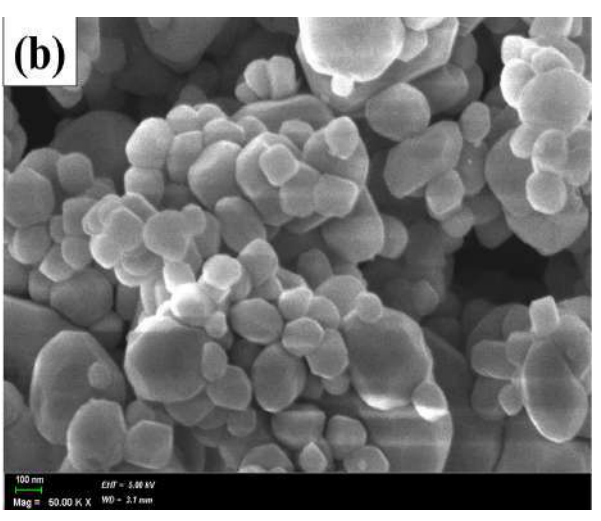


Fig. 1. SEM images of obtained (a) SrTiO₃ and (b) SrTiO₃@Al.

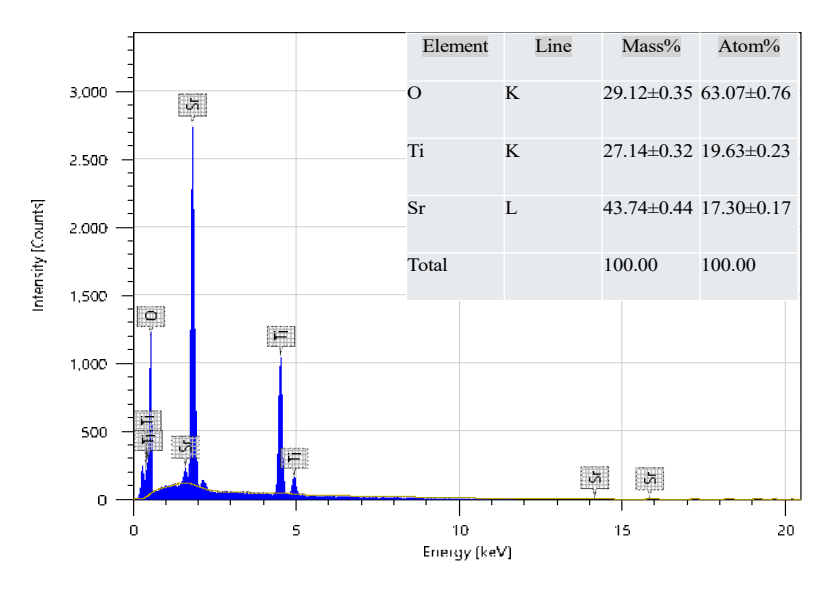
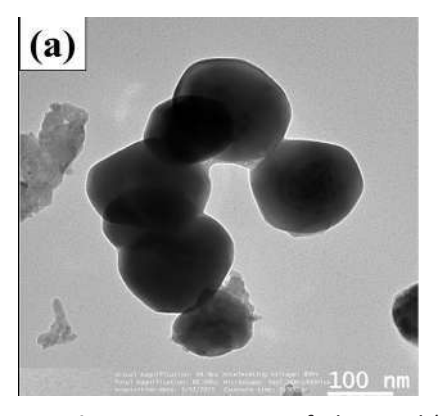
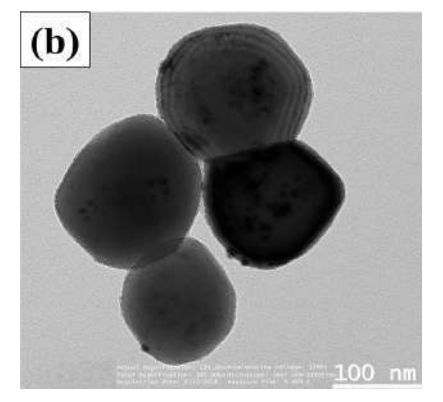


Fig. 2. EDX spectrum of SrTiO₃ particles.





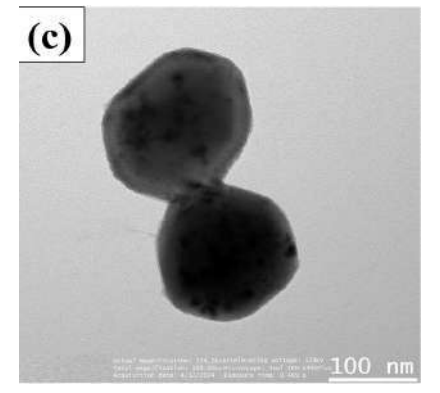


Fig. 3. TEM images of obtained (a) SrTiO₃@Al and (b,c) obtained cocatalyst loaded SrTiO₃@Al samples.

XRD spectra were studied for a detailed analysis of the crystal structure of the synthesized samples. Figure 4a shows the X-ray diffraction spectra for SrTiO₃, SrTiO₃@Al and SrTiO₃@Al samples with deposited co-catalysts. Diagnosis of the diffraction data shows that pure SrTiO₃ has a cubic perovskite

structure [21]. The defined peaks for SrTiO $_3$ are recorded at 20 angles of 32.40°, 40.50°, 46.50°, 58.50° and 68.50°, which correspond to the lattice planes of the cubic phase of SrTiO $_3$ ((110), (111), (200), (211) and (220) as reported in JCPDS Card #35-0734 [23]. Comparison of X-ray diffraction patterns for doped

and undoped SrTiO₃ shows a significant enhancement of peak intensities in the SrTiO₃@Al samples, indicating that aluminum doping improves the crystalline quality of SrTiO₃. Further, EDX mapping confirmed the presence of Ti, O, Sr and Al without any other impurities in the composition (Supplementary, Figs. S1, S2). At the same time, the presence of aluminum and co-catalysts does not change the crystal structure of SrTiO₃, since their peaks are not observed in the X-ray spectra. This is probably due to their low concentration, high dispersibility and low crystallinity [22].

XPS was used to analyze the changes in the chemical states and surface composition of $SrTiO_3$ samples before and after aluminum doping. The results are presented in Fig. 4 (b-d). In particular, the Ti 2p spectra (Fig. 4b) show two peaks: at 457.5 and 463.3 eV, corresponding to Ti $2p_{3/2}$ and Ti $2p_{1/2}$ states, respectively, indicating the presence of Ti^{4+} ions. The peak at 462.4 eV indicates the presence of Ti^{3+} ions in the $SrTiO_3$ sample [24]. After aluminum doping, Ti^{3+} ions completely disappear and the Ti 2p spectrum

for SrTiO₃@Al contains only two peaks: 457.9 and 463.6 eV, which are associated exclusively with Ti⁴⁺ ions [24]. The energy level analysis for oxygen (O 1s) presented in Fig. 4 c shows two Gaussian peaks: one at 528.3 eV, corresponding to O²⁻ ions in the crystal lattice, and the other at 529.9 eV, indicating oxygen defects associated with oxygen vacancies. Aluminum doping leads to an increase in the defective oxygen ratio from 15.9 % to 54.2 %, which is consistent with data from other studies where the effect of aluminum on the photocatalytic properties of SrTiO₃ was investigated [25]. The optimal increase [12] in the number of oxygen defects upon aluminum doping contributes to the reduction of photogenerated carrier recombination and positively affects photocatalytic activity. The Sr 3d spectra show two peaks at 132.4 and 134.1 eV, corresponding to Sr 3d_{5/2} and Sr 3d_{3/2} states, respectively (Fig. 4d), confirming the presence of Sr²⁺ ions in SrTiO₃, which remains stable after aluminum doping. Overall, the XPS results for the synthesized samples are in agreement with other studies [24, 25].

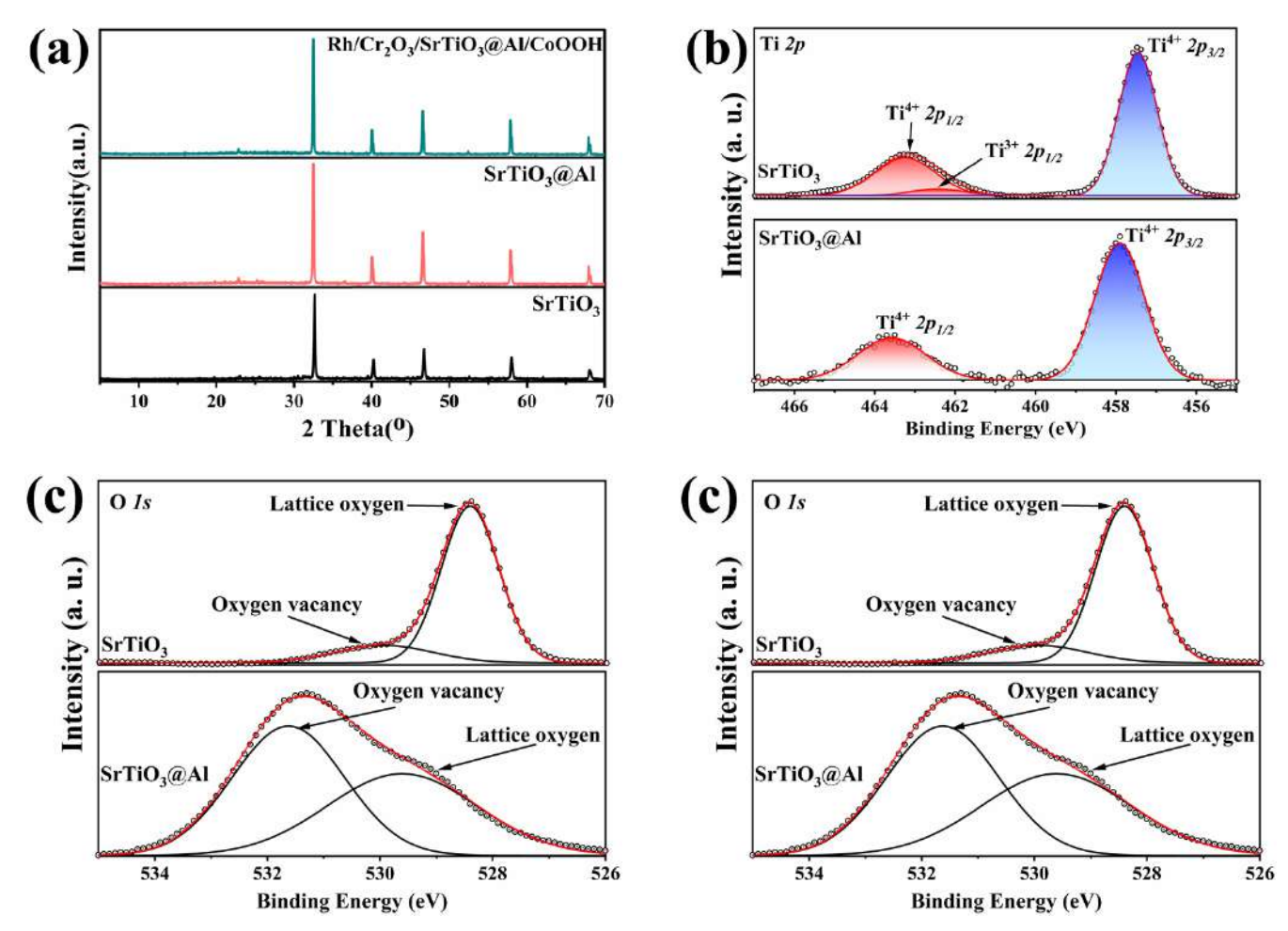


Fig. 4. (a) XRD patterns of prepared samples; XPS spectra of the $SrTiO_3$ and $SrTiO_3$ @Al samples – (b) high-resolution Ti 2p, (c) O 1s and (d) Sr 3d.

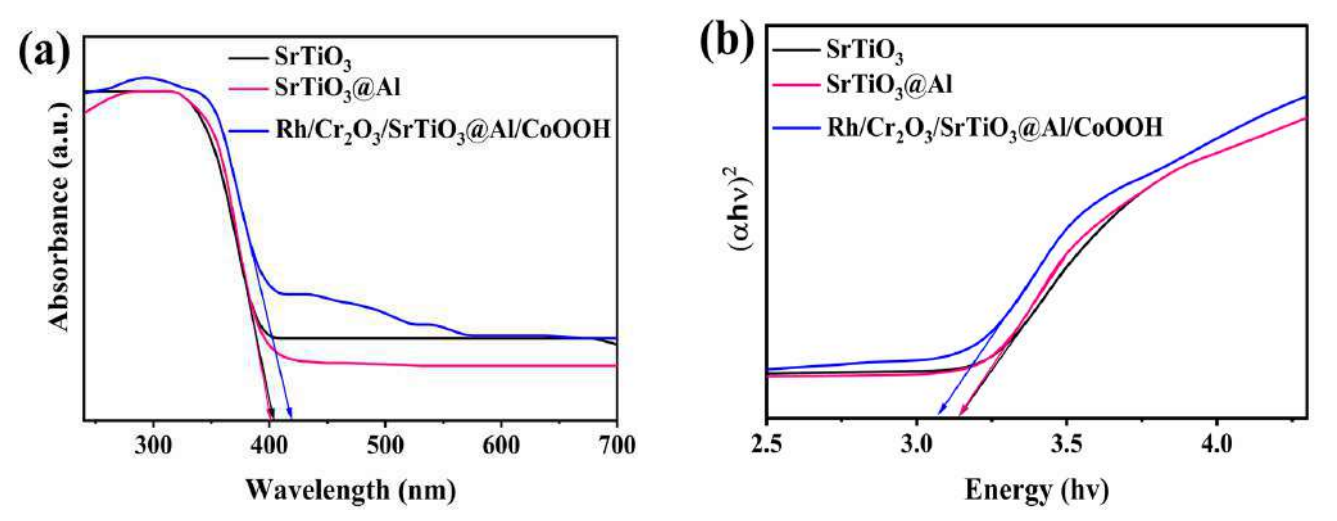


Fig. 5. (a) the UV-Vis DRS of the prepared samples and (b) the corresponding Tauc plots.

Figure 5 shows the UV-Vis absorption spectra for SrTiO₃, SrTiO₃@Al and SrTiO₃@Al with separately deposited co-catalysts in diffuse reflectance. The synthesized SrTiO₃ and SrTiO₃@Al samples exhibit light absorption up to a wavelength of 400 nm. At the same time, SrTiO₃@Al with co-catalysts shows a pronounced absorption peak around 425 nm shifted to the visible spectrum. To estimate the forbidden band width of photocatalysts, the dependence of $(\alpha h v)^2$ on photon energy was analyzed, where α is the absorption coefficient, h is Planck's constant, and v is the photon frequency [26]. The forbidden band width was 3.13 eV for SrTiO₃@Al and 3.07 eV for SrTiO₃@Al with co-catalysts. These results show that aluminum doping has no significant effect on the light absorption properties compared to pure SrTiO₃ (Fig. 5b). Similar results have been obtained in other studies on the doping of SrTiO₃ with aluminum [12]. In particular, it is noted that doping with aluminum does not change the width of the forbidden band, but mainly reduces the undesirable defects Ti³⁺, which serve as recombination centers for photogenerated charge carriers. For SrTiO₃@Al with co-catalysts, the bandgap width was slightly improved compared to SrTiO₃ and SrTiO₃@Al, indicating enhanced light absorption in the visible spectrum, especially in the violet and blue regions. However, the main advantage of co-catalysts is to reduce the recombination of photogenerated electrons and holes by improving their transport and separation [12].

3.2 Photocatalytic overall water splitting performance

Photocatalytic studies of total water splitting in the prepared samples were carried out and the results are presented in Fig. 6. The hydrogen and

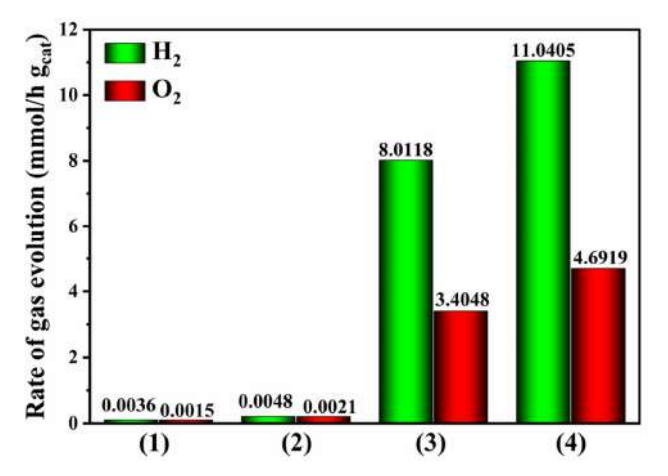


Fig. 6. Line graphs of photocatalytic H_2 and O_2 production performance of (1) bare $SrTiO_3$, (2) $SrTiO_3@AI$, (3) $Rh/Cr_2O_3/SrTiO_3/CoOOH$ and (4) $Rh/Cr_2O_3/SrTiO_3@AI/CoOOH$ under UV light irradiation.

oxygen production rates per hour of the used photocatalysts are in the expected stoichiometric ratio for water splitting and are shown in Fig. 6. The bare SrTiO₃ and SrTiO₃@Al samples showed very low H₂ release rates of \sim 0.0036 and 0.0048 mmol h^{-1} g^{-1} due to less efficient reaction sites. After loading the co-catalysts, the photocatalytic total water splitting activity of the samples increased significantly (Fig. 6). In particular, the highest activity was achieved for the Rh/Cr₂O₃/SrTiO₃@Al/CoOOH sample with gas release rates of 11.04 and 4.69 mmol h⁻¹ g⁻¹ for H₂ and O₂, respectively, which significantly exceeded bare SrTiO₃ and SrTiO₃@Al by a factor of 3067 and 2300, respectively. It should be considered that the nonaluminum-doped Rh/Cr₂O₃/SrTiO₃/CoOOH photocatalyst showed a hydrogen evolution rate of 8.01 mmol h⁻¹ g⁻¹ under identical conditions. This confirms the results of previous studies, according to which the improved solar energy conversion

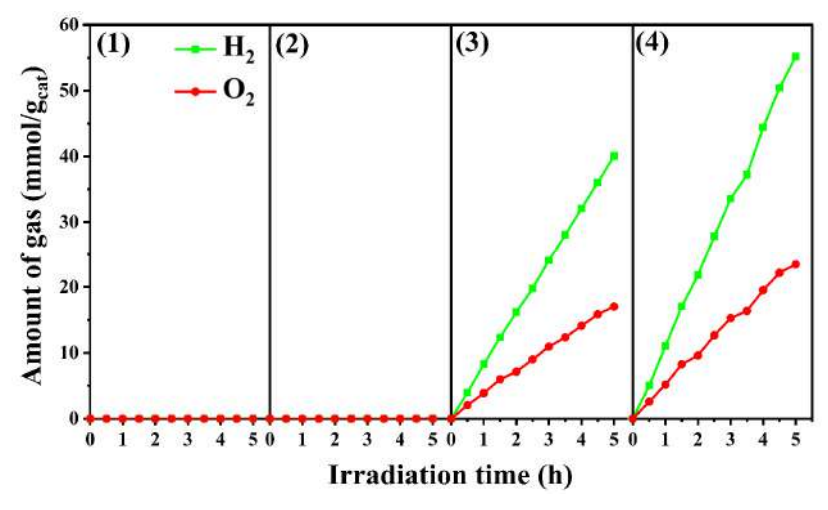


Fig. 7. Comparison of photocatalytic hydrogen production rates of (1) bare $SrTiO_3$, (2) $SrTiO_3$ @Al, (3) $Rh/Cr_2O_3/SrTiO_3/CoOOH$ and (4) $Rh/Cr_2O_3/SrTiO_3$ @Al/CoOOH.

ability of Al:SrTiO₃ correlates with the Al content [17, 27]. As the reaction time increased, the rate of photocatalytic hydrogen formation increased linearly and reached 55.2 and 40.06 mmol g⁻¹ after 5 h in the case of Rh/Cr₂O₃/SrTiO₃/CoOOH and Rh/ Cr₂O₃/SrTiO₃@Al/CoOOH, respectively (Fig. 7). The linearity of the hydrogen production rate at different time steps is almost the same, indicating that the catalyst performance is relatively stable during this hydrogen production process. The high photocatalytic activity of the photocatalysts with loaded co-catalysts is due to the synergistic effect of separately photodeposited Rh/Cr₂O₃ and CoOOH (reducing and oxidizing) co-catalysts, which promotes efficient separation and transfer of photogenerated electrons and holes. Where the photodeposited Rh/ Cr₂O₃ co-catalyst is responsible for the collection of electrons with subsequent hydrogen production, whereas CoOOH releases hydrogen due to the efficient collection of holes [17, 27]. In this way, charge recombination is minimized by sequential charge transfers between the photocatalyst and co-catalysts. In addition, the results of morphology and XPS analysis show that the use of flux method for aluminum doping resulted in the separation of reduction and oxidation zones by facet engineering, as well as the suppression of defects in the form of Ti³+, which can serve as recombination centers.

Table shows comparisons with recent composite photocatalysts, which have relatively high results in photocatalytic water splitting. However, the photocatalyst synthesized in our laboratory significantly outperforms analogs in both H_2 and O_2 production. In addition, the above works used UV lamps with

Table. Comparison of the synthesized Cocat/STO@Al photocatalyst with the results of recent research

Year	Photocatalyst	Light source	Sacrificial agent	H ₂ evolution rate (mmol h ⁻¹ g ⁻¹)	O_2 evolution rate (mmol h^{-1} g^{-1})	Ref.
2021	C–SrTiO₃/PAN/WS-FLG	120 W UV lamp, 254 nm	15 vol. % methanol	5.375	-	[9]
2022	Cr₂O₃@CoP/Al:STO	300 W Xe arc lamp	None	3.558	1.002	[28]
2023	$Rh/Cr_2O_3/SrTiO_3@AI/$ CoOOH (hydrothermal method)	300W Xe-lamp	20 vol.% methanol	4.100	1.900	[27]
2024	Pd-loaded Al: SrTiO ₃	300W Xe-lamp	20 vol.% methanol	1.430	-	[29]
2024	Rh/Cr ₂ O ₃ /SrTiO ₃ /CoOOH	10 W Mercury lamp	None	8.01	3.04	This work
2024	Rh/Cr₂O₃/SrTiO₃@Al/ CoOOH	10 W Mercury lamp	None	11.04	4.69	This work

120 and 300 W power and used sacrificial agents to reduce recombination, which are undesirable and may cause difficulties in scaling [9].

4. Conclusion

This study successfully developed and investigated an aluminum-doped SrTiO₃ photocatalyst with dual, separately photo-deposited cocatalysts (Rh/ Cr₂O₃ and CoOOH) for efficient water splitting. The results demonstrated a significant enhancement in photocatalytic activity, with the Rh/Cr₂O₃/SrTiO₃@ Al/CoOOH sample achieving a hydrogen evolution rate of 11.04 mmol g⁻¹ h⁻¹, which is substantially higher than non-modified samples. The enhanced performance is attributed to the synergistic effect of the cocatalysts, which effectively separate and transfer photogenerated charge carriers, minimizing recombination. Additionally, aluminum doping through a flux method improved crystal facet engineering and reduced defects like Ti3+, further contributing to the catalyst's efficiency. These findings highlight the potential of aluminum-doped SrTiO₃ and dual cocatalysts in advancing photocatalytic water splitting technologies and offer a promising approach for future research in this field.

Acknowledgments

This research has been funded by the Science Committee of the Ministry of Science and Higher Education of the Republic of Kazakhstan (Grant No AP14869381).

References

- [1]. G. Yergaziyeva, Z. Kuspanov, M. Mambetova, et al., J. CO2 Util. 80 (2024) 102682. DOI: 10.1016/j. jcou.2024.102682
- [2]. J. Wang, W. Azam, Geosci. Front. 15 (2024) 101757.DOI: 10.1016/j.gsf.2023.101757
- [3]. E. Dmitriyeva, I. Lebedev, E. Bondar, et al., *Eurasian Chem.-Technol. J.* 25 (2024) 211–217. DOI: 10.18321/ecti1543
- [4]. G. Yergaziyeva, E. Kutelia, K. Dossumov, et al., Eurasian Chem.-Technol. J. 25 (2023) 21–32. DOI: 10.18321/ectj1492
- [5]. E. Kutelia, K. Dossumov, M. Mambetova, et al., AIP Conf. Proc. 2803 (2023) 040015. DOI: 10.1063/5.0143475
- [6]. V. Pavlenko, K. Temirkulova, A. Zakharov, et al., Eurasian Chem.-Technol. J. 25 (2024) 201–210. DOI: 10.18321/ectj1542
- [7]. Q. Hassan, A.Z. Sameen, H.M. Salman, et al., J. Energy Storage 72 (2023) 108404. DOI: 10.1016/j. est.2023.108404

- [8]. M. Yue, H. Lambert, E. Pahon, et al., Renew. Sustain. Energy Rev. 146 (2021) 111180. DOI: 10.1016/j. rser.2021.111180
- [9]. E.V. Matus, I.Z. Ismagilov, E.S. Mikhaylova, Z.R. Ismagilov, Eurasian Chem.-Technol. J. 24 (2022) 69–91. DOI: 10.18321/ectj1320
- [10]. I.Z. Ismagilov, E.V. Matus, V.V. Kuznetsov, H.C.L. Abbenhuis, *Eurasian Chem.-Technol. J.* 19 (2017) 3–16. DOI: 10.18321/ectj497
- [11]. Z. Kuspanov, A. Umirzakov, A. Serik, *Int. J. Hydrogen Energy* 48 (2023) 38634–38654. DOI: 10.1016/j. ijhydene.2023.06.168
- [12]. Z. Zhao, R. Goncalves, S. Barman, et al., Energy Environ. Sci. 12 (2019) 1385–1395. DOI: 10.1039/ C9EE00310J
- [13]. Y. Sakata, Y. Miyoshi, T. Maeda, et al., Appl. Catal. A-Gen. 521 (2016) 227–232. DOI: 10.1016/j. apcata.2015.12.013
- [14]. Y. Liu, Y.-H. Li, X. Li, et al., ACS Nano 14 (2020) 14181–14189. DOI: 10.1021/acsnano.0c07089
- [15]. Q. Shen, W. Kang, L. Ma, et al., Chem. Eng. J. 478 (2023) 147338. DOI: 10.1016/j.cej.2023.147338
- [16]. M. Tayyab, Y. Liu, Z. Liu, et al., *Chem. Eng. J.* 455 (2023) 140601. DOI: 10.1016/j.cej.2022.140601
- [17]. T. Takata, J. Jiang, Y. Sakata, et al., *Nature* 581 (2020) 411–414. DOI: 10.1038/s41586-020-2278-9
- [18]. A.D. Kudaibergen, Z.B. Kuspanov, A.N. Issadykov, et al., *Eurasian Chem.-Technol. J.* 25 (2023) 139–146. DOI: 10.18321/ectj1516
- [19]. M. Bissenova, A. Umirzakov, K. Mit, et al., *Molecules* 29 (2024) 1101. DOI: 10.3390/molecules29051101
- [20]. A. Serik, Z. Kuspanov, M. Bissenova, N. Idrissov, et al., *J. Water Process Eng.* 66 (2024) 106052. DOI: 10.1016/j.jwpe.2024.106052
- [21]. Y. Ma, Z. Wu, H. Wang, et al., *CrystEngComm* 21 (2019) 3982–3992. DOI: 10.1039/C9CE00495E
- [22]. Y.-G. Lee, Y.-C. Cheng, Y.-T. Lin, et al., *J. Phys. Chem. C* 127 (2023) 9981–9991. DOI: 10.1021/acs. jpcc.3c00483
- [23]. E. Rocha-Rangel, W.J. Pech-Rodríguez, J. López-Hernández, et al., *Arch. Metall. Mater.* 65 (2020) 621–626. DOI: 10.24425/amm.2020.132801
- [24]. R. Li, T. Takata, B. Zhang, et al., *Angew. Chem. Int. Ed.* 62 (2023) e202313537. DOI: 10.1002/anie.202313537
- [25]. H. Tan, Z. Zhao, W. Zhu, et al., ACS Appl. Mater. Interfaces 6 (2014) 19184–19190. DOI: 10.1021/ am5051907
- [26]. N. Ashurov, B. Oksengendler, S. Maksimov, et al., Eurasian Chem.-Technol. J. 24 (2022) 229–239. DOI: 10.18321/ectj1436
- [27]. L. Tian, X. Guan, Y. Dong, et al., *Environ. Chem. Lett.* 21 (2023) 1257–1264. DOI: 10.1007/s10311-023-01580-8
- [28]. S. Zong, L. Tian, X. Guan, et al., *J. Colloid Interface Sci.* 606 (2022) 491–499. DOI: 10.1016/j.jcis.2021.08.049
- [29]. J. Jiang, Y. Zhou, J. Zhang, et al., *Int. J. Hydrogen Energy* 82 (2024) 646–654. DOI: 10.1016/j. ijhydene.2024.07.441





Communication

Synthesis and Study of SrTiO₃/TiO₂ Hybrid Perovskite Nanotubes by Electrochemical Anodization

Madina Bissenova ^{1,2}, Arman Umirzakov ^{1,2,3}, Konstantin Mit ¹, Almaz Mereke ^{1,3}, Yerlan Yerubayev ⁴, Aigerim Serik ^{2,3} and Zhengisbek Kuspanov ^{2,3,*}

- ¹ Institute of Physics and Technology, Almaty 050032, Kazakhstan; m-bisenova@list.ru (M.B.); arman_umirzakov@mail.ru (A.U.); konstantin-mit@yandex.ru (K.M.)
- Institute of Nuclear Physics, Almaty 050032, Kazakhstan; aigerimserik3508@gmail.com
- Department of Materials Science, Nanotechnology and Engineering Physics, Satbaev University, Almaty 050032, Kazakhstan
- Department of Mechanics and Mechanical Engineering, M.Kh. Dulaty Taraz Regional University, Taraz 080000, Kazakhstan
- * Correspondence: zhenis.kuspanov@gmail.com; Tel.: +7-707-605-04-64

Abstract: Layers of TiO $_2$ nanotubes formed by the anodization process represent an area of active research in the context of innovative energy conversion and storage systems. Titanium nanotubes (TNTs) have attracted attention because of their unique properties, especially their high surface-to-volume ratio, which makes them a desirable material for various technological applications. The anodization method is widely used to produce TNTs because of its simplicity and relative cheapness; the method enables precise control over the thickness of TiO $_2$ nanotubes. Anodization can also be used to create decorative and colored coatings on titanium nanotubes. In this study, a combined structure including anodic TiO $_2$ nanotubes and SrTiO $_3$ particles was fabricated using chemical synthesis techniques. TiO $_2$ nanotubes were prepared by anodizing them in ethylene glycol containing NH $_4$ F and H $_2$ O while applying a voltage of 30 volts. An anode nanotube array heat-treated at 450 °C was then placed in an autoclave filled with dilute SrTiO $_3$ solution. Scanning electron microscopy (SEM) analysis showed that the TNTs were characterized by clear and open tube ends, with an average outer diameter of 1.01 μ m and an inner diameter of 69 nm, and their length is 133 nm. The results confirm the successful formation of a structure that can be potentially applied in a variety of applications, including hydrogen production by the photocatalytic decomposition of water under sunlight.

Keywords: photocatalyst; TiO₂; TNT; SrTiO₃; anodizing



Citation: Bissenova, M.; Umirzakov, A.; Mit, K.; Mereke, A.; Yerubayev, Y.; Serik, A.; Kuspanov, Z. Synthesis and Study of SrTiO₃/TiO₂ Hybrid Perovskite Nanotubes by Electrochemical Anodization. *Molecules* **2024**, 29, 1101. https://doi.org/10.3390/molecules29051101

Academic Editors: Isabella Natali Sora and Lin Ju

Received: 24 January 2024 Revised: 23 February 2024 Accepted: 23 February 2024 Published: 29 February 2024



Copyright: © 2024 by the authors. Licensee MDPI, Basel, Switzerland. This article is an open access article distributed under the terms and conditions of the Creative Commons Attribution (CC BY) license (https://creativecommons.org/licenses/by/4.0/).

1. Introduction

Rapid growth in the world population has increased the demand for energy, the bulk of which is provided by fossil fuels for power generation, industrial needs, and transportation [1–4]. However, in addition to limited availability, the use of fossil fuels has a negative impact on the environment, creating by-products such as carbon, nitrogen, and sulfur oxides [5,6]. Therefore, there is an urgent need to develop cleaner alternative energy sources that are sustainable and have a minimal impact on the environment [7,8]. Hydrogen stands out as a clean and efficient energy source, and its production is becoming an important challenge in the field of sustainable energy sources.

Water is an abundant source of hydrogen, but given the need to introduce energy to overcome the energy barrier associated with chemical stability, it is difficult to separate water into stoichiometric hydrogen and oxygen on an industrial scale. Nevertheless, one method of hydrogen production is the photocatalytic splitting of water. Photocatalysis can efficiently utilize solar energy to split water into its individual elements [9–11]. This is a unique and promising method of hydrogen production based on the use of solar energy to convert water into hydrogen and oxygen [12]. This process could be an important

Molecules **2024**, 29, 1101 2 of 8

step toward sustainable energy sources, as it combines the efficiency of solar panels with the ability to produce clean hydrogen. In particular, photocatalysis has been shown to be a more efficient form of wastewater treatment because of the impressive efficiency of photocatalytic removal, rapid oxidation process, lower costs, and a lack of toxicity [13]. Photocatalytic water splitting involves the use of semiconductors as photocatalysts. The most studied photocatalysts are TiO₂, ZnO, CdS, and SrTiO₃, which are used for various photocatalytic applications including photocatalytic water splitting [14–16]. To achieve efficient photocatalytic water splitting, a sophisticated photocatalyst is required that can overcome problems in the water oxidation process.

Titanium dioxide (titanium, TiO₂) is considered the most promising and versatile material. Over the past decades, TiO₂ has been extensively investigated in various fields because of its unique properties such as outstanding corrosion resistance, high biocompatibility, suitable bandgap for water splitting, and stable physicochemical characteristics [17,18]. The narrow-bandgap facilitates the more efficient collection of solar energy, making it an ideal material for creating an electron-hole pair. This pair is actively involved in redox reactions and finds applications in various fields, such as dyes, food, biomedicine, photocatalysis, photodegradation of water, photosensitive materials, dye-sensitized solar cells, and gas-sensitive devices. In recent years, significant research efforts have been devoted to the development of new nanomaterials, including nanostructured titanium obtained via anodization, sol-gel, hydrothermal treatment, and vapor deposition techniques [19]. Nowadays, a wide range of materials are required to develop and research advanced devices suitable for various commercial applications. Nanomaterials play a key role in emerging technologies, enabling the creation of high-performance devices [20,21]. The performance of such devices is largely determined by the geometry, shape, and morphology of the nanostructures [7]. The exponential growth in the literature indicates that interest in the nanoscale began in the 1990s. Interest in the nanoscale is driven by the commercial availability of tools used to manipulate and measure nanoscale characteristics for several reasons: (1) the anticipation of the novel physical, chemical, and biological properties of nanostructures; (2) the assumption that nanostructures will provide new building blocks for innovative materials with unique properties; (3) the miniaturization of the semiconductor industry to the nanoscale; and (4) the recognition that molecular mechanisms in biological cells function at the nanoscale [22].

2. Results and Discussion

The morphology of the obtained $SrTiO_3$ samples was studied using scanning (SEM) and transmission (TEM) electron microscopes at different resolutions. The scanning electron microscopy results (Figure 1a–c) show that the $SrTiO_3$ particles that calcined at 900 °C possess cubic shapes and have sizes ranging from 150 nm to 300 nm. Calcination at 800 °C leads to the formation of finer particles but with more significant numbers of impurities such as $SrCO_3$. Based on the literature and experimental data [23,24], the optimal calcination temperature is 900 °C, which is followed by treatment in 1 m nitric acid solution to remove residual $SrCO_3$. However, it is worth noting that the particle sizes are highly heterogeneous. Given studies in the literature, doping $SrTiO_3$ with other elements, such as Al or Mn, can contribute to the size reduction and distortion in $SrTiO_3$'s crystal shape.

In the case of TEM, clearly formed cubes of $SrTiO_3$ with anisotropic structures with an average size of about 200 nm are clearly visible, as shown in Figure 1d–f. An important feature of these particles is the anisotropic structure, which creates a difference in energy at different faces, leading to the formation of p–n junctions. This allows the charge within each photocatalyst particle to be separated using an inter-domain electric field. Thus, electrons are concentrated on some faces and holes on other faces, which provides for the separation of photocatalytic reduction and oxidation processes on different faces. Given the anisotropic crystal structure, the selective deposition of catalysts takes place, which leads to the release of hydrogen and oxygen on the faces of the cubic photocatalyst.

Molecules **2024**, 29, 1101 3 of 8

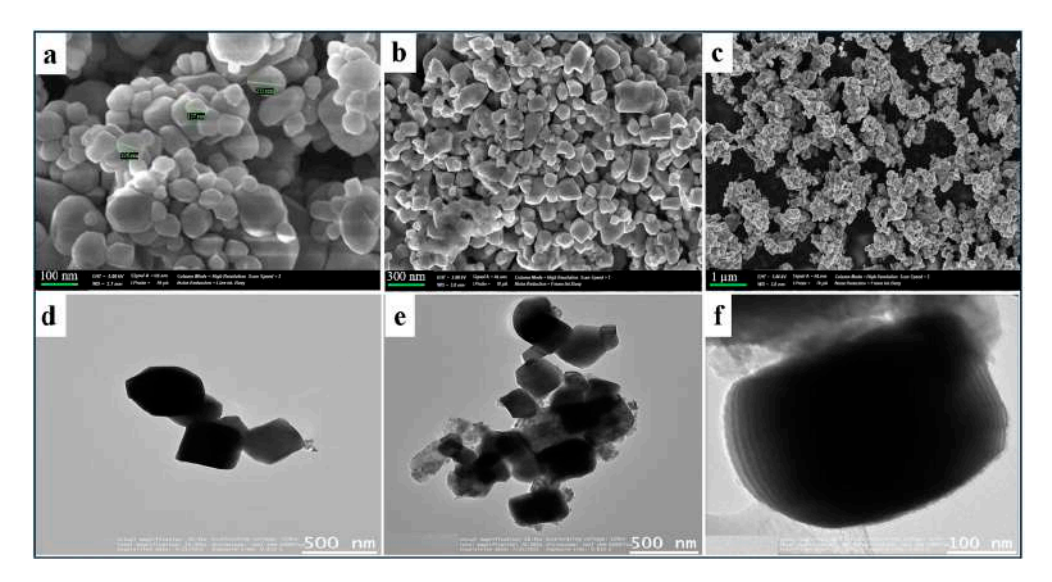


Figure 1. SEM (**a**–**c**) and TEM (**d**–**f**) images at different magnifications of cubic SrTiO₃ obtained by a chemical precipitation method.

Among various nanostructured oxide materials, TiO₂ nanotubes have been emphasized because of their improved properties, economical design, and higher surface-tovolume ratio [25]. TNTs with high specific surface areas, ion exchange abilities, and photocatalytic properties have been considered for various potential applications and can be excellent candidates as catalysts in photocatalysis [26]. Figure 2 shows images of the top surfaces of the anodized TiO₂ nanotube samples before and after the deposition of SrTiO₃ on their surfaces. The top surfaces of the anodized and annealed TNTs at 450 °C shown in Figure 2a show well-defined tubes with open ends that form a hexagonal order. This is typical of anodization, as previously noted in [27]. After applying SrTiO₃, pronounced morphological changes are observed with the presence of interface regions between SrTiO₃ and TNT, which indicates the success of the combination (Figure 2b). During 6 h of autoclave treatment, the surface showed a tendency to be coated with nanoparticles, and uneven deposition was also found. Agglomerates are formed on the surface, and round holes corresponding to TNT are still visible. Note that increasing the treatment time to 6 h significantly affects the surface morphology, leading to the formation of larger agglomerates and the blocking of the tube tops [28]. Figure 2c shows that the initial TNTs have an average outer diameter of 1 µm, while Figure 2a shows an inner diameter of 69 nm. The length of the tubes is 133 nm, as seen in the inset. A cross-sectional view of a freestanding titanium dioxide membrane with an average thickness of more than 50 nm is shown in Figure 2d, mechanically collapsed for visualization. In a related study [25], Paulose et al. obtained nanotubes measuring 360 µm in length over a 96 h period, utilizing a voltage of 60 V. They employed a titanium foil with a thickness of 0.25 mm, immersed in a solution comprising 0.3 wt% NH₄F and 2% H₂O in ethylene glycol. Our results—derived from anodization in a solution comprising 0.7 wt% NH₄F and 3.5 wt% distilled water at 30 V—revealed the length of the TNT nanotubes to be 133 nm at the nanoscale. The SEM images also demonstrate that the obtained nanotubes are ordered and have clear open ends. Despite the low voltage (30 V), we compensated for this by increasing the concentrations of NH₄F and H₂O in the anode solution. Given the higher mass percentage of NH₄F, compensation is accomplished by increasing the concentration of H₂O, resulting in faster growth and, hence, longer nanotube lengths.

Molecules **2024**, 29, 1101 4 of 8

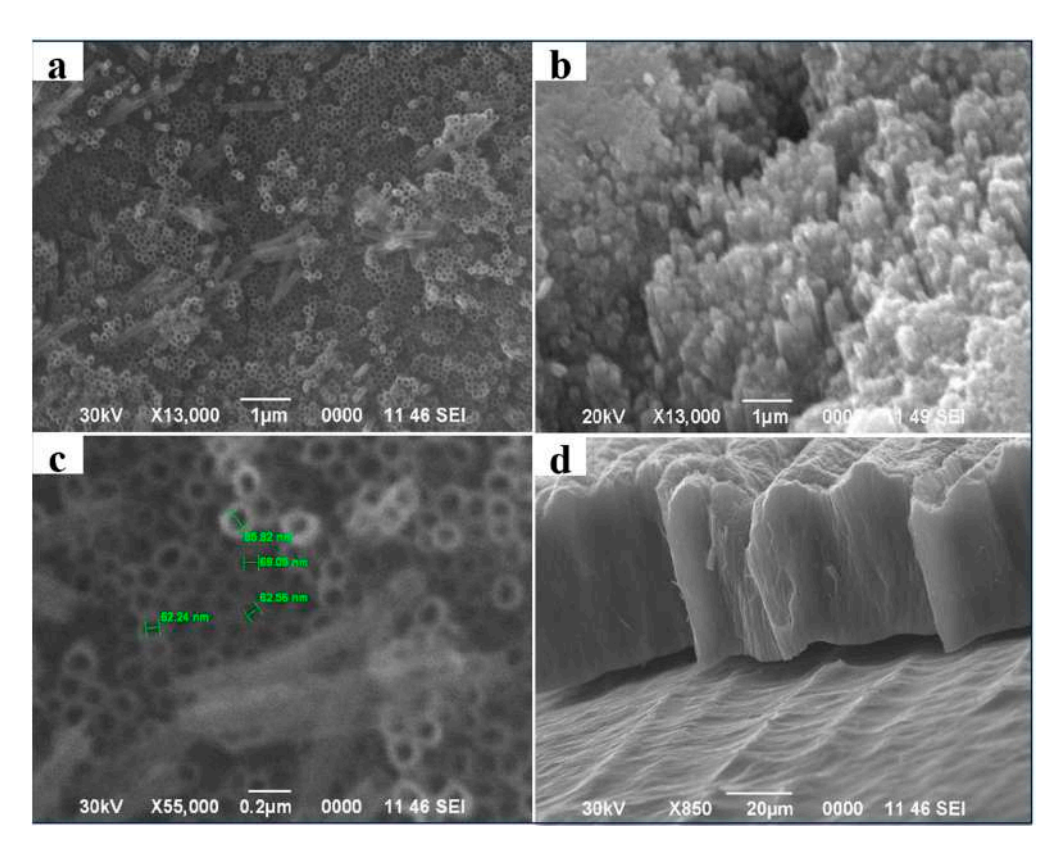


Figure 2. (a) SEM images showing the top surface of the TNT anode array; (b) the TNT@SrTiO₃ array; (c) the top view and (d) side view of samples with magnification of the surface of the anode array prepared at 30 V.

XRD analysis of the TNT@SrTiO₃ samples was performed on an X-ray diffractometer with detection unit rotation angles ranging from 20° to 80° and a minimum detection unit movement step of 0.01, as shown in Figure 3a. The characteristic peaks of the TNT samples appear at 2θ 25.4°, 37.9°, and 53.4°, 71.5°, indicating the polycrystalline structure of the anatase, in good agreement with the standard map for TNT (JCPDS map 1286) [20]. In addition, the appearance of new peaks at 32.2°, 46.9°, and 57.8° in the X-ray diffraction spectrum of the TNT@SrTiO₃ samples indicates the combination of two components in the composite, which additionally proves the successful connection and interaction between the components. This confirmation is based on a comparison of the diffraction spectra of the composite with TNT, which makes it possible to determine whether changes have occurred in the crystal structure during their combination. It is particularly important to note that the peak at 20, equal to 71.23°, has a high intensity, indicating the high crystallinity of the semiconductor. This is significant because the transport efficiency of charged carriers generated during photogeneration can be strongly dependent on the crystallinity of the material. Low crystallinity can lead to the inefficient migration of charged particles. In addition, semi-quantitative elemental analysis of the particles confirmed the composition of the obtained samples. The presence of the elements Ti and Sr was confirmed without detecting other impurities. According to the atomic percentages in the index (Figure 3b), it can be established that Ti/Sr is 81.10%/18.90%, respectively. These results confirm that the designs contain the expected elements and have no significant impurities.

Low-temperature electron paramagnetic resonance (EPR) spectra were determined on the $SrTiO_3/TiO_2$ samples to confirm the presence of Ti^{3+} and oxygen vacancies. The initial $SrTiO_3/TiO_2$ (Figure 4c, marked in red), containing mainly Ti^{4+} 3d0 states, exhibits a weak EPR signal, which may be due to the surface adsorption of O_2 from air. For $SrTiO_3$ and TiO_2 , a strong signal from Ti^{3+} spins (marked in blue and black) is also observed. It is generally believed that photoelectrons can be captured by Ti^{4+} and lead to the reduction of

Molecules **2024**, 29, 1101 5 of 8

 ${\rm Ti^{4+}}$ cations to the ${\rm Ti^{3+}}$ state, which is usually accompanied by the loss of oxygen from the surface of ${\rm TiO_2}$ and ${\rm SrTiO_3}$. Thus, these data clearly confirm that ${\rm Ti^{3+}}$ and oxygen vacancies were formed in all ${\rm SrTiO_3/TiO_2}$, ${\rm TiO_2}$, and ${\rm SrTiO_3}$ samples.

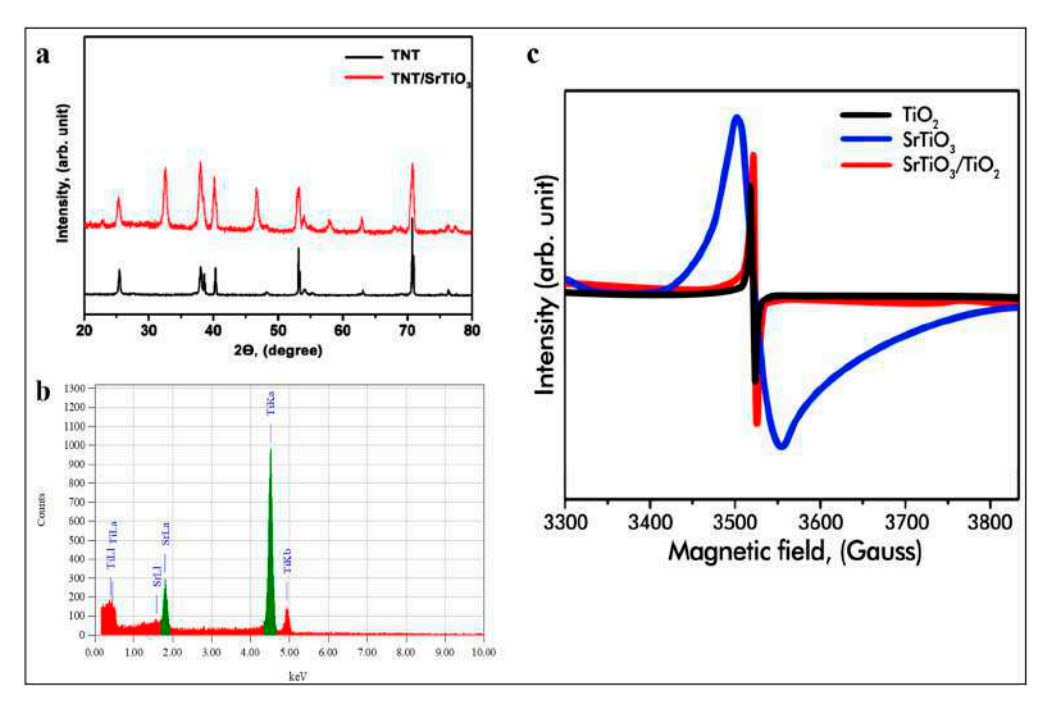


Figure 3. (a) X-ray diffraction analysis of combined TNT@ $SrTiO_3$; (b) semi-quantitative elemental analysis of TNT@ $SrTiO_3$ particles; (c) EPR spectra of pristine TiO_2 and $SrTiO_3$ and pristine $SrTiO_3/TiO_2$ nanotube arrays after hydrothermal reaction of 5 h duration.

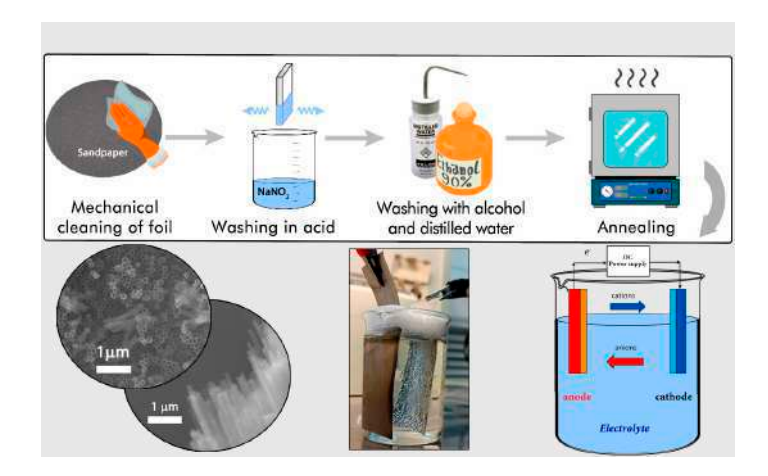


Figure 4. Schematic illustration of the stages of obtaining TNT.

 ${
m TiO_2}$ nanotubes can be produced in various ways [29], among which, the most widely studied is the use of electrochemical anodization. The advantage of anodic ${
m TiO_2}$ nanotubes over ${
m TiO_2}$ nanotubes produced by other methods is their availability and cost-effectiveness. Also, one of the advantages of this method is that the anodic ${
m TiO_2}$ nanotubes grow vertically on the Ti substrate with nanotube holes on top and closed nanotube bottoms attached to the Ti substrate. Thus, no further immobilization on the substrate is required. The TNT layers are highly ordered, which favors a direct diffusion pathway. In addition, the nanotube layers can be removed from the Ti substrate and used as powders if required. Another advantage is that the nanotube layer thickness and nanotube diameter can be controlled by adjusting the anodization electrolyte, potential, and time [30].

Molecules **2024**, 29, 1101 6 of 8

3. Materials and Methods

3.1. Materials

Ti foil (99.9%; thickness, 0.1 mm; China), ethanol (45%), ethylene glycol (99.9%, Russia), ammonium fluoride, and sodium nitrate (70%) were used without further purification. Distilled water was used as a solvent in all experiments.

3.2. Synthesis of SrTiO₃

SrTiO $_3$ was obtained using a chemical precipitation method [24,31–33]. For this purpose, 2.54 g of Sr (NO $_3$) $_2$ was mixed with 100 mL of distilled water; then, 0.958 g of TiO $_2$ was added in a 1:1 ratio of Ti and SrTiO $_3$ to this solution. The solution was then treated for 30 min in an ultrasonic bath. The solution was gradually added while maintaining vigorous stirring, and the pH of the mixture was brought to 6–7 using 10% NH $_3$ OH solution. The suspension was washed several times with distilled water. The resulting powder was dried at 60 °C overnight and then calcined at 900 °C for 1 h.

3.3. Nanotube Synthesis

 ${
m TiO_2}$ was obtained using an anodization method. The 0.1 mm thick Ti foil was initially cut into 1 cm \times 6 cm samples and mechanically polished with P150 sandpaper. The sheets were then ultrasonically treated in sodium nitrate, ethanol, and distilled water for final cleaning. Electrochemical anodization experiments were carried out in a two-electrode electrochemical cell, where titanium foil served as the working electrode and a sheet of nickel foil as the counter electrode at constant potential and room temperature (\approx 22 °C). Figure 1 shows a schematic of the titanium nanotube formation process. A constant current power supply unit model, UNI-T UTP3315TPL from UNI-TREND Technology, China, was used. This unit was used as a voltage source to control the anodization. The electrolyte for anodizing consisted of ethylene glycol with 0.7 wt% NH4F and 3.5 wt% distilled water added. The anodization process was carried out at 30 V for 96 h at room temperature. The anodized titanium nanotube samples were then placed in ethylene glycol and subjected to ultrasonic stirring until the nanotube film separated from the titanium substrate. The suspension was filtered; the residue was washed several times with distilled water. The resulting powder was dried at 60 °C for 3 h and then calcined at 450 °C for 1 h.

3.4. Synthesis of TNT@SrTiO₃

To create the combined TNT@ SrTiO $_3$ structure, powders of 0.2 g of TNT and 0.1 g of SrTiO $_3$ were taken, mixed with 40 mL of distilled water, and placed in a stainless autoclave. The sealed autoclave was heated to 90 °C and incubated for 6 h. At the end of the experiment, the autoclave was cooled to room temperature. The samples were then washed with distilled water and dried in an oven for 5 h at 60 °C.

3.5. Material Characterization Techniques

The morphologies of the TNT and the combined TNT@SrTiO $_3$ were analyzed using a JSM-6490LA scanning electron microscope from JEOL, Tokyo, Japan. TESCAN MAIA3 XMU scanning transmission electron microscopy (STEM) was used to further investigate the morphology at high resolution. The crystal structure of the samples was studied using a Drone-8 X-ray diffractometer. An EPR spectrometer "JEOL" (JES-FA200, Japan) was also used. Measurements were in ranges of ~9.4 GHz (X-Band) and ~35 GHz (Q-Band). Microwave frequency stability—~10 $^{-6}$. Sensitivity—7 \times 109/10 $^{-4}$ Tl. Resolution—2.35 μ T. Output power—from 200 mW to 0.1 μ W. Quality factor (Q-factor)—18,000.

4. Conclusions

In this paper, the synthesis of arrays of TiO_2 nanotubes using an electrochemical anodization method was successfully demonstrated. The obtained nanotubes have clear and open ends and are 133.9 nm long, and their membranes are more than 1 μ m thick. The anodization process of 0.1 mm thick Ti foil at 450 °C can easily produce such nanotube

Molecules **2024**, 29, 1101 7 of 8

arrays. SEM analysis showed that the TNTs are characterized by clear and open tube ends, with an average outer diameter of 1 μ m and an inner diameter of 69 nm, and their length is 133 nm. In addition, a combined structure of TNT@SrTiO3 was fabricated in this study using chemical autoclave synthesis techniques. X-ray phase analysis confirmed the high crystallinity and orientation of crystallites along the preferential growth direction, indicating the successful formation of the structure. The results obtained here have potential significance for various fields including the sunlight-induced photocatalytic decomposition of water and other applications in energy conversion and storage. Further research and development in this area can contribute to the development of innovative technologies and improve the efficiency of energy systems.

Author Contributions: Conceptualization, methodology, writing—original draft preparation, investigation: M.B.; resources, visualization, project administration, funding acquisition: A.U., K.M., A.M. and Y.Y.; formal analysis: A.S.; supervision, data curation, writing—review and editing: Z.K. All authors have read and agreed to the published version of the manuscript.

Funding: This research was funded by the Science Committee of the Ministry of Science and Higher Education and of the Republic of Kazakhstan (Grant No AP19680604).

Institutional Review Board Statement: Not applicable.

Informed Consent Statement: Not applicable.

Data Availability Statement: The data are contained within the article.

Conflicts of Interest: There are no conflicts of interest to declare.

References

1. Zhang, Z.; Wang, Q.; Xu, H.; Zhang, W.; Zhou, Q.; Zeng, H.; Yang, J.; Zhu, J.; Zhu, X. TiO₂ Nanotube Arrays with a Volume Expansion Factor Greater than 2.0: Evidence against the Field-Assisted Ejection Theory. *Electrochem. Commun.* **2020**, 114, 106717. [CrossRef]

- 2. Prikhodko, N.; Yeleuov, M.; Abdisattar, A.; Askaruly, K.; Taurbekov, A.; Tolynbekov, A.; Rakhymzhan, N.; Daulbayev, C. Enhancing Supercapacitor Performance through Graphene Flame Synthesis on Nickel Current Collectors and Active Carbon Material from Plant Biomass. *J. Energy Storage* 2023, 73, 108853. [CrossRef]
- 3. Askaruly, K.; Yeleuov, M.; Taurbekov, A.; Sarsembayeva, B.; Tolynbekov, A.; Zhylybayeva, N.; Azat, S.; Abdisattar, A.; Daulbayev, C. A Facile Synthesis of Graphite-Coated Amorphous SiO₂ from Biosources as Anode Material for Libs. *Mater. Today Commun.* **2023**, *34*, 105136. [CrossRef]
- 4. Yeleuov, M.; Daulbayev, C.; Taurbekov, A.; Abdisattar, A.; Ebrahim, R.; Kumekov, S.; Prikhodko, N.; Lesbayev, B.; Batyrzhan, K. Synthesis of Graphene-like Porous Carbon from Biomass for Electrochemical Energy Storage Applications. *Diam. Relat. Mater.* **2021**, *119*, 108560. [CrossRef]
- 5. Galstyan, V.; Macak, J.M.; Djenizian, T. Anodic TiO₂ Nanotubes: A Promising Material for Energy Conversion and Storage. *Appl. Mater. Today* **2022**, 29, 101613. [CrossRef]
- Taurbekov, A.; Abdisattar, A.; Atamanov, M.; Yeleuov, M.; Daulbayev, C.; Askaruly, K.; Kaidar, B.; Mansurov, Z.; Castro-Gutierrez, J.; Celzard, A.; et al. Biomass Derived High Porous Carbon via CO₂ Activation for Supercapacitor Electrodes. J. Compos. Sci. 2023, 7, 444. [CrossRef]
- 7. Saddique, Z.; Imran, M.; Javaid, A.; Kanwal, F.; Latif, S.; dos Santos, J.C.S.; Kim, T.H.; Boczkaj, G. Bismuth-Based Nanomaterials-Assisted Photocatalytic Water Splitting for Sustainable Hydrogen Production. *Int. J. Hydrogen Energy* **2024**, *52*, 594–611. [CrossRef]
- Yergaziyeva, G.; Kuspanov, Z.; Mambetova, M.; Khudaibergenov, N.; Makayeva, N.; Daulbayev, C. Advancements in Catalytic, Photocatalytic, and Electrocatalytic CO₂ Conversion Processes: Current Trends and Future Outlook. J. CO2 Util. 2024, 80, 102682. [CrossRef]
- 9. Wang, S.-J.; Su, D.; Zhu, Y.-F.; Lu, C.-H.; Zhang, T. The State-of-the-Art Review on Rational Design for Cavitation Assisted Photocatalysis. *Mater. Des.* **2023**, 234, 112377. [CrossRef]
- 10. Kuspanov, Z.; Bakbolat, B.; Baimenov, A.; Issadykov, A.; Yeleuov, M.; Daulbayev, C. Photocatalysts for a Sustainable Future: Innovations in Large-Scale Environmental and Energy Applications. *Sci. Total Environ.* **2023**, *885*, 163914. [CrossRef]
- 11. Megbenu, H.K.; Daulbayev, C.; Nursharip, A.; Tauanov, Z.; Poulopoulos, S.; Busquets, R.; Baimenov, A. Photocatalytic and Adsorption Performance of MXene@Ag/Cryogel Composites for Sulfamethoxazole and Mercury Removal from Water Matrices. *Environ. Technol. Innov.* **2023**, 32, 103350. [CrossRef]
- 12. Baimenov, A.; Montagnaro, F.; Inglezakis, V.J.; Balsamo, M. Experimental and Modeling Studies of Sr²⁺ and Cs⁺ Sorption on Cryogels and Comparison to Commercial Adsorbents. *Ind. Eng. Chem. Res.* **2022**, *61*, 8204–8219. [CrossRef]

Molecules **2024**, 29, 1101 8 of 8

13. Lee, D.-E.; Kim, M.-K.; Danish, M.; Jo, W.-K. State-of-the-Art Review on Photocatalysis for Efficient Wastewater Treatment: Attractive Approach in Photocatalyst Design and Parameters Affecting the Photocatalytic Degradation. *Catal. Commun.* **2023**, *183*, 106764. [CrossRef]

- 14. Indira, K.; Mudali, U.K.; Nishimura, T.; Rajendran, N. A Review on TiO₂ Nanotubes: Influence of Anodization Parameters, Formation Mechanism, Properties, Corrosion Behavior, and Biomedical Applications. *J. Bio- Tribo-Corros.* **2015**, *1*, 28. [CrossRef]
- 15. Kuspanov, Z.; Umirzakov, A.; Serik, A.; Baimenov, A.; Yeleuov, M.; Daulbayev, C. Multifunctional Strontium Titanate Perovskite-Based Composite Photocatalysts for Energy Conversion and Other Applications. *Int. J. Hydrogen Energy* **2023**, *48*, 38634–38654. [CrossRef]
- 16. Bakbolat, B.; Daulbayev, C.; Sultanov, F.; Beissenov, R.; Umirzakov, A.; Mereke, A.; Bekbaev, A.; Chuprakov, I. Recent Developments of TiO₂-Based Photocatalysis in the Hydrogen Evolution and Photodegradation: A Review. *Nanomaterials* **2020**, *10*, 1790. [CrossRef] [PubMed]
- 17. Moon, S.; Nagappagari, L.R.; Lee, J.; Lee, H.; Lee, W.; Lee, K. Electrochemical Detection of 2,4,6-Trinitrotoluene Reduction in Aqueous Solution by Using Highly Ordered 1D TiO₂ Nanotube Arrays. *Mater. Today Commun.* **2020**, 25, 101389. [CrossRef]
- 18. An, X.; Hua, W.; Rui, L.; Liu, P.; Li, X. Application of a New Nano-TiO₂ Composite Antibacterial Agent in Nursing Management of Operating Room: Based on Real-Time Information Push Assistant System. *Prev. Med.* **2023**, 172, 107541. [CrossRef]
- 19. Yin, H.; Liu, H.; Shen, W.Z. The Large Diameter and Fast Growth of Self-Organized TiO₂ Nanotube Arrays Achieved via Electrochemical Anodization. *Nanotechnology* **2009**, *21*, 035601. [CrossRef]
- 20. Ghani, T.; Mujahid, M.; Mehmood, M.; Zhang, G.; Naz, S. Highly Ordered Combined Structure of Anodic TiO₂ Nanotubes and TiO₂ Nanoparticles Prepared by a Novel Route for Dye-Sensitized Solar Cells. *J. Saudi Chem. Soc.* **2019**, 23, 1231–1240. [CrossRef]
- 21. Jandosov, J.; Alavijeh, M.; Sultakhan, S.; Baimenov, A.; Bernardo, M.; Sakipova, Z.; Azat, S.; Lyubchyk, S.; Zhylybayeva, N.; Naurzbayeva, G.; et al. Activated Carbon/Pectin Composite Enterosorbent for Human Protection from Intoxication with Xenobiotics Pb(II) and Sodium Diclofenac. *Molecules* 2022, 27, 2296. [CrossRef]
- 22. Zhang, W.; Sun, Y.; Tian, R.; Gao, Q.; Wang, J.; Liu, Y.; Yang, F. Anodic Growth of TiO₂ Nanotube Arrays: Effects of Substrate Curvature and Residual Stress. *Surf. Coat. Technol.* **2023**, 469, 129783. [CrossRef]
- 23. Roy, P.K.; Bera, J. Formation of SrTiO₃ from Sr-Oxalate and TiO₂. Mater. Res. Bull. 2005, 40, 599–604. [CrossRef]
- Kudaibergen, A.D.; Kuspanov, Z.B.; Issadykov, A.N.; Beisenov, R.E.; Mansurov, Z.A.; Yeleuov, M.A.; Daulbayev, C.B. Synthesis, Structure, and Energetic Characteristics of Perovskite Photocatalyst SrTiO3: An Experimental and DFT Study. Eurasian Chem.-Technol. J. 2023, 25, 139–146. [CrossRef]
- 25. Paulose, M.; Prakasam, H.E.; Varghese, O.K.; Peng, L.; Popat, K.C.; Mor, G.K.; Desai, T.A.; Grimes, C.A. TiO₂ Nanotube Arrays of 1000 μm Length by Anodization of Titanium Foil: Phenol Red Diffusion. *J. Phys. Chem. C* **2007**, 111, 14992–14997. [CrossRef]
- 26. Moulis, F.; Krýsa, J. Photocatalytic Degradation of Several VOCs (*n*-Hexane, *n*-Butyl Acetate and Toluene) on TiO₂ Layer in a Closed-Loop Reactor. *Catal. Today* **2013**, 209, 153–158. [CrossRef]
- 27. Hou, X.; Lund, P.D.; Li, Y. Controlling Anodization Time to Monitor Film Thickness, Phase Composition and Crystal Orientation during Anodic Growth of TiO₂ Nanotubes. *Electrochem. Commun.* **2022**, *134*, 107168. [CrossRef]
- 28. Sopha, H.; Samoril, T.; Palesch, E.; Hromadko, L.; Zazpe, R.; Skoda, D.; Urbanek, M.; Ng, S.; Prikryl, J.; Macak, J.M. Ideally Hexagonally Ordered TiO₂ Nanotube Arrays. *ChemistryOpen* **2017**, *6*, 480–483. [CrossRef] [PubMed]
- 29. Beketova, D.; Motola, M.; Sopha, H.; Michalicka, J.; Cicmancova, V.; Dvorak, F.; Hromadko, L.; Frumarova, B.; Stoica, M.; Macak, J.M. One-Step Decoration of TiO₂ Nanotubes with Fe₃O₄ Nanoparticles: Synthesis and Photocatalytic and Magnetic Properties. *ACS Appl. Nano Mater.* **2020**, *3*, 1553–1563. [CrossRef]
- 30. Tak, M.; Tomar, H.; Mote, R.G. Synthesis of Titanium Nanotubes (TNT) and Its Influence on Electrochemical Micromachining of Titanium. *Procedia CIRP* **2020**, *95*, 803–808. [CrossRef]
- 31. Daulbayev, C.; Sultanov, F.; Korobeinyk, A.V.; Yeleuov, M.; Azat, S.; Bakbolat, B.; Umirzakov, A.; Mansurov, Z. Bio-Waste-Derived Few-Layered Graphene/SrTiO₃/PAN as Efficient Photocatalytic System for Water Splitting. *Appl. Surf. Sci.* **2021**, *549*, 149176. [CrossRef]
- 32. Sultanov, F.; Daulbayev, C.; Azat, S.; Kuterbekov, K.; Bekmyrza, K.; Bakbolat, B.; Bigaj, M.; Mansurov, Z. Influence of Metal Oxide Particles on Bandgap of 1D Photocatalysts Based on SrTiO₃/PAN Fibers. *Nanomaterials* **2020**, *10*, 1734. [CrossRef] [PubMed]
- 33. Sultanov, F.; Daulbayev, C.; Bakbolat, B.; Daulbayev, O.; Bigaj, M.; Mansurov, Z.; Kuterbekov, K.; Bekmyrza, K. Aligned Composite SrTiO₃/PAN Fibers as 1D Photocatalyst Obtained by Electrospinning Method. *Chem. Phys. Lett.* **2019**, 737, 136821. [CrossRef]

Disclaimer/Publisher's Note: The statements, opinions and data contained in all publications are solely those of the individual author(s) and contributor(s) and not of MDPI and/or the editor(s). MDPI and/or the editor(s) disclaim responsibility for any injury to people or property resulting from any ideas, methods, instructions or products referred to in the content.

Synthesis, Structure, and Energetic Characteristics of Perovskite Photocatalyst SrTiO₃: an Experimental and DFT Study

A.D. Kudaibergen¹, Zh.B. Kuspanov^{1,3*}, A.N. Issadykov^{3,4}, R.E. Beisenov⁵, Z.A. Mansurov^{2,3}, M.A. Yeleuov^{1,2,3}, Ch.B. Daulbayev^{3,6}

¹Satbayev University, 22a Satbayev str., Almaty, Kazakhstan

²Institute of Combustion Problems, 172 Bogenbay Batyr str., Almaty, Kazakhstan

³Institute of Nuclear Physics, 1 Ibragimova str., Almaty, Kazakhstan

⁴Joint Institute for Nuclear Research, 6 Joliot-Curie str., Dubna, Moscow Region, Russia

⁵Kazakh-British Technical University, 59 Tole by Str., Almaty, Kazakhstan

⁶National Laboratory Astana, Nazarbayev University, 53 Kabanbay Batyr Ave., Astana, Kazakhstan

Article info

Abstract

Received:

Received in revised form:

Accepted:

Keywords:

Photocatalysts SrTiO₃ Precipitation method DFT Quantum ESPRESSO PBE $SrTiO_3$ -based photocatalysts have become widely used due to their excellent properties such as high thermal stability, photocorrosion resistance and stable structure that can be modified by doping and making composites. In this work, $SrTiO_3$ powder was prepared from $Sr(NO_3)_2$ and TiO_2 precursors by a simple chemical precipitation method followed by calcination. It was determined that calcination at 900 °C followed by treatment in nitric acid solution produced cubic $SrTiO_3$ particles without the presence of any impurities. In addition, structural, morphology and energetic characterization using experimental and theoretical aspects are presented. Within the framework of density functional theory, the electronic properties of $SrTiO_3$ have been investigated in the Quantum ESPRESSO software package using the PBE functional under the generalized gradient approximation (GGA). The band structure and density of states were obtained, and the width of the bandgap was determined.

1. Introduction

The transition to renewable energy sources is becoming an essential step in solving modern environmental problems and meeting the growing energy needs of society. Effective utilization of the most widespread and promising energy source – solar radiation is one of the most critical problems, for the solution of which the search for new materials with improved optical properties is underway. Among them semiconductor photocatalysts are of the greatest interest due to their good study and wide range of possible applications: water splitting for hydrogen production [1–3], CO₂ reduction [4, 5], water purification from pollutants [6–11], degradation of dyes [12, 13] and others. However, due to the presence of a wide bandgap, the optical spectrum of semicon-

ductor photocatalysts is limited to the ultraviolet zone [1], which is 3–5% of the total energy of solar radiation [14]. For example, titanium dioxide, which is a well-studied material among photocatalysts, has a bandgap of 3.2 eV [14, 15]. In addition to the bandgap width, the critical parameters for photocatalysts are low recombination rate of charge carriers and resistance to photocorrosion [16, 17]. To obtain materials with the required properties, doping is most often used as a method of modifying the crystal lattice of the photocatalyst by adding impurities.

The class of perovskites with the general formula ABO₃ has more photocatalytic active centers on the surface compared to conventional metal oxides [18] due to their crystal structure in which A cations are located in the center of the BO₃ octahedron. Among them, SrTiO₃ is considered as one of the promising

materials, whose attractiveness consists of its environmental friendliness, low cost, high thermal and chemical stability, and excellent resistance to photocorrosion [17-19]. The cubic structure of SrTiO₃ perovskite makes it possible to vary the composition of A and B nodes, to control the charge balance and by using various impurities such as Cr, Al, Pt, Ag, Rh, Mo, Fe, etc., it is possible to achieve an improvement in photocatalytic activity [16], since the doping or formation of heterostructure due to the replacement of A cations by cations with a different ionic radius reduces the band structure of the material [18]. Goto et al. [20] in 2018 conducted a study of the photocatalytic water splitting activity of RhCrOx/ SrTiO₃:Al, they achieved an efficiency of converting solar energy into hydrogen energy (STH) of 0.4% using a panel photocatalytic reactor with an area of 1 m² in sunlight. This achievement demonstrates the prospects for using photocatalysts based on Sr-TiO₃ for large-scale photocatalytic water splitting. Recently, attention to the use of density functional theory (DFT) to calculate the electronic structure of many-particle systems in quantum physics and chemistry, in particular for modeling the properties of photocatalysts [14, 17, 18], has increased significantly.

Density functional theory (DFT), developed by Hohenberg and Cohn, is a method for calculating the electronic structure of molecules and condensed matter that is widely used in computational chemistry and physics [21]. This theory's essence is using electron density instead of the many-electron wave function in the Schrödinger equation to describe the electronic subsystem. The advantage of DFT over ab initio methods (e.g., the Hartree-Fock method) is higher accuracy and speed of calculations because, unlike the wave function, which depends on the three spatial coordinates of each of the N electrons (3N), the electron density is a function of only three spatial coordinates. However, DFT-based calculations cannot be applied in all cases because the exchange-correlation functionals responsible for approximating electron-electron interactions have limitations in accuracy due to the fact that no single functional can correctly describe all types of systems and interactions. Also, significant computational resources may be required to handle systems with a large number of atoms. Nevertheless, numerous studies show successful examples of the use of DFT computational methods [22–25]. Thus, it is obvious that the use of DFT calculations can help in finding and predicting the properties of new materials.

In this work, SrTiO₃ was synthesized, X-ray diffrac-

tion analysis, and EDX analysis were performed, and surface morphology was investigated by scanning electron microscopy (SEM) and transmission electron microscopy (TEM). To calculate the electronic properties of SrTiO₃, a model simulation of the crystal structure of SrTiO₃ was carried out using the Quantum-Espresso software code and applying the GGA-PBE exchange-correlation functional. The modeling results helped to evaluate the electronic properties of SrTiO₃, such as energy structure and bandgap width. The obtained results made it possible to better understand the behavior of the material and its potential applications as an efficient photocatalyst.

2. Experimental section

2.1. Photocatalyst preparation

To synthesize SrTiO₃ of high purity, a chemical precipitation method based on previous works was used [26–30]. $Sr(NO_3)_2$ (> 98% purity, Sigma Aldrich), TiO₂ (Sigma Aldrich, particle size: 0.27 μm, 0.35 μm, $0.48 \mu m$) and (COOH)₂*2H₂O (> 99.5%, Sigma Aldrich) were used as initial reagents. A concentrated 0.12 M solution of Sr(NO₃)₂ was prepared using distilled water. TiO₂ powder was then added in the ratio of Ti and Sr 1:1. The resulting suspension was treated for 30 min in an ultrasonic bath. After that, 0.4 M solution of (COOH)₂*2H₂O was added dropwise with vigorous stirring. The pH of the resulting mixture was adjusted to 6-7 with 10% NH₃OH solution. The suspension was filtered, and the residue was washed several times with distilled water. The obtained powder was dried at 60 °C overnight and then calcined at 900 °C for 1 h. Figure 1 shows a schematic representation of the methodology for the synthesis of SrTiO₃ powder.

2.2. Photocatalyst characterization technique

The surface morphology of the samples was investigated using a scanning electron microscope (SEM) JEM-2100 (JEOL, Japan). Scanning transmission electron microscopy (STEM) TESCAN MAIA3 XMU was used to further study morphology in high resolution. XRD analysis was performed on a Drone-8 X-ray diffractometer with detection unit rotation angles ranging from 5° to 70° and a minimum step of 0.001°. The permissible deviation of the detection unit from the specified rotation angle was ±0.015°.

2.3. Computational study

Based on the density functional theory, the electronic structure of SrTiO₃ was investigated; the



Fig. 1. Schematic illustration of the process of SrTiO₃ synthesis by chemical precipitation method.

open-source Quantum ESPRESSO program package was used as a computer code. The cubic structure of SrTiO₃ shown in Fig. 2 belongs to the space group Pm3m at room temperature, the lattice constants (a = b = c) were co-valued to 3.905 Å [24]. The Perdew-Burke-Ernzerhof (PBE) functional was adopted for the exchange-correlation potential (XC) in the generalized gradient approximation (GGA). The ultra-soft pseudo potential (USPP) was applied to approximate the electron-nucleus interaction. A 6 × 6 × 6 × 6 k-point Monkhorst-Pack grid was used to integrate the Brillouin zone for the calculation of the self-consistent field, and a 20 × 20 × 20 × 20 grid for the inconsistent field. The electronic structure was determined for relaxed cells along the Γ-X-M-Γ-R-X [17] symmetry points in the Brillouin zone.

3. Results and discussion

3.1. Photocatalyst characterization

The crystal structure of the semiconductor SrTiO₃ synthesized by chemical precipitation followed by

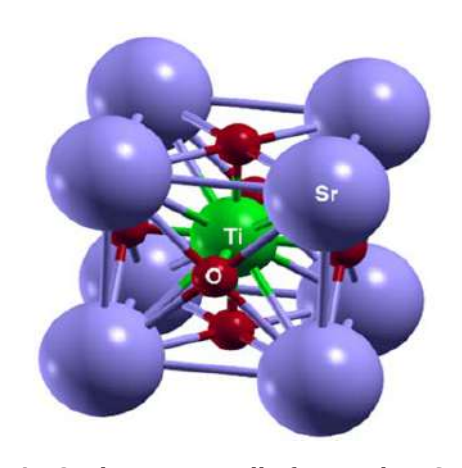


Fig. 2. Elementary cell of perovskite SrTiO₃.

calcination at 900 °C was studied by X-ray diffraction. Figure 3a shows typical diffraction peaks at 20 equal to 32.23°, 39.98°, 46.50°, 57.83° and 67.64° corresponding to (110), (111), (200), (211), and (220) orientations of the SrTiO₃ crystal lattice. These peaks indicate that the semiconductor sample obtained via chemical precipitation is cubic SrTiO₃ and is consistent with standard data for SrTiO₃ (JCPDS Card No. 35-0734). It is particularly important to note that the peak at 2θ , equal to 32.23° , has a very high intensity, indicating that the semiconductor is highly crystalline. This is important because the transport efficiency of charged carriers arising from photogeneration can strongly depend on the crystallinity of the material. If the crystallinity is low, this can lead to inefficient migration of charged particles.

The choice of strontium titanate precursors with different sizes is due to the fact that, according to experimental data [31], when using smaller particles of TiO_2 precursors, the synthesis reaction is completed at lower temperatures and in less time, which indicates the dependence of the reaction rate on the surface area precursors. It was also established [31] that the initial particle size of the TiO_2 precursor strongly affects the particle size of the reaction product obtained as a result of hydrothermal synthesis.

EDX analysis confirms the presence of O, Ti, and Sr in the obtained SrTiO₃ samples without any other impurities. Considering the atomic percentages of the synthesized sample as shown in Fig. 3d it can be found that Sr/Ti/O are 17.30%/19.63%/63.07%, respectively. In addition, the FIB-SEM technique was used to determine the distribution of elements in the obtained sample. Figure 3(c-f) shows the elemental maps for Sr, Ti and O in the SrTiO₃ sample. From the

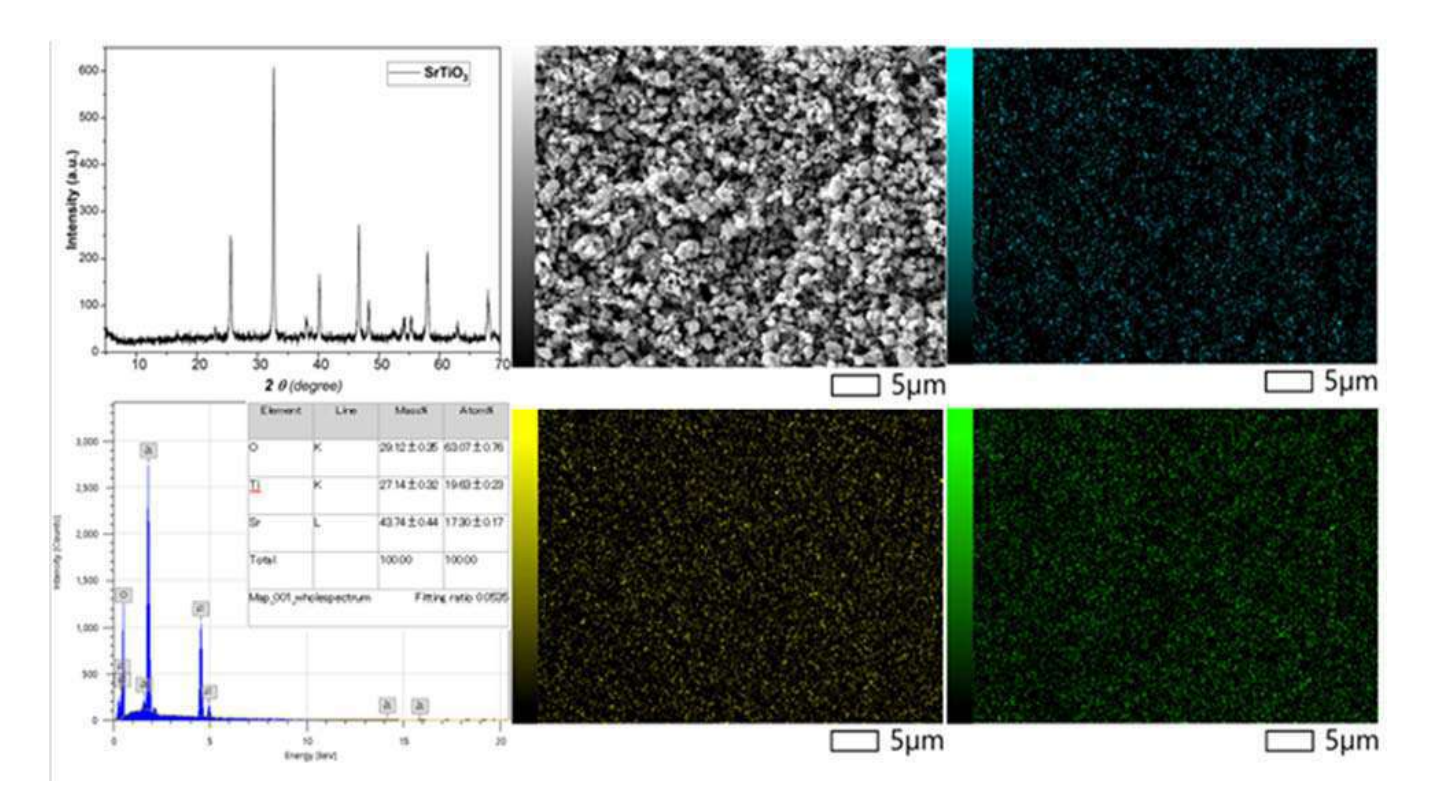


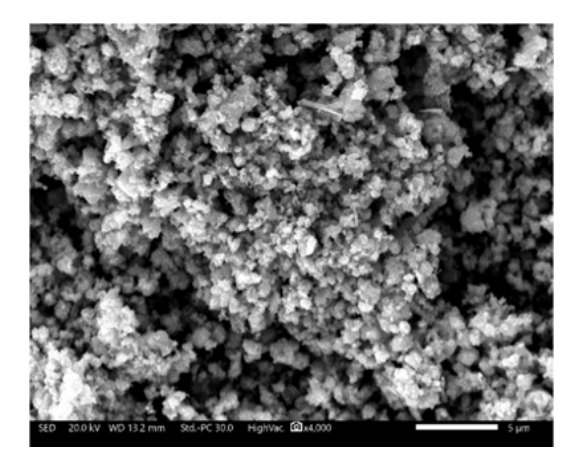
Fig. 3. X-ray spectra of synthesized $SrTiO_3$ powder – (a); energy dispersive X-ray spectrum of $SrTiO_3$ particles – (b); distributions of elements in the obtained sample by FIB-SEM method – (c-f).

obtained maps, it can be seen that Sr, Ti, and O are uniformly distributed throughout the sample area.

The morphology of the obtained SrTiO₃ samples was studied by scanning (SEM) and transmission (TEM) electron microscope at different resolutions. As the results of scanning electron microscopy (Fig. 4) showed, we found that SrTiO₃ particles calcined at 900 °C have cubic shapes and sizes from 150 to 300 nm. Whereas increasing the calcination temperature to 1000 °C and 1100 °C increases the size of SrTiO₃ particles to the micrometer scale, which can negatively affect their photoactivity due to the increased distance that the photogenerated electrons and holes need to travel to the surface where the reactions occur. This increases the probability of recombination (charge fusion) and can reduce the efficiency of the reactions [30, 32]. Calcination at 800 °C leads to the formation of smaller particles but with more impurities such as SrCO₃ [33]. Based on literature and experimental data, the optimum calcination temperature is 900 °C followed by treatment in 1M nitric acid solution to remove residual SrCO₃. However, it should be noted that the particle sizes are very heterogeneous. From studies in the literature, it is clear that doping SrTiO₃ with other elements such as Al or Mn can contribute to the size reduction and distortion of the shape of SrTiO₃ crystals [34, 35].

In the case of TEM, one can see clearly formed cubes of SrTiO₃ with anisotropic structure, the average size of which is about 200 nm as can be seen from Fig. 5. An important feature of these particles is the anisotropic structure, which creates a difference in energy on different faces, leading to the formation of p-n junctions [36]. This allows the charge within each photocatalyst particle to be separated using an internal electric field. Thus, electrons are concentrated on some facets and holes on other facets, which helps to separate the photocatalytic reduction and oxidation processes on different facets [37]. Due to the anisotropic crystal structure, selective precipitation of co-catalysts occurs, which leads to the release of hydrogen and oxygen on the faces of the cubic photocatalyst [37].

The efficiency of solar energy conversion in semi-conductor photocatalysts depends on the efficiency of charge separation. Without the presence of suitable active sites for photocatalytic reactions, photogenerated electrons and holes can easily recombine. It was found [38] that semiconductors such as ${\rm TiO_2}$ and ${\rm BiVO_4}$, which have characteristic anisotropic facets, can separate photogenerated electrons and holes into different facets. This separation provides selective reductive and oxidative reactivity on different facets. Mu et al. [38, 39] achieved the transformation of an isotropic 6-facet ${\rm SrTiO_3}$ photocatalyst



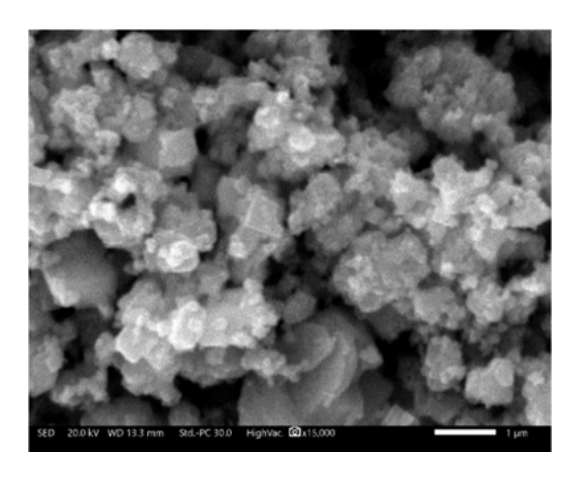
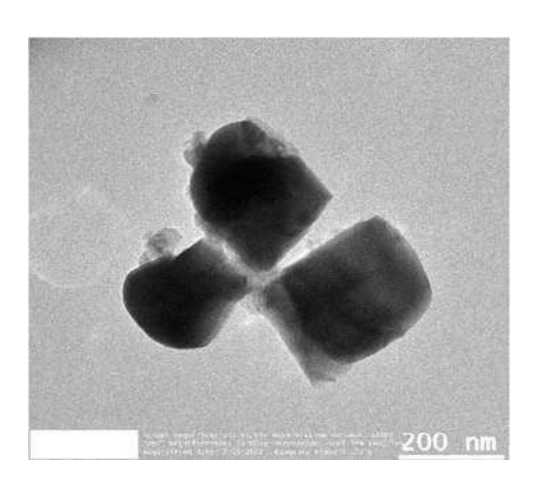


Fig. 4. SEM images of obtained SrTiO₃ at different magnifications.



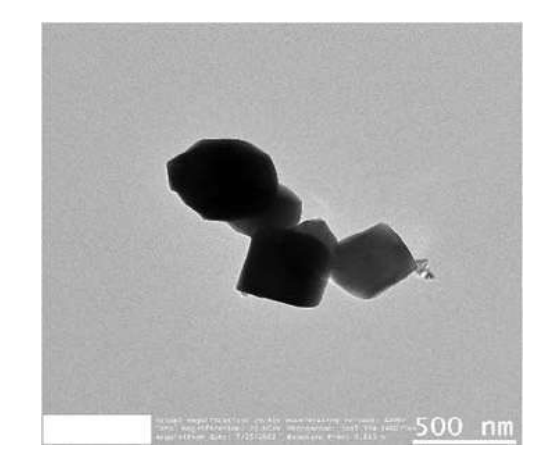


Fig. 5. SEM images of obtained SrTiO₃ at different magnifications.

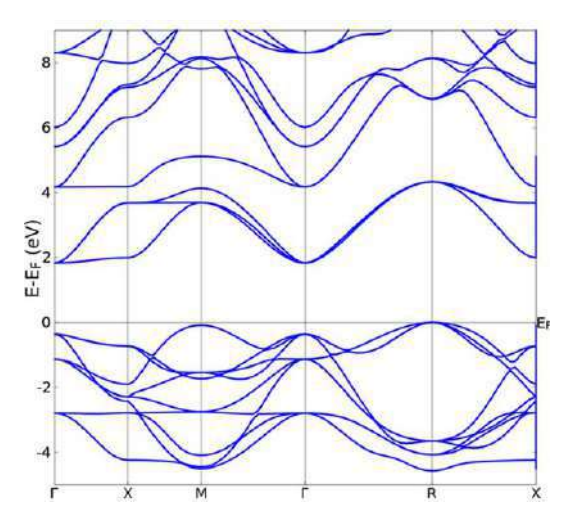
into an anisotropic 18-facet SrTiO₃ crystal and thereby significantly improved the separation of electrons and holes. They also found that the release of hydrogen and oxygen occurs at different crystal facets after the formation of an anisotropic SrTiO₃ facet. This strategy is the most promising way to increase photocatalytic activity since it allows to reduce charge recombination and reduces the need to search for various semiconductors necessary for the formation of a heterojunction.

3.2. DFT calculations

To investigate the electronic structure, the band structure and total density of states (TDOS) calculations were performed. The band structure shown in Fig. 6 (the Fermi energy is set equal to 0 eV on the ordinate axis) shows that the conduction zone minima lie at the Γ symmetry point, while the valence band maxima are at the R symmetry point. Thus, the indirect width of the bandgap (R- Γ) in the electronic structure for SrTiO₃ is 1.83 eV. There is an

underestimation of the bandgap width compared to the experimental value of 3.20 eV, which is a typical problem for DFT-based calculations using the GGA-PBE method due to discontinuities present in the energy derivative of the number of electrons [17]. The value of the direct bandgap width (conduction band minima and valence band maxima at the Γ symmetry point) was 2.197 eV. The obtained results are in agreement with the data from other studies [40–43], but unlike them, in this work we did not carry out modeling of the SrTiO₃ supercell to minimize the computational resources consumed and because we did not consider the doping of the crystal structure with impurity atoms.

It is well known that the band gap is a key factor that characterizes the electronic structure of materials and determines their application in electronics, so the accurate prediction of the band gap is a key issue in the development of new semiconductor materials. The PBE functional, which is very popular in DFT calculations due to its efficiency, due to the tendency to underestimate the band gap for semi-



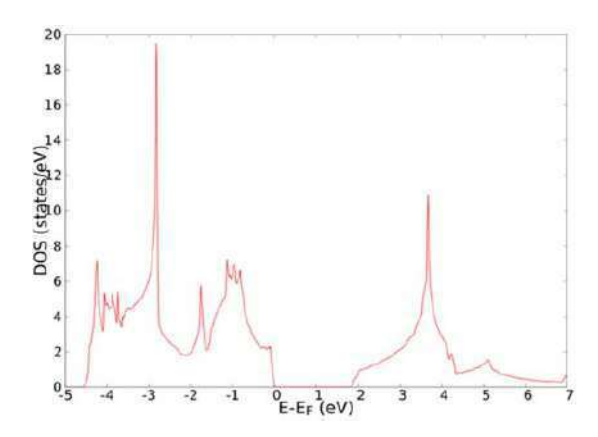


Fig. 6. Band structure and total density of states of SrTiO₃.

conductor compounds and insulators, as has been demonstrated in many studies [17, 22, 43], as well as in this work, does not suitable for calculations of the electronic structure of semiconductor materials.

In order to achieve better accuracy in determining the width of the bandgap, some authors [24, 44] use hybrid functionals in calculations, such as PBEO, HSE, which provide better accuracy in calculating the lattice parameters of most solids and the bandgap width in semiconductors and insulators, give an excellent description of insulating antiferromagnetic oxides of rare-earth and transition metals [45]. For example, the paper [46] compares PBE, SCAN and HSE06 in DFT calculations for cesium antimonide and telluride and the authors conclude that SCAN is the best option for this type of materials, PBE is suitable for modeling structural parameters but should be avoided when quantitatively describing electronic properties, and HSE06 is excellent for determining electronic and optical gaps because it was designed for this purpose, but requires significant computational resources. Another approach to improve computational results is to introduce semiempirical terms into the GGA functional, such as GGA+U, in which the fitted Hubbard parameter U, is fitted to reproduce the experimental forbidden band width, geometry, and other parameters [25, 40, 45]. Therefore, it is worthwhile to further perform calculations relying on hybrid functionals to achieve the best fit to the experimental data.

To study the influence of doping on the structural and electronic properties of SrTiO₃, it is necessary to synthesize complex composites and perform DFT calculations. For this purpose, it is necessary to construct supercells with the introduction of impurity atoms, as was done in many works [1, 17, 24, 25,

41], as well as to calculate the optical properties of the materials.

4. Conclusion

SrTiO₃ was synthesized by a simple chemical precipitation method. X-ray diffraction data reveal the cubic structure of the synthesized SrTiO₃ and indicate the high crystallinity of the semiconductor. Elemental analysis was carried out using EDX analysis and FIB-SEM technique which showed the absence of impurities. Morphology study using SEM and TEM demonstrated the cubic structure of the formed particles of the obtained samples. The structural and electronic properties of SrTiO₃ were also investigated. The results were obtained using density functional theory in the framework of the GGA-PBE approximation. The band structure and density of states of SrTiO₃ demonstrate the presence of an indirect band gap, and the calculated parameters are suitable with the literature results.

Acknowledgments

This research is funded by the Science Committee of the Ministry of Science and Higher Education and of the Republic of Kazakhstan (No AP14869381).

References

- [1]. A.C. Wardhana, A. Yamaguchi, S. Shoji, M. Liu, T. Fujita, T. Hitosugi, M. Miyauchi, *Appl. Catal. B: Environ.* 270 (2020) 118883. DOI: 10.1016/j.apcatb.2020.118883
- [2]. T.K. Maji, Md.N. Hasan, S. Ghosh, D. Wulferding, C. Bhattacharya, P. Lemmens, D. Karmakar, S.K.

- Pal, *J. Photochem. Photobiol. A: Chem.* 397 (2020) 112575. DOI: 10.1016/j.jphotochem.2020.112575
- [3]. Y. Liu, R. Li, H. Yang, J. Song, J. Hu, C. Yang, Z. Zheng, Int. J. Hydrog. Energy 47 (2022) 14563–14569. DOI: 10.1016/j.ijhydene.2022.02.207
- [4]. P.K. Prajapati, A. Malik, N. Nandal, S. Pandita, R. Singh, S. Bhandari, S. Saran, S.L. Jain, Appl. Surf. Sci. 588 (2022) 152912. DOI: 10.1016/j. apsusc.2022.152912
- [5]. J. Zhao, Z. Xiong, J. Wang, Y. Qiu, P. Liu, Y. Zhao, J. Zhang, Chem. Eng. J. 446 (2022) 137242. DOI: 10.1016/j.cej.2022.137242
- [6]. J. Duan, X. Fang, C. Li, J. Qu, L. Guo, Y. Zou, M. Xiang, W. Wang, Colloids Surf. Physicochem. Eng. Asp. 659 (2023) 130759. DOI: 10.1016/j. colsurfa.2022.130759
- [7]. K. Kato, T. Shirai, J. Alloys Compd. 901 (2022) 163434. DOI: 10.1016/j.jallcom.2021.163434
- [8]. F.R. Sultanov, C. Daulbayev, B. Bakbolat, Z.A. Mansurov, *Eurasian J. Phys. Funct. Mater.* 2 (2018) 104–109. DOI: 10.29317/ejpfm.2018020202
- [9]. F.R. Sultanov, Ch. Daulbayev, B. Bakbolat, Z.A. Mansurov, Eurasian Chem.-Technol. J. 20 (2018) 195-200. DOI: 10.18321/ectj721
- [10]. H.K. Megbenu, Z. Tauanov, C. Daulbayev, S.G. Poulopoulos, A. Baimenov, J. Chem. Technol. Biotechnol. 97 (2022) 3375–3384. DOI: 10.1002/ jctb.7197
- [11]. A. Baimenov, F. Montagnaro, V.J. Inglezakis, M. Balsamo, *Ind. Eng. Chem. Res.* 61 (2022) 8204–8219. DOI: 10.1021/acs.iecr.2c00531
- [12]. J.S. Gan, X.B. Li, U. Arif, F. Ali, A. Ali, F. Raziq, N. Ali, Y. Yang, Z. Wang, Surf. Interfaces. 39 (2023) 102938. DOI: 10.1016/j.surfin.2023.102938
- [13]. M. Mousavi, J.B. Ghasemi, *J. Taiwan Inst. Chem. Eng.* 121 (2021) 168–183. DOI: 10.1016/j. jtice.2021.04.009
- [14]. W. Navarra, I. Ritacco, O. Sacco, L. Caporaso, M. Farnesi Camellone, V. Venditto, V. Vaiano, *J. Phys. Chem. C* 126 (2022) 7000–7011. DOI: 10.1021/acs. jpcc.2c00152
- [15]. D.I. Chenchik, J.M. Jandosov, Eurasian Chem.-Technol. J. 19 (2017) 191–195. DOI: 10.18321/ ectj651
- [16]. M.M.J. Sadiq, U.S. Shenoy, D.K. Bhat, Front. Mater. Sci. 12 (2018) 247–263. DOI: 10.1007/ s11706-018-0433-0
- [17]. H. Bantawal, U.S. Shenoy, D.K. Bhat, Appl. Surf. Sci. 513 (2020) 145858. DOI: 10.1016/j. apsusc.2020.145858
- [18]. Y. Fo, M. Wang, Y. Ma, H. Dong, X. Zhou, *J. Solid State Chem.* 292 (2020) 121683. DOI: 10.1016/j. issc.2020.121683

- [19]. Z.A. Mansurov, *Eurasian Chem.-Technol. J.* 22(4) (2020) 241-253. DOI: 10.18321/ectj994
- [20]. Y. Goto, T. Hisatomi, Q. Wang, T. Higashi, K. Ishikiriyama, T. Maeda, Y. Sakata, S. Okunaka, H. Tokudome, M. Katayama, S. Akiyama, H. Nishiyama, Y. Inoue, T. Takewaki, T. Setoyama, T. Minegishi, T. Takata, T. Yamada, K. Domen, *Joule* 2 (2018) 509–520. DOI: 10.1016/j.joule.2017.12.009
- [21]. A.A. Aldongarov, A.M. Assilbekova, I.S. Irgibaeva, A.I. Mantel, *Eurasian J. Phys. Funct. Mater.* 4 (2020) 255–260. DOI: 10.29317/ejpfm.2020040308
- [22]. R. Garcia-Diaz, M.T. Romero de la Cruz, R. Ochoa Valiente, J. Guerrero-Sanchez, G. Hernández Cocoletzi, Appl. Surf. Sci. 487 (2019) 1394–1402. DOI: 10.1016/j.apsusc.2019.05.134
- [23]. H. Bentour, M. El Yadari, A. El Kenz, A. Benyoussef, Solid State Commun. 312 (2020) 113893. DOI: 10.1016/j.ssc.2020.113893
- [24]. F. Opoku, K.K. Govender, C.G. Catharina Elizabeth van Sittert, P.P. Govender, *Int. J. Hydrog. Energy* 43 (2018) 22253–22264. DOI: 10.1016/j. ijhydene.2018.10.072
- [25]. J. Wang, Y. Wang, Y. Wang, X. Zhang, Y. Fan, Y. Liu, Z. Yi, Int. J. Hydrog. Energy 46 (2021) 20492–20502. DOI: 10.1016/j.ijhydene.2021.03.147
- [26]. F. Sultanov, C. Daulbayev, B. Bakbolat, O. Daulbayev, M. Bigaj, Z. Mansurov, K. Kuterbekov, K. Bekmyrza, Chem. Phys. Lett. 737 (2019) 136821.
 DOI: 10.1016/j.cplett.2019.136821
- [27]. C. Daulbayev, F. Sultanov, A.V. Korobeinyk, M. Yeleuov, S. Azat, B. Bakbolat, A. Umirzakov, Z. Mansurov, Appl. Surf. Sci. 549 (2021) 149176. DOI: 10.1016/j.apsusc.2021.149176
- [28]. F. Sultanov, C. Daulbayev, S. Azat, K. Kuterbekov, K. Bekmyrza, B. Bakbolat, M. Bigaj, Z. Mansurov, Nanomaterials 10 (2020) 1734. DOI: 10.3390/ nano10091734
- [29]. Z. Kuspanov, B. Bakbolat, A. Baimenov, A. Issadykov, M. Yeleuov, C. Daulbayev, Sci. Total Environ. 885 (2023) 163914. DOI: 10.1016/j. scitotenv.2023.163914
- [30]. Z. Kuspanov, A. Umirzakov, A. Serik, A. Baimenov, M. Yeleuov, C. Daulbayev, Int. J. Hydrog. Energy (2023). DOI: 10.1016/j.ijhydene.2023.06.168
- [31]. A. Habib, R. Haubner, N. Stelzer, Mater. Sci. Eng. B. 152 (2008) 60–65. DOI: 10.1016/j. mseb.2008.06.018
- [32]. B. Bakbolat, C. Daulbayev, F. Sultanov, R. Beissenov, A. Umirzakov, A. Mereke, A. Bekbaev, I. Chuprakov, *Nanomaterials* 10 (2020) 1790. DOI: 10.3390/nano10091790
- [33]. P.K. Roy, J. Bera, *Mater. Res. Bull.* 40 (2005) 599–604. DOI: 10.1016/j.materresbull.2005.01.010

- [34]. Y. Yang, B. Sun, G. Zhou, C. Ke, J. Zhang, Y. Zhou, S. Mao, J. Qin, Y. Zhao, *Mater. Today Commun.* 35 (2023) 105512. DOI: 10.1016/j. mtcomm.2023.105512
- [35]. Z. Su, F. Fang, S. Liu, N. Wang, Y. Wan, D. Guo, W. Han and K. Chang, *Catal. Sci. Technol.* 12 (2022) 5003–5008. DOI: 10.1039/d2cy01146h
- [36]. H. Nishiyama, T. Yamada, M. Nakabayashi, Y. Maehara, M. Yamaguchi, Y. Kuromiya, Y. Nagatsuma, H. Tokudome, S. Akiyama, T. Watanabe, R. Narushima, S. Okunaka, N. Shibata, T. Takata, T. Hisatomi, K. Domen, *Nature* 598 (2021) 304–307. DOI: 10.1038/s41586-021-03907-3
- [37]. T. Takata, J. Jiang, Y. Sakata, M. Nakabayashi, N. Shibata, V. Nandal, K. Seki, T. Hisatomi, K. Domen, *Nature* 581 (2020) 411–414. DOI: 10.1038/s41586-020-2278-9
- [38]. S.-C. Chan, Y.-L. Cheng, B.K. Chang, C.-W. Hong, *RSC Adv.* 11 (2021) 18500–18508. DOI: 10.1039/d1ra01711j
- [39]. L. Mu, Y. Zhao, A. Li, S. Wang, Z. Wang, J. Yang, Y. Wang, T. Liu, R. Chen, Z. Jian, F. Fan, R. Li, C. Li, *Energy Env. Sci.* 9 (2016). DOI: 10.1039/ C6EE00526H

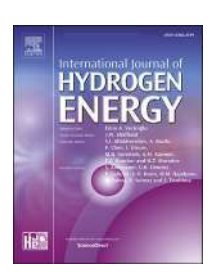
- [40]. A. Adewale, C. Abdullah, *Int. J. Nanoelectron. Mater.* 12 (2019) 11–18.
- [41]. M. Rizwan, M. Anwar, Z. Usman, M. Shakil, S.S.A. Gillani, H.B. Jin, C.B. Cao, U. Mushtaq, Chin. J. Phys. 62 (2019) 388–394. DOI: 10.1016/j. cjph.2019.09.036
- [42]. M. Rizwan, Z. Khadija, T. Mahmood, S.S.A. Gillani, M.I. Khan, *Phys. B Condens. Matter.* 602 (2021) 412553. DOI: 10.1016/j.physb.2020.412553
- [43]. S.S.A. Gillani, R. Ahmad, Islah-u-din, M. Rizwan, M. Shakil, M. Rafique, G. Murtaza, H.B. Jin, *Optik* 201 (2020) 163481. DOI: 10.1016/j.ijleo.2019.163481
- [44]. Y.S. Hou, S. Ardo, R.Q. Wu, Phys. Rev. Mater. 5 (2021) 065801. DOI: 10.1103/ PhysRevMaterials.5.065801
- [45]. J. Morin, J.M. Pelletier, Density Functional Theory: Principles, Applications and Analysis. Nova Science Publishers, Incorporated, New York, 2013, p. 3.
- [46]. H.-D. Saßnick, C. Cocchi, *Electron. Struct.* 3 (2021) 027001. DOI: 10.1088/2516-1075/abfb08



Available online at www.sciencedirect.com

ScienceDirect

journal homepage: www.elsevier.com/locate/he



Review Article

Multifunctional strontium titanate perovskitebased composite photocatalysts for energy conversion and other applications



Zhengisbek Kuspanov a,b, Arman Umirzakov a,b,d, Aigerim Serik a,b, Alzhan Baimenov a,b, Mukhtar Yeleuov a,b, Chingis Daulbayev a,b,

- ^a Satbayev University, 050013, Almaty, Kazakhstan
- ^b Institute of Nuclear Physics, 050032, Almaty, Kazakhstan
- ^c Al Farabi Kazakh National University, 050040, Almaty, Kazakhstan
- ^d National Laboratory Astana, Nazarbayev University, 010000, Astana, Kazakhstan

HIGHLIGHTS

- The main strategies to overcome the limitations of SrTiO₃ based photocatalysts in various applications are presented.
- The synthesis methods of composites based on SrTiO₃ for photocatalytic applications were discussed.
- The potential applications of SrTiO₃-based composites in solving environmental and energyrelated problems are explored.

ARTICLE INFO

Article history:
Received 23 April 2023
Received in revised form
12 June 2023
Accepted 14 June 2023
Available online 01 July 2023

Keywords: Photocatalysis SrTiO₃-Based heterostructures CO₂ reduction

GRAPHICAL ABSTRACT



ABSTRACT

The detrimental impact of human activity on the global ecological situation has resulted in the active exploration and development of alternative energy sources. Efficient solar energy utilization can significantly contribute to resolving the current energy crisis, because approximately 1.36 kW m⁻² of solar radiation reaches the Earth's surface, and this can be used to satisfy the global energy requirements. Among various prevalent sunlight conversion technologies, photocatalytic materials are potentially useful for hydrogen production and other relevant applications. Existing technologies for the production and use of photocatalysts do not sufficiently address the target characteristics owing to the low solar conversion efficiency and service life in addition to high costs. However, recent advances in SrTiO₃-based heterostructures indicate that photocatalysts can potentially compete with modern solar energy technologies in terms of their practical application. In

^{*} Corresponding author. Institute of Nuclear Physics, 050032, Almaty, Kazakhstan. E-mail address: chingis.daulbayev@nu.edu.kz (C. Daulbayev). https://doi.org/10.1016/j.ijhydene.2023.06.168

 ${
m H}_2$ evolution ${
m N}_2$ fixation Pollutants degradation this review, we systematically consider the advancement in the production and application of SrTiO₃-based photocatalysts in various fields. The methods for obtaining complex heterostructures with different classes of nanomaterials are comprehensively discussed. The aim of this review is to highlight the advantages and limitations of using SrTiO₃-based photocatalytic systems. Finally, the future prospects of using SrTiO₃-based photocatalysts are considered from the perspective of their practical applications.

© 2023 Hydrogen Energy Publications LLC. Published by Elsevier Ltd. All rights reserved.

Contents

Introduction	
Methods for obtaining SrTiO ₃ and SrTiO ₃ -based composites	38636
Hydrothermal method	38637
Solvothermal method	38637
Sol-gel method	38638
Precipitation/co-precipitation	38638
Other methods for obtaining heterostructured SrTiO ₃ -based photocatalysts	38639
Application of heterostructured SrTiO₃-based photocatalysts	38639
Photocatalytic water splitting with the release of hydrogen	38639
Photocatalytic decomposition of organic pollutants and antibiotics	38642
Photocatalytic decomposition of organic air pollutants	38644
Photocatalytic sterilisation	38644
Other applications of heterostructured SrTiO ₃ -based photocatalysts	38644
Photoanodes for dye-sensitized solar cells	38644
Electrochemical sensors/biosensors	38645
Energy storage	38647
Biodiesel production	38647
Conclusions and future prospects	38648
Declaration of competing interest	38648
Acknowledgments	38648
References	38649

Abbreviations

ALD atomic layer deposition

BRO bromhexine
CB conduction band
CIP ciprofloxacin
CNT carbon nanotube

CTC \bullet HCl aureomycin hydrochloride D_{max} - D_{rem} electric displacement difference

DPH diphenhydramine
Eb breakdown strength
FAME fatty acid methyl ester
J_{sc} short circuit current density

MB methylene blue
MO methyl orange
NHE hydrogen electrode
PBS phosphate-buffered saline

RhB rhodamine B

SILAR sequential ion layer adsorption reaction

SMX carbamazepine

TBT tetra-n-butyl orthotitanate

 $\begin{array}{ll} \text{TC} & \text{tetracycline} \\ \text{TEOA} & \text{triethanolamine} \\ \text{U_e} & \text{energy storage density} \end{array}$

VB valence band V_{OC} circuit voltage

Introduction

Studies aimed at identifying sustainable and environmentally friendly energy sources are of considerable interest owing to the negative impact of fossil fuels on the environment [1-5]. Therefore, several programs and strategies have been adopted to develop and implement technologies for the use of alternative energy sources. The 2019-2025 Global Strategy for Sustainable Energy is one such program adopted by the United Nations and the Green Deal project (with an annual investment of €260 billion), which aims to reduce greenhouse gas emissions in the European Union by up to 32% and shift to a carbon-neutral society by 2030 [6]. Such strategic development programs are also being adopted in the Central Asian region. For example, Kazakhstan has adopted a concept for the development of the fuel and energy sector until 2030, with the aim of developing and expanding the role of alternative and renewable energy sources and implementing a decarbonisation policy.

Efficient solar energy utilization can significantly contribute to the successful implementation of these programs and development strategies. Although technologies are available for the efficient conversion of sunlight into energy, photocatalysts that can produce pure hydrogen and purify water and air from various pollutants by converting light have attracted considerable interest. The discovery of photocatalytic decomposition of water in 1972 [7] marked the beginning of numerous studies, and this field has witnessed significant progress thus far. Numerous types of photocatalysts, such as TiO2, SrTiO3, NaTaO3, ZnO, Co3O4, and Fe₂O₃, have been discovered and investigated [8-12]. The quantum efficiencies of solar light conversion for all photocatalysts are typically low and depend on the sensitivity of the photocatalytic system to the visible spectrum. For example, theoretical calculations indicate that solar energy can be converted into hydrogen by at efficiencies up to 15% if a solar spectrum below 600 nm is used [13,14]. The actual quantum efficiency for the photocatalytic decomposition of water is only 1% [15].

The quantum efficiency of a photocatalyst for converting light into electrochemical energy depends on the following parameters: 1) the band gap, which should be comparable to the photon energy in the visible region of the spectrum (2.0-2.4 eV); 2) a low number of recombination of photoinduced electron-hole pairs, which have high mobility; 3) resistance to the aquatic environment, temperature, acid-base solutions, and sunlight; 4) free diffusion of water molecules. A possible solution to improve the solar conversion efficiency is the creation of hybrid composite structures, which can reduce the band gap of the photocatalyst and improve light absorption. In this regard, strontium titanate (SrTiO₃) is suitable for creating hybrid composite photocatalyst systems owing to several advantages. First, this semiconductor material is a well-researched photocatalyst with a band gap of 3.2 eV [16]; second, numerous studies have indicated the formation of SrTiO₃-based composite structures, whereby the photocatalytic decomposition of water is improved by 69% compared with the process using pure SrTiO₃ powder [17-20]. In addition, SrTiO₃ has been

successfully used in the manufacture of panels with a total area of 100 m² for hydrogen production [21].

Over the past decade, numerous research articles containing the keyword SrTiO₃ have been published. The growing interest in SrTiO₃ is evidenced by fundamental research [22-26] devoted to theoretical and practical aspects, which allow us to consider the prospects and problems of using this perovskite in various fields. These studies indicate that the type of co-catalyst and the method of synthesising the heterostructure significantly affect the SrTiO3 structure; consequently, the properties of the SrTiO3-based composite structures are modified. From this perspective, we believe that the properties of SrTiO₃-based heterostructures must be comprehensively examined to elucidate the relationship between the synthesis parameters of SrTiO₃-based composites and the characteristics of their applications. In this review, methods for obtaining SrTiO₃-based composites and recent advances in their practical application are considered. We analyse the influence of the method of obtaining $SrTiO_3$ -based composites on the mechanism and efficiency of their practical application in various fields. Finally, the problems and future prospects for the use of SrTiO₃ and its composites in various fields are discussed.

Methods for obtaining SrTiO₃ and SrTiO₃-based composites

The use of pure SrTiO₃ is not of particular interest owing to several factors, such as extremely low efficiency, attributed to the rapid recombination of photogenerated electrons and holes, and a wide bandgap, which reduces the solar energy absorption spectrum. Creating heterojunctions based on SrTiO₃ and various other materials addresses their limitations and significantly contributes to the creation of new types of photocatalysts. Conventional methods for synthesising SrTiO₃ include hydro/solvothermal [27–29], solid-phase [30], sol-gel [31], co-precipitation [32], and hybrid methods. SrTiO₃ nanoparticles with various shapes and sizes can be obtained through the application of various methods and their combinations. In particular, the solid-phase method results in chemically pure cube-like SrTiO₃ particles with an average size of 75 nm [33]. The hybrid sol-gel-solid phase method is environmentally friendly and enables the synthesis of SrTiO₃ nanoparticles with a smaller size (34 nm) [34]. The advantages of hydro/solvothermal methods include the ability to control the morphology of the SrTiO₃ nanoparticles by adjusting the synthesis conditions. Graphic illustrations of different approaches for obtaining SrTiO₃-based composites are shown in Fig. 1.

When heterostructures are created by methods that affect the photocatalytic properties, the main problems are: 1) insufficiently close contact between two or more phases for free exchange of charge carriers; 2) inability to control the size, morphology, and crystallinity to obtain pure, homogeneous heterostructures of the required shape; and 3) difficulty in creating unique surfaces or mesoporous structures with a high specific area to provide numerous reaction centres. In this section, we discuss recent advances in the synthesis of SrTiO₃-based photocatalysts, because the production of

highly efficient heterostructured photocatalysts at low cost and without environmental harm is an urgent challenge.

Hydrothermal method

The conventional hydrothermal method can be used to efficiently synthesise both crystalline SrTiO₃ and related heterostructured composite materials. The primary advantage of this method is the improvement in the crystallinity, crystallite size, and morphology at moderate temperatures. The other advantages of this method include simplicity, environmental friendliness, and the ability to control the surface chemical composition by controlling the type of solvent, sol composition, holding time, pressure, and reaction temperature. Particularly, multilayer composites with desired shapes can be created. Thus, a simple hydrothermal method can yield hollow multi-shell homogeneous structures of SrTiO3 doped with La and Rh (STOLa/Rh) [35] and SrTiO3-TiO2 [36]. In addition to multi-shell structures, nanocomposites (CdSe/ SrTiO₃) with quasi-spherical structures and rough surfaces can be obtained through the hydrothermal method [37]. Simultaneously, the structure of such a heterojunction, which is formed by modifying quantum dots (CdSe) on the surface of SrTiO₃ nanoparticles, improves its photocatalytic characteristics. Another promising hybrid photocatalytic system is the ZnO/SrTiO3 nanocomposite, which is obtained through a lowcost hydrothermal method and consists of ZnO nanosheets modified with SrTiO₃ nanospherical particles [38]. For this system, analysing the chemical composition using X-ray photoelectron spectroscopy and maps of the spatial distribution of atoms indicate that pure composites are produced with ZnO-SrTiO₃ atomic interfacial contact; thus, successful hydrothermal synthesis is confirmed. Hybridisation and creation of a heterogeneous ZnO semiconductor with a wide-band SrTiO₃ photocatalyst reduces the recombination of photoexcited excitons, thereby increasing the photocatalytic activity.

Obtaining sufficient close contact and a strong chemical bond between the components is crucial for the successful synthesis of highly efficient heterojunction photocatalysts. For example, the composite photocatalyst rGO@SrTiO3 obtained through the hydrothermal method demonstrates the formation of a sufficiently strong chemical bond, which is associated with a possible improvement in the photocatalytic properties of the rGO@SrTiO3 nanocomposite, in contrast to the separate use of pure SrTiO₃ or rGO [39]. In addition, a heterostructure composite consisting of Ag-doped STO/g-CN was synthesised for the efficient photocatalytic production of hydrogen and decomposition of the pesticide dicofol; the hydrothermal reaction was found to contribute to the close contact between the g-CN nanosheets and STO and Ag nanoparticles, thus increasing the efficiency for photocatalytic applications [40].

Fast recombination of electron—hole pairs and a relatively narrow absorption region of visible light are regarded as the predominant problems that reduce the photocatalytic performance. The construction of heterojunctions from two suitable semiconductors, that is, in the form of a Z-scheme, is of considerable interest because such a structure suppresses the recombination of photoinduced charge carriers. For example, the formation of such Z-scheme heterojunctions with zero-dimensional carbon nanomaterials through a simple hydrothermal method can consequently expand the light absorption range [41].

Solvothermal method

In contrast to the hydrothermal synthesis method, wherein water is used, the solvothermal process involves heating the initial solutions in organic or inorganic compounds in special Teflon-coated autoclaves at temperatures exceeding the boiling point of the solvent and under pressures exceeding 0.1 MPa. The desired crystal structure, morphology, and

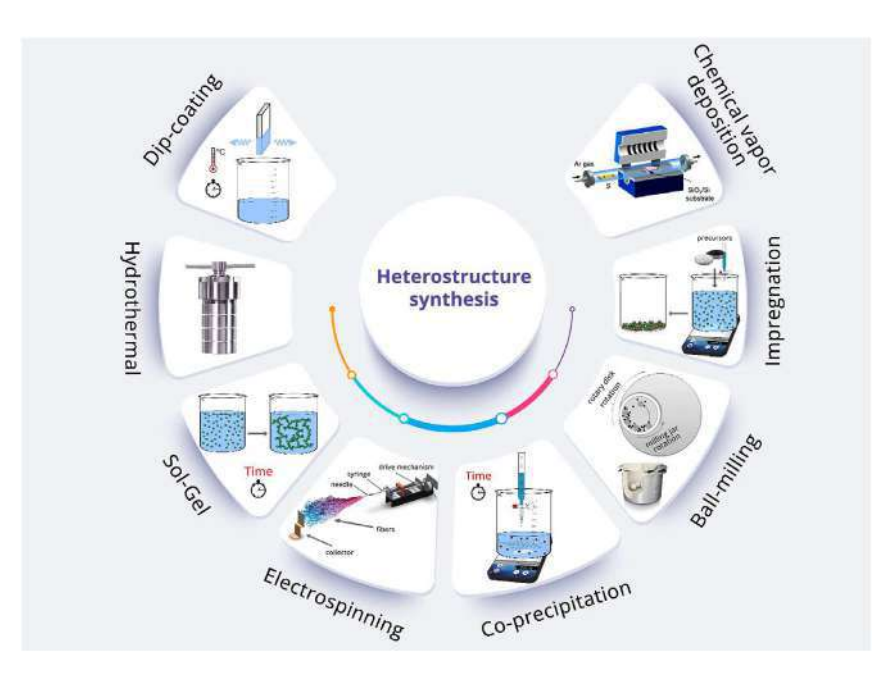


Fig. 1 – Different methods for obtaining SrTiO₃-based heterostructures.

particle size can be achieved by adjusting the reaction conditions. The solvothermal method also facilitates sufficiently close contact between the photocatalyst heterojunctions of SrTiO₃-based nanocomposites. For example, the solvothermal method can promote close contact between La-WO3 and SrTiO₃ in a nanostructured heterojunction composite, La-WO₃@SrTiO₃ [42]. In addition, under certain reaction conditions, ultrathin nanovilli with an average diameter of 50 nm grow on the surface of the La-WO₃ particles in the samples, contributing to the high adsorption of reactive substances and efficient absorption of visible light. In another study [43], BiOIdecorated SrTiO3 nanofibres were obtained via rapid solvothermal treatment using microwave radiation for methyl orange (MO) photodegradation under visible-light irradiation. The solvothermal method resulted in the formation of a p-n junction at the interface between $SrTiO_3$ and BiOI, which improved the electron-hole transfer. Simultaneously, the resulting nanocomposite has a spike-like structure with mesopores (size = 31 nm) providing a large contact area, thereby increasing the photocatalytic efficiency during dye decomposition, with a degradation rate of 0.015 min⁻¹. In addition, the solvothermal method has been used to synthesise a porous graphene/SrTiO3 nanocomposite with a morphology similar to that of a washcloth, wherein SrTiO₃ nanospheres are wrapped in sheets of porous graphene. Such a structure increases the contact area between porous graphene and SrTiO₃, thus improving the charge carrier transport 44].

Sol-gel method

The advantages of the sol-gel method over various other methods for synthesising nanocomposite heterostructured SrTiO₃-based photocatalysts include the high purity of the synthesised homogeneous nanopowders and the possibility of controlling their chemical properties. These advantages are achieved by mixing liquid starting reagents at the molecular level during synthesis. For example, a high-purity mesoporous heterostructured TiO2@SrTiO3 nanocomposite was obtained through the sol-gel method by mixing pre-dispersed tetra-n-butyl orthotitanate (TBT) and Sr(NO₃)₂ precursors in 20 mL of ethanol and thoroughly stirring for 30 min until a transparent sol and gel were formed. Using the sol-gel method, a relatively small size (approximately 24.49 nm) of the TiO2@SrTiO3 nanocomposite with a considerably high porosity of 126.8 m² g⁻¹ could be obtained [45]. Owing to the complete control of the reaction conditions in the sol-gel method, a highly efficient CoAlMnO₄@SrTiO₃ heterojunction with optimal morphology and particle size could be synthesised; this heterojunction was subsequently used for producing hydrogen by the photocatalytic decomposition of water under both ultraviolet (UV) and visible radiation [46]. Furthermore, optimised synthesis conditions facilitated the configuration of a type-I heterojunction with a core-shell structure, wherein CoAlMnO4 nanoparticles (10 nm) and SrTiO₃ (20 nm) served as the core and shell, respectively.

The sol-gel technology is distinguished by its simplicity; moreover, high temperatures and pressures are not required during synthesis. For example, a porous heterojunction SrTiO₃/SrSO₄ nanocomposite was created using a one-pot

sol-gel method at a moderate temperature, followed by annealing and photodeposition of Pt nanoparticles [47]. The resulting data indicate the high crystallinity and porosity of the SrTiO₃@SrSO₄ heterojunction with increased photocatalytic activity. The characteristics of multicomponent nanocomposite photocatalysts are significantly superior to those of photocatalysts with individual components; for example, ternary systems improve the photogeneration of electron-hole pairs and enhance the light-absorbing ability of the photocatalyst. The use of carbon nanotubes (CNTs), which have excellent properties such as high conductivity and large specific surface area in ternary systems, makes the photocatalyst promising for photocatalytic applications. Ternary plasmon nanocomposites Ag@SrTiO3@CNT were successfully synthesised using the sol-gel method for the efficient photocatalytic degradation of organic dyes [48]. The resulting composite had a high efficiency in the photodecomposition of dyes, while the CNT surface was densely covered and wrapped with Ag and SrTiO₃ nanoparticles.

Another distinctive advantage of the sol-gel method is the possibility of combining it with other methods, which is known as hybridisation. Various researchers have reported the successful hybridisation of sol-gel with other synthesis methods. Thus, a combination of sol-gel and hydrothermal methods was used for the synthesis of SrTiO₃ photocatalysts doped with La and Cr for hydrogen production [49,50]. Consequently, the composite obtained by the hybrid sol-gel hydrothermal method demonstrated excellent photocatalytic performance for the release of H₂ in the visible-light spectrum compared to another hybrid polymerised complex method [49]. Based on these studies, a highly porous Pt STO:C, N heterostructure was synthesised via a two-stage sol-gel method using a polymer in addition to a solvothermal method [51]. A distinctive feature of this technology is the production of mesopores inside the volume of cubic nanoparticles, whereas the specific surface area is attained owing to voids between nanoparticles in the previously described methods.

Precipitation/co-precipitation

Precipitation and co-precipitation are conventional methods for synthesising semiconductor heterostructures. Generally, a heterojunction based on SrTiO3 is obtained through a reaction in a liquid solution with SrTiO3, dropwise addition of the second component to the solution, and pH adjustment, followed by mixing and precipitate formation. Thus, a SrTiO3@Ag@Ag3PO4 photocatalyst was obtained via precipitation, wherein Ag₃PO₄ nanoparticles had a spherical shape with an average diameter of 50-100 nm and were uniformly grown on the acicular surface of SrTiO3 particles, which were obtained using the hydrothermal method. Compared with pure SrTiO₃ and Ag₃PO₄, the synthesised sample demonstrated excellent photocatalytic activity for tetracycline photodegradation [52]. Similarly, an N-SrTiO₃/BiOBr heterostructure was obtained with a flake nanoparticle morphology; irregularly shaped N-SrTiO₃ nanoparticles (size = 20-30 nm) formed a close interfacial contact with the BiOBr nanosheets, which facilitated rapid separation and improved the transport of photogenerated electrons and holes between N-SrTiO₃ and BiOBr [53].

The photocatalytic efficiency of SrTiO₃ and other types of photocatalysts can be considerably improved by forming a morphology with a large specific surface area, which increases the number of active centres. Thus, the formation of the Ag₃PO₄/SrTiO₃ composite by the deposition of homogeneous Ag₃PO₄ nanoparticles on the surface of SrTiO₃ nanofibres increases the photocatalytic activity by 10 times compared with that of pure SrTiO₃ in the visible light range [54].

Other methods for obtaining heterostructured $SrTiO_3$ -based photocatalysts

In addition to the above-mentioned methods, other methods include the chemical reduction [55,56], impregnation [57], polymer precursor [58,59], low-temperature process [60], chemical vapour deposition [61], atomic layer deposition (ALD) [62], sequential ion layer adsorption reaction (SILAR) [63], and simple high-energy ultrasound [64] methods, which can be used to synthesise heterostructured nanocomposites, of which one component is SrTiO₃; these nanocomposites are used for various photocatalytic applications under the influence of visible light. However, all these methods have limitations that hinder their widespread practical application for the synthesis of SrTiO₃-based heterojunctions. For example, a composite with Ag nanoparticles decorated on the acicular surface of SrTiO₃ particles was obtained via the ALD method; however, the complexity of mass production and prolonged deposition time are disadvantages of this method [62]. The SILAR method is a simple and cost-effective technology for producing ternary semiconductors. Accordingly, it has been used to obtain nanocomposite photocatalysts with a Zscheme and H-type SrTiO₃/(BiFeO₃@ZnS), wherein SrTiO₃ nanoparticles (100 nm) are connected to elliptical BiFeO₃ nanoparticles (50 nm) coated with a ZnS nanofilm (thickness = 22 nm). The synergistic effect of the Z-scheme and heterojunction contributed to the high photocatalytic activity with a 2,4-dichlorophenol photodecomposition rate and Cr(VI) conversion of 91.32% and 97.87%, respectively. However, the relatively long synthesis duration is the primary disadvantage of this method [63]. Another promising production technology is the high-energy ultrasonic treatment method, which enables the synthesis of a heterostructured rGO@SrTiO3 nanocomposite by dispersing graphene oxide and SrTiO₃ nanoparticles in a ternary solvent [64]. This method can be used to significantly reduce the size of crystallites and the band gap, enhance the optical properties of SrTiO3, and improve the morphology of SrTiO3 and RGO/SrTiO3 samples by increasing the specific surface area. The RGO/SrTiO₃ heterostructure photocatalyst exhibited degradation rates of 94.5% and 90% within 100 min with reference to rhodamine B (RhB) and Rose Bengal dyes, respectively.

The synthetic method used to prepare SrTiO₃-based composites can have a significant impact on their performance. The choice of synthetic method can affect various characteristics of the composites, such as their composition, structure, morphology, surface area, and crystallinity. These factors, in turn, influence the photocatalytic activity, stability, efficiency, and selectivity of the composites. Different synthesis methods may result in variations in the size and distribution of SrTiO3 particles, the presence of impurities or defects, or the

incorporation of dopants or additional components. These factors can influence the charge transfer, light absorption, and surface reactivity of the composites, ultimately affecting their photocatalytic performance.

Table 1 presents the methods used to develop various $SrTiO_3$ -based composites and the primary parameters of these composites that affect their performance. However, although the characteristics of the synthesised composites are successfully improved using these methods, all synthesis processes have been typically performed under laboratory conditions; consequently, commercialisation can be achieved only by introducing technology for the large-scale production of hybrid composite $SrTiO_3$ -based photocatalysts.

Application of heterostructured SrTiO₃-based photocatalysts

Composites with SrTiO₃-based heterojunctions are extensively used in the hydrogen, solar energy, and energy storage industries. In addition, the relatively high photocatalytic characteristics of SrTiO₃-based composites, compared with those of pure components, are beneficial for producing biodiesel and environmentally friendly hydrogen, purifying wastewater and the atmosphere from various pollutants (dyes, antibiotics, CO₂, and NO), and sterilisation under the influence of electromagnetic radiation. The electrocatalytic and dielectric properties of SrTiO₃-based composites have been used to fabricate high-performance solar cells [84,85], biosensors [86], and supercapacitors [87]. Graphic illustrations of different applications of SrTiO₃-based composites are shown in Fig. 2.

Photocatalytic water splitting with the release of hydrogen

Photocatalytic water splitting with the release of hydrogen upon irradiation with sunlight is considered a promising technology owing to its environmental friendliness and low cost. This process primarily requires the photocatalyst, light energy, and water; the process essentially involves the decomposition of a water molecule into hydrogen and oxygen. Breaking the intermolecular bonds of water requires energy; for example, electrolysis requires electrical energy. Generally, upon irradiation, the photocatalyst absorbs a photon of energy to form an electron-hole pair, provided that the energy of the light is equal to or greater than the bandgap energy of the semiconductor. Consequently, the excited negatively charged electrons are transferred to the conduction band (CB), followed by the reduction of water and release of gaseous hydrogen. Simultaneously, a positively charged hole in the valence band (VB) oxidises water to form oxygen gas. The two conditions necessary for the photocatalytic decomposition of water into H2 and O2 under the influence of light are as follows.

- 1) The minimum photon energy for photoabsorption should be 1.23 eV;
- 2) The energy position of the CB of the photocatalyst is more negative than the redox potential $\rm H^+/H_2$ (0 V versus normal hydrogen electrode (NHE) at pH = 0), and the energy

	Table	1- Recent methods for t	the development of various SrTiO ₃ -l	pased composites and	l the main parameters of	these composites th	nat affect their p	performance.	
2019 268-SFTiO ₂ Hydrothermal	Year	Photocatalyst	Synthetic Methods	Heterojunction	Structure	Particle size, nm	Band gap, eV	SSA, m ² /g	Ref
2021 SrTiO ₁ Lay/Ba-PNO Hydrothermal Z-scheme hollow multishell 90 24 8.222 [31] 2022 C-dusty/FiO ₂ /Min Hydrothermal Z-scheme nanoshests/spherical — 2.98(F10) [41] 2018 STIO ₁ /Min*Po ₂ Q Hydrothermal — nord-like 80 120 3.04 — [65] 2020 STIO ₂ /Min*Po ₂ Q Hydrothermal Type II annosphetics 167 (F170) 2.2 14.49 [55] 2019 FOTO ¹ (NSTIO) Hydrothermal Type II quasi-spherical 20 -0 (S770) 2.24 — [60] 2011 FOTO ¹ (TO) Hydrothermal — pherical 33.1 3.1 — [30] 2021 STIO ₂ -TIO ₂ Hydrothermal — hollow multi-spherical 20 — 58 [63] 2018 PNT TO(110T STIO) Hydrothermal — nonopaticles 20 — — [70] 2018 STIO ₂ -TIO ₂ Hydrothermal	2022	Ag(x)STO/g-CN	Hydrothermal	Type II	nanoparticles	20-35 (SrTiO ₃)	2.72	298.12	[40]
2022 2. closs/STIO/NHIA/Nos Hydrothermal 2. spekerno 10.61 (c-dots) 2.54 2.96 4.11 1.81	2019	CdSe/SrTiO ₃	Hydrothermal	_	quasi-spherical	120.5	1.85	_	[37]
2022 2. closs/STIO/NHIA/Nos Hydrothermal 2. spekerno 10.61 (c-dots) 2.54 2.96 4.11 1.81	2021	SrTiO ₃ :La/Rh-BVO	Hydrothermal	Z-scheme	hollow multishell	90	2.4	8.232	
2015 2πO/STIO; Hydrothermal col-like 50-10 30-6 62-5 53-5	2022	C-dots/SrTiO ₃ /NH ₄ V ₄ O ₁₀	Hydrothermal	Z-scheme	nanosheets	10.61 (C-dots)	2.54	29.6	
STIO_PMnie_Q_0 Hydrothermal Z-scheme quasi-spherical 16.7 (STIO_Q) 2.2 14.49 5.9	2018	ZnO/SrTiO ₃	Hydrothermal	_	nanosheets/spherical	-	2.99(SrTiO ₃)	18.18	
STIO_PMnie_Q_0 Hydrothermal Z-scheme quasi-spherical 16.7 (STIO_Q) 2.2 14.49 5.9	2019	SrTiO ₃ /TiO ₂	Hydrothermal	_	rod-like	80-120	3.04	_	[65]
2012 Co., y.To., y.e., y.e. y.e. y.e. y.e. y.e. y.e. y	2020	SrTiO ₃ /MnFe ₂ O ₄	Hydrothermal	Z-scheme	quasi-spherical	16.7 (SrTiO ₃)	2.2	14.49	
2021 STOTiO_0 Hydrothermal	2019	FTO/TiO ₂ /SrTiO ₃	Hydrothermal	Type II	nanoparticles	30-50 (SrTiO ₃)	3.24	_	[66]
	2019	$Co_{0.7}Zn_{0.3}Fe_2O_4$ -SrTiO ₃	Hydrothermal	Type II	quasi-spherical	20	2.89	27.82	[67]
	2021	rGO/SrTiO₃	Hydrothermal	-	spherical	33.1	3,1	_	[39]
2018 Pt/N-TiO/ITIO-STITO; Hydrothermal - hollow multi-shelled 6 - 298.3 [69] 108 STIO, -TiO/Cat/ns Hydrothermal - hollow multi-shelled 45 3.3 (STIO ₃) - 17 2019 Porous graphene/SrTIO ₃ Solvothermal - spherical 28.8 2.93 65.35 [4] 2019 STIO, PilOI Solvothermal - nanocubic 30 (STIO ₃) 2.2 61.1 [4] 2019 SCHYTS Solvothermal 2-scheme nanocubic 5-100 3.15 (STIO ₃) 3.2 27.5 71 2019 STIO, N-ONS Solvothermal 2-scheme nanoparticles 5-100 3.15 (STIO ₃) 3.2 7.2 2011 Agmodified STO Sol-gel - 171,3 73 2012 Agmodified STO Sol-gel - 179,1 275 128.8 45 2013 Agmodified STO Sol-gel - 199,1 10 12-1	2021	SrTiO ₃ -TiO ₂	Hydrothermal	Type II	spherical	250	_	58	
2018 SrTiO ₂ —TiO ₂ Hydrothermal - hollow multi-shelled 4 § 3.3 (SrTiO ₂) - [2] 2019 Portous graphene/SrTiO ₃ Solvothermal - nanoparticles 20.8 2.93 65.35 [4] 2019 Portous graphene/SrTiO ₃ Solvothermal - nanofibers 30.4 (SrTiO ₃) 2.3 6.1 42.3 2019 Agmodified STO Solvothermal - nanoparticles 5-100 3.15 (SrTiO ₃) 3.367 [7] 2021 STOMPN-GNS Solvothermal - nanoparticles 5-100 3.15 (SrTiO ₃) 3.367 [7] 2021 STOMPN-GNS Solvothermal - nanoparticles 50 - 17.1 17.3 7.3 2021 STOPA-CNTO Sol-gel - cyberical 21 2.7 7.8 [48] 2021 STOO, STOO, STOO Sol-gel - cyberical 24.9 2.7 12.6 8.9 2021 STOO, STOO, STOO	2018	Pt/N-TiO ₂ /110T-SrTiO ₃	Hydrothermal		nanotube	66	_	298.3	
2019 SrTiO ₂ —T/CdZnS Hydrothermal - nanoparticles 20 - [70] 199 Portous graphene/SrTiO ₃ Solvothermal - sphenola 28.8 293 65.55 [44] 2019 SrTiO/BiOI Solvothermal p-n junction nanocabic 30 (SrTiO ₃) 23 6.1 [43] 2021 CSWT7S Solvothermal Z-scheme nanocabic 30 (SrTiO ₃) 3.26 (SrTiO ₃) 3.36 (T) 7.2 2019 SrTiO ₃ /N-CNS Solvothermal Z-scheme nanoparticles 5-10 (O 1.2 7.7 8.4 [48] 2018 SrTiO ₃ /N-CNS Solvothermal Z-scheme spherical 24.49 2.7 12.6 [48] 2018 TiO ₂ /SrSO ₂ /Pt Sol-gel - cubic 20 2.7 12.6 [47] 2018 SrTiO ₃ (La,Cr) Sol-gel-hydrothermal Z-scheme nanoparticles 680 3.0 2.1 1.7 1.9 1.0 2012	2018	SrTiO ₃ -TiO ₂	Hydrothermal	-	hollow multi-shelled	45	3.3 (SrTiO ₃)	_	
2019 Sortion graphene/SriiO ₃ Solvothermal	2019		Hydrothermal	-	nanoparticles	20	-	_	
2019 SrTiO/BiOI Solvothermal p-n junction nanofibers 30.43 (SrTiO ₃) 2.3 6.1 4.3 2019 Ag modified STO Solvothermal - nanoparticles 5-100 3.15 (SrTiO ₃) 3.36 7.2 2019 SrTiO ₃ /N-GNS Solvothermal - cylindrical 50 - 17.1 7.3 2012 AgeSTIO ₃ /N-GNS Solvothermal - cylindrical 50 - 17.1 7.3 2018 By TiO ₃ /N-GNS Sol-gel Schottky junction spherical 24.49 2.7 78 48 2018 SrTiO ₃ /SrO ₄ /Pt Sol-gel Type I cvubic 100 (SrTiO ₃) 3.2 - 46 2018 SrTiO ₃ /SrO ₄ /Pt Sol-gel-hydrothermal 2-scheme nanoparticles 100 (SrTiO ₃) 3.2 - 47 2018 SrTiO ₃ /SrO ₄ (BaC ₄) Sol-gel-hydrothermal 2-scheme nanoparticles 100 (SrTiO ₃) 3.2 2.5 2.6 49 2019	2019		Solvothermal	_	spherical	28.8	2.93	65.35	
Ag modified STO Solvothermal	2019	SrTiO ₃ /BiOI	Solvothermal	p–n junction	nanofibers	30.43 (SrTiO ₃)	2.3	6.1	
2-c C C C C C C C C C	2019	Ag modified STO	Solvothermal	-	nanocubic	30 (SrTiO ₃)	3.28	27.51	
STIO_y/N-CNS Solvothernal -	2021	CSWT75	Solvothermal	Z-scheme	nanoparticles		3.15 (SrTiO ₃)	3.367	
Agg STTiO Agg CNT Sol-gel Schottky junction spherical 21 2.7 78 48 48 102 57 103 Sol-gel 7 7 7 126.8 45 102 102 102 103 1	2019	SrTiO ₃ /N-GNS	Solvothermal	_	cylindrical	50	- ` '	171.3	
2012 STIO ₂ -STIO ₃ Sol-gel Type I Core-shell 20 24.49 2.75 126.8 [45] 2021 STIO ₃ /StSO ₄ /Pt Sol-gel Type I Core-shell 20 20 2.4 - 46] 46] 2021 STIO ₃ /StSO ₄ /Pt Sol-gel - Cubic 100 (StTIO ₃) 3.2 - 47] 2018 STIO ₃ /TiO ₂ Sol-gel - Cubic 100 (StTIO ₃) 3.2 2.4 [74] 2018 STIO ₃ /TiO ₄ Sol-gel Type I Cubic 100 (StTIO ₃) 3.2 2.4 [74] 2018 STIO ₃ /TiO ₄ Sol-gel-hydrothermal Z-scheme nanoparticles 10-50 2.52 20.6 [49] 2019 STIO ₃ (La,Cr)-6 Sol-gel-hydrothermal Z-scheme nanoparticles 10-50 2.52 20.6 [49] 2019 STIO ₃ (La,Cr)-6 Sol-gel-hydrothermal Z-scheme nanoparticles 10-50 2.97 176 [51] 2020 STIO ₃ A/ZSTO Sol-gel-electrospinning P-n junction nanocibrous 210 2.49 30.4 [75] 2020 STIO ₃ A/ZSTO Precipitation Z-scheme urchin-like several μm 3.12 (StTIO ₃) - [52] 2020 N-StTIO ₃ B/Gs ₃ PO ₄ Precipitation Type II nanopitres 100-200 2.71 8.05 [53] 2020 N-StTIO ₃ B/Gs ₃ PO ₄ Precipitation Type II nanopitres 100-200 2.72 2760 [76] 2021 C-StTIO ₃ /PAN/WS-FLG Electrospinning - nanobibres 200-400 2.72 2760 [76] 2021 C-StTIO ₃ /PAN/WS-FLG Electrospinning - nanofibers 2191 1.68 48.92 [78] 2020 TO ₃ /StTIO ₃ Electrospinning and gas-solid reaction Z-scheme nanofibers 2191 1.68 48.92 [78] 2020 TO ₃ /StTIO ₃ Electrospinning and gas-solid reaction Z-scheme nanofibers 210 STIO ₃ (BiC ₃) 3.2 (StTIO ₃) 2.4 80] 2020 StTIO ₃ (BiC ₃) SILAR Z-scheme 2.5 cheme 2.5	2021	Ag@SrTiO ₃ @CNT	Sol-gel	Schottky junction	spherical	21	2.7	78	
	2018	TiO ₂ —SrTiO ₃		_	spherical	24.49	2.75	126.8	
2011 SrTiO ₃ /TSrSO ₄ /Pt Sol-gel	2022		•	Type I	-	20	2.4	_	
2018 SrTiO ₃ (La,Cr) Sol-gel Nanoparticles 680 3.03 21.4 [74] 2018 SrTiO ₃ (La,Cr) Sol-gel-hydrothermal Spherical 30-80 17.9 50] 2019 SrTiO ₃ (La,Cr)-6 Sol-gel-hydrothermal Spherical 30-80 17.9 50] 2011 ZSTO, AZSTO Sol-gel-electrospinning P-n junction nanofibrous 210 2.49 30.4 [75] 2018 Pt/STDC,N Polymer-assisted sol-gel Schottky junction nanocuboid 90-100 2.97 176 [51] 2018 Pt/STDC,N Precipitation Z-scheme urchin-like several μm 3.12 (SrTiO ₃) [52] 2020 SrTiO ₃ /Ag/Ag,PO ₄ Precipitation Nanowires 100-200 2.71 8.05 [53] 2018 Ag,PO ₄ /STIO ₃ Precipitation Nanowires 100-200 [54] 2018 SrTiO ₃ Mo ₂ C Electrospinning Nanowires 200-400 2.72 2760 [76] 2018 SrTiO ₃ SMo ₂ C Electrospinning Nanofibers 210 2.25 276 [76] 2018 Ag,SrTiO ₃ Electrospinning Nanofibers 210 2.25 276 [76] 2018 Ag,SrTiO ₃ SO ₄ A Electrospinning Nanofibers 210 2.25 276 [76] 2018 Ag,SrTiO ₃ G,Aq Electrospinning and gas-solid reaction Z-scheme Annofibers 210 2.25 2.25 [78] 2020 SrTiO ₃ /Ag,Ag Electrospinning and gas-solid reaction Nanofibers 210 2.25 2.25 [78] 2020 SrTiO ₃ /Ag ALD Urchin-like 150 129.7 [62] 2018 RGO/SrTiO ₃ Mechanically milling and calcination Type II Cubic 25 2.65 2.76 8.3 [78] 2020 SrTiO ₃ /SrTiO ₃ Mechanically milling and calcination Cubic 25 2.76 8.3 [78] 2020 SrTiO ₃ /Ag,CuPd-Bi ₂ O ₃ Chemical reduction and high 2-scheme Schottky junction Carl-like 2.30-50 3.26 (SrTiO ₃) 2.26 (SrTiO ₃) 2.26 (SrTiO ₃) 2.27 [79] 2021 CuPd/SrTiO ₃ -CuPd-Bi ₂ O ₃ Mechanically milling and calcination Cubic 2.50 2.76 2.76 8.3 [78] 2022 SrTiO ₃ /Ag ₂ O-NDC Polymeric precursor Cubic 2.50 2.76 2.76 2.76 2.76 2.76	2021		•	_	cubic	100 (SrTiO ₃)	3.2	_	
2018 SrTiO ₃ (La,Cr) Sol-gel-hydrothermal Z-scheme nanoparticles 10-50 2.52 20.6 [49] 2019 SrTiO ₃ (La,Cr)-6 Sol-gel-hydrothermal - 17.9 [50] 2011 SZTO, AZSTO Sol-gel-electrospinning p-n junction nanofibrous 2.0 2.49 30.4 [75] 2018 PYSTO:C,N Polymer-assisted sol-gel Schottky junction nanocuboid 90-100 2.97 176 [51] 2020 SrTiO ₃ /BA/AgsPO ₄ Precipitation Z-scheme urchin-like several μm 3.12 (SrTiO ₃) - [52] 2018 Ags,PO ₄ /SrTiO ₃ Precipitation - nanowires 100-200 - - [52] 2018 Ags,PO ₄ /SrTiO ₃ Precipitation - nanowires 100-200 - - [52] 2018 Ags,PO ₄ /SrTiO ₃ Plectrospinning - nanowires 100-200 2.72 2760 [76] 2018 Ag-SrTiO ₃ /PA,WaysTiO ₃ Electrosp	2018	SrTiO ₃ /TiO ₂	Sol-gel	_	nanoparticles	680	3.03	21.4	
2019 STTiO ₃ (La,Cr)-6 Sol-gel-hydrothermal - Spherical 30-80 - 17.9 [50] 2021 ZSTO, AZSTO Sol-gel-electrospinning p-n junction nanofibrous 210 2.49 30.4 [75] 2021 STTiO ₃ /Ag/Ag ₃ PO ₄ Polymer-assisted sol-gel Schottky junction nanocuboid 90-100 2.97 176 [51] 2022 STTiO ₃ /Ag/Ag ₃ PO ₄ Precipitation Z-scheme urchin-like several μm 3.12 (StTiO ₃) - [52] 2023 N-STTiO ₃ /BiOBr Precipitation Type II Spherical 20-30 2.71 8.05 [53] 2024 C-STIO ₃ /PAN/WS-FLG Electrospinning - nanowires 100-200 - - [54] 2021 C-STIO ₃ /PAN/WS-FLG Electrospinning Type I core-shell nanofibers 200-400 2.72 2760 76] 2021 STTiO ₃ (Mo ₂ C Electrospinning Type I core-shell nanofibers 210 3.23 (StTiO ₃) - [77] 2020 TiO ₃ /STIO ₃ Electrospinning - nanofibers 210 3.25 (StTiO ₃) 46.7 [79] 2020 TiO ₃ /STIO ₃ Electrospinning - nanofibers 210 3.25 (StTiO ₃) 46.7 [79] 2020 STTiO ₃ /Ag Electrospinning - nanofibers 210 3.25 (StTiO ₃) 46.7 [79] 2020 STTiO ₃ /STIO ₃ High energy ultrasonication - cubic 53 2.87 31 [64] 2020 STTiO ₃ /(BiFeO ₃ @ZnS) SILAR Z-scheme and H-type cubic 210 (StTiO ₃) 3.26 (StTiO ₃) - [63] 2020 PVSTO Chemical reduction and high Z-scheme and H-type cubic ≈150-180 3.16 (StTiO ₃) 3.24 [80] 2021 CuPd/StTiO ₃ - CuPd-Bi ₂ O ₃ Chemical reduction and high Z-scheme Spherical 25 (StTiO ₃) 3.26 (StTiO ₃) - [17] 2022 STTiO ₃ /Ag ₂ O-NDC Polymeric precursor - cubic 20-30 (StTiO ₃) 3.24 247.32 [57] 2023 STTiO ₃ /g ₂ O-NDC Polymeric precursor - cubic 20-30 (StTiO ₃) 3.24 247.32 [57] 2024 STTiO ₃ /g ₂ O-NDC Polymeric precursor Type II nanoparticles 32-45 (StTiO ₃) 2,7 37 [57] 2025 STTiO ₃ /g ₂ O-NDC Polymeric precursor Type II nanoparticles 32-45 (StTiO ₃) 3.24 324 327 324 327 324	2018	SrTiO ₃ (La,Cr)	Sol-gel-hydrothermal	Z-scheme	nanoparticles	10-50	2.52	20.6	
Pt/STO:C,N Polymer—assisted sol—gel Schottky junction nanocuboid 90–100 2.97 176 51	2019	SrTiO ₃ (La,Cr)-6	Sol-gel-hydrothermal	_	spherical	30-80	_	17.9	
Pt/STO:C,N Polymer—assisted sol—gel Schottky junction nanocuboid 90–100 2.97 176 51	2021	ZSTO, AZSTO	Sol-gel-electrospinning	p–n junction	nanofibrous	210	2.49	30.4	[75]
2020 SrTiO ₃ /Ag/Ag ₃ PO ₄ Precipitation Z-scheme urchin-like several μm 3.12 (SrTiO ₃) - [52] 2020 N-SrTiO ₃ BioBr Precipitation Type II spherical 20-30 2.71 8.05 [53] 2018 Ag ₃ PO ₄ /SrTiO ₃ Precipitation - nanowires 100-200 - - 5.24 2021 C-SrTiO ₃ /PAN/WS-FLG Electrospinning - microfibers 200-400 2.72 2760 [76] 2018 SrTiO ₃ @Mo ₂ C Electrospinning Type I core-shell nanofibers 120 3.23 (SrTiO ₃) - [77] 2018 Ag ₃ -SrTiO ₃ Electrospinning - nanofibers 210 3.25 (SrTiO ₃) - [77] 2018 Ag ₃ -SrTiO ₃ Electrospinning - nanofibers 210 3.25 (SrTiO ₃) - [77] 2018 Ag ₃ -SrTiO ₃ Electrospinning and gas-solid reaction Z-scheme nanofibers × 100 3.25 (SrTiO ₃) 46.7 [79] 2020 SrTiO ₃ /Ag ALD - urchin-like 150 - 129.7 [62] 2018 RGO/SrTiO ₃ High energy ultrasonication - cubic 53 2.87 31 [64] 2020 SrTiO ₃ /(BiFeO ₃ @ZnS) SILAR Z-scheme and H-type cubic × 150-180 3.16 (SrTiO ₃) 3.24 80] 2020 PySTO Chemical reduction Schottky junction coral-like × 30-50 3.26 (SrTiO ₃) - [40] 2021 CuPd/SrTiO ₃ -CuPd-Bi ₂ O ₃ Chemical reduction and high Z-scheme Spherical 25 (SrTiO ₃) 3.2 (SrTiO ₃) - [40] 2022 SrTiO ₃ /Ag ₂ O-NDC Polymeric precursor - cubic 20-30 (SrTiO ₃) 2.84 247.32 [58] 2022 SrTiO ₃ /Ag ₂ O-NDC Polymeric precursor Type II nanoparticles 32-45 (SrTiO ₃) 2.75 37 [59] 2020 SrTiO ₃ /G ₂ O-NDC Polymeric precursor Type II nanoparticles 32-45 (SrTiO ₃) 2.75 37 [59] 2020 SrTiO ₃ /G ₂ O-NDC Polymeric precursor Type II nanoparticles 32-45 (SrTiO ₃) 2.75 37 [59] 2020 SrTiO ₃ /G ₂ O-NDC Polymeric precursor Type II Nanoparticles 32-45 (SrTiO ₃) 2.75 37 [59] 2020 SrTiO ₃ /G ₂ O-NDC Polymeric precursor Type II Nanoparticles 32-45 (SrTiO ₃) 2.75 37 [59] 2020 SrTiO ₃ /G ₂ O-NDC Polyme	2018	Pt/STO:C,N	Polymer—assisted sol—gel	Schottky junction	nanocuboid	90-100	2.97	176	
2020 N-SrTiO ₃ /BiOBr Precipitation Type II spherical 20-30 2.71 8.05 [53] 2018 Ag ₃ PO ₄ /SrTiO ₃ Precipitation - nanowires 100-200 - - [54] 2021 C-SrTiO ₃ /PAN/WS-FLG Electrospinning - microfibers 200-400 2.72 2760 [76] 2018 SrTiO ₃ /Mo ₂ C Electrospinning Type I core-shell nanofibers 120 3.23 (SrTiO ₃) - [77] 2018 Ag-SrTiO ₃ Electrospinning - nanofibers ≈ 191 1.68 48.92 [78] 2020 TiO ₂ /SrTiO ₃ /gC ₃ N ₄ Electrospinning and gas-solid reaction Z-scheme nanofibers ≈ 100 3.25 (SrTiO ₃) 46.7 [79] 2020 SrTiO ₃ /Ag ALD - urchin-like 150 - 129.7 [62] 2018 RGO/SrTiO ₃ High energy ultrasonication - cubic 53 2.8 2.8 31 [62] <td< td=""><td>2020</td><td>SrTiO₃/Ag/Ag₃PO₄</td><td>Precipitation</td><td>Z-scheme</td><td>urchin-like</td><td>several μm</td><td>3.12 (SrTiO3)</td><td>_</td><td></td></td<>	2020	SrTiO ₃ /Ag/Ag ₃ PO ₄	Precipitation	Z-scheme	urchin-like	several μm	3.12 (SrTiO3)	_	
2018 AggPO_4/SrTiO3 Precipitation - nanowires 100-200 - - [54] 2021 C-SrTiO3/PAN/WS-FLG Electrospinning - microfibers 200-400 2.72 2760 [76] 2018 SrTiO3/MO2C Electrospinning Type I core-shell nanofibers 120 3.23 (SrTiO3) - [77] 2018 Ag-SrTiO3/GC3N4 Electrospinning and gas-solid reaction - nanofibers *191 1.68 48.92 [78] 2020 SrTiO3/Ag ALD - urchin-like 150 - 129.7 [62] 2018 RGO/SrTiO3 High energy ultrasonication - cubic 53 2.87 31 [64] 2020 SrTiO3/(BiFeO3/@ZIS) SILAR Z-scheme and H-type cubic 100 (SrTiO3) 3.3(SrTiO3) - [63] 2019 gC3N4/SrTiO3 Mechanically milling and calcination Type II cubic *150-180 3.16 (SrTiO3) 3.24 [80] 2021	2020		Precipitation	Type II	spherical	20-30		8.05	
2021 C-SrTiO ₃ /PAN/WS-FLG Electrospinning — microfibers 200-400 2.72 2760 [76] 2018 SrTiO ₃ @Mo ₂ C Electrospinning Type I core-shell nanofibers 120 3.23 (SrTiO ₃) — [77] 2018 Ag-SrTiO ₃ Electrospinning — nanofibers ≈ 191 1.68 48.92 [78] 2020 TiO ₂ /SrTiO ₃ /gC ₃ N ₄ Electrospinning and gas-solid reaction Z-scheme nanofibers ≈ 100 3.25 (SrTiO ₃) 46.7 [79] 2020 SrTiO ₃ /Ag ALD — urchin-like 150 — 129.7 [62] 2018 RGO/SrTiO ₃ High energy ultrasonication — cubic 53 2.87 31 [64] 2020 SrTiO ₃ /(BiFeO ₃ @ZnS) SILAR Z-scheme and H-type cubic ≈ 150—180 3.16 (SrTiO ₃) 3.24 [80] 2020 Pt/STO Chemical reduction Schottky junction coral-like ≈ 30—50 3.26 (SrTiO ₃) - [40]	2018	Ag ₃ PO ₄ /SrTiO ₃			nanowires	100-200	_	_	
2018 SrTiO₃@Mo₂C Electrospinning Type I core-shell nanofibers 120 3.23 (SrTiO₃) − [77] 2018 Ag−SrTiO₃ Electrospinning − nanofibers ≈ 191 1.68 48.92 [78] 2020 TiO₂/SrTiO₃/gC₃N₄ Electrospinning and gas-solid reaction Z-scheme nanofibers ≈ 100 3.25 (SrTiO₃) 46.7 [79] 2020 SrTiO₃/Ag ALD − urchin-like 150 − 129.7 [62] 2018 RGO/SrTiO₃ High energy ultrasonication − cubic 53 2.87 31 [64] 2020 SrTiO₃/(BiFeO₃@ZnS) SILAR Z-scheme and H-type cubic ≈ 150−180 3.16 (SrTiO₃) 3.2 (SrTiO₃) − [63] 2019 gC₃N₄/SrTiO₃ Mechanically milling and calcination Type II cubic ≈ 150−180 3.16 (SrTiO₃) 3.2 (SrTiO₃) 3.2 (SrTiO₃) 3.2 (SrTiO₃) 2.6 (SrTiO₃) 2.7 (Mo₂) 17 2021 CuPd/SrTiO₃-CuPd−Bi₂O₃ Chemical reduction and high </td <td>2021</td> <td>C-SrTiO₃/PAN/WS-FLG</td> <td>Electrospinning</td> <td>_</td> <td>microfibers</td> <td>200-400</td> <td>2.72</td> <td>2760</td> <td></td>	2021	C-SrTiO ₃ /PAN/WS-FLG	Electrospinning	_	microfibers	200-400	2.72	2760	
2018 Ag−SrTiO₃ Electrospinning - nanofibers ≈ 191 1.68 48.92 [78] 2020 TiO₂/SrTiO₃/gC₃N₄ Electrospinning and gas-solid reaction Z-scheme nanofibers ≈ 100 3.25 (SrTiO₃) 46.7 [79] 2020 SrTiO₃/Ag ALD - urchin-like 150 - 129.7 [62] 2018 RGO/SrTiO₃ High energy ultrasonication - cubic 53 2.87 31 [64] 2020 SrTiO₃/gBiFeO₃@ZnS) SILAR Z-scheme and H-type cubic 100 (SrTiO₃) 3.3(SrTiO₃) - [63] 2019 gC₃N₄/SrTiO₃ Mechanically milling and calcination Type II cubic ≈ 150−180 3.16 (SrTiO₃) 32.4 [80] 2020 Pt/STO Chemical reduction Schottky junction coral-like ≈ 30−50 3.26 (SrTiO₃) - [40] 2021 CuPd/SrTiO₃-CuPd-Bi₂O₃ Chemical reduction and high Z-scheme spherical 25 (SrTiO₃) 3.2 (SrTiO₃) - [7] 2018 pGCN-ST Impregnation - cubic	2018	SrTiO ₃ @Mo ₂ C	Electrospinning	Type I	core-shell nanofibers	120	3.23 (SrTiO ₃)	_	[77]
2020 TiO₂/SrTiO₃/gC₃N₄ Electrospinning and gas-solid reaction Z-scheme nanofibers ≈ 100 3.25 (SrTiO₃) 46.7 [79] 2020 SrTiO₃/Ag ALD — urchin-like 150 — 129.7 [62] 2018 RGO/SrTiO₃ High energy ultrasonication — cubic 53 2.87 31 [64] 2020 SrTiO₃/(BiFeO₃@ZnS) SILAR Z-scheme and H-type cubic 100 (SrTiO₃) 3.3(SrTiO₃) — [63] 2019 gC₃N₄/SrTiO₃ Mechanically milling and calcination Type II cubic ≈150−180 3.16 (SrTiO₃) 32.4 [80] 2020 Pt/STO Chemical reduction Schottky junction coral-like ≈30-50 3.26 (SrTiO₃) — [40] 2021 CuPd/SrTiO₃-CuPd-Bi₂O₃ Chemical reduction and high Z-scheme spherical 25 (SrTiO₃) 3.2 (SrTiO₃) — [17] 2021 pGCN-ST Impregnation — cubic 25 2.76 83,3 [57]	2018	Ag-SrTiO ₃		_	nanofibers	≈191	1.68	48.92	
2020 SrTiO ₃ /Ag ALD — urchin-like 150 — 129.7 [62] 2018 RGO/SrTiO ₃ High energy ultrasonication — cubic 53 2.87 31 [64] 2020 SrTiO ₃ /(BiFeO ₃ @ZnS) SILAR Z-scheme and H-type cubic 100 (SrTiO ₃) 3.3(SrTiO ₃) — [63] 2019 gC ₃ N ₄ /SrTiO ₃ Mechanically milling and calcination Type II cubic ≈ 150-180 3.16 (SrTiO ₃) 32.4 [80] 2020 Pt/STO Chemical reduction Schottky junction coral-like ≈ 30-50 3.26 (SrTiO ₃) — [40] 2021 CuPd/SrTiO ₃ —CuPd—Bi ₂ O ₃ Chemical reduction and high Z-scheme spherical 25 (SrTiO ₃) 3.2 (SrTiO ₃) — [17] very company pGCN—ST Impregnation — cubic 25 2.76 83,3 [57] 2022 SrTiO ₃ /Ag ₂ O—NDC Polymeric precursor — cubic 20-30 (SrTiO ₃) 2.84 247.32 [58] 2020 SrTiO ₃ /G=C ₃ N ₄ Polymeric precursor Type II<	2020	TiO ₂ /SrTiO ₃ /gC ₃ N ₄	Electrospinning and gas-solid reaction	Z-scheme	nanofibers	≈100	3.25 (SrTiO ₃)	46.7	
2018 RGO/SrTiO ₃ High energy ultrasonication — cubic 53 2.87 31 [64] 2020 SrTiO ₃ /(BiFeO ₃ @ZnS) SILAR Z-scheme and H-type cubic 100 (SrTiO ₃) 3.3(SrTiO ₃) — [63] 2019 gC ₃ N ₄ /SrTiO ₃ Mechanically milling and calcination Type II cubic ≈ 150-180 3.16 (SrTiO ₃) 32.4 [80] 2020 Pt/STO Chemical reduction Schottky junction coral-like ≈ 30-50 3.26 (SrTiO ₃) — [40] 2021 CuPd/SrTiO ₃ —CuPd—Bi ₂ O ₃ Chemical reduction and high Z-scheme spherical 25 (SrTiO ₃) 3.2 (SrTiO ₃) — [17] very complex	2020		ALD	_	urchin-like	150	- ` '	129.7	
2020 SrTiO ₃ /(BiFeO ₃ @ZnS) SILAR Z-scheme and H-type cubic 100 (SrTiO ₃) 3.3(SrTiO ₃) - [63] 2019 gC ₃ N ₄ /SrTiO ₃ Mechanically milling and calcination Type II cubic $\approx 150-180$ 3.16 (SrTiO ₃) 32.4 [80] 2020 Pt/STO Chemical reduction Schottky junction coral-like $\approx 30-50$ 3.26 (SrTiO ₃) - [40] 2021 CuPd/SrTiO ₃ —CuPd—Bi ₂ O ₃ Chemical reduction and high Z-scheme spherical 25 (SrTiO ₃) 3.2 (SrTiO ₃) - [17] temperature calcination - cubic 25 2.76 83,3 [57] 2022 SrTiO ₃ /Ag ₂ O—NDC Polymeric precursor - cubic 20-30 (SrTiO ₃) 2.84 247.32 [58] 2020 SrTiO ₃ /G=C ₃ N ₄ Polymeric precursor Type II nanoparticles 32-45 (SrTiO ₃) 2,7 37 [59]	2018	RGO/SrTiO ₃	High energy ultrasonication	_	cubic	53	2.87	31	
2019 gC ₃ N ₄ /SrTiO ₃ Mechanically milling and calcination Type II cubic $\approx 150-180$ 3.16 (SrTiO ₃) 32.4 [80] 2020 Pt/STO Chemical reduction Schottky junction coral-like $\approx 30-50$ 3.26 (SrTiO ₃) - [40] 2021 CuPd/SrTiO ₃ -CuPd-Bi ₂ O ₃ Chemical reduction and high Z-scheme spherical 25 (SrTiO ₃) 3.2 (SrTiO ₃) - [17] Lemperature calcination - cubic 25 2.76 83,3 [57] 2022 SrTiO ₃ /Ag ₂ O-NDC Polymeric precursor - cubic 20-30 (SrTiO ₃) 2.84 247.32 [58] 2020 SrTiO ₃ /g-C ₃ N ₄ Polymeric precursor Type II nanoparticles 32-45 (SrTiO ₃) 2,7 37 [59]	2020	SrTiO ₃ /(BiFeO ₃ @ZnS)	SILAR	Z-scheme and H-type	cubic	100 (SrTiO ₃)	3.3(SrTiO ₃)	-	
2020 Pt/STO Chemical reduction Schottky junction coral-like ≈ 30-50 3.26 (SrTiO ₃) - [40] 2021 CuPd/SrTiO ₃ -CuPd-Bi ₂ O ₃ Chemical reduction and high temperature calcination Z-scheme spherical 25 (SrTiO ₃) 3.2 (SrTiO ₃) - [17] 2018 pGCN-ST Impregnation - cubic 25 2.76 83,3 [57] 2022 SrTiO ₃ /Ag ₂ O-NDC Polymeric precursor - cubic 20-30 (SrTiO ₃) 2.84 247.32 [58] 2020 SrTiO ₃ /g-C ₃ N ₄ Polymeric precursor Type II nanoparticles 32-45 (SrTiO ₃) 2,7 37 [59]	2019		Mechanically milling and calcination	Type II	cubic		3.16 (SrTiO ₃)	32.4	
2021 CuPd/SrTiO ₃ —CuPd—Bi ₂ O ₃ Chemical reduction and high temperature calcination Z-scheme spherical 25 (SrTiO ₃) 3.2 (SrTiO ₃) — [17] 2018 pGCN—ST Impregnation — cubic 25 2.76 83,3 [57] 2022 SrTiO ₃ /Ag ₂ O—NDC Polymeric precursor — cubic 20—30 (SrTiO ₃) 2.84 247.32 [58] 2020 SrTiO ₃ /g—C ₃ N ₄ Polymeric precursor Type II nanoparticles 32—45 (SrTiO ₃) 2,7 37 [59]	2020	Pt/STO	Chemical reduction	Schottky junction	coral-like	≈30-50	3.26 (SrTiO ₃)	-	
2022 SrTiO ₃ /Ag ₂ O-NDC Polymeric precursor - cubic 20-30 (SrTiO ₃) 2.84 247.32 [58] 2020 SrTiO ₃ /g-C ₃ N ₄ Polymeric precursor Type II nanoparticles 32-45 (SrTiO ₃) 2,7 37 [59]	2021	CuPd/SrTiO ₃ -CuPd-Bi ₂ O ₃		Z-scheme	spherical	25 (SrTiO ₃)	3.2 (SrTiO ₃)	-	[17]
2022 SrTiO ₃ /Ag ₂ O-NDC Polymeric precursor - cubic 20-30 (SrTiO ₃) 2.84 247.32 [58] 2020 SrTiO ₃ /g-C ₃ N ₄ Polymeric precursor Type II nanoparticles 32-45 (SrTiO ₃) 2,7 37 [59]	2018	pGCN-ST	Impregnation	=	cubic	25	2.76	83,3	[57]
2020 SrTiO ₃ /g-C ₃ N ₄ Polymeric precursor Type II nanoparticles 32–45 (SrTiO ₃) 2,7 37 [59]	2022	SrTiO ₃ /Ag ₂ O-NDC	Polymeric precursor	-	cubic	20-30 (SrTiO ₃)	2.84	247.32	
	2020			Type II	nanoparticles	, ,	2,7	37	
	2018		Hydrothermal		nanoparticles			33.1	

[30]	[81]	[28]	[27]			[83]	[31]	[34]	[32]
ı	1	14.38	27.43	20, 70.3, 106.6,	115.9, 131.8	I	I	I	20.971
ı	3.063					I	I	3.173	3.241
10	1000	6000 in length	35-40	97, 390, 530, 1500		120-170		34	50.07
spherical	cubic	nanofibers	cubic	golf-like, star-like,	urchin-like and flower-like	ribbon-like	cubic	nanocrystalline	spherical
I	ı	I	I	ı		I	ı	ı	1
Sol-gel	Hydrothermal	Hydrothermal	Hydrothermal	Solvothermal		Solvothermal	Sol-gel	Sol—gel—solid phase	Co-precipitation
SrTiO ₃		SrTiO ₃	SrTiO ₃	SrTiO ₃	SrTiO ₃				
2017	2018	2022	2020	2020		2020	2021	2019	2022

position of the VB is more positive than the redox potential O_2/H_2O (1.23 V versus NHE at pH = 0).

The SrTiO₃ semiconductor has a wide band gap of 3.2 eV, which contributes to the photoinduction of electrons and holes under UV light irradiation ($\lambda \leq 387.5$ nm); the CB and VB potentials are -0.61 and 2.59 eV, respectively. Therefore, owing to its redox potential, SrTiO₃ is a suitable material for photocatalytic water decomposition [88]. However, owing to its wide band gap and consequently low efficiency, pure SrTiO₃ requires modification with oxides of metals, nonmetals, and other semiconductors, thereby forming heterojunctions and composites. The photocatalytic characteristics of SrTiO₃-based heterojunctions for hydrogen production are improved to increase the light absorption spectrum by decreasing the recombination of photogenerated electron-hole pairs. The efficient separation and transfer of charge carriers is crucial in SrTiO3-based heterojunctions. Incorporating other materials like graphene into the SrTiO₃ structure enhances the efficiency of charge separation. The presence of a heterojunction between SrTiO3 and another material provides additional pathways for charge transfer. Photogenerated electrons can move to the conduction band of the co-catalyst material, while photogenerated holes can be effectively captured by SrTiO₃. This spatial separation reduces recombination of the charges, leading to higher overall efficiency in the photocatalytic process.

Currently, nanocomposite semiconductor photocatalysts based on SrTiO₃ are widely used for releasing H₂ through the photocatalytic decomposition of water upon visible-light irradiation. The efficiency of heterostructured composite photocatalysts can be improved by the synergistic effect of several combined components. Particularly, this effect is observed in the STO-TiO2NTs@Au composite, which demonstrates excellent photocatalytic efficiency for water decomposition, with a high hydrogen evolution rate under artificial solar radiation (7200 μ mol h⁻¹g⁻¹) [89]. This high efficiency is attributed to the possible synergistic effect of the STO-TiO2NTs@Au structure itself, because the synthesised composite facilitates the charge carrier separation and increases the oxidation potential of Au nanoparticles. Furthermore, the SrTiO₃-T/Cd_{0.5}Zn_{0.5}S nanocomposite demonstrates the highest rate of photocatalysis with H2 release, that is, 25.01 mmol $h^{-1}g^{-1}$ in the visible light spectrum [70]. In this case, the high efficiency is attributed to the high concentration of oxygen vacancies on the SrTiO₃ nanocrystal surface, which results in the effective separation of photoinduced charge carriers. A nanocomposite based on gC3N₄/SrTiO₃ resulted in a considerably high efficiency of hydrogen production via water decomposition under visible light (hydrogen formation rate = 966.8 μ mol h⁻¹g⁻¹), owing to the effect of interfacial coupling between g-C₃N₄ and SrTiO₃ [80].

Doping SrTiO₃ with metals subsequently increases the light absorption capacity in the visible spectrum because the band gap of the semiconductor is narrowed by the creation of a d-level in the middle of the band gap. However, phase impurities formed during doping can serve as recombination sites for photoinduced electrons and holes, thereby suppressing the electrical conductivity and reducing the photocatalytic efficiency. Despite this, numerous studies have



Fig. 2 – Various applications of SrTiO₃-based composites.

demonstrated the successful use of metals in heterostructured composites based on $SrTiO_3$. For example, the composite photocatalyst $Au-Al/SrTiO_3$ demonstrates a high hydrogen evolution rate (347 μ mol $h^{-1}g^{-1}$) under illumination in the visible light range, and this is associated with the effect of the Au-Al pair on light absorption [90].

In contrast, doping SrTiO $_3$ with non-metals such as N and C is more practical and beneficial for several reasons. First, N 3 -ions, which partially replace (O 2 -) in the oxide lattice, do not significantly contribute to the exciton recombination process. Second, the band gap of the semiconductor is narrowed owing to the overlap of the p-state with oxygen 2p-orbitals, which ultimately improves the photocatalytic performance under visible light. For example, the mesoporous Pt/SrTiO $_3$:C,N photocatalyst used for water splitting exhibited an excellent hydrogen formation rate (3400 μ mol h $^{-1}$ g $^{-1}$) under UV/visible light, with reliable stability during 15 h of irradiation [51].

The shape of the heterostructure is another important factor that affects the increase in the photocatalytic activity. For example, using a heterostructured nanocomposite in the form of one-dimensional SrTiO3@2Mo2C nanofibres with a core and shell, the hydrogen evolution rate was increased by 15 times compared with that of the initial SrTiO3, upon irradiation with sunlight [77]. The closed heterostructure and high electrical conductivity of Mo₂C improve the light absorbing capacity and phase conductivity and prevent the recombination of the generated charge carriers, facilitating the transfer of photogenerated electrons and holes to active centres. Tubular photocatalysts are also of considerable interest. The nanotubular multijunction photocatalyst Pt/N-TiO2@SrTiO3 exhibited excellent efficiency with a hydrogen production rate of 3873 μ mol h⁻¹ g⁻¹ under the influence of sunlight [69]. The 150T-SrTiO₃ sample had a specific area of 298.3 m² g⁻¹ and an average nanotube diameter of 66 nm, with well-dispersed square SrTiO₃ particles (diameter = 52-66 nm) [120]. A similar surface area (300 m² g⁻¹), but with a scaly shape, was successfully obtained during synthesis of the triple heterostructure SrTiO₃@TiO₂/C by freeze-casting in a mixture with

colloidal silica as a solid template and combining hierarchically lined (micro-, meso-, and macro-) pores [91]. Under UV irradiation, the synthesised SrTiO₃/TiO₂/C sample exhibited the optimal photocatalytic activity for $\rm H_2$ evolution at a rate of 2.52 mmol $\rm h^{-1}$ g⁻¹, which is 1.5 times higher than that of the reference P25 photocatalyst.

Based on the above-mentioned studies, although pure SrTiO₃-based photocatalysts are considered inefficient, the careful design and creation of SrTiO3-based composites can increase the photocatalytic activity for hydrogen production during the photocatalytic decomposition of water under solar radiation. The photocatalytic efficiency of SrTiO3-based composites can be increased because of a combination of several factors, such as: 1) providing an improved specific surface area to create numerous reaction centres; 2) narrowing the band gap by synthesising wide-gap SrTiO3 and narrow-gap semiconductors or using metals to increase light absorption in the UV-visible region; 3) doping with metals and non-metals, inclusion of oxygen vacancies on the SrTiO3 nanoparticle surface, and creation of a heterojunction to prevent recombination of photogenerated electron-hole pairs; 4) deposition of the desired type of co-catalyst to provide a driving force between the redox potential of H₂O and H₂.

Photocatalytic decomposition of organic pollutants and antibiotics

The use of photocatalysts for organic pollutant decomposition has attracted particular attention in recent years because it involves solar energy, which is inexhaustible, environmentally friendly, and affordable. Recent studies have demonstrated the effect of using various types of photocatalysts for decomposing hydrocarbons [92], dyes [44,93,94], pesticides [40,58], carboxylic acids [95,96], antibiotics [41,97], and other organic pollutants [98,99]. According to the principle of photocatalysis, as described previously, light irradiation with energy equal to or greater than the band gap of the photocatalyst consequently forms holes (h⁺) in the VB as electrons

are photoexcited into the CB. The photoexcited electrons allow the O_2 reduction reactions to proceed until highly reactive radicals are formed. The holes, which are simultaneously excited in the VB, oxidise H_2O into highly reactive hydroxyl radicals. The induced active radicals and the photoexcited holes accelerate the decomposition of the adsorbed organic pollutant particles. However, active photogenerated charge carriers also decompose the pollutant molecules. The main stages of the decomposition process upon light irradiation are as follows [31]:

$$SrTiO_3 + hv \rightarrow e^- + h^+$$

$$O_2 + e^- \rightarrow O^*_2$$

$$OH + h^+ \rightarrow OH^*$$

$$OH^- + O_2^- + Dyes \rightarrow Decomposition products$$

Among the numerous photocatalysts, SrTiO₃ is one of the most suitable candidates for the photocatalytic decomposition of organic pollutants because of its high photoactivity, thermal and chemical stability, low cost, non-toxicity, and environmental friendliness [31]. As specified in the previous section, pure SrTiO₃ absorbs light only in the UV spectrum owing to its wide bandgap (3.2 eV) and rapid recombination of photogenerated carriers. The modification of SrTiO3 and development of photocatalyst heterojunctions are effective solutions for expanding the absorption region towards the visible spectrum. In addition, the charge separation process in SrTiO₃-based heterojunctions is crucial for efficient photocatalytic degradation of organic pollutants and antibiotics. By creating heterojunctions with other materials, such as graphene or metal oxides, the charge separation efficiency can be enhanced. In these heterojunctions, the photogenerated electrons in SrTiO3 can transfer to the conduction band of the co-catalyst material. This facilitates the rapid separation of charge carriers and minimizes their recombination, which would otherwise reduce the overall photocatalytic activity. For example, a complex composite photocatalytic system, SrTiO₃@Bi₅O₇I, can be used to decompose an RhB solution upon irradiation with artificial sunlight [100]. Using 30 wt% SrTiO₃@Bi₅O₇I nanocomposite, dye degradation reaches 89.6% within 150 min of photocatalysis. However, this result is not the most efficient; the SrTiO₃@Fe₂TiO₅ composite modified with CNTs shows unique photocatalytic performance in the complete decomposition of the methylene blue (MB) dye within 71 min, whereas MO and RhB dyes are degraded by 64% and 89%, respectively, in the same duration [101]. This can be explained by the improvement in the photocatalytic characteristics of SrTiO₃ owing to CNTs, thereby promoting the efficient separation of electrons and holes and minimising the recombination rate of photogenerated charge carriers. In addition, increasing the specific surface area of the resulting system improves the visible-light absorption. Furthermore, including CNTs in the system can contribute to the photosensitization of semiconductor particles, electron-hole pairs are generated on their surface [102].

For water decomposition with hydrogen evolution, comprehensively understanding the effect of the morphology of photocatalysts on their activity can help to improve the photocatalytic purification of water from organic pollutants. One such example is the highly efficient Co_{0.7}Zn_{0.3}Fe₂O₄--SrTiO₃ nanocomposite with an improved pore hierarchy and core-shell structure [67]. Additionally, studies have shown that Co_{0.7}Zn_{0.3}Fe₂O₄-SrTiO₃ has a high photodecomposition rate for the Congo red dye (5.08 \times 10⁻¹ min⁻¹) owing to the core-shell structure, chemical behaviour of the dye, and increased hierarchy of photocatalyst pores. The generation of charge carriers on the surface of a nanomaterial owing to the piezoelectric effect can produce free radical groups for organic pollutant degradation. Combining a piezoelectric material with a photocatalytic semiconductor effectively improves the photocatalytic characteristics of composites [97,103,104]. The SrTiO₃ photocatalyst is an effective material for obtaining such nanocomposite structures. For example, heterogeneous BaTiO₃/SrTiO₃ nanocomposites in the form of fibres demonstrate highly efficient and rapid photodecomposition of RhB (~97.4% in 30 min) under simultaneous exposure to ultrasound and UV. The high efficiency is attributed to the piezoelectric effect, which decreases the bandgap and provides a built-in polarisation field, thereby facilitating the separation of photoinduced electrons and holes [105].

Antibiotics and pharmaceuticals (such as carbamazepine (SMX) [106], aureomycin hydrochloride (CTC•HCl) [41], ciprofloxacin (CIP) [107], and tetracyclines (TCs) [108,109], are other pollutants in wastewater that severely affect human health, owing to their toxicity and chemical stability. This problem can potentially be solved through the photocatalytic degradation of antibiotics under light irradiation. Despite the high efficiency of several photocatalytic systems with reference to antibiotic decomposition, most systems are based on UV irradiation, which significantly limits their use in vivo [55]. However, heterostructured photocatalysts have recently been synthesised and demonstrate high efficiency in wider radiation spectra; examples include the heterojunction composite CSWT75 based on the Z-scheme (100% decomposition of TC rings B, C, and D in 60 min and 98% decomposition of the A ring of TC in 90 min) [72], ZSTO nanofibre membranes modified with silver phosphate (85% decomposition of tetracycline hydrochloride in 60 min) [75], and triple C-dots/Cu₂O/SrTiO₃ composites (92.6% decomposition of chlortetracycline hydrochloride in 90 min) [110]. The above-mentioned photocatalysts are suitable for only one type of antibiotic, whereas in another study [41] a new Z-scheme heterojunction of SrTiO₃/NH₄V₄O₁₀ decorated with C-dots was developed for the simultaneous decomposition of SMX, CTC•HCl, and CIP under artificial sunlight irradiation; the photocatalyst demonstrated efficiencies of 94.7, 88.3, and 86.05%, respectively, without significant inactivation after four treatment cycles.

Creation of heterojunctions, doping, surface modification, and metal/non-metal deposition are employed to improve the efficiency of composite SrTiO₃-based photocatalysts for the photocatalytic degradation of various organic pollutants and antibiotics. Consequently, 1) the band gap width is reduced, leading to photoabsorption in the visible radiation spectrum;

2) VB and CB are optimally arranged, thereby suppressing the recombination of photoinduced e⁻/h⁺ pairs; 3) unique, flexible, and nanoscale surfaces are created to facilitate the transfer of charge carriers to the photocatalyst surface; 4) sufficiently hierarchical porosity is generated to allow the substance to penetrate into the interior and provide multiple reaction centres for the redox process; 5) the photocatalysts can possibly be reused. Because environmental problems are a cause for concern, and considering the above-mentioned studies on the use of photocatalysts for the effective decomposition of organic pollutants and antibiotics, modified SrTiO₃-based composites are promising photocatalysts for environmental and health applications.

Photocatalytic decomposition of organic air pollutants

Global environmental problems associated with excessive CO₂ emissions are detrimental to the planet. In this regard, researchers have investigated the reduction of CO2 and its conversion into organic fuel in the presence of semiconductor photocatalysts [111-113]. The mechanism for photocatalytic reduction of air pollutants is similar to photocatalytic water purification, but with a slight difference. In the case of photocatalytic reduction of CO2, the photogenerated electrons on the surface of the photocatalyst interact with the adsorbed CO2 molecules, resulting in their conversion into hydrocarbons or other valuable chemical compounds. This process involves the transfer of electrons from the photocatalyst to CO₂, effectively transforming CO₂ into a more useful form. Recently published reports on the photoreduction of CO₂ to CO emphasise that the photocatalytic efficiency is affected by the ability of the photocatalyst to adsorb CO and light, and the rapid separation and transport of photogenerated charge carriers [114,115]. The use of SrTiO₃-based composites has also attracted considerable interest for CO2 photorecovery and organic pollutant decomposition. Thus, the SrCO₃/SrTiO₃ heterostructure demonstrates a sufficiently high rate of CO formation ~23.82 mmol $h^{-1}g^{-1}$, which is ~11.34 and ~6.75 times higher than those of pure SrTiO₃ and SrCO₃, respectively [116]. The SrTiO₃ heterojunction photocatalyst decorated with Ag nanoparticles can also be used to produce hydrogen [71]. This composite demonstrates high photoactivity, reducing CO_2 to CO (80.24 mmol g^{-1}), and the rate of H_2 release is 264.5 mmol h⁻¹g⁻¹. Such high rates are associated with the influence of Ag nanoparticles, which contribute to the passage of localised surface plasmon resonance (LSPR). Owing to the synergistic effect of the photocatalytic activity and LSPR of the resulting composite, it can be used both for CO2 reduction and hydrogen production. Furthermore, heterostructured SrTiO₃based photocatalysts have been used to remove NO, which is harmful to the environment and human life [117,118]. The SrTiO₃ photocatalyst is promising for removing NO, and decorating it with a co-catalyst composed of inexpensive SrCO₃ eco-material avoids disadvantages such as catalyst poisoning and rapid recombination of photoinduced electrons and holes. For example, the SrCO₃/SrTiO₃ composite with a band gap of 2.9 eV exhibited optimal photoactivity when 47% NO was removed after 12 min of artificial sunlight irradiation [119]. In another similar study, a heterostructured Bi/SrTiO₃ photocatalyst, synthesised via a simple sol-gel method, was

used to achieve a high photocatalytic activity, with 37% NO removal efficiency during 10 min of visible light irradiation [120].

Photocatalytic sterilisation

Semiconductor photocatalysts are promising materials for sterilisation owing to their characteristics, such as high oxidisability, non-toxicity, photostability, and chemical resistance [121]. Photocatalysts have the capability to generate reactive oxygen species (ROS), like hydroxyl radicals (-OH), which possess powerful oxidative properties when they interact with photons. When microorganisms come into contact with the surface of the photocatalyst, these ROS can initiate attacks on their cell membranes, proteins, and DNA, causing damage. This oxidative stress ultimately results in the sterilisation or deactivation of the microorganisms. Nanocomposite semiconductor photocatalysts based on SrTiO₃ can be used as bactericidal or antimicrobial systems under suitable light irradiation. Typically, photocatalytic sterilisation occurs because of the synthesis of antibacterial materials and SrTiO₃ and the creation of a composite with a heterojunction; the photoabsorption area of SrTiO₃ can be expanded to the visible light spectrum. In SrTiO3-based heterojunctions, an interface is created between SrTiO₃ and another material. This interface aids in the separation of electron-hole pairs generated by light. Electrons move towards the surface of the photocatalyst, while holes either stay within the bulk material or diffuse towards the surface of the other material. Such hybrid composites are widely used for the inhibition and sterilisation of Escherichia coli (E. coli) and Staphylococcus aureus (S. aureus) [75,110,122-124]. For example, a nanocomposite structure of polydopamine-functionalized (PDA) SrTiO₃ gallium-doped nanotubes (PDA-SrTiO3NT) was synthesised and studied for stability in vivo. The PDA-SrTiO₃ NT sample retained approximately 72% of its antibacterial activity for 14 days and could sterilize both E. coli and S. Aureus [122]. Another composite photocatalyst CuxO/Ag/SrTiO3 designed in the form of a Z-scheme, is highly effective in removing toluene and E. coli because of the presence of Ag nanoparticles and Cu⁺ [123].

However, compared with these heterostructured composites, triple C-dots/Cu₂O/SrTiO₃ exhibit the highest efficiency, with a photocatalytic inactivation of 91.58% for 60 min with reference to E. coli under sunlight; however, under the same conditions, the results were extremely low for pure Cu₂O and SrTiO₃. The photocatalytic characteristics were primarily optimised by the synergy of the p—n heterojunction and the introduction of carbon quantum dots, which promoted the separation and migration of charge carriers and improved the absorption capacity in the longer-wavelength light spectrum of the photocatalysts [110].

Other applications of heterostructured $SrTiO_3$ -based photocatalysts

Photoanodes for dye-sensitized solar cells

In contrast to conventional semiconductor solar cells, dyesensitized solar cells (DSSC) convert solar energy into electricity at relatively low costs, demonstrating adequate

mL of $H_2O/(0.35 \text{ mol L}-1 \text{ Na}_2\text{S}\cdot9H_2\text{O}$ and 0.25 mol $\text{L}^{-1} \text{ Na}_2\text{SO3})$

STO/g-CN

100

50 mg catalyst,

420 nm

300 W Xe lamp, 300 W Xe lamp

37] 135] 136] 136] 137] 60] 60] 76] 76]

efficiency. The primary components of traditional DSSC are the photoanode, electrolyte, and anti-electrode [125]. Consequently, most of the studies aimed at improving the efficiency of DSSC have concentrated on modernising the photoanode. The photoanode materials are mesoporous semiconductors, such as SnO2, Nb2O5, WO3, and TiO2, deposited on a transparent electrically conductive electrode, and light-sensitive dye molecules adsorbed on the semiconductor surface. When irradiated with light, the dye molecule, which absorbs photons, generates an electron in the CB and is directed along an external circuit. From the electrolyte, an electron from the iodine ion (I⁻) regenerates the excited dye molecule, oxidising it to the triiodide ion (I³⁻), which in turn is regenerated by an electron from the counter electrode.

One reason for the decrease in the efficiency of DSSC is the rapid recombination of charge carriers produced by the photosensitive dye [125]. Because all the induced electrons do not reach the photoanode, the magnitude of the photocurrent is not proportional to the number of excited electrons. To solve this problem, many studies have used a blocking layer that suppresses the charge carrier recombination and consequently increases the efficiency of DSSC. Perovskite SrTiO3 is a promising material for blocking layers. Heterostructured SrTiO3-based photocatalysts are promising materials for creating highly efficient photoanodes for DSSC. For example, the hetero-structured composite SrTiO₃/TiO₂ exhibits a photocatalytic conversion efficiency of 2.68%, which is 38% higher than that of pure TiO₂ (1.93%). Electrochemical impedance spectroscopy results indicate that the improved efficiency of DSSC is because of an increase in the charge lifetime and resistance of electron transport in the photoanode owing to the presence of SrTiO₃ in the blocking layer [65]. In two-layer DSSC photoanodes composed of 0.05% AC/TiO2 and SrTiO3 composites, the second layer of SrTiO3 improved the photovoltaic characteristics by reducing the recombination of charge carriers at the interface, and a similar band structure increased the electron lifetime, thereby increasing JSGs and V_{OC} . In addition, the efficiency of DSSC increased by ~57% compared with that of a device consisting of TiO2 [126]. In another study, SrTiO3 nanoparticles synthesised via coprecipitation were used as photoanodes in quantum dot solar cells (QDSCs). The QDSCs constructed from a heterostructured composite SrTiO₃/CDs/Bi₂S₃/ZnS:Cu demonstrated a maximum current of 2.38 mA cm^{-2} and a voltage (V_{OC}) of 0.37 V [127].

Electrochemical sensors/biosensors

Currently, the manufacture of SrTiO₃-based nanostructures for use in electrochemical sensors and biosensors is an urgent research area. SrTiO3-based composites improve the electrocatalytic characteristics in terms of detecting necessary molecules. A hybrid SrTiO₃/N-GNS nanocomposite has been used for the simultaneous determination of diphenhydramine (DPH) and bromhexine (BRO). The creation of a mesoporous heterojunction with nitrogen-doped graphene (N-GNS), which has excellent conductivity, subsequently generates numerous reaction centres in SrTiO3 and improves its electrocatalytic characteristics. An electrochemical sensor based on SrTiO₃/N-GNS demonstrates a wide dynamic range of 0.038-100.0 µm for DPH and 0.030-90.0 μm for BRO in a phosphate-buffered

Ref.	[77]	[69]	[06]	[21]	[32]	[49]	[38]	[70]	[80]	[91]	[37]	[135]	[136]	[88]	[137]	[09]	[36]	[92]	[138]
Efficiency, $\mu mol \ h^{-1}g^{-1}$	7900	3873	347	3400	212	91	263,49	25,010	8'996	2520	418,75	305,9	1322	7200	1304	471	462	5375	396,82
Sacrificial Agents	25 mg catalyst, 90 mL of $H_2O/(10 \text{ vol}\%)$ TEOA	50 mL solution containing 25% v/v methanol	$2,5$ mg catalyst, 1000 mL of $H_2O/30\%$ isopropyl alcohol	20 mg catalyst, 50 mL of H ₂ O/20% v/v methanol	50 mg catalyst, 150 mL of DI H ₂ O/H ₂ PtC _{I6} solution (0.73 mg/mL)	100 mg catalyst, 200-mL of $\mathrm{H_2O/Nai}~(\mathrm{2~mmol~L^{-1}})$	50 mg catalyst, 100 mL of $H_2O/Na_2S-Na_2SO_3$ (0.43:0.5)	50 mg catalyst, 100 mL f $\mathrm{H}_2\mathrm{O}/(0,25\mathrm{M}\ \mathrm{Na}_2\mathrm{S}\ \mathrm{and}\ 0,35\mathrm{M}\ \mathrm{Na}_2\mathrm{SO}_3)$	50 mg catalyst, 100 mL of $H_2O/(10 \text{ vol}\%)$ TEOA	100 mg catalyst, 100 mL of $H_2O/20\%$ v/v methanol	25 mg catalyst, 100 mL of H ₂ O/(0,35M Na ₂ S, 0,25M Na ₂ SO ₃)	10 wt% catalyst in H ₂ O/20 vol% CH ₃ OH solution	20 mg catalyst, 80 mL of $\rm H_2O/10\%$ v/v methanol	30 mg catalyst, 80 mL of $\mathrm{H}_2\mathrm{O}/10\%$ v/v methanol	15 mg catalyst, 30 mL of $\rm H_2O/10\%$ v/v methanol	1 g/L catalyst, 25% TEOA	100 mg catalyst, 100 mL of $H_2O/20\%$ v/v ethanol	1 g catalyst, 20 mL of H ₂ O/15% methanol	50 mg catalyst, 10% v/v methanol
Light Source	300 W Xe lamp, 313 nm	310 W/m ² Xe lamp, simulated sunlight	150 W Xe lamp, simulated sunlight	300 W Xe lamp, 360 nm	300 W Xe lamp, >400 nm	300 W Xe lamp, >420 nm	300 W Xe lamp	300 W Xe lamp, 420 nm	300 W Xe lamp, 420 nm	300 W Xe lamp, >420 nm	300 W Xe lamp	40 W UV lamp, 320 nm	300 W Xe lamp, AM 1.5 cut-off filter	300 W Xe lamp, Simulated sunlight	300 W Xe lamp, AM 1.5 cut-off filter	500 W xenon lamp, >500 nm	300 W Xe lamp, >400 nm	120 W UV lamp, 254 nm	300 W Xe lamp
Photocatalyst	SrTiO ₃ @Mo ₂ C	Pt/N-TiO2/110T-SrTiO3	Au-Al/SrTiO3	Pt-STO:C,N	SrTiO ₃ – TiO ₂	SrTiO ₃ (La,Cr)	ZnO/SrTiO ₃	$SrTiO_3 - T/Cd_{0,5}Zn_{0,5}S$	gC ₃ N4/SrTiO ₃	SrTiO ₃ /TiO ₂ /C	CdSe/SrTiO ₃	SrTiO ₃ /PAN	CdS/SrTiO ₃	STO-TiO ₂ NTs@Au	TiO ₂ /SrTiO ₃ /gC ₃ N ₄	Pt/gC ₃ N ₄ /SrTiO ₃	SrTiO ₃ :La/Rh	C-SrTiO ₃ /PAN/WS-FLG	SrTiO ₃ /SrSO ₄ /Pt
Year	2018	2018	2018	2018	2018	2018	2018	2019	2019	2019	2019	2019	2019	2020	2020	2020	2021	2021	2021

– The results of recent studies (2018–2022) on the use of SrTiO₃- based heterostructured photocatalysts nanoparticles in the H₂ production appi

Table 3 — The results of recent studies (2018–2022) on the use of SrTiO₃-based heterostructured photocatalysts nanoparticles in the environmental remediation application.

чррт						
Year	Photocatalyst	Organic Pollutant	Light Source	Irradiation Time	Efficiency	Ref.
2018	SrTiO ₃ /Bi ₅ O ₇ I	Rhodamine B	300 W Xe lamp	150 min	89,60%	[100]
2018	SrTiO ₃ /graphene	Rhodamine B	350 W Halogen lamp, 300–400 nm	70 min	97,60%	[139]
2019	CaO/SrTiO ₃	Rhodamine B	11 W UV light, 254 nm	120 min	92,50%	[140]
2021	BaTiO ₃ /SrTiO ₃	Rhodamine B	30 W, LED UV lamp, 365 nm	30 min	97,40%	[105]
2020	N-SrTiO ₃ /BiOBr	Rhodamine B	300 W Xe lamp, 400 nm	60 min	100%	[53]
2020	SrTiO ₃ /Ag	Rhodamine B	300 W Xe lamp	90 min	92,50%	[62]
2018	RGO/SrTiO ₃	Rhodamine B; Rose Bengal	sunlight	100 min	94.5; 90%	[64]
2018	Ag-SrTiO ₃	Rhodamine B; Methylene blue	visible light	60 min	93,5%; 94,7%	[78]
2019	SrTiO ₃ /TiO ₂	Methylene blue	High-power LED, 365 nm	220 min	100%	[66]
2018	PTh-SrTiO ₃	Methylene blue	250 W visible lamp	210 min	90%	[141]
2019	Porous graphene-SrTiO ₃	Methylene blue	250 W Hg, 410–700 nm	120 min	92%	[44]
2021	CuPd/SrTiO ₃ -CuPd-Bi ₂ O ₃	Methylene blue	300 W Xe lamp	4 h	93.87%	[17]
2021	Ag@SrTiO ₃ @CNT	Methylene blue; Methyl orange; Rhodamine B	150 W OSRAM lamp, <420 nm	30 min	100%; 71%; 46%	[48]
2022	SrTiO ₃ /Fe ₂ TiO ₅ /CNT	Methylene blue; Methyl orange; Rhodamine B	150 W visible light lamp	71 min	97%; 64%; 89%	[101]
2020	SrTiO ₃ /g-C ₃ N ₄	Methylene blue; Drug amiloride	visible light	420 min	1.3*10 ⁻³ (min ⁻¹); 1,82*10 ⁻³ (min ⁻¹)	[59]
2021	rGO/SrTiO ₃	Methylene blue; 2-nitrophenol	500 W Halogen lamp	150 min	91%; 81%	[39]
2019	Co _{0.7} Zn _{0.3} Fe ₂ O ₄ @SrTiO ₃	Congo Red; Methylene blue	Halogen lamp	12min; 60 min	94,9%; 91,8%	[67]
2019	SrTiO ₃ /BiOI	Methyl orange	250 W metal ha lamp, >400 nm	3 h	94,60%	[43]
2018	La-WO ₃ /SrTiO ₃	Methyl orange	300 W Xe lamp, 420 nm	75 min	100%	[142]
2020	Pt/gC ₃ N4/SrTiO ₃	Acid red 1	500 W xenon lamp >420 nm	120 min	83%	[60]
2018	pGCN-ST	Reactive blue 198; Reactive black 5; Reactive yellow 145	500 W tungsten lamp, 420 nm	120 min	100%	[57]
2022	SrTiO ₃ /CoAlMnO ₄	Erio Chrom Black T; Methylene Viole	300 W Xe lamp, ≥420 nm		92.42%; 90.34%	[46]
2020	SrTiO ₃ /PbBiO ₂ Br	Crystal violet	500 W Xe lamp	120 min	94,2	[143]
2021	SrTiO ₃ -TiO ₂	Cr ^{VI}	300 W Xe lamp, AM 1.5	4 h	100%	[68]
2020	SrTiO ₃ /(BiFeO ₃ @ZnS)	2,4-dichlorophenol	300 W Xe lamp	180 min	91.32%; 97.87%	[63]
2019	Ag-S-STO	4-chlorophenol	Solar light	120 min	96%	[144]
2022	SrTiO ₃ /Ag ₂ O-NDC	Dichlorodiphenyltrichloroethane	350 W Xe lamp, $\lambda \geq 420 \text{ nm}$	180 min	94,20%	[58]
2018	TiO ₂ /SrTiO ₃	4-nitrophenol	125 W mercury lamp, UV light	150 min	99%	[74]
2021	SrTiO ₃ /MnFe ₂ O ₄	Tetracycline	200 W Hg lamp, 253.7 nm	20 min	100%	[55]
2019	SrTiO ₃ (La,Cr)-6	Tetracycline	300 W Xe lamp, ≥420 nm	90 min	83%	[50]
2020	SrTiO ₃ /Ag/Ag ₃ PO ₄	Tetracycline	500 W Xe lamp >420 nm	15 min	72%	[52]
2021	CSWT75	Tetracycline	350 W Xe lamp	90 min	98%	[72]
2022	C-dots/SrTiO ₃ /NH ₄ V ₄ O ₁₀	SMX; CTC·HCl; CIP	500 W Xe lamp, >420 nm	120 min	94,7%; 88,3%; 86,05%	[41]
2022	SrCO ₃ /SrTiO ₃	CO ₂ to CO	300 W Xe lamp, $\lambda \geq 420 \text{ nm}$	_	23.82 μ mol $h^{-1}g^{-1}$	[116]
2019	Ag modified SrTiO ₃	CO ₂ to CO	300 W Xe lamp, $\lambda \geq 420 \text{ nm}$	_	6.69 μ mol h ⁻¹ g ⁻¹	[71]
2018	SrTiO ₃ /SrCO ₃	NO	300 W Xe lamp, 420 nm	12 min	47%	[119]
2020	Bi/SrTiO ₃	NO	300 W Xe lamp, 420 nm	10 min	37%	[120]
2021	AZSTO	Tetracycline hydrochloride; Gram bacteria	350 W Xe lamp, $\lambda \geq 400 \text{ nm}$	60 min; 24 h	85%; 99,99%	[75]
2022	Ti ₆ Al ₄ V/TiO ₂ /SrTiO ₃	E. coli	UV lamp, 253.7 nm	24 h	3% (proliferation rate)	[124]
2019	Ga:PDA-SrTiO₃	E. coli and S. aureus	in vivo	24 h	100%	[122]
2022	Cu _x O/Ag/SrTiO ₃	E. coli; toluene	visible light	24 h, 90 min	$0.0989 \mathrm{min}^{-1}$	[123]
2022	C-dots/Cu ₂ O/SrTiO ₃	E. coli; CTC·HCl	500 W Xe lamp >420 nm	60 min; 90 min	91,58%; 92,6%	[110]

saline solution with a pH of 7.0, and the detection limit reaches 2.1 and 1.9 nM for these preparations, respectively [73].

Energy storage

Energy can be stored in $SrTiO_3$ owing to its excellent dielectric properties. A recent study reported the construction of a nanocomposite based on $SrTiO_3@SiO_2$ plates in the form of a core—shell and polyvinylidene fluoride as a polymer matrix with excellent energy storage capacity. The design of the plates oriented along the direction of the electric field and the structural compatibility of the components are attributed to the improved values of E_b and U_e ($E_b = 402$ MV m⁻¹, $U_{e-} = 14.4$ J cm⁻³) compared with similar $SrTiO_3$ -based nanocomposites in the form of nanoparticles (NP), nanofibres (NF), nanowires (NW), platelets (ST PS), $ST@Al_2O_3$ nanofibres (ST@Al_2O_3 NF), ST@PVP nanofibres (ST@PVP NF), and ST@PDA platelets (ST@PDA PS) [128—132,145].

In addition, effective MgFe $_2$ O $_4$ /SrTiO $_3$ and MgFe $_2$ O $_4$ /SiO $_2$ nanocomposites modified by the sol—gel method have been manufactured as anodes for lithium-ion batteries. The manufactured MgFe $_2$ O $_4$ /SrTiO $_3$ sample (crystallite size = 18 nm) exhibits an increased Coulomb efficiency of 64.1%. The results of electrochemical studies show that the MgFe $_2$ O $_4$ /SrTiO $_3$ sample has a high velocity index with a capacity of 330 mAh g $^{-1}$ and 65% retention in the second cycle, which is higher than that of MgFe $_2$ O $_4$ /SiO $_2$ (with a capacity of 252 mAh g $^{-1}$ and 42% retention in the second cycle) after recovering current densities to 100 mA g $^{-1}$ [133].

Biodiesel production

Nanocomposites based on SrTiO₃ can be used for biodiesel production owing to the catalytic reduction of acidic waste cooking oil. In a recent study [134], a heterogeneous SrTiO₃ catalyst doped with graphene oxide iron nanoparticles (IGO@SrTi) was used for producing fatty acid methyl esters (FAME) of biodiesel by reforming triglycerides and free fatty acids. The presence of SrTiO₃ nanoparticles in the composite facilitated the highly efficient production of FAME (96% within 180 min) owing to its potential properties such as high catalytic ability, chemical and thermal stability, and large surface area with abundant charge carriers.

Tables 2–4 list recent research results on the use of heterostructured photocatalysts based on $SrTiO_3$ nanoparticles in H_2 production, environmental remediation, and other electrochemical and dielectric applications, respectively. The effectiveness of composites in photocatalytic applications directly depends on the experimental conditions. These results confirm the considerable potential of composite $SrTiO_3$ -based photocatalysts in photocatalytic, electrochemical, and dielectric applications. However, most of the results were obtained under laboratory conditions and require further study under more natural conditions for commercial and industrial purposes.

Nevertheless, autonomous prototypes have been developed for large-scale hydrogen production by the photocatalytic separation of water exposed to sunlight under natural conditions. In particular, photocatalytic panels with a total size of 100 m² have been developed using the composite SrTiO₃:Al, resulting in a solar-to-hydrogen (STH) efficiency of 0.76% and safe operation for several months under natural

Table 4	- The results of recent studies ((2017-2022) on the use of SrTi	O_3 - based heterostructured $_{ m I}$	Table 4 – The results of recent studies (2017–2022) on the use of SrTiO3- based heterostructured photocatalysts nanoparticles in the electrochemical and dielectric	ic
applications.	ons.				
Year	Photocatalyst	Application	Synthesis method	Efficiency	Ref.
2021	$ST@SiO_2/PVDF$	Energy storage	Solution casting	$D_{\rm max}\text{-}D_{\rm rem} = 9.14~\mu\text{C}~\text{cm}^{-2}, U_e = 14.4\text{J}~\text{cm}^{-3}$ at $E_b = 402~\text{MV}~\text{m}^{-1}$	[145]
2021	SrTiO ₃ @PDA	Energy storage	Three-step molten salt	D_{max} - $D_{rem} = 8.65 \ \mu C \ cm^{-2}, \ U_e = 12.45 \ J \ cm^{-3} \ at \ E_b = 350 \ MV \ m^{-1}$	128
2019	ST@Al ₂ O ₃ NF/PVDF	Energy storage	Coaxial electrospinning	$U_e = 15.3 J cm^{-3} at E_b = 475 MV m^{-1}, \eta = 68.5 \%$	129
2018	STnws/P(VDF-CTFE)	Energy storage	Solution casting	$U_e = 8.8 \text{ J cm}^{-3} \text{ at } E_b = 3381 \text{ kV cm}^{-1}, \eta = 45\%$	[130]
2018	ST@PDA NFs	Energy storage	Solution casting	$U_e = 9,12\mathrm{J~cm^{-3}}$ at $E_b = 360\mathrm{MV~m^{-1}},\eta = 61.1\%$	[131]
2017	ST NP/PVDF	Energy storage	Solution casting	$U_e = 5.1 J cm^{-3} at E_b = 2700 kV cm^{-1}, \eta = 64.6\%$	[132]
2022	0.05%AC/TiO ₂ -25 %SrTiO ₃	Photoanode for DSSC	Sol-gel	$\eta = 5,90\%$, $J_{SC} = 14,91$ mA/cm ² , $V_{OC} = 714,71$ V, FF = 55,46%	126
2019	SrTiO ₃ /TiO ₂	Photoanode for DSSC	Hydrothermal	$\eta = 2,68\%$, $J_{SC} = 7.01$ (MA/cM ²), $V_{OC} = 0.65$ V, FF = 58%	9
2019	TiO2: SrTiO3	Photoanode for QDSC	Doctor-blade	$\eta = 0.32\%$, Jsc = 2,38 (MA/cM ²), Voc = 0,37 V, FF = 31%	[127]
2019	SrTiO ₃ /N-GNS	Electrochemical sensor	Solvothermal	0.038-100.0 µM for DPH and 0.030-90.0 µM for BRO	[73]
2022	MgFe ₂ O ₄ /SrTiO ₃	Li-ion battery anodes	Sol-gel auto combustion	$1098 \text{ mAh g}^{-1} \text{ at } 100 \text{ mA g}^{-1}$	133
2022	IGO@SrTiO ₃	Biodiesel production	Ultrasonication	96% FAME at 180 min	134

conditions [21]. However, despite the considerably low STH efficiency compared with that of a potential competitor such as a photovoltaic water electrolyser (30% STH), this photocatalytic reactor is in the initial stage of development and can serve as the basis for highly efficient prototypes for large-scale hydrogen production via photocatalytic water separation under natural solar radiation [14].

Conclusions and future prospects

Cubic perovskite SrTiO₃ is considered a promising material for photocatalytic applications because of its excellent physical and chemical characteristics such as high thermal stability, resistance to photocorrosion, high surface hydrophilicity, and a sufficiently stable structure to create heterogeneous composites. Moreover, SrTiO3 has a higher electrical mobility at room temperature (5-8 cm² V⁻¹ s⁻¹) than its potential competitor titanium dioxide (TiO_2) (0.1–4 cm² V⁻¹ s⁻¹) in addition to a higher CB potential, which is favourable for photocatalytic applications. However, the wide bandgap, which narrows the spectrum of light absorption to the UV region, and the rapid recombination of photogenerated electrons and holes are the primary limitations of SrTiO₃. Based on the above-mentioned problems, we reviewed recent studies on the development of new heterogeneous SrTiO3-based photocatalysts with reduced charge carrier recombination and operation in the visible radiation spectrum. Initially, we presented the primary methods for the synthesis of heterogeneous SrTiO3-based photocatalysts with different morphologies and described the salient advantages and disadvantages of each method. However, considering these studies, highly effective SrTiO3-based composites were obtained only in the laboratory, and further development is required with industrial and commercial technologies. Subsequently, we discussed various applications of modified SrTiO₃ particles that are obtained by alloying with metals and nonmetals, creation of heterojunctions with highly conductive carbon modifications, deposition of co-catalysts, creation of oxygen vacancies, and modification of SrTiO3 surfaces and their results were summarized. These strategies are aimed at improving the photocatalytic, electrochemical, and dielectric properties of SrTiO3-based composites, which are expected to have wide practical applications. Numerous studies clearly indicate that the limiting factors of thermally and chemically stable SrTiO3 can be modified because of the adjustable bandgap width, and the creation of a heterojunction increases the lifetime of photogenerated charge carriers, which makes this material more promising than its competitors for future applications. Although the synthesised SrTiO3-based composites yielded highly effective results in a laboratory environment, they can be considerably different under natural conditions. Thus, further efforts should be directed towards developing modified SrTiO₃-based photocatalysts that function effectively over a wide UV-visible radiation spectrum in vivo for largescale applications. As described previously, owing to their photocatalytic, electrochemical, and dielectric properties, SrTiO₃-based composites have broad prospects for practical applications to address environmental pollution, energy shortage, and storage of the generated energy. Therefore, to

improve the efficiency of large-scale operations, the key strategies for development over the next decade should focus on.

- (1) Enhanced performance and efficiency. It is anticipated that significant advancements will be made in optimizing the performance of SrTiO₃-based composites. This could involve improving their photocatalytic efficiency, stability, and selectivity. Strategies such as novel synthesis techniques, bandgap engineering, and surface modification may be explored to achieve superior performance.
- (2) Tailored properties for specific applications. Future developments will focus on tailoring the properties of SrTiO₃-based composites to meet specific application requirements. This may involve precise control over composition, structure, morphology, and surface properties. By customizing these parameters, researchers can optimize the photocatalytic activity and selectivity of SrTiO₃-based composites for targeted environmental and energy applications.
- (3) Integration with emerging technologies. Over the next decade, there may be an increasing focus on integrating SrTiO₃-based composites with other technologies to enhance their functionality and applicability. For instance, coupling with energy storage systems, catalysts, or electrochemical devices could enable more efficient utilization of the generated energy or facilitate multi-step reactions for complex photocatalytic transformations.
- (4) Sustainable and scalable production methods. As the demand for efficient and environmentally friendly materials grows, the development of sustainable and scalable production methods for SrTiO₃-based composites will be crucial. This may involve the exploration of green synthesis approaches, utilization of renewable resources, and efficient recycling strategies to ensure the eco-friendly production and utilization of SrTiO₃based composites on a larger scale.

We expect that this review will provide new insights for future research on synthesis technologies and consequently improve the various applications of modified SrTiO₃-based photocatalysts to solve modern problems related to the environment, health, and energy.

Declaration of competing interest

The authors declare the following financial interests/personal relationships which may be considered as potential competing interests: Zh. Kuspanov A. Umirzakov A. Serik A. Baimenov M. Yeleuov Ch. Daulbayev.

Acknowledgments

This research is funded by the Science Committee of the Ministry of Science and Higher Education of the Republic of Kazakhstan (Grant No AP14869381).

REFERENCES

- [1] Spillias S, Kareiva P, Ruckelshaus M, McDonald-Madden E. Renewable energy targets may undermine their sustainability. Nat Clim Change 2020;10:974—6. https:// doi.org/10.1038/s41558-020-00939-x.
- [2] Razmjoo A, Gandomi AH, Pazhoohesh M, Mirjalili S, Rezaei M. The key role of clean energy and technology in smart cities development. Energy Strategy Rev 2022;44:100943. https://doi.org/10.1016/j.esr.2022.100943.
- [3] Abdisattar A, Yeleuov M, Daulbayev C, Askaruly K, Tolynbekov A, Taurbekov A, et al. Recent advances and challenges of current collectors for supercapacitors. Electrochem Commun 2022;142:107373. https://doi.org/ 10.1016/j.elecom.2022.107373.
- [4] Baimenov A, Montagnaro F, Inglezakis VJ, Balsamo M. Experimental and modeling studies of Sr2+ and Cs+ sorption on cryogels and comparison to commercial adsorbents. Ind Eng Chem Res 2022;61:8204–19. https:// doi.org/10.1021/acs.iecr.2c00531.
- [5] Askaruly K, Yeleuov M, Taurbekov A, Sarsembayeva B, Tolynbekov A, Zhylybayeva N, et al. A facile synthesis of graphite-coated amorphous SiO2 from biosources as anode material for libs. Mater Today Commun 2023;34:105136. https://doi.org/10.1016/j.mtcomm.2022.105136.
- [6] Veum K, Bauknecht D. How to reach the EU renewables target by 2030? An analysis of the governance framework. Energy Pol 2019;127:299–307. https://doi.org/10.1016/ j.enpol.2018.12.013.
- [7] Fujishima A, Honda K. Electrochemical photolysis of water at a semiconductor electrode. Nature 1972;238:37—8. https://doi.org/10.1038/238037a0.
- [8] Maeda K, Domen K. Photocatalytic water splitting: recent progress and future challenges. J Phys Chem Lett 2010;1:2655-61. https://doi.org/10.1021/jz1007966.
- [9] Wang Q, Domen K. Particulate photocatalysts for lightdriven water splitting: mechanisms, challenges, and design strategies. Chem Rev 2020;120:919–85. https://doi.org/ 10.1021/acs.chemrev.9b00201.
- [10] Fajrina N, Tahir M. A critical review in strategies to improve photocatalytic water splitting towards hydrogen production. Int J Hydrogen Energy 2019;44:540-77. https:// doi.org/10.1016/j.ijhydene.2018.10.200.
- [11] Ni M, Leung MKH, Leung DYC, Sumathy K. A review and recent developments in photocatalytic water-splitting using TiO2 for hydrogen production. Renew Sustain Energy Rev 2007;11:401–25. https://doi.org/10.1016/j.rser.2005.01.009.
- [12] Chen S, Takata T, Domen K. Particulate photocatalysts for overall water splitting. Nat Rev Mater 2017;2:17050. https:// doi.org/10.1038/natrevmats.2017.50.
- [13] Pan C, Takata T, Nakabayashi M, Matsumoto T, Shibata N, Ikuhara Y, et al. A complex perovskite-type oxynitride: the first photocatalyst for water splitting operable at up to 600 nm. Angew Chem Int Ed 2015;54:2955–9. https://doi.org/ 10.1002/anie.201410961.
- [14] Kuspanov Z, Bakbolat B, Baimenov A, Issadykov A, Yeleuov M, Daulbayev C. Photocatalysts for a sustainable future: innovations in large-scale environmental and energy applications. Sci Total Environ 2023;885:163914. https://doi.org/10.1016/j.scitotenv.2023.163914.
- [15] Hisatomi T, Domen K. Reaction systems for solar hydrogen production via water splitting with particulate semiconductor photocatalysts. Nat Catal 2019;2:387–99. https://doi.org/10.1038/s41929-019-0242-6.
- [16] Patial S, Hasija V, Raizada P, Singh P, Khan Singh AAP, Asiri AM. Tunable photocatalytic activity of SrTiO3 for water splitting: strategies and future scenario. J Environ

- Chem Eng 2020;8:103791. https://doi.org/10.1016/j.jece.2020.103791.
- [17] Piao C, Lin Y, Liu Z, Chen L, Tang J, Fang D, et al. Fabrication of Z-scheme CuPd/SrTiO3—CuPd—Bi2O3 photocatalyst for converting organic dye containing N and S elements into (NH4)2SO4. J Environ Chem Eng 2021;9:105537. https:// doi.org/10.1016/j.jece.2021.105537.
- [18] Gu Z, Wang Q, Sun X, Lu L, Zhang Y, Wang R, et al. SrTiO3-CaCr0.5Nb0.5O3 solid solutions as p-type photocatalysts for Z-scheme water splitting under visible light illumination. J Mater Sci Technol 2021;87:46-53. https://doi.org/10.1016/j.jmst.2021.01.039.
- [19] Wagner FT, Somorjai GA. Photocatalytic hydrogen production from water on Pt-free SrTiO3 in alkali hydroxide solutions. Nature 1980;285:559–60. https://doi.org/10.1038/ 285559a0.
- [20] Qin Y, Fang F, Xie Z, Lin H, Zhang K, Yu X, et al. La,Al-Codoped SrTiO 3 as a photocatalyst in overall water splitting: significant surface engineering effects on defect engineering. ACS Catal 2021;11:11429–39. https://doi.org/10.1021/acscatal.1c02874.
- [21] Nishiyama H, Yamada T, Nakabayashi M, Maehara Y, Yamaguchi M, Kuromiya Y, et al. Photocatalytic solar hydrogen production from water on a 100-m2 scale. Nature 2021;598:304—7. https://doi.org/10.1038/s41586-021-03907-3.
- [22] Tilley RJD. An electron microscope study of perovskiterelated oxides in the Sr Ti O system. J Solid State Chem 1977;21:293–301. https://doi.org/10.1016/0022-4596(77) 90128-1.
- [23] Liang Y, Bonnell DA. Structures and chemistry of the annealed SrTiO3(001) surface. Surf Sci 1994;310:128–34. https://doi.org/10.1016/0039-6028(94)91378-1.
- [24] Haeni JH, Irvin P, Chang W, Uecker R, Reiche P, Li YL, et al. Room-temperature ferroelectricity in strained SrTiO3. Nature 2004;430:758–61. https://doi.org/10.1038/ nature02773.
- [25] Szot K, Speier W, Bihlmayer G, Waser R. Switching the electrical resistance of individual dislocations in singlecrystalline SrTiO3. Nat Mater 2006;5:312–20. https://doi.org/ 10.1038/nmat1614.
- [26] Ji L, McDaniel MD, Wang S, Posadas AB, Li X, Huang H, et al. A silicon-based photocathode for water reduction with an epitaxial SrTiO3 protection layer and a nanostructured catalyst. Nat Nanotechnol 2015;10:84–90. https://doi.org/ 10.1038/nnano.2014.277.
- [27] Ramos-Sanchez JE, Camposeco R, Lee S-W, Rodríguez-González V. Sustainable synthesis of AgNPs/strontium-titanate-perovskite-like catalysts for the photocatalytic production of hydrogen. Catal Today 2020;341:112–9. https://doi.org/10.1016/j.cattod.2019.08.020.
- [28] Cao J, Jia Y, Wan X, Li B, Zhang Y, Huang S, et al. Strong tribocatalysis of strontium titanate nanofibers through harvesting friction energy for dye decomposition. Ceram Int 2022;48:9651–7. https://doi.org/10.1016/ j.ceramint.2021.12.164.
- [29] Kobayashi M, Suzuki Y, Goto T, Cho SH, Sekino T, Asakura Y, et al. Low-temperature hydrothermal synthesis and characterization of $SrTiO_3$ photocatalysts for NO_x degradation. J Ceram Soc Japan 2018;126:135–8. https://doi.org/10.2109/jcersj2.17195.
- [30] Youssef AM, Farag HK, El-Kheshen A, Hammad FF. Synthesis of nano-structured strontium titanate by sol-gel and solid state routes. Silicon 2018;10:1225–30. https:// doi.org/10.1007/s12633-017-9596-z.
- [31] Deshmukh VV, Ravikumar CR, Kumar MRA, Ghotekar S, Kumar AN, Jahagirdar AA, et al. Structure, morphology and electrochemical properties of SrTiO3 perovskite: photocatalytic and supercapacitor applications.

- Environmental Chemistry and Ecotoxicology 2021;3:241–8. https://doi.org/10.1016/j.enceco.2021.07.001.
- [32] Aravinthkumar K, Praveen E, Jacquline Regina Mary A, Raja Mohan C. Investigation on SrTiO3 nanoparticles as a photocatalyst for enhanced photocatalytic activity and photovoltaic applications. Inorg Chem Commun 2022;140:109451. https://doi.org/10.1016/ j.inoche.2022.109451.
- [33] El-Sadek MH, Farahat MM, Ali HH, Zaki ZI. Synthesis of SrTiO3 from celestite and rutile by mechanical activation assisted Solid-State reaction. Adv Powder Technol 2022;33:103548. https://doi.org/10.1016/j.apt.2022.103548.
- [34] Ma Y, Wu Z, Wang H, Wang G, Zhang Y, Hu P, et al. Synthesis of nanocrystalline strontium titanate by a sol-gel assisted solid phase method and its formation mechanism and photocatalytic activity. CrystEngComm 2019;21:3982-92. https://doi.org/10.1039/C9CE00495E.
- [35] Wei Y, Wang J, Yu R, Wan J, Wang D. Constructing SrTiO₃-TiO₂ heterogeneous hollow multi-shelled structures for enhanced solar water splitting. Angew Chem 2018:201812364. https://doi.org/10.1002/ange.201812364.
- [36] Wei Y, Wan J, Wang J, Zhang X, Yu R, Yang N, et al. Hollow multishelled structured SrTiO3 with La/Rh Co-doping for enhanced photocatalytic water splitting under visible light. Small 2021;17:2005345. https://doi.org/10.1002/ smll.202005345.
- [37] Han J, Dai F, Liu Y, Zhao R, Wang L, Feng S. Synthesis of CdSe/SrTiO3 nanocomposites with enhanced photocatalytic hydrogen production activity. Appl Surf Sci 2019;467–468:1033–9. https://doi.org/10.1016/ j.apsusc.2018.10.267.
- [38] Wu Y, Dong B, Zhang J, Song H, Yan C. The synthesis of ZnO/SrTiO3 composite for high-efficiency photocatalytic hydrogen and electricity conversion. Int J Hydrogen Energy 2018;43:12627–36. https://doi.org/10.1016/ j.ijhydene.2018.03.206.
- [39] Venkatesh G, Vignesh S, Srinivasan M, Palanisamy G, Elavarasan N, Bhuvaneswari K, et al. Construction and investigation on perovskite-type SrTiO3@ reduced graphene oxide hybrid nanocomposite for enhanced photocatalytic performance. Colloids Surf A Physicochem Eng Asp 2021;629:127523. https://doi.org/10.1016/ j.colsurfa.2021.127523.
- [40] Ahamad T, Alshehri SM. Fabrication of Ag@SrTiO3/g-C3N4 heterojunctions for H2 production and the degradation of pesticides under visible light. Separ Purif Technol 2022;297:121431. https://doi.org/10.1016/ j.seppur.2022.121431.
- [41] Zhang Y, Li Y, Yuan Y, Lin K. C-dots decorated SrTiO3/ NH4V4O10 Z-scheme heterojunction for sustainable antibiotics removal: reaction kinetics, DFT calculation and mechanism insight. Separ Purif Technol 2022;295:121268. https://doi.org/10.1016/j.seppur.2022.121268.
- [42] Wu Y, Wei Y, Guo Q, Xu H, Gu L, Huang F, et al. Solvothermal fabrication of La-WO3/SrTiO3 heterojunction with high photocatalytic performance under visible light irradiation. Sol Energy Mater Sol Cell 2018;176:230–8. https://doi.org/10.1016/j.solmat.2017.12.005.
- [43] Hu C, Huang H-X, Lin Y-F, Yoshida M, Chen T-H. Decoration of SrTiO3 nanofibers by BiOI for photocatalytic methyl orange degradation under visible light irradiation. J Taiwan Inst Chem Eng 2019;96:264–72. https://doi.org/10.1016/ j.jtice.2018.11.020.
- [44] Bantawal H, Sethi M, Shenoy US, Bhat DK. Porous graphene wrapped SrTiO3 nanocomposite: Sr—C bond as an effective coadjutant for high performance photocatalytic

- degradation of methylene blue. ACS Appl Nano Mater 2019;2:6629–36. https://doi.org/10.1021/acsanm.9b01513.
- [45] Swathi Padmaja J, Rao TS, Lakshmi KVD, Raju IM. Fabrication of hetero-structured mesoporours TiO2-SrTiO3 nanocomposite in presence of Gemini surfactant: characterization and application in catalytic degradation of Acid Orange. J Environ Chem Eng 2018;6:6457–67. https:// doi.org/10.1016/j.jece.2018.09.016.
- [46] Valian M, Soofivand F, Yusupov MM, Salavati-Niasari M. Facile synthesis of SrTiO3/CoAlMnO4 nanocomposite: a rechargeable heterojunction photocatalyst with superior hydrogen storage capability. Int J Hydrogen Energy 2022;47:31624–37. https://doi.org/10.1016/j.ijhydene.2022.07.073.
- [47] Cai J, Wei H, Zhang Y, Cai R, Zhang X, Wang Y, et al. Designed construction of SrTiO3/SrSO4/Pt heterojunctions with boosted photocatalytic H2 evolution activity. Chem Eur J 2021;27:7300–6. https://doi.org/10.1002/chem.202100101.
- [48] Sharifian K, Mahdikhah V, Sheibani S. Ternary Ag@SrTiO3@CNT plasmonic nanocomposites for the efficient photodegradation of organic dyes under the visible light irradiation. Ceram Int 2021;47:22741–52. https:// doi.org/10.1016/j.ceramint.2021.04.291.
- [49] Jia Y, Zhao D, Li M, Han H, Li C. La and Cr Co-doped SrTiO3 as an H2 evolution photocatalyst for construction of a Zscheme overall water splitting system. Chin J Catal 2018;39:421–30. https://doi.org/10.1016/S1872-2067(18) 63027-X.
- [50] Jiang J, Jia Y, Wang Y, Chong R, Xu L, Liu X. Insight into efficient photocatalytic elimination of tetracycline over SrTiO3(La,Cr) under visible-light irradiation: the relationship of doping and performance. Appl Surf Sci 2019;486:93–101. https://doi.org/10.1016/ j.apsusc.2019.04.261.
- [51] Tamiolakis I, Liu D, Xiao F-X, Xie J, Papadas IT, Salim T, et al. Mesoporous implantable Pt/SrTiO3:C,N nanocuboids delivering enhanced photocatalytic H2-production activity via plasmon-induced interfacial electron transfer. Appl Catal B Environ 2018;236:338–47. https://doi.org/10.1016/ j.apcatb.2018.05.036.
- [52] Yu X, Wang J, Fu X, Meng H, Zhu Y, Zhang Y. Construction of Z-scheme SrTiO3/Ag/Ag3PO4 photocatalyst with oxygen vacancies for highly efficient degradation activity towards tetracycline. Separ Purif Technol 2020;241:116718. https:// doi.org/10.1016/j.seppur.2020.116718.
- [53] Chen L, Shi L, Wu J, Tong Z, Huang C, Li C, et al. N-SrTiO3 nanoparticle/BiOBr nanosheet as 0D/2D heterojunctions for enhanced visible light photocatalytic dye degradation. Mater Sci Eng, B 2020;261:114667. https://doi.org/10.1016/ j.mseb.2020.114667.
- [54] Zhao W, Zhang J, Pan J, Zhao W, Niu J, Qiu J, et al. Fabrication and photocatalytic performance of onedimensional Ag3PO4 sensitized SrTiO3 nanowire. Ceram Int 2018;44:18337–43. https://doi.org/10.1016/ j.ceramint.2018.07.049.
- [55] Wang X, Jiang L, Li K, Wang J, Fang D, Zhang Y, et al. Fabrication of novel Z-scheme SrTiO3/MnFe2O4 system with double-response activity for simultaneous microwaveinduced and photocatalytic degradation of tetracycline and mechanism insight. Chem Eng J 2020;400:125981. https:// doi.org/10.1016/j.cej.2020.125981.
- [56] Han K, Li W, Ren C, Li H, Liu X, Li X, et al. Dye-sensitized SrTiO3-based photocatalysts for highly efficient photocatalytic hydrogen evolution under visible light. J Taiwan Inst Chem Eng 2020;112:4–14. https://doi.org/ 10.1016/j.jtice.2020.07.014.
- [57] Sureshkumar T, Thiripuranthagan S, Paskalis SMK, Kumaravel S, Kannan K, Devarajan A. Synthesis,

- characterization and photodegradation activity of graphitic C3N4-SrTiO3 nanocomposites. J Photochem Photobiol Chem 2018;356:425–39. https://doi.org/10.1016/j.jphotochem.2018.01.027.
- [58] Alhokbany N, Ahamad T, Ahmed J, Alshehri SM. SrTiO3/ Ag2O embedded in N-doped carbon nanocomposite for advanced photocatalytic degradation of dichlorodiphenyltrichloroethane (DDT). Mater Lett 2022;319:132271. https://doi.org/10.1016/ j.matlet.2022.132271.
- [59] Ferreira MA, da Silva GTST, Lopes OF, Mastelaro VR, Ribeiro C, Pires MJM, et al. Fabrication of SrTiO3/g-C3N4 heterostructures for visible light-induced photocatalysis. Mater Sci Semicond Process 2020;108:104887. https://doi.org/10.1016/j.mssp.2019.104887.
- [60] Tan C-E, Lee J-T, Su E-C, Wey M-Y. Facile approach for Z-scheme type Pt/g-C3N4/SrTiO3 heterojunction semiconductor synthesis via low-temperature process for simultaneous dyes degradation and hydrogen production. Int J Hydrogen Energy 2020;45:13330–9. https://doi.org/10.1016/j.ijhydene.2020.03.034.
- [61] He C, Bu X, Yang S, He P, Ding G, Xie X. Core-shell SrTiO3/ graphene structure by chemical vapor deposition for enhanced photocatalytic performance. Appl Surf Sci 2018;436:373–81. https://doi.org/10.1016/ j.apsusc.2017.12.063.
- [62] Shi L, Zhang Z, Wang R, Zhou C, Sun C. Synthesis and postannealing of Ag nanoparticles decorated urchin-like SrTiO3 particles for enhanced electron/hole separation and photocatalytic activity. Ceram Int 2020;46:19460–8. https://doi.org/10.1016/ j.ceramint.2020.04.294.
- [63] Qu Z, Liu Z, Wu A, Piao C, Li S, Wang J, et al. Preparation of a coated Z-scheme and H-type SrTiO3/(BiFeO3@ZnS) composite photocatalyst and application in degradation of 2,4-dichlorophenol with simultaneous conversion of Cr(VI). Separ Purif Technol 2020;240:116653. https://doi.org/10.1016/j.seppur.2020.116653.
- [64] Rosy A, Kalpana G. Reduced graphene oxide/strontium titanate heterostructured nanocomposite as sunlight driven photocatalyst for degradation of organic dye pollutants. Curr Appl Phys 2018;18:1026–33. https://doi.org/10.1016/ j.cap.2018.05.019.
- [65] Somdee A, Osotchan T. Effect of precipitating agent NaOH on the synthesis of SrTiO3/TiO2 heterostructure for dyesensitized solar cells. Mater Chem Phys 2019;229:210–4. https://doi.org/10.1016/j.matchemphys.2019.03.018.
- [66] Łęcki T, Zarębska K, Sobczak K, Skompska M. Photocatalytic degradation of 4-chlorophenol with the use of FTO/TiO2/ SrTiO3 composite prepared by microwave-assisted hydrothermal method. Appl Surf Sci 2019;470:991–1002. https://doi.org/10.1016/j.apsusc.2018.11.200.
- [67] Thomas B, Alexander LK. Nanoreactor based enhancement of photocatalysis with Co0.7Zn0.3Fe2O4@SrTiO3 core-shell nanocomposites. J Alloys Compd 2019;788:257–66. https:// doi.org/10.1016/j.jallcom.2019.02.190.
- [68] Cao S, Ye X, Hu H, Jin H, Wang Y, Ye J. Rational synthesis of SrTiO3 nanodots anchored mesocrystalline anatase TiO2 submicrospheres for photocatalytic reduction of CrVI. Separ Purif Technol 2021;275:119096. https://doi.org/10.1016/ j.seppur.2021.119096.
- [69] Su E-C, Huang B-S, Lee J-T, Wey M-Y. Excellent dispersion and charge separation of SrTiO3-TiO2 nanotube derived from a two-step hydrothermal process for facilitating hydrogen evolution under sunlight irradiation. Sol Energy 2018;159:751–9. https://doi.org/10.1016/ j.solener.2017.11.048.

- [70] Yu T, Lv Z, Wang K, Sun K, Liu X, Wang G, et al. Constructing SrTiO3-T/CdZnS heterostructure with tunable oxygen vacancies for solar-light-driven photocatalytic hydrogen evolution. J Power Sources 2019;438:227014. https://doi.org/10.1016/j.jpowsour.2019.227014.
- [71] Wan S, Chen M, Ou M, Zhong Q. Plasmonic Ag nanoparticles decorated SrTiO3 nanocubes for enhanced photocatalytic CO2 reduction and H2 evolution under visible light irradiation. J CO2 Util 2019;33:357–64. https://doi.org/ 10.1016/j.jcou.2019.06.024.
- [72] Zheng M, Chen Z, Lun Y, Liu B, Zhai W, He Q. Hybridization of SrTiO3 and strontium wolframates with very-highpotential photogenerated carriers for degrading the A-ring of tetracycline. Appl Surf Sci 2021;570:151138. https:// doi.org/10.1016/j.apsusc.2021.151138.
- [73] Punde NS, Rajpurohit AS, Srivastava AK. Sensitive electrochemical platform based on nano-cylindrical strontium titanate/N-doped graphene hybrid composite for simultaneous detection of diphenhydramine and bromhexine. Electrochim Acta 2019;319:727–39. https:// doi.org/10.1016/j.electacta.2019.07.025.
- [74] Devi LG, Anitha BG. Exploration of vectorial charge transfer mechanism in TiO 2/SrTiO 3 composite under UV light illumination for the degradation of 4-Nitrophenol: a comparative study with TiO 2 and SrTiO 3. Surface Interfac 2018;11:48–56. https://doi.org/10.1016/j.surfin.2018.02.005.
- [75] Gao X, Li M, Zhou F, Wang X, Chen S, Yu J. Flexible zirconium doped strontium titanate nanofibrous membranes with enhanced visible-light photocatalytic performance and antibacterial activities. J Colloid Interface Sci 2021;600:127–37. https://doi.org/10.1016/ j.jcis.2021.05.005.
- [76] Daulbayev C, Sultanov F, Korobeinyk AV, Yeleuov M, Azat S, Bakbolat B, et al. Bio-waste-derived few-layered graphene/ SrTiO3/PAN as efficient photocatalytic system for water splitting. Appl Surf Sci 2021;549:149176. https://doi.org/ 10.1016/j.apsusc.2021.149176.
- [77] Yue X, Yi S, Wang R, Zhang Z, Qiu S. Well-controlled SrTiO3@Mo2C core-shell nanofiber photocatalyst: boosted photo-generated charge carriers transportation and enhanced catalytic performance for water reduction. Nano Energy 2018;47:463-73. https://doi.org/10.1016/ j.nanoen.2018.03.014.
- [78] Wu Y, He T. Ag loading induced visible light photocatalytic activity for pervoskite SrTiO3 nanofibers. Spectrochim Acta Mol Biomol Spectrosc 2018;199:283–9. https://doi.org/ 10.1016/j.saa.2018.03.078.
- [79] Tao R, Li X, Li X, Shao C, Liu Y. TiO 2/SrTiO 3/g-C 3 N 4 ternary heterojunction nanofibers: gradient energy band, cascade charge transfer, enhanced photocatalytic hydrogen evolution, and nitrogen fixation. Nanoscale 2020;12:8320–9. https://doi.org/10.1039/D0NR00219D.
- [80] Luo Y, Deng B, Pu Y, Liu A, Wang J, Ma K, et al. Interfacial coupling effects in g-C3N4/SrTiO3 nanocomposites with enhanced H2 evolution under visible light irradiation. Appl Catal B Environ 2019;247:1–9. https://doi.org/10.1016/ j.apcatb.2019.01.089.
- [81] Gao H, Yang H, Wang S. Hydrothermal synthesis, growth mechanism, optical properties and photocatalytic activity of cubic SrTiO3 particles for the degradation of cationic and anionic dyes. Optik 2018;175:237–49. https://doi.org/ 10.1016/j.ijleo.2018.09.027.
- [82] Zhou M, Chen J, Zhang Y, Jiang M, Xu S, Liang Q, et al. Shape-controlled synthesis of golf-like, star-like, urchinlike and flower-like SrTiO3 for highly efficient photocatalytic degradation and H2 production. J Alloys Compd 2020;817:152796. https://doi.org/10.1016/ j.jallcom.2019.152796.

- [83] Zhang Z, Miao L, Zhao F, Li L, Yao M, Wang Y, et al. Dielectric SrTiO3 mesocrystal derived from a H2Ti4O9·H2O single crystal. Inorg Chem Commun 2020;114:107840. https://doi.org/10.1016/j.inoche.2020.107840.
- [84] Bera A, Wu K, Sheikh A, Alarousu E, Mohammed OF, Wu T. Perovskite oxide SrTiO 3 as an efficient electron transporter for hybrid perovskite solar cells. J Phys Chem C 2014;118:28494–501. https://doi.org/10.1021/jp509753p.
- [85] Okamoto Y, Fukui R, Fukazawa M, Suzuki Y. SrTiO3/TiO2 composite electron transport layer for perovskite solar cells. Mater Lett 2017;187:111–3. https://doi.org/10.1016/ j.matlet.2016.10.090.
- [86] Wang Y, Ma J, Zhang N, Chen D, Tu J, Cao Y, et al. Enhancing the performance of photoelectrochemical glucose sensor via the electron cloud bridge of Au in SrTiO ₃/PDA electrodes. RSC Adv 2021;11:13624–34. https://doi.org/ 10.1039/D1RA00812A.
- [87] Hou C, Huang W, Zhao W, Zhang D, Yin Y, Li X. Ultrahigh energy density in SrTiO 3 film capacitors. ACS Appl Mater Interfaces 2017;9:20484–90. https://doi.org/10.1021/ acsami.7b02225.
- [88] Moniruddin M, Ilyassov B, Zhao X, Smith E, Serikov T, Ibrayev N, et al. Recent progress on perovskite materials in photovoltaic and water splitting applications. Mater Today Energy 2018;7:246–59. https://doi.org/10.1016/ j.mtener.2017.10.005.
- [89] Han B, Wu L, Li J, Wang X, Peng Q, Wang N, et al. A nanoreactor based on SrTiO3 coupled TiO2 nanotubes confined Au nanoparticles for photocatalytic hydrogen evolution. Int J Hydrogen Energy 2020;45:1559–68. https:// doi.org/10.1016/j.ijhydene.2019.11.095.
- [90] Saadetnejad D, Yıldırım R. Photocatalytic hydrogen production by water splitting over Au/Al-SrTiO3. Int J Hydrogen Energy 2018;43:1116–22. https://doi.org/10.1016/ j.ijhydene.2017.10.154.
- [91] Xu T, Wang S, Li L, Liu X. Dual templated synthesis of trimodal porous SrTiO3/TiO2@ carbon composites with enhanced photocatalytic activity. Appl Catal Gen 2019;575:132–41. https://doi.org/10.1016/ i.apcata.2019.02.017.
- [92] Kang Q, Wang T, Li P, Liu L, Chang K, Li M, et al. Photocatalytic reduction of carbon dioxide by hydrous hydrazine over Au-Cu alloy nanoparticles supported on SrTiO ₃/TiO ₂ coaxial nanotube arrays. Angew Chem 2015;127:855–9. https://doi.org/10.1002/ange.201409183.
- [93] Cui J, Liu J, Xia X, Chai X, Guo H, Gao J, et al. Carbonized propagation synthesis of porous CQDs—SrTiO ₃/graphene and its photocatalytic performance for removal of methylene blue. Environ Sci: Water Res Technol 2022;8:671—85. https://doi.org/10.1039/D1EW00758K.
- [94] Nunes MJ, Lopes A, Pacheco MJ, Ciríaco L. Visible-light-Driven AO7 photocatalytic degradation and toxicity removal at Bi-doped SrTiO3. Materials 2022;15:2465. https:// doi.org/10.3390/ma15072465.
- [95] Lv X, Lam FL-Y, Hu X. Developing SrTiO3/TiO2 heterostructure nanotube array for photocatalytic fuel cells with improved efficiency and elucidating the effects of organic substrates. Chem Eng J 2022;427:131602. https:// doi.org/10.1016/j.cej.2021.131602.
- [96] Guo M, Liu Q, Wu M, Lv T, Jia L. Novel reduced graphene oxide wrapped-SrTiO3 flower-like nanostructure with Ti–C bond for free noble metal decomposition of formic acid to hydrogen. Chem Eng J 2018;334:1886–96. https://doi.org/ 10.1016/j.cej.2017.11.120.
- [97] Qian W, Zhao K, Zhang D, Bowen CR, Wang Y, Yang Y. Piezoelectric material-polymer composite porous foam for efficient dye degradation via the piezo-catalytic effect. ACS

- Appl Mater Interfaces 2019;11:27862–9. https://doi.org/10.1021/acsami.9b07857.
- [98] Konstas P-S, Konstantinou I, Petrakis D, Albanis T. Synthesis, characterization of g-C3N4/SrTiO3 heterojunctions and photocatalytic activity for organic pollutants degradation. Catalysts 2018;8:554. https://doi.org/10.3390/catal8110554.
- [99] Chang C-W, Hu C. Graphene oxide-derived carbon-doped SrTiO3 for highly efficient photocatalytic degradation of organic pollutants under visible light irradiation. Chem Eng J 2020;383:123116. https://doi.org/10.1016/j.cej.2019.123116.
- [100] Xia Y, He Z, Su J, Liu Y, Tang B. Fabrication and photocatalytic property of novel SrTiO3/Bi5O7I nanocomposites. Nanoscale Res Lett 2018;13:148. https:// doi.org/10.1186/s11671-018-2558-6.
- [101] Alimohammadi E, Mahdikhah V, Sheibani S. Type-II band alignment in CNT-modified SrTiO3-Fe2TiO5 heterostructure nanocomposite for photocatalytic degradation of organic dyes. Appl Surf Sci 2022;598:153816. https://doi.org/10.1016/ j.apsusc.2022.153816.
- [102] Syed N, Huang J, Feng Y, Wang X, Cao L. Carbon-based nanomaterials via heterojunction serving as photocatalyst. Front Chem 2019;7.
- [103] Zhou X, Wu S, Li C, Yan F, Bai H, Shen B, et al. Piezophototronic effect in enhancing charge carrier separation and transfer in ZnO/BaTiO3 heterostructures for high-efficiency catalytic oxidation. Nano Energy 2019;66:104127. https://doi.org/10.1016/ j.nanoen.2019.104127.
- [104] Raju TD, Veeralingam S, Badhulika S. Polyvinylidene fluoride/ZnSnO3 nanocube/Co3O4 nanoparticle thermoplastic composites for ultrasound-assisted piezocatalytic dye degradation. ACS Appl Nano Mater 2020;3:4777-87. https://doi.org/10.1021/acsanm.0c00771.
- [105] Liu X, Shen X, Sa B, Zhang Y, Li X, Xue H. Piezotronic-enhanced photocatalytic performance of heterostructured BaTiO3/SrTiO3 nanofibers. Nano Energy 2021;89:106391. https://doi.org/10.1016/j.nanoen.2021.106391.
- [106] Yu C, Lan S, Cheng S, Zeng L, Zhu M. Ba substituted SrTiO3 induced lattice deformation for enhanced piezocatalytic removal of carbamazepine from water. J Hazard Mater 2022;424:127440. https://doi.org/10.1016/ j.jhazmat.2021.127440.
- [107] Liu Z, Ma Z. Ag-SrTiO3/TiO2 composite nanostructures with enhanced photocatalytic activity. Mater Res Bull 2019;118:110492. https://doi.org/10.1016/ j.materresbull.2019.110492.
- [108] Chen Y, Peng Z, Li Y, Liu Y, Chen Y, Wu Y, et al. Photocatalytic performance of Z-scheme SrCO3-SrTiO3/ Ag3PO4 heterojunction for tetracycline hydrochloride degradation. J Mater Sci 2021;56:4356–65. https://doi.org/ 10.1007/s10853-020-05529-y.
- [109] Qiao J, Zhang H, Li G, Li S, Qu Z, Zhang M, et al. Fabrication of a novel Z-scheme SrTiO3/Ag2S/CoWO4 composite and its application in sonocatalytic degradation of tetracyclines. Separ Purif Technol 2019;211:843–56. https://doi.org/ 10.1016/j.seppur.2018.10.058.
- [110] Zhang Y, Li Y, Ruan Z, Yuan Y, Lin K. Extensive solar light utilizing by ternary C-dots/Cu2O/SrTiO3: highly enhanced photocatalytic degradation of antibiotics and inactivation of E. coli. Chemosphere 2022;290:133340. https://doi.org/ 10.1016/j.chemosphere.2021.133340.
- [111] Li N, Kong Y, Shen Q, Wang K, Wang N, Zhou J. Enhanced photocatalytic performance of direct Z-scheme Bi4Ti3O12/ SrTiO3 photocatalysts for CO2 reduction to solar fuel. J Photon Energy 2021:11. https://doi.org/10.1117/ 1.JPE.11.026501.

- [112] Wang L, Li Y, Wu C, Li X, Shao G, Zhang P. Tracking charge transfer pathways in SrTiO3/CoP/Mo2C nanofibers for enhanced photocatalytic solar fuel production. Chin J Catal 2022;43:507–18. https://doi.org/10.1016/S1872-2067(21) 63898-6.
- [113] Humayun M, Xu L, Zhou L, Zheng Z, Fu Q, Luo W. Exceptional co-catalyst free photocatalytic activities of B and Fe co-doped SrTiO3 for CO2 conversion and H2 evolution. Nano Res 2018;11:6391–404. https://doi.org/ 10.1007/s12274-018-2164-z.
- [114] Gong S, Zhu G, Wang R, Rao F, Shi X, Gao J, et al. Synergistically boosting highly selective CO2-to-CO photoreduction over BiOCl nanosheets via in-situ formation of surface defects and non-precious metal nanoparticles. Appl Catal B Environ 2021;297:120413. https://doi.org/ 10.1016/j.apcatb.2021.120413.
- [115] Hu Y, Qu Y, Zhou Y, Wang Z, Wang H, Yang B, et al. Single Pt atom-anchored C3N4: a bridging Pt—N bond boosted electron transfer for highly efficient photocatalytic H2 generation. Chem Eng J 2021;412:128749. https://doi.org/10.1016/j.cej.2021.128749.
- [116] Li Z, Zheng P, Zhang W, Gong S, Zhu L, Xu J, et al. Constructing SrCO3/SrTiO3 nanocomposites with highly selective photocatalytic CO2-to-CO reduction. Colloids Surf A Physicochem Eng Asp 2022;650:129686. https://doi.org/ 10.1016/j.colsurfa.2022.129686.
- [117] Carlotto S, Natile MM, Glisenti A, Vittadini A. Catalytic mechanisms of NO reduction in a CO-NO atmosphere at Co- and Cu-doped SrTiO ₃ (100) surfaces. J Phys Chem C 2018;122:449-54. https://doi.org/10.1021/acs.jpcc.7b09279.
- [118] Zhou Z, Chen D, Dong S, Li N, Xu Q, Li H, et al. Enhancing the photodegradation property of NO through the construction of a SrTiO ₃/GQDs/NH ₂ -UiO-66 heterojunction. Ind Eng Chem Res 2022;61:3550–60. https:// doi.org/10.1021/acs.iecr.1c04894.
- [119] Jin S, Dong G, Luo J, Ma F, Wang C. Improved photocatalytic NO removal activity of SrTiO3 by using SrCO3 as a new cocatalyst. Appl Catal B Environ 2018;227:24—34. https:// doi.org/10.1016/j.apcatb.2018.01.020.
- [120] Guo Y, Zhou S, Sun X, Yuan H. Improving photocatalytic activity in NO removal by adding metallic bismuth to SrTiO3 nanoparticles. Ceram Int 2020;46:14257–61. https://doi.org/10.1016/j.ceramint.2020.02.062.
- [121] Tauanov Z, Zakiruly O, Baimenova Z, Baimenov A, Akimbekov NS, Berillo D. Antimicrobial and antiviral properties of triclosan-containing polymer composite: aging effects of pH, UV, and sunlight exposure. Polymers 2023;15:1236. https://doi.org/10.3390/polym15051236.
- [122] Qiao H, Zhang C, Dang X, Yang H, Wang Y, Chen Y, et al. Gallium loading into a polydopamine-functionalised SrTiO3 nanotube with combined osteoinductive and antimicrobial activities. Ceram Int 2019;45:22183–95. https://doi.org/ 10.1016/j.ceramint.2019.07.240.
- [123] Chen J, Guo X, Lang L, Yin X, Wang A, Rui Z. Multifunctional Z-scheme CuxO/Ag/SrTiO3 heterojunction for photothermocatalytic VOCs degradation and antibiosis. Appl Surf Sci 2022:153275. https://doi.org/10.1016/ j.apsusc.2022.153275.
- [124] Si Y, Liu H, Yu H, Jiang X, Sun D. A heterogeneous TiO2/ SrTiO3 coating on titanium alloy with excellent photocatalytic antibacterial, osteogenesis and tribocorrosion properties. Surf Coating Technol 2022;431:128008. https://doi.org/10.1016/ j.surfcoat.2021.128008.
- [125] Babar F, Mehmood U, Asghar H, Mehdi MH, Khan AUH, Khalid H, et al. Nanostructured photoanode materials and their deposition methods for efficient and economical third generation dye-sensitized solar cells: a comprehensive

- review. Renew Sustain Energy Rev 2020;129:109919. https://doi.org/10.1016/j.rser.2020.109919.
- [126] Imani S, Alizadeh A, Roudgar-Amoli M, Shariatinia Z. Bilayered photoelectrodes of TiO2/activated carbon modified with SrTiO3 films boosted sunlight harvesting of dyesensitized solar cells. Inorg Chem Commun 2022;145:110045. https://doi.org/10.1016/ j.inoche.2022.110045.
- [127] Peter IJ, Vignesh G, Vijaya S, Anandan S, Ramachandran K, Nithiananthi P. Enhancing the power conversion efficiency of SrTiO3/CdS/Bi2S3quantum dot based solar cell using phosphor. Appl Surf Sci 2019;494:551–60. https://doi.org/ 10.1016/j.apsusc.2019.07.092.
- [128] Chen J, Wang Y, Chen W. Superior capacitive energy storage capability in polymer composites induced by polydopamine-coated paraelectric platelets. J Mater Sci 2021;56:9395–407. https://doi.org/10.1007/s10853-021-05883-5.
- [129] Pan Z, Yao L, Liu J, Liu X, Pi F, Chen J, et al. Superior discharge energy density and efficiency in polymer nanocomposites induced by linear dielectric core—shell nanofibers. J Mater Chem C 2019;7:405—13. https://doi.org/ 10.1039/C8TC04555K.
- [130] Zhang H, Zhu Y, Li Z, Fan P, Ma W, Xie B. High discharged energy density of polymer nanocomposites containing paraelectric SrTiO3 nanowires for flexible energy storage device. J Alloys Compd 2018;744:116–23. https://doi.org/ 10.1016/j.jallcom.2018.02.052.
- [131] Yao L, Pan Z, Zhai J, Zhang G, Liu Z, Liu Y. High-energy-density with polymer nanocomposites containing of SrTiO3 nanofibers for capacitor application. Compos Appl Sci Manuf 2018;109:48–54. https://doi.org/10.1016/j.compositesa.2018.02.040.
- [132] Wang J, Liu S, Wang J, Hao H, Zhao L, Zhai J. Improving dielectric properties and energy storage performance of poly(vinylidene fluoride) nanocomposite by surfacemodified SrTiO3 nanoparticles. J Alloys Compd 2017;726:587–92. https://doi.org/10.1016/ j.jallcom.2017.07.341.
- [133] Taha TA, Fayed MG, Mohamed SG. Enhanced electrochemical performance of MgFe2O4/SrTiO3 and MgFe2O4/SiO2 nanocomposite structures. J Alloys Compd 2022;925:166660. https://doi.org/10.1016/j.jallcom.2022.166660.
- [134] Hadi Jume B, Joolaei Ahranjani P, Farshineh Saei S, Zeki Mahmood FM, Vasseghian Y, Rezania S. Strontium titanium trioxide doped magnetic graphene oxide as a nanocatalyst for biodiesel production from waste cooking oil. Sustain Energy Technol Assessments 2022;54:102619. https:// doi.org/10.1016/j.seta.2022.102619.
- [135] Sultanov F, Daulbayev C, Bakbolat B, Daulbayev O, Bigaj M, Mansurov Z, et al. Aligned composite SrTiO3/PAN fibers as 1D photocatalyst obtained by electrospinning method. Chem Phys Lett 2019;737:136821. https://doi.org/10.1016/ j.cplett.2019.136821.
- [136] Yin X-L, Li L-L, Li D-C, Wei D-H, Hu C-C, Dou J-M. Room temperature synthesis of CdS/SrTiO3 nanodots-onnanocubes for efficient photocatalytic H2 evolution from water. J Colloid Interface Sci 2019;536:694—700. https:// doi.org/10.1016/j.jcis.2018.10.097.
- [137] Tao R, Li X, Li X, Shao C, Liu Y. TiO2/SrTiO3/g-C3N4 ternary heterojunction nanofibers: gradient energy band, cascade charge transfer, enhanced photocatalytic hydrogen evolution, and nitrogen fixation. Nanoscale 2020;12:8320—9. https://doi.org/10.1039/D0NR00219D.
- [138] Cai J, Wei H, Zhang Y, Cai R, Zhang X, Wang Y, et al. Designed construction of SrTiO3/SrSO4/Pt heterojunctions with boosted photocatalytic H2 evolution activity. Chem

- Eur J 2021;27:7300-6. https://doi.org/10.1002/chem.202100101.
- [139] He C, Bu X, Yang S, He P, Ding G, Xie X. Core-shell SrTiO3/ graphene structure by chemical vapor deposition for enhanced photocatalytic performance. Appl Surf Sci 2018;436:373–81. https://doi.org/10.1016/ j.apsusc.2017.12.063.
- [140] Coleto U, Amoresi RAC, Pereira CAM, Simões AZ, Zaghete MA, Monteiro Filho ES, et al. Influence of defects on photoluminescent and photocatalytic behavior of CaO/ SrTiO3 heterojunctions. Ceram Int 2019;45:15244-51. https://doi.org/10.1016/j.ceramint.2019.05.013.
- [141] Faisal M, Harraz FA, Ismail AA, El-Toni AM, Al-Sayari SA, Al-Hajry A, et al. Polythiophene/mesoporous SrTiO3 nanocomposites with enhanced photocatalytic activity under visible light. Separ Purif Technol 2018;190:33–44. https://doi.org/10.1016/j.seppur.2017.08.037.
- [142] Wu Y, Wei Y, Guo Q, Xu H, Gu L, Huang F, et al. Solvothermal fabrication of La-WO3/SrTiO3 heterojunction

- with high photocatalytic performance under visible light irradiation. Sol Energy Mater Sol Cell 2018;176:230–8. https://doi.org/10.1016/j.solmat.2017.12.005.
- [143] Xia Y, He Z, Su J, Zhu S, Tang B. Sustainable solar-light-driven SrTiO3/PbBiO2Br nanocomposites with enhanced photocatalytic activity. J Electron Mater 2020;49:3259—68. https://doi.org/10.1007/s11664-020-08022-z.
- [144] Anitha BG, Devi LG. Study of reaction dynamics of photocatalytic degradation of 4-chlorophenol using SrTiO3, sulfur doped SrTiO3, silver metallized SrTiO3 and silver metallized sulfur doped SrTiO3 catalysts: detailed analysis of kinetic results. Surface Interfac 2019;16:50–8. https:// doi.org/10.1016/j.surfin.2019.04.009.
- [145] Chen J, Zhang X, Yang X, Li C, Wang Y, Chen W. High breakdown strength and energy storage density in aligned SrTiO3@SiO2 core—shell platelets incorporated polymer composites. Membranes 2021;11:756. https://doi.org/ 10.3390/membranes11100756.

EI SEVIER

Contents lists available at ScienceDirect

Science of the Total Environment

journal homepage: www.elsevier.com/locate/scitotenv



Review

Photocatalysts for a sustainable future: Innovations in large-scale environmental and energy applications



Zhengisbek Kuspanov ^{a,b}, Baglan Bakbolat ^{b,c}, Alzhan Baimenov ^{c,d}, Aidos Issadykov ^{b,e}, Mukhtar Yeleuov ^{a,b}, Chingis Daulbayev ^{b,d,*}

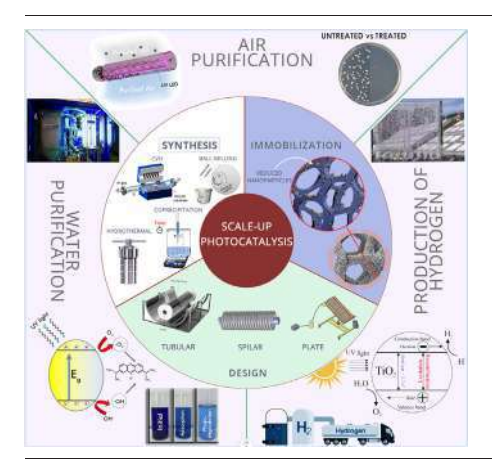
- ^a Satbayev University, 050013 Almaty, Kazakhstan
- ^b Institute of Nuclear Physics, 050032 Almaty, Kazakhstan
- ^c Al Farabi Kazakh National University, 050040 Almaty, Kazakhstan
- ^d National Laboratory Astana, Nazarbayev University, 010000 Astana, Kazakhstan
- ^e Joint Institute for Nuclear Research, 141980 Dubna, Russian Federation

HIGHLIGHTS

Photocatalytic systems for solving energy and environmental problems.

- The main challenges in the development of large-scale photocatalytic systems.
- Pilot applications of photocatalytic reactors for large-scale water and air purification and solar hydrogen production.

GRAPHICAL ABSTRACT



ARTICLE INFO

Editor: Huu Hao Ngo

Keywords: Photocatalysis Scale up Water purification Hydrogen production Air purification

ABSTRACT

The growing environmental and energy crises have prompted researchers to seek new solutions, including large-scale photocatalytic environmental remediation and the production of solar hydrogen using photocatalytic materials. To achieve this goal, scientists have developed numerous photocatalysts with high efficiency and stability. However, the large-scale application of photocatalytic systems under real-world conditions is still limited. These limitations arise at every step, including the large-scale synthesis and deposition of photocatalyst particles on a solid support, and the development of an optimal design with high mass transfer and efficient photon absorption. The purpose of this article is to provide a detailed description of the primary challenges and potential solutions encountered in scaling up photocatalytic systems for use in large-scale water and air purification and solar hydrogen production. Additionally, based on a review of current pilot developments, we draw conclusions and make comparisons regarding the main operating parameters that affect performance, as well as propose strategies for future research.

^{*} Corresponding author at: Institute of Nuclear Physics, 050032 Almaty, Kazakhstan. E-mail address: chingis.daulbayev@nu.edu.kz (C. Daulbayev).

Contents

1.	Introduction							
2.	Challe	nges for scale-up						
	2.1.	Large-scale synthesis of photocatalysts						
	2.2.	Immobilization of photocatalysts						
	2.3.	Design of photocatalytic reactors						
3.	Recent	t developments of photocatalytic reactors for a variety of large-scale applications						
	3.1.	Large-scale solar hydrogen generation						
	3.2.	Large-scale water purification						
	3.3.	Large-scale air purification						
4.	Conclu	isions and strategies for the future						
CRec	liT auth	orship contribution statement						
		ility						
Decla	Declaration of competing interest							
Ackn	cknowledgments							
Refer	ences							

Nomenclature

PANI polyaniline NF nickel foam

MIL Matériaux Institut Lavoisier
ALD atomic layer deposition

PE-ALD plasma-enhanced atomic layer deposition

ICP-PECVD inductively coupled radiofrequency plasmas - plasma

enhanced chemical vapour deposition

APP atmospheric pressure plasma

CFD combined Computational Fluid Dynamics

DOM discrete Ordinates Method

SFM six-flow model

STH solar-to-hydrogen conversion
FTO fluorine-doped tin oxide
OWS overall water splitting
CPC compound parabolic collector
PMR photocatalytic membrane reactor

PVDF polyvinylidene fluoride

DCF diclofenac

LSC fluorescent solar concentrator
VOC volatile organic compound
TOC total organic carbon
COD chemical oxygen demand

 $\begin{array}{ll} BEN & bentonite \\ VER & vermiculite \\ \eta_{Rxn} & quantum \ efficiency \end{array}$

1. Introduction

Although photocatalysis is a promising technology that could partially solve the environmental and energy problems associated with excessive use of fossil fuels, the production and application of photocatalysts capable of operating in visible light on a large scale remains an unsolved problem (J. Chen et al., 2022a; Ozin, 2022; Patowary and Kalita, 2022). At the same time, basic research on the photocatalysis process shows its marketing attractiveness for widespread application in the near future (Khan, 2023). Despite significant advancements in developing photocatalysts with high efficiency, thermal stability, purity, and environmental compatibility, low efficiency in photocatalytic reactors remains a major hurdle in their large-scale application. To enhance the efficiency of photocatalytic reactors, it

is imperative to address the fundamental challenges related to large-scale synthesis and deposition of photocatalysts on solid substrates using simple yet high-quality methods. Additionally, there is a need to develop optimal designs and geometries to overcome the existing limitations (Low et al., 2023). For example, the use of photocatalysts for water purification of different kinds of organic pollutants is a promising technology. However, due to the mass transfer of nanoparticles, it is necessary to collect nanoparticles later, which complicates the process of their repeated use. Mass transfer in turn may lead to incomplete oxidation of the pollutants on the surface of the nanoparticles due to the lack of optimum time for the process. As a result, the formation of byproducts becomes possible. When treating large volumes of water, it becomes necessary to carry out an additional timeconsuming process of filtering water from nanoscale photocatalysts, which calls into question the economic viability of nanoparticles. Such technological disadvantages limit investment in the application of photocatalysis for environmental problems. One solution is the creation of special photocatalytic reactors capable of eliminating emissions of pollutants into the environment at minimum costs in comparison with similar methods. For example, the creation of photocatalysts in the form of thin films on a special surface by different methods of deposition capable of functioning in a stable mode was suggested for operation on an industrial scale (Dolai et al., 2022; L. Wang et al., 2022c). In the case of repeated use, it is important to pay attention to the mechanical stability of such films, as they are prone to deformation at high flows (Y. Liu et al., 2022d; D. R. Ramos et al., 2021b).

The development of alternative energy sources can free mankind from its dependence on oil and gas resources. Today's global environmental problems, such as the greenhouse effect, are forcing us to focus on renewable energy sources such as solar, hydrogen and wind power. In addition to being environmentally friendly, cost-effective end products are also important for large-scale production. Unfortunately, there are some disadvantages to the currently available technology that prevent a full transition to renewable energy consumption. Intensive research has been carried out on the conversion of solar energy into photovoltaic energy (solar panels) and chemical reaction energy (reduction of CO2 into hydrocarbons and formation of H₂) (Photocatalytic Hydrogen Production: A Rift into the Future Energy Supply - Christoforidis - 2017 - ChemCatChem - Wiley Online Library, n.d.). The widespread introduction of hydrogen energy is one possible solution to decarbonization in the world economy. The search and development of innovative hydrogen technologies could lead to the creation of a quite competitive industry of large-scale hydrogen production. Currently, hydrogen is produced worldwide by the conversion of methane from fossil energy resources, which requires high temperature and pressure (Li Liu et al., 2022a; Liu et al., 2023). A developing method of hydrogen production is the photocatalytic decomposition of water. Despite the advantages of photocatalysis in their ability to work in usual environmental conditions, at the scale of hydrogen production, it is important to take

into consideration some parameters that can influence production efficiency. For example, an even distribution of radiation of suspension inside the reactor increases the amount of absorbed photons and optimum speed of agitation. Most scientific works characterize the photocatalyst efficiency using artificial light sources (different lamps) in which only a certain part of sunlight is presented. In the long term, it is necessary to use sunlight for photocatalysis considering that solar radiation is an environmentally friendly and renewable energy resource.

A number of studies on photocatalytic systems and their performances in real environments have been reported in the last few years (Jimenéz-Calvo et al., 2023). However, a few factors, such as high cost, low quality, and difficulty in controlling the morphology and structure obtained in large quantities of powders, cause difficulties in producing nanosized photocatalyst particles in large volume and simultaneously with high photocatalytic activity. Consequently, the focus in the bulk production of nanoscale photocatalysts should be on cost-effectiveness, the ability to control morphology and size, high photoactivity and environmental friendliness. To realize these goals, we hope to develop the shortest, most convergent routes with reliable and sustainable methods for the synthesis of photocatalysts functioning in a wide UV–visible range using readily available and inexpensive reagents and cocatalysts without releasing harmful byproducts and waste.

Significant advances in the production and application of photocatalytic systems allow us to speak with confidence about their large-scale implementation in the promising future. This is indicated by numerous works aimed at creating effective systems under laboratory conditions. From this perspective, we believe that a comprehensive review of photocatalytic systems with the potential for large-scale implementation in areas such as water and air purification and hydrogen production is needed. This review compiles research on photocatalytic systems with respect to their practical applications. The main problems hindering the large-scale application of the photocatalytic process for environmental cleaning and solar hydrogen generation have been analyzed and discussed in detail to deeply understand and explore the relationship between their synthesis parameters and applications. Finally, the problems, solutions, and prospects for the widespread application of photocatalytic systems in areas such as water and air purification and solar hydrogen generation are discussed in conclusion.

2. Challenges for scale-up

To achieve the full efficiency of the photocatalytic process, the main problems hindering large-scale photocatalytic applications for environmental cleaning and solar hydrogen generation must be solved. The first important obstacle to realizing this goal is the production of highly active photocatalysts on a large scale through low-energy, economical and environmentally friendly synthesis methods. The next hurdle is selecting the optimal substrate structure, material and immobilization method. In addition, difficulties arise in selecting the necessary geometry and design of photocatalytic reactors depending on the conditions and mode of operation. In the following sections, the main obstacles and solutions encountered in large-scale photocatalyst particle synthesis, substrate immobilization and the selection of the optimal photocatalytic reactor design will be discussed in detail.

2.1. Large-scale synthesis of photocatalysts

Fundamentally, all methods for producing nanomaterials, including photocatalytic materials, can be divided into two types: top-down and bottom-up. In the first case, the methods are characterized by their simplicity and scalability and in many cases represent the delamination of nanolayers from more massive materials but are limited by the low yield and lack of control over the size, thickness, and morphology of nanomaterials (Burke et al., 2020; Xiudong Chen et al., 2019d; Li et al., 2016; Yusran et al., 2020). Bottom-up methods, on the other hand, have broad prospects for synthesizing pure, homogeneous, and controlled nanoparticles with a complex structure with scalability (Cui et al., 2018; Liu et al.,

2019). However, among the various bottom-up methods, economical one-pot (B. Tian et al., 2018a) and in situ growth methods (M. Liu et al., 2021b) are best suited for large-scale production. In particular, the one-pot methods are characterized by easy availability of starting reagents, a small number of reaction steps and full use of precursors (J. Chen et al., 2022a; Parthibavarman et al., 2018; L. Wang et al., 2020b), whereas the in situ synthesis technique allows size and morphology control (G. Li et al., 2019b; Xin et al., 2020).

Regarding the large-scale production of nanoscale photocatalysts, the methods should not only be simple and stable but also allow the control of size and morphology, which play a key role in improving charge carrier mobility and enhancing light collection in various photocatalytic applications. For instance, various studies have indicated that mesoporous polymorphs (Xiong et al., 2019), nanosheets, nanotubes (Zhou et al., 2018), three-dimensional hierarchical porous structures, flower-shaped structures (Huang et al., 2018) or needle-shaped structures show better photocatalytic activity than commercial samples (Mamaghani et al., 2020; H.-X. Wang et al., 2020a). On the other hand, scaling up should also be considered to increase the reaction yield and create complex heterostructures with high efficiency, as simple photocatalysts such as TiO2, ZnS, gC3N4, and CdS are ineffective due to their wide bandgap and small conductivity (Kang et al., 2019; C. Liu et al., 2021a; Liu et al., 2019). For example, a BP/CN photocatalyst with high efficiency with respect to H2 release (at 786 μ mol h⁻¹ g⁻¹) and relatively low cost (€0.235/g) has been reported on a large scale (Min Wen et al., 2019b). The use of cocatalysts allows composite photocatalysts with higher yields and higher photocatalytic activity for H2 release to be obtained; however, despite high results, precious metals such as Pt are often used as cocatalysts, which considerably increase the cost of photocatalysts (Ma et al., 2018).

Under laboratory conditions, it is possible to obtain photocatalysts in grams, but the subsequent increase in yields requires the introduction of larger scale reaction apparatuses with high control of heating and mass transfer (Yi et al., 2021). Transition to large-scale photocatalyst production is also possible using a combination of several methods, including the abovementioned single-step and in situ methods (Deng et al., 2023). In addition, the ecological purity of solvents should be considered when applying the synthesis methods on a large scale, as there will be byproducts and wastes from reagents on the way to making photocatalysts in large quantities (Jahanshahi et al., 2020; G. Li et al., 2019b).

To date, several studies have been conducted to produce highperformance photocatalysts, both in the laboratory and on a larger scale, with the aim of achieving full-scale commercialization of photocatalytic applications. For a seamless transition from laboratory to industrial production, modern methods of large-scale synthesis should prioritize high reaction yield, scalability, and reliability while also allowing control of the morphological and structural characteristics of nanomaterials. Furthermore, the synthesis methods should ensure the rational use of the environment and maximum environmental safety to facilitate sustainable production practices.

2.2. Immobilization of photocatalysts

Modern photocatalytic experiments for hydrogen extraction or environmental purification are carried out to a large extent using a particle suspension in bespoke laboratory reactors. These are usually quartz reactors with a total volume of 50 to 500 mL. Such systems have achieved considerable photocatalytic success on the laboratory scale by using the entire active surface of the photocatalyst, which in turn leads to high reaction rates. However, particle-suspended reactors for large-scale use have a few limitations, such as the energy cost of dispersing large amounts of liquid before and during light irradiation so that particles do not settle to the bottom of the reactor, separation, and collection of the photocatalyst from liquid for maintenance purposes, as photocatalyst efficiency decreases with time. Studies aimed at reducing the limitations (e.g., electromagnetic, mechanical agitation) could not significantly reduce the limitations of suspended photocatalysts due to the impracticality of their applications at the

production scale. Thus, particle-immobilized photocatalysts on a solid substrate are used to enable large-scale photocatalyst applications, the main advantage of which is to ensure continuous operability and easy extraction of the photocatalyst from the spent solution (Bui et al., 2020; Loeb et al., 2019). Potential difficulties in the practical operation of immobilized photocatalytic systems are related to the mass transfer of reagents and products to the catalyst, both in liquid and gaseous phases, as well as the reduced illuminated surface area and fast photon scattering rate (Phan et al., 2018).

Depending on the photocatalyst application, the substrate design can vary, e.g., for hydrogen production, solid substrates are used, whereas for water and air purification systems, emphasis is placed on porous membranes and substrates because in addition to increasing the active centers, the bandwidth for unimpeded transport of pollutants is improved (Schwarze et al., 2022b). For large-scale photocatalytic hydrogen production, thin film photocatalysts immobilized on various substrates, such as 2D glass (Cerrato et al., 2019), PANI/cotton (Yu et al., 2019), and nonwoven fiber (Kacem et al., 2017; Schwarze et al., 2022a), are mainly used. Compared to suspended photocatalysts, thin-film photocatalysts are the most efficient in producing solar hydrogen due to the following advantages: thin films absorb photons uniformly with low scattering, contributing to efficient generation of charge carriers in large amounts; good scalability compared to suspended photocatalysts due to continuous H2 production and minimal consumption of immobilized photocatalyst powder with high activity (Gopinath and Nalajala, 2021). In particular, a thin film photocatalyst with immobilized CdS and Ni₃S₂ particles as cocatalysts on a flat foam surface showed excellent results with a maximum hydrogen extraction rate of 100.5 mmol g⁻¹ h⁻¹, which corresponds to obtaining 132 L H₂ using 1 m² of CdS-Ni₃S₂/NF photocatalyst under irradiation with light in the visible spectrum for 12 h (Chao et al., 2018). Unlike 2D photocatalytic purification of water and air from various pollutants, 3D substrates are applied, which are the most practical. The advantages of such 3D substrates are a large active specific surface area and low surface resistance, which provides improved mass transfer and photon absorption, which in turn increases the photocatalytic properties of the immobilized photocatalyst and the possibility of multiple uses.

To date, the following three-dimensional photoreactors have been reported: Duranit (Karavasilis et al., 2022), borosilicate glass (pros: continuous flow, transparent, reuse without loss of efficiency) (Karavasilis and Tsakiroglou, 2022), and ceramics with immobilized photocatalytic TiO₂ and ZnO nanoparticles (Sraw et al., 2018). Such spherical substrates for photocatalysts are mainly made of transparent materials and are notable for their durability and reusability without losses in continuous-flow systems, but the rate of pollutant decomposition (70 % chemical oxygen demand in 180 min) (Vaiano and Iervolino, 2018) is significantly lower in comparison with their suspended particle counterparts (90-95 % chemical oxygen demand in 120 min) (Kanakaraju et al., 2019). Other membranelike substrates have rather high prospects for both water and air purification, such as graphene oxide (GO)/polysulfone (PSF) membranes (Cheng et al., 2021), ceramic membranes/TiO₂-P25 (Lumbaque et al., 2021), poly(vinylidene fluoride)/TiO2-GO (Tran et al., 2020), porous stainless steel/TiO₂ (Rodríguez-Chueca et al., 2019), Al₂O₃/N-TiO₂ (Horovitz et al., 2018), and carbon nanofibers/TiO2 nanowires/MIL-100 (Zhang et al., 2018).

Another important factor is the choice of photocatalyst deposition method on the substrate surface, as the thickness of the immobilized layer should be thin enough to reduce photon scattering. One of the simple, economical and often used methods for both 2D (Rana et al., 2022; Schwarze et al., 2022b) and 3D substrates (Allen et al., 2018; Levchuk et al., 2016; D. Li et al., 2019a; Omerzu et al., 2021; Su et al., 2018) is the wet impregnation method, which involves immersion of the support material in a photocatalyst suspension or application of photocatalyst suspension drops to the substrate surface followed by drying at moderate temperatures up to 150 °C. Although this method is simple and cost-effective, it is not suitable for large-scale deposition, nor can it accurately control the growth of thin films on the surface, and it is not suitable for thermal treatment of inorganic substrates such as matrices and polymers (Rana et al., 2022).

Immobilization of low-size particles is also possible using other low-cost and low-temperature chemical methods, such as sol-gel and hydrothermal methods, but in the case of polymeric materials, organic residues promote excessive crystallization and increase in grain size, which in turn reduce photocatalyst activity (Allen et al., 2018). Recent work has been reported on the use of gas-phase methods that can accurately control growth and thickness. In particular, TiO₂/Al₂O₃ and separate TiO₂/ZnO layers have been deposited on the surface of a polycarbonate membrane matrix by the gas-phase atomic layer deposition method (Su et al., 2018). Similarly, ${
m TiO_2}$ powders have been deposited on porous aluminum foams (Levchuk et al., 2016), which indicates the possibility of this method to deliver photocatalyst particles to difficult-to-access complex surfaces; however, the ALD method is limited by a low deposition rate and deposition temperature range (120-180 °C), which does not allow for the use of heat-sensitive substrates. To reduce the deposition temperature, optimization methods have been proposed by using a low-temperature plasma process. Thus, low-temperature PE-ALD (Omerzu et al., 2021), ICP-PECVD (D. Li et al., 2019a), and APP (Banerjee et al., 2020) methods have been applied for photocatalyst deposition on polymer substrates. For instance, using low-temperature plasma-controlled deposition, we managed to deposit a thin layer of TiO2 on a complex three-dimensional porous foam surface and obtain high photocatalytic activity in a special recirculating reactor during dye decomposition with multiple use (20 cycles) capability (Uricchio et al., 2021). In view of the abovementioned works, an ideal substrate for modern photocatalytic systems for large-scale applications should meet criteria such as sufficiently strong contact with photocatalysts, high specific surface area, high adsorption to reaction products, chemical stability and structural strength. In addition, the choice of a suitable photocatalyst immobilization method is based primarily on the material and shape of the substrate used, as the quality of photocatalyst adhesion and the stability of photocatalytic activity directly depend on this.

2.3. Design of photocatalytic reactors

Research into photocatalytic environmental cleaning and hydrogen production has increased significantly in recent years. The main elements of heterogeneous photocatalysis are the light source and the photocatalytic reactor. The main function of photoreactors is to bring the illuminated photocatalyst and reaction product (contaminated water/air or product for H_2 generation) into contact. Consequently, the photoreactor for large-scale applications must have such a geometry and configuration to ensure the largest possible three-phase contact area.

The geometry of the photoreactor must be chosen according to the size and shape of the radiation source to maximize the collection of irradiated radiation. Reactor irradiation can take place outside or inside the reactor. In internally illuminated reactors, photocatalysts are irradiated by an ultraviolet or visible lamp located inside the reactor with cylindrical (Reilly et al., 2018), spiral (Jo et al., 2015) or circular geometry (Rincón and La Motta, 2019). Photocatalysts immobilized on glass spheres (Kamaei et al., 2018; Vaiano and Iervolino, 2018), clay balls (Sraw et al., 2018) or powder suspensions (Peralta Muniz Moreira and Li Puma, 2021; Rincón and La Motta, 2019) are commonly used. Such photoreactors with internal illumination are distinguished by high mass transfer, as they possess a large photocatalytic surface area per unit volume of liquid or volatile gas (Bafaqeer et al., 2018; Khan and Tahir, 2019). However, internally illuminated photoreactors for commercial applications are limited by efficiency drop due to scattering and reflection on immobilized photocatalyst layers when using photoreactors with large diameters (Ramos et al., 2019), and in suspension reactors in the case of nanoscale photocatalysts, these particles can adhere to the tube inner surface, thus also reducing light penetration efficiency (Khan and Tahir, 2019). In addition, there are cases of optimizing such photoreactors by using intensely and uniformly distributed light optical fibers (Harrisankar et al., 2021; O'Neal Tugaoen et al., 2018; Zhong et al., 2019), economical LEDs (Khodadadian et al., 2018; O'Neal Tugaoen et al., 2018) or designing reactors that are irradiated by LEDs

from both inside and outside to minimize dead spots (Manassero et al., 2023).

In contrast to photocatalytic reactors with internal illumination, externally illuminated photoreactors are irradiated by multiple external lamps, which are situated perpendicularly (Claes et al., 2019), above (Fang et al., 2019; Kassahun et al., 2020) or on the focal axis of a parabolic reflector (Casado et al., 2019). Externally illuminated reactor designs are usually transparent tubular and can be irradiated by direct sunlight rich in UV radiation (Ochoa-Gutiérrez et al., 2018). Solar collector-based photocatalytic reactor designs, namely, compound parabolic collectors (CPCs), have broad applications for photocatalytic environmental cleaning (Gutiérrez-Alfaro et al., 2018; Luna-Sanguino et al., 2020; Moreira et al., 2018) and hydrogen generation (Cao et al., 2018b; Ma et al., 2020; Ren et al., 2022). CPC photoreactors are more suitable for large-scale applications because they maximize the use of sunlight by redirecting direct and scattered rays by reflectors to the tube reactor and perfectly cross-mix suspensions due to low-cost turbulent flow (Cabral, 2022; Talwar et al., 2020). As a rule, such reactors are hermetically sealed and made of economical materials (Fendrich et al., 2019). This paper (M. Tian et al., 2018b) details the factors to consider when selecting the most efficient CPC-based photoreactor design with 2D and 3D, asymmetric, seashell-shaped and convex geometry for large-scale operation. However, externally illuminated photoreactors are limited due to the incomplete irradiation of the photocatalyst slurry through the reactor surface's depth. In addition, reactors of this type are difficult to scale in natural direct sunlight conditions.

Reactors with flat geometry in the form of fixed plates (Ahmed et al., 2022; Devia-Orjuela et al., 2019; B. Ramos et al., 2021a) or rotating disks/drums (Zelić et al., 2022a, 2022b) are more suitable for such purposes. The main advantages of planar photocatalytic reactors are as follows: control of liquid flow rate; absence of possible dead zones and provision of continuous liquid flow mode in case of contaminated water treatment; and easy maintenance and operation (very important in production scale and with the possibility of uniform irradiation by sunlight (Bahmani et al., 2020a) and illumination by additional emitters (Zhou et al., 2023)). For example, using these advantages, a thin film sludge reactor irradiated with blue LEDs for urea degradation was designed. In addition, various operating parameters, such as light source, flux rate (Ahmed et al., 2022), catalyst dosage, emitted surface area, and pH, on photocatalytic efficiency have been investigated (Babić et al., 2021; Bahmani et al., 2020b). At present, modern mathematical modeling techniques such as combined computational fluid dynamics (CFD) (Lira et al., 2022; Tong et al., 2020; Yusuf et al., 2018, 2020), the discrete ordinates method (DOM) (Armaković et al., 2020; Moreno et al., 2019), the six-flow model (SFM), and others (Tolosana-Moranchel et al., 2019; van Walsem et al., 2018) can accurately analyze internal kinetic processes to optimize photocatalytic reactors of any given photoreactor configuration if the required parameters are correctly considered. In particular, a real photoreactor simulated using CFD and the discrete element method increased the photocatalytic reaction rate by adjusting the size and shape (Tong et al., 2020). Methods such as CFD and DOM have made great progress in estimating the radiation field and contaminant removal by photoreactors with simple geometry and with laboratory artificial light sources, but they are limited in scaling solar photoreactors because they are time-consuming and require large computing resources, whereas the SFM model is more accurate in describing radiation transport phenomena in real-life solar photoreactor operating conditions. SFM has been used to simulate different geometries of photocatalytic reactors, including solar flat films, tubular CPC, and mixed multitubular photoreactors (Acosta-Herazo et al., 2020; Nchikou et al., 2021; Ochoa-Gutiérrez et al., 2018; Otálvaro-Marín et al., 2019).

Thus, the design of the selected photocatalytic reactor plays a key role in ensuring that the photocatalysts obtain the maximum benefit from light energy and provide a platform with a large contact area between the irradiated photocatalysts and the reaction products used. From the above data, it can be concluded that the choice of optimum geometry and configuration must first be based on the photocatalytic application method and the shape and variety of the radiation source. Consequently, when designing modern

high-efficiency photocatalysts for large-scale applications, researchers should focus on stable reactors operating in the visible region of radiation, using artificial radiation sources (cost-effective LEDs and optical fibers) and natural sunlight, with high reaction rates of both pollutant degradation and water splitting and the possibility of easy photocatalytic reduction and increased mass transfer. In addition, modern computer modeling techniques have made progress in optimizing the geometry of photoreactors, which will help to save time and money in designing the required large-scale photoreactors.

3. Recent developments of photocatalytic reactors for a variety of large-scale applications

3.1. Large-scale solar hydrogen generation

The rising global energy demand and depletion of fossil fuels are accelerating the transition to renewable energy sources, including green hydrogen. The direct conversion of solar energy into hydrogen through a photocatalytic process is distinguished by its simplicity and economy compared to competitive technologies such as photoelectrochemistry and photovoltaic-electrochemistry, which require more complex designs than a photocatalytic system. The photocatalytic process also has an ultralow energy consumption as the main source of energy is solar energy, making it more cost-effective per kg of hydrogen compared to other processes, costing around 3.12 \$/kgH2 (Frowijn and van Sark, 2021) and 1.60-3.20 \$/kgH2 (Chen et al., 2017). Meanwhile, in photoelectrochemical and photovoltaic-electrochemical processes, under optimal conditions, the cost is expected to decrease to \$6.05/kgH2 and \$3.72/ kgH2, respectively (Frowijn and van Sark, 2021). Additionally, the installation of local photocatalytic systems in remote locations can further reduce logistics costs. Green H2 is usually obtained by photocatalysis using two processes: photocatalytic water splitting and biomass photoreforming (Qian et al., 2022). While many high-performance materials have been developed in both systems (Lu et al., 2023; Xia et al., 2023), the reactor design to improve photocatalytic reaction conditions are often neglected. Most laboratory-scale photoreactors are not suitable for scaling up as they do not require complex engineering efforts and are designed for testing the main photocatalyst. Therefore, the development of an efficient and simple photoreactor for large-scale applications requires more engineering effort.

Suspension photocatalytic plants, due to their simplicity and economical manufacturing, have an advantage over panel photocatalytic and photoelectrochemical plants (Hisatomi and Domen, 2019). Based on suspension photocatalytic particles, not a few scale-up pilot programs have been proposed since the 2000s (Cao et al., 2018b, 2018a; Chen et al., 2019a, 2019b, 2019c, 2019d; Jing et al., 2010; Maldonado et al., 2018; Priya and Kanmani, 2013; Ruiz-Aguirre et al., 2022; Wei et al., 2017). Parabolic photocatalytic concentrator reactor (CPC) types are popular because they effectively capture and focus direct and scattered solar rays. There are many CPCs based on different photocatalysts and different capacities (Cao et al., 2018b, 2018a; Maldonado et al., 2018; Ruiz-Aguirre et al., 2022; Toledo-Camacho et al., 2021; Wei et al., 2018, 2017). For example, tubular CPC reactors with a total volume of 25 L based on TiO₂-CuO with the addition of glycerol as a sacrificial agent can produce hydrogen with a maximum STH efficiency of 0.9 % (Ruiz-Aguirre et al., 2022), while a system of 76 tubular CPC reactors with a total light area of 103.7 m² can produce 42.84 L of H₂ a day (Wei et al., 2017). It should be noted that when designing suspension photoreactors, such parameters as flow rate, catalyst and sacrificial agent concentration, and tube radius, which directly affect the productivity of the plant (Jing et al., 2010; Wei et al., 2018), should be considered. However, despite the relatively high achievements, suspension systems in large-scale applications have a few major limitations, in particular:

(1) More water is needed, making photocatalytic systems bulky and uneconomic:

- (2) Constant agitation is required because particles will settle to the bottom and will not receive enough solar energy, and some systems require constant availability of sacrificial agents;
- (3) Difficulties associated with the extraction of the photocatalyst from the suspension.

Thus, for instance, to maintain constant mixing of the photocatalyst and sacrificial agent suspension in a unit with a total area of 2.1 m² containing a water volume equal to 14.25 L, a pump with a flowrate of 20 L/min is necessary (Toledo-Camacho et al., 2021). To solve these problems, photocatalytic reactors with immobilized photocatalytic particles on flat plates made of a Au layer (Chen et al., 2019a, 2019b, 2019c, 2019d, 2021), carbon electrically conductive layer (Wang et al., 2017), nickel mesh (Zhang et al., 2023), nickel foam (Liu et al., 2020), 25 cm² matte stele (Xiong et al., 2014) and FTO (Zhu et al., 2022) were suggested. However, the hydrophilicity and porosity of the photocatalyst need to be controlled for the effective use of such panels, as these parameters significantly affect the safety and efficiency of photocatalytic panels (Goto et al., 2018). Another advantage of fixed-particle installations is that the pH value and gradient do not affect the photocatalytic activity of the particles because the immobilized particles are tightly fixed on the electroconductive layer and H2 and O2 are released in the immediate vicinity (Hisatomi and Domen, 2019).

To date, work is underway to improve the performance and efficiency of photocatalytic installations with immobilized photocatalytic particles. In 2015, for example, the development of a large-scale panel-type reactor for general water splitting under direct sunlight based on gC₃N₄ immobilized on stainless steel plates by drip coating was reported for the first time (Schröder et al., 2015). Despite 10 vol% triethanolamine aqueous content and the use of an energy-consuming pump for solution circulation, the reactor showed an insignificant STH equal to 0.12; however, it operated for 30 days and became a starting point for further large-scale development of modern photocatalytic reactors functioning in natural conditions. As the use of sacrificial agents and circulating pumps limited the large-scale use of photocatalytic reactors in vivo in 2018, a 1 \times 1 m² panel reactor filled with water without sacrificial agents with a thickness of 1 mm and capable of operating without forced circulation was designed (Goto et al., 2018). A flat reactor based on immobilized SrTiO₃@Al particles demonstrated hydrogen yield with an STH efficiency of 0.4 %. A water layer depth of 1 mm did not affect the activity, and the hydrophilic surface of the panel window improved the unobstructed escape of gases. In addition, based on this work, a 100 m² pilot scale plant was established (Nishiyama et al., 2021), which operated for several months off-line with negligible loss of efficiency. It should be noted that the plant, which consisted of a system of 1600 reactor units, operated for one year without obvious safety problems. However, although the efficiency of such plants was only STH 0.76 %, this work proves the viability and prospects of large-scale hydrogen production and the possibility of putting it into operation. To this end, photocatalytic stand-alone systems with STH efficiencies >6 % and low catalyst concentrations (<0.2 g (catalyst)/L) (Hisatomi and Domen, 2019; Schneidewind, 2022) under natural solar radiation should be developed for economically viable photocatalytic hydrogen production on a production scale. The authors (Toe et al., 2022) report that developing efficient photocatalysts and engineering systems capable of increasing STH from 1 % to 5 % will reduce costs by 75 %. Moreover, reducing the cost of photocatalysts (by using base materials), increasing their service life (to at least 1 year), and introducing solar concentrators can further decrease costs by 20-30 %.

All this led to the active development of this field, and recently, an InGaN/GaN composite photocatalyst with Rh/Cr_2O_3 core/shell and Co_3O_4 nanoparticles as cocatalysts and deposited on a silicon wafer was developed that achieved a high STH efficiency of 9.2 % in pure water splitting under the action of concentrated natural sunlight (Zhou et al., 2023). Such high performance is due to the synergistic effect of InGaN/GaN-based high-efficiency composites and cocatalysts (Chowdhury et al., 2018; Y. Wang et al., 2019c) and the suppression of the recombination of separated hydrogen and oxygen gases at a moderate reaction temperature of approximately

70 °C, which helps to increase the reaction rate by enhancing mass transfer and chemical bond breaking (Tembhurne et al., 2019; Zhang et al., 2017). In addition, this composite photocatalyst showed an STH efficiency of 7 % in seawater splitting and 6.2 % in a large-scale photocatalytic OWS test with 257 W natural sunlight power on a 4 \times 4 cm² plate unit.

Thus, despite the simplicity and efficiency of particle suspended photocatalyst reactors, reactors based on immobilized photocatalyst particles are the most scalable for large-scale photocatalytic production of solar hydrogen. Pilot studies of flat panels have proven the viability of safe industrial production of solar H_2 by photocatalysis. In addition, based on the study mentioned above (Nishiyama et al., 2021), a large-scale photocatalytic process has shown that hydrogen can be produced from abundant solar energy without additional energy input and without emitting by-products such as solid waste, polluted water, or harmful volatile gases. This can significantly reduce the overall cost of hydrogen production. These developments are currently the most feasible for commercialization despite the low efficiency of STH and require further upgrading of photoreactor design, operating conditions and the use of composite high efficiency photocatalysts operating over a wide range of light emissions, thereby improving overall efficiency.

Table 1 compares the above-described solar photoreactors for large-scale solar H_2 production. The overall efficiency of photocatalytic solar H_2 production directly depends on such parameters, as photoreactor geometry, type and amount of photocatalysts, availability and concentration of sacrificial agent and solar radiation intensity.

3.2. Large-scale water purification

The demand for very high purity water has posed new challenges for scientists in the field of water purification. Traditional water treatment technologies such as adsorption, biological treatment, chemical treatment with chlorine, ozone, and hydrogen peroxide, thermal and catalytic oxidation, and high-energy UV irradiation all have their own drawbacks, such as problems with waste disposal or the emission of harmful intermediate products. In contrast, the photocatalytic water purification process allows for the complete mineralization of water pollutants, making it an effective and environmentally friendly option for water treatment. In addition, the process is able to remove a wide range of pollutants, including organic compounds, heavy metals, and microorganisms. Overall, the use of photocatalytic water purification can lead to a more sustainable and cost-effective solution for water treatment compared to conventional technologies.

Photocatalytic pilot or prospective for implementation on a large-scale installation for effective treatment of formaceous, textile and other polluted water can be divided into two main groups, i.e., photoreactors either with suspended photocatalysts (Janssens et al., 2021) or with immobilized photocatalysts (Kane et al., 2022). Photocatalytic reactors with suspended photocatalysts are characterized by simplicity and relatively high efficiency: particles are effectively irradiated by light and interact smoothly with pollutants in aqueous suspension (Manassero et al., 2017). To date, numerous photoreactors with artificial illumination methods have been developed through pilot projects (Ahmadpour et al., 2022; Baaloudj et al., 2022). Such reactors exhibit improved performance in water purification compared to other types of reactors, but the high efficiency is limited by the not insignificant energy consumption costs of lamps and mixers. Suspension photoreactors operating under the action of free natural sunlight are highly scalable and economical in this respect (Saran et al., 2019). In particular, a slurry pilot plant based on a solar photocatalytic tube reactor has been tested for wastewater treatment by reusing local materials at low cost. In addition, there are many pilot developments of parabolic solar concentrator photoreactors for wastewater treatment with total volumes of 85 L (Rapti et al., 2022), 39 L (Davididou et al., 2019; Grilla et al., 2019), 35 L (Luna-Sanguino et al., 2020), 16 L (Martínez-Costa et al., 2020), 9 L (Esteban García et al., 2021), 7.7 L (Diaz-Angulo et al., 2019) and 2 L (Martín-Sómer et al., 2021). However, it should be kept in mind that such reactors, although having small pipe diameters, occupy a

Table 1Recent applications of different photocatalytic reactors for solar hydrogen production.

Photoreactor type	Total working volume (area)	Photocatalyst	Photocatalyst concentration	Average solar intensity (W·m ⁻²)	Efficiency	Sacrificial agent (conc.)	Ref.
CPC	207 L (32.4 m ²)	$Cd_{1-x}Zn_xS$	2.77 g·L ⁻¹	800	10.321 L·h ⁻¹	Na ₂ S and Na ₂ SO ₃ (0.1 mol·L ⁻¹)	(Cao et al., 2018a)
CPC	25 L (2.10 m ²)	Cu/TiO ₂	0.2 g·L ⁻¹	N/A	STH 2.6 %	Glycerol at pH = $9 (0.05 \text{ M})$	(Maldonado et al., 2018)
CPC	25 L (2.10 m ²)	TiO ₂ -CuO	0.1 g·L ⁻¹	N/A	STH 0.9 %	Glycerol (0.075 M)	(Ruiz-Aguirre et al., 2022)
CPC	720 L (103.7 m ²)	$NiS/Cd_{x}Zn_{1-x}S$	0.5 g·L ⁻¹	965.5	7.14 L·h^{-1} ($\eta = 0.087 \%$)	Na_2SO_3 (0.25 mol·L ⁻¹), Na_2S (0.35 mol·L ⁻¹)	(Wei et al., 2017)
CPC	25 L (2.10 m ²)	Au/TiO ₂	0.2 g·L ⁻¹	67.4	1.3 mmol $h^{-1} \cdot L^{-1}$ ($\eta = 1.8 \%$)	Formic acid (0.05 M)	(Arzate Salgado et al., 2016)
SUC	70 L	$NiS\text{-}Cd_{x}Zn_{1\text{-}x}S$	0,5 g·L ⁻¹	876.7	2.148 L·h ⁻¹ ($\eta = 0.475 \%$)	Na_2SO_3 (0.75 mol·L ⁻¹), Na_2S (1.05 mol·L ⁻¹)	(Wei et al., 2018)
CPC	25 L	Pd/TiO ₂	0.2 g·L ⁻¹	N/A	$0.618 \text{ L}\cdot\text{h}^{-1}\cdot\text{g}^{-1}$	Clycerol (5 vol%)	(Toledo-Camacho et al., 2021)
Flat panel	10 L (0.756 m ²)	Pt/g-C ₃ N ₄	13 g·m ⁻²	~ 800	STH 0,12 %	Triethanolamine (10 vol%)	(Schröder et al., 2015)
Flat panel	1 m ²	RhCrO _x /SrTiO ₃ :Al	8 g·m ⁻²	650–750	1.016 L·h ⁻¹ (STH 0.4 %)	None	(Goto et al., 2018)
Flat panel	100 m^2	SrTiO ₃ :Al/(Rh, Cr, Co)	$8.9\mathrm{g\cdot m}^{-2}$	880	216–222 L·h ⁻¹ (STH 0,76 %)	None	(Nishiyama et al., 2021)
Flat wafer+ Fresnel lens	0.0016 m ² + 1.21 m ² (lens)	InGaN/GaN@Rh/ Cr ₂ O ₃ /Co ₃ O ₄	88.1 mmol·m ⁻²	850	STH 6,2 %	None	(Zhou et al., 2023)

relatively large volume and require large areas for such systems to avoid shading each other, and, in addition, nighttime or cloudy days reduce the efficiency of such SRS reactors. Although authors have reported the separation of photocatalyst powder by filtration techniques, the potential separation of particles in the case of dispersed powders is hampered by its energy intensity (Lee et al., 2018), which is another serious disadvantage of such systems, as toxicity and adverse environmental and health effects are not excluded (von Gunten, 2018). Alternatives to such photoreactors are fluidized bed photoreactors modified with inexpensive and economical LEDs (Surenjan et al., 2019) that do not require photocatalyst collection and a constant stirring stage (Aimeur et al., 2021). In such systems, an immobilized photocatalyst on a retained substrate is maintained inside the reactor by circulating water flow at a certain rate, preventing it from settling to the bottom of the reactor. For example, fluidized bed reactors with immobilized photocatalysts on sand (Aimeur et al., 2021), silica (Rincón and La Motta, 2019), polymers (Surenjan et al., 2019), and graphene macrostructures (Fang et al., 2019) as substrates, without the need for separation and to increase the active area of photon-irradiated catalysts, have been proposed for large-scale continuous use. In addition, fluidized bed photoreactors are well combined with ozone aeration and membrane filtration for water purification (Wei et al., 2020). Guillermo J. Rincón and others (Rincón and La Motta, 2019) reported that as the diameter of silica particles decreases, the photooxidation efficiency increases in a fluidized bed unit, i.e., the carrier particle size directly affects the unit efficiency. Consequently, increasing the carrier size to reduce high catalyst dispersibility is not effective, limiting the scalability of such systems.

Another variety of photocatalytic reactors for water treatment are immobilized catalyst photoreactors. Such photoreactors have been proposed as the most suitable for conversion from laboratory scale to full scale water/wastewater treatment due to the absence of photocatalyst collection and provision of direct continuous flow (Alalm et al., 2021; Fouad et al., 2021). The most popular are photoreactors with immobilized particles on solid fixed membranes (Lotfi et al., 2022). Based on the photocatalytic membrane reactor (PMR) made of hollow fibers of PVDF, a pilot project was implemented to treat diclofenac (DCF) from wastewater (Plakas et al., 2016). The proposed PMR had a total volume of 25 L and was fully automated to continuously produce 1.2 m³/day of treated water. In such continuous flow devices, the flow rate plays an important role, and the photocatalytic oxidation reaction occurs by passing a slurry of pollutant through the pores irradiated by the loaded photocatalyst (Pascariu et al., 2019). Recently, Chechia Hu (Hu et al., 2021) designed a photocatalytic membrane reactor (PMR) and compared flat and hollow

substrates based on Al_2O_3 fibers, where the stable flux was 4250 \pm $100 \ L \ m^{-2} \ h^{-1} \ bar^{-1}$ versus $80\text{--}100 \ L \ m^{-2} \ h^{-1} \ bar^{-1}$ for hollow and flat substrates, respectively, and the phenol degradation efficiency reached 90 %, whereas in a similar study (Hu et al., 2019) with the same hollow substrates but with a different photocatalyst, phenol degradation was over 92 %. However, in PMR, the difficulty is related to the penetration of light deep into the porous structure and the relatively weak mass transfer, which can affect the efficiency of the whole system. In addition, such reactors face the problem of membrane clogging by degradation products due to photocatalysis (Sundar and Kanmani, 2020). An alternative is thin-film photoreactors, which have a high degree of light absorption and mass transfer regulation (Samy et al., 2020a). In such plants, water flows in a laminar stream along an inclined plane covered with a thin layer of photocatalyst in recirculation mode (Samy et al., 2020b). Mahmoud Samy et al. (Samy et al., 2021) in a pilot scale purified real agrochemical and pharmaceutical aqueous pollutants using planar photoreactors based on immobilized CNT/ MOF-808 photocatalysts with 93 % and 76 % efficiency, respectively, and reusability with no loss of efficiency after 5 cycles. A study of depreciation and operating costs showed that such a large-scale plant costs \$2.523/m³. However, the use of sunlight, reuse of photocatalyst film and simplicity can significantly reduce operating costs (Pava-Gómez et al., 2021).

The main problem with immobilized photoreactors is the large difference in photon-photocatalyst interaction time (~1 µs) and reagent diffusion inside the porous catalyst (~1 s), which limits the interaction between the illuminated catalyst and pollutant molecules (Kayahan et al., 2020). Compacted bed reactors (Manassero et al., 2022) and macroporous foam reactors (Goetz et al., n.d.) operating in continuous mode are of most interest to improve mass transfer at large scales in immobilized particle photoreactors. Such photoreactors are scaled by continuously pumping contaminated water into the photoreactor and placing several units in parallel (Pestana et al., 2020; Sacco et al., 2018). The compacted structure improves the mass transfer efficiency and light absorption by reducing the light path and effective mass transfer caused by laminar flow perturbation by properly selected photocatalyst carriers (Zhang et al., 2020), thus requiring a short time for complete decomposition and making it possible to treat large amounts of contaminated water in a continuous operation mode (Sacco et al., 2019; Vaiano et al., 2020). Among many immobilized particle photoreactors, this compacted bed photoreactor (Claes et al., 2019) proved to be much more productive, with a reactor rate constant of 0.82 min⁻¹ at a flow rate of 216 mL per minute, which is 3-4 orders of magnitude higher than other immobilized bed photoreactors, such as compacted flat $\sim 10^{-5} \text{ s}^{-1}$ (Vaiano et al., 2015) or immobilized foam $\sim 10^{-5} \text{ s}^{-1}$ (Kouamé et al., 2013) continuous reactors. In addition, the authors

analyzed 29 photoreactors and sorted them according to their performance, where this photoreactor was the most efficient in terms of scaling on par with suspension and microreactor systems. To reduce energy costs, flow photochemistry is combined with fluorescent solar concentrators (LSCs) (Cambié et al., 2017, 2019). LSCs are systems where phosphors such as fluorescent dyes or quantum dots are ground into a polymer or glass, with the ability to convert solar radiation into light of a specific wavelength. Based on LSCs, an optimized photomicroreactor with densely packed photocatalyst-coated glass beads (850 μm) has been designed (Zhao et al., 2020) with high performance. Such optimized photoreactors not only increase the efficiency but also represent a new direction to simultaneously improve mass and light transfer for enhanced photocatalysis.

In light of the research work described above, it can be concluded that photocatalytic installations for large-scale photocatalytic treatment of water, both with suspension and immobilized photocatalysts, are at the stage of development. Each type of photoreactor has advantages and disadvantages, and the choice of one or another photoreactor depends on the operating conditions. For example, in regions with a warm climate, solar photocatalytic installation with the possibility of working year-round would be more effective, whereas in cold regions, the most suitable reactors are economic with effective artificial light sources. In addition, hybrid photocatalytic reactors need to be developed to improve efficiency and reduce operating costs by combining the optimal qualities of these devices.

Table 2 lists recent pilot-scale photocatalytic developments and compares their operating parameters directly affecting the overall efficiency in photocatalytic water purification.

3.3. Large-scale air purification

As air pollution is a serious concern in today's society, attempts are being made to create technologies to clean the air of various kinds of pollutants. Among air pollutant control methods such as adsorption with highly porous materials, UV irradiation and nonthermal plasma causing unwanted byproducts such as ozone and thermal oxidation requiring high costs of additional energy supply, photocatalysis technology has the following advantages: it can do without external additional energy or chemical supply as it is powered by free sunlight; it can completely degrade volatile organic compounds (VOCs); it is fully capable of treating air in a safe and environmentally sound manner; and it has the ability to clean air at all times. As in the case of water purification, large-scale photocatalytic air purification is at a developmental stage and is limited by low purification rates, the possibility of photocatalyst deactivation and the difficulty of scaling (Sharma et al., 2022). However, on the way to scale, pilot developments have been proposed to clean various air pollutants ranging from small rooms to huge production facilities (Lekshmi et al., 2020; Muscetta and Russo, 2021), which will be discussed in this section.

UV disinfection is mainly used to disinfect indoor air from bacteria, viruses and other pathogens (C. Wang et al., 2019a). However, UV irradiation is not effective enough to fully inactivate bacteria with multiple layers, such as *Bacillus subtilis* spores (Zacarías et al., 2019). In contrast to UV sterilization, photocatalysis (Ahmadi et al., 2021) can fully disinfect airborne pathogens on a large scale. For example, antibacterial experiments have been carried out using a pilot-scale flat photocatalytic reactor on a continuous scale (Abou Saoud et al., 2021). Cu-Ag/TiO₂ was used as the photocatalyst and showed good results in sterilizing bacteria and removing volatile organic compounds (VOCs). Another TiO₂/MXene composite based on a dynamic photocatalytic reactor was more effective in inactivating antibiotic-resistant bacteria compared to conventional bacteria, providing a basis for industrial application of this development (Liming Liu et al., 2022b).

In addition to sterilization, photocatalytic oxidation is one of the most effective methods of degrading VOCs in indoor air (Mata et al., 2022; Sharma et al., 2022; Shayegan et al., 2022). Highly toxic VOCs such as formaldehyde (He et al., 2022), benzene (L. Chen et al., 2022b), toluene (Zhang et al., 2022b), chlorobenzene (Zhang et al., 2022a) and others can

be safely removed by photocatalysis using both UV and UV-visible lamps and energy-efficient UV-emitting diodes (Rouhani and Taghipour, 2022; Wu et al., 2022). There are not a few large-scale technologies aimed at cleaning premises from VOCs in natural conditions (Alkaabi et al., 2022; Malayeri et al., 2021; F. Wang et al., 2022a; Xu et al., 2021). Nevertheless, industrial application is very difficult due to scaling and real conditions in contrast to laboratory applications (F. Wang et al., 2022a). The results of studies on photoreactors of three scales (full scale, pilot scale and laboratory scale) for removal showed that the key operating parameters limiting the efficiency of large-scale photocatalytic oxidation are a high flow rate, high concentration and short residence time of VOCs at the inlet (Shayegan et al., 2019).

Recently, solar photocatalysis technology has attracted much scientific attention in the photocatalytic reduction of the greenhouse gas CO₂ into renewable fuels (Dilla et al., 2019; Nguyen and Wu, 2018). Although there are not few photocatalytic materials for converting CO2 into carbon fuel (e.g., into methane (Kumar et al., 2020; Sun et al., 2022), ethane (G. Wang et al., 2022b; Xie et al., 2022), CO (Dong et al., 2022; Liu et al., 2019), HCOOH (X. Liu et al., 2022c; Zhou et al., 2022)), research has been conducted on a laboratory scale, and there is a need for photoreactors for industrial operation (Khan and Tahir, 2019). Advances in this field have contributed to the development of a mesoscale photocatalytic reactor, which can operate in continuous mode for photoconversion of CO2 (Nabil et al., 2021, 2022). The advantages of the proposed plant for large-scale implementation are the possibility of continuous operation; productivity in a relatively large volume (several g/day); use of energy-saving LEDs; uniform illumination; high area relative to volume for efficient mass and photon exchange; and additional integration of a chilled water bath to improve CO₂ solubility. In addition, membrane photocatalytic reactors can also be operated in continuous mode and show high efficiency in the photoconversion of CO2 to carbon fuel (Baniamer et al., 2021; Kandy et al., 2021). For example, continuous membrane photoreactors using naphion as a photocatalyst carrier are 10 times more efficient in the production of carbon fuel compared to batch photoreactors (Pomilla et al., 2018).

Another important aspect in photocatalytic air purification is the reduction of photocatalyst activity due to deactivation during the photoreaction. At the gas-solid interface, the reduction of activity is more noticeable in comparison with the liquid-solid interface because in the latter case, water by dissolution can clean the photocatalyst surface, whereas the solvent capacity of the air medium is limited. Thus, undesirable components such as decomposition intermediates can accumulate on the photocatalyst surface, which not only limits light input but also blocks the diffusion of oxygen and other products to the reaction centers, thereby seriously limiting large-scale application under realistic conditions (Weon et al., 2019). There are several methods to regenerate deactivated photocatalysts at the expense of heteroatoms and carbonaceous deposits, including UV treatment with deionized water (Pei et al., 2021; Pylnev and Wong, 2019), thermal treatment (Chen et al., 2020), and washing with aqueous H2O2 solution (Serge-Correales et al., 2022). However, these regeneration methods, due to their added complexity and cost, may limit their practical application on a full scale; hence, preventing and minimizing photocatalyst deactivation by optimizing photocatalysts and photoreactors is a priority (Cha et al., 2019; Kim et al., 2022; Ran et al., 2019; H. Wang et al., 2019b).

Another problem with photocatalytic air purification technology is the low purification rate. To increase the process efficiency, photocatalytic treatment is combined with other methods of air purification, e.g., thermal catalytic oxidation (Wei et al., 2021), nonthermal plasma (Guo et al., 2022; Kvss et al., 2023), and adsorption (Meicheng Wen et al., 2019a; Zou et al., 2019). This synergy can help to level out the disadvantages and take advantage of each of the methods; for example, the photocatalysis process can be used as an end stage in VOC purification, as it is more effective in purifying pollutants with low concentrations (below ppm) (Weon et al., 2019), whereas other methods are more effective for air purification only with high concentrations (Krishnamurthy et al., 2020). For example, in the plasma-photocatalytic method, plasma splits high concentration air pollutants and their decomposition

Science of the 10tal Environment 885 (2023) 103

 Table 2

 Recent pilot-scale photocatalytic reactors for the efficient degradation of water pollutants.

	-			-	-					
Reactor type	Reactor design	Total volume, (L)	Flow rate, (L·h ⁻¹)	Polutant	Concentration (mg·L ⁻¹)	Photocatalyst (conc.)	Light source	Efficiency	Reusability	Ref.
Slurry reactor	CPC	85	N/A	O-desmethyl venlafaxine	6074.28×10^{-6}	TiO ₂ (200 mg·L ⁻¹)	Sunlight	90 % degradation at 240 min	From 70 % to 63 % after 3 cycles.	(Rapti et al., 2022)
Slurry reactor	CPC	35	N/A	Pesticides	0.2	TiO ₂ -rGO (200 mg·L ⁻¹)	Sunlight, 30 W·m ⁻²	100 % degradation at <25 min	N/A	(Luna-Sanguino et al., 2020)
Slurry reactor	CPC	16	1584	Sulfamethoxazole, diclofenac	0.1	BEN и VER (200 mg·L ⁻¹)	Sunlight, 40 W·m ⁻²	80 % degradation at 180 min	N/A	(Martínez-Costa et al., 2020)
Slurry membrane reactor	Cylindrical	25	1200	Diclofenac, TOC	470×10^{-6}	TiO ₂ (500 mg·L ⁻¹)	UV-C, 2.08 W·L ⁻¹ , 253.7 nm	90,5 % and 52,4 % degradation at 180 min	N/A	(Plakas et al., 2016)
Slurry reactor	Cylindrical	2	N/A	COD	0.030	TiO ₂ (990 mg·L ⁻¹)	8-W UV-C 8 lamps	77 % degradation at 90 min	N/A	(Ahmadpour et al., 2022)
Slurry reactor	Cylindrical		0.06	Clofibric acid	20	TiO ₂ (500 mg·L ⁻¹)	150 W Ha-Hg lamp, 350–410 nm	$\eta_{Rxn} = 4,59 \%$	N/A	(Manassero et al., 2017)
Slurry reactor	Cylindrical	280	60	Cefixime, cefaclor, cefuroxime	10	Bi ₁₂ TiO ₂₀ (1500 mg·L ⁻¹)	24 W UV, 200 W·m ⁻² , 270 nm	94 %, 81 %, and 69.71 % degradation at 210 min	N/A	(Baaloudj et al., 2022)
Slurry reactor	Tubular	25	15	COD	1420	Ag-TiO ₂ (200 mg·L ⁻¹)	Sunlight, 10 W·m ⁻²	99 % degradation at 120 min	High stability after 5 cycles	(Saran et al., 2019)
Fixed-film reactor	Staircase	2	29	Flumequine	5	TiO_2 (film thickness ~ 1 mm)	UV + H_2O_2 , 38 mW·m ⁻² , 365 nm	97 % degradation at 150 min	N/A	(Kane et al., 2022)
Fixed-film reactor	Cylindrical	1	0.06	Clofibric acid	20	TiO_2 (film thickness - 2,7 μ m)	150 W Ha-Hg lamp, 350–410 nm	$\eta_{Rxn}~=~2,\!02~\%$	N/A	(Manassero et al., 2017)
Fixed-film reactor	Inclined plate	0.2	0.02	Carbamazepine, diazinon	4.8, 34.2	CNTs/MOF-808 (film thickness - 1 mm)	400 W metal-halide lamps, 511 nm	91.6 % degradation at 90 min, 99,7 % degradation at 60 min	From 91.6 % to 83.1 % after 5 cycles. From 99,7 % to 92,1 % after 5 cycles	(Samy et al., 2021)
Fixed-film reactor	Annular	0.6	90	Clofibric acid	1.8×10^{-7} mol/cm ³	TiO_2 (film thickness - 3.2 μ m)	40 UV-LEDs, 365 nm	70 % degradation at 360 min	N/A	(Manassero et al., 2022)
Fixed-film reactor	Inclined plate	5	1.20	Methylene blue	N/A	Cu:TiO ₂ -glass, Cu: TiO ₂ -LDPE	Sunlight, 609.6 W·m ⁻²	73,7 % degradation at 360 min 68,1 % degradation at 360 min	From 73,7 % to 51,2 % after 3 cycles. From 68,1 % to 66,3 % after 5 cycles	(Pava-Gómez et al., 2021)
Fluidized-bed reactor	Cylindrical	4	0.60	Diclofenac	0.05	C-TiO ₂ - polymer (500 mg·L ⁻¹)	8000 lx 27 vis-LEDs, > 400 nm	100 % degradation at 120 min	high stability after 6 cycles (washed Di water)	(Surenjan et al., 2019)
Fluidized-bed reactor	Cylindrical	0.1	0.06	Bisphenol A	5	TiO ₂ -graphene (100 mg·L ⁻¹)	350 W Xe lamp	97 % degradation at 30 min	From 97 % to 92 % after 5 cycles	(Fang et al., 2019)
Fluidized-bed reactor	Tubular	0.8	31.8	Phenol	1.0 mmol L ⁻¹	TiO ₂ -silica gel (20 g·L ⁻¹)	UV-C lamp 1.2 W·m ⁻² , 254 nm	100 % degradation at 240 min	N/A	(Rincón and La Motta, 2019)
Fluidized-bed reactor	Cylindrical	37.8	44,961	Tebuconazole	0.02	Phenalenone-sand (30 g·L ⁻¹)	5-W blue LED, 435–465 nm	73 % degradation at 480 min	From 73 % to 49 % after 3 cycles	(Aimeur et al., 2021)
Packed-bed reactor	Cylindrical	1	0.06	Clofibric acid	20	TiO_2 (film thickness $\sim 0.44 \mu m$)	150 W Ha-Hg lamp, 350–410 nm	$\eta_{Rxn}~=~2,96~\%$	N/A	(Manassero et al., 2017)
Packed-bed reactor	Cylindrical	0.007	0.07	Crystal violet	10	ZnO- zeolite (4 g)	UV-LEDs 12 W·m ⁻¹ 365 nm	93 % degradation at 4,7 min	N/A	(Sacco et al., 2018)
Packed-bed reactor	Cylindrical	70.68×10^{-6}	0.01	Methylene blue	4.6	${ m TiO_2}$ -Glass beads (film thickness $\sim 200~\mu { m m}$)	300 W Xe-lamp, ~1070 W·m ⁻²	96 % degradation at 20 c	From 93,73 % to 83 % after 25.5 h	(Zhang et al., 2020)
Packed-bed reactor	Cylindrical	0.5	3	Methylene blue, TOC	7, 5	N-TiO ₂ /polystyrene spheres	vis-LEDs, 780 W·m ⁻² , 400–700 nm	100 % degradation at 120 min 80 % degradation at 180 min	High stability after 5 cycles	(Sacco et al., 2019)
Packed-bed reactor	Rectangular	0.05	12.96	Methylene blue	10	TiO₂-Glass beads (1.9 g·L ⁻¹)	3.264 W 192 LEDs, 191 W·m ⁻² , 375 nm	$k_{app}=0.82min^{-1}$	N/A	(Claes et al., 2019)

intermediates, preventing accumulation on the surface, thus regenerating the photocatalyst and producing byproducts in the form of NO_x and O₃, which are decomposed by photogenerated radicals (H^- , HO). In particular, scientists on a pilot scale using a photocatalysis/nonthermal plasma hybrid have achieved improved efficiency in the removal of ammonia, oil aldehyde (Abou Saoud et al., 2018) and toluene (Mohammadi et al., 2020) compared to using these methods alone. The combination of adsorbent and photocatalyst promotes instant adsorption of target molecules and gradual degradation by photogenerated active centers (Zou et al., 2019). Such hybridization helps to overcome the mismatch in the timing of rapid mass influx and slow photodegradation of airborne pollutants (Li et al., 2020). On the other hand, thermal photocatalysis makes it possible to utilize the full spectrum of sunlight by utilizing both solar and thermal energy, whereas the potential of traditional high-performance photocatalytic materials is in the UV and visible region, which accounts for approximately 47 % of the entire solar spectrum (Xi Chen et al., 2019c). In addition, thermocatalysis extends the lifetime of photocatalysts by additional high-temperature oxidation of undesirable intermediates accumulating on the catalyst surface (Krishnamurthy et al., 2020). In such systems, catalysts made of noble materials (Pt/TiO2 (Vikrant et al., 2021), Pt/MO (Yu et al., 2020) and MnO₂-Au (da Silva et al., 2018)) show high catalytic activity in air purification but have high cost and low thermal stability. However, transition metal oxides have recently been used as an alternative to noble metals to improve efficiency (Xi Chen et al., 2019c). In particular, a CeO2@LaMnO3 composite with a wide light absorption band (800-1800 nm) can be used as an efficient photothermal catalyst with an efficiency of 15.3 % in toluene conversion (J.-J. Li et al., 2019c). Based on this strategy, a pilot photothermocatalytic system was proposed, with simultaneous space heating and air purification under the influence of solar energy. The authors used a MnOx-CeO2/TiO2 composite as a catalytic material, and the air-cleaning rate of the developed system was in the range of 5-23 m³/h with the possibility of application for indoor air cleaning (Li et al., 2023).

A detailed analysis of works on photocatalytic air purification research suggests that further research is still needed for large-scale photocatalytic air purification under realistic conditions to bridge the gap between laboratory and production testing. Further strategies should be directed (1) toward the cleaning of multicomponent mixtures, which is more feasible under natural conditions, whereas only one component is mainly cleaned; (2) to develop inexpensive and simple photocatalytic systems that will prevent or regenerate the deactivation of photocatalysts; and (3) to introduce hybrid technologies together with the photocatalytic process whose advantages have been summarized above.

4. Conclusions and strategies for the future

The photocatalytic process is recognized as a promising technology for solving environmental and energy problems as a clean and safe method that does not require additional energy-consuming systems. However, although much effort has been directed to the study of photocatalysts, the practical application of photocatalysis on an industrial scale is still limited. This article details the main limiting obstacles and possible solutions for moving from a laboratory to a large-scale process, including large-scale production of high-performance photocatalysts in a simple and environmentally friendly way, efficient immobilization of photocatalyst particles on the surface of the desired material and support design, and criteria for choosing a photocatalytic reactor with the required optimal geometry to provide an effective three-phase boundary with maximum area. In addition, a review and comparison of operational parameters from recent pilot studies for large-scale photocatalytic hydrogen production and water and air purification was made. Based on the analysis of the above studies, future strategies in developing the ideal photocatalytic system for practical full-scale use should have the following directions:

 The development of highly efficient photocatalysts with the possibility of multiple reuses with minimal loss of photoactivity. The regeneration

- of photocatalysts deactivated by contaminants or prevention of photocatalyst deactivation to help increase the service life and maximize material savings. Numerous studies show that the immobilization of photocatalyst particles on a solid base is the most suitable option for reuse with minimal loss of efficiency. Despite this, more research should be carried out aimed at measuring the service life and developing a method to combat the deactivation of photocatalysts.
- More efforts need to be directed toward the efficient use of free sunlight for the large-scale photocatalytic process through the introduction of additional systems capable of concentrating and focusing direct and diffuse beams
- Modifications of optimal designs of photocatalytic reactors with increased mass transfer of reaction products and maximum use of incident photons to increase overall performance.
- 4. Consideration of the possibility of combining the photocatalytic process with other methods for solving environmental and energy problems, thereby serving to balance the disadvantages and optimize the advantages of each.
- To conduct a comprehensive cost estimate of a photocatalytic system for commercialization and comparison with other technologies, it is necessary to provide data on the prices of the materials used and the costs of operation.
- 6. Finally, the photocatalytic process is a "green" technology, and scientists need to make more effort to spread its benefits in order to address energy and environmental problems by overcoming barriers to commercialization and improving economic efficiency.

It is expected that this comprehensive review will assist future research in obtaining up-to-date insights and overcoming possible barriers to scaling up and commercializing photocatalytic systems.

CRediT authorship contribution statement

Zhengisbek Kuspanov: Conceptualization, Methodology, Investigation. Baglan Bakbolat: Conceptualization, Methodology, Investigation. Alzhan Baimenov: Resources, Formal analysis. Aidos Issadykov: Writing – review & editing. Mukhtar Yeleuov: Writing – review & editing. Chingis Daulbayev: Writing – original draft, Project administration.

Data availability

No data was used for the research described in the article.

Declaration of competing interest

The authors declare that they have no known competing financial interests or personal relationships that could have appeared to influence the work reported in this paper.

Acknowledgments

This research is funded by the Science Committee of the Ministry of Science and Higher Education and of the Republic of Kazakhstan (Grant No. BR18574073).

References

Abou Saoud, W., Assadi, A.A., Guiza, M., Bouzaza, A., Aboussaoud, W., Soutrel, I., Ouederni, A., Wolbert, D., Rtimi, S., 2018. Abatement of ammonia and butyraldehyde under non-thermal plasma and photocatalysis: oxidation processes for the removal of mixture pollutants at pilot scale. Chem. Eng. J. 344, 165–172. https://doi.org/10.1016/j.cej.2018.03.068.

Abou Saoud, W., Kane, A., Le Cann, P., Gerard, A., Lamaa, L., Peruchon, L., Brochier, C., Bouzaza, A., Wolbert, D., Assadi, A.A., 2021. Innovative photocatalytic reactor for the degradation of VOCs and microorganism under simulated indoor air conditions: cu-Ag/TiO2-based optical fibers at a pilot scale. Chem. Eng. J. 411, 128622. https://doi.org/10.1016/j.cej.2021.128622.

- Acosta-Herazo, R., Valadés-Pelayo, P.J., Mueses, M.A., Pinzón-Cárdenas, M.H., Arancibia-Bulnes, C., Machuca-Martínez, F., 2020. An optical and energy absorption analysis of the solar compound parabolic collector photoreactor (CPCP): the impact of the radiation distribution on its optimization. Chem. Eng. J. 395, 125065. https://doi.org/10.1016/j.cej.2020.125065.
- Ahmadi, Y., Bhardwaj, N., Kim, K.-H., Kumar, S., 2021. Recent advances in photocatalytic removal of airborne pathogens in air. Sci. Total Environ. 794, 148477. https://doi.org/10.1016/j.scitotenv.2021.148477.
- Ahmadpour, A., Bozorgian, A., Eslamimanesh, A., Mohammadi, A.H., 2022. Treatment of a low-salt petrochemical effluent using a slurry photocatalytic reactor. Water Air Soil Pollut. 233, 409. https://doi.org/10.1007/s11270-022-05877-2.
- Ahmed, S., Rasul, M.G., Sattar, M.A., Jahirul, M.I., 2022. Phenol degradation of waste and stormwater on a flat plate photocatalytic reactor with TiO2 on glass slide: an experimental and modelling investigation. J. Water Process Eng. 47, 102769. https://doi.org/10. 1016/i.iwpe.2022.102769.
- Aimeur, M., Godard, J., Baudu, M., Bregier, F., Villandier, N., Zermane, F., 2021. Photodegradation of tebuconazole in a fluidized bed reactor mediated by phenalenone supported on sand. Chem. Eng. J. 410, 128332. https://doi.org/10.1016/j.cej.2020.128332.
- Alalm, M.G., Djellabi, R., Meroni, D., Pirola, C., Bianchi, C.L., Boffito, D.C., 2021. Toward scaling-up photocatalytic process for multiphase environmental applications. Catalysts 11, 562. https://doi.org/10.3390/catal11050562.
- Alkaabi, M., Mohamed, M., Almanea, A., AlShehhi, M., Farousha, K., Yusuf, A., Palmisano, G., 2022. Design of a Microfluidic Photocatalytic Reactor for removal of volatile organic components: process simulation and techno-economic assessment. ACS Omega 7, 8306–8313. https://doi.org/10.1021/acsomega.1c05431.
- Allen, N.S., Mahdjoub, N., Vishnyakov, V., Kelly, P.J., Kriek, R.J., 2018. The effect of crystalline phase (anatase, brookite and rutile) and size on the photocatalytic activity of calcined polymorphic titanium dioxide (TiO2). Polym. Degrad. Stab. 150, 31–36. https://doi.org/ 10.1016/j.polymdegradstab.2018.02.008.
- Armaković, S.J., Armaković, S., Šibul, F., Četojević-Simin, D.D., Tubić, A., Abramović, B.F., 2020. Kinetics, mechanism and toxicity of intermediates of solar light induced photocatalytic degradation of pindolol: experimental and computational modeling approach. J. Hazard. Mater. 393, 122490. https://doi.org/10.1016/j.jhazmat.2020.122490.
- Arzate Salgado, S.Y., Ramírez Zamora, R.M., Zanella, R., Peral, J., Malato, S., Maldonado, M.I., 2016. Photocatalytic hydrogen production in a solar pilot plant using a Au/TiO2 photo catalyst. Int. J. Hydrog. Energy 41, 11933–11940. https://doi.org/10.1016/j.ijhydene.2016.05.039.
- Baaloudj, O., Badawi, A.K., Kenfoud, H., Benrighi, Y., Hassan, R., Nasrallah, N., Assadi, A.A., 2022. Techno-economic studies for a pilot-scale Bi12TiO20 based photocatalytic system for pharmaceutical wastewater treatment: from laboratory studies to commercial-scale applications. J. Water Process Eng. 48, 102847. https://doi.org/10.1016/j.jwpe.2022.102847.
- Babić, K., Tomašić, V., Gilja, V., Le Cunff, J., Gomzi, V., Pintar, A., Žerjav, G., Kurajica, S., Duplančić, M., Zelić, I.E., Pavičić, T.V., Grčić, I., 2021. Photocatalytic degradation of imidacloprid in the flat-plate photoreactor under UVA and simulated solar irradiance conditions—The influence of operating conditions, kinetics and degradation pathway. J. Environ. Chem. Eng. 9, 105611. https://doi.org/10.1016/j.jece.2021.105611.
- Bafaqeer, A., Tahir, M., Amin, N.A.S., 2018. Synergistic effects of 2D/2D ZnV2O6/RGO nanosheets heterojunction for stable and high performance photo-induced CO2 reduction to solar fuels. Chem. Eng. J. 334, 2142–2153. https://doi.org/10.1016/j.cej.2017.11.1111.
- Bahmani, M., Dashtian, K., Mowla, D., Esmaeilzadeh, F., Ghaedi, M., 2020a. UiO-66(Ti)-Fe3O4-WO3 photocatalyst for efficient ammonia degradation from wastewater into continuous flow-loop thin film slurry flat-plate photoreactor. J. Hazard. Mater. 393, 122360. https://doi.org/10.1016/j.jhazmat.2020.122360.
- Bahmani, M., Mowla, D., Esmaeilzadeh, F., Ghaedi, M., 2020b. BiFeO3–BiOI impregnation to UiO-66(Zr/Ti) as a promising candidate visible-light-driven photocatalyst for boosting urea photodecomposition in a continuous flow-loop thin-film slurry flat-plate photoreactor. J. Solid State Chem. 286, 121304. https://doi.org/10.1016/j.jssc.2020.121304.
- Banerjee, S., Adhikari, E., Sapkota, P., Sebastian, A., Ptasinska, S., 2020. Atmospheric pressure plasma deposition of TiO2: a review. Materials 13, 2931. https://doi.org/10.3390/ ma13132931.
- Baniamer, M., Aroujalian, A., Sharifnia, S., 2021. Photocatalytic membrane reactor for simultaneous separation and photoreduction of CO2 to methanol. Int. J. Energy Res. 45, 2353–2366. https://doi.org/10.1002/er.5930.
- Bui, V.K.H., Tran, V.V., Moon, J.-Y., Park, D., Lee, Y.-C., 2020. Titanium dioxide microscale and macroscale structures: a mini-review. Nanomaterials 10, 1190. https://doi.org/10. 3390/nano10061190.
- Burke, D.W., Sun, C., Castano, I., Flanders, N.C., Evans, A.M., Vitaku, E., McLeod, D.C., Lambeth, R.H., Chen, L.X., Gianneschi, N.C., Dichtel, W.R., 2020. Acid exfoliation of imine-linked covalent organic frameworks enables solution processing into crystalline thin films. Angew. Chem. Int. Ed. 59, 5165–5171. https://doi.org/10.1002/anie.201913975.
- Cabral, D., 2022. Development and performance comparison of a modified glazed CPC hybrid solar collector coupled with a bifacial PVT receiver. Appl. Energy 325, 119653. https:// doi.org/10.1016/j.apenergy.2022.119653.
- Cambié, D., Dobbelaar, J., Riente, P., Vanderspikken, J., Shen, C., Seeberger, P.H., Gilmore, K., Debije, M.G., Noël, T., 2019. Energy-efficient solar photochemistry with luminescent solar concentrator based photomicroreactors. Angew. Chem. Int. Ed. 58, 14374–14378. https://doi.org/10.1002/anie.201908553.
- Cambié, D., Zhao, F., Hessel, V., Debije, M.G., Noël, T., 2017. A leaf-inspired luminescent solar concentrator for energy-efficient continuous-flow photochemistry. Angew. Chem. Int. Ed. 56, 1050–1054. https://doi.org/10.1002/anie.201611101.
- Cao, F., Liu, H., Wei, Q., Zhao, L., Guo, L., 2018a. Experimental study of direct solar photocatalytic water splitting for hydrogen production under natural circulation conditions. Int. J. Hydrog. Energy 43, 13727–13737. https://doi.org/10.1016/j.ijhydene.2017.12.107 Special Issue on The 8th International Conference on Hydrogen Production (ICHP-2017).
- Cao, F., Wei, Q., Liu, H., Lu, N., Zhao, L., Guo, L., 2018b. Development of the direct solar photocatalytic water splitting system for hydrogen production in Northwest China: design

- and evaluation of photoreactor. Renew. Energy 121, 153–163. https://doi.org/10.1016/j.renene.2018.01.016.
- Casado, C., García-Gil, Á., van Grieken, R., Marugán, J., 2019. Critical role of the light spectrum on the simulation of solar photocatalytic reactors. Appl. Catal. B Environ. 252, 1–9. https://doi.org/10.1016/j.apcatb.2019.04.004.
- Cerrato, G., Bianchi, C.L., Galli, F., Pirola, C., Morandi, S., Capucci, V., 2019. Micro-TiO2 coated glass surfaces safely abate drugs in surface water. J. Hazard. Mater. 363, 328–334. https://doi.org/10.1016/j.jhazmat.2018.09.057.
- Cha, B.J., Saqlain, S., Seo, H.O., Kim, Y.D., 2019. Hydrophilic surface modification of TiO2 to produce a highly sustainable photocatalyst for outdoor air purification. Appl. Surf. Sci. 479, 31–38. https://doi.org/10.1016/j.apsusc.2019.01.261.
- Chao, Y., Zheng, J., Zhang, H., Ma, Y., Li, F., Tan, Y., Zhu, Z., 2018. Constructing film photocatalyst with abundant interfaces between CdS and Ni3S2 nanosheets for efficient photocatalytic hydrogen production. Energy Technol. 6, 2132–2138. https://doi.org/ 10.1002/ente.201800180.
- Chen, J., Xu, W., Zuo, H., Wu, X., E, J., Wang, T., Zhang, F., Lu, N., 2019. System development and environmental performance analysis of a solar-driven supercritical water gasification pilot plant for hydrogen production using life cycle assessment approach. Energy Convers. Manag. 184, 60–73. https://doi.org/10.1016/j.enconman.2019.01.041.
- Chen, J., Tang, T., Feng, W., Liu, X., Yin, Z., Zhang, X., Chen, Juanrong, Cao, S., 2022. Large-scale synthesis of p-n heterojunction Bi2O3/TiO2 nanostructures as photocatalysts for removal of antibiotics under visible light. ACS Appl. Nano Mater. 5, 1296–1307. https://doi.org/10.1021/acsanm.1c03851.
- Chen, L., Wang, X., Rao, Z., Tang, Z., Shi, G., Wang, Y., Lu, G., Xie, X., Chen, D., Sun, J., 2022. One-pot synthesis of the MIL-100 (Fe) MOF/MOX homojunctions with tunable hierarchical pores for the photocatalytic removal of BTXS. Appl. Catal. B Environ. 303, 120885. https://doi.org/10.1016/j.apcatb.2021.120885.
- Chen, S., Ma, G., Wang, Q., Sun, S., Hisatomi, T., Higashi, T., Wang, Z., Nakabayashi, M., Shibata, N., Pan, Z., Hayashi, T., Minegishi, T., Takata, T., Domen, K., 2019. Metal selenide photocatalysts for visible-light-driven Z-scheme pure water splitting. J. Mater. Chem. A 7, 7415–7422. https://doi.org/10.1039/C9TA00768G.
- Chen, S., Takata, T., Domen, K., 2017. Particulate photocatalysts for overall water splitting. Nat. Rev. Mater. 2, 1–17. https://doi.org/10.1038/natrevmats.2017.50.
- Chen, S., Vequizo, J.J.M., Pan, Z., Hisatomi, T., Nakabayashi, M., Lin, L., Wang, Z., Kato, K., Yamakata, A., Shibata, N., Takata, T., Yamada, T., Domen, K., 2021. Surface modifications of (ZnSe)0.5(CuGa2.5Se4.25)0.5 to promote photocatalytic Z-scheme overall water splitting. J. Am. Chem. Soc. 143, 10633–10641. https://doi.org/10.1021/jacs.1c03555.
- Chen, Xi, Cai, S., Yu, E., Li, J., Chen, J., Jia, H., 2019. Photothermocatalytic performance of ACo2O4 type spinel with light-enhanced mobilizable active oxygen species for toluene oxidation. Appl. Surf. Sci. 484, 479–488. https://doi.org/10.1016/j.apsusc.2019.04.093.
- Chen, Xiudong, Li, Y., Wang, L., Xu, Y., Nie, A., Li, Q., Wu, F., Sun, W., Zhang, X., Vajtai, R., Ajayan, P.M., Chen, L., Wang, Y., 2019. High-lithium-affinity chemically exfoliated 2D covalent organic frameworks. Adv. Mater. 31, 1901640. https://doi.org/10.1002/adma.201901640.
- Chen, Z., Peng, Y., Chen, J., Wang, C., Yin, H., Wang, H., You, C., Li, J., 2020. Performance and mechanism of photocatalytic toluene degradation and catalyst regeneration by Thermal/UV treatment. Environ. Sci. Technol. 54, 14465–14473. https://doi.org/10.1021/ acs.est.0c06048.
- Cheng, J., Wu, X., Jin, B., Zhang, C., Zheng, R., Qin, L., 2021. Coupling of immobilized photosynthetic bacteria with a graphene Oxides/PSF composite membrane for textile wastewater treatment: biodegradation performance and membrane anti-fouling behavior. Membranes 11, 226. https://doi.org/10.3390/membranes11030226.
- Chowdhury, F.A., Trudeau, M.L., Guo, H., Mi, Z., 2018. A photochemical diode artificial photosynthesis system for unassisted high efficiency overall pure water splitting. Nat. Commun. 9, 1707. https://doi.org/10.1038/s41467-018-04067-1.
- Claes, T., Dilissen, A., Leblebici, M.E., Van Gerven, T., 2019. Translucent packed bed structures for high throughput photocatalytic reactors. Chem. Eng. J. 361, 725–735. https://doi.org/10.1016/j.cej.2018.12.107.
- Cui, L., Liu, Y., Fang, X., Yin, C., Li, S., Sun, D., Kang, S., 2018. Scalable and clean exfoliation of graphitic carbon nitride in NaClO solution: enriched surface active sites for enhanced photocatalytic H2 evolution. Green Chem. 20, 1354–1361. https://doi.org/10.1039/ C7GC03704J.
- da Silva, A.G.M., Rodrigues, T.S., Candido, E.G., de Freitas, I.C., da Silva, A.H.M., Fajardo, H.V., Balzer, R., Gomes, J.F., Assaf, J.M., de Oliveira, D.C., Oger, N., Paul, S., Wojcieszak, R., Camargo, P.H.C., 2018. Combining active phase and support optimization in MnO2-au nanoflowers: enabling high activities towards green oxidations. J. Colloid Interface Sci. 530, 282–291. https://doi.org/10.1016/j.jcis.2018.06.089.
- Davididou, K., Chatzisymeon, E., Perez-Estrada, L., Oller, I., Malato, S., 2019. Photo-Fenton treatment of saccharin in a solar pilot compound parabolic collector: use of olive mill wastewater as iron chelating agent, preliminary results. J. Hazard. Mater. 372, 137–144. https://doi.org/10.1016/j.jhazmat.2018.03.016.
- Deng, S., Liu, C., Zhang, Y., Ji, Y., Mei, B., Yao, Z., Lin, S., 2023. Large-scale preparation of ultrathin bimetallic nickel iron sulfides branch nanoflake arrays for enhanced hydrogen evolution reaction. Catalysts 13, 174. https://doi.org/10.3390/catal13010174.
- Devia-Orjuela, J.S., Betancourt-Buitrago, L.A., Machuca-Martinez, F., 2019. CFD modeling of a UV-A LED baffled flat-plate photoreactor for environment applications: a mining wastewater case. Environ. Sci. Pollut. Res. 26, 4510–4520. https://doi.org/10.1007/s11356-018-2431-2.
- Diaz-Angulo, J., Arce-Sarria, A., Mueses, M., Hernandez-Ramirez, A., Machuca-Martinez, F., 2019. Analysis of two dye-sensitized methods for improving the sunlight absorption of TiO2 using CPC photoreactor at pilot scale. Mater. Sci. Semicond. Process. 103, 104640. https://doi.org/10.1016/j.mssp.2019.104640.
- Dilla, M., Becerikli, A.E., Jakubowski, A., Schlögl, R., Ristig, S., 2019. Development of a tubular continuous flow reactor for the investigation of improved gas—solid interaction in photocatalytic CO2 reduction on TiO2. Photochem. Photobiol. Sci. 18, 314–318. https://doi.org/10.1039/c8pp00518d.

- Dolai, S., Vanluchene, A., Stavárek, P., Dzik, P., Fajgar, R., Soukup, K., Klusoň, P., 2022. Graphitic carbon nitride thin films for light-induced photocatalysis in a slit geometry microreactor. J. Environ. Chem. Eng. 10, 108790. https://doi.org/10.1016/j.jece.2022. 108790
- Dong, W.-W., Jia, J., Wang, Y., An, J.-R., Yang, O.-Y., Gao, X.-J., Liu, Y.-L., Zhao, J., Li, D.-S., 2022. Visible-light-driven solvent-free photocatalytic CO2 reduction to CO by Co-MOF/ Cu2O heterojunction with superior selectivity. Chem. Eng. J. 438, 135622. https://doi. org/10.1016/j.cej.2022.135622.
- Esteban García, A.B., Szymański, K., Mozia, S., Sánchez Pérez, J.A., 2021. Treatment of laundry wastewater by solar photo-Fenton process at pilot plant scale. Environ. Sci. Pollut. Res. 28, 8576–8584. https://doi.org/10.1007/s11356-020-11151-x.
- Fang, Z., Hu, Y., Cheng, J., Chen, Y., 2019. Continuous removal of trace bisphenol a from water by high efficacy TiO2 nanotube pillared graphene-based macrostructures in a photocatalytically fluidized bed. Chem. Eng. J. 372, 581–589. https://doi.org/10.1016/ i.cei.2019.04.129.
- Fendrich, M.A., Quaranta, A., Orlandi, M., Bettonte, M., Miotello, A., 2019. Solar concentration for wastewaters remediation: a review of materials and technologies. Appl. Sci. 9, 118. https://doi.org/10.3390/app9010118.
- Fouad, K., Bassyouni, M., Alalm, M.G., Saleh, M.Y., 2021. Recent developments in recalcitrant organic pollutants degradation using immobilized photocatalysts. Appl. Phys. A Mater. Sci. Process. 127, 612. https://doi.org/10.1007/s00339-021-04724-1.
- Frowijn, L.S.F., van Sark, W.G.J.H.M., 2021. Analysis of photon-driven solar-to-hydrogen production methods in the Netherlands. Sustainable Energy Technol. Assess. 48, 101631. https://doi.org/10.1016/j.seta.2021.101631.
- V. Goetz C. Dezani E. Ribeiro C. Caliot G. Plantard Continuous flow photocatalytic reactor using TiO2-coated foams, modeling and experimental operating mode AICHE J. n/a e17972 n.d. 10.1002/aic.17972
- Gopinath, C.S., Nalajala, N., 2021. A scalable and thin film approach for solar hydrogen generation: a review on enhanced photocatalytic water splitting. J. Mater. Chem. A 9, 1353–1371. https://doi.org/10.1039/D0TA09619A.
- Goto, Y., Hisatomi, T., Wang, Q., Higashi, T., Ishikiriyama, K., Maeda, T., Sakata, Y., Okunaka, S., Tokudome, H., Katayama, M., Akiyama, S., Nishiyama, H., Inoue, Y., Takewaki, T., Setoyama, T., Minegishi, T., Takata, T., Yamada, T., Domen, K., 2018. A particulate photocatalyst water-splitting panel for large-scale solar hydrogen generation. Joule 2, 509–520. https://doi.org/10.1016/j.joule.2017.12.009.
- Grilla, E., Matthaiou, V., Frontistis, Z., Oller, I., Polo, I., Malato, S., Mantzavinos, D., 2019. Degradation of antibiotic trimethoprim by the combined action of sunlight, TiO2 and persulfate: a pilot plant study. Catal. Today 328 (SI: SPEA10), 216–222. https://doi.org/10.1016/j.cattod.2018.11.029.
- Guo, H., Yang, H., Huang, J., Tong, J., Liu, X., Wang, Y., Qiao, W., Han, J., 2022. Theoretical and experimental insight into plasma-catalytic degradation of aqueous p-nitrophenol with graphene-ZnO nanoparticles. Sep. Purif. Technol. 295, 121362. https://doi.org/ 10.1016/j.seppur.2022.121362.
- Gutiérrez-Alfaro, S., Rueda-Márquez, J.J., Perales, J.A., Manzano, M.A., 2018. Combining sun-based technologies (microalgae and solar disinfection) for urban wastewater regeneration. Sci. Total Environ. 619–620, 1049–1057. https://doi.org/10.1016/j.scitotenv. 2017.11.110.
- Harrisankar, N., Levecque, P., van Steen, E., 2021. An automated coating process to produce TiO2-coated optical fibre for photocatalytic reactor systems. Chem. Eng. Process. Process Intensif. 166, 108479. https://doi.org/10.1016/j.cep.2021.108479.
- He, L., Guan, W., Zeng, Y., Zhao, D., Qiu, X., Jia, G., 2022. Molybdenum sulfide (MoS2)/ordered mesoporous carbon (OMC) tubular mesochannel photocatalyst for enhanced photocatalytic oxidation for removal of volatile organic compounds (VOCs). Front. Chem. 9.
- Hisatomi, T., Domen, K., 2019. Reaction systems for solar hydrogen production via water splitting with particulate semiconductor photocatalysts. Nat. Catal. 2, 387–399. https:// doi.org/10.1038/s41929-019-0242-6.
- Horovitz, I., Avisar, D., Luster, E., Lozzi, L., Luxbacher, T., Mamane, H., 2018. MS2 bacterio-phage inactivation using a N-doped TiO2-coated photocatalytic membrane reactor: influence of water-quality parameters. Chem. Eng. J. 354, 995–1006. https://doi.org/10.1016/j.cej.2018.08.083.
- Hu, C., Wang, M.-S., Chen, C.-H., Chen, Y.-R., Huang, P.-H., Tung, K.-L., 2019. Phosphorus-doped g-C3N4 integrated photocatalytic membrane reactor for wastewater treatment. J. Membr. Sci. 580, 1–11. https://doi.org/10.1016/j.memsci.2019.03.012.
- Hu, C., Yoshida, M., Huang, P.-H., Tsunekawa, S., Hou, L.-B., Chen, C.-H., Tung, K.-L., 2021. MIL-88B(Fe)-coated photocatalytic membrane reactor with highly stable flux and phenol removal efficiency. Chem. Eng. J. 418, 129469. https://doi.org/10.1016/j.cej.2021. 129469.
- Huang, J., Jin, B., Liu, H., Li, X., Zhang, Q., Chu, Shijin, Peng, R., Chu, Sheng, 2018. Controllable synthesis of flower-like MoSe2 3D microspheres for highly efficient visible-light photocatalytic degradation of nitro-aromatic explosives. J. Mater. Chem. A 6, 11424–11434. https://doi.org/10.1039/C8TA02287A.
- Jahanshahi, R., Khazaee, A., Sobhani, S., Sansano, J.M., 2020. G-C3N4/γ-Fe2O3/TiO2/Pd: a new magnetically separable photocatalyst for visible-light-driven fluoride-free hiyama and Suzuki-miyaura cross-coupling reactions at room temperature. New J. Chem. 44, 11513–11526. https://doi.org/10.1039/D0NJ01599G.
- Janssens, R., Hainaut, R., Gillard, J., Dailly, H., Luis, P., 2021. Performance of a slurry photocatalytic membrane reactor for the treatment of real secondary wastewater effluent polluted by anticancer drugs. Ind. Eng. Chem. Res. 60, 2223–2231. https://doi.org/10. 1021/acs.iecr.0c04846.
- Jimenéz-Calvo, P., Muñoz-Batista, M.J., Isaacs, M., Ramnarain, V., Ihiawakrim, D., Li, X., Ángel Muñoz-Márquez, M., Teobaldi, G., Kociak, M., Paineau, E., 2023. A compact photoreactor for automated H2 photoproduction: revisiting the (Pd, pt, Au)/TiO2 (P25) schottky junctions. Chem. Eng. J. 459, 141514. https://doi.org/10.1016/j.cej.2023. 141514.
- Jing, D., Guo, L., Zhao, L., Zhang, Ximin, Liu, H., Li, M., Shen, S., Liu, G., Hu, X., Zhang, Xianghui, Zhang, K., Ma, L., Guo, P., 2010. Efficient solar hydrogen production by

- photocatalytic water splitting: from fundamental study to pilot demonstration. Int. J. Hydrog. Energy ISMF-09 35, 7087–7097. https://doi.org/10.1016/j.ijhydene.2010. 01 030
- Jo, W.-K., Park, G.T., Tayade, R.J., 2015. Synergetic effect of adsorption on degradation of malachite green dye under blue LED irradiation using spiral-shaped photocatalytic reactor. J. Chem. Technol. Biotechnol. 90, 2280–2289. https://doi.org/10.1002/jctb.4547.
- Kacem, M., Plantard, G., Brienza, M., Goetz, V., 2017. Continuous-flow aqueous system for heterogeneous photocatalytic disinfection of gram-negative Escherichia coli. Ind. Eng. Chem. Res. 56, 15001–15007. https://doi.org/10.1021/acs.iecr.7b03644.
- Kamaei, M., Rashedi, H., Dastgheib, S.M.M., Tasharrofi, S., 2018. Comparing photocatalytic degradation of gaseous ethylbenzene using N-doped and pure TiO2 Nano-catalysts coated on glass beads under both UV and visible light irradiation. Catalysts 8, 466. https://doi. org/10.3390/catal8100466.
- Kanakaraju, D., Yahya, M.S., Wong, S.-P., 2019. Removal of chemical oxygen demand from agro effluent by ZnO photocatalysis and photo-Fenton. SN Appl. Sci. 1, 738. https:// doi.org/10.1007/s42452-019-0782-z.
- Kandy, M.M., K, A.R., Sankaralingam, M., 2021. Development of proficient photocatalytic systems for enhanced photocatalytic reduction of carbon dioxide. Sustainable Energy Fuels 5, 12–33. https://doi.org/10.1039/D0SE01282C.
- Kane, A., Assadi, Achraf Amir, El Jery, A., Badawi, A.K., Kenfoud, H., Baaloudj, O., Assadi, Aymen Amin, 2022. Advanced photocatalytic treatment of wastewater using immobilized titanium dioxide as a photocatalyst in a pilot-scale reactor: process intensification. Materials 15, 4547. https://doi.org/10.3390/ma15134547.
- Kang, X., Liu, S., Dai, Z., He, Y., Song, X., Tan, Z., 2019. Titanium dioxide: from engineering to applications. Catalysts 9, 191. https://doi.org/10.3390/catal9020191.
- Karavasilis, M.V., Theodoropoulou, M.A., Tsakiroglou, C.D., 2022. Photocatalytic degradation of dissolved phenol by immobilized zinc oxide nanoparticles: batch studies, continuous flow experiments, and numerical modeling. Nanomaterials 12, 69. https://doi.org/10. 3390/nano12010069.
- Karavasilis, M.V., Tsakiroglou, C.D., 2022. Use of immobilized zinc oxide photocatalysts for wastewater treatment: application to methylene blue degradation. Can. J. Chem. Eng. 100, 893–910. https://doi.org/10.1002/cjce.24199.
- Kassahun, S.K., Kiflie, Z., Kim, H., Gadisa, B.T., 2020. Effects of operational parameters on bacterial inactivation in Vis-LEDs illuminated N-doped TiO2 based photoreactor. J. Environ. Chem. Eng. 8, 104374. https://doi.org/10.1016/j.jece.2020.104374.
- Kayahan, E., Jacobs, M., Braeken, L., Thomassen, L.C.J., Kuhn, S., van Gerven, T., Leblebici, M.E., 2020. Dawn of a new era in industrial photochemistry: the scale-up of micro- and mesostructured photoreactors. Beilstein J. Org. Chem. 16, 2484–2504. https://doi.org/10.3762/bjoc.16.202.
- Khan, A.A., Tahir, M., 2019. Recent advancements in engineering approach towards design of photo-reactors for selective photocatalytic CO2 reduction to renewable fuels. J. $\rm CO_2$ Util. 29, 205–239. https://doi.org/10.1016/j.jcou.2018.12.008.
- Khan, M.M., 2023. Chapter 8 photocatalysis: laboratory to market. In: Mansoob Khan, M. (Ed.), Theoretical Concepts of Photocatalysis. Elsevier, pp. 187–212 https://doi.org/10.1016/B978-0-323-95191-3.00013-4.
- Khodadadian, F., de Boer, M.W., Poursaeidesfahani, A., van Ommen, J.R., Stankiewicz, A.I., Lakerveld, R., 2018. Design, characterization and model validation of a LED-based photocatalytic reactor for gas phase applications. Chem. Eng. J. 333, 456–466. https://doi.org/10.1016/j.cej.2017.09.108.
- Kim, Sungwon, Kim, Saemi, Park, H.-J., Park, S., Kim, J.Y., Jeong, Y.W., Yang, H.H., Choi, Y., Yeom, M., Song, D., Lee, C., 2022. Practical scale evaluation of a photocatalytic air purifier equipped with a titania-zeolite composite bead filter for VOC removal and viral inactivation. Environ. Res. 204, 112036. https://doi.org/10.1016/j.envres.2021.112036.
- Kouamé, A.N., Masson, R., Robert, D., Keller, N., Keller, V., 2013. β-SiC foams as a promising structured photocatalytic support for water and air detoxification. Catal. Today 209, 13–20. https://doi.org/10.1016/j.cattod.2012.12.008.
- Krishnamurthy, A., Adebayo, B., Gelles, T., Rownaghi, A., Rezaei, F., 2020. Abatement of gaseous volatile organic compounds: a process perspective. Catal. Today 350, 100–119. https://doi.org/10.1016/j.cattod.2019.05.069 Frontier of Catalysis of Energy and Fuels: From Catalyst Synthesis to Production Yield.
- Kumar, S., Regue, M., Isaacs, M.A., Freeman, E., Eslava, S., 2020. All-inorganic CsPbBr 3 nanocrystals: gram-scale mechanochemical synthesis and selective photocatalytic CO2 reduction to methane. ACS Appl. Energy Mater. 3, 4509–4522. https://doi.org/10.1021/ acsaem.0c00195.
- Kvss, B., Ray, D., Chawdhury, P., B.S, R., Thatikonda, S., Challapalli, S., 2023. Catalytic non-thermal plasma reactor for oxidative degradation of toluene present in low concentration. Catal. Today https://doi.org/10.1016/j.cattod.2023.01.005.
- Lee, C.-G., Javed, H., Zhang, D., Kim, J.-H., Westerhoff, P., Li, Q., Alvarez, P.J.J., 2018. Porous electrospun fibers embedding TiO2 for adsorption and photocatalytic degradation of water pollutants. Environ. Sci. Technol. 52, 4285–4293. https://doi.org/10.1021/acs. est.7b06508.
- Lekshmi, M.V., Shiva Nagendra, S.M., Maiya, M.P., 2020. Heterogeneous photocatalysis for indoor air purification: Recent advances in technology from material to reactor modeling. In: Sharma, A., Goyal, R., Mittal, R. (Eds.), Indoor Environmental Quality. Lecture Notes in Civil Engineering. Springer, Singapore, pp. 147–166 https://doi.org/10.1007/978-981-15-1334-3_16.
- Levchuk, I., Guillard, C., Dappozze, F., Parola, S., Leonard, D., Sillanpää, M., 2016. Photocatalytic activity of TiO2 films immobilized on aluminum foam by atomic layer deposition technique. J. Photochem. Photobiol. A Chem. 328, 16–23. https://doi.org/10.1016/j. jphotochem.2016.03.034.
- Li, D., Gautier, N., Dey, B., Bulou, S., Richard-Plouet, M., Ravisy, W., Goullet, A., Choquet, P., Granier, A., 2019. TEM analysis of photocatalytic TiO2 thin films deposited on polymer substrates by low-temperature ICP-PECVD. Appl. Surf. Sci. 491, 116–122. https://doi. org/10.1016/j.apsusc.2019.06.045.
- Li, G., Zhang, K., Li, C., Gao, R., Cheng, Y., Hou, L., Wang, Y., 2019. Solvent-free method to encapsulate polyoxometalate into metal-organic frameworks as efficient and recyclable

- photocatalyst for harmful sulfamethazine degrading in water. Appl. Catal. B Environ. 245, 753–759. https://doi.org/10.1016/j.apcatb.2019.01.012.
- Li, J.-J., Yu, E.-Q., Cai, S.-C., Chen, X., Chen, J., Jia, H.-P., Xu, Y.-J., 2019. Noble metal free, CeO2/LaMnO3 hybrid achieving efficient photo-thermal catalytic decomposition of volatile organic compounds under IR light. Appl. Catal. B Environ. 240, 141–152. https:// doi.org/10.1016/j.apcatb.2018.08.069.
- Li, N., Gu, T., Xie, H., Ji, J., Liu, X., Yu, B., 2023. The kinetic and preliminary performance study on a novel solar photo-thermal catalytic hybrid trombe-wall. Energy 269, 126839. https://doi.org/10.1016/j.energy.2023.126839.
- Li, P., Yan, X., He, Z., Ji, J., Hu, J., Li, G., Lian, K., Zhang, W., 2016. α-Fe2O3 concave and hollow nanocrystals: top-down etching synthesis and their comparative photocatalytic activities. CrystEngComm 18, 1752–1759. https://doi.org/10.1039/C5CE02097B.
- Li, Y., Wu, S., Wu, J., Hu, Q., Zhou, C., 2020. Photothermocatalysis for efficient abatement of CO and VOCs. J. Mater. Chem. A 8, 8171–8194. https://doi.org/10.1039/DOTA00029A.
- Lira, J.O.B., Riella, H.G., Padoin, N., Soares, C., 2022. Computational fluid dynamics (CFD), artificial neural network (ANN) and genetic algorithm (GA) as a hybrid method for the analysis and optimization of micro-photocatalytic reactors: NOx abatement as a case study. Chem. Eng. J. 431, 133771. https://doi.org/10.1016/j.cej.2021.133771.
- Liu, C., Feng, Y., Han, Z., Sun, Y., Wang, X., Zhang, Q., Zou, Z., 2021. Z-scheme N-doped K4Nb6O17/g-C3N4 heterojunction with superior visible-light-driven photocatalytic activity for organic pollutant removal and hydrogen production. Chin. J. Catal. 42, 164–174. https://doi.org/10.1016/S1872-2067(20)63608-7.
- Liu, Li, Jiang, P., Qian, H., Mu, L., Lu, X., Zhu, J., 2022. CO2-negative biomass conversion: an economic route with co-production of green hydrogen and highly porous carbon. Appl. Energy 311, 118685. https://doi.org/10.1016/j.apenergy.2022.118685.
- Liu, Liming, Meng, G., Laghari, A.A., Chen, H., Wang, C., Xue, Y., 2022. Reducing the risk of exposure of airborne antibiotic resistant bacteria and antibiotic resistance genes by dynamic continuous flow photocatalytic reactor. J. Hazard. Mater. 429, 128311. https:// doi.org/10.1016/j.jhazmat.2022.128311.
- Liu, M., Xing, Z., Li, Z., Zhou, W., 2021. Recent advances in core-shell metal organic frame-based photocatalysts for solar energy conversion. Coord. Chem. Rev. 446, 214123. https://doi.org/10.1016/j.ccr.2021.214123.
- Liu, Wenbo, Li, X., Wang, C., Pan, H., Liu, Wenping, Wang, K., Zeng, Q., Wang, R., Jiang, J., 2019. A scalable general synthetic approach toward ultrathin imine-linked two-dimensional covalent organic framework nanosheets for photocatalytic CO2 reduction. J. Am. Chem. Soc. 141, 17431–17440. https://doi.org/10.1021/jacs.9b09502.
- Liu, X., Chen, T., Xue, Y., Fan, J., Shen, S., Hossain, Md.S.A., Amin, M.A., Pan, L., Xu, X., Yamauchi, Y., 2022. Nanoarchitectonics of MXene/semiconductor heterojunctions toward artificial photosynthesis via photocatalytic CO2 reduction. Coord. Chem. Rev. 459, 214440. https://doi.org/10.1016/j.ccr.2022.214440.
- Liu, Y., Li, R., Yang, H., Song, J., Hu, J., Yang, C., Zheng, Z., 2022. In situ modification by graphidyne as interlayer in titanium dioxide thin film / platinum for water splitting photocatalysis. Int. J. Hydrog. Energy 47, 14563–14569. https://doi.org/10.1016/j. iihydene.2022.02.207.
- Liu, Y., Osta, E.H., Poryvaev, A.S., Fedin, M.V., Longo, A., Nefedov, A., Kosinov, N., 2023. Direct conversion of methane to zeolite-templated carbons, light hydrocarbons, and hydrogen. Carbon 201, 535–541. https://doi.org/10.1016/j.carbon.2022.09.050.
- Liu, Z., Wang, F., Zhang, Z., Min, S., 2020. Interfacing CdS particles on ni foam as a three-dimensional monolithic photocatalyst for efficient visible-light-driven H2 evolution. Int. J. Hydrog. Energy 45, 31678–31688. https://doi.org/10.1016/j.ijhydene.2020.09.031.
- Loeb, S.K., Alvarez, P.J.J., Brame, J.A., Cates, E.L., Choi, W., Crittenden, J., Dionysiou, D.D., Li, Q., Li-Puma, G., Quan, X., Sedlak, D.L., David Waite, T., Westerhoff, P., Kim, J.-H., 2019. The technology horizon for photocatalytic water treatment: sunrise or Sunset? Environ. Sci. Technol. 53, 2937–2947. https://doi.org/10.1021/acs.est.8b05041.
- Lotfi, S., Fischer, K., Schulze, A., Schäfer, A.I., 2022. Photocatalytic degradation of steroid hormone micropollutants by TiO2-coated polyethersulfone membranes in a continuous flow-through process. Nat. Nanotechnol. 17, 417–423. https://doi.org/10.1038/s41565-022-01074-8.
- Low, J., Zhang, C., Ma, J., Murzin, D.Y., Xiong, Y., 2023. Heterogeneous photocatalysis: what is being overlooked? TRECHEM 5, 121–132. https://doi.org/10.1016/j.trechm.2022.11.007.
- Lu, Q., Zhang, L.-L., Xu, T.-T., Zhang, B.-Y., Gong, W.-J., 2023. Highly efficient photocatalytic water splitting in direct Z-scheme α -In2Se3/Are van der waals heterostructures. Surf. Interfaces 36, 102608. https://doi.org/10.1016/j.surfin.2022.102608.
- Lumbaque, E.C., Lüdtke, D.S., Dionysiou, D.D., Vilar, V.J.P., Sirtori, C., 2021. Tube-in-tube membrane photoreactor as a new technology to boost sulfate radical advanced oxidation processes. Water Res. 191, 116815. https://doi.org/10.1016/j.watres.2021.116815.
- Luna-Sanguino, G., Ruíz-Delgado, A., Tolosana-Moranchel, A., Pascual, L., Malato, S., Bahamonde, A., Faraldos, M., 2020. Solar photocatalytic degradation of pesticides over TiO2-rGO nanocomposites at pilot plant scale. Sci. Total Environ. 737, 140286. https:// doi.org/10.1016/j.scitotenv.2020.140286.
- Ma, B., Zhang, R., Lin, K., Liu, H., Wang, X., Liu, W., Zhan, H., 2018. Large-scale synthesis of noble-metal-free phosphide/CdS composite photocatalysts for enhanced H2 evolution under visible light irradiation. Chin. J. Catal. 39, 527–533. https://doi.org/10.1016/ S1872-2067(17)62931-0.
- Ma, R., Sun, J., Li, D.H., Wei, J.J., 2020. Exponentially self-promoted hydrogen evolution by uni-source photo-thermal synergism in concentrating photocatalysis on co-catalyst-free P25 TiO2. J. Catal. 392, 165–174. https://doi.org/10.1016/j.jcat.2020.10.007.
- Malayeri, M., Lee, C.-S., Haghighat, F., 2021. Modeling of photocatalytic oxidation reactor for methyl ethyl ketone removal from indoor environment: systematic model development and validation. Chem. Eng. J. 409, 128265. https://doi.org/10.1016/j.cej.2020.128265.
- Maldonado, M.I., López-Martín, A., Colón, G., Peral, J., Martínez-Costa, J.I., Malato, S., 2018. Solar pilot plant scale hydrogen generation by irradiation of Cu/TiO2 composites in presence of sacrificial electron donors. Appl. Catal. B Environ. 229, 15–23. https://doi.org/10.1016/j.apcatb.2018.02.005.

- Mamaghani, A.H., Haghighat, F., Lee, C.-S., 2020. Role of titanium dioxide (TiO2) structural design/morphology in photocatalytic air purification. Appl. Catal. B Environ. 269, 118735. https://doi.org/10.1016/j.apcatb.2020.118735.
- Manassero, A., Alfano, O.M., Satuf, M.L., 2023. Radiation modeling and performance evaluation of a UV-LED photocatalytic reactor for water treatment. J. Photochem. Photobiol. A Chem. 436, 114367. https://doi.org/10.1016/j.jphotochem.2022.114367.
- Manassero, A., Alfano, O.M., Satuf, M.L., 2022. Degradation of emerging pollutants by photocatalysis: radiation modeling and kinetics in packed-bed reactors. Water 14, 3608. https://doi.org/10.3390/w14223608.
- Manassero, A., Satuf, M.L., Alfano, O.M., 2017. Photocatalytic reactors with suspended and immobilized TiO2: comparative efficiency evaluation. Chem. Eng. J. 326, 29–36. https://doi.org/10.1016/j.cej.2017.05.087.
- Martínez-Costa, J.I., Maldonado Rubio, M.I., Leyva-Ramos, R., 2020. Degradation of emerging contaminants diclofenac, sulfamethoxazole, trimethoprim and carbamazepine by bentonite and vermiculite at a pilot solar compound parabolic collector. Catal. Today 2017 (341), 26–36. https://doi.org/10.1016/j.cattod.2018.07.021 SI: 5th LACP3.
 Martín-Sómer, M., Moreno-SanSegundo, J., Álvarez-Fernández, C., van Grieken, R., Marugán,
- Martín-Sómer, M., Moreno-SanSegundo, J., Álvarez-Fernández, C., van Grieken, R., Marugán, J., 2021. High-performance low-cost solar collectors for water treatment fabricated with recycled materials, open-source hardware and 3d-printing technologies. Sci. Total Environ. 784, 147119. https://doi.org/10.1016/j.scitotenv.2021.147119.
- Mata, T.M., Martins, A.A., Calheiros, C.S.C., Villanueva, F., Alonso-Cuevilla, N.P., Gabriel, M.F., Silva, G.V., 2022. Indoor air quality: a review of cleaning technologies. Environments 9, 118. https://doi.org/10.3390/environments9090118.
- Mohammadi, P., Ghorbani-Shahna, F., Bahrami, A., Rafati, A.A., Farhadian, M., 2020. Plasma-photocatalytic degradation of gaseous toluene using SrTiO3/rGO as an efficient heterojunction for by-products abatement and synergistic effects. J. Photochem. Photobiol. A Chem. 394, 112460. https://doi.org/10.1016/j.jphotochem.2020.112460.
- Moreira, N.F.F., Narciso-da-Rocha, C., Polo-López, M.I., Pastrana-Martínez, L.M., Faria, J.L., Manaia, C.M., Fernández-Ibáñez, P., Nunes, O.C., Silva, A.M.T., 2018. Solar treatment (H2O2, TiO2-P25 and GO-TiO2 photocatalysis, photo-Fenton) of organic micropollutants, human pathogen indicators, antibiotic resistant bacteria and related genes in urban wastewater. Water Res. 135, 195–206. https://doi.org/10.1016/j.watres.2018.01.064.
- Moreno, J., Casado, C., Marugán, J., 2019. Improved discrete ordinate method for accurate simulation radiation transport using solar and LED light sources. Chem. Eng. Sci. 205, 151–164. https://doi.org/10.1016/j.ces.2019.04.034.
- Muscetta, M., Russo, D., 2021. Photocatalytic applications in wastewater and air treatment: a patent review (2010–2020). Catalysts 11, 834. https://doi.org/10.3390/catal11070834.
- Nabil, S., Hammad, A.S., El-Bery, H.M., Shalaby, E.A., El-Shazly, A.H., 2021. The CO2 photoconversion over reduced graphene oxide based on Ag/TiO2 photocatalyst in an advanced meso-scale continuous-flow photochemical reactor. Environ. Sci. Pollut. Res. 28, 36157–36173. https://doi.org/10.1007/s11356-021-13090-7.
- Nabil, S., Shalaby, E.A., Elkady, M.F., Matsushita, Y., El-Shazly, A.H., 2022. Optimizing the performance of the meso-scale continuous-flow photoreactor for efficient photocatalytic CO2 reduction with water over Pt/TiO2/RGO composites. Catal. Lett. 152, 3243–3258. https://doi.org/10.1007/s10562-021-03915-y.
- Nchikou, C., Loredo-Medrano, J.Á., Hernández-Ramírez, A., Colina-Marquez, J.Á., Mueses, M. A., 2021. Estimation of the radiation field for CPC photocatalytic reactors using a novel six-flux model in two dimensions (SFM-2D). J. Environ. Chem. Eng. 9, 106392. https://doi.org/10.1016/j.jece.2021.106392.
- Nguyen, V.-H., Wu, J.C.S., 2018. Recent developments in the design of photoreactors for solar energy conversion from water splitting and CO2 reduction. Appl. Catal. A Gen. 550, 122–141. https://doi.org/10.1016/j.apcata.2017.11.002.
- Nishiyama, H., Yamada, T., Nakabayashi, M., Maehara, Y., Yamaguchi, M., Kuromiya, Y., Nagatsuma, Y., Tokudome, H., Akiyama, S., Watanabe, T., Narushima, R., Okunaka, S., Shibata, N., Takata, T., Hisatomi, T., Domen, K., 2021. Photocatalytic solar hydrogen production from water on a 100–m2 scale. Nature 598, 304–307. https://doi.org/10.1038/s41586-021-03907-3.
- Ochoa-Gutiérrez, K.S., Tabares-Aguilar, E., Mueses, M.Á., Machuca-Martínez, F., Li Puma, G., 2018. A novel prototype offset multi tubular photoreactor (OMTP) for solar photocatalytic degradation of water contaminants. Chem. Eng. J. 341, 628–638. https://doi.org/10.1016/j.cej.2018.02.068.
- Omerzu, A., Peter, R., Jardas, D., Turel, I., Salamon, K., Podlogar, M., Vengust, D., Jelovica Badovinac, I., Kavre Piltaver, I., Petravic, M., 2021. Large enhancement of photocatalytic activity in ZnO thin films grown by plasma-enhanced atomic layer deposition. Surf. Interfaces 23, 100984. https://doi.org/10.1016/j.surfin.2021.100984.
- O'Neal Tugaoen, H., Garcia-Segura, S., Hristovski, K., Westerhoff, P., 2018. Compact light-emitting diode optical fiber immobilized TiO2 reactor for photocatalytic water treatment. Sci. Total Environ. 613–614, 1331–1338. https://doi.org/10. 1016/j.scitotenv.2017.09.242.
- Otálvaro-Marín, H.L., González-Caicedo, F., Arce-Sarria, A., Mueses, M.A., Crittenden, J.C., Machuca-Martinez, F., 2019. Scaling-up a heterogeneous H2O2/TiO2/solar-radiation system using the Damköhler number. Chem. Eng. J. 364, 244–256. https://doi.org/10.1016/j.cej.2019.01.141.
- Ozin, G., 2022. Accelerated optochemical engineering solutions to CO2 photocatalysis for a sustainable future. Matter 5, 2594–2614. https://doi.org/10.1016/j.matt.2022.07.033.
- Parthibavarman, M., Karthik, M., Prabhakaran, S., 2018. Facile and one step synthesis of WO3 nanorods and nanosheets as an efficient photocatalyst and humidity sensing material. Vacuum 155, 224–232. https://doi.org/10.1016/j.vacuum.2018.06.021.
- Pascariu, P., Tudose, I.V., Suchea, M., 2019. Surface morphology effects on photocatalytic activity of metal oxides nanostructured materials immobilized onto substrates. J. Nanosci. Nanotechnol. 19, 295–306. https://doi.org/10.1166/jnn.2019.15777.
- Patowary, M., Kalita, H., 2022. 19 Large-scale materials for visible light photocatalysis. In: Nayak, A.K., Sahu, N.K. (Eds.), Nanostructured Materials for Visible Light Photocatalysis, Micro and Nano Technologies. Elsevier, pp. 511–533 https://doi.org/10.1016/B978-0-12-823018-3.00007-5.

- Pava-Gómez, B., Vargas-Ramírez, X., Díaz-Uribe, C., Romero, H., Duran, F., 2021. Evaluation of copper-doped TiO2 film supported on glass and LDPE with the design of a pilotscale solar photoreactor. Sol. Energy 220, 695–705. https://doi.org/10.1016/j. solener.2021.03.071.
- Pei, C., Zhu, J.-H., Xing, F., 2021. Photocatalytic property of cement mortars coated with graphene/TiO2 nanocomposites synthesized via sol–gel assisted electrospray method. J. Clean. Prod. 279, 123590. https://doi.org/10.1016/j.jclepro.2020.123590.
- Peralta Muniz Moreira, R., Li Puma, G., 2021. Multiphysics Computational Fluid-Dynamics (CFD) Modeling of Annular Photocatalytic Reactors by the Discrete Ordinates Method (DOM) and the Six-Flux Model (SFM) and Evaluation of the Contaminant Intrinsic Kinetics Constants. Catalysis Today, Environmental Applications of Advanced Oxidation Processes (EAAOP-6). 361, pp. 77–84. https://doi.org/10.1016/j.cattod.2020.01.012.
- Pestana, C.J., Hobson, P., Robertson, P.K.J., Lawton, L.A., Newcombe, G., 2020. Removal of microcystins from a waste stabilisation lagoon: evaluation of a packed-bed continuous flow TiO2 reactor. Chemosphere 245, 125575. https://doi.org/10.1016/j.chemosphere. 2019.125575.
- Phan, D.D., Babick, F., Trinh, T.H.T., Nguyen, M.T., Samhaber, W., Stintz, M., 2018. Investigation of fixed-bed photocatalytic membrane reactors based on submerged ceramic membranes. Chem. Eng. Sci. 191, 332–342. https://doi.org/10.1016/j.ces.2018.06.062.
- Photocatalytic Hydrogen Production: A Rift into the Future Energy Supply Christoforidis 2017 ChemCatChem Wiley Online Library, ... [WWW document]. URL https://chemistry-europe.onlinelibrary.wiley.com/doi/10.1002/cctc.201601659. (Accessed 6 March 2023).
- Plakas, K.V., Sarasidis, V.C., Patsios, S.I., Lambropoulou, D.A., Karabelas, A.J., 2016. Novel pilot scale continuous photocatalytic membrane reactor for removal of organic micropollutants from water. Chem. Eng. J. 304, 335–343. https://doi.org/10.1016/j. cei 2016.06.075
- Pomilla, F.R., Brunetti, A., Marcì, G., Fontananova, E., Palmisano, L., Barbieri, G., García-López, E.I., 2018. CO2 to liquid fuels: photocatalytic conversion in a continuous membrane reactor. ACS Sustain. Chem. Eng. 6, 8743–8753. https://doi.org/10.1021/ acssuschemeng.8b01073.
- Priya, R., Kanmani, S., 2013. Design of pilot-scale solar photocatalytic reactor for the generation of hydrogen from alkaline sulfide wastewater of sewage treatment plant. Environ. Technol. 34, 2817–2823. https://doi.org/10.1080/09593330.2013.790081.
- Pylnev, M., Wong, M.-S., 2019. Comparative study of photocatalytic deactivation of pure and black titania thin films. J. Photochem. Photobiol. A Chem. 378, 125–130. https://doi. org/10.1016/j.jphotochem.2019.04.020.
- Qian, H., Hou, Q., Zhang, W., Nie, Y., Lai, R., Ren, H., Yu, G., Bai, X., Wang, H., Ju, M., 2022. Construction of electron transport channels and oxygen adsorption sites to modulate reactive oxygen species for photocatalytic selective oxidation of 5-hydroxymethylfurfural to 2,5-diformylfuran. Appl. Catal. B Environ. 319, 121907. https://doi.org/10.1016/j.apcatb.2022.121907.
- Ramos, B., Carneiro, J.G.M., Nagamati, L.I., Teixeira, A.C.S.C., 2021. Development of intensified flat-plate packed-bed solar reactors for heterogeneous photocatalysis. Environ. Sci. Pollut. Res. 28, 24023–24033. https://doi.org/10.1007/s11356-020-11806-9.
- Ramos, B., Couri, A.P., Ookawara, S., Costa Teixeira, A.C.S., 2019. Micro-structured packed bed reactors for solar photocatalysis: impacts of packing size and material on light harnessing. Photochem. Photobiol. Sci. 18, 577–582. https://doi.org/10.1039/c8 pp00371h
- Ramos, D.R., Iazykov, M., Fernandez, M.I., Santaballa, J.A., Canle, M., 2021. Mechanical stability is key for large-scale implementation of photocatalytic surface-attached film technologies in water treatment. Front. Chem. Eng. 3.
- Ran, M., Wang, H., Cui, W., Li, J., Chen, P., Sun, Y., Sheng, J., Zhou, Y., Zhang, Y., Dong, F., 2019. Light-induced generation and regeneration of oxygen vacancies in BiSbO4 for sustainable visible light photocatalysis. ACS Appl. Mater. Interfaces 11, 47984–47991. https://doi.org/10.1021/acsami.9b18154.
- Rana, A.G., Schwarze, M., Tasbihi, M., Sala, X., García-Antón, J., Minceva, M., 2022. Influence of cocatalysts (Ni co, and Cu) and synthesis method on the photocatalytic activity of exfoliated graphitic carbon nitride for hydrogen production. Nanomaterials 12, 4006. https://doi.org/10.3390/nano12224006.
- Rapti, I., Kosma, C., Albanis, T., Konstantinou, I., 2022. Solar photocatalytic degradation of inherent pharmaceutical residues in real hospital WWTP effluents using titanium dioxide on a CPC pilot scale reactor. Catal. Today https://doi.org/10.1016/j.cattod.2022.08.026.
- Reilly, K., Wilkinson, D.P., Taghipour, F., 2018. Photocatalytic water splitting in a fluidized bed system: computational modeling and experimental studies. Appl. Energy 222, 423–436. https://doi.org/10.1016/j.apenergy.2018.03.020.
- Ren, T., Ma, T., Liu, S., Li, X., 2022. Bi-level optimization for the energy conversion efficiency improvement in a photocatalytic-hydrogen-production system. Energy 253, 124138. https://doi.org/10.1016/j.energy.2022.124138.
- Rincón, G.J., La Motta, E.J., 2019. A fluidized-bed reactor for the photocatalytic mineralization of phenol on TiO2-coated silica gel. Heliyon 5, e01966. https://doi.org/10.1016/j.heliyon.2019.e01966.
- Rodríguez-Chueca, J., Mesones, S., Marugán, J., 2019. Hybrid UV-C/microfiltration process in membrane photoreactor for wastewater disinfection. Environ. Sci. Pollut. Res. 26, 36080–36087. https://doi.org/10.1007/s11356-018-3262-x.
- Rouhani, S., Taghipour, F., 2022. Modeling of UV-LED photocatalytic reactors for the degradation of gaseous volatile organic compounds (VOCs) in indoor environments. J. Environ. Chem. Eng. 10, 107657. https://doi.org/10.1016/j.jece.2022.107657.
- Ruiz-Aguirre, A., Villachica-Llamosas, J.G., Polo-López, M.I., Cabrera-Reina, A., Colón, G., Peral, J., Malato, S., 2022. Assessment of pilot-plant scale solar photocatalytic hydrogen generation with multiple approaches: valorization, water decontamination and disinfection. Energy 260, 125199. https://doi.org/10.1016/j.energy.2022.125199
- Sacco, O., Matarangolo, M., Vaiano, V., Libralato, G., Guida, M., Lofrano, G., Carotenuto, M., 2018. Crystal violet and toxicity removal by adsorption and simultaneous photocatalysis in a continuous flow micro-reactor. Sci. Total Environ. 644, 430–438. https://doi.org/10. 1016/j.scitotenv.2018.06.388.

- Sacco, O., Sannino, D., Vaiano, V., 2019. Packed bed photoreactor for the removal of water pollutants using visible light emitting diodes. Appl. Sci. 9, 472. https://doi.org/10. 3390/app9030472.
- Samy, M., Ibrahim, M.G., Fujii, M., Diab, K.E., ElKady, M., Gar Alalm, M., 2021. CNTs/MOF-808 painted plates for extended treatment of pharmaceutical and agrochemical wastewaters in a novel photocatalytic reactor. Chem. Eng. J. 406, 127152. https://doi.org/10.1016/j.cei.2020.127152.
- Samy, M., İbrahim, M.G., Gar Alalm, M., Fujii, M., 2020a. MIL-53(Al)/ZnO coated plates with high photocatalytic activity for extended degradation of trimethoprim via novel photocatalytic reactor. Sep. Purif. Technol. 249, 117173. https://doi.org/10.1016/j.seppur. 2020.117173.
- Samy, M., Ibrahim, M.G., Gar Alalm, M., Fujii, M., Diab, K.E., ElKady, M., 2020b. Innovative photocatalytic reactor for the degradation of chlorpyrifos using a coated composite of ZrV2O7 and graphene nano-platelets. Chem. Eng. J. 395, 124974. https://doi.org/10. 1016/j.cej.2020.124974.
- Saran, S., Arunkumar, P., Manjari, G., Devipriya, S.P., 2019. Reclamation of grey water for non-potable purposes using pilot-scale solar photocatalytic tubular reactors. Environ. Technol. 40, 3190–3199. https://doi.org/10.1080/09593330.2018.1468486.
- Schneidewind, J., 2022. How much technological progress is needed to make solar hydrogen cost-competitive? Adv. Energy Mater. 12, 2200342. https://doi.org/10.1002/aenm. 202200342.
- Schröder, M., Kailasam, K., Borgmeyer, J., Neumann, M., Thomas, A., Schomäcker, R., Schwarze, M., 2015. Hydrogen evolution reaction in a large-scale reactor using a carbon nitride photocatalyst under natural sunlight irradiation. Energy Technol. 3, 1014–1017. https://doi.org/10.1002/ente.201500142.
- Schwarze, M., Thiel, T.A., Rana, A.G., Yang, J., Acharjya, A., Nguyen, A.D., Tameu Djoko, S., Kutorglo, E.M., Tasbihi, M., Minceva, M., Huseyinova, S., Menezes, P., Walter, C., Driess, M., Schomäcker, R., Thomas, A., 2022a. Screening of heterogeneous photocatalysts for water splitting. Chem. Ing. Tech. 94, 1739–1746. https://doi.org/10.1002/cite. 202200070.
- Schwarze, M., Thiel, T.A., Tasbihi, M., Schroeter, M., Menezes, P.W., Walter, C., Driess, M., Schomäcker, R., 2022b. Use of cellulose for the production of photocatalytic films for hydrogen evolution along the lines of paper production. Energy Technol. 10, 2100525. https://doi.org/10.1002/ente.202100525.
- Serge-Correales, Y.E., Ullah, S., Ferreira-Neto, E.P., Rojas-Mantilla, H.D., Hazra, C., Ribeiro, S.J.L., 2022. A UV-visible-NIR active smart photocatalytic system based on NaYbF4: Tm3+ upconverting particles and Ag3PO4/H2O2 for photocatalytic processes under light on/light off conditions. Mater. Adv. 3, 2706–2715. https://doi.org/10.1039/DIMA010281
- Sharma, S., Kumar, R., Raizada, P., Ahamad, T., Alshehri, S.M., Nguyen, V.-H., Thakur, S., Nguyen, C.C., Kim, S.Y., Le, Q.V., Singh, P., 2022. An overview on recent progress in photocatalytic air purification: metal-based and metal-free photocatalysis. Environ. Res. 214, 113995. https://doi.org/10.1016/j.envres.2022.113995.
- Shayegan, Z., Bahri, M., Haghighat, F., 2022. A review on an emerging solution to improve indoor air quality: application of passive removal materials. Build. Environ. 219, 109228. https://doi.org/10.1016/j.buildenv.2022.109228.
- Shayegan, Z., Haghighat, F., Lee, C.-S., 2019. Photocatalytic oxidation of volatile organic compounds for indoor environment applications: three different scaled setups. Chem. Eng. J. 357, 533–546. https://doi.org/10.1016/j.cej.2018.09.167.
- Sraw, A., Kaur, T., Pandey, Y., Sobti, A., Wanchoo, R.K., Toor, A.P., 2018. Fixed bed recirculation type photocatalytic reactor with TiO2 immobilized clay beads for the degradation of pesticide polluted water. J. Environ. Chem. Eng. 6, 7035–7043. https://doi.org/10.1016/j.jece.2018.10.062.
- Su, C.-Y., Wang, L.-C., Liu, W.-S., Wang, C.-C., Perng, T.-P., 2018. Photocatalysis and hydrogen evolution of Al- and zn-doped TiO2 nanotubes fabricated by atomic layer deposition. ACS Appl. Mater. Interfaces 10, 33287–33295. https://doi.org/10.1021/acsami.8b12299.
- Sun, Q.-M., Xu, J.-J., Tao, F.-F., Ye, W., Zhou, C., He, J.-H., Lu, J.-M., 2022. Boosted inner surface charge transfer in perovskite Nanodots@Mesoporous titania frameworks for efficient and selective photocatalytic CO2 reduction to methane. Angew. Chem. Int. Ed. 61, e202200872. https://doi.org/10.1002/anie.202200872.
- Sundar, K.P., Kanmani, S., 2020. Progression of photocatalytic reactors and it's comparison: a review. Chem. Eng. Res. Des. 154, 135–150. https://doi.org/10.1016/j.cherd.2019.11.035.
- Surenjan, A., Pradeep, T., Philip, L., 2019. Application and performance evaluation of a cost-effective Vis- LED based fluidized bed reactor for the treatment of emerging contaminants. Chemosphere 228, 629–639. https://doi.org/10.1016/j.chemosphere.2019.04.179.
- Talwar, S., Verma, A.K., Sangal, V.K., Štangar, U.L., 2020. Once through continuous flow removal of metronidazole by dual effect of photo-Fenton and photocatalysis in a compound parabolic concentrator at pilot plant scale. Chem. Eng. J. 388, 124184. https://doi.org/10.1016/j.cej.2020.124184.
- Tembhurne, S., Nandjou, F., Haussener, S., 2019. A thermally synergistic photoelectrochemical hydrogen generator operating under concentrated solar irradiation. Nat. Energy 4, 399–407. https://doi.org/10.1038/s41560-019-0373-7.
- Tian, B., Tian, Bining, Smith, B., Scott, M.C., Lei, Q., Hua, R., Tian, Y., Liu, Y., 2018. Facile bottom-up synthesis of partially oxidized black phosphorus nanosheets as metal-free photocatalyst for hydrogen evolution. Proc. Natl. Acad. Sci. 115, 4345–4350. https:// doi.org/10.1073/pnas.1800069115.
- Tian, M., Su, Y., Zheng, H., Pei, G., Li, G., Riffat, S., 2018. A review on the recent research progress in the compound parabolic concentrator (CPC) for solar energy applications. Renew. Sust. Energ. Rev. 82, 1272–1296. https://doi.org/10.1016/j.rser.2017.09.050.
- Toe, C.Y., Pan, J., Scott, J., Amal, R., 2022. Identifying key design criteria for large-scale photocatalytic hydrogen generation from engineering and economic perspectives. ACS EST Eng. 2, 1130–1143. https://doi.org/10.1021/acsestengg.2c00030.
- Toledo-Camacho, S.Y., Rey, A., Maldonado, M.I., Llorca, J., Contreras, S., Medina, F., 2021.

 Photocatalytic hydrogen production from water-methanol and -glycerol mixtures using

- Pd/TiO2(-WO3) catalysts and validation in a solar pilot plant. Int. J. Hydrog. Energy 46, 36152–36166. https://doi.org/10.1016/j.ijhydene.2021.08.141.
- Tolosana-Moranchel, Á., Manassero, A., Satuf, M.L., Alfano, O.M., Casas, J.A., Bahamonde, A., 2019. TiO2-rGO photocatalytic degradation of an emerging pollutant: kinetic modelling and determination of intrinsic kinetic parameters. J. Environ. Chem. Eng. 7, 103406. https://doi.org/10.1016/j.jece.2019.103406.
- Tong, K., Yang, L., Du, X., 2020. Modelling of TiO2-based packing bed photocatalytic reactor with raschig rings for phenol degradation by coupled CFD and DEM. Chem. Eng. J. 400, 125988. https://doi.org/10.1016/j.cej.2020.125988.
- Tran, M.L., Fu, G.-C., Chiang, L.-Y., Hsieh, C.-T., Liu, S.-H., Juang, R.-S., 2020. Immobilization of TiO2 and TiO2-GO hybrids onto the surface of acrylic acid-grafted polymeric membranes for pollutant removal: analysis of photocatalytic activity. J. Environ. Chem. Eng. 8, 104422. https://doi.org/10.1016/j.jece.2020.104422.
- Uricchio, A., Nadal, E., Plujat, B., Plantard, G., Massines, F., Fanelli, F., 2021. Low-temperature atmospheric pressure plasma deposition of TiO2-based nanocomposite coatings on open-cell polymer foams for photocatalytic water treatment. Appl. Surf. Sci. 561, 150014. https://doi.org/10.1016/j.apsusc.2021.150014.
- Vaiano, V., Iervolino, G., 2018. Facile method to immobilize ZnO particles on glass spheres for the photocatalytic treatment of tannery wastewater. J. Colloid Interface Sci. 518, 192–199. https://doi.org/10.1016/j.icis.2018.02.033.
- Vaiano, V., Sacco, O., Libralato, G., Lofrano, G., Siciliano, A., Carraturo, F., Guida, M., Carotenuto, M., 2020. Degradation of anionic azo dyes in aqueous solution using a continuous flow photocatalytic packed-bed reactor: influence of water matrix and toxicity evaluation. J. Environ. Chem. Eng. 8, 104549. https://doi.org/10.1016/j. jece.2020.104549.
- Vaiano, V., Sacco, O., Pisano, D., Sannino, D., Ciambelli, P., 2015. From the design to the development of a continuous fixed bed photoreactor for photocatalytic degradation of organic pollutants in wastewater. Chem. Eng. Sci. 137, 152–160. https://doi.org/10.1016/j.ces.2015.06.023.
- van Walsem, J., Roegiers, J., Modde, B., Lenaerts, S., Denys, S., 2018. Determination of intrinsic kinetic parameters in photocatalytic multi-tube reactors by combining the NTUmmethod with radiation field modelling. Chem. Eng. J. 354, 1042–1049. https://doi.org/10.1016/j.cej.2018.08.010.
- Vikrant, K., Weon, S., Kim, K.-H., Sillanpää, M., 2021. Platinized titanium dioxide (Pt/TiO2) as a multi-functional catalyst for thermocatalysis, photocatalysis, and photothermal catalysis for removing air pollutants. Appl. Mater. Today 23, 100993. https://doi.org/10.1016/j.apmt.2021.100993.
- von Gunten, U., 2018. Oxidation processes in water treatment: are we on track? Environ. Sci. Technol. 52, 5062–5075. https://doi.org/10.1021/acs.est.8b00586.
- Wang, C., Lu, S., Zhang, Z., 2019. Inactivation of airborne bacteria using different UV sources: performance modeling, energy utilization, and endotoxin degradation. Sci. Total Environ. 655, 787–795. https://doi.org/10.1016/j.scitotenv.2018.11.266.
- Wang, F., Li, W., Zhang, W., Ye, R., Tan, X., 2022. Facile fabrication of the ag nanoparticles decorated graphitic carbon nitride photocatalyst film for indoor air purification under visible light. Build. Environ. 222, 109402. https://doi.org/10.1016/j.buildenv.2022.109402.
- Wang, G., Chen, Z., Wang, T., Wang, D., Mao, J., 2022. P and cu dual sites on graphitic carbon nitride for photocatalytic CO2 reduction to hydrocarbon fuels with high C2H6 evolution. Angew. Chem. Int. Ed. 61, e202210789. https://doi.org/10. 1002/anie.202210789.
- Wang, H., Liu, Q., You, C., 2019. Regeneration of sulfur-deactivated TiO2 photocatalysts. Appl. Catal. A Gen. 572, 15–23. https://doi.org/10.1016/j.apcata.2018.12.031.
- Wang, H.-X., Li, X.-X., Tang, L., 2020. Effects of surfactants on the morphology and properties of TiO2. Appl. Phys. A Mater. Sci. Process. 126, 448. https://doi.org/10.1007/s00339-020-03638-8.
- Wang, L., Hong, Y., Liu, E., Wang, Z., Chen, J., Yang, S., Wang, J., Lin, X., Shi, J., 2020. Rapid polymerization synthesizing high-crystalline g-C3N4 towards boosting solar photocatalytic H2 generation. Int. J. Hydrog. Energy 45, 6425–6436. https://doi.org/10.1016/j. iihydene.2019.12.168.
- Wang, L., Mogan, T.R., Wang, K., Takashima, M., Ohtani, B., Kowalska, E., 2022. Fabrication and characterization of inverse-opal titania films for enhancement of photocatalytic activity. ChemEngineering 6, 33. https://doi.org/10.3390/chemengineering6030033.
- Wang, Q., Hisatomi, T., Suzuki, Y., Pan, Z., Seo, J., Katayama, M., Minegishi, T., Nishiyama, H., Takata, T., Seki, K., Kudo, A., Yamada, T., Domen, K., 2017. Particulate photocatalyst sheets based on carbon conductor layer for efficient Z-scheme purewater splitting at ambient pressure. J. Am. Chem. Soc. 139, 1675–1683. https://doi.org/10.1021/jacs.6b12164.
- Wang, Y., Wu, Y., Sun, K., Mi, Z., 2019. A quadruple-band metal-nitride nanowire artificial photosynthesis system for high efficiency photocatalytic overall solar water splitting. Mater. Horiz. 6, 1454–1462. https://doi.org/10.1039/C9MH00257J.
- Wei, K., Wang, Z., Ouyang, C., Cao, X., Liang, P., Huang, X., Zhang, X., 2020. A hybrid fluidized-bed reactor (HFBR) based on arrayed ceramic membranes (ACMs) coupled with powdered activated carbon (PAC) for efficient catalytic ozonation: a comprehensive study on a pilot scale. Water Res. 173, 115536. https://doi.org/10.1016/j. watres.2020.115536.
- Wei, L., Yu, C., Yang, K., Fan, Q., Ji, H., 2021. Recent advances in VOCs and CO removal via photothermal synergistic catalysis. Chin. J. Catal. 42, 1078–1095. https://doi.org/10. 1016/S1872-2067(20)63721-4.
- Wei, Q., Yang, Y., Hou, J., Liu, H., Cao, F., Zhao, L., 2017. Direct solar photocatalytic hydrogen generation with CPC photoreactors: system development. Sol. Energy 153, 215–223. https://doi.org/10.1016/j.solener.2017.05.064.
- Wei, Q., Yang, Y., Liu, H., Hou, J., Liu, M., Cao, F., Zhao, L., 2018. Experimental study on direct solar photocatalytic water splitting for hydrogen production using surface uniform concentrators. Int. J. Hydrog. Energy 43, 13745–13753. https://doi.org/10.1016/j.ijhydene.2018.01.135 Special Issue on The 8th International Conference on Hydrogen Production (ICHP-2017).

- Wen, Meicheng, Li, G., Liu, H., Chen, J., An, T., Yamashita, H., 2019. Metal-organic framework-based nanomaterials for adsorption and photocatalytic degradation of gaseous pollutants: recent progress and challenges. Environ. Sci.: Nano 6, 1006–1025. https://doi.org/10.1039/C8EN01167B.
- Wen, Min, Wang, J., Tong, R., Liu, D., Huang, H., Yu, Y., Zhou, Z.-K., Chu, P.K., Yu, X.-F., 2019. A low-cost metal-free photocatalyst based on black phosphorus. Adv. Sci. 6, 1801321. https://doi.org/10.1002/advs.201801321.
- Weon, S., He, F., Choi, W., 2019. Status and challenges in photocatalytic nanotechnology for cleaning air polluted with volatile organic compounds: visible light utilization and catalyst deactivation. Environ. Sci. Nano 6, 3185–3214. https://doi.org/10.1039/ C9EN00891H.
- Wu, J., Alipouri, Y., Luo, H., Zhong, L., 2022. Ultraviolet photocatalytic oxidation technology for indoor volatile organic compound removal: a critical review with particular focus on byproduct formation and modeling. J. Hazard. Mater. 421, 126766. https://doi.org/10. 1016/j.jhazmat.2021.126766.
- Xia, T., Hou, Q., Qian, H., Lai, R., Bai, X., Yu, G., Zhang, W., Laiq Ur Rehman, M., Ju, M., 2023. Fabricating metal-free Z-scheme heterostructures with nitrogen-deficient carbon nitride for fast photocatalytic removal of acetaminophen. Sep. Purif. Technol. 308, 122964. https://doi.org/10.1016/j.seppur.2022.122964.
- Xie, S., Li, Y., Sheng, B., Zhang, W., Wang, W., Chen, C., Li, J., Sheng, H., Zhao, J., 2022. Self-reconstruction of paddle-wheel copper-node to facilitate the photocatalytic CO2 reduction to ethane. Appl. Catal. B Environ. 310, 121320. https://doi.org/10.1016/j.apcatb. 2022.121320.
- Xin, X., Song, Y., Guo, S., Zhang, Y., Wang, B., Yu, J., Li, X., 2020. In-situ growth of high-content 1T phase MoS2 confined in the CuS nanoframe for efficient photocatalytic hydrogen evolution. Appl. Catal. B Environ. 269, 118773. https://doi.org/10.1016/j.apcatb.2020.118773.
- Xiong, A., Ma, G., Maeda, K., Takata, T., Hisatomi, T., Setoyama, T., Kubota, J., Domen, K., 2014. Fabrication of photocatalyst panels and the factors determining their activity for water splitting. Catal. Sci. Technol. 4, 325–328. https://doi.org/10.1039/C3CY00845B.
- Xiong, H., Wu, L., Liu, Y., Gao, T., Li, K., Long, Y., Zhang, R., Zhang, L., Qiao, Z.-A., Huo, Q., Ge, X., Song, S., Zhang, H., 2019. Controllable synthesis of mesoporous TiO2 polymorphs with tunable crystal structure for enhanced photocatalytic H2 production. Adv. Energy Mater. 9, 1901634. https://doi.org/10.1002/aenm.201901634.
- Xu, Z., Chai, W., Cao, J., Huang, F., Tong, T., Dong, S., Qiao, Q., Shi, L., Li, H., Qian, X., Bian, Z., 2021. Controlling the gas-water Interface to enhance photocatalytic degradation of volatile organic compounds. ACS EST Eng. 1, 1140–1148. https://doi.org/10.1021/acsestengg.1c00120.
- Yi, J., Fei, T., Li, L., Yu, Q., Zhang, S., Song, Y., Lian, J., Zhu, X., Deng, J., Xu, H., Li, H., 2021. Large-scale production of ultrathin carbon nitride-based photocatalysts for high-yield hydrogen evolution. Appl. Catal. B Environ. 281, 119475. https://doi.org/10.1016/j.apcatb.2020.119475.
- Yu, E., Li, J., Chen, Jin, Chen, Jing, Hong, Z., Jia, H., 2020. Enhanced photothermal catalytic degradation of toluene by loading pt nanoparticles on manganese oxide: photoactivation of lattice oxygen. J. Hazard. Mater. 388, 121800. https://doi.org/10.1016/j.jhazmat. 2019.121800
- Yu, J., Pang, Z., Zheng, C., Zhou, T., Zhang, J., Zhou, H., Wei, Q., 2019. Cotton fabric finished by PANI/TiO2 with multifunctions of conductivity, anti-ultraviolet and photocatalysis activity. Appl. Surf. Sci. 470, 84–90. https://doi.org/10.1016/j.apsusc.2018.11.112.
- Yusran, Y., Li, H., Guan, X., Li, D., Tang, L., Xue, M., Zhuang, Z., Yan, Y., Valtchev, V., Qiu, S., Fang, Q., 2020. Exfoliated mesoporous 2D covalent organic frameworks for high-rate electrochemical double-layer capacitors. Adv. Mater. 32, 1907289. https://doi.org/10.1002/adma.201907289.
- Yusuf, A., Garlisi, C., Palmisano, G., 2018. Overview on microfluidic reactors in photocatalysis: applications of graphene derivatives. Catal. Today 315, 79–92. https:// doi.org/10.1016/j.cattod.2018.05.041 Graphitic materials in photo(electro)catalysis.
- Yusuf, A., Oladipo, H., Yildiz Ozer, L., Garlisi, C., Loddo, V., Abu-Zahra, M.R.M., Palmisano, G., 2020. Modelling of a recirculating photocatalytic microreactor implementing mesoporous N-TiO2 modified with graphene. Chem. Eng. J. 391, 123574. https://doi.org/10.1016/j.cej.2019.123574.
- Zacarías, S.M., Pirola, S., Manassero, A., Visuara, M.E., Alfano, O.M., Satuf, M.L., 2019. Photocatalytic inactivation of bioaerosols in a fixed-bed reactor with TiO2-coated glass rings. Photochem. Photobiol. Sci. 18, 884–890. https://doi.org/10.1039/c8 pp00297e.
- Zelić, I.E., Povijač, K., Gilja, V., Tomašić, V., Gomzi, Z., 2022. Photocatalytic degradation of acetamiprid in a rotating photoreactor - determination of reactive species. Catal. Commun. 169, 106474. https://doi.org/10.1016/j.catcom.2022.106474.
- Zelić, Ivana Elizabeta, Tomašić, V., Gomzi, Z., 2022. Development of a new rotating photocatalytic reactor for the degradation of hazardous pollutants. Int. J. Chem. React. Eng. https://doi.org/10.1515/ijcre-2022-0084.
- Zhang, B., Daniel, Q., Cheng, M., Fan, L., Sun, L., 2017. Temperature dependence of electrocatalytic water oxidation: a triple device model with a photothermal collector and photovoltaic cell coupled to an electrolyzer. Faraday Discuss. 198, 169–179. https://doi.org/ 10.1039/C6FD00206D.
- Zhang, G., Sheng, H., Chen, D., Li, N., Xu, Q., Li, H., He, J., Lu, J., 2018. Hierarchical titanium dioxide nanowire/metal-organic framework/carbon nanofiber membranes for highly efficient photocatalytic degradation of hydrogen sulfide. Chem. Eur. J. 24, 15019–15025. https://doi.org/10.1002/chem.201802747.
- Zhang, J., Zeng, D., Xu, C., Hu, W., Liu, P., Cao, S., Chen, Y., 2023. One-step electrodeposition of amorphous MoSx - CdS on ti mesh as a monolithic heterostructured photocatalyst for enhanced photocatalytic H2 evolution. Surf. Interfaces 36, 102588. https://doi.org/10. 1016/j.surfin.2022.102588.
- Zhang, S., Zhang, J., Sun, J., Tang, Z., 2020. Capillary microphotoreactor packed with TiO2-coated glass beads: an efficient tool for photocatalytic reaction. Chem. Eng. Process. Process Intensif. 147, 107746. https://doi.org/10.1016/j.cep.2019.107746.
- Zhang, X., Yue, K., Rao, R., Chen, J., Liu, Q., Yang, Y., Bi, F., Wang, Y., Xu, J., Liu, N., 2022a.
 Synthesis of acidic MIL-125 from plastic waste: significant contribution of N orbital for

- efficient photocatalytic degradation of chlorobenzene and toluene. Appl. Catal. B Environ. 310, 121300. https://doi.org/10.1016/j.apcatb.2022.121300.
- Zhang, X., Zhu, Z., Rao, R., Chen, J., Han, X., Jiang, S., Yang, Y., Wang, Y., Wang, L., 2022b. Highly efficient visible-light-driven photocatalytic degradation of gaseous toluene by rutile-anatase TiO2@MIL-101 composite with two heterojunctions. J. Environ. Sci. https://doi.org/10.1016/j.jes.2022.03.014.
- Zhao, F., Chen, Z., Fan, W., Dou, J., Li, L., Guo, X., 2020. Reactor optimization and process intensification of photocatalysis for capillary-based PMMA LSC-photomicroreactors. Chem. Eng. J. 389, 124409. https://doi.org/10.1016/j.cej.2020.124409.
- Zhong, N., Chen, M., Luo, Y., Wang, Z., Xin, X., Rittmann, B.E., 2019. A novel photocatalytic optical hollow-fiber with high photocatalytic activity for enhancement of 4-chlorophenol degradation. Chem. Eng. J. 355, 731–739. https://doi.org/10.1016/j.cej.2018.08.167.
- Zhou, C., Shi, R., Shang, L., Wu, L.-Z., Tung, C.-H., Zhang, T., 2018. Template-free large-scale synthesis of g-C3N4 microtubes for enhanced visible light-driven photocatalytic H2 production. Nano Res. 11, 3462–3468. https://doi.org/10.1007/s12274-018-2003-2.
- Zhou, J., Li, J., Kan, L., Zhang, L., Huang, Q., Yan, Y., Chen, Y., Liu, J., Li, S.-L., Lan, Y.-Q., 2022. Linking oxidative and reductive clusters to prepare crystalline porous catalysts for photocatalytic CO2 reduction with H2O. Nat. Commun. 13, 4681. https://doi.org/ 10.1038/s41467-022-32449-z.
- Zhou, P., Navid, I.A., Ma, Y., Xiao, Y., Wang, P., Ye, Z., Zhou, B., Sun, K., Mi, Z., 2023. Solar-to-hydrogen efficiency of more than 9% in photocatalytic water splitting. Nature 613, 66–70. https://doi.org/10.1038/s41586-022-05399-1.
- Zhu, H., Zhen, C., Chen, X., Feng, S., Li, B., Du, Y., Liu, G., Cheng, H.-M., 2022. Patterning alternate TiO2 and Cu2O strips on a conductive substrate as film photocatalyst for Z-scheme photocatalytic water splitting. Sci. Bull. 67, 2420–2427. https://doi.org/10.1016/j.scib.2022.11.018.
- Zou, W., Gao, B., Ok, Y.S., Dong, L., 2019. Integrated adsorption and photocatalytic degradation of volatile organic compounds (VOCs) using carbon-based nanocomposites: a critical review. Chemosphere 218, 845–859. https://doi.org/10.1016/j.chemosphere.2018.11.175.





Review

Recent Progress in Photocatalytic Applications of Electrospun Nanofibers: A Review

Aigerim Serik ^{1,2}, Nurlan Idrissov ^{1,2}, Aibol Baratov ^{1,2}, Alexey Dikov ², Sergey Kislitsin ², Chingis Daulbayev ^{2,3} and Zhengisbek Kuspanov ^{1,2,*}

- Department of Materials Science, Nanotechnology and Engineering Physics, Satbayev University, Almaty 050032, Kazakhstan; aigerimserik3508@gmail.com (A.S.)
- Institute of Nuclear Physics, Almaty 050032, Kazakhstan; dikov@inp.kz (A.D.); skislitsin@inp.kz (S.K.)
- ³ Bes Saiman Group, Almaty 050057, Kazakhstan
- * Correspondence: zhenis.kuspanov@gmail.com; Tel.: +7-707-605-0464

Abstract: Electrospun fiber-based photocatalysts demonstrate significant potential in addressing global environmental and energy challenges, primarily due to their high specific surface areas and unique properties. This review examines recent advances in the application of these materials in photocatalytic processes, with a particular focus on water splitting and hydrogen production. The principles of the electrospun method are described in detail, along with the operating parameters, material characteristics, and environmental conditions that affect the fiber formation. Additionally, the review discusses the challenges, advantages, and future prospects of photocatalysts incorporating carbon materials, metals, semiconductors, and hybrid structures with improved performance. These materials have the potential to significantly improve the efficiency of hydrogen energy production, water purification, and CO₂ recovery, highlighting their importance in engineering sciences.

Keywords: electrospinning; photocatalysis; nanofibers; hydrogen; semiconductors; wastewater treatment; CO₂ utilization



Citation: Serik, A.; Idrissov, N.; Baratov, A.; Dikov, A.; Kislitsin, S.; Daulbayev, C.; Kuspanov, Z. Recent Progress in Photocatalytic Applications of Electrospun Nanofibers: A Review. *Molecules* **2024**, *29*, 4824. https://doi.org/ 10.3390/molecules29204824

Academic Editor: Lan Xu

Received: 11 September 2024 Revised: 7 October 2024 Accepted: 9 October 2024 Published: 11 October 2024



Copyright: © 2024 by the authors. Licensee MDPI, Basel, Switzerland. This article is an open access article distributed under the terms and conditions of the Creative Commons Attribution (CC BY) license (https://creativecommons.org/licenses/by/4.0/).

1. Introduction

Global environmental and energy issues have increasingly attracted attention from the scientific community due to the detrimental effects of fossil fuels on ecosystems [1]. The excessive use of oil, coal, and gas has led to a significant increase in greenhouse gas emissions, resulting in global warming and associated challenges, such as extreme weather events and rising sea levels [2,3]. For example, according to the World Health Organization (WHO), approximately 99 percent of the global population breathes air that fails to meet adequate quality standards, posing serious health risks. Each year, over 13 million people die worldwide due to air pollution and environmental causes [4].

One solution to these problems is to reduce reliance on fossil fuels and partially transition to clean renewable energy sources. A notable example of such a transition is the European Union, which, for the first time in 2021, produced 10.3% of the world's electricity from wind and solar energy, doubling its share since 2015, when the Paris Agreement was signed [5]. In May 2022, the European Commission presented the REPowerEU plan to phase out fossil fuels, proposing an investment of EUR 210 billion in renewable energy and energy efficiency. According to this plan, the capacity of renewable energy in the EU is expected to reach 1236 GW by 2030 [6]. Similar initiatives are being adopted in other countries. For example, the United States passed legislation in 2022 aimed at reducing greenhouse gas emissions by 1 Gt, including tax credits for the production of clean hydrogen, the development of new clean technologies, air capture, and clean fuels [7].

Hydrogen, in particular, has garnered significant interest as an environmentally friendly energy carrier that is expected to play a key role in the decarbonization and electrification of major energy systems in the near future [8,9]. Its high energy density and unique

Molecules **2024**, 29, 4824 2 of 18

properties make it suitable for a wide range of applications, including fuel cell vehicles, stationary power generation, and industrial processes. However, the existing difficulties in hydrogen production, storage, and transportation limit its widespread adoption [10,11]. Hydrogen production methods can be classified based on the hydrogen or energy source. These methods are divided into renewable [12] (e.g., wind energy [13], solar energy [14], geothermal energy [15,16]) and non-renewable [17] (e.g., fossil resources [13], coal gasification, catalytic reforming, partial oxidation) [18]. The use of solar energy to produce hydrogen has several advantages over traditional methods, including lower costs and scalability [19,20].

Photocatalytic water decomposition, discovered in 1972 [21], is a promising, efficient, and simple method for producing renewable hydrogen. However, despite numerous studies, the large-scale practical application of photocatalytic water decomposition to produce pure hydrogen remains challenging [22]. Nevertheless, ongoing research allows us to confidently discuss the prospects and competitiveness of this method for effective hydrogen production [23]. The primary issue limiting the practical application of current photocatalysts is the low quantum efficiency of solar energy conversion. This challenge can be addressed by creating hybrid composite structures based on photocatalysts, achieved through doping with various elements or combining them with the plasmonic effect of noble metals (Au, Ag, or Pt) or narrow-bandwidth semiconductors [24]. From this perspective, electrospinning is a versatile, simple, and cost-effective technique for producing composite structures with a high specific surface area-to-volume ratio and the ability to regulate their composition and morphology. Given that this method is widely used in various fields, such as water purification [25], tissue engineering [26,27], and the production and delivery of medicinal products [28,29], and its scalability, it has significant potential for developing effective photocatalytic systems. Unlike conventional photocatalysts, electrospun nanofiber photocatalysts have several advantages, such as significant specific surface area, high porosity, and the possibility of surface modification to enhance photoactivity [30].

Over the past decade, there has been a notable increase in research articles featuring the keywords "photocatalysis" and "electrospinning". An analysis of publications indexed in the Scopus database from 2014 to 2024 reveals that 60,851 publications include the keyword "electrospinning" and 36,138 publications feature "photocatalysis". Figure 1 suggest that research in this area will continue to increase. A quantitative analysis of the countries, institutions, and journals most engaged in research on photocatalysis and electrospinning shows that China is the most active, followed by India, the United States, South Korea, Japan, Germany, and Iran. In terms of citation impact, the United States leads, followed by Germany and Japan, indicating the wide use of the electrospinning method for developing composite photocatalytic systems. This review discusses the latest achievements in the formation of hybrid photocatalytic systems using electrospinning, specifically for hydrogen production. A detailed analysis of the effect of the method on the mechanism and efficiency of photocatalytic water decomposition is performed, along with the exploration of future prospects and challenges. Electrospinning is demonstrated as an efficient, low-cost approach to developing hybrid composite photocatalytic systems.

Molecules **2024**, 29, 4824 3 of 18

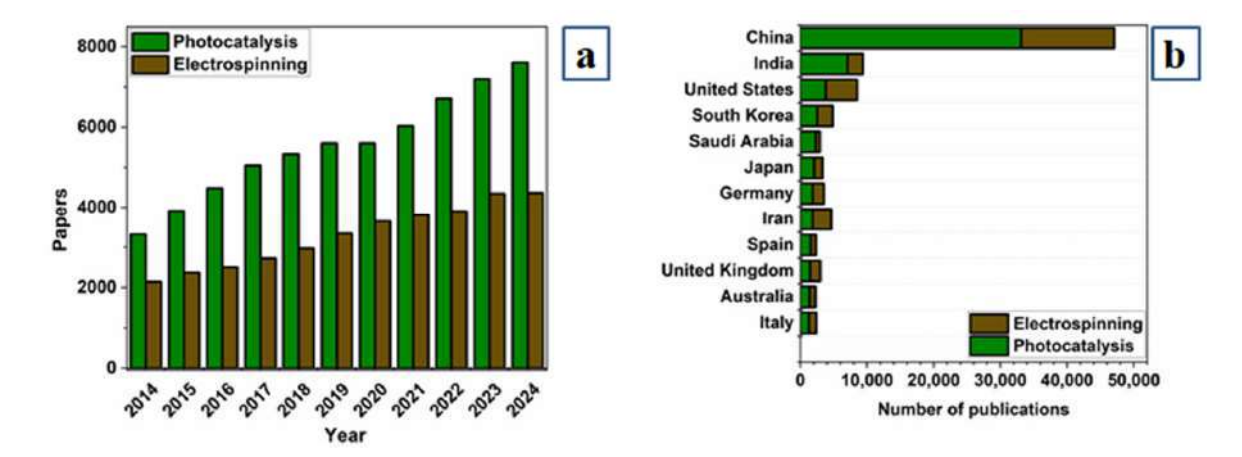


Figure 1. (a) Statistics from the Scopus database showing publication trends and keyword matches with the search string TITLE ("photocatalysis") AND TITLE-ABS-KEY ("electrospinning") from 2014 to 4 September 2024. (b) Distribution of publications by country.

2. Principle of Electrospinning Method

Electrospinning is a method used to fabricate one-dimensional (1D) nanofibers from organic, inorganic, and hybrid materials [31,32]. The concept of electrospinning originated in 1600 with William Gilbert, who observed the formation of a drop of water in an electric field. In 1902, John Cooley and William Morton filed the first patents describing a prototype electrospinning rig. In 1934 and 1944, Anton Formhals filed several more patents, improving equipment to commercialize the electrospinning process [33]. The foundation of electrospinning research can be traced back to the pioneering work by Taylor from 1964 to 1969, which modelled the formation of spherical and conical shapes in polymer solutions or melt droplets under the influence of an electric field [34]. These studies initiated the development of the electrospinning method. In the early 1980s, Donaldson Co. Inc. in the United States began producing and marketing air filters fabricated using this method [33]. A new impetus for the development of electrospinning came with the introduction of electron microscopes in the early 1990s, which enabled the examination of nanoscale structures. Researchers, including Reneker and Rutledge, discovered that nanoscale fibers could be drawn from solutions of various organic polymers [35,36].

Electrospinning operates based on an electrohydrodynamic process in which a droplet of a liquid polymer is electrified to form a jet that is then stretched and elongated to produce a fiber. The typical electrospinning setup is relatively simple (Figure 2), making it accessible to most laboratories. The main elements of an electrospinning apparatus include a high-voltage power source, a needle through which the polymer solution is dispensed, and a conductive collector to collect the incoming polymer. These elements are combined into a single electrical circuit. During electrospinning, the liquid is squeezed out of the needle, forming pendant droplets due to surface tension. As the electrical voltage at the tip of the needle increases, the surface tension of the polymer solution is overcome, resulting in the formation of a Taylor cone from which a charged jet is ejected. Once the voltage is sufficient, the polymer jet rushes from the top of the cone towards the collector. The diameter of the resulting fibers depends on several factors. In air, part of the solvent evaporates, and the jet splits, depositing pure polymer on the collector as randomly or directionally aligned nanofibers with sizes ranging from nanometers or micrometers. The resulting material resembles a fibrous, porous soft fabric or a thin elastic coating. The fiber formation process can be divided into four stages [33].

Molecules **2024**, 29, 4824 4 of 18

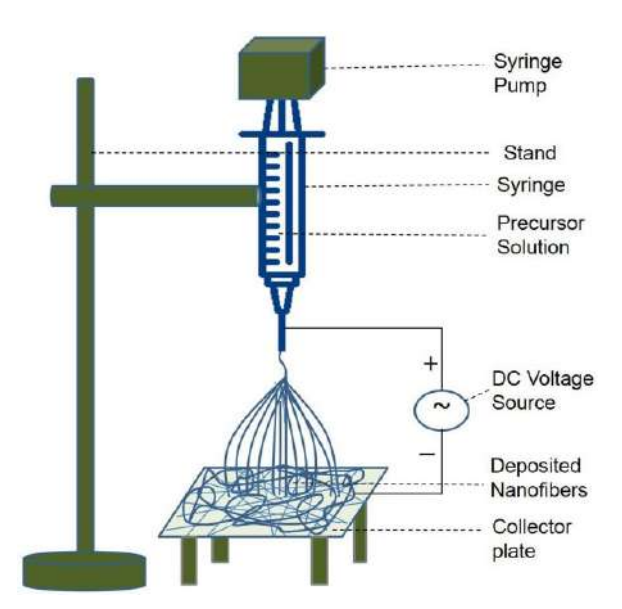


Figure 2. Schematic diagram of a typical electrospinning set up for preparation of nanofibers (reproduced from [37] with permission of Elsevier, 2019).

Formation of a Taylor cone from which liquid is released.

Expansion of the charged jet along a straight line.

- Stretching of the jet due to the increased electric field voltage, leading to electrical bending instability.
- Solidification of the jet in the form of solid fiber(s) on a grounded collector.

The process of fiber formation by electrospinning is influenced by various operating, material, and environmental parameters.

First, the formation and deposition of fibers are affected by the electric field strength. Thinner fibers are usually formed at higher voltages, while thicker fibers or no fibers are formed at low voltages [38–40]. For example, increasing the voltage to 60 kV produced the thinnest nanofibers with a diameter of 190.21 \pm 36.65 nm [41].

Second, the diameter and morphology of the resulting fibers are affected by the flow rate at which the polymer solution is fed into or ejected from the spinneret. To maintain a stable Taylor cone, the liquid flow rate must be adjusted continuously to match the voltage. A uniform Taylor cone results in the production of uniform nanofibers with narrow dispersion [42–45].

Third, the distance between the needle tip and the collector impacts the diameter and shape of the fibers. The minimum distance required ensures that the solvent has sufficient time to evaporate before the fiber reaches the collector. Increasing this distance results in thinner fibers. However, if the distance is too large or small, bead formation may occur [46,47].

Fourth, material properties, including the molecular weight of the polymer, viscosity of the solution, and concentration, play a crucial role in determining fiber size and structure. A higher polymer molecular weight or concentration increases fiber size. A study on the effects of PVA concentration and molecular weight (low, medium, and high) on the morphology of electrospun fibers showed that the formation of beads decreased with higher polymer concentration and molecular weight. However, at high molecular weights and concentrations, uneven and thick fibers were observed due to the increased solution viscosity [48]. High-viscosity colloidal polymer solutions can lead to an unstable jet state, resulting in fibers with a banded structure [49]. If the viscosity is too high, the solution may dry at the tip of the needle before electrospinning begins, complicating the process [47]. Notably, the choice of polymer significantly affects the formation of fibers; higher-viscosity polymer solutions typically produce fibers with larger diameters [50]. For example, using 14 wt% and 16 wt% polyvinylidene fluoride (PVDF) solutions, the 16 wt% solution yielded

Molecules **2024**, 29, 4824 5 of 18

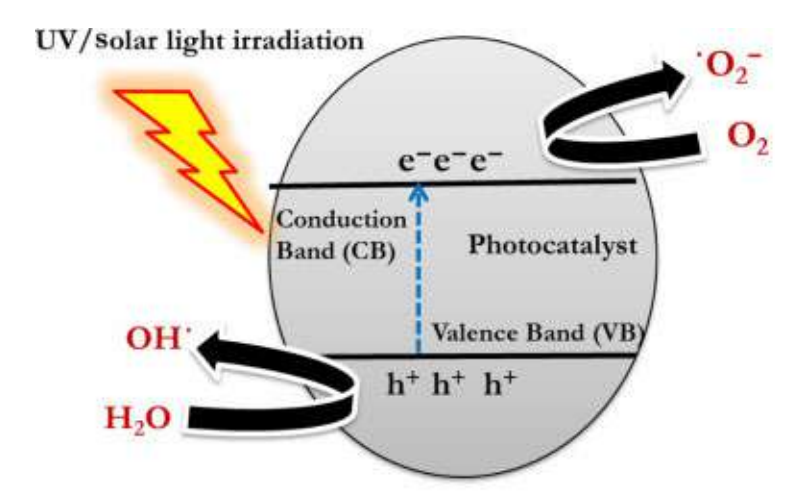
fewer beads and formed a membrane-like structure [51]. This is attributed to the formation of long-chain linkages in the polymer, which ensure the continuity of the jet [52].

Finally, environmental parameters such as temperature [53] and humidity significantly affect the electrospinning process and fiber morphology. Increasing the temperature to 45 °C decreased fiber diameter from 600 nm to 213 nm due to decreased solution viscosity and surface tension [54]. Similarly, increasing the relative humidity from 5.1% to 48.7% decreased fiber diameters from 253 nm to 144 nm. At humidity levels above 50%, beads formed on the fibers due to capillary instability [55].

3. Application of Electrospun One-Dimensional Photocatalysts

Electrospinning is a versatile, simple, and cost-effective method for producing high-quality 1D nanomaterials. However, there are certain problems associated with photocatalysts made from electrospun fibers. These problems include the recombination of charge carriers: the rapid recombination of electrons and holes reduces the efficiency of photocatalysis. Additionally, degradation of materials under ultraviolet light can lead to a loss of activity, and low quantum efficiency limits their application in visible light conditions [56].

To address these issues, the surfaces of the materials can be modified. Since the photocatalytic properties of fibers primarily depend on the catalytic components, this opens up opportunities for creating 1D fibrous materials with tunable chemical composition, morphology, high specific surface area, high porosity, and varying fiber diameters. Such 1D photocatalysts are particularly promising for various applications, as they provide better light harvesting and enhanced reaction efficiency. Additionally, doping and composite formation are possible: incorporating metallic or non-metallic dopants, as well as creating composites with other semiconductors, can reduce electron–hole recombination and extend the activity of photocatalysts (Figure 3) in the visible spectrum [57].



Organic contaminants + 'O₂-(or OH ')→ CO₂ + H₂O

Figure 3. General mechanism of a photocatalytic reaction (reproduced from [58] with permission of Elsevier, 2020).

This section discusses the unique properties of 1D nanofibers and their applications in photocatalytic water decomposition, with a focus on various photocatalyst options incorporating carbon materials, metals, and semiconductors.

3.1. Development of Various Electrospun Composite Nanofibers for Photocatalytic Applications

One of the most effective ways to improve the properties of 1D photocatalysts involves the incorporation of carbon materials, such as graphene, carbon nanotubes, and carbon nanoparticles. Graphene, a 2D carbon material with a honeycomb lattice structure, exhibits high electrical conductivity, sufficient mechanical strength, and good chemical sta-

Molecules **2024**, 29, 4824 6 of 18

bility, making it an ideal co-catalyst. It can be easily incorporated into conductive fibers by dispersing it in a polymer solution before electrospinning. The resulting fibers exhibit high electrical conductivity and a large surface area, facilitating efficient light absorption and charge separation on the catalyst surface [59–61]. In addition, graphene can be modified with various surfactants to enhance its adsorption efficiency. For example, reduced graphene oxide (rGO) and titanium dioxide (TiO₂) composite fibers have shown significant improvements in the photocatalytic degradation of methyl orange compared to pure TiO_2 [62]. Similar studies demonstrated that C/TiO₂ nanofibers carbonized at 400 °C exhibit superior photocatalytic activity for MB degradation. This increased efficiency is attributed to the transfer of photogenerated electrons from the conduction band of TiO_2 to the carbon during photocatalysis, leading to a more efficient separation of electrons and holes [63].

However, the primary limitation of graphene and graphene oxide as photocatalysts is their poor absorption of visible light. To address this, dye molecules that absorb visible light have been used as effective photosensitizers [64]. Positively charged dye molecules that absorb visible light are easily attracted to the negatively charged graphene oxide system due to the electrostatic forces of attraction. Studies [65] demonstrated that a photocatalyst comprising graphene oxide and positively charged dye molecules, without the inclusion of noble metals, exhibited activity two orders of magnitude higher than that of conventional TiO₂-based catalysts.

There is also growing interest in carbon nitride, with approximately 10–12% of research on photocatalytic hydrogen production focusing on photocatalysts based on graphite-like carbon nitride (gC_3N_4) [66]. It is known for its stability, good light absorption (up to 460 nm) [67], large surface area and cost-effectiveness [68]. However, its photocatalytic efficiency is limited due to the high rate of electron–hole recombination, which prevents efficient reduction of H_2 [69].

Semiconductor-based photocatalysts, particularly in the form of nanofibers, such as TiO₂ [70], ZnO [71,72], and SrTiO₃ [73–75], are known for their light-absorbing properties, high surface-area-to-volume ratio, and mechanical strength. TiO₂ [76,77] exhibits high photocatalytic activity owing to its three main crystal structures with bandgap energies of 3.2, 3.0 and 3.1 eV. ZnO [78] has a higher light absorption capacity than TiO₂; however, the issue of photocorrosion under UV radiation remains [79].

While these materials are extensively studied, semiconductors face challenges related to high bandgap energy and chemical stability. To improve their efficiency, many researchers have used metal or non-metal doping or combined them with other semiconductors that operate effectively under visible-light irradiation [80,81]. However, this approach limits the ability of semiconductors to absorb visible light, which constitutes the majority of the solar spectrum.

In this context, sulfide (CdS, MoS₂) [82] and nitride (GaN, InN) [83] semiconductors have attracted considerable interest due to their small bandgaps, which enable efficient visible-light absorption. Sulfide semiconductors possess bandgaps ranging from 2.0 to 2.4 eV, enhancing their performance in the visible spectrum. However, a significant challenge with these materials is the high recombination rate of electron–hole pairs [84], which reduces their photocatalytic efficiency. Various approaches have been used to address this problem, including the addition of cocatalysts and the creation of heterojunctions [85], which aim to increase the lifetime of the charge carriers and improve photocatalytic efficiency.

Noble metals such as platinum, gold and palladium are widely used as cocatalysts for semiconductors [86–89]. These metals facilitate efficient electron transfer and reduce the probability of recombination. Additionally, they act as "traps" for electrons, extending their lifetime and increasing the number of photogenerated charge carriers.

Base metals such as iron, copper, nickel, and cobalt [90–92], are also used as cocatalysts. Although they are less efficient than noble metals, they offer a more cost-effective

Molecules **2024**, 29, 4824 7 of 18

solution by creating additional active sites on the photocatalyst surface and enhancing charge-carrier dissociation.

3.2. Application of Electrospun Nanofibers for Hydrogen Production

Nanofibers obtained by electrospinning have recently been considered as promising candidates for applications in the photocatalytic production of solar hydrogen [73,93]. The process of photocatalytic water splitting to produce hydrogen involves three stages: light absorption leading to the formation of electron–hole pairs, charge separation and transport, followed by oxidation–reduction reactions. To efficiently split water, the photocatalyst must have a sufficient bandgap and suitable potentials for hydrogen and oxygen generation [94–97]. Therefore, there is a demand for the development of new, more efficient photocatalysts to harness solar energy effectively. A promising direction is the use of nanofiber photocatalysts, which have unique properties such as high surface area, improved charge transfer, and the ability to finely tune the morphology and structure of the material.

Electrospinning is an effective approach for synthesizing nanofiber photocatalysts [98]. The composites obtained using this method demonstrated improved characteristics compared to traditional photocatalysts, making them promising candidates for practical applications in hydrogen energy. In particular, sulfur-doped g- C_3N_4 nanofibers demonstrate 2.84 times higher activity in hydrogen evolution (632 μ mol/h g) compared to bulk sulfur-doped g- C_3N_4 , under similar conditions [93].

In addition, powder photocatalysts tend to settle, complicating recovery and reuse. In contrast, composite nanofiber membranes do not require mechanical stirring or ultrasound, which improves reaction stability. In particular, the ZIS/PAN membrane showed 3.7 times higher hydrogen production than ZIS powder while also simplifying the recovery process and demonstrating good stability, making it a promising solution for practical photocatalyst applications [99,100].

Carbon nanofibers obtained by electrospinning are highly effective at accumulating and transporting charge [74,101]. However, their photocatalytic efficiency may be hindered by issues such as limited active sites, rapid charge recombination, and high overpotential during hydrogen generation [93]. Possible solutions include the decoration of co-catalysts, which can increase the absorption of visible light, create more active sites, and influence charge carrier dynamics. For example, hydrogen evolution on electrospun porous TiO₂ nanofibers with NiS and Pt cocatalysts, deposited via wet-chemical and self-assembly methods, increased 292 times compared to pure TiO₂ nanofibers [102]. This significant increase in visible-light photocatalytic activity of the TiO₂/NiS/Pt nanofibers upon deposition with cocatalysts can be attributed to enhanced absorption of visible light and more efficient separation of photogenerated electrons and holes.

In cocatalyst-electrospun nanofiber systems, selecting the optimal amount of cocatalyst is crucial for maximizing hydrogen generation efficiency. For example, one study [103] showed that as the content of the cocatalyst $Cd_{0.5}Co_{0.5}S$ increased from 1.0 to 9.0 wt. %, the rate of hydrogen production using solar energy initially increased and then decreased. The highest efficiency of 4.55 mmol g^{-1} h⁻¹ was achieved at 5.0 wt. % $Cd_{0.5}Co_{0.5}S$. The decrease in efficiency at higher concentrations was attributed to excessive cocatalyst content, which hinders charge separation, blocks active centers, and promotes the recombination of charge carriers, thus inhibiting photocatalytic water splitting [104]. As demonstrated in Table 1, the highest efficiency of photocatalytic hydrogen evolution was achieved with the nanofibers decorated with nanoparticle cocatalysts.

Molecules **2024**, 29, 4824 8 of 18

Table 1. Recent research results (2022–2024) on the use of electrospun nanofiber-based photocatalysts in H_2 production.

Year	Photocatalyst	Light Source	Sacrificial Agent	H ₂ Evolution Rate (mmol h ⁻¹ g ⁻¹) and AQY	Ref.
2023	Sg-C ₃ N ₄ nanofiber	Metal halide 400 W, full spectrum	20 vol.% methanol	0.632	[105]
2023	TiO ₂ /NiS/Pt nanofiber	5 W blue LED light, λmax = 420 nm	50 vol.% methanol	4.411	[102]
2024	NiGa ₂ O ₄ /ZnIn ₂ S ₄ nanofiber	300 W Xe-lamp, AM 1.5 filter, 41.7 mW/cm ²	10 vol.% TEOA	9.292	[93]
2024	CoGa ₂ O ₄ /ZnIn ₂ S ₄ nanofiber	300 W Xe-lamp, AM 1.5 filter, 41.7 mW/cm ²	10 vol.% TEOA	6.283	[93]
2022	Cd0.5Co0.5S/SN-TiO2 nanofiber	300 W Xe-lamp	$2.4 \text{ g Na}_2\text{S}$, and 1.26 g Na_2SO_3 into 100 mL deionized H_2O	4.55 and AQY of 19.01% at 410 nm	[103]
2024	ZnIn ₂ S ₄ /PAN nanofiber membrane	Visible light (420 nm $\leq \lambda \leq 700$ nm)	10 vol.% TEOA	1.836 and AQY of 1.77% at 365 nm	[99]
2023	S-scheme BaTiO ₃ /Ag ₂ S nanofiber	300 W Xe-lamp	Na2S (0.35 mol/L) and Na ₂ SO ₃ (0.25 mol/L)	0.597	[106]
2024	In ₂ S ₃ -In(OH) ₃ -ZnS nanofibers	5 W blue LED light $(\lambda max = 420 \text{ nm}, 41.7 \text{ mW cm}^{-2})$	0.1 M Na ₂ S solution	0.2236	[107]
2024	C-Ni ₂ P/ZnCr ₂ O ₄ nanofibers	Xe lamp intensity of 350 mW cm ⁻²	$0.2~{\rm g~Na_2S}$, and $0.2~{\rm g}$ ${\rm Na_2SO_3}$ into $100~{\rm mL}$ deionized ${\rm H_2O}$	0.5759 and AQY of 15.25% at 420 nm	[108]
2023	CdS NPs-decorated ZnO nanofibers	500 W Xe lamp with 425 nm band pass filter	0.35 M Na ₂ S and 0.25 M Na ₂ SO ₃	0.820	[109]

Photocatalytic hydrogen production based on electrospun nanofibers has great potential. However, several challenges remain for its practical implementation. These include (1) increasing the mechanical strength of nanofibers after heat treatment and (2) using safe and non-toxic solvents during electrospinning [37]. To achieve high-efficiency hydrogen generation, the development of photocatalytic material that absorbs light over a broad wavelength range and ensures efficient separation and migration of charged particles is essential. A particularly promising research direction is the fabrication of electrospun nanofibers with controlled properties and the formation of heterostructures with integrated nanoparticles, which could significantly increase their photocatalytic activity.

3.3. Application of Electrospun Nanofibers for Water Treatment

Composite photocatalysts synthesized by electrospinning are promising materials for purifying water from organic pollutants [87]. As previously noted, nanofibers obtained using this method exhibit a high specific surface area and a developed porous structure, enhancing their adsorption properties and access to active photocatalytic centers. This facilitates the effective destruction of stable organic compounds, such as benzene rings and carbonyl groups [110].

The most widely used photocatalysts in nanofibers are metal oxides, such as TiO_2 and ZnO, due to their high catalytic activity and environmental safety [111]. When exposed to ultraviolet or visible light, these materials generate electrons and holes, which react with oxygen to form active oxides and hydroxyl radicals. These highly reactive species break the stable chemical bonds in pollutant molecules, such as C=C and CN bonds, mineralizing them into carbon dioxide and water. However, the bandgaps of these materials, 3.2 eV (for TiO_2) and 3.37 eV (for ZnO), limit their absorption to ultraviolet radiation, which constitutes only 4–5% of the solar spectrum, reducing their effectiveness in the visible range [112]. In addition, the rapid recombination of photogenerated electron–hole pairs reduces the

Molecules **2024**, 29, 4824 9 of 18

number of charge carriers involved in redox reactions, thereby diminishing the photocatalytic efficiency [113].

To increase the photosensitivity and efficiency of TiO_2 , various modifications including doping with noble metals, transition metals, rare-earth elements, and nonmetals have been explored [30]. In particular, N,F-doping of TiO_2 - δ nanofibers, developed by researchers [114], increased the degradation rate of RhB, MB and Cr(VI) dyes by 11.8, 3.2 and 2.8 times, respectively, compared to commercial TiO_2 . Doping narrows the bandgap, enabling the photocatalyst to function under visible light. This effect is attributed to the hybridization of the 2p orbitals of nitrogen with the 2p orbitals of oxygen in the valence band of TiO_2 , enhancing the separation of electron–hole pairs and reducing recombination [115,116]. Fluorine doping also improves light absorption at long wavelengths due to the similarity in ionic radii between fluorine and oxygen. The researchers further suggested that multi-element doping could provide even more improvements in photocatalytic performance compared to single-component doping.

Another promising approach to improving the photocatalytic properties of materials involves the creation of binary and ternary composites based on various metal oxides. For example, combining TiO_2 with ZnO or Bi_2WO_6 leads to the formation of heterostructures that promote more efficient charge separation and broaden the spectrum of photocatalytic activity [117,118]. Ternary composites, such as NT@BMO and NT@BWO, exhibit high photocatalytic efficiency due to the synergistic interaction between components, resulting in improved adsorption of pollutants and more effective degradation of organic molecules.

Similarly, the composite NT@BWMO, a ternary heterostructure with controlled morphology and composition, was obtained by depositing BWMO on the surface of N-TiO₂ NF [114]. The NT@BWMO-0.25, NT@BWMO-0.5 and NT@BWMO-0.75 samples synthesized at different W/Mo molar ratios (0.25, 0.75, 0.5, 0.5, and 0.75/0.25, respectively) exhibited > 99% tetracycline removal efficiency under visible-light irradiation. Among them, the NT@BWMO-0.25 sample showed the highest tetracycline degradation rate (TC) of 0.0054 min^{-1} , which is 9.0, 2.5 and 1.8 times higher than that of N-TiO₂, NT@BMO and NT@BWO, respectively. The enhanced photocatalytic activity of NT@BWMO-0.25 is attributed to the improved adsorption, optimal crystal size, a narrower bandgap, and enhanced visible-light absorption. Photoluminescence (PL) and photoelectrochemical performance (PEC) analyses confirmed that a lower tungsten ion content improved carrier mobility and increased the carrier separation rate. Radical scavenging experiments and electron paramagnetic resonance (EPR) results showed that O_2^- radicals and h^+ holes played a crucial role in the photocatalytic degradation process, while the influence of hydroxyl radicals was minimal. The photocatalytic activity of NT@BWMO-0.25 slightly decreased from 99.4% to 91%, indicating that the material can be reused multiple times without significant loss of efficiency.

Based on the data presented in Table 2, it can be concluded that the use of composites with multicomponent heterostructures achieves 99–100% water purification from various organic pollutants under the influence of visible light. However, the addition of g- C_3N_4 to nanofibers does not result in equally high photocatalytic activity. This is attributed to the limitations of the material, such as high charge recombination rates, low conductivity, and a tendency to aggregate, which reduces surface area. However, graphite-like carbon nitride (g- C_3N_4), consisting of tri-s-triazine structural units, is the most stable isomer, providing nanofibers with high thermal and chemical stability, thereby increasing their durability in photocatalytic applications [119].

Electrospinning allows the synthesis of materials with unique adsorption and photocatalytic properties, ensuring the complete removal of organic pollutants [120]. Nanofiber composites also exhibit high wear resistance, making them suitable for repeated use. However, scaling this technology for industrial application remains a challenge. To integrate this technology into mass production, new approaches that increase productivity without compromising material quality must be developed. Promising areas include increasing

the speed of nanofiber formation, introducing multijet electrospinning, and developing cost-effective raw materials.

Year	Photocatalyst	Light Source	Pollutant	Time	Efficiency	Ref.
2021	ZnFe ₂ O ₄ /Ag/AgBr	UV light	Rhodamine B	100 min	86%	[121]
2020	Bimetal-PANNM	UV-visible	Reactive blue	60 min	99.99%	[122]
2021	TiO ₂ @Ag@Cu ₂ O	Visible light	Methylene Blue	90 min	99%	[123]
2020	$ZnIn_2S_4/SnO_2$	Visible light	Čr(VI)	80 min	100%	[124]
2020	Co-CdSe@ECNFs	Visible light	Methylene Blue	90 min	87%	[125]
2021	ZnO	UV light	Methylene Blue	85 min	90%	[87]
2021	Bi_2O_3/g - C_3N_4	Visible light	Tetracycline	180 min	~60%	[126]
2020	Mn_2+/ZnO	Visible light	Rhodamine B	260 min	~80%	[127]
2021	Ag ₃ PO ₄ -TiO ₂ CNFs	Visible light	Methylene Blue	10 min	100%	[128]
2021	Ag/BiVO ₄	Visible light	Rhodamine B	20 min	~100%	[129]
2020	ZnO-TiO ₂ CNFs	Visible light	Methylene Blue	120 min	~95%	[130]
2023	g-C ₃ N ₄ (TiO ₂ /g-C ₃ N ₄ @LCNFs	UV light	Rhodamine B	90 min	83.8%	[131]
2022	Chitin-modified and graphene oxide (GO) bridged TiO ₂ /carbon fibers (CGTC)	Visible light	Rhodamine B	60 min	86.8%	[132]
2022	PAN/Bi ₂ MoO ₆ /Ti ₃ C ₂ (PAN/BT)	UV-visible	Tetracycline	180 min	90.3%	[133]
2023	CuBi ₂ O ₄ @WO ₃	Visible light	Tetracycline hydrochloride (TCH)	120 min	70.42%	[134]

3.4. Application of Electrospun Nanofibers for CO₂ Reduction

One of the most promising applications of composite photocatalysts produced via electrospinning is the reduction of CO_2 into high-value-added products [135]. This process not only mitigates carbon dioxide emissions but also generates clean energy sources, playing a pivotal role in sustainable development and the fight against climate change. In recent years, significant research efforts have been directed towards the development and optimization of materials for photocatalytic CO_2 reduction [136].

A particularly promising approach for enhancing photocatalytic CO₂ reduction efficiency is the synthesis of graphene-based nanostructured materials. Graphene, due to its superior charge carrier mobility, large surface area, structural flexibility, and chemical stability, has been widely investigated for improving the photocatalytic performance of semiconductors. Specifically, the development of homogeneous ternary nanocomposites composed of graphene, noble metals, and semiconductors—without agglomeration or overpacking of grapheme—is emerging as a reliable approach for CO₂ photoreduction [137]. Utilizing negative electric potential in the coaxial electrospinning technique enables the production of core-shell nanofibers (NFs), where metal ions concentrate beneath the rGO layer that uniformly wraps the entire fiber. These rGO monolayers, concentrated on the surface of silver (Ag), efficiently transport and collect photogenerated electrons for CO₂ reduction while enhancing light-capturing abilities, allowing the utilization of a broader light spectrum, from ultraviolet to visible. Under visible light, rGO/Ag/TiO2 NFs demonstrated 25 times higher CO₂ photoreduction efficiency, producing 4301 μmol gNF⁻¹ CH₄ in 7 h, compared to conventional semiconductor nanofibers. Similarly, graphene's efficacy is highlighted in a study combining graphene with PVDF (polyvinylidene fluoride) and TiO_2 , which achieved a yield of 363 µmol g^{-1} in 1 h, significantly higher than the result without graphene (28.3 μ mol g⁻¹ in 1 h) [138]. However, it is important to note that an excessive amount of graphene may complicate the electrospinning process and reduce

Molecules **2024**, 29, 4824 11 of 18

photocatalytic efficiency due to aggregation, which blocks incident light and hinders photocatalysis.

In addition to graphene, doping semiconductors with single-atom metal catalysts has been recognized as an effective strategy for enhancing the efficiency of photocatalytic CO_2 reduction [139]. Titanium dioxide (TiO_2), known for its high photocatalytic activity, thermodynamic stability, non-toxicity, and low cost, has been widely utilized in CO_2 reduction processes [140]. Electrospun TiO_2 nanoparticles serve as ideal substrates for the growth of secondary nanostructures, facilitating the creation of heterojunction photocatalysts. These hybrid heterojunctions improve electron–hole separation, enhance light absorption, and promote reactant activation, resulting in superior photocatalytic performance. For instance, TiO_2 nanofibers coated with graphitic carbon nitride (gC_3N_4) achieved CO and CH_4 yields of 5.19 and 1.65 μ mol/g, respectively, representing a 1.8-fold increase in CO_2 conversion performance compared to gC_3N_4 alone [141]. However, TiO_2 faces limitations such as low surface active site density, a high recombination rate of photogenerated charge carriers, and limited CO_2 capture efficiency. To overcome these challenges, various modification strategies have been explored [142].

In parallel with TiO₂, alternative semiconductor materials have been investigated for photocatalytic CO₂ reduction, including metal oxides (e.g., ZnO), metal chalcogenides (e.g., ZnS, CdS), perovskite halides (e.g., CsPbBr₃), MXenes (e.g., Ti₃C₂), layered double hydroxides, and metal–organic frameworks [143–145]. However, these materials often exhibit low practical efficiency due to rapid electron–hole recombination and limited sunlight utilization. Consequently, significant efforts have been made to develop more efficient photocatalysts by manipulating their morphology, adjusting the bandgap, and introducing metals to improve performance [146].

Recently, single-atom catalysts (SACs) have gained considerable attention in various catalytic reactions due to their unique physical and chemical properties [147]. Several SAC-based photocatalysts, including Cu/CN [148] and Pt@WS₂ [149], have been synthesized. In particular, doping TiO₂ with noble metals significantly enhances catalytic activity through three primary mechanisms: Fermi level alignment, efficient electron trapping, and the creation of thermal catalytic sites for adsorbed molecules and reaction intermediates [123]. For instance, co-deposition of Pt on TiO₂ has demonstrated exceptional activity in CO₂ conversion to CH₄, outperforming pure TiO₂ by a factor of 10 [150]. This enhanced performance is attributed to Pt nanoparticles acting as electron traps, facilitating charge separation on the TiO₂ surface. On the other hand, Au/TiO₂ nanofibers exhibit lower activity in CH₄ production but demonstrate higher CO production, highlighting new possibilities for selective control of photocatalytic reaction products.

The key parameters and results of recent studies on the photocatalytic reduction of CO_2 into value-added products are summarized in Table 3. Based on a comparative analysis, the Ni-MoP@NCPF photocatalyst exhibits the highest efficiency in reducing CO_2 to CO [151] (953.33 µmol $g^{-1}h^{-1}$), while the Graphene@PVDF@TiO2 composite [138] shows superior efficiency in CH_4 formation (363 µmol g^{-1} h^{-1}) under visible-light irradiation. When comparing photocatalysts, it is essential to consider the use of sacrificial agents, carbon and hydrogen sources, and the type of radiation.

Molecules **2024**, 29, 4824 12 of 18

Table 3. Recent research results (2020–2024) on the use of electrospun nanofiber-based photocatalysts for CO₂ reduction into value-added products.

Photocatalytic Nanofibers	Light Source	Reagent	Products	Reaction Rate	Ref.
g-C ₃ N ₄ /black titania	300 W Xe-arc lamp	$CO_2 + H_2O + TEOA$	CO and CH ₄	5.19 and 1.65 μmol/g	[141]
(rGO)-wrapped Ag/TiO ₂	500 W Xe lamp with a 400-nm long pass filter	$CO_2 + H_2O$ vapor	CH_4	$4.301~\mu mol~g^{-1}$	[137]
Ni-NiS/C/ZnO	350 W simulated solar Xe arc lamp, 10,117 μW cm ⁻²	CO ₂ + H ₂ O + NaHCO ₃	CO and CH ₄	$5.86~{ m and} \ 1.14~{ m \mu mol}~{ m g}^{-1}~{ m h}^{-1}$	[152]
NiS@Ta ₂ O ₅	Xe lamp, 920 mW cm ⁻²	$CO_2 + H_2O$	CO and CH ₄	43.27 and 6.56 μ mol g ⁻¹ h ⁻¹	[153]
TiO ₂ /MoSe ₂	300 W Xe-arc lamp, 12 mW/cm ²	$CO_2 + H_2O + TEOA$	CH ₄ and CO	174.02 and 478.46 μmol/g	[154]
Nb_2O_5	18 W mercury lamp, 254 nm	$CO_2 + H_2O$ vapor	CO and CH ₄	8.5 and 0.55 μ mol g ⁻¹	[155]
Ni-MoP@NCPF	300 W Xe lamp with a UVCUT 420-nm filter	CO ₂ + acetonitrile/H ₂ O + TEOA	СО	953.33 μ mol $g^{-1}h^{-1}$	[151]
C doped TiO ₂	300 W Xe lamp, AM 1.5 filter	CO ₂ + H ₂ O + NaHCO ₃ + H ₂ SO ₄	CH_4	$55.17~\mu mol~g^{-1}~h^{-1}$	[156]
SrTi1-xCuxO ₃ -H ₂	300 W Xe lamp, (400 nm $< \lambda < 780$ nm)	$CO_2 + H_2O$	CH ₃ OH	$5.38~\mu mol~g^{-1}~h^{-1}$	[157]
Graphene@PVDF@TiO2	Two 300 W visible light sources (UV < 5%)	$CO_2 + H_2O$	CH_4	$363~\mu mol~g^{-1}~h^{-1}$	[138]
TiO ₂ /MoS ₂ /g-C ₃ N	300 W Xe-arc lamp, 12 mW/cm ²	$CO_2 + H_2O + TEOA$	$\mathrm{CH_4}$	21.78 μ mol g $^{-1}$	[158]

4. Conclusions

In conclusion, electrospun nanofiber photocatalysts demonstrate significant potential for practical application in hydrogen energy, water purification and CO₂ recovery. The advantages and prospects of various photocatalyst modifications, including the addition of carbon materials, metals, and semiconductors, as well as the development of hybrid structures with improved characteristics, are discussed. Due to their unique physicochemical properties, such as large specific surface area and improved charge separation, these materials can significantly improve photocatalytic efficiency. However, for widespread implementation, several technical challenges must be addressed, including increasing the mechanical strength of nanofibers post-heat treatment and using safe, non-toxic solvents during synthesis. The prospects for further development of electrospun composite materials offer broad opportunities to enhance their photocatalytic properties. Research in this area can focus on optimizing the composition and structure of nanofibers, utilizing new cocatalysts, and modifying the surface to improve the efficiency of light absorption and solar energy conversion processes. A key challenge is addressing the issues related to electron hole recombination, as well as developing cost-effective solutions to increase the lifespan and stability of photocatalysts. These directions could significantly expand the application of electrospun materials in environmentally friendly technologies and energy-saving processes, including photocatalytic hydrogen production and water purification.

Author Contributions: Writing—original draft preparation, A.S.; Conceptualization, methodology, investigation, N.I. and A.B.; Project administration, funding acquisition, A.D. and S.K.; Writing—review and editing, C.D. and Z.K. All authors have read and agreed to the published version of the manuscript.

Funding: This research is funded by the Science Committee of the Ministry of Science and Higher Education and of the Republic of Kazakhstan (Grant No. BR18574073).

Institutional Review Board Statement: The study did not require ethical approval.

Informed Consent Statement: Not applicable.

Data Availability Statement: Data are contained within the article.

Conflicts of Interest: The authors declare no conflict of interest.

References

 Letcher, T.M. 9.01—Introduction to Environmental and Social Issues. In Comprehensive Renewable Energy, 2nd ed.; Letcher, T.M., Ed.; Elsevier: Oxford, UK, 2022; pp. 1–8. ISBN 978-0-12-819734-9.

- 2. Sharma, S.; Basu, S.; Shetti, N.P.; Kamali, M.; Walvekar, P.; Aminabhavi, T.M. Waste-to-Energy Nexus: A Sustainable Development. *Environ. Pollut.* **2020**, *267*, 115501. [CrossRef] [PubMed]
- 3. Yergaziyeva, G.; Kuspanov, Z.; Mambetova, M.; Khudaibergenov, N.; Makayeva, N.; Daulbayev, C. Advancements in Catalytic, Photocatalytic, and Electrocatalytic CO₂ Conversion Processes: Current Trends and Future Outlook. *J. CO2 Util.* **2024**, *80*, 102682. [CrossRef]
- 4. Nations, U. Renewable Energy—Powering a Safer Future. Available online: https://www.un.org/en/climatechange/raising-ambition/renewable-energy (accessed on 5 April 2023).
- 5. Nations, U. The Paris Agreement. Available online: https://www.un.org/en/climatechange/paris-agreement (accessed on 5 April 2023).
- 6. Directorate-General for Communication (European Commission). *REPowerEU with Clean Energy*; Publications Office of the European Union: Luxembourg, 2022; ISBN 978-92-76-52458-8.
- 7. Environment, U.N. Emissions Gap Report. 2022. Available online: http://www.unep.org/resources/emissions-gap-report-2022 (accessed on 5 April 2023).
- 8. Hermesmann, M.; Müller, T.E. Green, Turquoise, Blue, or Grey? Environmentally Friendly Hydrogen Production in Transforming Energy Systems. *Prog. Energy Combust. Sci.* **2022**, *90*, 100996. [CrossRef]
- 9. Daulbayev, C.; Lesbayev, B.; Bakbolat, B.; Kaidar, B.; Sultanov, F.; Yeleuov, M.; Ustayeva, G.; Rakhymzhan, N. A Mini-Review on Recent Trends in Prospective Use of Porous 1D Nanomaterials for Hydrogen Storage. *S. Afr. J. Chem. Eng.* **2022**, *39*, 52–61. [CrossRef]
- 10. Ratnakar, R.R.; Gupta, N.; Zhang, K.; van Doorne, C.; Fesmire, J.; Dindoruk, B.; Balakotaiah, V. Hydrogen Supply Chain and Challenges in Large-Scale LH2 Storage and Transportation. *Int. J. Hydrogen Energy* **2021**, *46*, 24149–24168. [CrossRef]
- 11. Qureshi, F.; Yusuf, M.; Arham Khan, M.; Ibrahim, H.; Ekeoma, B.C.; Kamyab, H.; Rahman, M.M.; Nadda, A.K.; Chelliapan, S. A State-of-The-Art Review on the Latest Trends in Hydrogen Production, Storage, and Transportation Techniques. *Fuel* **2023**, 340, 127574. [CrossRef]
- 12. Insights into Renewable Hydrogen Energy: Recent Advances and Prospects. *Mater. Sci. Energy Technol.* **2020**, *3*, 319–327. [Cross-Ref]
- 13. Razzhivin, I.A.; Andreev, M.V.; Kievec, A.V. Increasing the Stability of Hydrogen Production in the Wind Energy-Hydrogen System through the Use of Synthetic Inertia of the Wind Turbine. *Int. J. Hydrogen Energy* **2022**, *47*, 38495–38505. [CrossRef]
- 14. Partho, A.T.; Tahir, M.; Tahir, B. Recent Advances in Covalent Organic Framework (COF) Nanotextures with Band Engineering for Stimulating Solar Hydrogen Production: A Comprehensive Review. *Int. J. Hydrogen Energy* **2022**, 47, 34323–34375. [CrossRef]
- 15. Steingrímsson, B.; Gunnlaugsson, E.; Saemundsson, K.; Axelsson, G. 7.02—Nature and Classification of Geothermal Resources. In *Comprehensive Renewable Energy*, 2nd ed.; Letcher, T.M., Ed.; Elsevier: Oxford, UK, 2022; pp. 3–17. ISBN 978-0-12-819734-9.
- 16. Mahmoud, M.; Ramadan, M.; Naher, S.; Pullen, K.; Ali Abdelkareem, M.; Olabi, A.-G. A Review of Geothermal Energy-Driven Hydrogen Production Systems. *Therm. Sci. Eng. Prog.* **2021**, 22, 100854. [CrossRef]
- 17. Muritala, I.K.; Guban, D.; Roeb, M.; Sattler, C. High Temperature Production of Hydrogen: Assessment of Non-Renewable Resources Technologies and Emerging Trends. *Int. J. Hydrogen Energy* **2020**, *45*, 26022–26035. [CrossRef]
- 18. Monga, D.; Shetti, N.P.; Basu, S.; Kakarla, R.R. Recent Advances in Various Processes for Clean and Sustainable Hydrogen Production. *Nano-Struct. Nano-Objects* **2023**, *33*, 100948. [CrossRef]
- 19. Mandade, P. Chapter 5—Introduction, Basic Principles, Mechanism, and Challenges of Photocatalysis. In *Handbook of Nanomate-rials for Wastewater Treatment*; Bhanvase, B., Sonawane, S., Pawade, V., Pandit, A., Eds.; Micro and Nano Technologies; Elsevier: Amsterdam, The Netherlands, 2021; pp. 137–154. ISBN 978-0-12-821496-1.
- 20. Kuspanov, Z.; Bakbolat, B.; Baimenov, A.; Issadykov, A.; Yeleuov, M.; Daulbayev, C. Photocatalysts for a Sustainable Future: Innovations in Large-Scale Environmental and Energy Applications. *Sci. Total Environ.* **2023**, *885*, 163914. [CrossRef]
- 21. Ahmed, S.N.; Haider, W. Heterogeneous Photocatalysis and Its Potential Applications in Water and Wastewater Treatment: A Review. *Nanotechnology* **2018**, 29, 342001. [CrossRef]
- 22. Nishiyama, H.; Yamada, T.; Nakabayashi, M.; Maehara, Y.; Yamaguchi, M.; Kuromiya, Y.; Nagatsuma, Y.; Tokudome, H.; Akiyama, S.; Watanabe, T.; et al. Photocatalytic Solar Hydrogen Production from Water on a 100-M2 Scale. *Nature* **2021**, *598*, 304–307. [CrossRef]
- 23. Goto, Y.; Hisatomi, T.; Wang, Q.; Higashi, T.; Ishikiriyama, K.; Maeda, T.; Sakata, Y.; Okunaka, S.; Tokudome, H.; Katayama, M.; et al. A Particulate Photocatalyst Water-Splitting Panel for Large-Scale Solar Hydrogen Generation. *Joule* 2018, 2, 509–520. [CrossRef]
- 24. Tai, L.N.; Long, P.D.; Hong Le, N.T.; Van Hong, L.; Linh, P.T.; Khuyen, B.X.; Tung, B.S.; Lam, V.D. Photocatalytic and Water-Splitting Properties of TiO₂ and Ag–TiO₂ Films in the Visible Light Region. *AIP Adv.* **2021**, *11*, 075118. [CrossRef]
- 25. Peng, R.; Zhang, S.; Yao, Y.; Wang, J.; Zhu, X.; Jiang, R.; Zhang, J.; Zhang, W.; Wang, C. MOFs Meet Electrospinning: New Opportunities for Water Treatment. *Chem. Eng. J.* **2023**, 453, 139669. [CrossRef]
- 26. Liverani, L.; Guarino, V.; La Carrubba, V.; Boccaccini, A.R. Porous Biomaterials and Scaffolds for Tissue Engineering. In *Encyclopedia of Biomedical Engineering*; Narayan, R., Ed.; Elsevier: Oxford, UK, 2019; pp. 188–202. ISBN 978-0-12-805144-3.

27. Mohammadalizadeh, Z.; Bahremandi-Toloue, E.; Karbasi, S. Recent Advances in Modification Strategies of Pre- and Post-Electrospinning of Nanofiber Scaffolds in Tissue Engineering. *React. Funct. Polym.* **2022**, *172*, 105202. [CrossRef]

- 28. Ghosal, K.; Augustine, R.; Zaszczynska, A.; Barman, M.; Jain, A.; Hasan, A.; Kalarikkal, N.; Sajkiewicz, P.; Thomas, S. Novel Drug Delivery Systems Based on Triaxial Electrospinning Based Nanofibers. *React. Funct. Polym.* **2021**, *163*, 104895. [CrossRef]
- 29. Tan, S.M.; Teoh, X.Y.; Le Hwang, J.; Khong, Z.P.; Sejare, R.; Almashhadani, A.Q.; Assi, R.A.; Chan, S.Y. Electrospinning and Its Potential in Fabricating Pharmaceutical Dosage Form. *J. Drug Deliv. Sci. Technol.* **2022**, *76*, 103761. [CrossRef]
- 30. Asgari, S.; Mohammadi Ziarani, G.; Badiei, A.; Ajalloueian, F.; Vasseghian, Y. Electrospun Composite Nanofibers as Novel High-Performance and Visible-Light Photocatalysts for Removal of Environmental Pollutants: A Review. *Environ. Res.* 2022, 215, 114296. [CrossRef] [PubMed]
- 31. Tebyetekerwa, M.; Ramakrishna, S. What Is Next for Electrospinning? Matter 2020, 2, 279–283. [CrossRef]
- 32. SalehHudin, H.S.; Mohamad, E.N.; Mahadi, W.N.L.; Muhammad Afifi, A. Multiple-Jet Electrospinning Methods for Nanofiber Processing: A Review. *Mater. Manuf. Process.* **2018**, *33*, 479–498. [CrossRef]
- 33. Xue, J.; Wu, T.; Dai, Y.; Xia, Y. Electrospinning and Electrospun Nanofibers: Methods, Materials, and Applications. *Chem. Rev.* **2019**, *119*, 5298–5415. [CrossRef]
- Ghosal, K.; Agatemor, C.; Tucker, N.; Kny, E.; Thomas, S. Electrical Spinning to Electrospinning: A Brief History; The Royal Society of Chemistry: Cambridge, UK, 2018. [CrossRef]
- 35. Haider, A.; Haider, S.; Kang, I.-K. A Comprehensive Review Summarizing the Effect of Electrospinning Parameters and Potential Applications of Nanofibers in Biomedical and Biotechnology. *Arab. J. Chem.* **2018**, *11*, 1165–1188. [CrossRef]
- 36. Shepa, I.; Mudra, E.; Dusza, J. Electrospinning through the Prism of Time. Mater. Today Chem. 2021, 21, 100543. [CrossRef]
- 37. Panda, P.K.; Sahoo, B.; Ramakrishna, S. Electrospun Nanofibers for Photocatalytic Water Treatment and Hydrogen Generation Application: A Review. *Int. J. Hydrogen Energy* **2023**, *48*, 37193–37208. [CrossRef]
- 38. Joshi, B.; Samuel, E.; Kim, Y.; Yarin, A.L.; Swihart, M.T.; Yoon, S.S. Review of Recent Progress in Electrospinning-Derived Free-standing and Binder-Free Electrodes for Supercapacitors. *Coord. Chem. Rev.* **2022**, *460*, 214466. [CrossRef]
- 39. Can-Herrera, L.A.; Oliva, A.I.; Dzul-Cervantes, M.a.A.; Pacheco-Salazar, O.F.; Cervantes-Uc, J.M. Morphological and Mechanical Properties of Electrospun Polycaprolactone Scaffolds: Effect of Applied Voltage. *Polymers* **2021**, *13*, 662. [CrossRef]
- Tlili, I.; Alkanhal, T.A. Nanotechnology for Water Purification: Electrospun Nanofibrous Membrane in Water and Wastewater Treatment. J. Water Reuse Desalination 2019, 9, 232–248. [CrossRef]
- 41. Wei, L.; Sun, R.; Liu, C.; Xiong, J.; Qin, X. Mass Production of Nanofibers from Needleless Electrospinning by a Novel Annular Spinneret. *Mater. Des.* **2019**, *179*, 107885. [CrossRef]
- 42. Zhao, K.; Wang, W.; Yang, Y.; Wang, K.; Yu, D.-G. From Taylor Cone to Solid Nanofiber in Tri-Axial Electrospinning: Size Relationships. *Results Phys.* **2019**, *15*, 102770. [CrossRef]
- 43. Ngadiman, N.H.A.; Noordin, M.Y.; Idris, A.; Kurniawan, D. Effect of Electrospinning Parameters Setting towards Fiber Diameter. *Adv. Mater. Res.* **2014**, *845*, 985–988. [CrossRef]
- 44. Sharma, G.K.; James, N.R.; Sharma, G.K.; James, N.R. Electrospinning: The Technique and Applications. In *Recent Developments in Nanofibers Research*; IntechOpen: London, UK, 2022; ISBN 978-1-80356-387-9.
- 45. Abdul Hameed, M.M.; Mohamed Khan, S.A.P.; Thamer, B.M.; Rajkumar, N.; El-Hamshary, H.; El-Newehy, M. Electrospun Nanofibers for Drug Delivery Applications: Methods and Mechanism. *Polym. Adv. Technol.* **2023**, *34*, 6–23. [CrossRef]
- 46. Shi, X.; Zhou, W.; Ma, D.; Ma, Q.; Bridges, D.; Ma, Y.; Hu, A. Electrospinning of Nanofibers and Their Applications for Energy Devices. *J. Nanomater.* **2015**, 2015, e140716. [CrossRef]
- 47. Li, Y.; Li, Q.; Tan, Z. A Review of Electrospun Nanofiber-Based Separators for Rechargeable Lithium-Ion Batteries. *J. Power Sources* **2019**, 443, 227262. [CrossRef]
- 48. Mwiiri, F.K.; Daniels, R. Influence of PVA Molecular Weight and Concentration on Electrospinnability of Birch Bark Extract-Loaded Nanofibrous Scaffolds Intended for Enhanced Wound Healing. *Molecules* **2020**, 25, 4799. [CrossRef]
- 49. Lin, H.-N.; Peng, T.-Y.; Kung, Y.-R.; Chiou, Y.-J.; Chang, W.-M.; Wu, S.-H.; Mine, Y.; Chen, C.-Y.; Lin, C.-K. Effects of the Methyl Methacrylate Addition, Polymerization Temperature and Time on the MBG@PMMA Core-Shell Structure and Its Application as Addition in Electrospun Composite Fiber Bioscaffold. *Ceram. Int.* **2023**, 49, 7630–7639. [CrossRef]
- 50. Ki, C.S.; Baek, D.H.; Gang, K.D.; Lee, K.H.; Um, I.C.; Park, Y.H. Characterization of Gelatin Nanofiber Prepared from Gelatin–Formic Acid Solution. *Polymer* **2005**, *46*, 5094–5102. [CrossRef]
- 51. Suresh, S.; Becker, A.; Glasmacher, B. Impact of Apparatus Orientation and Gravity in Electrospinning-A Review of Empirical Evidence. *Polymers* **2020**, *12*, 2448. [CrossRef] [PubMed]
- 52. Ramakrishna, S. *An Introduction to Electrospinning and Nanofibers*; World Scientific: Hackensack, NJ, USA, 2005; ISBN 978-981-256-761-1.
- 53. Yang, G.-Z.; Li, H.-P.; Yang, J.-H.; Wan, J.; Yu, D.-G. Influence of Working Temperature on The Formation of Electrospun Polymer Nanofibers. *Nanoscale Res. Lett.* **2017**, *12*, 55. [CrossRef] [PubMed]
- 54. Ramazani, S.; Karimi, M. Investigating the Influence of Temperature on Electrospinning of Polycaprolactone Solutions. *e-Polymers* **2014**, *14*, 323–333. [CrossRef]
- 55. Wang, J.; Wang, Z.; Ni, J.; Li, L. Electrospinning for Flexible Sodium-Ion Batteries. *Energy Storage Mater.* **2022**, 45, 704–719. [CrossRef]

56. Joly, D.; Jung, J.-W.; Kim, I.-D.; Demadrille, R. Electrospun Materials for Solar Energy Conversion: Innovations and Trends. *J. Mater. Chem. C* **2016**, *4*, 10173–10197. [CrossRef]

- 57. Lu, X.; Wang, C.; Wei, Y. One-Dimensional Composite Nanomaterials: Synthesis by Electrospinning and Their Applications. Small 2009, 5, 2349–2370. [CrossRef]
- 58. Hariganesh, S.; Vadivel, S.; Maruthamani, D.; Rangabhashiyam, S. Chapter 12—Disinfection by-Products in Drinking Water: Detection and Treatment Methods. In *Disinfection By-Products in Drinking Water*; Prasad, M.N.V., Ed.; Butterworth-Heinemann: Oxford, UK, 2020; pp. 279–304, ISBN 978-0-08-102977-0.
- 59. Mayorov, A.S.; Gorbachev, R.V.; Morozov, S.V.; Britnell, L.; Jalil, R.; Ponomarenko, L.A.; Blake, P.; Novoselov, K.S.; Watanabe, K.; Taniguchi, T.; et al. Micrometer-Scale Ballistic Transport in Encapsulated Graphene at Room Temperature. *Nano Lett.* **2011**, 11, 2396–2399. [CrossRef]
- 60. Novoselov, K.S.; Geim, A.K.; Morozov, S.V.; Jiang, D.; Zhang, Y.; Dubonos, S.V.; Grigorieva, I.V.; Firsov, A.A. Electric Field Effect in Atomically Thin Carbon Films. *Science* **2004**, *306*, 666–669. [CrossRef]
- 61. Stoller, M.D.; Park, S.; Zhu, Y.; An, J.; Ruoff, R.S. Graphene-Based Ultracapacitors. Nano Lett. 2008, 8, 3498–3502. [CrossRef]
- 62. Nasr, M.; Balme, S.; Eid, C.; Habchi, R.; Miele, P.; Bechelany, M. Enhanced Visible-Light Photocatalytic Performance of Electrospun rGO/TiO₂ Composite Nanofibers. *J. Phys. Chem. C* **2017**, *121*, 261–269. [CrossRef]
- 63. Song, M.; Cao, H.; Zhu, Y.; Wang, Y.; Zhao, S.; Huang, C.; Zhang, C.; He, X. Electrochemical and Photocatalytic Properties of Electrospun C/TiO₂ Nanofibers. *Chem. Phys. Lett.* **2020**, 747, 137355. [CrossRef]
- 64. Yao, Y. Visible-Light Photocatalysis of Carbon-Based Materials; IntechOpen Limited: London, UK, 2018; ISBN 978-1-78923-029-1.
- 65. Latorre-Sánchez, M.; Lavorato, C.; Puche, M.; Fornés, V.; Molinari, R.; Garcia, H. Visible-Light Photocatalytic Hydrogen Generation by Using Dye-Sensitized Graphene Oxide as a Photocatalyst. *Chem. A Eur. J.* **2012**, *18*, 16774–16783. [CrossRef] [PubMed]
- 66. Zhurenok, A.V.; Vasilchenko, D.B.; Kozlova, E.A. Comprehensive Review on G-C3N4-Based Photocatalysts for the Photocatalytic Hydrogen Production under Visible Light. *Int. J. Mol. Sci.* **2023**, *24*, 346. [CrossRef] [PubMed]
- 67. Singla, S.; Sharma, S.; Basu, S.; Shetti, N.P.; Reddy, K.R. Graphene/Graphitic Carbon Nitride-Based Ternary Nanohybrids: Synthesis Methods, Properties, and Applications for Photocatalytic Hydrogen Production. *FlatChem* **2020**, 24, 100200. [CrossRef]
- 68. Mishra, A.; Mehta, A.; Kainth, S.; Basu, S. A Comparative Study on the Effect of Different Precursors for Synthesis and Efficient Photocatalytic Activity of G-C3N4/TiO₂/Bentonite Nanocomposites. *J. Mater. Sci.* **2018**, *53*, 13126–13142. [CrossRef]
- 69. Kim, Y.K.; Kim, M.; Hwang, S.-H.; Lim, S.K.; Park, H.; Kim, S. CdS-Loaded Flexible Carbon Nanofiber Mats as a Platform for Solar Hydrogen Production. *Int. J. Hydrogen Energy* **2015**, *40*, 136–145. [CrossRef]
- 70. Dai, Z.; Ren, P.; Cao, Q.; Gao, X.; He, W.; Xiao, Y.; Jin, Y.; Ren, F. Synthesis of TiO₂@lignin Based Carbon Nanofibers Composite Materials with Highly Efficient Photocatalytic to Methylene Blue Dye. *J. Polym. Res.* **2020**, 27, 108. [CrossRef]
- 71. Abbasi, S.; Hasanpour, M.; Ekrami-Kakhki, M.-S. Removal Efficiency Optimization of Organic Pollutant (Methylene Blue) with Modified Multi-Walled Carbon Nanotubes Using Design of Experiments (DOE). *J. Mater. Sci. Mater. Electron.* **2017**, 28, 9900–9910. [CrossRef]
- 72. Roozban, N.; Abbasi, S.; Ghazizadeh, M. The Experimental and Statistical Investigation of the Photo Degradation of Methyl Orange Using Modified MWCNTs with Different Amount of ZnO Nanoparticles. *J. Mater. Sci. Mater. Electron.* **2017**, 28, 7343–7352. [CrossRef]
- 73. Sultanov, F.; Daulbayev, C.; Bakbolat, B.; Daulbayev, O.; Bigaj, M.; Mansurov, Z.; Kuterbekov, K.; Bekmyrza, K. Aligned Composite SrTiO3/PAN Fibers as 1D Photocatalyst Obtained by Electrospinning Method. *Chem. Phys. Lett.* **2019**, 737, 136821. [CrossRef]
- 74. Daulbayev, C.; Sultanov, F.; Korobeinyk, A.V.; Yeleuov, M.; Azat, S.; Bakbolat, B.; Umirzakov, A.; Mansurov, Z. Bio-Waste-Derived Few-Layered Graphene/SrTiO3/PAN as Efficient Photocatalytic System for Water Splitting. *Appl. Surf. Sci.* **2021**, 549, 149176. [CrossRef]
- Serik, A.; Kuspanov, Z.; Bissenova, M.; Idrissov, N.; Yeleuov, M.; Umirzakov, A.; Daulbayev, C. Effective Photocatalytic Degradation of Sulfamethoxazole Using PAN/SrTiO3 Nanofibers. J. Water Process Eng. 2024, 66, 106052. [CrossRef]
- Pereira, M.F.G.; Nascimento, M.M.; Cardoso, P.H.N.; Oliveira, C.Y.B.; Tavares, G.F.; Araújo, E.S. Preparation, Microstructural Characterization and Photocatalysis Tests of V5+-Doped TiO₂/WO₃ Nanocomposites Supported on Electrospun Membranes. *Inorganics* 2022, 10, 143. [CrossRef]
- 77. Guerrero-Pérez, M.O. Research Progress on the Applications of Electrospun Nanofibers in Catalysis. *Catalysts* **2022**, *12*, 9. [Cross-Ref]
- 78. Hilal Elhousseini, M.; Isık, T.; Kap, Ö.; Verpoort, F.; Horzum, N. Dual Remediation of Waste Waters from Methylene Blue and Chromium (VI) Using Thermally Induced ZnO Nanofibers. *Appl. Surf. Sci.* **2020**, *514*, 145939. [CrossRef]
- 79. Navidpour, A.H.; Salehi, M.; Salimijazi, H.R.; Kalantari, Y.; Azarpour Siahkali, M. Photocatalytic Activity of Flame-Sprayed Coating of Zinc Ferrite Powder. *J. Therm. Spray Technol.* **2017**, *26*, 2030–2039. [CrossRef]
- 80. Karim, A.V.; Shriwastav, A. Degradation of Amoxicillin with Sono, Photo, and Sonophotocatalytic Oxidation under Low-Frequency Ultrasound and Visible Light. *Environ. Res.* **2021**, 200, 111515. [CrossRef]
- 81. Bharathi, P.; Harish, S.; Archana, J.; Navaneethan, M.; Ponnusamy, S.; Muthamizhchelvan, C.; Shimomura, M.; Hayakawa, Y. Enhanced Charge Transfer and Separation of Hierarchical CuO/ZnO Composites: The Synergistic Effect of Photocatalysis for the Mineralization of Organic Pollutant in Water. *Appl. Surf. Sci.* **2019**, *484*, 884–891. [CrossRef]
- 82. Ullah, H.; Haneef, Z.; Ahmad, A.; Butler, I.S.; Nasir Dara, R.; Rehman, Z. MoS₂ and CdS Photocatalysts for Water Decontamination: A Review. *Inorg. Chem. Commun.* **2023**, *153*, 110775. [CrossRef]

83. Paraskevopoulou, A.; Pandis, P.; Argirusis, C.; Sourkouni, G. Sonochemical Synthesis of Indium Nitride Nanoparticles and Photocatalytic Composites with Titania. *Ceramics* **2024**, *7*, 478–490. [CrossRef]

- 84. Alahmadi, N. Recent Progress in Photocatalytic Removal of Environmental Pollution Hazards in Water Using Nanostructured Materials. *Separations* **2022**, *9*, 264. [CrossRef]
- 85. Samadi, M.; Moshfegh, A.Z. Recent Developments of Electrospinning-Based Photocatalysts in Degradation of Organic Pollutants: Principles and Strategies. *ACS Omega* **2022**, *7*, 45867–45881. [CrossRef] [PubMed]
- 86. Duan, Z.; Huang, Y.; Zhang, D.; Chen, S. Electrospinning Fabricating Au/TiO₂ Network-like Nanofibers as Visible Light Activated Photocatalyst. *Sci. Rep.* **2019**, *9*, 8008. [CrossRef] [PubMed]
- 87. Pantò, F.; Dahrouch, Z.; Saha, A.; Patanè, S.; Santangelo, S.; Triolo, C. Photocatalytic Degradation of Methylene Blue Dye by Porous Zinc Oxide Nanofibers Prepared via Electrospinning: When Defects Become Merits. *Appl. Surf. Sci.* **2021**, 557, 149830. [CrossRef]
- 88. Ruiz-Ramírez, L.R.; Torres-Pérez, J.; Medellín-Castillo, N.; Reyes-López, S.Y. Photocatalytic Degradation of Oxytetracycline by SiO₂–TiO₂–Ag Electrospun Fibers. *Solid State Sci.* **2023**, *140*, 107188. [CrossRef]
- 89. Zhang, Y.; Liu, Y.; Xie, S.; Huang, H.; Guo, G.; Dai, H.; Deng, J. Supported Ceria-Modified Silver Catalysts with High Activity and Stability for Toluene Removal. *Environ. Int.* **2019**, *128*, 335–342. [CrossRef]
- 90. Lontio Fomekong, R.; Saruhan, B. Synthesis of Co³⁺ Doped TiO₂ by Co-Precipitation Route and Its Gas Sensing Properties. *Front. Mater.* **2019**, *6*, 252. [CrossRef]
- 91. Na, K.-H.; Kim, B.-S.; Yoon, H.-S.; Song, T.-H.; Kim, S.-W.; Cho, C.-H.; Choi, W.-Y. Fabrication and Photocatalytic Properties of Electrospun Fe-Doped TiO₂ Nanofibers Using Polyvinyl Pyrrolidone Precursors. *Polymers* **2021**, *13*, 2634. [CrossRef]
- 92. Ghoreishian, S.M.; Ranjith, K.S.; Lee, H.; Park, B.; Norouzi, M.; Nikoo, S.Z.; Kim, W.-S.; Han, Y.-K.; Huh, Y.S. Tuning the Phase Composition of 1D TiO₂ by Fe/Sn Co-Doping Strategy for Enhanced Visible-Light-Driven Photocatalytic and Photoelectrochemical Performances. *J. Alloys Compd.* **2021**, *851*, 156826. [CrossRef]
- 93. Wang, L.; Sun, M.; Zhou, B.; Rao, Y.; Yan, T.; Du, B.; Shao, Y. Electrospinning Mediated Solvothermal Preparation of Hierarchical MGa2O4/ZnIn2S4 (M = Ni, Co) Hollow Nanofibers with p-n Heterojunction for Boosting Photocatalytic H2 Evolution. *Fuel* **2024**, 374, 132448. [CrossRef]
- 94. Kuspanov, Z.; Umirzakov, A.; Serik, A.; Baimenov, A.; Yeleuov, M.; Daulbayev, C. Multifunctional Strontium Titanate Perovskite-Based Composite Photocatalysts for Energy Conversion and Other Applications. *Int. J. Hydrogen Energy* **2023**, 48, 38634–38654. [CrossRef]
- 95. Kudaibergen, A.D.; Kuspanov, Z.B.; Issadykov, A.N.; Beisenov, R.E.; Mansurov, Z.A.; Yeleuov, M.A.; Daulbayev, C.B. Synthesis, Structure, and Energetic Characteristics of Perovskite Photocatalyst SrTiO3: An Experimental and DFT Study. *Eurasian Chem.-Technol. J.* 2023, 25, 139–146. [CrossRef]
- 96. Bissenova, M.; Umirzakov, A.; Mit, K.; Mereke, A.; Yerubayev, Y.; Serik, A.; Kuspanov, Z. Synthesis and Study of SrTiO₃/TiO₂ Hybrid Perovskite Nanotubes by Electrochemical Anodization. *Molecules* **2024**, 29, 1101. [CrossRef] [PubMed]
- 97. Matus, E.V.; Ismagilov, I.Z.; Mikhaylova, E.S.; Ismagilov, Z.R. Hydrogen Production from Coal Industry Methane. *Eurasian Chem.-Technol. J.* **2022**, 24, 69–91. [CrossRef]
- 98. Sun, F.; Qi, H.; Xie, Y.; Ma, Q.; He, W.; Xu, D.; Wang, G.; Yu, W.; Wang, T.; Dong, X. Flexible Self-Supporting Bifunctional [TiO₂/C]//[Bi2WO6/C] Carbon-Based Janus Nanofiber Heterojunction Photocatalysts for Efficient Hydrogen Evolution and Degradation of Organic Pollutant. *J. Alloys Compd.* **2020**, *830*, 154673. [CrossRef]
- 99. Zhang, Y.; Niu, L.; Li, Z.; Yang, T.; Liu, Y.; Kang, Z. A Recyclable ZnIn2S4/PAN Photocatalytic Nanofiber Membrane for Boosting Visible Light Hydrogen Evolution in Seawater without Cocatalyst. *Appl. Catal. B Environ. Energy* **2024**, *357*, 124300. [CrossRef]
- 100. Ismagilov, I.Z.; Matus, E.V.; Kuznetsov, V.V.; Yashnik, S.A.; Kerzhentsev, M.A.; Gerritsen, G.; Abbenhuis, H.C.; Ismagilov, Z.R. Application of POSS Nanotechnology for Preparation of Efficient Ni Catalysts for Hydrogen Production. *Eurasian Chem.-Technol. J.* 2017, 19, 3–16. [CrossRef]
- 101. Sultanov, F.; Daulbayev, C.; Azat, S.; Kuterbekov, K.; Bekmyrza, K.; Bakbolat, B.; Bigaj, M.; Mansurov, Z. Influence of Metal Oxide Particles on Bandgap of 1D Photocatalysts Based on SrTiO3/PAN Fibers. *Nanomaterials* **2020**, *10*, 1734. [CrossRef]
- 102. Chang, Y.-C.; Zeng, C.-J.; Chen, C.-Y.; Tsay, C.-Y.; Lee, G.-J.; Wu, J.J. NiS/Pt Loaded on Electrospun TiO₂ Nanofiber with Enhanced Visible-Light-Driven Photocatalytic Hydrogen Production. *Mater. Res. Bull.* **2023**, *157*, 112041. [CrossRef]
- 103. Peng, H.; Yong, J.; Wang, H.; Gou, Y.; Wang, F.; Zheng, X. Dual CdS–CoS/S,N-Doped TiO₂ Nanofibers for Efficient Visible-Light Induced H2 Evolution. *Int. J. Hydrogen Energy* **2022**, 47, 31269–31278. [CrossRef]
- 104. Li, R.; Luan, J.; Zhang, Y.; Jiang, L.; Yan, H.; Chi, Q.; Yan, Z. A Review of Efficient Photocatalytic Water Splitting for Hydrogen Production. *Renew. Sustain. Energy Rev.* **2024**, 206, 114863. [CrossRef]
- 105. Abu-Sari, S.M.; Ang, B.C.; Wan Daud, W.M.A.; Patah, M.F.A. Visible-Light-Driven Photocatalytic Hydrogen Production on Defective, Sulfur Self-Doped g-C3N4 Nanofiber Fabricate via Electrospinning Method. *J. Environ. Chem. Eng.* **2023**, *11*, 109318. [CrossRef]
- 106. Shang, Q.; Wang, J.; Yang, J.; Wang, Z.; Wang, G.; Wang, K.; Wu, X.; Li, J. Photocatalytic Hydrogen Evolution Coupled with Tetracycline Photodegradation over S-Scheme BaTiO3/Ag2S Dual-Function Nanofibers: Performance and Mechanism. *Appl. Surf. Sci.* 2023, 635, 157760. [CrossRef]
- 107. Chang, Y.-C.; Syu, S.-Y.; Hsu, P.-C. Construction of In₂S₃–In(OH)₃–ZnS Nanofibers for Boosting Photocatalytic Hydrogen Evolution. *Int. J. Hydrogen Energy* **2024**, *86*, 24–35. [CrossRef]

108. Peng, H.; Luo, M.; Zheng, X. Boosting Solar-Light Photocatalytic Activity of Ni2P-Decorated ZnCr₂O₄ Nanofibers for H₂ Evolution and Tetracycline Elimination. *Ceram. Int.* **2024**, *50*, 26474–26481. [CrossRef]

- 109. Al-Enizi, A.M.; Karim, A.; Yousef, A. A Novel Method for Fabrication of Electrospun Cadmium Sulfide Nanoparticles-Decorated Zinc Oxide Nanofibers as Effective Photocatalyst for Water Photosplitting. *Alex. Eng. J.* **2023**, *65*, 825–835. [CrossRef]
- 110. Aravind, M.; Amalanathan, M.; Aslam, S.; Noor, A.E.; Jini, D.; Majeed, S.; Velusamy, P.; Alothman, A.A.; Alshgari, R.A.; Saleh Mushab, M.S.; et al. Hydrothermally Synthesized Ag-TiO₂ Nanofibers (NFs) for Photocatalytic Dye Degradation and Antibacterial Activity. *Chemosphere* 2023, 321, 138077. [CrossRef]
- 111. Mousa, H.M.; Alenezi, J.F.; Mohamed, I.M.A.; Yasin, A.S.; Hashem, A.-F.M.; Abdal-hay, A. Synthesis of TiO₂@ZnO Heterojunction for Dye Photodegradation and Wastewater Treatment. *J. Alloys Compd.* **2021**, *886*, 161169. [CrossRef]
- 112. Villa, K.; Galán-Mascarós, J.R.; López, N.; Palomares, E. Photocatalytic Water Splitting: Advantages and Challenges. *Sustain. Energy Fuels* **2021**, *5*, 4560–4569. [CrossRef]
- 113. Ahmed, M.A.; Mohamed, A.A. Recent Progress in Semiconductor/Graphene Photocatalysts: Synthesis, Photocatalytic Applications, and Challenges. *RSC Adv.* **2022**, *13*, 421–439. [CrossRef]
- 114. Chen, Y.; Li, A.; Fu, X.; Peng, Z. Electrospinning-Based (N,F)-Co-Doped TiO₂-δ Nanofibers: An Excellent Photocatalyst for Degrading Organic Dyes and Heavy Metal Ions under Visible Light. *Mater. Chem. Phys.* **2022**, 291, 126672. [CrossRef]
- 115. Yasin, A.S.; Mohamed, I.M.A.; Mousa, H.M.; Park, C.H.; Kim, C.S. Facile Synthesis of TiO₂/ZrO₂ Nanofibers/Nitrogen Co-Doped Activated Carbon to Enhance the Desalination and Bacterial Inactivation via Capacitive Deionization. *Sci. Rep.* **2018**, *8*, 541. [CrossRef] [PubMed]
- 116. Le, P.H.; Hieu, L.T.; Lam, T.-N.; Hang, N.T.N.; Truong, N.V.; Tuyen, L.T.C.; Phong, P.T.; Leu, J. Enhanced Photocatalytic Performance of Nitrogen-Doped TiO₂ Nanotube Arrays Using a Simple Annealing Process. *Micromachines* **2018**, *9*, 618. [CrossRef] [PubMed]
- 117. Enculescu, M.; Costas, A.; Evanghelidis, A.; Enculescu, I. Fabrication of ZnO and TiO₂ Nanotubes via Flexible Electro-Spun Nanofibers for Photocatalytic Applications. *Nanomaterials* **2021**, *11*, 1305. [CrossRef] [PubMed]
- 118. Chen, G.; Wang, Y.; Shen, Q.; Xiong, X.; Ren, S.; Dai, G.; Wu, C. Fabrication of TiO₂ Nanofibers Assembled by Bi₂WO₆ Nanosheets with Enhanced Visible Light Photocatalytic Activity. *Ceram. Int.* **2020**, *46*, 21304–21310. [CrossRef]
- 119. Lou, C.-W.; Xie, M.-M.; Yang, Y.-D.; Wang, H.-Y.; Wang, Z.-K.; Zhang, L.; Hsieh, C.-T.; Liu, L.-Y.; Lin, M.-C.; Li, T.-T. Carbon Nanofiber Membranes Loaded with MXene@g-C3N4: Preparation and Photocatalytic Property. *Nanomaterials* **2024**, *14*, 896. [CrossRef]
- 120. Liu, Y.; Hao, M.; Zhou, C.; Yang, B.; Jiang, S.; Huang, J.; Chen, Z.; Liu, Y.; Ramakrishna, S. Chapter 9—Scale-up Strategies for Electrospun Nanofiber Production. In *Electrospun and Nanofibrous Membranes*; Kargari, A., Matsuura, T., Shirazi, M.M.A., Eds.; Elsevier: Amsterdam, The Netherlands, 2023; pp. 205–266. ISBN 978-0-12-823032-9.
- 121. Sabzehmeidani, M.M.; Karimi, H.; Ghaedi, M.; Avargani, V.M. Construction of Efficient and Stable Ternary ZnFe₂O₄/Ag/AgBr Z-Scheme Photocatalyst Based on ZnFe₂O₄ Nanofibers under LED Visible Light. *Mater. Res. Bull.* **2021**, *143*, 111449. [CrossRef]
- 122. Yi, S.; Sun, S.; Zhang, Y.; Zou, Y.; Dai, F.; Si, Y. Scalable Fabrication of Bimetal Modified Polyacrylonitrile (PAN) Nanofibrous Membranes for Photocatalytic Degradation of Dyes. *J. Colloid Interface Sci.* **2020**, *559*, 134–142. [CrossRef]
- 123. Li, X.; Raza, S.; Liu, C. Directly Electrospinning Synthesized Z-Scheme Heterojunction TiO₂@Ag@Cu₂O Nanofibers with Enhanced Photocatalytic Degradation Activity under Solar Light Irradiation. *J. Environ. Chem. Eng.* **2021**, *9*, 106133. [CrossRef]
- 124. Li, X.; Chen, D.; Li, N.; Xu, Q.; Li, H.; He, J.; Lu, J. Hollow SnO₂ Nanotubes Decorated with ZnIn₂S₄ Nanosheets for Enhanced Visible-Light Photocatalytic Activity. *J. Alloys Compd.* **2020**, *8*43, 155772. [CrossRef]
- 125. Panthi, G.; Kwon, O.H.; Kuk, Y.-S.; Gyawali, K.R.; Park, Y.W.; Park, M. Ternary Composite of Co-Doped CdSe@electrospun Carbon Nanofibers: A Novel Reusable Visible Light-Driven Photocatalyst with Enhanced Performance. *Catalysts* **2020**, *10*, 348. [CrossRef]
- 126. Zhang, L.; Shen, Q.; Zheng, S.; Yu, L.; Huang, F.; Zhang, C.; Sheng, J.; Yang, H. Direct Electrospinning Preparation of Z-Scheme Mixed-Crystal Bi₂O₃/g-C₃N₄ Composite Photocatalysts with Enhanced Visible-Light Photocatalytic Activity. New J. Chem. 2021, 45, 14522–14531. [CrossRef]
- 127. Wang, Y.; Hao, X.; Wang, Z.; Dong, M.; Cui, L. Facile Fabrication of Mn²⁺-Doped ZnO Photocatalysts by Electrospinning. *R. Soc. Open Sci.* **2020**, *7*, 191050. [CrossRef] [PubMed]
- 128. Pant, B.; Prasad Ojha, G.; Acharya, J.; Park, M. Ag₃PO₄-TiO₂-Carbon Nanofiber Composite: An Efficient Visible-Light Photocatalyst Obtained from Electrospinning and Hydrothermal Methods. *Sep. Purif. Technol.* **2021**, 276, 119400. [CrossRef]
- 129. Xing, Y.; Cheng, J.; Li, H.; Lin, D.; Wang, Y.; Wu, H.; Pan, W. Electrospun Ceramic Nanofibers for Photocatalysis. *Nanomaterials* **2021**, *11*, 3221. [CrossRef]
- 130. Pant, B.; Ojha, G.P.; Kuk, Y.-S.; Kwon, O.H.; Park, Y.W.; Park, M. Synthesis and Characterization of ZnO-TiO2/Carbon Fiber Composite with Enhanced Photocatalytic Properties. *Nanomaterials* **2020**, *10*, 1960. [CrossRef]
- 131. Zhai, G.; Zhou, J.; Xie, M.; Jia, C.; Hu, Z.; Xiang, H.; Zhu, M. Improved Photocatalytic Property of Lignin-Derived Carbon Nanofibers through Catalyst Synergy. *Int. J. Biol. Macromol.* **2023**, 233, 123588. [CrossRef]
- 132. Yu, W.; Zheng, B.; Mao, K.; Jiang, J.; Luo, B.; Wu, X.; Tao, T.; Min, X.; Mi, R.; Huang, Z.; et al. Interfacial Structure and Photocatalytic Degradation Performance of Graphene Oxide Bridged Chitin-Modified TiO₂/Carbon Fiber Composites. *J. Clean. Prod.* **2022**, *361*, 132261. [CrossRef]

133. Zhang, J.-J.; Kai, C.-M.; Zhang, F.-J.; Wang, Y.-R. Novel PAN/Bi₂MoO₆/Ti₃C₂ Ternary Composite Membrane via Electrospinning with Enhanced Photocatalytic Degradation of Tetracycline. *Colloids Surf. A Physicochem. Eng. Asp.* **2022**, *648*, 129255. [CrossRef]

- 134. Zhang, L.; Shen, Q.; Huang, F.; Jiang, L.; Liu, J.; Sheng, J.; Li, Y.; Yang, H. Electrospinning Directly Synthesis of 0D/1D CuBi₂O₄@WO₃ Nanofiber Photocatalyst with S-Scheme Heterojunction. *Appl. Surf. Sci.* **2023**, *608*, 155064. [CrossRef]
- 135. Fu, J.; Jiang, K.; Qiu, X.; Yu, J.; Liu, M. Product Selectivity of Photocatalytic CO₂ Reduction Reactions. *Mater. Today* **2020**, 32, 222–243. [CrossRef]
- 136. Adekoya, D.; Tahir, M.; Amin, N.A.S. Recent Trends in Photocatalytic Materials for Reduction of Carbon Dioxide to Methanol. *Renew. Sustain. Energy Rev.* **2019**, *116*, 109389. [CrossRef]
- 137. Kang, S.; Hwang, J. rGO-Wrapped Ag-Doped TiO₂ Nanofibers for Photocatalytic CO₂ Reduction under Visible Light. *J. Clean. Prod.* **2022**, *374*, 134022. [CrossRef]
- 138. Wang, X.; Zhang, Z.; Huang, Z.; Dong, P.; Nie, X.; Jin, Z. Electrospun PVDF Nanofibers Decorated with Graphene and Titania for Improved Visible Light Photocatalytic Methanation of CO₂. *Plasmonics* **2020**, *15*, 717–725. [CrossRef]
- 139. Lu, N.; Zhang, M.; Jing, X.; Zhang, P.; Zhu, Y.; Zhang, Z. Electrospun Semiconductor-Based Nano-Heterostructures for Photocatalytic Energy Conversion and Environmental Remediation: Opportunities and Challenges. *Energy Environ. Mater.* **2023**, *6*, e12338. [CrossRef]
- 140. Xu, F.; Tan, H.; Fan, J.; Cheng, B.; Yu, J.; Xu, J. Electrospun TiO₂-Based Photocatalysts. Sol. RRL 2021, 5, 2000571. [CrossRef]
- 141. Kang, S.; Im, T.; Koh, M.; Lee, C.S. Facile Fabrication of Electrospun Black Titania Nanofibers Decorated with Graphitic Carbon Nitride for the Application of Photocatalytic CO₂ Reduction. *J. CO2 Util.* **2020**, *41*, 101230. [CrossRef]
- 142. Song, J.; Guan, R.; Xie, M.; Dong, P.; Yang, X.; Zhang, J. Advances in Electrospun TiO₂ Nanofibers: Design, Construction, and Applications. *Chem. Eng. J.* **2022**, *431*, 134343. [CrossRef]
- 143. Ma, H.; Wu, X.; Li, X.; Liu, J.; Dong, H.; Liu, Y.; Niu, L.; Zhang, F.; Wang, W.; Shao, C.; et al. Photocatalytic CO₂ Reduction to Ethanol by ZnCO₂O4/ZnO Janus Hollow Nanofibers. *Inorg. Chem.* **2024**, *63*, 15735–15751. [CrossRef]
- 144. Wei, Z.; Ji, T.; Zhou, X.; Guo, J.; Yu, X.; Liu, H.; Wang, J. Synergistic Enhancement of Photocatalytic CO₂ Reduction by Built-in Electric Field/Piezoelectric Effect and Surface Plasmon Resonance via PVDF/CdS/Ag Heterostructure. *Small* **2023**, *19*, 2304202. [CrossRef]
- 145. Wu, Y.; Wu, J.; Zhu, C.; Zhang, L.; Yan, J. MXene-Intercalation Induced Ordered Brick-Mortar Structures of Allomorph Junctions for Enhanced Flexibility in TiO₂ Nanofibers and Photocatalytic Efficiency. *Chem. Eng. J.* **2023**, 465, 142798. [CrossRef]
- 146. Sun, Y.; Zhang, X.; Zhang, M.; Ge, M.; Wang, J.; Tang, Y.; Zhang, Y.; Mi, J.; Cai, W.; Lai, Y.; et al. Rational Design of Electrospun Nanofibers for Gas Purification: Principles, Opportunities, and Challenges. *Chem. Eng. J.* 2022, 446, 137099. [CrossRef]
- 147. Wang, S.; Wang, L.; Wang, D.; Li, Y. Recent Advances of Single-Atom Catalysts in CO₂ Conversion. *Energy Environ. Sci.* **2023**, 16, 2759–2803. [CrossRef]
- 148. Li, L.; ul Hasan, I.M.; Farwa1; He, R.; Peng, L.; Xu, N.; Niazi, N.K.; Zhang, J.-N.; Qiao, J. Copper as a Single Metal Atom Based Photo-, Electro-, and Photoelectrochemical Catalyst Decorated on Carbon Nitride Surface for Efficient CO₂ Reduction: A Review. *Nano Res. Energy* **2022**, *1*, e9120015. [CrossRef]
- 149. Zhu, L.; Qin, C.; Wang, Y.; Cao, J. Single-Atom Pt Supported on Non-Metal Doped WS2 for Photocatalytic CO₂ Reduction: A First-Principles Study. *Appl. Surf. Sci.* **2023**, 626, 157252. [CrossRef]
- 150. Zhang, Z.; Wang, Z.; Cao, S.-W.; Xue, C. Au/Pt Nanoparticle-Decorated TiO₂ Nanofibers with Plasmon-Enhanced Photocatalytic Activities for Solar-to-Fuel Conversion. *J. Phys. Chem. C* **2013**, *117*, 25939–25947. [CrossRef]
- 151. Gong, S.; Hou, M.; Niu, Y.; Teng, X.; Liu, X.; Xu, M.; Xu, C.; Ka-Man Au, V.; Chen, Z. Molybdenum Phosphide Coupled with Highly Dispersed Nickel Confined in Porous Carbon Nanofibers for Enhanced Photocatalytic CO₂ Reduction. *Chem. Eng. J.* **2022**, 427, 131717. [CrossRef]
- 152. Photocatalytic CO2 Reduction of C/ZnO Nanofibers Enhanced by an Ni-NiS Cocatalyst—Nanoscale (RSC Publishing). Available online: https://pubs.rsc.org/en/content/articlelanding/2020/nr/c9nr10451h (accessed on 11 September 2024).
- 153. Shao, X.; Li, K.; Li, J.; Cheng, Q.; Wang, G.; Wang, K. Investigating S-Scheme Charge Transfer Pathways in NiS@Ta₂O₅ Hybrid Nanofibers for Photocatalytic CO₂ Conversion. *Chin. J. Catal.* **2023**, *51*, 193–203. [CrossRef]
- 154. Kang, S.; Khan, H.; Lee, C.; Kwon, K.; Sunyong Lee, C. Investigation of Hydrophobic MoSe₂ Grown at Edge Sites on TiO₂ Nanofibers for Photocatalytic CO₂ Reduction. *Chem. Eng. J.* **2021**, *420*, 130496. [CrossRef]
- 155. Prado, A.C.F.; Malafatti, J.O.D.; Oliveira, J.A.; Ribeiro, C.; Joya, M.R.; Luz, A.P.; Paris, E.C. Preparation and Application of Nb₂O₅ Nanofibers in CO₂ Photoconversion. *Nanomaterials* **2021**, *11*, 3268. [CrossRef]
- 156. Li, Y.; Ren, Z.; Gu, M.; Duan, Y.; Zhang, W.; Lv, K. Synergistic Effect of Interstitial C Doping and Oxygen Vacancies on the Photoreactivity of TiO₂ Nanofibers towards CO₂ Reduction. *Appl. Catal. B Environ.* **2022**, *317*, 121773. [CrossRef]
- 157. Zhang, Z.; Chen, R.; Wang, L.; Chen, X.; Ding, J.; Zhang, J.; Wan, H.; Guan, G. Synergistic Effect of Cu²⁺ and Cu⁺ in SrTiO₃ Nanofibers Promotes the Photocatalytic Reduction of CO₂ to Methanol. *Appl. Surf. Sci.* **2023**, 609, 155297. [CrossRef]
- 158. Kang, S.; Khan, H.; Lee, C.S. CO₂ Selectivity of Flower-like MoS₂ Grown on TiO₂ Nanofibers Coated with Acetic Acid-Treated Graphitic Carbon Nitride. *Sol. Energy Mater. Sol. Cells* **2021**, 221, 110890. [CrossRef]

Disclaimer/Publisher's Note: The statements, opinions and data contained in all publications are solely those of the individual author(s) and contributor(s) and not of MDPI and/or the editor(s). MDPI and/or the editor(s) disclaim responsibility for any injury to people or property resulting from any ideas, methods, instructions or products referred to in the content.

ELSEVIER

Contents lists available at ScienceDirect

Journal of CO2 Utilization

journal homepage: www.elsevier.com/locate/jcou



Review article

Advancements in catalytic, photocatalytic, and electrocatalytic CO₂ conversion processes: Current trends and future outlook

Gaukhar Yergaziyeva ^{a,b,*}, Zhengisbek Kuspanov ^{c,d}, Manshuk Mambetova ^{a,b}, Nurlan Khudaibergenov ^{a,b}, Nursaya Makayeva ^{a,b}, Chingis Daulbayev ^{d,e}

- a Institute of Combustion Problems, Almaty, Kazakhstan
- ^b Al Farabi Kazakh National University, Almaty, Kazakhstan
- Satbayev University, Almaty, Kazakhstan
- ^d Institute of Nuclear Physics, Almaty, Kazakhstan
- ^e National Laboratory Astana, Nazarbayev University, Astana, Kazakhstan

ARTICLE INFO

Keywords: CO₂ conversion Tandem catalysis Photocatalytic CO₂ reduction Electrocatalytic CO₂ reduction

ABSTRACT

Climate change, which is caused by increasing greenhouse gas (GHG) emissions, poses a serious threat to humanity, impacting economies, societies, and the environment. Carbon dioxide (CO_2), which is a major contributor to the greenhouse effect, is responsible for climate change and thus must be reduced. Carbon capture, conversion, and storage (CCUS) technology, which involves catalytic, photocatalytic, and electrocatalytic conversions, is a promising method for reducing CO_2 emissions and converting CO_2 into valuable products. Recent advances in catalytic, electrocatalytic, and photocatalytic reduction of CO_2 have highlighted the potential environmental and economic benefits of these technologies. However, the practical application of these techniques is challenging and requires scientific research and engineering efforts to develop efficient materials capable of simultaneously capturing CO_2 and converting it into valuable products. Therefore, this review presents a comprehensive analysis of various catalytic systems for CO_2 capture and conversion. This review aims to identify the advantages and limitations of catalytic systems for CO_2 capture and conversion. In addition, the identified challenges and future prospects in the application of the proposed methods are outlined. Thus, this article covers the current trends and perspectives in the field of combating climate change through efficient CO_2 management.

1. Introduction

Global climate change is a serious threat to humanity, affecting economic, social, and environmental aspects of life. The main cause of climate change is an increase in greenhouse gases, including water vapour, methane, carbon dioxide, ozone, nitrogen oxides, and freons. The main driver of the process is carbon dioxide, which slowly and inevitably contributes to the greenhouse effect. For example, anthropogenic activities have caused $1.0~^{\circ}$ C of global warming compared to pre-industrial levels. If $\rm CO_2$ emissions continue to rise at current levels, global warming will likely reach $1.5~^{\circ}$ C by 2030 [1]. In 2016, the Paris Agreement marked a historic transformation of global climate change as world leaders from 195 countries agreed to combat climate change and its adverse impacts by limiting the increase in global warming below $2~^{\circ}$ C above pre-industrial levels by the end of this century [1]. To date,

more than 130 countries have committed to zero-carbon emissions, as evidenced by recent governmental policies statements. More than 90% of these countries, including the US, the European Union, the UK, and Japan, have set targets to achieve carbon neutrality by 2050. However, according to the Climate Action Tracker, countries or regions that have adopted or are considering carbon-neutral targets account for more than 70% of the global carbon dioxide emissions.

 ${\rm CO_2}$ emissions can be reduced by switching to cleaner fuels, improving ${\rm CO_2}$ capture methods, and altering the Earth's radiation balance [2]. Moreover, carbon capture, conversion and storage (CCUS) technology based on catalytic, photocatalytic, and electrocatalytic conversion is a new and promising approach for effectively reducing ${\rm CO_2}$ emissions and concentration in ambient air [3]. ${\rm CO_2}$ capture technologies can be divided into three types: pre-combustion, post-combustion, and oxy-fuel combustion methods. Because pre-combustion

^{*} Corresponding author at: Institute of Combustion Problems, Almaty, Kazakhstan. *E-mail address*: ergazieva_g@mail.ru (G. Yergaziyeva).

and oxy-fuel combustion capture technologies require appropriate materials and certain conditions to meet high-temperature requirements, little research has been conducted on the application of these two technologies. Post-combustion capture is a widely used, mature technology with good CO_2 selectivity and efficiency [4].

Although climate policy-driven CCUS projects have great potential, the return on investment is still low because of the high capital investment requirements for CO₂ capture and infrastructure, uncertainty about the liability for CO₂ storage and technical failures, the need for risk-sharing mechanisms across multiple sectors and stakeholders, incomplete insurance and financial markets, and low public willingness to store CO₂ in some of the world's most vulnerable countries [2]. These difficulties have prompted research into the theoretical and practical aspects of various methods to solve these problems, as evidenced by the growth dynamics of scientific publications on CCUS from 2000 to 2023 [5–8]. These and many other studies have demonstrated that the ideal solution is to treat CO₂ as a commodity by capturing and converting it into useful products using dual-function materials (DFMs).

On the other hand, converting carbon dioxide into valuable products is a significant challenge that requires optimizing energy consumption, reducing greenhouse gas emissions and achieving economic competitiveness. Converting CO₂ into other substances is hampered by its stability, creating energy barriers, and many technologies suffer from limitations such as high costs, low efficiency, instability, and high fossil energy consumption when breaking C=O bonds. Catalysts are promising tools for practical applications that can convert CO2 into valueadded products and at the same time solve modern energy problems. In addition, combining technologies such as photocatalysis, electrocatalysis and thermal catalysis is seen as a new approach to improve the efficiency of converting CO2 into value-added products. This solution reduces the reaction temperature caused by the thermal catalyst and is capable of achieving sustainable energy conversion. However, the practical application of this technology still requires a significant amount of effort.

Based on this perspective, we believe that a comprehensive analysis of recent advances in CO_2 conversion via catalytic hydrogenation, as well as research into electrocatalytic and photocatalytic approaches to produce high-value chemical compounds, is required. This analysis aims to identify general guiding principles that facilitate the optimisation of these processes. This review presents an analysis of the recent literature on CO_2 capture and its conversion to methane and synthesis gas in the presence of DFM in terms of CO_2 adsorbents and catalysts for methanation and dry reforming of methane. Because the conversion of CO_2 to methane and synthesis gas requires a specific temperature, a thorough understanding of the synergies between catalysts and adsorbents in DFMs is required. Finally, the conclusion summarizes a detailed review of the identified problems and discusses the future prospects of the proposed methods.

2. CO_2 utilization to methane and syngas in the presence of dual function materials (DFM)

Tandem catalysts, or dual-function materials (DFMs), are named based on the structure and roles of the two active components [9]. The term "tandem catalysis" first appeared in synthetic chemistry at the end of the 20th century and has since been used in various reaction systems [10,11]. The first study on the application of DFMs for $\rm CO_2$ capture and conversion into value-added substances was reported in [12,13]. Tandem catalysis not only shifts the reaction via efficient binding between the active components but also eliminates the purification and isolation of intermediates and reduces the energy intensity of the reaction. In recent years, significant progress has been made in the use of tandem synthesis to produce value-added chemicals, liquid fuels from synthesis gases, and $\rm CO_2$ hydrogenation [14–17].

2.1. CO₂ capture and methanation

Under current environmental, legal, and economic conditions, the ${\rm CO}_2$ capture by adsorption and its subsequent hydrogenation to ${\rm CH}_4$ via catalytic methanation is a promising area of research and development. In recent years, progress has been made in both chemotechnological aspects and the development of innovative and efficient adsorbents and catalysts. The DFM for ${\rm CO}_2$ methanation consists of an alkaline adsorbent and a catalytic metal, in some cases supported on the same high surface area support. Its functional mechanism involves the adsorption of ${\rm CO}_2$ to saturation (stage 1), followed by the addition of ${\rm H}_2$ (Eq. 1) fed separately into stage 2 to catalyse the methanation of the adsorbed ${\rm CO}_2$ [10,11].

$$CO_{2adsorbed} + 4 H_2 \rightarrow CH_4 + H_2O$$
 (1)

2.1.1. Sorbents in DFM for CO₂ methanation

The most common sorbents in DFM for CO₂ capture and methanation are alkali metal oxides such as Na₂O, K₂O, MgO, and CaO. Owing to its high theoretical adsorption capacity (17.8 mmol/g) and low cost, CaO is widely used as a CO₂ adsorbent. However, the main problem with CaObased sorbents is their high decay rate, which reduces their efficiency after 20-30 cycles because of abrasion and sintering. The stability of CaO is affected by its textural characteristics, which depend on the precursor from which it is derived. Highly dispersed CaO provides better stability than CaO derived from limestone. For example, Cao dispersion and deposition on porous g-Al₂O₃ increase methane yields owing to CO₂ diffusion to active centres within the DFM, i.e. from the CaO sites to the Ru sites [12]. Owing to the temperature limitations of CO₂ hydrogenation to methane, Na₂O and K₂O are popular CO₂ methanation sorbents in the DFM. The dispersions of Na₂O, CaO, and K₂O on g-Al₂O₃ also showed that Na₂O and CaO exhibited the best adsorption capacities. The highest methanation rate was observed for Na₂O-containing DFM (0.614 mmol CH₄/g DFM) as the adsorbent. CaO (0.610 mmol CH₄/g DFM) was also an acceptable candidate for sorbents in the DFM compared to K2O (0.466 mmol CH₄/g DFM). The increase in the adsorption properties of the Na₂O sorbent compared to those of CaO and K₂O is because the addition of Na to g-Al₂O₃ promotes the formation of Al-O ionic centres, which allow access to more hydroxyl centres for CO₂ adsorption to form reversible bidentate and polydentate carbonates [18].

Magnesium-based adsorbents are also widely used in DFM owing to their low cost and sintering stability compared to CaO. MgO adsorbents exhibit a higher theoretical CO2 absorption capacity of 24.8 mmol/g than CaO (17.8 mmol/g), making them more promising for CO₂ capture and utilisation. MgCO₃ regenerates 100% at 300 °C in a pure H₂ stream, whereas CaCO₃ regeneration requires a significantly higher temperature of 600 °C. Moreover, MgCO3 regeneration in a pure H2 stream can provide CH_4 selectivity of > 95% at 300 °C [19]. Thus, a study of the cyclic stability of hydrotalcite-based DFM during CO2 capture and methanation showed that the decrease in the CO2 sorption capacity of DFM from 0.52 mmol/g to 0.32 mmol/g is attributed to the formation of irreversible bulk polydentate carbonate. To stabilize MgO during CO2 capture, Li can be used as a promoter [20]. To promote MgO in DFM, various alkali metal precursors (Li, Na, and K) are used to increase the sorption capacity of DFM up to 4 mmolCO₂/g DFM. DFM operates stably for 10 cycles at temperatures below 300 °C [21]. The cycling performance of DFM can be increased at lower temperatures (250 °C) using Ni/MgO-Al₂O₃ composites. However, the low Ni content in the DFM composition leads to the formation of difficult-to-recover particles such as Ni-O-Mg and/or Ni-O-Al, reducing DFM recoverability.

The nature of the sorbent precursor also plays a role in the DFM preparation. For example, replacing the Na₂CO₃ precursor with NaNO₃ in DFM synthesis [22] showed that, unlike nitrate precursors, alkali metal carbonates do not completely decompose during the reductive

pretreatment in $\rm H_2$ at 400 °C; thus, some amorphous particles remain on the catalyst surface, requiring temperatures above 600 °C to decompose. In turn, these particles tend to obscure the active Ru centres, limiting the catalytic activity of the hydrogenation catalyst while reducing the process selectivity towards methane in favour of CO. However, this can be partially avoided if the carrier is pre-impregnated with a similar amount of $\rm Na_2CO_3$ or $\rm K_2CO_3$.

Furthermore, the sorption capacity of the DFM is affected by the sorbent content [13]. A relationship was established between the contents of dispersed K_2CO_3 , Na_2CO_3 , and MgO adsorbents and the CO_2 sorption capacity of the DFM. The sorbent content in the DFM varied from 5 to 20 wt%. It has been shown that a high sorbent content does not always lead to a higher sorption capacity of the DFM. The optimum contents of Na_2CO_3 and MgO for increasing their capacity were 10 wt% [23].

The sorption characteristics of the sorbents in the DFM are influenced by both the temperature of the methanation process and the composition of the initial reaction feedstock. The performance of the CaO-based DFMs showed a significantly more positive correlation with increasing temperature than the Na₂O-based DFMs [24]. Moreover, the performance of Na₂O-based DFMs improved significantly when the ambient air was humidified. Adsorption under humid conditions was 2.36 times greater than that under dry conditions because of the formation of dispersed NaHCO₃, whereas DFM containing CaO performed poorly in the presence of moisture during the adsorption step [24].

Another factor affecting the sorption capacity of a sorbent is the nature of the carrier used to disperse it. An investigation into different carriers (such as CeO $_2$, CeO $_2$ /ZrO $_2$, CeC, SiO $_2$, ZrO $_2$ -Y, and zeolites) have demonstrated that g-Al $_2$ O $_3$ is the most effective carrier for DFM and can adsorb CO $_2$ on Al $_2$ O $_2$ -OH groups. The authors [25] investigating the DFM surface using DRIFTS in situ at 320 °C proposed that the interaction of Na $_2$ O and Al $_2$ O $_3$ produces Al-O-Na $^+$ on which CO $_2$ adsorption occurs with the formation of bidentate carbonates. Thus, developing DFMs with adsorbents capable of adsorbing and releasing CO $_2$ in the temperature range effective for CO $_2$ hydrogenation to methane is crucial for CO $_2$ capture and methanation.

2.1.2. Catalysts in DFM for CO₂ methanation

 CO_2 methanation is a complex process involving kinetic constraints. Therefore, developing active and selective catalysts for CO_2 methanation is important. For this purpose, Ni- [18,26,27], Ru- [12,13,18,21,22,28–31], and Li-based [32,33] catalysts have been investigated. As shown in Fig. 2, the temperature range of 290–330 $^{\text{o}}\text{C}$ is favourable for

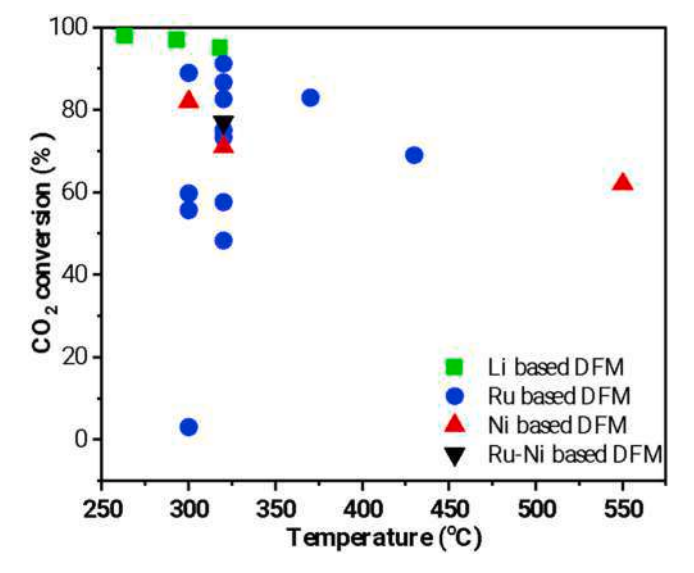


Fig. 1. - Influence of the nature of DFM on CO₂ conversion during methanation.

methanation in the presence of DFM. Ni-based catalysts are the most widely studied because of their high catalytic activity and low cost [28].

The high Ni content of DFMs favours CO_2 capture and methanation because of the close contact between the adsorbent and metal phase [34]. In addition, a high Ni content favours carbonate decomposition at lower temperatures. Presumably, the recoverability of the Ni particles increased in the presence of the adsorbent because it prevented the interaction of Ni with the carrier (Al₂O₃), favouring the formation of easily recoverable NiO particles. The characteristics of the DFM depend upon the content of metallic Ni⁰, the concentration of oxygen vacancies, and the content of alkali element salts in the samples. Both the bulk diffusion kinetics of CO_2 adsorption and methanation kinetics can be facilitated by increasing the metallic Ni⁰ and oxygen vacancy concentrations [35].

The main disadvantage of Ni catalysts is the oxidation of metallic Ni in the presence of oxygen in the reaction mixture. Ni alone cannot methanate adsorbed CO₂; small amounts of precious metal (≤1% Pt, Pd or Ru) are required for enhancing the Ni reduction and activation even after exposure to O2-containing flue gas. The addition of 1% wt. of precious metals enhanced the reduction of NiO_x to metallic Ni (at 320 °C), allowing methanation to proceed, with Ru outperforming Pt and Pd. The best results for CO₂ capture (0.52 mmol CO₂/g) and CH₄ formation (0.38 mmol CH₄/g) were obtained using a composite of 1% Ru, 10% Ni, and 6.1% Na₂O/Al₂O₃ with proven stability over 20 cycles, indicating the excellent long-term stability of Ru-promoted Ni-based DFM [26]. In addition, the reduction of NiO_x to metallic Ni can be enhanced by rare earth elements. For example, lanthanum (La) in Ni-La/ZrO2 improved the Ni reduction ability without changing the reaction mechanism by forming active formate intermediates to yield CH₄. In addition, La in Ni-La/ZrO₂ allows a moderate increase in the CO₂ capture capacity and, importantly, a very fast conversion of captured CO₂ to CH₄ with a high H₂ utilisation efficiency [36].

A study of the effect of alkali metals on the activity of 15 wt% NiO/Al $_2$ O $_3$ showed that methane productivity and cyclic stability strongly depend on the type of alkali metal and the temperature of cyclic tests [37]. DFM containing K and Na showed optimal performance in the highest temperature range (350–400 °C), while the Ba containing material showed optimal performance in the lowest temperature range (250–300 °C). CH $_4$ productivity is decreased when the flue gas also contains O $_2$ and H $_2$ O due to Ni oxidation, competitive adsorption of H $_2$ O and accumulation of unreactive carbonate species. Methane production is restored when capture is carried out under dry and anaerobic conditions. K-Ni/Al provided the highest performance and CH $_4$ selectivity in simulated flue gas cyclic testing at 350 °C. This is due to the increased reducibility of nickel and the higher reactivity of carbonate particles formed during the capture stage, resulting in higher methane productivity.

Modification of nickel-based DFM with cesium made it possible to increase its operating stability to 250 h in the cyclic process of CO_2 capture and methanation [38]. The authors of [39] associate the increase in the ability of DFM to capture CO_2 and methanate with the introduction of cesium to an increase in the number of basic sites, mainly related to centers with medium and strong strength. However, modification with cesium slows down the rate of CH_4 formation and also CH_4 selectivity decreases to 92% due to the parallel formation of CO.

Noble metals can be used not only as modifiers of Ni-containing DFM but also as the main active metal to improve catalytic properties. The capture and hydrogenation processes were compared at 320 $^{\circ}$ C with Ni, Ru, and Rh as candidates for methanation [18]. The findings indicated that Rh is the second-best methanation catalyst after Ru; however, its higher cost requires a reduction in metal content, resulting in fewer catalytic centres and a lower reaction rate compared to Ru. Because of its high catalytic activity, Ru has proven to be the most promising catalyst among noble metals in the following ways: first, even a small Ru content (5% Ru, 10% CaO/Al₂O₃) can provide high methane yield (7.07 mmolCH₄/gcat) and CO₂ conversion (89%); second, Ru-based DFMs

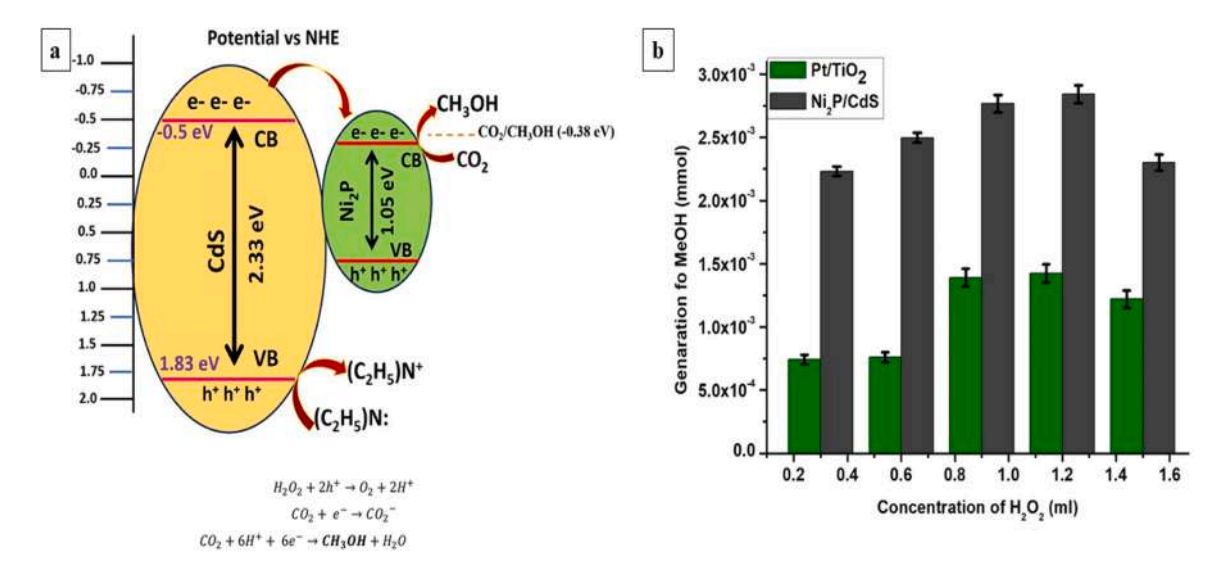


Fig. 2. – Possible pathways for charge transfer and the reduction of CO2 by the 5 wt% Ni2P/CdS composite, along with the corresponding chemical equations (a); effect of increasing concentration of H₂O₂ from 0.2 to 1.6 ml on the conversion of CO₂ to MeOH generation (b) [87].

demonstrated good stable performance in CO_2 capture and methanation [12]. For example, a composite of 5%Ru-6.1%Na₂O/g-Al₂O₃ demonstrated stable performance for 80 h with a methane yield of 0.35 mmol CH₄/gDFM. Moreover, its BET, chemisorption, and transmission electron microscopy analysis confirmed its stable characteristics, indicating no significant changes in surface area and a slight increase in Ru dispersion.

Additionally, Ru-based DFMs exhibit good performance in the presence of oxygen in the reaction mixture. Thus, Ru-based catalysts (5% Ru, 10% CaO/Al₂O₃) can be easily reduced to an active metallic state because of the high H2 flow rate required for methanation after exposure to O2-containing flue gas [29]. The high dispersibility of Ru also affects its activity in CO2 capture and methanation. For example, increasing the weight ratio of CaO to Ru promoted the spillover of CO2 from the CaO sites to Ru and improved the methanation efficiency. The introduction of a CeO2 carrier also favoured Ru dispersion and improved methanation efficiency. Ru deposited on CeO₂ in rod and particle forms, compared with cubic CeO2, possesses a larger surface area and better dispersion and carrier-metal interactions, resulting in improved process performance. In addition, the oxygen vacancies on CeO2 enhance the CO₂ adsorption efficiency. Combined CeO₂ materials in rod and particle forms (Ru/rod-CeO2-MgO and Ru/particle-CeO2-MgO) exhibit higher catalytic efficiencies than Ru/cube-CeO₂-MgO [30].

Rizzetto et al. [40] investigated the influence of the nature of the support on the activity of $2\% Ru + 30\% CeO_2$, showing that the deposition of ruthenium-cerium on a support with a large surface area is critical for maintaining the methanating activity of this catalytic system under conditions of cyclic adsorption-hydrogenation of CO_2 . The ruthenium-cerium catalyst supported on Al_2O_3 adsorbed smaller amount of CO_2 (about $200~\mu mol~g^{-1}$ per cycle) compared to the sample supported on ZSM-5 (about $300~\mu mol~g^{-1}$); however, 2% Ru + 30% CeO_2/Al_2O_3 showed better methanation performance due to the intermediate reaction of ruthenium and cerium, giving a maximum of 51% converted CO_2 and producing up to $111~\mu mol~g^{-1}$ CH_4 at $250~^{\circ}C$.

The catalytic efficiency of DFMs for CO_2 capture and methanation can be enhanced by adding promoters. For example, Li-promoted 1% Ru/Al $_2O_3$ outperforms its Na- and K-promoted counterparts in terms of CO_2 capacity and methanation of trapped CO_2 [32]. Temperature-programmed reaction tests in H_2 showed that the Li-Ru/Al catalyst can catalytically convert pre-adsorbed CO_2 to methane with high selectivity at temperatures between 200 and 350 °C upon doping with LiNO $_3$, which can react with Al $_2O_3$ to form a mixed spinel phase. Li-doped Ru/Al $_2O_2$ has been extensively tested in integrated CO_2

capture and methanation to evaluate the effects of basic particles (O_2 and H_2O) and poisonous impurities (SO_2) on real flue gases [33]. A study involving SO_2 contents of up to 100 ppmv demonstrated remarkable resistance to sulphur poisoning and a delayed loss of CO_2 capacity owing to long-term sulphur accumulation.

The work [41] investigated the mechanisms of sulfur poisoning and the ability to self-regenerate the catalytic properties of Li-Ru DFM. The authors showed that Li-Ru/Al $_2$ O $_3$ can achieve integrated capture and methanation of CO $_2$ at low temperatures, demonstrating remarkable tolerance to SO $_2$ impurities that are captured and stored as Li $_2$ SO $_4$. Long-term accumulation of sulfates on DFM affects its ability to capture CO $_2$, but only minorly affects the catalytic activity of methanation. The authors developed a Li-Ru/Al $_2$ O $_3$ regeneration procedure that completely restored the DFM's CO $_2$ capture capacity and methanation catalytic activity.

Thus, Ru appears to be the most active methanation catalyst; however, its content should be as low as possible to reduce costs and limit the H_2 consumption associated with its redox cycle. For the same reason, strongly reduced sorbent/promoter phases, such as CeO_2 , should be avoided. The possibility of replacing some Ru with Ni requires further investigation for additional cost reductions. Promoting Ru-containing DFM using Li outperforms its Na- and K-promoted counterparts in terms of CO_2 capacity and methanation of sorbed CO_2 .

For industrial applications of bifunctional materials, they should be tested in realistic feed streams to evaluate the effects of O_2 , water vapor, and other substances present in trace concentrations in real flue gas streams on DFM activity and stability. In addition, cycling operation at higher pressures and for longer periods of time should also be studied to test the stability of the DFM under more severe conditions.

2.2. Capture and dry reforming of methane

Dry reforming of methane (DRM) is an endothermic process that converts CO_2 and CH_4 in the presence of a catalyst into a mixture of CO and H_2 (Eq. 2), a synthesis gas. Synthesis gas is a valuable building block for the production of liquid fuels and chemicals [42]. Owing to the large reserves of CH_4 in the form of natural and shale gases, DRM has great potential for CO_2 utilization.

$$CO_2 + CH_4 \rightarrow 2CO + 2H_2 \Delta H_{298 \text{ K}}^0 = 247 \text{ kJ mol}^{-1}$$
 (2)

Recently, the successful integration of CO_2 capture with DRM has been reported [43]. This combination simultaneously realises the utilization of flue gas as a resource while increasing the amount of CH_4 . This

integrated process involves time-separated CO_2 capture and conversion steps. CO_2 is first captured using a sorbent (typically an alkaline oxide) and then calcined in a CH_4 atmosphere to regenerate the sorbent and produce the synthesis gas. The CO_2 capture and DRM processes can be realised in a single reactor, reducing operating and capital costs and energy consumption; however, the key to success is the use of a suitable bifunctional material consisting of two main active components: CO_2 sorbents and a catalyst to convert the sorbed CO_2 into synthesis gas.

2.2.1. Sorbents in DFM for dry reforming of methane

The selection of CO₂ adsorbents for developing DFMs for methane capture and DRM is challenging because they must adsorb and desorb CO₂ in cycles at the higher temperatures at which DRM occurs [44]. Because sorbents for CO2 capture and DRM are intended to work with a reforming catalyst, a solid adsorbent should be selected [45]. CaO and MgO are the most available solid sorbents for CO₂ capture owing to their significant theoretical CO₂ capture capacity compared to other sorbents [46]. However, the most serious problem with CaO sorbents is their sintering, which decreases their ability to capture CO2 after 10 cycles and DRM [47]. To increase the sintering stability of CaO, high-temperature stabilisers such as Al₂O₃, ZrO₂, or MgO are used [48, 49]. In this case, decreasing the molar ratio of Ca²⁺ to Mg²⁺ resulted in materials with larger surface areas and pore volumes and improved the thermal stability of the CaO-containing material [49]. In addition to stabiliser incorporation, the presence of numerous mesopores and grains < 100 nm in the CaO composite enhances CO2 adsorption on CaO

The efficiency of the adsorbents for CO_2 capture and DRM is also affected by the presence of catalysts. The deposition of NiO on CaO accelerates the $CaCO_3$ decomposition by almost three times [53]. In addition, the nature of the carbonates formed during CO_2 adsorption on the sorbent is affected by the carrier, which is typically used to increase sorbent dispersibility. Thus, strongly bonded monoidal carbonates are formed on massive CaO at 300 °C, which partially rearrange at 450 °C to form bridging carbonates and evolve towards the crystalline phase. In contrast, dispersed CaO/Al_2O_3 adsorbs CO_2 exclusively as weakly and reversibly bound carbonates, regardless of temperature or loading, and prevents the formation of strongly bound carbonates [54]. MgO is another widely used CO_2 adsorbent; however, it is not suitable for DFM for CO_2 capture and DRM. The lower adsorption capacity of MgO compared to CaO [55] is attributed to its narrower operating conditions (300–400 °C).

Lithium silicate-based materials have been widely investigated for CO_2 capture and DRM at high temperatures [56,57]. However, compared with CaO-based adsorbents, their adsorption capacities are limited. To improve the adsorption characteristics of lithium silicate-based materials at lower CO_2 concentrations, additional alkaline treatment or metal alloying is necessary [57].

Thus, adsorbents for DFM must be stable at high temperatures and must not degrade over time during CO_2 capture and DRM. Lithium silicate-based materials are suitable for the cyclic adsorption and desorption of CO_2 at high temperatures. However, their adsorption capacity is limited compared to high-capacity CaO -based adsorbents. Therefore, CaO is the most effective adsorbent for DFM for CO_2 capture and DRM; however, its thermal stability must be improved by introducing stabilisers.

2.2.2. Catalysts in DFM for dry reforming of methane

DRM involves high temperatures and energy costs [58]. Catalysts based on Ni, Rh, Mo, and Co can lower the thermodynamic barrier and reduce the temperature [59,60]. The most common catalysts for DRM are Ni-based catalysts. The conversion of methane and trapped CO₂ was affected by the Ni dispersion in the bifunctional material. Thus, the hydrogen and carbon monoxide yields decreased during the reaction [58]; this was associated with the loss of active surface area caused by the gradual sintering of Ni particles, which increased Ni particle size

from 11.0 to 27.2 nm. The interactions between the metal and adsorbent prevent Ni sintering [53]. Catalyst sintering can also be prevented by introducing stabilising additives. Because of the stabilising effect of the $\rm ZrO_2$ layer, both CaO and Ni particles were more resistant to sintering, ensuring isothermal $\rm CO_2$ capture and release at a temperature favourable for DRM [61]. In addition to sintering, one reason for the decontamination of Ni-containing DFMs is the carbonisation of the catalyst surface caused by methane decomposition with increasing DRM temperature. The addition of cerium oxide to a CaO-Ni-based bifunctional material promotes carbon gasification during DRM, suppresses the accumulation of inactive carbon on Ni during a long reaction, and enhances the activation of $\rm CO_2$ and $\rm CH_4$ because of its redox properties, thereby increasing the production of synthesis gas during $\rm CO_2$ capture and DRM [61,62].

Studies on CO_2 capture and DRM have mainly focused on ideal CO_2 capture conditions. However, in real factory flue gases, many components, such as oxygen and water vapour, affect the DFM efficiency. The authors showed that CO_2 capture and DRM under simulated flue gas conditions using Ni10-CaO (DFM) as the bifunctional material were sensitive to steam and oxygen [63]. The water in the flue gas aided the kinetics of CO_2 capture, whereas oxygen oxidised Ni to NiO and prevented further CO_2 conversion by methane during DRM. The reduction of NiO to metallic Ni resulted in instantaneous CO_2 formation, making it difficult for methane to interact with Ni. In cyclic CO_2 capture and DRM, the deposited carbon is gasified into CO via a reverse Boudoir reaction. However, after the DRM reaction, the steam gasification of carbon deposited on the bifunctional material enables carbon removal with the formation of synthesis gas byproduct and does not adversely affect the overall performance of the process.

Additionally, iron-containing DFMs have exhibited good characteristics for CO_2 capture and DRM [64]. DFMs based on Ca-Fe can restore their state and activity during flue gas oxidation and carbonation. A reaction occurs between methane, CaCO_3 , and $\mathrm{Fe}_2\mathrm{O}_3$, with the complete oxidation of methane to CO_2 and $\mathrm{H}_2\mathrm{O}$. During the reaction, all the $\mathrm{Fe}_2\mathrm{O}_3$ was converted into $\mathrm{Fe}_3\mathrm{O}_4$, which was further transformed into $\mathrm{Fe}_3\mathrm{O}_4$ and $\mathrm{Fe}_3\mathrm{O}_4$ with the formation of H_2 and CO_3 . In the last stage, CaCO_3 reappeared because $\mathrm{Fe}_3\mathrm{O}_4$ was reduced by methane to form CO_2 , which was then sorbed by CaO_3 [64].

Therefore, bifunctional CO_2 capture and DRM materials must be stable at high temperatures and should not degrade over time. Lithium-silicate-based materials are suitable for the cyclic adsorption and desorption of CO_2 at high temperatures. However, their adsorption capacities are limited compared to CaO-based high-capacity adsorbents. Bifunctional materials based on CaO-Ni can capture and release CO_2 at temperatures favourable for DRM. The carbonation of CaO during CO_2 capture is strongly influenced by the basicity of the material, and the conversion of methane and captured CO_2 is influenced by Ni dispersion in the bifunctional material. The addition of cerium oxide to a CaO-Ni-based bifunctional material enhances the activation of CO_2 and CH_4 because of its redox properties, thus lowering the required temperatures and activation energies of carbonation and decarbonisation stimulated by dry reforming.

3. Photocatalytic disposal of CO2

An alternative approach to solving environmental problems related to CO_2 emissions and sustainable production of chemical fuels is photocatalysis, which simulates typical photosynthesis [67]. Various methods, such as carbon capture and storage, electrochemical, thermochemical, and catalytic conversion, and biological fixation, are available for reducing CO_2 emissions. However, these methods incur additional compression and transportation costs [68], high energy and heat consumption [69,70], and restrictions on enzyme production and regeneration [71]. In contrast, photocatalysis is environmentally friendly and economically efficient because it uses abundant solar energy as the main source of energy and water as a reactive substance and

does not produce toxic products or waste. Typically, photocatalysis involves the conversion of CO2 and water into solar fuels such as methane (CH₄), carbon monoxide (CO), methanol (CH₃OH), formic acid (HCOOH), and formaldehyde (HCHO) when various semiconductor photocatalysts are irradiated with sunlight. In general, photocatalytic CO₂ reduction involves three main stages: (1) the absorption of light by a semiconductor, resulting in the generation of electron-hole pairs; (2) the separation of photogenerated electrons and holes and their transport to the photocatalyst surface; (3) the occurrence of surface reactions when electrons reduce CO2 and holes oxidise H2O [72]. The formation of the final reduction product depends on multistage CO2 reduction and is determined by the number and speed of transferred electrons in the system and the mode of adsorption between CO2 and the photocatalyst surface [73]. The overall photocatalytic efficiency of CO₂ reduction depends on the combined thermodynamic and kinetic aspects of the aforementioned processes [67].

Among the various CO_2 reduction photocatalysts, the most widely used materials are TiO_2 [74], ZnO [75], $SrTiO_3$ [76,77], and ZnS [78]. Unfortunately, the efficiency of traditional photocatalysts does not meet modern requirements because of (1) sensitivity to light in a narrow range due to a wide band gap, (2) rapid recombination of photogenerated charge carriers due to the short lifetime of electrons, and (3) weak adsorption of CO_2 and low diffusion of electrons to the reaction sites of photocatalysts. To overcome these disadvantages, many studies have proposed increasing the efficiency of photocatalysts by alloying them with various metals and non-metals, modifying structures into new forms, surface modification with noble metals, and fabricating heterojunctions and nanocomposites with various semiconductors [79]. This also increases the photosensitivity range and the effective separation and transfer of photogenerated charges. The main techniques used to improve the efficiency of CO_2 reduction photocatalysts are as follows:

Defect engineering: One of the important strategies for improving the photocatalytic characteristics and selectivity of CO2 conversion into hydrocarbon fuel is to modify defects by alloying the photocatalyst with metals and nonmetals. In particular, Li et al. [80] engineered ultrathin (~4.1 nm) Bi₂WO₆ nanosheets by doping them with carbon heteroatoms using a hydrothermal method, followed by calcination. The modified photocatalyst C-Bi₂WO₆ with an ultrathin nanosheet structure demonstrated twice the photocatalytic reduction of CO2 as pure Bi2WO6 nanosheets. Carbon doping successfully broadened the light absorption spectrum and improved charge separation, thereby reducing recombination. In another study [81], the Sn_vNb_{1-v}O₂ photocatalyst obtained by strongly substituting Nb in SnO2 using hydrothermal treatment demonstrated significantly increased photocatalytic CO2 reduction activity with a generation rate of \sim 292.47 μ mol/(g h), which is 19 times higher than that of pure SnO2 without using any sacrificial agent under artificial sunlight. The authors reported that the strong substitution of Sn⁴⁺ with a more valent Nb⁵⁺ resulted in the formation of a band structure with improved properties, including a more efficient photocatalytic CO₂ reduction and the formation of a preferred multi-carbon compound, C₂H₅OH. This demonstrated that strong doping of metal oxides with high-valent cations enables the enhancement and modulation of the photocatalytic CO₂ reduction to obtain value-added products.

Morphology improvement: The morphology of semiconductor photocatalysts is important for the separation of charge carriers, effective capture of incident light, and surface area of contact with reagents (CO₂, H₂O, and sacrificial reagents) [82]. Recently, significant progress has been made in the development of highly efficient photocatalysts with complex architectures for photocatalytic CO₂ reduction in a wide range of light wavelengths. For example, Wang et al. [83] synthesised hierarchical TiO₂ @ZnIn₂S₄ CSHS heterojunctions with hollow spheres possessing a large surface area and abundant active sites, which contributed to effective charge separation and improved reflection and scattering of light. This hierarchical design and heterojunction significantly increased the rate of the multielectronic photocatalytic CO₂ reduction, with the total yields of CO, CH₃OH, and CH₄ being 2.75 and

4.43 times higher than pure $ZnIn_2S_4$ and TiO_2 , respectively. Cheng et al. [84] successfully synthesized a three-dimensional hierarchical flower-like composite based on $Cd_{0.8}Zn_{0.2}S$ (C_8Z_2S -F) with ultrathin petals via in situ self-assembly, using sodium citrate as a morphology regulator. Owing to the hierarchical flower-like structure, which makes excellent use of a wide range of light and possesses desirable properties of CO_2 adsorption, effective CO production was 41.4 μ mol g⁻¹ during photocatalytic CO_2 reduction under visible light for 3 h; this was 2 times more than that of $Cd_{0.8}Zn_{0.2}S$ (C_8Z_2S -NP) (14.7 μ mol g⁻¹) without the addition of any sacrificial agent or cocatalyst.

Composite formation. The formation of semiconductor composites in photocatalytic systems is gaining popularity because of their high activity, charge separation, and low recombination. The formation of heterojunctions between semiconductors allows individual photocatalysts to improve their photostability, charge transfer, and light absorption [79]. Nitrogen-doped graphene (NG) on TiO₂ hollow spheres (HS) with a large area and close interfacial contact were synthesised via chemical vapour deposition [85]. The optimised TiO₂/NG HS composite showed an increased CO2 conversion rate (total yield of CO, CH3OH, and CH₄) of 18.11 μmol g⁻¹ h⁻¹, which is approximately 4.6 times higher than pure TiO₂ HS. The significantly improved photocatalytic activity was attributed to the close interfacial contact and abundant pyridine N-sites, which contributed to the efficient separation of photogenerated electron-hole pairs and charge carrier transfer. Similarly, a new AgBr/BiOBr heterojunction with surface oxygen vacancies obtained using a simple chemical method has demonstrated significantly increased photocatalytic activity for the reduction of CO2 to CO and CH4 [86]. The reaction rates were 212.6 and 5.7 µmol g⁻¹ h⁻¹, respectively, which were 9.2 and 5.2 times higher than those achieved by pure BiOBr. Experiments and DFT calculations confirmed that the AgBr/BiOBr heterojunction bands possesses an S-scheme, which contributes to a more efficient sunlight usage, improved charge separation, increased redox properties, and CO2 activation.

Cocatalyst loading: Cocatalyst loading onto the photocatalyst surface facilitates the separation and transport of photogenerated charge carriers, thus increasing their photocatalytic activity and selectivity for CO₂ reduction. In particular, using Ni₂P-containing CDs as a cocatalyst results in a higher efficiency of methanol formation from CO2 under visible light compared to pure CDs [87]. Due to the more negative conduction band (CB) edge of CdS compared to Ni₂P under visible light exposure, photo-generated electrons efficiently migrate from the CB of CdS to Ni₂P. Electrons accumulated at the surface of Ni₂P particles facilitate the reduction of CO_2 to CO^{2-} , while the valence band holes on CdS act as oxidants for H₂O₂ (serving as a sacrificial donor), resulting in the production of O₂ and H⁺. Subsequently, the generated CO²⁻ undergoes a reaction with H⁺ to yield methanol in the presence of triethylamine, functioning as the sacrificial electron donor (Fig. 2). The optimal catalyst ratio was 5% of the mass of Ni₂P loaded onto the CDs, which led to the highest methanol yield (2843 µmol/g). In contrast, a Pt/TiO₂ reference photocatalyst containing noble metals demonstrated a methanol yield of 1424.8 µmol/g. In addition, the cocatalyst/photocatalyst system always has an optimal load of the cocatalysts at which the highest photoactivity is achieved. For example, Wang [88] reported that the amount of Ag loaded as a cocatalyst changes CO selectivity during CO2 photorecovery. Moreover, the maximum CO selectivity of 60.9% was found at 0.5 wt% Ag/HST, whereas CO selectivities at 0.3 wt% Ag/HST and 1 wt% Ag/HST were 54.8% and 52.6%, respectively. A decrease in selectivity at 1 wt% Ag/HST is because the excessive loading of the photocatalyst negatively affects the charge separation and hinders the absorption of photons of light, which ultimately reduces the photocatalytic activity. In addition, increasing the loading may decrease photoactivity because an excess of photocatalyst blocks the surface-active centres of the photocatalyst and prevents its interaction with CO₂, H₂O, or sacrificial reagents [89].

3.1. Synergy of photocatalysis and adsorption for CO₂ reduction and conversion to carbon fuel

Despite considerable efforts to develop effective visible-lightcontrolled photocatalysts for converting CO2 into chemical fuel, their effectiveness remains insufficient for practical use because of their small specific surface area and poor ability to adsorb and diffuse CO2. To achieve the desired efficiency of the CO₂ photo-recovery process, an ideal photocatalytic system must possess high catalytic activity and a high ability to adsorb CO₂. The integration of a material with high CO₂ capture ability into a photocatalytic system has great potential to increase CO2 conversion efficiency [90]. For example, the synergistic effect of 1D highly crystalline polymer nitride (CNs) nanorods arranged in an orderly manner on 2D graphene with a high specific surface area provides more efficient light collection, CO2 capture, and electron diffusion at the interface compared to the nanorods alone or without any sacrificial agent [91]. The most attractive adsorbents are porous materials, owing to their highly developed porous structures with increased specific surface areas. The CO₂ conversion process occurs in two stages: CO2 and H2O capture and surface diffusion along the surface of the photocatalyst, occupying the active sites [92,93]. Porous materials for trapping possess numerous adsorption centers; however, compared to semiconductors or noble metals, they are less active in photocatalytic CO₂ conversion [51]. Thus, to achieve higher photo-transformation of CO2, the porous material must possess abundant adsorption sites and a short diffusion length. In accordance with systematic studies on gas adsorption and separation, the development of photocatalysts for CO2 conversion is based on porous materials such as porous carbon materials, metal-organic polymers (MOP), metal-organic frameworks (MOF), and covalent organic frameworks (COFs). In particular, Wang et al. [90] have developed a composite based on porous hyperstitched polymer-structured TiO2-graphene with a large surface area of 988 m² g-1 and high CO2 absorption capacity, demonstrating a high photocatalytic performance of CH₄ equal to 27.62 µmol g⁻¹h⁻¹ without using any sacrificial reagents or noble metal co-catalysts. The authors claimed that combining microporous organic polymers with photocatalysts improves CO₂ adsorption and diffusion, visible light absorption, and the effective separation of photoinduced electron-hole pairs. In addition, combining porous carbon materials with photocatalysts increases their photocatalytic activity for CO₂ reduction by increasing the possibility of CO₂ absorption and coexposure [51,52]. Sun et al. [94] reported the synthesis of a 0D/3D composite photocatalyst of Cu-NPs/g-C₃N₄ foam by originally loading Cu NPs onto g-C₃N₄ foam using combined template and microwave approaches. The optimised Cu-NPs/g-C₃N₄ composite demonstrated increased photocatalytic activity for CRR owing to its three-dimensional micron-scale pores, and the amount of CO2 adsorption by Cu-NPs/g-C₃N₄ was $0.179 \mu mol g^{-1}$ at 1.00 bar and 273.15 K, which was approximately 2.63 times higher than that of pure g- C₃N₄ powder. Compared with other porous materials, MOFs with high porosity and stability in strongly acidic and basic media can act as a matrix for these active photocatalytic substances, preventing their damage and accumulation while maintaining high availability [95]. In this regard, the sequential deposition of affordable and inexpensive MAPbI₃ perovskite quantum dots into the pores of Fe-porphyrin-based MOF PCN-221(Fe_x) facilitates record-high photocatalytic reduction performance of CO2 to CO (34%) and CH4 (66%), with a yield of 1559 µmol g⁻¹, which is 38 times higher than that obtained using PCN-221(Fe_{0.2}) without perovskite QDs [96]. The significant improvement in the photocatalytic CO2 reduction is attributed to the sufficiently close contact between the QDs and the Fe catalytic site in the MOF, which facilitated the rapid transport of photoinduced charges in the QDs to the Fe photocatalytic sites. In addition to combining photocatalysts with porous materials, photocatalysts can also be modified by adding alkaline and alkaline earth metals or their oxides to improve their ability to absorb and effectively reduce CO₂ [97,98]. Tang et al. [99] showed that the substitution of magnesium ions (Mg²⁺) in hydrogen titanate

nanotubes (H-TNTs) significantly improved the chemisorption and activation of CO_2 on photocatalysts. Compared with pure H-TNTs, 0.1 M-Mg-H-TNTs exhibited the highest reaction performance among the Mg^{2+} -modified samples, and their photocatalytic activity in reducing CO_2 to CO and CH_4 increased by 3.8 and 16.5 times, respectively.

In addition to metal-organic polymers and metal-organic frameworks, covalent organic frameworks (COFs) represent porous materials without metallic components that exhibit significant potential in photocatalytic systems and possess excellent carbon dioxide capture capabilities. COFs offer a high surface area and crystallinity, serving as excellent supports for anchoring photocatalytically active centers through coordinated interactions among their components and various types of catalysts [100,101]. In comparison to MOFs and MORs, COFs consist of organic elements, making them more accessible and cost-effective. Moreover, the majority of COFs demonstrate high chemical stability in various conditions, such as high temperatures and alkaline or acidic environments, thanks to robust covalent bonds. Meanwhile, in most MOFs, metal ions often lose control over organic ligands, becoming free ions in the bulk solution due to weak coordination bonds [102].

Based on these findings, the development of universal photocatalytic systems possessing a high ability to capture CO_2 and effective photocatalytic activity is one of the most promising approaches for converting CO_2 using solar energy.

3.2. Photoreactors for CO₂ recovery and future prospects

Currently, the practical use of photocatalytic systems for CO₂ reduction is limited because of the low efficiency of photocatalysts, slow reaction rates and insufficient efficiency of the photocatalytic reactors. Photocatalysis requires a good light source and a photoreactor that ensures maximum contact between light, CO2, and the photocatalyst surface with high mass transfer [103]. The development of commercially viable photoreactors requires serious engineering efforts in terms of configuration and design. Three types of reactors are commonly used in photocatalytic processes: suspension, fixed bed, and membrane reactors [104]. In addition, the design of photoreactors for CO₂ reduction may vary depending on the operating mode (continuous or periodic), number of phases (three-phase or two-phase), and type of photocatalyst layer (stationary or fluidized) [105]. Suspension photoreactors are most commonly used because of their simplicity and low production costs. In such systems, a triple-phase (gas-liquid-solid) photocatalyst is used; it is combined in a fluidised form to ensure mass transfer between the catalyst and reagents and provide a large illuminated surface [106]. Based on a suspension reactor, Nabil et al. [107] developed a mesomachine photocatalytic reactor capable of converting CO₂ into fuel in a continuous mode. This enables high productivity on a relatively large scale, producing several grammes of fuel per day. In addition, the introduction of energy-saving LEDs and uniform lighting with a high area-to-volume ratio ensures efficient exchange of mass and photons, and the additional presence of a cooled water bath promotes CO2 solubility. However, suspension systems have limitations for large-scale use, owing to the difficult extraction of the photocatalyst from the suspension, the low active surface area of the photocatalyst because of the absorption of main light energy by the liquid, and additional costs for constant mixing and circulation, making them less economical [106, 108]. Suspension photoreactors are typically used to evaluate the photoactivity of the main photocatalyst [109], whereas fixed-bed reactors are more suitable for scaling. In fixed-bed reactors, the photocatalyst is fixed to a supporting material such as monoliths, balls, or fibres placed inside the reactor [110]. In these photoreactors, the light source is usually located in the middle of the reactor or near its surface, providing uniform illumination over the entire surface of the photocatalyst layer [108,111]. The main advantages of fixed-layer photoreactors are the ability to operate continuously with high gas output and the ease of extraction of the photocatalyst from the spent solution [112]. However, potential difficulties in the practical application of immobilised photocatalytic systems are associated with the small area of the illuminated surface and the fast photon scattering rate [103]. Membrane photocatalytic reactors operate in a continuous mode and efficiently convert $\rm CO_2$ into chemical fuel [113,114]. For example, a photocatalytic reactor with a $\rm C_3N_4$ -based photocatalyst loaded onto a Nafion membrane turned out to be 10 times more efficient than a conventional photoreactor operating with a periodic regime during reduction of $\rm CO_2$ to alcohol (MeOH + EtOH) [115]. In addition, membrane reactors prevent a reverse reaction and facilitate high selective control of the products because $\rm H_2O$ oxidation and $\rm CO_2$ reduction occur in separate chambers [79]. However, these photoreactors have some limitations related to weak transfer of reagents to the photocatalyst surface and membrane contamination, which may reduce their effectiveness [104].

Based on the above research, it can be concluded that the photocatalytic conversion of CO2 into carbon fuel is still in its development stage and requires further research and engineering efforts. The main obstacle to the practical application of this process is a lack of effective photocatalytic materials that can reduce CO₂ using visible light. Despite continuous improvements in the performance of these photocatalysts via defect engineering, morphology improvement, composite formation, cocatalyst loading, and synergy with adsorbents, the efficiency of photocatalytic systems lags significantly behind that of other CO2 reduction technologies (Table 2). Another problem affecting the commercialisation of the photocatalytic process is the low efficiency of photocatalytic reactors. To date, various types of photoreactors have been developed depending on the operating conditions. However, aspects such as the design, reagent supply to the photocatalyst surface, effective surface illumination, and reliable application of the photocatalyst layer to the substrate require further research. Thus, future strategies for improving the photocatalytic reduction of CO₂ into chemical fuels should aim at (1) developing effective photocatalysts with high photoactivity and the ability to recover CO2 using the visible radiation spectrum; (2) improving the design of photocatalytic reactors using light more efficiently with uniform illumination of the surface layer and increasing the mass transfer of reagents; (3) improving the reliability and stability of photocatalytic systems and preventing contamination of photocatalysts; (4) optimising operating conditions by controlling operating parameters; (5) combining the photocatalytic CO2 reduction with other technologies such as CO2 capture, electrocatalysis, or thermocatalysis to increase the energy efficiency of photocatalysis and the costeffectiveness of other technologies.

4. Electrocatalytic reduction of CO₂

The use of a cost-effective method for industrial-scale CO2 conversion can mitigate the negative impact of large CO₂ emissions on the environment [121,122]. An attractive method to solve this problem is the electrochemical CO₂ reduction reaction (CO₂ RR), which can be performed under mild conditions [123]. The electrochemical conversion of CO2 into high-energy products has attracted attention owing to fast reaction kinetics, configurable conversion efficiency, controlled selectivity, use of reaction systems with environmental operating parameters (pressure and temperature), and compatibility with electricity obtained from renewable sources (e.g. hydropower, solar, and wind) [124]. The characteristic products of the electrocatalytic CO₂ RR are single-carbon (C₁) (e.g. carbon monoxide, methane, and formic acid) and multi-carbon (C₂₊) products (e.g. ethylene, ethanol, n-propanol, and acetic acid) [125]. However, the practical application of this process remains problematic because of the lack of effective electrocatalysts with good stability and high product selectivity, which are desirable for simplifying product purification and improving conversion energy efficiency [123].

The electrocatalytic process involves two processes at the cathode and anode, which occur in separate compartments separated by a

membrane to prevent the reaction products from mixing (Table 5). The electrocatalytic CO_2 RR occurs at the interface between the catalyst and the electrolyte, with CO_2 adsorbing at the cathode and electrons transferring from the cathode to CO_2 , leading to the desorption of the reduced products from the cathode. Meanwhile, oxygen is generated at the anode and H^+ is released, which moves to the cathode, resulting in CO_2 reduction. Because of the various reaction pathways available during CO_2 RR, the final products depend on many factors, such as the type of catalyst, solvent, electrolyte, and operating conditions (such as applied potential, temperature, and pressure of CO_2) [126,127]. A typical heterogeneous CO_2 RR involves four stages:

Adsorption of CO₂ onto the catalyst surface.

Reduction of adsorbed CO₂ to intermediately reduced CO₂.

Further reduction, protonation, or other chemical reactions necessary for the formation of the final products.

Desorption of end products.

The change in the number of electrons and protons transferred in Stages 2 and 3 depends significantly on the adsorption energy of the reaction intermediates, leading to the formation of various products [128].

- adsorption of CO₂ on the surface of the catalyst;.
- reduction of adsorbed CO₂ to intermediate reduced CO₂;.
- further reduction and protonation or other chemical reactions necessary for the formation of final products;.
- desorption of end products. The change in the number of electrons and protons transferred at stages 2 and 3 significantly depends on the adsorption energy of the reaction intermediates and leads to the formation of various products [128].

4.1. Catalysts for electrocatalytic reduction of CO₂

As a result of the electrochemical CO_2 RR, various reduction products ranging from C_1 to C_2 are formed. Despite extensive studies on CO_2 RR, there is an urgent need to develop highly efficient and selective electrocatalysts capable of meeting the demands of industrial applications for specific products [129,130]. Various catalytic systems, including metals and their alloys [123,131–133] metal compounds (oxides, nitrides, and sulphides) [44,134], metal-nitrogen-carbon structures [135, 136], heterogeneous molecular catalysts [137], and organometallic frameworks (MOF), have been used as electrocatalysts for CO_2 RR [138, 139]. In this review, we consider various types of electrocatalysts developed over the past five years for CO_2 RR.

4.1.1. Electrocatalysts for the conversion of CO_2 into products with C_1

Noble metals, including Au, Ag, and Pd, have been used in the electrochemical CO $_2$ RR and exhibit excellent characteristics. However, their high cost and scarcity limit their widespread use [140]. Various metals, such as zinc and copper, are used as alternatives to noble metal catalysts. For example, the CuO/SnO $_2$ heterojunction catalyst obtained by the hydrothermal method demonstrates a yield with respect to C $_1$ products with a Faraday efficiency (FE) of more than 80% [141]. The authors found that the CuO and SnO $_2$ heterojunction provides a large number of composite interfaces that facilitate electron transfer for CO $_2$ RR

Similar results were obtained for the Cu₂O/Cu composite, which was fabricated using a two-stage method involving thermal oxidation and electro-reduction; the Faraday efficiency of the HCOOH and CO products reached 84% at - 0.7 V [142]. In situ combinational analysis showed that Cu $^{+}$ on the Cu₂O/Cu electrode inhibited hydrogen formation and promoted the CO $_{2}$ RR by stabilising CO $_{2}$ adsorption.

In addition to Cu-containing catalysts, carbon-based materials have also been investigated as electrocatalysts for CO_2 RR. A catalyst doped with nitrogen from carbon black demonstrated a CO selectivity of 97.8% at a current density of 9.1 mA·cm⁻² [143]. The results showed that the nitrogen content effectively improves the CO selectivity in nitrogen-doped carbon materials; however, excessive oxygen content

Table 1
Tandem catalysts, their activity and selectivity for CO₂ hydrogenation to CH₄.

Year	DFMs	Pre-treatment of DFM	CO ₂ capture conditions	Methanation conditions	Cycle of adsorption/methanation	CO ₂ capacity *	CO ₂ conversion	CH ₄ yield*	Ref.
2015	5% Ru 10% CaO/ Al ₂ O ₃	4% H ₂ /N ₂ V= 26 ml/min T = 320°C	$10\% \text{ CO}_2/\text{N}_2$ $t = 30 \text{ min T} = 320^{\circ}\text{C}$ $P = 1 \text{ atm}$	$5\% H_2/N_2$ t = 20 min $T = 320^{\circ}\text{C}$	20	0.4	82.7	0.3	[12]
2016	5% Ru 10% Na ₂ CO ₃ /Al ₂ O ₃	$4\% H_2/N_2$ V= 26 ml/min T = 320 °C	$5\% \text{ CO}_2/\text{N}_2$ $t = 30 \text{ min T} = 320^{\circ}\text{C}$ P = 1 atm	$\begin{split} P &= 1 \text{ atm} \\ 5\% \text{ H}_2/\text{N}_2 \\ t &= 30 \text{ min} \\ T &= 320 \text{°C} \end{split}$	3	0.5	N/A	1.05	[13]
2016	5% Ru 10% K ₂ CO ₃ /Al ₂ O ₃ ,	$4\% \ H_2/N_2$ V= 26 ml/min T = 320° C	$5\% \text{ CO}_2/\text{N}_2$ $t = 30 \text{ min T} = 320^{\circ}\text{C}$ P = 1 atm	$P = 1$ atm $5\% \ H_2/N_2$ $t = 30 \ min$ $T = 320 \ ^{\circ}C$	N/A	0.1	N/A	0.91	[13]
2017	5% Ru, 10% Na ₂ CO ₃ /Al ₂ O ₃	5% H ₂ /N ₂ T-320°C P-1 atm	$7.5\% \ CO_2 + 15\%$ $H_2O + 4.5\%O_2 \ /N_2$ $V = 300 \ ml/min$ $T = 320^{\circ}C$	$\begin{split} P &= 1 \text{ atm} \\ 5\% \ H_2/N_2 \\ V &= 300 \ \text{ml/min} \\ t &= 30 \ \text{min} \\ T\text{-}320^{\circ}\text{C}, \end{split}$	12	0.29	73.3	0.21	[28]
2018	5% Ru, 6.1% $Na_2O/\gamma\text{-}Al_2O_3$	$5\%~H_2/N_2$ t = 15 min T = 320 °C	P-1 atm $7.5\% \text{ CO}_2 + 15\%$ $\text{H}_2\text{O} + 4.5\%\text{O}_2 / \text{N}_2$ t = 15 min $\text{GHSV} = 521 \text{ h}^{-1}$ $\text{T} = 300^{\circ}\text{C}$	P-1 atm, $15\% \text{ H}_2/\text{N}_2 \text{ GHSV}$ = 1389 h^{-1} t = 15 min T = 300 °C P = 1 atm	50	0.44	80	0.35	[65]
2019	5%Ru-6.1%Na ₂ O/ Al ₂ O ₃	$10\text{-}15\% \ H_2/N_2$ $T = 320 \ ^{\circ}\text{C}$	$\begin{array}{l} \text{P-1 atm} \\ 7.5\% \ \text{CO}_2 + 15\% \\ \text{H}_2\text{O} + 4.5\% \text{O}_2 \ / \text{N}_2 \\ \text{t} = 40 \ \text{min} \\ \text{V} = 30 \ \text{ml/min} \\ \text{T} = 320 ^{\circ} \text{C} \end{array}$	$10\%~H_2/N_2$ $V = 30~ml/min$ $t = 60~min$ $T = 320~^{\circ}C$ $P = 1~atm$	N/A	0.42	75	0.32	[18]
2022	$1\%~{\rm Ru} + 10\%$ ${\rm CaO/Al_2O_3}$	$20\% \text{ H}_2/\text{N}_2$ V= 16.7 ml/min T = 300 oC	P-1 atm 400 ppm CO_2 / air V=400 ml/min $T=25 \circ C$	$15\%~H_2/N_2$ V= 100 ml/ min t = 30 min	3	0.45	N/A	0.3	[24]
2022	1% Ru+ 10% Na ₂ O/Al ₂ O ₃	$20\%~H_2/N_2 \label{eq:h2}$ V= 16.7 ml/min T = 300 oC	400 ppm CO_2 / air $V=400 \text{ ml/min}$ $T=25 \circ C$	$T = 300 \circ C$ $15\% H_2/N_2$ V = 100 ml/min t = 30 min $T = 300 \circ C$	10	0.55	N/A	0.35	[24]
2022	Li-Ru/Al	5% H_2/Ar $T = 400 ^{\circ}C$ t = 1 h	$10\%CO_2/Ar \ t = 30 \ min$ $T = 263^{\circ}C$ $T = 293^{\circ}C$	$10\% \text{ H}_2/\text{Ar}$ $t = 30 \text{ min T} = 263^{\circ}\text{C}$ $T = 293^{\circ}\text{C}$	3 3 3	0.03 0.04 0.06	98 97 95	0.32 0.34 0.29	[32]
2023	Li-Ru/Al		$T = 318 ^{\circ}\text{C}$ $5\% \text{CO}_2/\text{N}_2$ V = 20 Sl/h $T = 300 ^{\circ}\text{C}$	T = 318 °C $15\% H_2/N_2$ V = 20 Sl/h T = 300 °C	4	0.29	89.2	0.20	[33]
2024	Li-Ru/Al	$20\% \text{ H}_2/\text{N}_2$ T = 450 oC t = 2 h	$5\% \text{ CO}_2/\text{N}_2$ V= 20 Sdm ³ /h T = 300 °C	$\begin{aligned} &CO_2/H_2/N_2 = 1/4/5\\ &GHSV = 33000\ h^{-\ 1} \end{aligned}$	N/A	0.29	94	0.19	[41]
2023	K-Ni/Al	N_2 T = 500 oC t = 1 h H_2 T = 500 oC t = 1 h	$5\% \text{ CO}_2 + 11\%$ $\text{H}_2\text{O} + 4.5\% \text{ O}_2/\text{Ar}$ $\text{T} = 350 ^{\circ}\text{C}$	$5\%~H_2/~Ar$ V= $60~ml/min$ T = $350~^{\circ}C$	7	0.35	N/A	0.32	[37]
2023	Na-Ni/Al	N_2 $T = 500 \circ C$ $t = 1 h$ H_2 $T = 500 \circ C$ $t = 1 h$	$5\% \ CO_2 + 11\% \\ H_2O + 4.5\% \ O_2 / \ Ar \\ T = 350 \ ^{\circ}C$	$5\%~H_{2}/~Ar$ $V=60~ml/min$ $T=350~^{\circ}C$	7	0.23	N/A	0.19	[37]
2023	Ba-Ni/Al	N_2 $T = 500 \circ C$ $t = 1 h$ H_2 $T = 500 \circ C$	$5\% \text{ CO}_2 + 11\%$ $\text{H}_2\text{O} + 4.5\% \text{ O}_2/\text{ Ar}$ T = 350 °C	$5\%~H_{2}/~Ar$ $V=60~ml/min$ $T=350~^{\circ}C$	7	0.14	N/A	0.10	[37]
2019	10%Ni - 6.1% Na ₂ O/Al ₂ O ₃	t = 1 h 10-15% H_2/N_2 $T = 650 ^{\circ}C$	$7.5\% \text{ CO}_2 + 15\%$ $\text{H}_2\text{O} + 4.5\%\text{O}_2 / \text{N}_2$ $\text{t} = 40 \text{ min}$ $\text{V} = 30 \text{ ml/min}$ $\text{T} = 320^{\circ}\text{C}$ P-1 atm	$\label{eq:hammonic} \begin{split} 10\%~H_2/N_2\\ V &= 30~ml/min\\ t &= 60~min\\ T &= 320~^{\circ}C\\ P &= 1~atm \end{split}$	3	0.43	71	0.61	[18]

(continued on next page)

Table 1 (continued)

Year	DFMs	Pre-treatment of DFM	CO_2 capture conditions	Methanation conditions	Cycle of adsorption/methanation	CO ₂ capacity	CO ₂ conversion	CH ₄ yield*	Ref.
2019	1% Ru, 10% Ni, 6,1% "Na ₂ O"/ Al ₂ O ₃	$15\% \text{ H}_2/\text{N}_2$ t = 150 min $T = 320 ^{\circ}\text{C P} = 1 \text{ atm}$	$10\%CO_2/N_2$ $T = 320 ^{\circ}C$ P-1 atm	$10\%H_2/N_2$ V= 30 ml/min, t = 1 h T = 320 °C	20	0.56	77	0.38	[31]
2024	2%Ru/30%CeO ₂ / Al ₂ O ₃	N_2 V= 150 ml/min T = 500 oC 5% H ₂ /N ₂ V= 150 ml/min T = 500 oC	$8\%CO_2/N_2$ $T = 250 ^{\circ}C$ $t = 30 ^{\circ}min$ $V = 150 ^{\circ}ml/min$	$5\%H_2/N_2$ V = 15 ml/min t = 63 min $T = 250 ^{\circ}\text{C}$	N/A	0.2	55	0.11	[40]
2024	2%Ru/30%CeO ₂ / ZSM-5	N_2 V= 150 ml/min T = 500 oC 5% H ₂ /N ₂ V= 150 ml/min T = 500 oC	$8\%CO_2/\ N_2$ $T=250\ ^\circ C$ $t=30\ min$ $V=150\ ml/min$	$\label{eq:sigma} \begin{split} 5\% H_2/N_2 \\ V &= 15 \text{ ml/min} \\ t &= 63 \text{ min} \\ T &= 250 ^{\circ}\text{C} \end{split}$	N/A	0.3	32	0.09	[40]
2021	1% Ni/CeO ₂ -CaO	$5\% \ H_2/N_2$ $t = 30 \ min$ $T = 350 \ ^{\circ}C \ P = 1 \ atm$	$15\%CO_2/N_2$ V= 50 ml/min, t = 1 h T = 550 °C P-1 atm	$100\%H_2/N_2$ V= 50 ml/min, t = 1 h T = 550 °C P-1 atm	N/A	15.3	62	8.0	[27]
2023	20% LaNiO ₃ /CeO ₂	$5\% \ H_2/N_2$ $t = 2 \ h$ $T = 550 \ ^{\circ}C \ P = 1 \ atm$	5% CO ₂ /He V= 50 ml/min	100%H ₂ V= 50 ml/min, t = 1 h T = 480 °C P-1 atm	N/A	0.11	N/A	0.074	[66]
2023	20% La _{0.5} Ca _{0.5} NiO ₃ / CeO ₂	$5\%~H_{2}/N_{2}$ $t=2~h$ $T=550~^{\circ}C~P=1~atm$	$5\% \text{ CO}_2/\text{He}$ V= 50 ml/min T = $480 ^{\circ}\text{C}$	$100\%H_{2}$ V= 50 ml/min, t = 1 h T = 480 °C P-1 atm	30	0.17	N/A	0.139	[66]
2022	Ru/cube -CeO ₂ - MgO	$5\% \text{ H}_2/\text{N}2 \text{ at}$ $V = 50 \text{ ml/min}$ $T = 3 \text{ h}$ $T = 300 \text{ oC}$	$35\% CO_2/N_2$ V = 100 ml/min t = 1 h T = 300 °C	$5\% H_2/N_2$ V= 50 ml/min t = 30 min T = 300 °C	N/A	N/A	3	0.05	[30]
2022	Ru/particle-CeO ₂ - MgO	$5\% \text{ H}_2/\text{N2} \text{ at}$ V = 50 ml/min T = 3 h T = 300 oC	$35\% \text{ CO}_2/\text{ N}_2$ V= 100 ml/min t = 1 h T = 300 °C	$5\% H_2/N_2$ V = 50 ml/min T = 30 min $T = 300 ^{\circ}\text{C}$	N/A	N/A	59.8	0.29	[30]
2022	Ru/rod-CeO ₂ -MgO	$5\% \text{ H}_2/\text{N}_2 \text{ at}$ V = 50 ml/min T = 3 h T = 300 oC	$35\% \text{ CO}_2/\text{ N}_2$ V = 100 ml/min t = 1 h $T = 300 ^{\circ}\text{C}$	$5\% H_2/N_2$ V = 50 ml/min t = 30 min $T = 300 ^{\circ}\text{C}$	9	N/A	55.7	0.33	[30]
2023	*AMS promoted Ni/MgO	1 = 350 GC $100\%\text{H}_2$ T = 450 °C	$65\%CO_2/N_2 t = 15 min$ $T = 300 ^{\circ}C$	$50\%H_2/N_2 t = 10 \text{ min}$ $T = 300 ^{\circ}\text{C}$	5	6.46	82.0	0.85	[26]

^{*} CO₂ capture capacity (mmol/gDFM); CO₂ conversion (%); CH₄ yield (mmol/gDFM)

inhibits the activity of the CO2 RR.

4.1.2. Electrocatalysts for the conversion of CO_2 into C_2 and C_{2+} products The synthesis of C₂ and C₂₊ products by the electrochemical CO₂ RR is more difficult than that of C1 because of the higher energy requirements and slower kinetics of C-C bond formation. The most effective catalysts in the CO₂ RR for the synthesis of carbon products are Cubased electrocatalysts because of their high catalytic activity and low cost [144–146]. However, high overvoltage and poor stability limit the further development of Cu-based catalysts [147,148]. To overcome these disadvantages, bimetallic Cu-based electrocatalysts have been proposed. For example, a Cu-Al electrocatalyst with an FE greater than 80% was used for ethylene formation at a current density of 400 mA·cm⁻². Excellent catalytic efficiency was achieved by several CO bonding centres and the surface orientation of Cu-Al alloys [144]. Another example is CuBi catalysts with a high Bi content and 85.4% FE obtained by electrodeposition at a partial current density of 38.4 mA·cm⁻² [149]. In addition, the CuBi catalyst was found to possess strongly acidic and basic Lewis centres that contribute to the formation of bidentate carbonates after CO_2 adsorption. The strong interactions between Cu and Bi, the presence of reduced copper (Cu⁺) particles, and oxygen defects on the catalyst surface determine the high efficiency of CO2 RR for propane.

Recently, the authors [150] investigated a catalyst by coating Cu-I with a hydrophobic polytetrafluoroethylene (PTFE) polymer, and the FE for C_2H_4 was 70.2% at - 1.4 V. Studies have shown that the hydrophobic surface of the Cu-I/PTFE electrode increases the local concentration of CO_2 , and Cu^+ particles are stabilised because of the continuous formation of OH radicals during CO_2 RR. MOF structures are also used because of their excellent properties, high conductivities, and large surface areas. Thus, CuO nanoparticles deposited on Cu-MOF nanosheets demonstrate 50% ethylene FE at - 1.10 V.

4.2. CO2 RR electrocatalysts for synthesis gas production

Obtaining a highly efficient electrocatalyst with excellent stability for the reduction of CO₂ to synthesis gas is a challenging task. Currently, the most effective electrocatalysts are precious metals such as gold and silver, owing to their selectivity and energy efficiency. Thus, catalysts based on the nanoporous AuCu₃ alloy demonstrated CO₂ RR depending on the surface composition; the more Cu atoms formed on the surface, the more H₂ was formed. This was attributed to an increase in $\Delta G_{\rm COOH^*}$ and a decrease in $\Delta G_{\rm H^*}$. Moreover, AuCu₃ exhibited a positive correlation between the applied potential and FE of CO, realising a CO/H₂ ratio range of 1:5–6:1 [151]. Surprisingly, using a highly efficient catalytic system (nano-Ag nickel-based for CO₂ RR in an electrolyte with an ionic

Table 2
Recent photocatalysts over the past five years, their productivity and selectivity in CO₂ conversion.

Photocatalyst	Light source	Reactant	Products	Reaction rate (μ mol (g h) ⁻¹) / Quantum efficiency	Selectivity	Ref.
^m CD/CN	300 W Xe lamp (420 nm)	$CO_2 + H_2O$	CH ₃ OH	13.9 / 2.1%	99.6%	[72]
Cu ₂ O-Pt/SiC/IrO _x	300 W Xe lamp ($\lambda \ge 420$ nm)	$CO_2 + H_2O$	HCOOH	896.7	-	[79]
C-Bi ₂ WO ₆ s	300 W Xe lamp	$NaHCO_3 + H_2SO_4 + H_2O$	CH ₃ OH and C ₂ H ₅ OH	1.15 and 0.65	-	[80]
$Sn_xNb_{1-x}O_2$	300 W Xe lamp, 200 mW/cm ²	-	CH_3OH , CH_3CHO and C_2H_5OH	5.25, 13.25 and 130.36	-	[81]
$3D-ZnIn_2S_4$	300 W Xe lamp (AM 1.5 G filter)	$CH_3CN + TEOA$	CO	276.7	-	[82]
TiO2 @ZnIn2S4 CSHS	300 W Xe lamp	$NaHCO_3 + H_2SO_4 + H_2O$	CO, CH ₃ OH and CH ₄	9.28, 4.78 and 4.26	-	[83]
$3D-Cd_{0.8}Zn_{0.2}S$	300 W Xe lamp	$CO_2 + H_2O$	CO	13.8	89.9%	[84]
TiO2/NG HS	300 W Xe lamp	$NaHCO_3 + H_2SO_4$	CO, CH ₃ OH and CH ₄	18.11 (Total)	-	[85]
AgBr/BiOBr	300 W Xe lamp	$CO_2 + H_2O$	CO and CH ₄	212.6 and 5.7	-	[86]
5 wt% Ni ₂ P/CdS	300 W Xe lamp (420 nm), 2.75 W/cm ²	$CO_2 + DMF + TEA$	CH ₃ OH	2843	-	[87]
Ag/H ₂ SrTa ₂ O ₇	300 W Xe lamp ($\lambda > 200 \text{ nm}$)	$CO_2 + H_2O$	CO	0.39	60.9%	[88]
HCP-TiO ₂ -FG	300 W Xe lamp (420 nm), 433 W/cm ²	$NaHCO_3 + H_2SO_4$	CH ₄	27.62	83.7%	[90]
CNNA/rGO	350 W Xe arc lamp (AM1.5 filter)	$CO_2 + H_2O$	CO, CH ₄ , CH ₃ OH and C ₂ H ₅ OH	6.65, 4.30, 0.53 and 1.15	87%	[91]
3Cs3Bi2Br9/Bi-MOF	300 W Xe lamp	$CO_2 + H_2O$	CO	572.24	-	[50]
A-PCN/CdSe-DETA	300 W Xe lamp ($\lambda > 420 \text{ nm}$), 5.56 mW/cm ²	$NaHCO_3 + H_2SO_4$	CO	25.87	-	[52]
2D/2D Ti ₃ C ₂ /porous g-C ₃ N ₄	300 W Xe arc lamp ($\lambda >$ 200 nm)	$CO_2 + H_2O$	CH ₄	0.99	-	[51]
0D/3D Cu-NPs/g- C ₃ N ₄	300 W Xe lamp (350 nm–780 nm)	$CO_2 + H_2O$	CO	10.247	97.9%	[94]
MAPbI ₃ @PCN-221 (Fe _{0.2})	300 W Xe lamp (420 nm), 100 mW/cm ²	$\mathrm{CH_{3}CN} + \mathrm{H_{2}O}$	CO and CH ₄	104 and 325	34% and 66%	[96]
S-K _{0.475} WO ₃	300 W Xe lamp	$Na_2CO_3 + H_2SO_4$	CH ₄	5.27	87.6%	[98]
Ni(OH) ₂ -10%GR	300 W Xe lamp ($\lambda \ge$ 420 nm), 405 mW/cm ²	$MeCN + TEOA + H_2O$	CO	10725	96%	[116]
Pt@Zn-TPY-TTF CPG	300 W Xe lamp (400-750 nm)	$CH_3CN + TEA + H_2O$	CH ₄	292	97%	[117]
TiO ₂ /rGO	300 W Xe lamp (400 nm), 2.75 mW/cm ²	$CO_2 + TEOA + H_2O$	CH ₄	49 / 3.17%	-	[118]
Bi ₂ MoO ₆ - SOVs@In ₂ S ₃	300 W Xe lamp ($\lambda \ge 420$ nm), 21 mW/cm ²	$CO_2 + H_2O$	СО	28.54	94.1%	[119]
NiPc-NiPOP	white LED (400 nm \leq $\lambda < 800$ nm)	$\mathrm{MeCN} + \mathrm{TEOA} + \mathrm{H_{2}O}$	CO	1942.5	96%	[120]
MoS ₂ @COF	300 W Xe lamp, (420–780 nm), 209 mW/cm ²	$H_2O+ CH_3CN + [Ru(bpy)_3]$ $Cl_2 \cdot 6 H_2O + TEOA$	C_2H_6	56.2	83.8%	[100]
CoNi-COF-3	300 W Xe lamp (400 nm)	$H_2O + CH_3CN + [Ru(bpy)_3]$ $Cl_2 \cdot 6 H_2O + TEOA$	CO	2567	92.2%	[101]

liquid (IL)-acetonitrile) to convert CO₂ into synthesis gas, the molar ratio of CO/H₂ in synthesis gas can be adjusted in the range of 1:5–26:1, with the current densities of 363.6, 458.2, and 644.7 mA·cm⁻² at molar CO/H_2 ratios of 1:1, 1:2, and 1:3, respectively [152]. This is comparable to the best results reported thus far for the electrochemical conversion of CO2 into synthesis gas. The high efficiency of CO2 RR-to-synthesis gas can be explained by the synergistic stabilising effect of nano-Ag and cationic IL C4/5-H for the intermediate product *COO- to form CO, as well as the contribution of cationic C2-H to hydrogen evolution. Additionally, Pd-based electrocatalysts have demonstrated increased activity for the CO2 RR because of the small crystallite size, correct particle distribution, and the formation of a solid solution, which modifies the lattice parameters, causing better adsorption for the CO2 RR. Pd nanoparticles are known to absorb H2 in their lattice structure, which contributes the hydrogenation of the intermediate CO₂ * to generate CO₂ reduction products. Thus, Pd-Cu₂O/C and Pd-SnO₂/C catalysts are suitable for the highly selective development of CO₂ RR electrocatalysts for pollution control and the production of useful chemical products and fuels at room temperature [153]. In work [154], Pd catalysts on transition metal nitride (TMN) substrates were studied. The authors found that Pd-modified niobium nitride (Pd/NbN) generates much higher CO and H2 partial current densities and greater CO FE than Pd-modified vanadium nitride (Pd/VN). This indicates that NbN is a promising substrate for Pd modification, resulting in increased electrochemical conversion of CO2 into synthetic gas with a potential reduction in precious metal content. However, the main disadvantage of noble metal-based catalysts is their high cost. Researchers have continued to explore

unconventional combinations of electrocatalysts to open new avenues for electrocatalysis. One such exciting achievement is the integration of Cu with In as an electrocatalyst, demonstrating the versatility and potential of this field. Thus, the use of Cu-In hydroxides with a controlled composition (Cu_xIn_y -OH) showed that the selectivity of the CO_2 reduction products shifted from CO to formate with increasing the In content of the Cu_xIn_y -OH electrocatalysts. The high copper electrocatalyst mainly produced CO, reaching FE up to 75.8% at -0.59 V[155].

Although zinc and nickel alloys have demonstrated their use as electrocatalysts, iron is another widely studied and versatile material in electrochemistry. In [156], the authors designed an electrocatalyst with Fe-containing double active centres on N-doped porous carbon (Fe/FeN₄C) to stimulate the CO₂ RR for controlled synthesis gas production. The Fe/FeN₄C catalyst exhibits high (FE) CO and H₂ equal to 100%, high overall current density (>39.33 mA·cm⁻²) and wide H₂/CO ratio (1.09–7.08). Density functional theory calculations indicate that individual Fe atoms dispersed in the N-doped carbon structure, along with the inclusion of Fe nanoparticles, can reduce the *CO adsorption energy, thereby synergistically enhancing the catalytic activity.

Recently, N-doped porous carbon materials containing base metals (called "M-N-C") have formed a group of functional materials to replace precious metal-based catalysts for the electrochemical ${\rm CO_2}$ RR. Gas sorption tests revealed a typical mesoporous structure with sufficient open active centres and convenient mass transfer channels. M-Ni-N-C electrocatalysts exhibit high catalytic activity when using a wide range of raw materials and are easily scaled up in production, contributing to the further development of advanced, economical M-N-C

Table 3 CO_2 RR electrocatalysts for C_1 and C_2 products.

Year	Reactor type	Catalyst	Electrolyte	Current density (mA·cm ⁻²)	Potential (V)	Stability (h)	FE, %	Products	Ref.
2020	H-type cell	MFM-300 (In)	0.5 M EmimBF ₄ (1-ethyl-3- methylimidazolium tetrafluoroborate	46,1	-2,15	2	99,1%	НСООН	[164]
2023	H-type cell	Fe/Ni-NC	-	4.5	- 0677	40	92,9	CO	[159]
2023	H-type cell	ZnSn(OH) ₆ (MCs)	0,5 mol•L ⁻¹ KHCO ₃	7,31	-0,9 ∼ − 1,3	12	71,88%	HCOOH and CO	[165]
2023	-	Cu-I/PTFE	-	-	-1,4	-	70,2%	C_2H_4	[143]
2023	H-type cell	Cu ₂ O/Cu	0,1 M KHCO ₃	12,21 ²	-0,7	10	52%/22%	HCOOH and CO	[142]
2022	flow cell	Ni@NC	-	220	-0,87	100	98%	CO	[166]
2023	H-type cell	Ni-Ag/PC-N	0,1 M KHCO ₃	12.6	-0,8	-	99.2	CO	[158]
2023	-	CuZn-SAs/NC	0,1 M KCl	49.7	- 1,1	45	84,7%	CH ₄	[160]
2021	flow cell	Cu/CeO ₂	1,0 M KOH	-	-0,7	-	78,3%	C_2H_4	[167]
2021	H-cell	Cu-MOF	0,5 M KHCO ₃	-	-1,17	-	50%	C_2H_4	[168]
2020	flow cell	Cu-Al	-	400	1,5	-	80%	C_2H_4	[144]
2023	H-type cell	Cu ₂ O/Ag	0,5 M KHCO ₃	17.8	-1,2	16	66.8%	C_2H_4	[161]
2021	H-type cell	Cu-N-C	0,1 M KHCO ₃	CO = 0.4 HCOOH = 1.4	-0.6/- 0.9	-	38.1%/ 40.8%	HCOOH and CO	[169]
2021	flow cell (MEA)	Cu- _{DS}	$0.1~\mathrm{M~KHCO_3}$	100	0,7	30	53%/18%	C ₂ H ₅ OH and C ₃ H ₇ OH	[121]
2021	H-type cell	CuO-ZnO_{x} without N-doped graphene support	0,1 M KHCO ₃	3.74	-0,80	12	15%/ 22,3%/ 10.2%/20%	CH ₃ OH C ₂ H ₅ OH, n-C ₃ H ₇ OH, HCOOH	[170]
2022	-	$CuO-ZnO-MoS_2$	-	121	-0.6 and – 0.9	-	24,6% and 11,1%	CH ₃ OH and C ₂ H ₅ OH	[171]
2022	-	CuCo-MOF-74	-	19.28	-0.75	110	79.2%	C ₂ products	[162]
2022	flow cell	Ag@C@Cu	1,0 M KOH	126	-0.64	-	31.5%	C ₂ H ₅ OH	[17]
2022	-	CuO/Ni SAs	-	1220,8	-	-	54.1%/ 28.8%	C_2H_5OH , C_2H_4	[163]

Table 4Characteristics of catalysts for electrocatalytic reduction of CO2 to synthesis gas over the past 5 years.

Year	Catalyst	Electrolyte	Current density (mA cm ⁻²) Molar ratio (CO/H ₂)	Adjustable range of molar ${\rm CO/H_2}$ ratio	Stability (h)	FE of CO	Ref.
2023	AuCu ₃	0,1 mol•L ⁻¹ KHCO ₃	< 100	0,20-6	10	95%	[151]
2023	nano-Ag@Ni	[C ₄ mim][PF ₆]/MeCN	363,6 (1:1) 458,2 (1:2) 644,7 (1:3)	0,2-26	10	96.1%	[152]
2018	Ag_2S	0.1 M KHCO_3	70	-	40	87.4%	[172]
2018	CdS	KHCO ₃	27.1 mA cm ⁻²	0.25-4	10	81%	[173]
2021	MoS_2	EMIM-BF ₄	42,2		30	91.5%	[174]
2020	Pd/C, Pd/NbN, Pd/VN	0,5 mol•L ⁻¹ NaHCO ₃	0,4 (3:4)	0,16-0,74	3	38,4	[154]
2020	Pd-Cu	0,1 mol•L ⁻¹ Na ₂ SO ₄	_	0-0,1	> 8	-	[175]
2021	Pd/C, Pd-C _{u2} O/C, Pd-SnO ₂ /C	0.1 M KHCO_3	~3		10	-	[153]
2021	Cu-In	0.1 M KHCO_3	~10	-	10	75.8%	[155]
2020	SnO ₂ /CuS	0,1 mol•L ⁻¹ KHCO ₃	~5 (1:1) ~3 (1:3)	0,11-3,86	24	85%	[176]
2020	Zn-Ni	0,1 mol•L ⁻¹ KCl	8,4 (11:9)	-	48	~50%	[177]
2022	BiZn/NC	0,5 mol•L ⁻¹ KHCO ₃	< 13	0,20-2,92	10	74,5%	[178]
2019	$Zn_xCd_{1-x}S$ -amine	0,5 mol•L ⁻¹ NaHCO ₃	~6 (1:1)	0-19,7	10	60%	[179]
2020	Co@CoNC	0,5 mol•L ⁻¹ KHCO ₃	25 (2:1)	0,25-5	20	~60%	[180]
2020	Co and Ni	0,5 mol•L ⁻¹ KHCO ₃	> 74	0,23-2,26	7	~53%	[181]
2021	HPC-Co/CoPc (5:1)	1 mol•L ⁻¹ KHCO ₃	90 (1:1) 130 (1:2) 225 (1:3)	0,33-1,21	30	91.5%	[182]
2019	γ-In ₂ Se ₃	30 wt% [Bmim][PF ₆] 65 wt.% MeCN 5 wt.% H ₂ O	90,1 (1:1)	0,33-24	25	96.5%	[183]
2022	Fe/FeN ₄ C	0,5 mol•L ⁻¹ KHCO ₃	> 39,33	1.09-7.08	15	90%	[156]
2019	Fe ³⁺ -NC	0,5 mol•L ⁻¹ KHCO ₃	< 100	0,25-2,00	30	90%	[184]
2020	CNTA	0,5 mol•L ⁻¹ NaHCO ₃	< 40	0,55-3,03	10	75%	[185]
2022	Ni-N-C	0.5 M KHCO ₃	21.29		7	95.85%	[186]
2019	PCN	0,5 mol•L ⁻¹ NaHCO ₃	< 10	0,67	24	42%	[187]

Table 5 Standard electrode potentials (E^0) for selected CO_2RR reactions [128].

Electrode	Hall Cell Reaction	E ⁰ (V vs. SHE)
Cathode	$CO_2 + 2 H^+ + 2e^- \rightarrow CO + H_2O$	-0.106
Anode	$CO_2 + 2 H^+ + 2e^- \rightarrow HCOOH$	-0.199
	$2CO_2 + 2 H^+ + 2e^- \rightarrow H_2C_2O_4$	-0.475
	$CO_2 + 4 H^+ + 4e^- \rightarrow HCOH + H_2O$	-0.070
	$CO_2 + 6 H^+ + 6e^- \rightarrow CH_3OH + H_2O$	0.030
	$CO_2 + 8 H^+ + 8e^- \rightarrow CH_4 + 2 H_2O$	0.169
	$CO_2 + 12 H^+ + 12e^- \rightarrow C_2H_4 + 4 H_2O$	0.064
	$2 \text{ H}^+ + 2 \text{e}^- \rightarrow \text{H}_2$	0.000
	$2 \text{ H}_2\text{O} \rightarrow \text{O}_2 + 4 \text{ H}^+ + 4e^-$	1.230

electrocatalysts. Electric CO_2 reduction is a sustainable approach for producing synthesis gas with controlled ratios, which is required as a specific reagent to optimise various industrial processes. However, controlled synthesis gas production with a wide range of CO/H_2 ratios while maintaining a high current density is difficult.

Based on the aforementioned information, it is difficult to determine the "best" catalyst without additional context or specific criteria. However, a Ni-based nano-Ag catalyst has been used to convert CO2 into synthesis gas. This catalytic system provided a high degree of control over the CO/H2 ratio during synthesis gas production while achieving a current density comparable to the previously published results. Its effectiveness is explained by the synergistic effect of nano-Ag and cationic IL, making it a promising candidate for CO2 conversion. Owing to the innovative combinations of materials and the strategic design of catalysts, the field of electrocatalysis for the CO2 and synthesis gas production continues to develop. Unconventional combinations, conventional materials, and catalysts alloyed with base metals contribute to expanding the possibilities of achieving high efficiency, a controlled product ratio, and cost-effective solutions for the sustainable synthesis gas production. These developments can revolutionise industrial processes and contribute to a greener and more sustainable future. Porous carbon materials doped with nitrogen and base metals, viz. "M-N-C", have emerged as a promising class of functional materials for replacing precious metal catalysts in the electrochemical CO₂ RR. Similarly, Fe/ FeN₄C catalyst took advantage of both the porous carbon structure and nitrogen-doped active centres. Despite the challenges in achieving controlled synthesis gas production with a wide range of CO/H2 ratios while maintaining a high current density, the development of the Fe/ FeN₄C catalyst is a promising step forward. Its adjustable H₂/CO ratio and improved catalytic activity provide potential solutions to these problems, paving the way for sustainable and optimised industrial processes. As researchers continue to explore the possibilities of Febased electrocatalysts and their integration into practical applications, the field of electrocatalysis is at the forefront of shaping a more sustainable future.

4.3. Tandem materials for CO₂ capture and electrochemical reduction

Among various strategies for improving electrocatalytic systems, tandem materials are a way to achieve promising results. Currently, there is increasing interest in the development and use of tandem materials that combine the capabilities of CO₂ adsorption and electrochemical reduction of CO₂. Tandem materials involves the use of two or more electrocatalytic systems that operate in series or parallel to achieve better performance and efficiency. This eliminates the shortcomings of each individual system and improves overall performance. The operating principle of tandem materials is to capture CO₂ from the atmosphere or other sources and then electrochemically reduce it to produce multicarbon products. By combining multiple chemical reactions, tandem catalysts increase the kinetic rate of the overall reaction and improve the Faraday efficiency of the products [157]. Based on the composition of tandem process catalysts, CO₂ RR can be divided into copper and copper-free tandem catalysts. In tandem catalysis, the

combination of catalysts, the assembly of two active groups, the porous structure and the reaction conditions have a significant impact on the resulting product [14]. For example, Zeyu Guo et al. [158] studied a Ni-Ag/PC-N catalyst prepared by cascade pyrolysis method, which FE $_{\rm CO}$ reaches 99.2% at - 0.8 V. Experimental data confirm that the synergistic Ni-Ag diatomic sites in the Ni-Ag/PC-N catalyst promote the physical adsorption of CO $_{\rm 2}$ molecules and stabilize the *CO $_{\rm 2}$ bicarbonate species. Calculations (DFT) show that the coordinated Ni atom reduces the energy barrier to the formation of *COOH intermediates on the Ni-Ag/PC-N surface, while the Ag atom reduces catalyst poisoning.

On the other hand, recently, reducing the cost of the catalyst and increasing its performance through the use of catalysts based on alloyed carbon materials, including transition metals, has attracted much attention. Thus, the Fe/Ni-N-C composite using an H-type cell demonstrates an efficiency of 92.9% at 0.677 V [159]. At the same time, theoretical calculations carried out using DFT methods showed that carbon doped with bimetallic nitrogen Fe and Ni effectively reduces the energy barriers to the formation of intermediates *COOH and *CO for CO, and the synergistic effect of bimetals effectively increases the rate of charge transfer. The heterodoping method was used in the synthesis of bimetallic catalysts to eliminate the disadvantages associated with the low activity of monoatomic catalytic systems. An example is a copper-zinc bimetallic monatomic catalyst supported on microporous nitrogen-doped carbon substrates (CuZn-SAs/NC), which gives an FE for CH_4 of 84.7% and at $-49.7 \text{ mA} \cdot \text{cm}^{-2}$, respectively. In addition, the catalyst showed stability for 45 h. The high efficiency of the catalyst is explained by the atomically dispersed Cu-Zn centers and the synergistic effect of the active centers of Cu and Zn, which significantly accelerated the formation of CH_4 [160].

Several studies have reported that Ag-Cu catalysts improve C2H4 selectivity. Thus, a Cu₂O/Ag tandem catalyst is used to produce C₂H₄, while Cu₂O/Ag exhibits electrochemical characteristics with a current density of 17.8 mA·cm⁻² and an ethylene selectivity of 66.8% at -1.2 V [161]. The authors claim that the high catalytic activity and selectivity for the C₂H₄ product is due to the synergistic effect of the crystal face control technology and tandem catalysis. Metal-organic frameworks (MOFs) have multiple active sites to capture CO2 and convert it into valuable products. He et al. [162] synthesized a CuCo-MOF-74 catalyst derived from MOF designed with Co₃O₄ and CuO_x centers for efficient electroreduction of CO2 to C2 products. This catalyst showed good activity towards CO2 RR in C2 with Faraday efficiency (FE) up to 79.2% and current density of $19.28 \text{ mA} \cdot \text{cm}^{-2}$, when operating at -0.75 V. Based on experimental and DFT results, they proposed that CO₂ could be efficiently converted to CO at Co₃O₄ sites, forming a local CO-enriched environment around adjacent CuO_x sites and further accelerating the C₂ formation process.

In [17] the authors synthesized Ag@C@Cu nanoparticles (NPs), including a silver core and a copper shell, separated by a carbon intermediate layer, reaching FE C_2H_5OH 31.5% at - 0.64 V with an Ag/Cu ratio of 0.1. They demonstrated that the synergistic effect promotes the selectivity of ethanol over ethylene by increasing the *CO coverage on the copper surface. However, such a strategy remains a challenge for high-speed production of C_{2+} products due to the limitation of long-distance CO transport to the point of consumption. A tandem CuO/Ni SAs catalyst for C_{2+} products with a Faraday efficiency FE (C_{2+}) of 81.4% was also obtained, including ethylene (FE 54.1%) and ethanol (FE 28.8%) at a high current density of 1220.8 mA·cm⁻². The efficiency of the CuO/Ni SAs catalyst is attributed to its co-loading of nanostructures [163].

Thus, according to research, the importance of tandem materials lies in their ability to combine various properties such as strength and corrosion resistance to achieve optimal performance of electrocatalysts, however, disadvantages such as complexity of production and high cost require further research for more efficient development and availability of electrocatalysts. Further improvement of tandem catalysts may lead to the creation of more efficient catalysts, the search for new materials

and structures to improve the stability and selectivity of the process. Therefore, it is important to focus on developing and scaling such technologies for their successful commercialization.

5. Conclusions and future perspectives

Global climate change is one of the most serious threats to humanity, affecting economic, social, and environmental aspects of our lives. The main driver of these changes is an increase in greenhouse gas emissions, particularly carbon dioxide, which has the greenhouse effect. Modern global efforts aim to reduce CO_2 emissions and achieve carbon neutrality. Numerous commitments and programs, notably, the Paris Agreement, have been undertaken by various countries and regions. However, obstacles such as high investment requirements, uncertainty in CO_2 storage, technical difficulties, and low public support necessitate finding new and effective solutions. Carbon capture, conversion, and storage (CCUS) technologies involving various conversion methods are promising for reducing CO_2 emissions. Notably, research into catalytic, electrocatalytic, and photocatalytic methods for capturing CO_2 and its further transformation is promising from environmental and economic viewpoints.

The CO₂ capture and disposal in the presence of DFMs allows the extraction of CO2 from exhaust gas streams and converts it into valueadded products. However, the practical application of this process requires comprehensive engineering efforts as well as economic and technical analyses. One solution is to develop inexpensive materials capable of capturing and converting CO2 at lower temperatures. In addition, a deeper understanding of the interactions between catalysts and adsorbents is required. During CO₂ capture and methanation, DFMs exhibit the best catalytic activity and selectivity for CH₄ at a temperature of 300 °C. At this temperature, DFMs based on precious metals exhibit good activity; however, their main drawback is their high cost. Ni-based DFMs can be an alternative to noble metals; however, they can be used only in the absence of oxygen in the reaction mixture. To develop a suitable DFM for CO2 capture and methanation, additional studies on the synergy between the adsorbent and catalyst are required, as the transfer of CO₂ from the adsorbent to the catalytic centres is a key stage of methanation. In addition, more in-depth studies of the interactions within the DFM are required to understand the methanation process and design the catalyst effectively. The future development of CO2 capture and disposal in the presence of DFM will be determined by an economic assessment of the process. The CO2 capture and DRM require a high temperature (>500 °C). At this temperature, Ni- and CaO-based DFMs are highly applicable. However, the main reason for the decreased catalytic activity of the DFM is the sintering of CaO and the agglomeration of active metals at high temperatures. CO2 capture and in-situ catalytic conversion are still in their infancy. CO2 capture and catalytic conversion in the presence of DFM is a cost-effective CO₂ utilisation strategy that combines extensive CO2 capture and conversion research while providing solutions to pressing environmental needs.

In the long run, the conversion of CO₂ into valuable fuels using solar energy has the potential to accumulate an infinite source of energy in the form of chemically rich substances. Although the photocatalytic conversion of CO2 into carbon fuel is under development, additional scientific and engineering research efforts are required. The main obstacle to the successful implementation of this process is the poor efficiency of photocatalysts capable of reducing ${\rm CO}_2$ under visible light. Despite constant improvements in photocatalyst performance, defect introduction and their morphology optimisation, composite formation, cocatalyst use, and collaboration with adsorbents, the actual efficiency of photocatalytic systems is still far from being on par with other methods for CO2 recovery. In addition, the poor performance of photocatalytic reactors hinders their commercialisation. Therefore, future studies should focus on the following approaches to improve the photocatalytic reduction of CO2 into chemical fuel: developing more efficient photocatalytic materials capable of operating effectively in visible light,

improving the design of photocatalytic reactors for more efficient reagent transport and radiation, ensuring the stability of photocatalytic systems, and combining the photocatalytic process with other methods such as $\rm CO_2$ capture, thermocatalysis, and electrocatalysis to achieve higher efficiency and efficient resource use.

Industrial-scale CO2 capture and its utilisation into methane and synthesis gas require either high temperatures (>500 °C) or high pressures (>20 bar). In addition, these processes require relatively expensive reducing agents (such as H2 and CH4) to convert CO2 into the target products. Therefore, it is important to develop materials that are active in the conversion of CO2 under mild conditions. Photocatalytic or electrocatalytic CO2 reduction is a promising approach for carbon dioxide disposal. However, the main problem with the electrocatalytic reduction of CO2 is the multiplicity of proton and electron transfer processes, as well as the chemical inertia of the CO2 molecule. In addition, high reagent purity is required to avoid the toxic effects of impuon electrocatalysts and equipment. Recently, electrocatalytic systems, along with various strategies for increasing the activity and selectivity of the catalysts, such as regulation, morphological structure, and surface/interface engineering, have been studied for the electrocatalytic reduction of CO₂. The development of inexpensive and highly stable catalysts with improved activity and selectivity requires systematic research. Currently, some single-carbon (C₁) products have achieved an FE up to 95%; however, overvoltage optimisation is still required. Owing to the competing hydrogen release reactions and multiple reduction pathways, the FE of the CO2 reduction products, particularly multicarbon C₂₊ products, requires improvement. The poor stability of electrocatalysts is another challenge for large-scale CO2 reduction applications.

By analysing modern achievements in this field, it can be concluded that the processes of $\rm CO_2$ capture and utilisation using catalytic methods represent a promising strategy for the transition to a more sustainable energy and industrial economy. Highlighting the prospects for the development of this area, we can draw the following conclusions:

Economic Analysis: One of the key steps towards the practical use of CO_2 capture and utilisation processes using the DFM is to conduct a comprehensive economic analysis. A comprehensive assessment of the production costs and benefits will help determine the practical feasibility of these methods.

Development of low-cost materials: The development of more affordable and stable DFM materials capable of capturing and converting CO_2 at low temperatures is a priority. This will help reduce production costs and expand the scope of their application.

Research on the synergism of catalysts and adsorbents: A deep understanding of the interactions between adsorbents and catalysts is important for improving the efficiency of CO_2 capture and conversion processes.

Photocatalytic and electrocatalytic conversion: Continued research in the field of the photocatalytic and electrocatalytic conversion of CO_2 will create more efficient methods for converting CO_2 into valuable chemical compounds.

Engineering and technological innovations: The development of new technologies and engineering solutions for scaling CO₂ capture and disposal processes using the DFM will create efficient and sustainable production processes.

Integration of methods: In the future, consideration should be given to integrating CO_2 capture and disposal methods with DFM, along with other methods, such as thermocatalysis and electrocatalysis, to achieve higher efficiency and maximise the use of available resources.

CRediT authorship contribution statement

Makayeva Nursaya: Conceptualization, Methodology. Daulbayev Chingis: Supervision, Writing – original draft, Writing – review & editing. Khudaibergenov Nurlan: Methodology, Resources, Writing – original draft. Yergaziyeva Gaukhar: Conceptualization, Writing –

original draft, Writing – review & editing. **Kuspanov Zhengisbek:** Conceptualization, Writing – original draft. **Mambetova Manshuk:** Conceptualization, Writing – review & editing.

Declaration of Competing Interest

The authors declare that they have no known competing financial interests or personal relationships that could have appeared to influence the work reported in this paper.

Data Availability

No data was used for the research described in the article.

Acknowledgments

This research has been funded by the Science Committee of the Ministry of Science and Higher Education of the Republic of Kazakhstan (Grant No AP14869034 and No BR18574084).

References

- C.A. Tracker, Climate summit momentum: Warming Projections Global Update, (2021). https://policycommons.net/artifacts/2482084/climate-summit-momentum/3504304/ (accessed July 18, 2023).
- [2] S. Fawzy, A.I. Osman, J. Doran, D.W. Rooney, Strategies for mitigation of climate change: a review, Environ. Chem. Lett. 18 (2020) 2069–2094, https://doi.org/ 10.1007/s10311-020-01059-w.
- [3] L. Jiang, W. Liu, R.Q. Wang, A. Gonzalez-Diaz, M.F. Rojas-Michaga, S. Michailos, M. Pourkashanian, X.J. Zhang, C. Font-Palma, Sorption direct air capture with CO₂ utilization, Prog. Energy Combust. Sci. 95 (2023) 101069, https://doi.org/ 10.1016/j.pecs.2022.101069.
- [4] 赵志强张贺, Z.H. ZHAO Zhi-qiang, 全球CCUS技术和应用现状分析, 现代化工. 41 (2021) 5–10. https://doi.org/10.16606/j.cnki.issn0253–4320.2021.04.002.
- [5] O. Alioui, S. Gueddida, Y. Benguerba, S. Lebègue, M. Badawi, Potential of nickel nanoclusters supported on α-Al2O3(0001) surface for CO₂ capture, energy production, and dry reforming of methane, Appl. Surf. Sci. 610 (2023) 155474, https://doi.org/10.1016/j.apsusc.2022.155474.
- [6] B. Jin, T. Ouyang, Z. Zhang, Y. Zhao, H. Zhang, W. Yao, G. Huang, Z. Liang, Prussian blue derived Ca-Fe bifunctional materials for chemical looping CO₂ capture and in-situ conversion, Sep. Purif. Technol. 320 (2023) 123975, https://doi.org/10.1016/j.seppur.2023.123975.
- [7] S. Sun, H. Sun, P.T. Williams, C. Wu, Recent advances in integrated CO₂ capture and utilization: a review, Sustain. Energy Fuels 5 (2021) 4546–4559, https://doi. org/10.1039/D1SE00797A.
- [8] T. Zhang, M. Li, P. Ning, Q. Jia, Q. Wang, J. Wang, K2CO3 promoted novel Li4SiO4-based sorbents from sepiolite with high CO₂ capture capacity under different CO₂ partial pressures, Chem. Eng. J. 380 (2020) 122515, https://doi. org/10.1016/j.cej.2019.122515.
- [9] S. Sun, H. Sun, P.T. Williams, C. Wu, Recent advances in integrated CO₂ capture and utilization: a review, Sustain. Energy Fuels 5 (2021) 4546–4559, https://doi. org/10.1039/D1SE00797A.
- [10] K. Zong, S. Shin, E.K. Ryu, A new method for preparing N -acyloxaziridines via tandem O,N -addition of hydroxamic acids to methyl propiolate, Tetrahedron Lett. 39 (1998) 6227–6228, https://doi.org/10.1016/S0040-4039(98)01281-7.
- [11] A. Jeevanandam, K. Narkunan, C. Cartwright, Y.-C. Ling, A novel palladium-catalyzed tandem dimerization and cyclization of acetylenic ketones. A convenient method for 3,3'-bifurans, Tetrahedron Lett. 40 (1999) 4841–4844, https://doi.org/10.1016/S0040-4039(99)00889-8.
- [12] M.S. Duyar, M.A.A. Treviño, R.J. Farrauto, Dual function materials for CO 2 capture and conversion using renewable H 2, Appl. Catal. B: Environ. 168–169 (2015) 370–376, https://doi.org/10.1016/j.apcatb.2014.12.025.
- [13] M.S. Duyar, S. Wang, M.A. Arellano-Treviño, R.J. Farrauto, CO 2 utilization with a novel dual function material (DFM) for capture and catalytic conversion to synthetic natural gas: An update, J. CO₂ Util. 15 (2016) 65–71, https://doi.org/ 10.1016/j.jcou.2016.05.003.
- [14] X. Wang, Y. Duan, J. Zhang, Y. Tan, Catalytic conversion of CO₂ into high value-added hydrocarbons over tandem catalyst, J. Fuel Chem. Technol. 50 (2022) 538–563, https://doi.org/10.1016/S1872-5813(21)60181-0.
- [15] S. Cui, C. Yu, X. Tan, W. Li, Y. Zhang, J. Qiu, A tandem catalyst with high CO₂ capture capability to achieve a promoted CO₂-to-CH4 electrochemical conversion, Chem. Eng. J. 470 (2023) 144083, https://doi.org/10.1016/j.cej.2023.144083.
- [16] N. Martín, F.G. Cirujano, Multifunctional heterogeneous catalysts for the tandem CO₂ hydrogenation-Fischer Tropsch synthesis of gasoline, J. CO₂ Util. 65 (2022) 102176, https://doi.org/10.1016/j.jcou.2022.102176.
- [17] J. Zhang, T.H.M. Pham, Y. Ko, M. Li, S. Yang, C.D. Koolen, L. Zhong, W. Luo, A. Züttel, Tandem effect of Ag@C@Cu catalysts enhances ethanol selectivity for

- electrochemical CO_2 reduction in flow reactors, Cell Rep. Phys. Sci. 3 (2022) 100949, https://doi.org/10.1016/j.xcrp.2022.100949.
- [18] M.A. Arellano-Treviño, Z. He, M.C. Libby, R.J. Farrauto, Catalysts and adsorbents for CO₂ capture and conversion with dual function materials: limitations of Nicontaining DFMs for flue gas applications, J. CO₂ Util. 31 (2019) 143–151, https://doi.org/10.1016/j.jcou.2019.03.009.
- [19] B.W. Hwang, J.H. Lim, H.J. Chae, H.-J. Ryu, D. Lee, J.B. Lee, H. Kim, S.C. Lee, J. C. Kim, CO₂ capture and regeneration properties of MgO-based sorbents promoted with alkali metal nitrates at high pressure for the sorption enhanced water gas shift process, Process Saf. Environ. Prot. 116 (2018) 219–227, https://doi.org/10.1016/j.psep.2018.02.008.
- [20] C.V. Miguel, M.A. Soria, A. Mendes, L.M. Madeira, A sorptive reactor for CO 2 capture and conversion to renewable methane, Chem. Eng. J. 322 (2017) 590–602, https://doi.org/10.1016/j.cej.2017.04.024.
- [21] H. Sun, Y. Zhang, S. Guan, J. Huang, C. Wu, Direct and highly selective conversion of captured CO₂ into methane through integrated carbon capture and utilization over dual functional materials, J. CO₂ Util. 38 (2020) 262–272, https://doi.org/10.1016/j.jcou.2020.02.001.
- [22] S. Cimino, F. Boccia, L. Lisi, Effect of alkali promoters (Li, Na, K) on the performance of Ru/Al2O3 catalysts for CO₂ capture and hydrogenation to methane, J. CO₂ Util. 37 (2020) 195–203, https://doi.org/10.1016/j. jcou.2019.12.010.
- [23] A. Bermejo-López, B. Pereda-Ayo, J.A. González-Marcos, J.R. González-Velasco, Mechanism of the CO₂ storage and in situ hydrogenation to CH4. Temperature and adsorbent loading effects over Ru-CaO/Al2O3 and Ru-Na2CO3/Al2O3 catalysts, Appl. Catal. B: Environ. 256 (2019) 117845, https://doi.org/10.1016/j. apcatb.2019.117845.
- [24] C. Jeong-Potter, M. Abdallah, C. Sanderson, M. Goldman, R. Gupta, R. Farrauto, Dual function materials (Ru+Na2O/Al2O3) for direct air capture of CO₂ and in situ catalytic methanation: the impact of realistic ambient conditions, Appl. Catal. B: Environ. 307 (2022) 120990, https://doi.org/10.1016/j.apeatb.2021.120990.
- [25] L. Proaño, E. Tello, M.A. Arellano-Trevino, S. Wang, R.J. Farrauto, M. Cobo, Insitu DRIFTS study of two-step CO₂ capture and catalytic methanation over Ru, "Na2O"/Al2O3 Dual Functional Material, Appl. Surf. Sci. 479 (2019) 25–30, https://doi.org/10.1016/j.apsusc.2019.01.281.
- [26] P. Huang, J. Chu, J. Fu, J. Yu, S. Li, Y. Guo, C. Zhao, J. Liu, Influence of reduction conditions on the structure-activity relationships of NaNO3-promoted Ni/MgO dual function materials for integrated CO₂ capture and methanation, Chem. Eng. J. 467 (2023) 143431, https://doi.org/10.1016/j.cej.2023.143431.
- [27] H. Sun, Y. Wang, S. Xu, A.I. Osman, G. Stenning, J. Han, S. Sun, D. Rooney, P. T. Williams, F. Wang, C. Wu, Understanding the interaction between active sites and sorbents during the integrated carbon capture and utilization process, Fuel 286 (2021) 119308, https://doi.org/10.1016/j.fuel.2020.119308.
- [28] S. Wang, E.T. Schrunk, H. Mahajan, A.R.J. Farrauto, The role of ruthenium in CO₂ capture and catalytic conversion to fuel by dual function materials (DFM), Catalysts 7 (2017) 88, https://doi.org/10.3390/catal7030088.
- [29] Q. Zheng, R. Farrauto, A. Chau Nguyen, Adsorption and methanation of flue gas CO₂ with dual functional catalytic materials: a parametric study, Ind. Eng. Chem. Res. 55 (2016) 6768–6776, https://doi.org/10.1021/acs.iecr.6b01275.
 [30] S. Sun, H. Sun, S. Guan, S. Xu, C. Wu, Integrated CO₂ capture and methanation on
- [30] S. Sun, H. Sun, S. Guan, S. Xu, C. Wu, Integrated CO₂ capture and methanation on Ru/CeO2-MgO combined materials: morphology effect from CeO2 support, Fuel 317 (2022) 123420, https://doi.org/10.1016/j.fuel.2022.123420.
- [31] M.A. Arellano-Treviño, N. Kanani, C.W. Jeong-Potter, R.J. Farrauto, Bimetallic catalysts for CO₂ capture and hydrogenation at simulated flue gas conditions, Chem. Eng. J. 375 (2019) 121953, https://doi.org/10.1016/j.cej.2019.121953.
- [32] S. Cimino, R. Russo, L. Lisi, Insights into the cyclic CO₂ capture and catalytic methanation over highly performing Li-Ru/Al2O3 dual function materials, Chem. Eng. J. 428 (2022) 131275, https://doi.org/10.1016/j.cej.2021.131275.
- [33] S. Cimino, E.M. Cepollaro, L. Lisi, Ageing study of Li-Ru/Al2O3 dual function material during the integrated CO₂ capture and methanation with SO2-containing flue gas, Carbon Capture Sci. Technol. 6 (2023) 100096, https://doi.org/ 10.1016/j.ccst.2022.100096.
- [34] A. Bermejo-López, B. Pereda-Ayo, J.A. González-Marcos, J.R. González-Velasco, Ni loading effects on dual function materials for capture and in-situ conversion of CO₂ to CH4 using CaO or Na2CO3, J. CO₂ Util. 34 (2019) 576–587, https://doi. org/10.1016/j.jcou.2019.08.011.
- [35] C. Wang, Y. Lu, Y. Zhang, H. Fu, S. Sun, F. Li, Z. Duan, Z. Liu, C. Wu, Y. Wang, H. Sun, Z. Yan, Ru-based catalysts for efficient CO₂ methanation: Synergistic catalysis between oxygen vacancies and basic sites, Nano Res (2023), https://doi. org/10.1007/s12274-023-5592-3.
- [36] L. Hu, A. Urakawa, Continuous CO₂ capture and reduction in one process: CO₂ methanation over unpromoted and promoted Ni/ZrO2, J. CO₂ Util. 25 (2018) 323–329, https://doi.org/10.1016/j.jcou.2018.03.013.
- [37] E. García-Bordejé, A. Belén Dongil, J.M. Conesa, A. Guerrero-Ruiz, I. Rodríguez-Ramos, Dual functional materials based on Ni and different alkaline metals on alumina for the cyclic stepwise CO₂ capture and methanation, Chem. Eng. J. 472 (2023) 144953, https://doi.org/10.1016/j.cej.2023.144953.
- [38] A. Catarina Faria, C.V. Miguel, A.F.P. Ferreira, A.E. Rodrigues, L.M. Madeira, CO₂ capture and conversion to methane with Ni-substituted hydrotalcite dual function extrudates, Chem. Eng. J. 476 (2023) 146539, https://doi.org/10.1016/j.cej.2023.146539.
- [39] A.C. Faria, R. Trujillano, V. Rives, C.V. Miguel, A.E. Rodrigues, L.M. Madeira, Cyclic operation of CO₂ capture and conversion into methane on Ni-hydrotalcite based dual function materials (DFMs), J. CO₂ Util. 72 (2023) 102476, https://doi. org/10.1016/j.jcou.2023.102476.

- [40] A. Rizzetto, M. Piumetti, R. Pirone, E. Sartoretti, S. Bensaid, Study of ceriacomposite materials for high-temperature CO₂ capture and their ruthenium functionalization for methane production, Catal. Today 429 (2024) 114478, https://doi.org/10.1016/j.cattod.2023.114478.
- [41] S. Cimino, E.M. Cepollaro, M. Pazzi, L. Lisi, Sulphur poisoning and regeneration of Li-Ru/Al2O3 dual function material for the integrated CO₂ capture and methanation, Catal. Today 426 (2024) 114366, https://doi.org/10.1016/j. cattod.2023.114366.
- [42] Y. Wang, X. Lang, S. Fan, Hydrate capture CO₂ from shifted synthesis gas, flue gas and sour natural gas or biogas, J. Energy Chem. 22 (2013) 39–47, https://doi. org/10.1016/S2095-4956(13)60004-2.
- [43] L.F. Bobadilla, J.M. Riesco-García, G. Penelás-Pérez, A. Urakawa, Enabling continuous capture and catalytic conversion of flue gas CO₂ to syngas in one process, J. CO₂ Util. 14 (2016) 106–111, https://doi.org/10.1016/j.jcou.2016.04.003.
- [44] W. Gao, S. Liang, R. Wang, Q. Jiang, Y. Zhang, Q. Zheng, B. Xie, C.Y. Toe, X. Zhu, J. Wang, L. Huang, Y. Gao, Z. Wang, C. Jo, Q. Wang, L. Wang, Y. Liu, B. Louis, J. Scott, A.-C. Roger, R. Amal, H. He, S.-E. Park, Industrial carbon dioxide capture and utilization: state of the art and future challenges, Chem. Soc. Rev. 49 (2020) 8584–8686, https://doi.org/10.1039/DOCS00025F.
- [45] G. Liu, S. Sun, H. Sun, Y. Zhang, J. Lv, Y. Wang, J. Zeng, Z. Yan, C. Wu, Integrated CO₂ capture and utilisation: a promising step contributing to carbon neutrality, Carbon Capture Sci. Technol. 7 (2023) 100116, https://doi.org/10.1016/j.ccst.2023.100116.
- [46] X. Shi, H. Xiao, H. Azarabadi, J. Song, X. Wu, X. Chen, K.S. Lackner, Sorbenten zur direkten Gewinnung von CO₂ aus der Umgebungsluft, Angew. Chem. 132 (2020) 7048–7072, https://doi.org/10.1002/ange.201906756.
- [47] S.M. Kim, P.M. Abdala, M. Broda, D. Hosseini, C. Copéret, C. Müller, Integrated CO₂ capture and conversion as an efficient process for fuels from greenhouse gases, ACS Catal. 8 (2018) 2815–2823, https://doi.org/10.1021/ acceptal.7b03063
- [48] A. Armutlulu, M.A. Naeem, H.-J. Liu, S.M. Kim, A. Kierzkowska, A. Fedorov, C. R. Müller, Multishelled CaO microspheres stabilized by atomic layer deposition of Al2O3 for enhanced CO₂ capture performance, Adv. Mater. 29 (2017) 1702896, https://doi.org/10.1002/adma.201702896.
- [49] M. Broda, A.M. Kierzkowska, C.R. Müller, Development of highly effective Ca0-based, MgO-stabilized CO₂ sorbents via a scalable "one-pot" recrystallization technique, Adv. Funct. Mater. 24 (2014) 5753–5761, https://doi.org/10.1002/adfm 201400862
- [50] L. Ding, Y. Ding, F. Bai, G. Chen, S. Zhang, X. Yang, H. Li, X. Wang, In situ growth of Cs3Bi2Br9 quantum dots on Bi-MOF nanosheets via cosharing bismuth atoms for CO₂ capture and photocatalytic reduction, Inorg. Chem. 62 (2023) 2289–2303, https://doi.org/10.1021/acs.inorgchem.2c04041.
- [51] J. Hu, J. Ding, Q. Zhong, Ultrathin 2D Ti3C2 MXene Co-catalyst anchored on porous g-C3N4 for enhanced photocatalytic CO₂ reduction under visible-light irradiation, J. Colloid Interface Sci. 582 (2021) 647–657, https://doi.org/ 10.1016/j.icis.2020.08.047.
- [52] Y. Huo, J. Zhang, K. Dai, C. Liang, Amine-modified S-scheme porous g-C3N4/ CdSe-diethylenetriamine composite with enhanced photocatalytic CO₂ reduction activity, ACS Appl. Energy Mater. 4 (2021) 956–968, https://doi.org/10.1021/ accept 0c02896
- [53] S. Tian, F. Yan, Z. Zhang, J. Jiang, Calcium-looping reforming of methane realizes in situ CO₂ utilization with improved energy efficiency, Sci. Adv. 5 (2019) eaay5077. https://doi.org/10.1126/sciady.aay5077.
- [54] P. Gruene, A.G. Belova, T.M. Yegulalp, R.J. Farrauto, M.J. Castaldi, Dispersed calcium oxide as a reversible and efficient CO₂—sorbent at intermediate temperatures, Ind. Eng. Chem. Res. 50 (2011) 4042–4049, https://doi.org/10.1021/je102475d
- [55] A. Al-Mamoori, A.A. Rownaghi, F. Rezaei, Combined capture and utilization of CO₂ for syngas production over dual-function materials, ACS Sustain. Chem. Eng. 6 (2018) 13551–13561, https://doi.org/10.1021/acssuschemeng.8b03769.
- [56] Z. Lv, C. Qin, S. Chen, D.P. Hanak, C. Wu, Efficient-and-stable CH4 reforming with integrated CO₂ capture and utilization using Li4SiO4 sorbent, Sep. Purif. Technol. 277 (2021) 119476, https://doi.org/10.1016/j.seppur.2021.119476.
- [57] M. Shokrollahi Yancheshmeh, H.R. Radfarnia, M.C. Iliuta, High temperature CO₂ sorbents and their application for hydrogen production by sorption enhanced steam reforming process, Chem. Eng. J. 283 (2016) 420–444, https://doi.org/10.1016/j.cej.2015.06.060.
- [58] Y. Sha, Y. Ling, Y. Yang, X. Wang, D. Meng, S. Wang, A finger-like anode with infiltrated Ni0.1Ce0.9O2-δ catalyst using new phase inversion combined tapecasting technology for optimized dry reforming of methane, Ceram. Int. (2023), https://doi.org/10.1016/j.ceramint.2023.06.195.
- [59] G.E. Ergazieva, M.M. Telbayeva, A.N. Popova, Z.R. Ismagilov, K. Dossumov, L. K. Myltykbayeva, V.G. Dodonov, S.A. Sozinov, A.I. Niyazbayeva, Effect of preparation method on the activity of bimetallic Ni-Co/Al2O3 catalysts for dry reforming of methane, Chem. Pap. 75 (2021) 2765–2774, https://doi.org/10.1007/s11696-021-01516-y.
- [60] K. Dossumov, G.E. Ergazieva, L.K. Myltykbaeva, M.M. Telbaeva, A.T. Batyrbaev, Effect of MoO3 on the catalytic properties of NiO/Al2O3 in the carbon dioxide conversion of methane, Theor. Exp. Chem. 55 (2019) 137–142, https://doi.org/ 10.1007/s11237-019-09605-6.
- [61] J. Hu, P. Hongmanorom, V.V. Galvita, Z. Li, S. Kawi, Bifunctional Ni-Ca based material for integrated CO₂ capture and conversion via calcium-looping dry reforming, Appl. Catal. B: Environ. 284 (2021) 119734, https://doi.org/10.1016/ j.apcatb.2020.119734.

- [62] Z. Xuan Law, Y.-T. Pan, D.-H. Tsai, Calcium looping of CO₂ capture coupled to syngas production using Ni-CaO-based dual functional material, Fuel 328 (2022) 125202, https://doi.org/10.1016/j.fuel.2022.125202.
- [63] S. Sun, Y. Zhang, C. Li, Y. Wang, C. Zhang, X. Zhao, H. Sun, C. Wu, Upgrading CO₂ from simulated power plant flue gas via integrated CO₂ capture and dry reforming of methane using Ni-CaO, Sep. Purif. Technol. 308 (2023) 122956, https://doi.org/10.1016/j.seppur.2022.122956.
- [64] Y. Zhao, B. Jin, Z. Liang, Synergistic Enhanced Ca–Fe Chemical Looping Reforming Process for Integrated CO₂ Capture and Conversion, Ind. Eng. Chem. Res. 59 (2020) 1298–1307, https://doi.org/10.1021/acs.iecr.9b05783.
- [65] S. Wang, R.J. Farrauto, S. Karp, J.H. Jeon, E.T. Schrunk, Parametric, cyclic aging and characterization studies for CO₂ capture from flue gas and catalytic conversion to synthetic natural gas using a dual functional material (DFM), J. CO₂ Util. 27 (2018) 390–397, https://doi.org/10.1016/j.jcou.2018.08.012.
- [66] J.A. Onrubia-Calvo, A. Bermejo-López, B. Pereda-Ayo, J.A. González-Marcos, J. R. González-Velasco, Ca doping effect on the performance of La1-xCaxNiO3/CeO2-derived dual function materials for CO₂ capture and hydrogenation to methane, Appl. Catal. B: Environ. 321 (2023) 122045, https://doi.org/10.1016/j.apcatb.2022.122045.
- [67] J. Fu, K. Jiang, X. Qiu, J. Yu, M. Liu, Product selectivity of photocatalytic CO₂ reduction reactions, Mater. Today 32 (2020) 222–243, https://doi.org/10.1016/j.mattod.2019.06.009.
- [68] Y. Zhang, L. Yu, K. Cui, H. Wang, T. Fu, Carbon capture and storage technology by steel-making slags: recent progress and future challenges, Chem. Eng. J. 455 (2023) 140552, https://doi.org/10.1016/j.cej.2022.140552.
- [69] S. Ajmal, G. Yasin, A. Kumar, M. Tabish, S. Ibraheem, K.A. Sammed, M. A. Mushtaq, A. Saad, Z. Mo, W. Zhao, A disquisition on CO₂ electroreduction to C2H4: an engineering and design perspective looking beyond novel choosy catalyst materials, Coord. Chem. Rev. 485 (2023) 215099, https://doi.org/10.1016/j.ccr.2023.215099.
- [70] F. Su, Z. Wang, H. Cao, H. Xie, W. Tu, Y. Xiao, S. Shi, J. Chen, X. Jin, X.Y. Kong, Oxygen-deficient MoO3—x evoked synergistic photo-thermal catalytic CO₂ reduction over g-C3N4, Catal. Sci. Technol. 13 (2023) 1325–1334, https://doi. org/10.1039/D2CY01944B.
- [71] Y. Xiong, Z. Hou, H. Xie, J. Zhao, X. Tan, J. Luo, Microbial-mediated CO₂ methanation and renewable natural gas storage in depleted petroleum reservoirs: a review of biogeochemical mechanism and perspective, Gondwana Res. (2022), https://doi.org/10.1016/j.gr.2022.04.017.
- [72] Y. Wang, X. Liu, X. Han, R. Godin, J. Chen, W. Zhou, C. Jiang, J.F. Thompson, K. B. Mustafa, S.A. Shevlin, J.R. Durrant, Z. Guo, J. Tang, Unique hole-accepting carbon-dots promoting selective carbon dioxide reduction nearly 100% to methanol by pure water, Nat. Commun. 11 (2020) 2531, https://doi.org/10.1038/s41467-020-16227-3.
- [73] J. Wang, S. Lin, N. Tian, T. Ma, Y. Zhang, H. Huang, Nanostructured metal sulfides: classification, modification strategy, and solar-driven CO₂ reduction application, Adv. Funct. Mater. 31 (2021) 2008008, https://doi.org/10.1002/ adfm.202008008.
- [74] Y. Li, Y. Wei, W. He, Z. Tang, J. Xiong, Z. Zhao, Ordered macroporous structured TiO2-based photocatalysts for CO₂ reduction: A review, Chin. Chem. Lett. (2023) 108417, https://doi.org/10.1016/j.cclet.2023.108417.
- [75] S. Patial, R. Kumar, P. Raizada, P. Singh, Q. Van Le, E. Lichtfouse, D. Le Tri Nguyen, V.-H. Nguyen, Boosting light-driven CO₂ reduction into solar fuels: Mainstream avenues for engineering ZnO-based photocatalysts, Environ. Res. 197 (2021) 111134, https://doi.org/10.1016/j.envres.2021.111134.
- [76] Z. Kuspanov, A. Umirzakov, A. Serik, A. Baimenov, M. Yeleuov, C. Daulbayev, Multifunctional strontium titanate perovskite-based composite photocatalysts for energy conversion and other applications, Int. J. Hydrog. Energy (2023), https:// doi.org/10.1016/j.ijhydene.2023.06.168.
- [77] Synthesis, Structure, and Energetic Characteristics of Perovskite Photocatalyst SrTiO3: an Experimental and DFT Study | Eurasian Chemico-Technological Journal, (2023). https://ect-journal.kz/index.php/ectj/article/view/1516 (accessed December 30, 2023).
- [78] Y. Meng, G. Liu, G. Zuo, X. Meng, T. Wang, J. Ye, A review on ZnS-based photocatalysts for CO₂ reduction in all-inorganic aqueous medium, Nanoscale 14 (2022) 14455–14465, https://doi.org/10.1039/D2NR03703C.
- [79] Y. Wang, X. Shang, J. Shen, Z. Zhang, D. Wang, J. Lin, J.C.S. Wu, X. Fu, X. Wang, C. Li, Direct and indirect Z-scheme heterostructure-coupled photosystem enabling cooperation of CO₂ reduction and H2O oxidation, Nat. Commun. 11 (2020) 3043, https://doi.org/10.1038/s41467-020-16742-3.
- [80] H. Li, J. Zhang, J. Yu, S. Cao, Ultra-thin carbon-doped Bi2WO6 nanosheets for enhanced photocatalytic CO₂ reduction, Trans. Tianjin Univ. 27 (2021) 338–347, https://doi.org/10.1007/s12209-021-00289-5.
- [81] S. Gao, H. Guan, H. Wang, X. Yang, W. Yang, Q. Li, Creation of SnxNb1-xO2 solid solution through heavy Nb-doping in SnO2 to boost its photocatalytic CO₂ reduction to C2+ products under simulated solar illumination, J. Adv. Ceram. 11 (2022) 1404–1416, https://doi.org/10.1007/s40145-022-0619-x.
- [82] Y. He, H. Rao, K. Song, J. Li, Y. Yu, Y. Lou, C. Li, Y. Han, Z. Shi, S. Feng, 3D hierarchical ZnIn2S4 nanosheets with Rich Zn vacancies boosting photocatalytic CO₂ reduction, Adv. Funct. Mater. 29 (2019) 1905153, https://doi.org/10.1002/adfm.201905153.
- [83] L. Wang, B. Cheng, L. Zhang, J. Yu, In situ irradiated XPS investigation on S-scheme TiO2@ZnIn2S4 photocatalyst for efficient photocatalytic CO₂ reduction, Small 17 (2021) 2103447, https://doi.org/10.1002/smll.202103447.
- [84] L. Cheng, D. Zhang, Y. Liao, J. Fan, Q. Xiang, Structural engineering of 3D hierarchical Cd0.8Zn0.2S for selective photocatalytic CO₂ reduction, Chin. J. Catal. 42 (2021) 131–140, https://doi.org/10.1016/S1872-2067(20)63623-3.

- [85] L. Wang, B. Zhu, B. Cheng, J. Zhang, L. Zhang, J. Yu, In-situ preparation of TiO2/ N-doped graphene hollow sphere photocatalyst with enhanced photocatalytic CO₂ reduction performance, Chin. J. Catal. 42 (2021) 1648–1658, https://doi. org/10.1016/51872-2067(21)63805-6.
- [86] Z. Miao, Q. Wang, Y. Zhang, L. Meng, X. Wang, In situ construction of S-scheme AgBr/BiOBr heterojunction with surface oxygen vacancy for boosting photocatalytic CO₂ reduction with H2O, Appl. Catal. B: Environ. 301 (2022) 120802, https://doi.org/10.1016/j.apcatb.2021.120802.
- [87] P. Nagababu, S.A.M. Ahmed, Y.T. Prabhu, A. Kularkar, S. Bhowmick, S.S. Rayalu, Synthesis of Ni2P/CdS and Pt/TiO2 nanocomposite for photoreduction of CO₂ into methanol, Sci. Rep. 11 (2021) 8084, https://doi.org/10.1038/s41598-021-87625-w
- [88] Y. Wang, M. Liu, W. Chen, L. Mao, W. Shangguan, Ag loaded on layered perovskite H2SrTa2O7 to enhance the selectivity of photocatalytic CO₂ reduction with H2O, J. Alloy. Compd. 786 (2019) 149–154, https://doi.org/10.1016/j. iallcom.2019.01.325.
- [89] J. Ran, M. Jaroniec, S.-Z. Qiao, Cocatalysts in semiconductor-based photocatalytic CO₂ reduction: achievements, challenges, and opportunities, Adv. Mater. 30 (2018) 1704649, https://doi.org/10.1002/adma.201704649.
- [90] S. Wang, M. Xu, T. Peng, C. Zhang, T. Li, I. Hussain, J. Wang, B. Tan, Porous hypercrosslinked polymer-TiO2-graphene composite photocatalysts for visiblelight-driven CO₂ conversion, Nat. Commun. 10 (2019) 676, https://doi.org/ 10.1038/s41467.019.08551.x
- [91] Y. Xia, Z. Tian, T. Heil, A. Meng, B. Cheng, S. Cao, J. Yu, M. Antonietti, Highly Selective CO₂ capture and its direct photochemical conversion on ordered 2D/1D heterojunctions, Joule 3 (2019) 2792–2805, https://doi.org/10.1016/j. ioule 2010 08 011
- [92] W.A. Thompson, E. Sanchez Fernandez, M.M. Maroto-Valer, Review and analysis of CO₂ photoreduction kinetics, ACS Sustain. Chem. Eng. 8 (2020) 4677–4692, https://doi.org/10.1021/acssuschemeng.9b06170.
- [93] S. Wang, X. Han, Y. Zhang, N. Tian, T. Ma, H. Huang, Inside-and-out semiconductor engineering for CO₂ photoreduction: from recent advances to new trends, Small Struct. 2 (2021) 2000061, https://doi.org/10.1002/ sstr.20200061
- [94] Z. Sun, W. Fang, L. Zhao, H. Wang, 3D porous Cu-NPs/g-C3N4 foam with excellent CO₂ adsorption and Schottky junction effect for photocatalytic CO₂ reduction, Appl. Surf. Sci. 504 (2020) 144347, https://doi.org/10.1016/j. apsusc 2019 144347
- [95] A. Bavykina, N. Kolobov, I.S. Khan, J.A. Bau, A. Ramirez, J. Gascon, Metal-organic frameworks in heterogeneous catalysis: recent progress, new trends, and future perspectives, Chem. Rev. 120 (2020) 8468–8535, https://doi. org/10.1021/acs.chemrev.9b00685.
- [96] L.-Y. Wu, Y.-F. Mu, X.-X. Guo, W. Zhang, Z.-M. Zhang, M. Zhang, T.-B. Lu, Encapsulating perovskite quantum dots in iron-based metal-organic frameworks (MOFs) for efficient photocatalytic CO₂ reduction, Angew. Chem. Int. Ed. 58 (2019) 9491–9495. https://doi.org/10.1002/anje.201904537.
- [97] I. Khan, N. Sun, Z. Zhang, Z. Li, M. Humayun, S. Ali, Y. Qu, L. Jing, Improved visible-light photoactivities of porous LaFeO3 by coupling with nanosized alkaline earth metal oxides and mechanism insight, Catal. Sci. Technol. 9 (2019) 3149–3157, https://doi.org/10.1039/C9CY00127A.
- [98] J. Li, X. Pei, Z. Wang, Y. Li, G. Zhang, Boosted charge transfer and selective photocatalytic CO₂ reduction to CH4 over sulfur-doped K0.475WO3 nanorods under visible light: performance and mechanism insight, Appl. Surf. Sci. 605 (2022) 154632, https://doi.org/10.1016/j.apsusc.2022.154632.
- [99] Q. Tang, Z. Sun, P. Wang, Q. Li, H. Wang, Z. Wu, Enhanced CO₂ photocatalytic reduction performance on alkali and alkaline earth metal ion-exchanged hydrogen titanate nanotubes, Appl. Surf. Sci. 463 (2019) 456–462, https://doi. org/10.1016/j.apsusc.2018.08.245.
- [100] X. Yang, X. Lan, Y. Zhang, H. Li, G. Bai, Rational design of MoS2@COF hybrid composites promoting C-C coupling for photocatalytic CO₂ reduction to ethane, Appl. Catal. B: Environ. 325 (2023) 122393, https://doi.org/10.1016/j. apcath 2023 122393
- [101] J. Wang, W. Zhu, F. Meng, G. Bai, Q. Zhang, X. Lan, Integrating dual-metal sites into covalent organic frameworks for enhanced photocatalytic CO₂ reduction, ACS Catal. 13 (2023) 4316–4329, https://doi.org/10.1021/acscatal.3c00126.
- [102] J. Li, D. Zhao, J. Liu, A. Liu, D. Ma, Covalent organic frameworks: a promising materials platform for photocatalytic CO₂ reductions, Molecules 25 (2020) 2425, https://doi.org/10.3390/molecules25102425.
- [103] Z. Kuspanov, B. Bakbolat, A. Baimenov, A. Issadykov, M. Yeleuov, C. Daulbayev, Photocatalysts for a sustainable future: Innovations in large-scale environmental and energy applications, Sci. Total Environ. 885 (2023) 163914, https://doi.org/ 10.1016/i.scitotenv.2023.163914.
- [104] A.A. Khan, M. Tahir, Recent advancements in engineering approach towards design of photo-reactors for selective photocatalytic CO₂ reduction to renewable fuels, J. CO₂ Util. 29 (2019) 205–239, https://doi.org/10.1016/j. icon. 2018.12.008
- [105] D. Ješić, D. Lašič Jurković, A. Pohar, L. Suhadolnik, B. Likozar, Engineering photocatalytic and photoelectrocatalytic CO₂ reduction reactions: Mechanisms, intrinsic kinetics, mass transfer resistances, reactors and multi-scale modelling simulations, Chem. Eng. J. 407 (2021) 126799, https://doi.org/10.1016/j. cei.2020.126799.
- [106] A.G. Variar, R. M.s, V.U. Ail, S.P. S, S. K, M. Tahir, Influence of various operational parameters in enhancing photocatalytic reduction efficiency of carbon dioxide in a photoreactor: a review, J. Ind. Eng. Chem. 99 (2021) 19–47, https://doi.org/10.1016/j.jiec.2021.04.017.

- [107] S. Nabil, E.A. Shalaby, M.F. Elkady, Y. Matsushita, A.H. El-Shazly, Optimizing the performance of the meso-scale continuous-flow photoreactor for efficient photocatalytic CO₂ reduction with water over Pt/TiO2/RGO composites, Catal. Lett. 152 (2022) 3243–3258, https://doi.org/10.1007/s10562-021-03915-y.
- [108] F. Iqbal, B. Abdullah, H. Oladipo, M. Yusuf, F. Alenazey, T.D. Nguyen, M. Ayoub, Chapter 18 - Recent developments in photocatalytic irradiation from CO₂ to methanol, in: V.-H. Nguyen, D.-V.N. Vo, S. Nanda (Eds.), Nanostructured Photocatalysts, Elsevier, 2021, pp. 519–540, https://doi.org/10.1016/B978-0-12-823007-7 00015-8
- [109] S. Nadeem, A. Mumtaz, M.S. Alnarabiji, M.I.A. Mutalib, B. Abdullah, Highly porous Zr-MCM-48 immobilized Cu-porphyrin for photocatalytic reduction of CO₂ to methanol in a slurry reactor, J. Mater. Sci: Mater. Electron 32 (2021) 22060–22075, https://doi.org/10.1007/s10854-021-06676-x.
- [110] S. Ali, J. Lee, H. Kim, Y. Hwang, A. Razzaq, J.-W. Jung, C.-H. Cho, S.-I. In, Sustained, photocatalytic CO₂ reduction to CH4 in a continuous flow reactor by earth-abundant materials: reduced titania-Cu2O Z-scheme heterostructures, Appl. Catal. B: Environ. 279 (2020) 119344, https://doi.org/10.1016/j. apcatb.2020.119344.
- [111] A. Alarcón, J. Guilera, T. Andreu, CO₂ conversion to synthetic natural gas: Reactor design over Ni–Ce/Al2O3 catalyst, Chem. Eng. Res. Des. 140 (2018) 155–165, https://doi.org/10.1016/j.cherd.2018.10.017.
- [112] X.Y. Kong, W.Q. Lee, A.R. Mohamed, S.-P. Chai, Effective steering of charge flow through synergistic inducing oxygen vacancy defects and p-n heterojunctions in 2D/2D surface-engineered Bi2WO6/BiOI cascade: towards superior photocatalytic CO₂ reduction activity, Chem. Eng. J. 372 (2019) 1183–1193, https://doi.org/10.1016/j.cej.2019.05.001.
- [113] E.C. Lumbaque, D.S. Lüdtke, D.D. Dionysiou, V.J.P. Vilar, C. Sirtori, Tube-in-tube membrane photoreactor as a new technology to boost sulfate radical advanced oxidation processes, Water Res. 191 (2021) 116815, https://doi.org/10.1016/j. watres.2021.116815.
- [114] M. Baniamer, A. Aroujalian, S. Sharifnia, A novel PEBAX-1657/PES-(BiFeO3@ ZnS) photocatalytic membrane for integrated hybrid systems coupling CO₂ separation and photoreduction, J. Environ. Chem. Eng. 9 (2021) 106529, https://doi.org/10.1016/j.jece.2021.106529.
- [115] F.R. Pomilla, A. Brunetti, G. Marcì, E.I. García-López, E. Fontananova, L. Palmisano, G. Barbieri, CO₂ to liquid fuels: photocatalytic conversion in a continuous membrane reactor, ACS Sustain. Chem. Eng. 6 (2018) 8743–8753, https://doi.org/10.1021/acssuschemeng.8b01073.
- [116] K.-Q. Lu, Y.-H. Li, F. Zhang, M.-Y. Qi, X. Chen, Z.-R. Tang, Y.M.A. Yamada, M. Anpo, M. Conte, Y.-J. Xu, Rationally designed transition metal hydroxide nanosheet arrays on graphene for artificial CO₂ reduction, Nat. Commun. 11 (2020) 5181. https://doi.org/10.1038/s41467-020-18944-1.
- [117] P. Verma, A. Singh, F.A. Rahimi, P. Sarkar, S. Nath, S.K. Pati, T.K. Maji, Charge-transfer regulated visible light driven photocatalytic H2 production and CO₂ reduction in tetrathiafulvalene based coordination polymer gel, Nat. Commun. 12 (2021) 7313. https://doi.org/10.1038/s41467-021-27457-4.
- [118] G. Ahmed, F. Raziq, M. Hanif, J. Khan, K.S. Munawar, M. Wu, X. Cao, Z. Liu, Oxygen-cluster-modified anatase with graphene leads to efficient and recyclable photo-catalytic conversion of CO₂ to CH4 supported by the positron annihilation study, Sci. Rep. 9 (2019) 13103, https://doi.org/10.1038/s41598-019-49694-w.
- [119] B. Yu, Y. Wu, F. Meng, Q. Wang, X. Jia, M. Wasim Khan, C. Huang, S. Zhang, L. Yang, H. Wu, Formation of hierarchical Bi2MoO6/ln2S3 S-scheme heterojunction with rich oxygen vacancies for boosting photocatalytic CO₂ reduction, Chem. Eng. J. 429 (2022) 132456, https://doi.org/10.1016/j. cei 2021 132456
- [120] X.-Y. Dong, Y.-N. Si, Q.-Y. Wang, S. Wang, S.-Q. Zang, Integrating single atoms with different microenvironments into one porous organic polymer for efficient photocatalytic CO₂ reduction, Adv. Mater. 33 (2021) 2101568, https://doi.org/ 10.1002/adma.202101568.
- [121] Z. Gu, H. Shen, Z. Chen, Y. Yang, C. Yang, Y. Ji, Y. Wang, C. Zhu, J. Liu, J. Li, T.-K. Sham, X. Xu, G. Zheng, Efficient electrocatalytic CO₂ reduction to C2+ alcohols at defect-site-rich Cu surface, Joule 5 (2021) 429–440, https://doi.org/10.1016/j.ioule.2020.12.011.
- [122] Y. Xia, S. Kashtanov, P. Yu, L.-Y. Chang, K. Feng, J. Zhong, J. Guo, X. Sun, Identification of dual-active sites in cobalt phthalocyanine for electrochemical carbon dioxide reduction, Nano Energy 67 (2020) 104163, https://doi.org/ 10.1016/j.nanoen.2019.104163.
- [123] J.J. Masana, J. Xiao, H. Zhang, X. Lu, M. Qiu, Y. Yu, Nitrogen-rich carbon nitride inducing electron delocalization of Co-N4 site to enhance electrocatalytic carbon dioxide reduction, Appl. Catal. B: Environ. 323 (2023) 122199, https://doi.org/ 10.1016/j.apcatb.2022.122199.
- [124] C.V. Hoang, T.M. Nguyen, D.L.T. Nguyen, K.N. Dinh, H.T. Dang, Q.V. Le, Recent advances in nanoengineering 2D metal-based materials for electrocatalytic conversion of carbon dioxide into fuels and value-added products, Fuel 343 (2023) 127873, https://doi.org/10.1016/j.fuel.2023.127873.
- [125] L. Wei, R. Li, W. Kong, P. Tan, Q. Fan, C. Yu, Highly selective electrocatalytic reduction of carbon dioxide to ethylene on CuCl-derived Cu, Mater. Chem. Phys. 291 (2022) 126660, https://doi.org/10.1016/j.matchemphys.2022.126660.
- [126] S.-Q. Xiang, S.-T. Gao, J.-L. Shi, W. Zhang, L.-B. Zhao, Developing micro-kinetic model for electrocatalytic reduction of carbon dioxide on copper electrode, J. Catal. 393 (2021) 11–19, https://doi.org/10.1016/j.jcat.2020.11.014.
- [127] S. Nitopi, E. Bertheussen, S.B. Scott, X. Liu, A.K. Engstfeld, S. Horch, B. Seger, I.E. L. Stephens, K. Chan, C. Hahn, J.K. Nørskov, T.F. Jaramillo, I. Chorkendorff, Progress and perspectives of electrochemical CO₂ reduction on copper in aqueous electrolyte, Chem. Rev. 119 (2019) 7610–7672, https://doi.org/10.1021/acs.chemrev.8b00705.

- [128] Y. Zhang, S.-X. Guo, X. Zhang, A.M. Bond, J. Zhang, Mechanistic understanding of the electrocatalytic CO₂ reduction reaction – New developments based on advanced instrumental techniques, Nano Today 31 (2020) 100835, https://doi. org/10.1016/j.nantod.2019.100835.
- [129] I. Hussain, H. Alasiri, W. Ullah Khan, K. Alhooshani, Advanced electrocatalytic technologies for conversion of carbon dioxide into methanol by electrochemical reduction: recent progress and future perspectives, Coord. Chem. Rev. 482 (2023) 215081, https://doi.org/10.1016/j.ccr.2023.215081.
- [130] Y. Yang, F. Li, Reactor design for electrochemical CO₂ conversion toward large-scale applications, Curr. Opin. Green. Sustain. Chem. 27 (2021) 100419, https://doi.org/10.1016/j.cogsc.2020.100419.
- [131] L.R.L. Ting, O. Piqué, S.Y. Lim, M. Tanhaei, F. Calle-Vallejo, B.S. Yeo, Enhancing CO₂ electroreduction to ethanol on copper-silver composites by opening an alternative catalytic pathway, ACS Catal. 10 (2020) 4059–4069, https://doi.org/ 10.1021/acscatal.9b05319.
- [132] Q.H. Low, N.W.X. Loo, F. Calle-Vallejo, B.S. Yeo, Enhanced electroreduction of carbon dioxide to methanol using zinc dendrites pulse-deposited on silver foam, Angew. Chem. Int. Ed. 58 (2019) 2256–2260, https://doi.org/10.1002/ anie 201810901
- [133] D. Yang, Q. Zhu, C. Chen, H. Liu, Z. Liu, Z. Zhao, X. Zhang, S. Liu, B. Han, Selective electroreduction of carbon dioxide to methanol on copper selenide nanocatalysts, Nat. Commun. 10 (2019) 677, https://doi.org/10.1038/s41467-019-08653-9
- [134] S.N.A. Zakaria, N. Hollingsworth, H.U. Islam, A. Roffey, D. Santos-Carballal, A. Roldan, W. Bras, G. Sankar, G. Hogarth, K.B. Holt, N.H. De Leeuw, Insight into the nature of iron sulfide surfaces during the electrochemical hydrogen evolution and CO₂ reduction reactions, ACS Appl. Mater. Interfaces 10 (2018) 32078–32085, https://doi.org/10.1021/acsami.8b08612.
- [135] C. Lv, K. Huang, Y. Fan, J. Xi, C. Lian, H. Jiang, Y. Zhang, C. Ma, W. Qiao, J. Wang, L. Ling, Electrocatalytic reduction of carbon dioxide in confined microspace utilizing single nickel atom decorated nitrogen-doped carbon nanospheres, Nano Energy 111 (2023) 108384, https://doi.org/10.1016/j.nanoen.2023.108384.
- [136] Z. Zhang, L. Yu, Y. Tu, R. Chen, L. Wu, J. Zhu, D. Deng, Unveiling the active site of metal-free nitrogen-doped carbon for electrocatalytic carbon dioxide reduction, Cell Rep. Phys. Sci. 1 (2020) 100145, https://doi.org/10.1016/j. xcrp.2020.100145.
- [137] B. Xu, I. Masood Ul Hasan, L. Peng, J. Liu, N. Xu, M. Fan, N.K. Niazi, J. Qiao, Anion-regulation engineering toward Cu/In/MOF bimetallic electrocatalysts for selective electrochemical reduction of CO₂ to CO/formate, Mater. Rep.: Energy 2 (2022) 100139, https://doi.org/10.1016/j.matre.2022.100139.
- [138] K.-G. Liu, F. Bigdeli, A. Panjehpour, A. Larimi, A. Morsali, A. Dhakshinamoorthy, H. Garcia, Metal organic framework composites for reduction of CO₂, Coord. Chem. Rev. 493 (2023) 215257, https://doi.org/10.1016/j.ccr.2023.215257.
- [139] K.A. Adegoke, N.W. Maxakato, Porous metal-organic framework (MOF)-based and MOF-derived electrocatalytic materials for energy conversion, Mater. Today Energy 21 (2021) 100816. https://doi.org/10.1016/j.mtener.2021.100816.
- Energy 21 (2021) 100816, https://doi.org/10.1016/j.mtener.2021.100816.
 [140] J. Jeong, J. Choi, S. Jang, H. Shin, S. Kim, J. Jang, H.S. Park, M. Choi, Y.-E. Sung, In situ fabrication of highly porous foam-like Zn nanostructures on gas diffusion layer for selective electrocatalytic reduction of carbon dioxide to carbon monoxide, J. Ind. Eng. Chem. 113 (2022) 325–331, https://doi.org/10.1016/j.iiec.2022.06.006.
- [141] C. Shen, K. Li, Y. Ma, S. Liu, X. Wang, J. Xu, M. Wang, Y. Meng, N. Chen, W. Chen, Electrochemical reduction of CO₂ via a CuO/SnO2 heterojunction catalyst, Chem. Phys. Lett. 818 (2023) 140438, https://doi.org/10.1016/j.cplett.2023.140438.
- [142] L. Diao, Y. Liu, F. Chen, H. Pan, D.P.D. Lara, H. Liu, Y. Cheng, F. Luo, Improving the activity of electrochemical reduction of CO₂ to C1 products by oxidation derived copper catalyst, Mater. Rep.: Energy 3 (2023) 100180, https://doi.org/ 10.1016/j.matre.2023.100180.
- [143] Q. Zeng, G. Yang, J. Chen, Q. Zhang, Z. Liu, B. Qin, F. Peng, Effects of nitrogen and oxygen on electrochemical reduction of CO₂ in nitrogen-doped carbon black, Carbon 202 (2023) 1–11, https://doi.org/10.1016/j.carbon.2022.10.038.
- [144] M. Zhong, K. Tran, Y. Min, C. Wang, Z. Wang, C.-T. Dinh, P. De Luna, Z. Yu, A. S. Rasouli, P. Brodersen, S. Sun, O. Voznyy, C.-S. Tan, M. Askerka, F. Che, M. Liu, A. Seifitokaldani, Y. Pang, S.-C. Lo, A. Ip, Z. Ulissi, E.H. Sargent, Accelerated discovery of CO₂ electrocatalysts using active machine learning, Nature 581 (2020) 178–183, https://doi.org/10.1038/s41586-020-2242-8.
- [145] F. Li, A. Thevenon, A. Rosas-Hernández, Z. Wang, Y. Li, C.M. Gabardo, A. Ozden, C.T. Dinh, J. Li, Y. Wang, J.P. Edwards, Y. Xu, C. McCallum, L. Tao, Z.-Q. Liang, M. Luo, X. Wang, H. Li, C.P. O'Brien, C.-S. Tan, D.-H. Nam, R. Quintero-Bermudez, T.-T. Zhuang, Y.C. Li, Z. Han, R.D. Britt, D. Sinton, T. Agapie, J. C. Peters, E.H. Sargent, Molecular tuning of CO₂-to-ethylene conversion, Nature 577 (2020) 509–513, https://doi.org/10.1038/s41586-019-1782-2.
- [146] R. Lin, J. Guo, X. Li, P. Patel, A. Seifitokaldani, Electrochemical Reactors for CO₂ Conversion, Catalysts 10 (2020) 473, https://doi.org/10.3390/catal10050473.
- [147] T. Luo, K. Liu, J. Fu, S. Chen, H. Li, J. Hu, M. Liu, Tandem catalysis on adjacent active motifs of copper grain boundary for efficient CO₂ electroreduction toward C2 products, J. Energy Chem. 70 (2022) 219–223, https://doi.org/10.1016/j. iechem.2022.02.050.
- [148] Y. Jia, F. Li, K. Fan, L. Sun, Cu-based bimetallic electrocatalysts for CO₂ reduction, Adv. Powder Mater. 1 (2022) 100012, https://doi.org/10.1016/j. apmate.2021.10.003.
- [149] C. Azenha, C. Mateos-Pedrero, M. Alvarez-Guerra, A. Irabien, A. Mendes, Binary copper-bismuth catalysts for the electrochemical reduction of CO₂: Study on surface properties and catalytic activity, Chem. Eng. J. 445 (2022) 136575, https://doi.org/10.1016/j.cej.2022.136575.

- [150] D. Zeng, C. Li, W. Wang, L. Zhang, Y. Zhang, J. Wang, L. Zhang, X. Zhou, W. Wang, Insights into the hydrophobic surface promoting electrochemical CO₂ reduction to ethylene, Chem. Eng. J. 461 (2023) 142133, https://doi.org/ 10.1016/j.eij.2023.142133
- [151] C. An, Y. Shen, W. Yan, L. Dai, C. An, Surface-tuning nanoporous AuCu3 engineering syngas proportion by electrochemical conversion of CO₂, Nano Res. 14 (2021) 3907–3912, https://doi.org/10.1007/s12274-021-3313-3.
- [152] Z. Min, B. Chang, C. Shao, X. Su, N. Wang, Z. Li, H. Wang, Y. Zhao, M. Fan, J. Wang, Enhancing CO₂ electroreduction to syngas by active protons of imidazolium ionic liquids: from performance to mechanism, Appl. Catal. B: Environ. 326 (2023) 122185, https://doi.org/10.1016/j.apcatb.2022.122185.
- [153] J.M. Mora-Hernandez, W.I. González-Suárez, A. Manzo-Robledo, M. Luna-Trujillo, A comparative differential electrochemical mass spectrometry (DEMS) study towards the CO₂ reduction on Pd, Cu, and Sn -based electrocatalyst, J. CO₂ Util. 47 (2021) 101504, https://doi.org/10.1016/j.jcou.2021.101504.
- [154] Y. Liu, D. Tian, A.N. Biswas, Z. Xie, S. Hwang, J.H. Lee, H. Meng, J.G. Chen, Transition metal nitrides as promising catalyst supports for tuning CO/H₂ syngas production from electrochemical CO₂ reduction, Angew. Chem. Int Ed. 59 (2020) 11345–11348, https://doi.org/10.1002/anie.202003625.
- [155] Q. Xie, G.O. Larrazábal, M. Ma, I. Chorkendorff, B. Seger, J. Luo, Copper-indium hydroxides derived electrocatalysts with tunable compositions for electrochemical CO₂ reduction, J. Energy Chem. 63 (2021) 278–284, https://doi. org/10.1016/j.jechem.2021.09.008.
- [156] Y. Hua, B. Zhang, W. Hao, Z. Gao, Boosting CO desorption on dual active site electrocatalysts for CO₂ reduction to produce tunable syngas, Cell Rep. Phys. Sci. 3 (2022) 100703, https://doi.org/10.1016/j.xcrp.2021.100703.
- [157] J. Ma, C. Liu, M. Bai, Z. Fu, P. Zhao, Y. Gao, M. Zhao, Y. He, H. Xiao, J. Jia, Recent advances in application of tandem catalyst for electrocatalytic CO₂ reduction, Mol. Catal. 551 (2023) 113632, https://doi.org/10.1016/j.mcat.2023.113632.
- [158] Z. Guo, H. Zhu, G. Yang, A. Wu, Q. Chen, Z. Yan, K. Loon Fow, H. Do, J.D. Hirst, T. Wu, M. Xu, Synergistic engineering of heteronuclear Ni-Ag dual-atom catalysts for high-efficiency CO₂ electroreduction with nearly 100% CO selectivity, Chem. Eng. J. 476 (2023) 146556, https://doi.org/10.1016/j.cej.2023.146556.
- [159] H. Tian, Z. Shui, M.A. Raza, L. Zhu, X. Chen, Synergistic catalysis of bimetallic nitrogen-doped carbon materials for efficient electrocatalytic CO₂ reduction, J. Alloy. Compd. 958 (2023) 170544, https://doi.org/10.1016/j. iallcom.2023.170544.
- [160] C. An, S. Wu, R. Huang, X. Chen, X. Han, H. Gomaa, Q. Deng, L. Zhao, N. Hu, Cooperated catalytic mechanism of atomically dispersed binary Cu-N4 and Zn-N4 in N-doped carbon materials for promoting electrocatalytic CO₂ reduction to CH4, Chem. Eng. J. 471 (2023) 144618. https://doi.org/10.1016/j.cej.2023.144618.
- [161] G. Dong, C. Xue, M. Li, T. Zhang, D. Geng, L.-M. Liu, Synergetic enhancement of selectivity for electroreduction of CO₂ to C2H4 by crystal facet engineering and tandem catalysis over silver-incorporated-cuprous oxides, Mater. Rep.: Energy 3 (2023) 100195. https://doi.org/10.1016/j.matre.2023.100195
- (2023) 100195, https://doi.org/10.1016/j.matre.2023.100195.
 [162] A. He, Y. Yang, Q. Zhang, M. Yang, Q. Zou, J. Du, C. Tao, Z. Liu, The enhanced local CO concentration for efficient CO₂ electrolysis towards C2 products on tandem active sites, Chem. Eng. J. 450 (2022) 138009, https://doi.org/10.1016/j.cei.2022.138009.
- [163] Y. Zhang, P. Li, C. Zhao, G. Zhou, F. Zhou, Q. Zhang, C. Su, Y. Wu, Multicarbons generation factory: CuO/Ni single atoms tandem catalyst for boosting the productivity of CO₂ electrocatalysis, Sci. Bull. 67 (2022) 1679–1687, https://doi.org/10.1016/j.scib.2022.07.029
- [164] X. Kang, B. Wang, K. Hu, K. Lyu, X. Han, B.F. Spencer, M.D. Frogley, F. Tuna, E.J. L. McInnes, R.A.W. Dryfe, B. Han, S. Yang, M. Schröder, Quantitative electro-reduction of CO₂ to liquid fuel over electro-synthesized metal-organic frameworks, J. Am. Chem. Soc. 142 (2020) 17384–17392, https://doi.org/10.1021/jacs.0c05913.
- [165] L. Han, C. Wang, S. Luo, Y. Zhou, B. Li, M. Liu, Facet effects on bimetallic ZnSn hydroxide microcrystals for selective electrochemical CO₂ reduction, Green. Energy Environ. (2023) S2468025723000584, https://doi.org/10.1016/j.gee.2023.04.004
- [166] M. Liang, Y. Liu, J. Zhang, F. Wang, Z. Miao, L. Diao, J. Mu, J. Zhou, S. Zhuo, Understanding the role of metal and N species in M@NC catalysts for electrochemical CO₂ reduction reaction, Appl. Catal. B: Environ. 306 (2022) 121115, https://doi.org/10.1016/j.apcatb.2022.121115.
- [167] D. Tan, B. Wulan, X. Cao, J. Zhang, Strong interactions of metal-support for efficient reduction of carbon dioxide into ethylene, Nano Energy 89 (2021) 106460, https://doi.org/10.1016/j.nanoen.2021.106460.
- [168] T. Yan, J.-H. Guo, Z.-Q. Liu, W.-Y. Sun, Metalloporphyrin encapsulation for enhanced conversion of CO₂ to C₂ H₄, ACS Appl. Mater. Interfaces 13 (2021) 25937–25945, https://doi.org/10.1021/acsami.1c03557.
- [169] S.-M. Cao, H.-B. Chen, B.-X. Dong, Q.-H. Zheng, Y.-X. Ding, M.-J. Liu, S.-L. Qian, Y.-L. Teng, Z.-W. Li, W.-L. Liu, Nitrogen-rich metal-organic framework mediated Cu–N–C composite catalysts for the electrochemical reduction of CO₂, J. Energy Chem. 54 (2021) 555–563, https://doi.org/10.1016/j.jechem.2020.06.038.
- [170] S. Dongare, N. Singh, H. Bhunia, P.K. Bajpai, Electrochemical reduction of CO₂ using oxide based Cu and Zn bimetallic catalyst, Electrochim. Acta 392 (2021) 138988, https://doi.org/10.1016/j.electacta.2021.138988.
- [171] N. Hussain, M.A. Abdelkareem, H. Alawadhi, S. Begum, K. Elsaid, A.G. Olabi, Novel ternary CuO–ZnO–MoS2 composite material for electrochemical CO₂ reduction to alcohols, J. Power Sources 549 (2022) 232128, https://doi.org/ 10.1016/j.jpowsour.2022.232128.
- [172] L. Zeng, J. Shi, J. Luo, H. Chen, Silver sulfide anchored on reduced graphene oxide as a high -performance catalyst for CO 2 electroreduction, J. Power Sources 398 (2018) 83–90, https://doi.org/10.1016/j.jpowsour.2018.07.049.

- [173] R. He, A. Zhang, Y. Ding, T. Kong, Q. Xiao, H. Li, Y. Liu, J. Zeng, Achieving the widest range of syngas proportions at high current density over cadmium sulfoselenide nanorods in CO 2 electroreduction, Adv. Mater. 30 (2018) 1705872, https://doi.org/10.1002/adma.201705872.
- [174] W. Huang, D. Zhou, H. Yang, X. Liu, J. Luo, Dual-doping promotes the carbon dioxide electroreduction activity of MoS₂ nanosheet array, ACS Appl. Energy Mater. 4 (2021) 7492–7496, https://doi.org/10.1021/acsaem.1c01300.
- [175] R. Cui, Q. Shen, C. Guo, B. Tang, N. Yang, G. Zhao, Syngas electrosynthesis using self-supplied CO₂ from photoelectrocatalytic pollutant degradation, Appl. Catal. B: Environ. 261 (2020) 118253, https://doi.org/10.1016/j.apcatb.2019.118253.
- [176] X. Wang, J. Lv, J. Zhang, X.-L. Wang, C. Xue, G. Bian, D. Li, Y. Wang, T. Wu, Hierarchical heterostructure of SnO₂ confined on CuS nanosheets for efficient electrocatalytic CO₂ reduction, Nanoscale 12 (2020) 772–784, https://doi.org/ 10.1039/C9NR08726E.
- [177] M. Beheshti, S. Kakooei, M.C. Ismail, S. Shahrestani, Investigation of CO₂ electrochemical reduction to syngas on Zn/Ni-based electrocatalysts using the cyclic voltammetry method, Electrochim. Acta 341 (2020) 135976, https://doi.org/10.1016/j.electacta.2020.135976.
- [178] L. Meng, E. Zhang, H. Peng, Y. Wang, D. Wang, H. Rong, J. Zhang, Bi/Zn dual single-atom catalysts for electroreduction of CO₂ to syngas, ChemCatChem 14 (2022) e202101801, https://doi.org/10.1002/cctc.202101801.
- [179] N. Meng, C. Liu, Y. Liu, Y. Yu, B. Zhang, Efficient electrosynthesis of syngas with tunable CO/H₂ ratios over Zn_x Cd_{1-x} S-amine inorganic–organic hybrids, Angew. Chem. Int Ed. 58 (2019) 18908–18912, https://doi.org/10.1002/ anie.201913003.
- [180] R. Daiyan, R. Chen, P. Kumar, N.M. Bedford, J. Qu, J.M. Cairney, X. Lu, R. Amal, Tunable syngas production through CO₂ electroreduction on cobalt–carbon

- composite electrocatalyst, ACS Appl. Mater. Interfaces 12 (2020) 9307–9315, https://doi.org/10.1021/acsami.9b21216.
- [181] Q. He, D. Liu, J.H. Lee, Y. Liu, Z. Xie, S. Hwang, S. Kattel, L. Song, J.G. Chen, Electrochemical conversion of CO₂ to syngas with controllable CO/H₂ ratios over Co and Ni single-atom catalysts, Angew. Chem. Int. Ed. 59 (2020) 3033–3037, https://doi.org/10.1002/anie.201912719.
- [182] W. Ni, Z. Liu, X. Guo, Y. Zhang, C. Ma, Y. Deng, S. Zhang, Dual single-cobalt atom-based carbon electrocatalysts for efficient CO₂-to-syngas conversion with industrial current densities, Appl. Catal. B: Environ. 291 (2021) 120092, https://doi.org/10.1016/j.apcatb.2021.120092.
- [183] D. Yang, Q. Zhu, X. Sun, C. Chen, W. Guo, G. Yang, B. Han, Electrosynthesis of a defective indium selenide with 3D structure on a substrate for tunable CO₂ electroreduction to syngas, Angew. Chem. 132 (2020) 2374–2379, https://doi. org/10.1002/ange.201914831.
- [184] J. Gu, C.-S. Hsu, L. Bai, H.M. Chen, X. Hu, Atomically dispersed Fe ³⁺ sites catalyze efficient CO₂ electroreduction to CO, Science 364 (2019) 1091–1094, https://doi.org/10.1126/science.aaw7515.
- [185] Y. Ji, Y. Shi, C. Liu, B. Zhang, Plasma-regulated N-doped carbon nanotube arrays for efficient electrosynthesis of syngas with a wide CO/H2 ratio, Sci. China Mater. 63 (2020) 2351–2357, https://doi.org/10.1007/s40843-020-1396-7.
- [186] W. Wang, K. Chen, Y. Sun, S. Zhou, M. Zhang, J. Yuan, Mesoporous Ni-N-C as an efficient electrocatalyst for reduction of CO₂ into CO in a flow cell, Appl. Mater. Today 29 (2022) 101619, https://doi.org/10.1016/j.apmt.2022.101619.
- [187] N. Meng, W. Zhou, Y. Yu, Y. Liu, B. Zhang, Superficial hydroxyl and amino groups synergistically active polymeric carbon nitride for CO₂ electroreduction, ACS Catal. 9 (2019) 10983–10989, https://doi.org/10.1021/acscatal.9b03895.

https://doi.org/10.18321/cpc21(2)71-80

ПОЛУЧАЕМЫЙ ИЗ БИООТХОДОВ МНОГОСЛОЙНЫЙ ГРАФЕН/SrTiO₃ КАК ЭФФЕКТИВНАЯ ФОТОКАТАЛИТИЧЕСКАЯ СИСТЕМА

Ж. Куспанов^{1,2}*, Ч. Даулбаев², М. Елеуов^{1,2}, З. Мансуров^{3,4}

¹Satbayev University, ул. Сатпаева 22, Алматы, Казахстан ²Институт ядерной физики, ул. Ибрагимова 1, Алматы, Казахстан ³Казахский национальный университет им. аль-Фараби, пр. аль-Фараби, 71, Алматы, Казахстан ⁴Институт проблем горения, ул. Богенбай батыра, 172 Алматы, Казахстан

АННОТАЦИЯ

Изучены фотоэлектрохимические свойства фотокатализаторов на основе композита $SrTiO_3$ /многослойный графен, синтезированного из биоотходов методом электроспиннинга, как перспективных и недорогих элементов и графен, полученный из рисовой шелухи и скорлупы грецкого ореха, как со-катализатор для производства водорода (H_2) путем разложения воды, которые впервые использованы в фотокаталитической системе. Результаты показали, что наличие нескольких слоев графена уменьшает ширину запрещенной зоны фотокаталитической системы и способствует эффективному разделению фотоиндуцированных зарядов. Материал — многослойный графен, синтезированный из биоотходов/ $SrTiO_3$, проявил более высокую скорость выделения водорода, чем чистый $SrTiO_3$. Полученные результаты могут быть использованы для создания новых и эффективных фотокатализаторов на основе материалов, синтезированных из биоотходов, с улучшенными свойствами для расщепления воды.

Ключевые слова: фотокатализатор; расщепление воды; графен; получение водорода.

1. Введение

Использование фотокаталитических материалов для преобразования энергии солнца в водород является многообещающим методом получения экологически чистой энергии [1]. Однако большинство способов, применяемых в настоящее время в водородной энергетике, имеют ряд ограничений, включая низкую эффективность разделения зарядов, слабое преобразование солнечного облучения из-за широкой запрещенной зоны полупроводникого материала и поверхностной морфологии, слабую подвижность фотоиндуцированных носителей заряда, а также высокую стоимость [2]. Единственным способом решения этих проблем является синтез композитных фотокаталитализаторов на основе благородных [3], переходных металлов [4] и неметаллических элементов [5]. Синергия современных способов синтеза фотокатализаторов и нанотехнологий способствует получению новых эффективных систем для получения водорода за счет эффективного разложения воды [5] и может открыть путь

для крупномасштабного фотокаталитического применения [6, 7].

Применение графена в фотокаталитических системах может повысить их эффективность благодаря уникальным оптическим и электрическим свойствам материала, а также его химической стабильности. В исследовании [5] авторы показывают, что графен может сам по себе обладать фотокаталитической активностью, например, в процессе выделения водорода. Графен также может улучшить эффективное разделение фотогенерируемых зарядов путем быстрой передачи фотоиндуцированных зарядов, что приводит к высокой плотности тока при облучении солнечным светом. На сегодняшний день проведено множество исследований по созданию наноматериалов на основе графена, в том числе различных композитов [8, 9]. Для получения графена используют разные методы, в том числе механическое расслоение графита, парофазное химическое осаждение и карбонизация биомассы и отходов [10-13]. Хотя эти методы позволяют получить графен хорошего качества, его широкое практическое использование ограни-

*Ответственный автор

E-mail: zhenis.kuspanov@gmail.com (Ж. Куспанов)

чено высокой стоимостью. Использование биологических отходов для получения графена является активной исследовательской областью. Несмотря на то, что полученный материал может содержать дефекты, он все же обладает оптическими и электрическими свойствами чистого графена.

Изучение скорости фотокаталитического получения H_2 при использовании композитной структуры на основе $SrTiO_3$ и графена представляет большой интерес, поскольку $SrTiO_3$ является наиболее эффективным фотокатализатором [14]. Добавление графена в композитную структуру способствует эффективному разделению и переносу фотогенерированных носителей зарядов, а также позволяет повысить эффективность преобразования энергии солнца благодаря своим уникальным оптическим свойствам.

В данной работе были изготовлены композитные структуры на основе синтезированного SrTiO₃ с добавлением графена, полученного из рисовой шелухи. Выбор графена был обусловлен их фотоактивностью при разложении воды под воздействием солнечной энергии и ожидаемым повышением фотоэффективности по выделению Н₂ за счет использования этого композита. Для создания композитных структур на основе синтезированного SrTiO₃ с добавлением графена был использован метод электроспиннинга. Этот метод является простой и эффективной технологией получения одномерных нановолокон из полимеров, неорганических материалов и композитов. Нановолокна, синтезированные электроспиннингом, обладают более высокой удельной площадью поверхности, более высоким соотношением сторон и лучшей пористостью структуры по сравнению с материалами, полученными другими методами. Это, в свою очередь, благоприятно оказывает влияние на фотокаталитическую активность по выделению Н₂ при солнечном облучении.

2. Материалы и методы

2.1. Синтез SrTiO₃

Для синтеза $SrTiO_3$ использовали исходные материалы, включая $Sr(NO_3)_2$ (чистотой > 98%, Sigma Aldrich), TiO_2 (Sigma Aldrich, с размером частиц: 0,27 мкм, 0,35 мкм, 0,48 мкм) и (COOH) $_2$ *2 H_2O (более 99,5%, Sigma Aldrich). Синтез осуществляли методом химического осаждения из раствора TiO_2 и $Sr(NO_3)_2$, а затем проводили кальцинацию при 1100 °C в течение 1 ч. Для получения однородных частиц без примесей в растворе использовали TiO_2 и $Sr(NO_3)_2$ при соотношении 1:1.

2.2. Синтез графена

Для получения графена из биологических отходов использовали рисовую шелуху (РШ) и скорлупу грецкого ореха (СГО) в качестве источника углерода, КОН как химический активатор и аргон для защиты от окисления. РШ и СГО измельчали и карбонизовали при температуре 500 °C в течение 100 мин с помощью аргона. Затем карбонизованные материалы активировали с помощью гидроксида калия при температуре 150 °C в течение 5 ч. Далее проводили термохимическую активацию при скорости подачи инертного газа ~250 sccm, температуре 850 °C и времени активации 60-90 мин. Образцы промывали дистиллированной водой и сушили в два этапа при температурах 120 и 150 °C в вакуумной сушильной камере для удаления соединений калия и получения готовых образцов графена.

2.3. Электроспиннинг

Для синтеза фотокаталитического композита графен/SrTiO₃ использовали метод электроспиннинга, позволяющий формировать волокна с различными диаметрами из раствора в зависимости от параметров процесса. Электроспиннинг проводили при напряжении 16 кВ, комнатной температуре, при скорости шприцевого насоса 1,5 мл/ч. Коллектором служила алюминиевая фольга (диаметр 20 см), находящаяся на расстоянии 15 см от иглы. Фольгу заменяли каждые 1,5 ч в период работы. Были использованы различные типы графена и синтезированный титанат стронция.

Полимерный раствор готовили из полиакрилонитрила (ПАН) средней молекулярной массы 1,300,000 (от Sigma Aldrich), который растворяли в 99,5% этаноле. Затем к раствору полимера добавляли 0,01 г нанопорошка SrTiO₃ и 0,015 г графена (R-FLGr, W-FLGr и C-Gr от «Cheap tubes inc», чистота 99%, толщина 0,7-1,2 нм, размер частиц менее 450 нм). Полученные волокна подвергали термостабилизации при 180 °C в течение 15 мин с последующей карбонизацией при 500 °C в кислородной атмосфере.

2.4. Определение фотокаталитической активности полученных образцов

1 г смеси композитных фотокатализаторов графен/SrTiO $_3$ растворяли в 20 мл раствора (вода-спирт), содержащего 15% метанола, и перемешивали в течение 30 мин. Для оценки фото-

каталитической активности образцов в процессе разложения смеси воды-метанола и выделения основных газов (водород, азот, кислород, оксид углерода и диоксид углерода) применяли хроматограф Chromos-1000 с использованием 3 мм колонок, заполненных NaX и PORAPAK Q. Фотокаталитическое разложение проводили с использованием ультрафиолетовой лампы мощностью 120 Вт.

2.5. Методы исследования

Для анализа морфологии поверхности частиц и нановолокон $SrTiO_3$ использовали сканирующий электронный микроскоп QUANTA 3D 200i (FEI, США) с ускоряющим напряжением 15 кВ. XRD-анализ проводили на рентгеновском дифрактометре Drone-8 с углами поворота блока детектирования в диапазоне от 100° до 168° и минимальным шагом перемещения блока детектирования $0,001^\circ$. Допустимое отклонение блока детектирования от заданного угла поворота составило $\pm 0,015^\circ$.

Проводили измерение пропускания и отражения света в волокнах, состоящих из SrTiO₃ с добавлением графена, с помощью спектрофотометра Shimadzu UV-3600, оснащенного тремя детекторами: фотоумножителем для работы в УФ и видимом диапазоне, полупроводниковым детектором InGaAs и охлаждаемым детектором PbS для эксплуатации в ближнем инфракрасном диапазоне. Указанный прибор обеспечивает широкий спектр спектрального анализа, включая ультрафиолетовое облучение с длиной волны 185 нм и ближнее инфракрасное облучение с длиной волны до 3600 нм.

Исследования образцов проводили с помощью Раман-спектрометра NTEGRA Spectra Raman с использованием сигнала диаметром 80 нм при длине волны $\lambda = 473$ нм. Для оценки удельной поверхности углеродных материалов, полученных из РШ и СГО, использовали анализаторы удельной поверхности «СОРБТОМЕТР-М» и «Місгомегітіся Instrument Corp. ASAP 2400 V3.07». Для исследования структуры образцов использовали просвечивающую электронную микроскопию JEM-2100 (JEOL, Япония).

3. Результаты и обсуждение

Графен/ $SrTiO_3$ фотокатализаторы изготавливали в три этапа: сначала синтезировали $SrTiO_3$, затем графен, далее методом электроспиннинга

получали композитный фотокатализатор. Ранее опубликованная работа [14] подробно описывает методику получения $SrTiO_3$ и исследования физико-химических параметров. Полученный порошок $SrTiO_3$ имел чистоту 97% и средние размеры частиц были около 100 нм.

Изучение влияния продолжительности карбонизации в диапазоне от 30 до 120 мин РШ и СГО проводили путем сопоставления времени карбонизации и потери массы образца. Основная потеря массы фиксировалась в первые 70-90 мин, что свидетельствует о том, что оптимальным временем карбонизации является 90 мин. Увеличение продолжительности карбонизации более 90 мин не имеет смысла из-за незначительного изменения массы, что свидетельствует о завершении процесса. После карбонизации РШ и СГО массовый выход материала составил 43,7% и 29,3% соответственно, при этом достигалась высокая удельная поверхность. В процессе карбонизации удалялись неуглеродные элементы (азот, кислород и водород), которые содержались в исходной РШ и СГО в виде летучих газов. Используя метод БЭТ, определили, что удельная поверхность карбонизованных РШ и СГО до активации составляла соответственно $350 \text{ м}^2/\Gamma$ и $270 \text{ м}^2/\Gamma$.

Процесс термохимической активации, осуществляемый при получении графена из РШ и СГО [10, 15], способствует расширению существующих пор путем сжигания стенок между ближайшими порами и удаления неупорядоченного углерода, который может блокировать поры в карбонизованных РШ и СГО. Изначальный массовый выход графена из РШ и СГО до карбонизации составлял соответственно 11 % и 20,6 % от массы начального продукта. Результаты анализа БЭТ показали, что удельная поверхность для графена из РШ составляет 3200 м²/г, средний диаметр пор – 1,7 нм, удельный объем пор – 1,8 см³/г; для графена из СГО – 2760 м²/г, удельный объем пор – 1,49 см³/г, средний диаметр пор – 2,30 нм.

Раман-исследования указывают на присутствие графена в структурах образцов, полученных из биоотходов (рис. 1). Образцы характеризуются неоднородностями, представляя собой двухкомпонентный материал, в основном состоящий из графена и аморфного углерода. Наличие графена в структуре образцов подтверждается тремя пиками: пик D при 1357 см⁻¹, пик G при 1573 см⁻¹ и пик 2D при 2712 см⁻¹. Оба спектра демонстрируют относительно схожую графеноподобную структуру, характеризующуюся двумя основными полосами, обозначенными как G и 2D. Третья

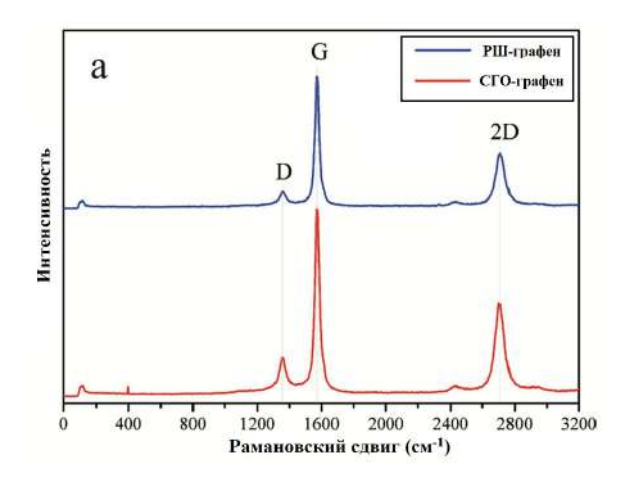


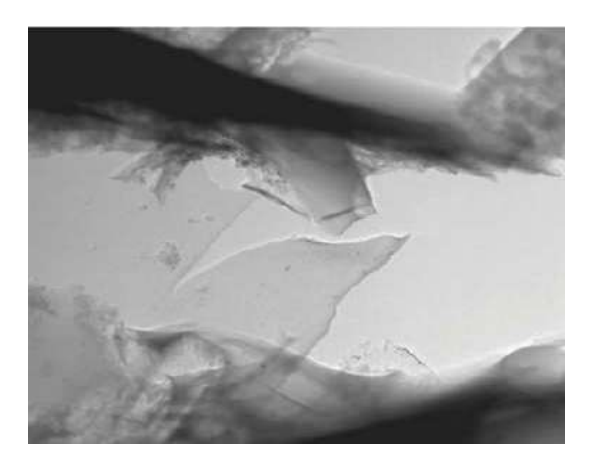
Рис. 1. Раман-спектры образцов.

D-полоса, появившаяся в обоих спектрах, свидетельствует о наличии дефектов в решетке углерода. Для определения количества слоев использовали метод, основанный на анализе отношений интенсивностей 2D- и G-пиков в спектрах, согласно которому эти отношения (I_{2D}/I_G) равны до 0,49 и 0,54 соответственно, что свидетельствует о том, что сформированная структура в большей степени состоит из нескольких слоев графена [10, 15]. На рис. 2 приведены ПЭМ снимки полученного графена.

Полимер, выбранный для использования в данном исследовании, полиакрилонитрил (ПАН), поскольку этот материал хорошо подходит для создания прочных и термостойких волокон. ПАН также широко используется в качестве модификатора для фиксации наночастиц на поверхности различных материалов. В результате проведенных экспериментов были получены полимерные волокна, в состав которых входили добавки $SrTiO_3$ и различных типов графена.

Полученные полимерные волокна на основе $SrTiO_3$ и графена имеют бездефектную форму в виде непрерывного цилиндра и расположены хаотично в пространстве. Экспериментальные образцы, полученные методом электроспиннинга на основе $SrTiO_3$ и графена, имеют типичную структуру волокон, взаимодействующих друг с другом и образующих трехмерную полимерную сеть. Для обеспечения равномерного распределения агломератов $SrTiO_3$ и частиц графена вдоль всех волокон были оптимизированы

Полученные полимерные волокна на основе SrTiO₃ и графена имеют бездефектную форму в виде непрерывного цилиндра и расположены хаотично в пространстве. Экспериментальные образцы, полученные методом электроспиннинга на основе SrTiO₃ и графена, имеют типичную струк-



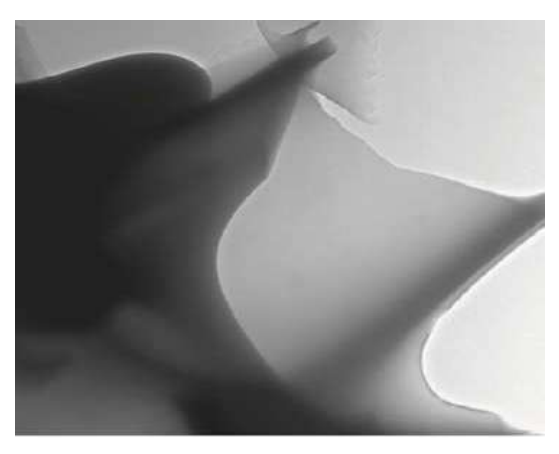


Рис. 2. ПЭМ-снимки полученного графена.

туру волокон, взаимодействующих друг с другом и образующих трехмерную полимерную сеть. Для обеспечения равномерного распределения агломератов SrTiO₃ и частиц графена вдоль всех волокон были оптимизированы соотношения раствора и добавок для электроспиннинга (рис. 3 (а), (б), (в), (г)). Полученные волокна имеют средний диаметр в диапазоне от 200 до 400 нм, который зависит от степени вязкости раствора и значения напряжения установки электроспиннинга. Добавление графена не оказывает значительного влияния на диаметр волокон. Повышение вязкости раствора за счет добавления частиц графена компенсируется увеличением электропроводности раствора, что приводит к образованию более тонких волокон за счет увеличения плотности заряда на электроспиннинговой струе и, в свою очередь, удлинения струи вдоль ее оси.

Полученные композитные волокна на основе $SrTiO_3$ /графена после синтеза подвергали кальцинации. Этот процесс позволяет рекристаллизировать материал и способствует достижению оптимальной кристаллической структуры. Для ПАНа, используемого в этой работе, кальцинирование позволяет достичь высокой степени

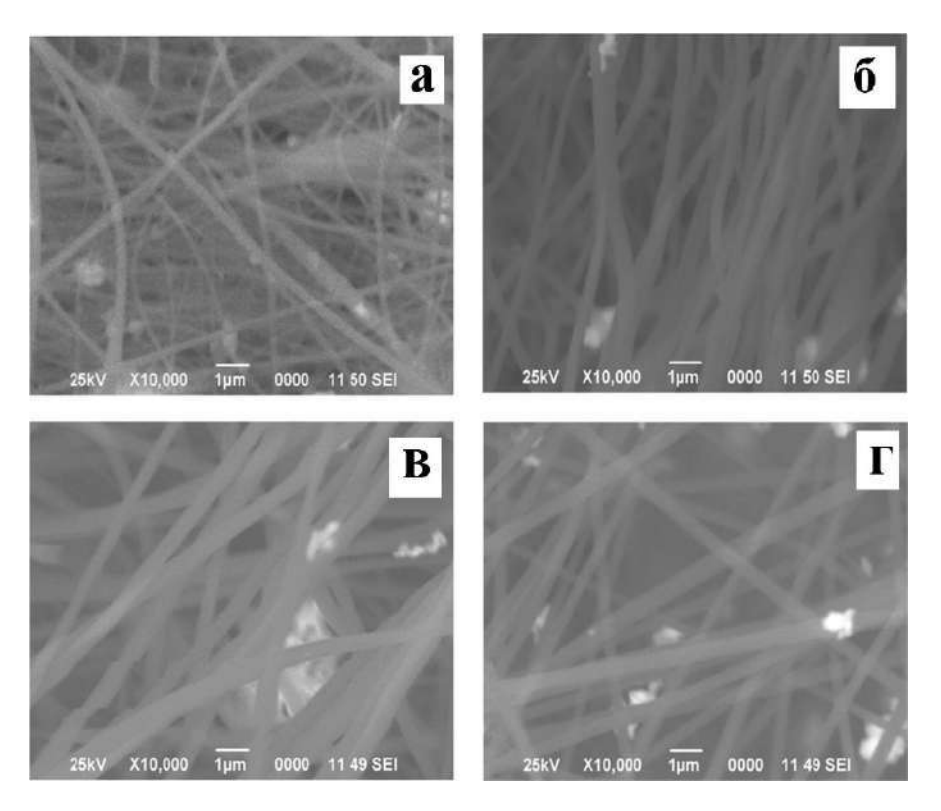


Рис. 3. СЭМ-снимки образцов: (a) – волокна с чистым $SrTiO_3$; (б) – волокна с добавлением гарфена и $SrTiO_3$; (в) – волокна с добавлением CFO-графена и $SrTiO_3$; (г) – волокна с добавлением коммерческого графена и $SrTiO_3$.

отверждения [14, 16]. Важно, чтобы термическая обработка, которая приводит к образованию углеродной структуры, происходила без плавления и с минимальным повреждением базовых волокон и его фибриллярной структуры, а также с меньшей усадкой. В отличие от других полимерных материалов, при термической обработке волокон из полиакрилонитрила легче происходит образование низкодефектной углеродной структуры. Это преимущество можно объяснить следующими факторами:

- 1. Для проведения кальцинации волокон из полиакрилонитрила не требуется разрушения основной полимерной цепи;
- 2. Атомы водорода, расположенные вдоль цепи макромолекул ПАНа, могут образовывать места с полисопряженной структурой во время дегидрирования, особенно при наличии О₂, служат зародышами для углеродной структуры;
- 3. Наличие нитрильных групп в полимерной цепи ПАНа позволяет полимеризироваться, образуя шестичленные конденсированные гетероциклы с гетероароматической полисопряженной структурой.

Процесс кальцинации композитных волокон на основе $SrTiO_3$ /графен состоит из двух этапов – термостабилизации и кальцинации. Этап тер-

мостабилизации включает термическую обработку при 180 °C в кислородной атмосфере, что приводит к объемным изменениям и формированию начальной твердофазной структуры. На этапе кальцинации волокна нагревают до 500 °C в токе воздухе в течение 30 мин, что вызывает окислительное дегидрирование и образование хромофорных сопряженных связей — C=N —. Это приводит к интенсивному окрашиванию полиакрилонитрила в оранжевый и коричневый цвета, а затем в черный.

Спектры РФА для композитов графен/SrTiO₃ (рис. 4) показывают высокую интенсивность дифракционных пиков при 31,62°, 39,22°, 45,69°, 57°, 67° и 76,33°, что подтверждает наличие кубической перовскитной фазы SrTiO₃ (JCPDS: 35-0734). В то же время ярко выраженные пики графена не наблюдаются для этих образцов из-за высокой интенсивности характерных полос перовскита. Результаты исследований показывают, что композитные фотокаталитические системы графен/ SrTiO₃ эффективно поглощают свет в интервале длин волн от 200 до 700 нм. Включение графена в состав системы приводит к повышению фотопоглощения в отличие от одномерных чистых SrTiO₃, особенно в видимом спектре, доказывая, что оптические свойства графена влияют на спо-

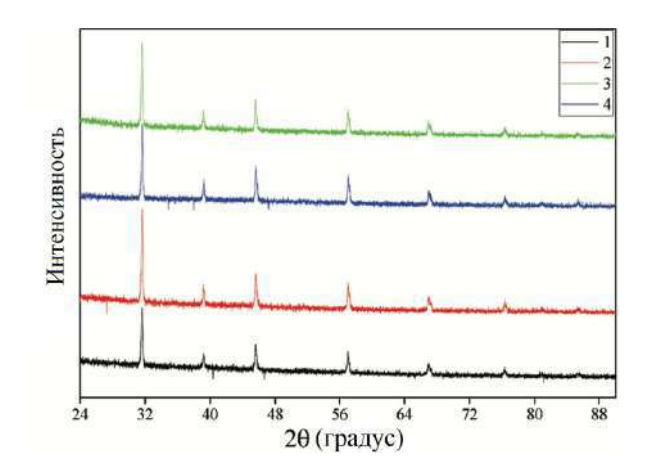


Рис. 4. РФА полученных волокон после прокаливания: РШ-графен/SrTiO₃ (1); СГО-графен/SrTiO₃ (2); коммерческий графен/SrTiO₃ (3); SrTiO₃/ Π AH (4).

собность всей композитной фотокаталитической системы поглошать свет.

Измерение ширины запрещенной зоны (Eg) и расчеты были выполнены с использованием методики анализа спектров поглощения и пропускания света, описанной в работе [17]. Полученные значения ширины запрещенной зоны для композитов графена и чистого $SrTiO_3$ были равны 2,89 eB, 2,72 eB, 2,6 eB; и 3,12 eB, соответственно.

Для оценки фотокаталитической активности образцов графен/SrTiO₃ в процессе разложения воды на Н2 использовали метод, заключающийся в размещении 1 г каждого образца в 20 мл водно-метанолового раствора (содержащего 15% метанола), а затем УФ облучении (мощность 120 Вт) суспензии при предварительной прокачке системы аргоном. Для более точного анализа полученных газов фотокаталитический реактор подсоединяли непосредственно к хроматографу Chromos 1000 с использованием 3 мм колонок, заполненных NaX и PORAPAK Q. На рис. 5 (a), (б) показаны графики скорости выделения Н, в зависимости от времени облучения для каждого из синтезированных композитов – графен/SrTiO₃ и чистый SrTiO₃.

Изображенные на рис. 5 данные показывают, что усредненные значения максимальной скорости образования H_2 для образцов коммерческий графен/SrTiO₃, PШ-графен/SrTiO₃, СГО-графен/SrTiO₃ и SrTiO₃/ПАН равны 5,35 ммоль/г·ч, 5,1 ммоль/ г·ч, 7,08 ммоль/ г·ч и 0,87 ммоль/ г·ч, соответственно. На рис. 5 (а) (кривая 1) снижение выделения водорода на чистом SrTiO₃ при УФ-облучении через 10 ч по сравнению с модифицированными аналогами (кривые 2, 3, 4) может быть объяснено пассивацией поверхности чистого

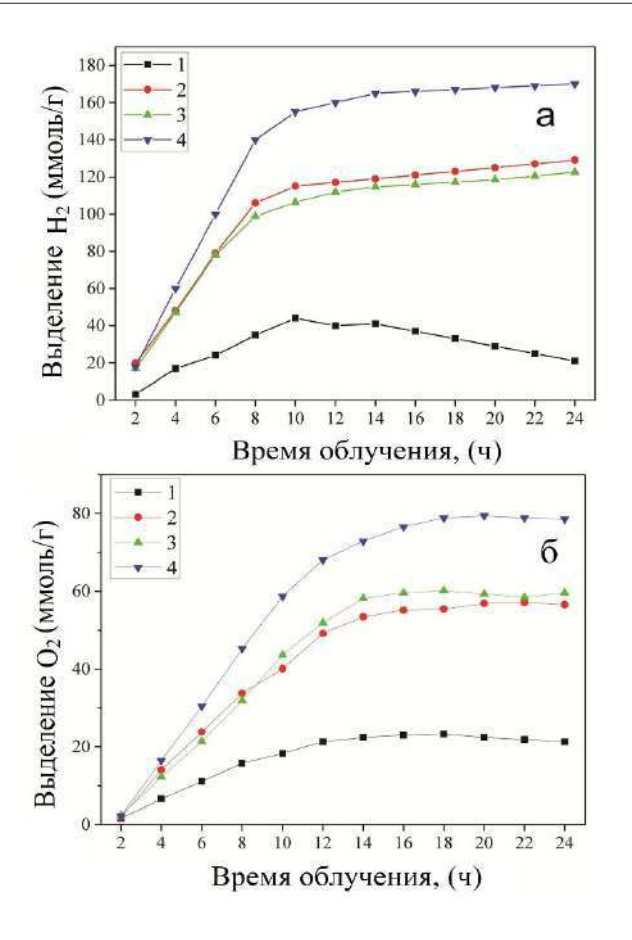


Рис. 5. Скорость выделения (а) водорода и (b) кислорода для: РШ-графен/SrTiO₃ (2); СГО-графен/SrTiO₃ (3); коммерческий графен/SrTiO₃ (4); SrTiO₃/ ПАН (1) при УФ облучении мощностью 120 Вт.

SrTiO₃ со временем, что означает, что активные участки, ответственные за выделение водорода, покрываются или блокируются промежуточными продуктами. Этот пассивирующий слой может снизить доступность реактивов к каталитическим участкам и затруднить реакцию выделения водорода. Модификация графеном может изменять свойства поверхности SrTiO₃, например, увеличивать площадь поверхности или вводить дополнительные активные участки для каталитических реакций. Эти модификации повышают доступность реактивов к каталитическим участкам и облегчают реакцию выделения водорода.

Несмотря на то, что коммерческий графен обладает более высокой фотоэффективностью по сравнению с графеном полученного из биологических отходов (рисовая шелуха и скорлупа грецкого ореха) при выделении H_2 при УФ облучении в фотокаталитической системе, скорость образования H_2 для графена/SrTiO₃ значительно соответствует многим другим эффективным фотокаталитическим системам [20, 21, 23, 24].

Данные, полученные в настоящем исследовании, находят подтверждение в ранее опубликованных работах [20, 21], которые демонстрируют положительное влияние дефектов в микроструктуре графена на активность фоторазложения воды. Кроме того, другое экспериментальное исследование [22] показывает, что использование композита графен/ TiO_2 увеличивает эффективность образования H_2 на 95% по сравнению с использованием чистого TiO_2 .

Максимальные значения скоростей образования H_2 , достигнутые при использовании дефектного графена в фотокаталитических системах, превышают аналоги [23, 24] и демонстрируют положительный эффект разделения фотогенерированных зарядов при облучении. Это связано с быстрой передачей фотоиндуцированных зарядов, что способствует высокой плотности тока при воздействии УФ облучения. Кроме того, одномерная структура фотокаталитического композита эффективно влияет на разделение носителей заряда, а благодаря высоким оптическим свойствам графена может использоваться как эффективный сборщик света.

Одномерные композитные фотокатализаторы на основе графен/SrTiO₃ представляют собой перспективный вариант для эффективного выделения Н2 из воды. В первую очередь, это связано с высокой удельной площадью поверхности волокон и оптическими свойствами графена, которые значительно повышают эффективность поглощения света при многократном отражении и рассеивании фотонов, взаимодействующих с фотокатализатором. Во-вторых, фотокаталитические системы графен/SrTiO₃ эффективно разделяют электронно-дырочные пары и значительно влияют на поглощение ультрафиолета. В-третьих, современные проблемы, связанные с фоторасщеплением воды для производства Н2, включают низкую стабильность, недостаточную эффективность производства Н2 и высокую стоимость фотокаталитических материалов. Использование композитных фотокатализаторов на основе графен/SrTiO₃ не только повышает активность фотовыделения Н2, но и значительно снижает затраты за счет применения биологических отходов.

Данные, полученные в ходе исследований, подтверждают, что использование комбинации различных типов наноматериалов значительно изменяет свойства композитных фотокатализаторов, что положительно сказывается на эффективности процесса выделения H_2 .

4. Заключение

В заключении следует отметить, что в результате применения метода электроспиннинга с использованием синтезированного графена из биологических отходов, успешно получили высокоэффективные фотокаталитические системы на основе графен/SrTiO₃. Измеренные значения ширины запрещенных зон составили 2,89, 2,72 и 3,12 эВ для образцов РШ-графен/SrTiO₃, СГО-графен/ SrTiO₃, коммерческий графен/SrTiO₃ и SrTiO₃/ ПАН, соответственно. Установлено, что усредненные значения максимальной скорости образования водорода из смеси «вода – метанол» для композитных образцов: коммерческий графен/ SrTiO₃, РШ-графен/SrTiO₃, СГО-графен/SrTiO₃, и $SrTiO_3/\Pi AH$ равны 5,35 ммоль/г·ч, 5,1 ммоль/г·ч, 7,08 ммоль/ Γ ·ч и 0,87 ммоль/ Γ ·ч, соответственно. Хотя в синтезированном по отдельности из рисовой шелухи и скорлупы грецкого ореха многослойном графене были обнаружены дефекты, однако они демонстрируют превосходные оптические и электрические свойства, что повысило фотокаталитическую эффективность выделения H_2 по сравнению с чистым $SrTiO_3$.

Результаты исследования указывают на потенциально перспективное применение новой стратегии производства эффективных композитных фотокатализаторов на основе графена, полученного из биомассы, для генерации водорода из воды.

Благодарность

Данное исследование финансируется Комитетом науки Министерства науки и высшего образования Республики Казахстан (грант №BR18574073).

Список литературы

- [1]. Li Y., Tsang S.C.E. Recent progress and strategies for enhancing photocatalytic water splitting // Materials Today Sustainability. 2020. № 9. P. 100032.
- [2]. Zhao Y., Zhang S., Shi R., Waterhouse G.I.N., Tang J., Zhang T. Two-dimensional photocatalyst design: A critical review of recent experimental and computational advances // Materials Today. 2020. № 34. P. 78–91.
- [3]. Kavitha R., Nithya P.M., Girish Kumar S. Noble metal deposited graphitic carbon nitride based heterojunction photocatalysts // Applied Surface Science. 2020. № 508. P. 145142.

- [4]. Rosman N.N., Mohamad Yunus R., Jeffery Minggu L., Arifin K., Salehmin M.N.I., Mohamed M.A., Kassim M.B. Photocatalytic properties of two-dimensional graphene and layered transition-metal dichalcogenides based photocatalyst for photoelectrochemical hydrogen generation: An overview // International Journal of Hydrogen Energy. − 2018. − № 43. − P. 18925–18945.
- [5]. Bellamkonda S., Thangavel N., Hafeez H.Y., Neppolian B., Ranga Rao G. Highly active and stable multi-walled carbon nanotubes-graphene-TiO₂ nanohybrid: An efficient non-noble metal photocatalyst for water splitting // Catalysis Today. − 2019. – № 321. – P. 120–127.
- [6]. Goto Y., Hisatomi T., Wang Q., Higashi T., Ishikiriyama K., Maeda T., Sakata Y., Okunaka S., Tokudome H., Katayama M., Akiyama S., Nishiyama H., Inoue Y., Takewaki T., Setoyama T., Minegishi T., Takata T., Yamada T., Domen K. A Particulate Photocatalyst Water-Splitting Panel for Large-Scale Solar Hydrogen Generation // Joule. 2018. № 2. P. 509–520.
- [7]. Nishiyama H., Yamada T., Nakabayashi M., Maehara Y., Yamaguchi M., Kuromiya Y., Nagatsuma Y., Tokudome H., Akiyama S., Watanabe T., Narushima R., Okunaka S., Shibata N., Takata T., Hisatomi T., Domen K. Photocatalytic solar hydrogen production from water on a 100-m² scale // Nature. − 2021. − № 598. − P. 304–307.
- [8]. Torrisi F., Carey T. Graphene, related two-dimensional crystals and hybrid systems for printed and wearable electronics // Nano Today. 2018. № 23. P. 73–96.
- [9]. Iqbal A.A., Sakib N., Iqbal A.K.M.P., Nuruzzaman D.M. Graphene-based nanocomposites and their fabrication, mechanical properties and applications // Materialia. – 2020. – № 12. – P. 100815.
- [10]. Mansurov Z.A., Atamanov M.K., Elemesova J., Lesbaev B.T., Chikradze M.N. New Nanocarbon High-Energy Materials // Physics of Combustion and Explosion. – 2019. – № 4. – P. 34-41. (In Russian).
- [11]. Yeleuov M., Daulbayev C., Taurbekov A., Abdisattar A., Ebrahim R., Kumekov S., Prikhodko N., Lesbayev B., Batyrzhan K. Synthesis of graphene-like porous carbon from biomass for electrochemical energy storage applications // Diamond and Related Materials. 2021. № 119. P. 108560.
- [12]. Daulbayev C., Kaidar B., Sultanov F., Bakbolat B., Smagulova G., Mansurov Z. The recent progress in pitch derived carbon fibers applications. A Review // South African Journal of Chemical Engineering. 2021. № 38. P. 9–20.
- [13]. Nazhipkyzy M., Maltay A.B., Askaruly K., Assylkhanova D.D., Seitkazinova A.R., Mansurov

- Z.A. Biomass-Derived Porous Carbon Materials for Li-Ion Battery // Nanomaterials. 2022. № 12. P. 3710.
- [14]. Sultanov F., Daulbayev C., Bakbolat B., Daulbayev O., Bigaj M., Mansurov Z., Kuterbekov K., Bekmyrza K. Aligned composite SrTiO₃/PAN fibers as 1D photocatalyst obtained by electrospinning method // Chemical Physics Letters. 2019. № 737. P. 136821.
- [15]. Мансуров 3. Получение наноматериалов в процессах горения // Горение и плазмохимия. 2019. № 17. С. 150—157.
- [16]. Daulbayev C., Sultanov F., Korobeinyk A.V., Yeleuov M., Azat S., Bakbolat B., Umirzakov A., Mansurov Z. Bio-waste-derived few-layered graphene/SrTiO₃/PAN as efficient photocatalytic system for water splitting // Applied Surface Science. 2021. № 549. P. 149176.
- [17]. Makuła P., Pacia M., Macyk W. How To Correctly Determine the Band Gap Energy of Modified Semiconductor Photocatalysts Based on UV–Vis Spectra // J. Phys. Chem. Lett. 2018. № 9. P. 6814–6817.
- [18]. Zong H., Yu K., Zhu Z. Heterostructure nanohybrids of Ni-doped MoSe₂ coupled with Ti₂NT_x toward efficient overall water splitting // Electrochimica Acta. 2020. № 353. P. 136598.
- [19]. Zheng D., Jing Z., Zhao Q., Kim Y., Li P., Xu H., Li Z., Lin J. Efficient Co-doped pyrrhotite Fe_{0.95}S_{1.05} nanoplates for electrochemical water splitting // Chemical Engineering Journal. 2020. № 402. P. 125069.
- [20]. Mateo D., García-Mulero A., Albero J., García H. N-doped defective graphene decorated by strontium titanate as efficient photocatalyst for overall water splitting // Applied Catalysis B: Environmental. 2019. № 252. P. 111–119.
- [21]. Marlinda A.R., Yusoff N., Sagadevan S., Johan M.R. Recent developments in reduced graphene oxide nanocomposites for photoelectrochemical water-splitting applications // International Journal of Hydrogen Energy. 2020. № 45. P. 11976–11994.
- [22]. Sajjadizadeh H.-S., Goharshadi E.K., Ahmadzadeh H.Photoelectrochemical water splitting by engineered multilayer TiO₂/GQDs photoanode with cascade charge transfer structure // International Journal of Hydrogen Energy. 2020. № 45. P. 123–134.
- [23]. Oh I., Youn J.-S., Park Y.-K., Jeon K.-J. Heterostructure of 3D sea-grape-like MoS₂/graphene on carbon cloth for enhanced water splitting // Applied Surface Science. 2020. № 529. P. 147089.
- [24]. Zhang S., Zhang X., Shi X., Zhou F., Wang R., Li X. Facile fabrication of ultrafine nickeliridium alloy nanoparticles/graphene hybrid with

enhanced mass activity and stability for overall water splitting // Journal of Energy Chemistry. – 2020. – № 49. – P. 166–173.

References

- [1]. Y. Li, S.C.E. Tsang, Materials Today Sustainability. 9 (2020) 100032. https://doi.org/10.1016/j.mtsust. 2020.100032
- [2]. Y. Zhao, S. Zhang, R. Shi, G.I.N. Waterhouse, J. Tang, T. Zhang, Materials Today. 34 (2020) 78–91. https://doi.org/10.1016/j.mattod.2019.10.022
- [3]. R. Kavitha, P.M. Nithya, S. Girish Kumar, Applied Surface Science. 508 (2020) 145142. https://doi.org/10.1016/j.apsusc.2019.145142
- [4]. N.N. Rosman, R. Mohamad Yunus, L. Jeffery Minggu, K. Arifin, M.N.I. Salehmin, M.A. Mohamed, M.B. Kassim, International Journal of Hydrogen Energy. 43 (2018) 18925–18945. https://doi.org/10.1016/j.ijhydene.2018.08.126
- [5]. S. Bellamkonda, N. Thangavel, H.Y. Hafeez, B. Neppolian, G. Ranga Rao, Catalysis Today. 321– 322 (2019) 120–127. https://doi.org/10.1016/j. cattod.2017.10.023
- [6]. Y. Goto, T. Hisatomi, Q. Wang, T. Higashi, K. Ishikiriyama, T. Maeda, Y. Sakata, S. Okunaka, H. Tokudome, M. Katayama, S. Akiyama, H. Nishiyama, Y. Inoue, T. Takewaki, T. Setoyama, T. Minegishi, T. Takata, T. Yamada, K. Domen, A Particulate Photocatalyst Water-Splitting Panel for Large-Scale Solar Hydrogen Generation, Joule. 2 (2018) 509–520. https://doi.org/10.1016/j.joule.2017.12.009
- [7]. H. Nishiyama, T. Yamada, M. Nakabayashi, Y. Maehara, M. Yamaguchi, Y. Kuromiya, Y. Nagatsuma, H. Tokudome, S. Akiyama, T. Watanabe, R. Narushima, S. Okunaka, N. Shibata, T. Takata, T. Hisatomi, K. Domen, Nature. 598 (2021) 304–307. https://doi.org/10.1038/s41586-021-03907-3
- [8]. F. Torrisi, T. Carey, Nano Today. 23 (2018) 73–96. https://doi.org/10.1016/j.nantod.2018.10.009
- [9]. A.A. Iqbal, N. Sakib, A.K.M.P. Iqbal, D.M. Nuruzzaman, Materialia. 12 (2020) 100815. https://doi.org/10.1016/j.mtla.2020.100815
- [10]. New Nanocarbon High-Energy Materials, FGV. (2019). https://doi.org/10.15372/FGV20190405
- [11]. M. Yeleuov, C. Daulbayev, A. Taurbekov, A. Abdisattar, R. Ebrahim, S. Kumekov, N. Prikhodko, B. Lesbayev, K. Batyrzhan, Diamond and Related Materials. 119 (2021) 108560. https:// doi.org/10.1016/j.diamond.2021.108560
- [12]. C. Daulbayev, B. Kaidar, F. Sultanov, B. Bakbolat, G. Smagulova, Z. Mansurov, A Review, South African Journal of Chemical Engineering. 38 (2021) 9–20. https://doi.org/10.1016/j.sajce.2021.07.001

- [13]. M. Nazhipkyzy, A.B. Maltay, K. Askaruly, D.D. Assylkhanova, A.R. Seitkazinova, Z.A. Mansurov, Nanomaterials. 12 (2022) 3710. https://doi.org/10.3390/nano12203710
- [14]. F. Sultanov, C. Daulbayev, B. Bakbolat, O. Daulbayev, M. Bigaj, Z. Mansurov, K. Kuterbekov, K. Bekmyrza, Chemical Physics Letters. 737 (2019) 136821. https://doi.org/10.1016/j.cplett.2019.136821
- [15]. Z. Mansurov, Горение и плазмохимия. 17 (2019) 150–157. https://doi.org/10.18321/cpc318
- [16]. C. Daulbayev, F. Sultanov, A.V. Korobeinyk, M. Yeleuov, S. Azat, B. Bakbolat, A. Umirzakov, Z. Mansurov, Applied Surface Science. 549 (2021) 149176. https://doi.org/10.1016/j.apsusc.2021.149176
- [17]. P. Makuła, M. Pacia, W. Macyk, J. Phys. Chem. Lett. 9 (2018) 6814–6817. https://doi.org/10.1021/ acs.jpclett.8b02892
- [18]. H. Zong, K. Yu, Z. Zhu, Electrochimica Acta. 353 (2020) 136598. https://doi.org/10.1016/j. electacta.2020.136598
- [19]. D. Zheng, Z. Jing, Q. Zhao, Y. Kim, P. Li, H. Xu, Z. Li, J. Lin, Chemical Engineering Journal. 402 (2020) 125069. https://doi.org/10.1016/j.cej.2020.125069
- [20]. D. Mateo, A. García-Mulero, J. Albero, H. García, Applied Catalysis B: Environmental. 252 (2019) 111–119. https://doi.org/10.1016/j.apcatb.2019.04.011
- [21]. A.R. Marlinda, N. Yusoff, S. Sagadevan, M.R. Johan, International Journal of Hydrogen Energy. 45 (2020) 11976–11994. https://doi.org/10.1016/j.ijhydene.2020.02.096
- [22]. H.-S. Sajjadizadeh, E.K. Goharshadi, H. Ahmadzadeh, International Journal of Hydrogen Energy. 45 (2020) 123–134. https://doi.org/10.1016/j.ijhydene.2019.10.161
- [23]. I. Oh, J.-S. Youn, Y.-K. Park, K.-J. Jeon, Applied Surface Science. 529 (2020) 147089. https://doi.org/10.1016/j.apsusc.2020.147089
- [24]. S. Zhang, X. Zhang, X. Shi, F. Zhou, R. Wang, X. Li, Journal of Energy Chemistry. 49 (2020) 166– 173. https://doi.org/10.1016/j.jechem.2020.02.022

Multilayer Graphene Derived from Biowaste/ SrTiO₃ as Effective Photocatalytic System

Zh. Kuspanov^{1,2*}, Ch. Daulbaev², M. Yeleuov^{1,2}, Z. Mansurov^{3,4}

¹Satpayev University, Almaty, Kazakhstan ²Institute of Nuclear Physics, Almaty, Kazakhstan ³Al-Farabi Kazakh National University, Almaty, Kazakhstan

⁴Institute of Combustion Problems, Almaty, Kazakhstan

Abstract

The photoelectrochemical properties of photocatalysts including SrTiO₃/multilayer graphene composite obtained using the electrospinning method were studied. Graphene obtained from rice husk and walnut shells was used as a co-catalyst for hydrogen (H₂) production by water decomposition. This was the first time it was used in a photocatalytic system. The results of the study showed that the presence of multiple layers of graphene reduces the band gap width of the photocatalytic system and contributes to the effective separation of photoinduced charges. The material consisting of multilayer graphene synthesized from biowaste and SrTiO₃ showed a higher rate of hydrogen release compared to pure SrTiO₃. The results can be used to develop new and effective photocatalysts based on materials derived from biowaste with improved properties for the separation of water.

Тиімді Фотокаталитикалық Жүйе Ретінде Биоқалықтардан Өндірілген Көп Қабатты Графен/SrTiO $_3$

Ж. Құспанов^{1,2}*, Ч. Даулбаев², М. Елеуов^{1,2}, 3. Мансұров^{3,4}

¹Сәтбаев Университеті, Алматы, Қазақстан ²Ядролық физика институты, Алматы, Қазақстан ³Әл-Фараби атындағы Қазақ ұлттық университеті, Алматы, Қазақстан

⁴Жану проблемалары институты, Алматы, Қазақстан

Андатпа

SrTiO₃/Көп қабатты графен электроспининг әдісін қолдану арқылы алынған композитті фотокатализаторлардың фотоэлектрохимиялық қасиеттері зерттелді. Суды ыдырату арқылы сутекті (Н2) өндіруге арналған сокатализатор ретінде күріш қабығы мен жаңғақ қабығынан алынған графен қолданылды. Бұл алғаш рет фотокаталитикалық жүйеде қолданылды. Зерттеу нәтижелері графеннің бірнеше қабаттарының болуы фотокаталитикалық жүйенің тыйым салынған аймағын азайтатынын және фотоиндукцияланған зарядтардың тиімді бөлінуіне ықпал ететінін көрсетті. Биоқалдықтардан синтезделген көп қабатты графен мен SrTiO₃-тен тұратын материал таза SrTiO₃-пен салыстырғанда сутектің жоғары бөліну жылдамдығын көрсетті. Алынған нәтижелер суды бөлу үшін жақсартылған қасиеттері бар биоқалдықтардан алынған материалдарға негізделген жаңа және тиімді фотокатализаторларды әзірлеу үшін пайдаланылуы мүмкін.